

UNCLASSIFIED

---

---

AD 273 305

*Reproduced  
by the*

ARMED SERVICES TECHNICAL INFORMATION AGENCY  
ARLINGTON HALL STATION  
ARLINGTON, VIRGINIA



---

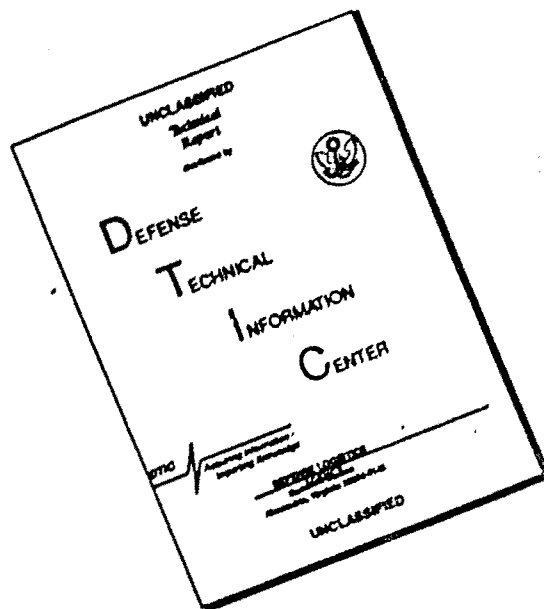
---

UNCLASSIFIED

NOTICE: When government or other drawings, specifications or other data are used for any purpose other than in connection with a definitely related government procurement operation, the U. S.

Government thereby incurs no responsibility, nor any obligation whatsoever; and the fact that the Government may have formulated, furnished, or in any way supplied the said drawings, specifications, or other data is not to be regarded by implication or otherwise as in any manner licensing the holder or any other person or corporation, or conveying any rights or permission to manufacture, use or sell any patented invention that may in any way be related thereto.

# DISCLAIMER NOTICE



THIS DOCUMENT IS BEST QUALITY AVAILABLE. THE COPY FURNISHED TO DTIC CONTAINED A SIGNIFICANT NUMBER OF PAGES WHICH DO NOT REPRODUCE LEGIBLY.

273305

ASD TECHNICAL REPORT 61-177

CATALOGED BY ASTIA

AS AD NO. \_\_\_\_\_

62-2-5  
NOX

# METHODS FOR ANALYZING FLIGHT VEHICLES DURING THE TAXI CONDITION

J. G. THEISEN

LOCKHEED-GEORGIA COMPANY  
ER 5179

CONTRACT AF 33(616)-7546

JANUARY 1962

FLIGHT DYNAMICS LABORATORY  
AERONAUTICAL SYSTEMS DIVISION  
AIR FORCE SYSTEMS COMMAND  
UNITED STATES AIR FORCE  
WRIGHT-PATTERSON AIR FORCE BASE, OHIO

## NOTICES

When Government drawings, specifications, or other data are used for any purpose other than in connection with a definitely related Government procurement operation, the United States Government thereby incurs no responsibility nor any obligation whatsoever; and the fact that the Government may have formulated, furnished, or in any way supplied the said drawings, specifications, or other data, is not to be regarded by implication or otherwise as in any manner licensing the holder or any other person or corporation, or conveying any rights or permission to manufacture, use, or sell any patented invention that may in any way be related thereto.

Qualified requesters may obtain copies of this report from the Armed Services Technical Information Agency, (ASTIA), Arlington Hall Station, Arlington 12, Virginia.

This report has been released to the Office of Technical Services, U. S. Department of Commerce, Washington 25, D. C., for sale to the general public.

Copies of ASD Technical Reports and Technical Notes should not be returned to the Aeronautical Systems Division unless return is required by security considerations, contractual obligations, or notice on a specific document.

ASD TECHNICAL REPORT 61-177

**METHODS FOR ANALYZING FLIGHT  
VEHICLES DURING THE TAXI CONDITION**

*J. G. THEISEN*

*LOCKHEED-GEORGIA COMPANY*

*JANUARY 1962*

FLIGHT DYNAMICS LABORATORY  
CONTRACT AF 33(616)-7546  
PROJECT No. 1367  
TASK No. 13451

AERONAUTICAL SYSTEMS DIVISION  
AIR FORCE SYSTEMS COMMAND  
UNITED STATES AIR FORCE  
WRIGHT-PATTERSON AIR FORCE BASE, OHIO

## FOREWORD

This report was prepared for the Flight Dynamics Laboratory, Aeronautical Systems Division, Wright-Patterson Air Force Base, Ohio. The research work was accomplished by Lockheed Aircraft Corporation, Georgia Division, Marietta, Georgia, under Air Force Contract AF 33(616)-7546, "Development of an Analytical Method to Determine Dynamic Loads Induced by Ground Operation of Aircraft", Project No. 1367, "Structural Design Criteria", Task No. 13451, "Design Criteria for Ground Induced Loads". The work was administered under the direction of the Dynamics Branch, Flight Dynamics Laboratory, with Mr. Walter Dunn acting as project engineer.

This report covers work conducted from June 1960 to June 1961.

The author wishes to express his sincere appreciation for the contributions of S. W. Robinson, C. H. Griffin, and J. W. Benson of the Mathematical Analysis Department whose valuable assistance was indispensable to the massive data processing involved in this program.


## ABSTRACT

Methods are developed for the prediction of ground taxiing loads for advanced flight vehicles. The theory presented is generally applicable to determining the taxiing response of vehicles operated on prepared or unprepared terrain with randomly distributed surface undulations. The vehicle, with many degrees of flexibility and nonlinearities of the shock strut, is represented in a generalized Lagrangian coordinate system. Nonlinear solutions are obtained in closed analytical form, and on analog and digital computers, to various degrees of approximation for taxiing over an existing runway profile. Equivalent linearized transfer functions are developed for comparison on the basis of power and cross spectral densities, load occurrences, and probabilities for a variety of speeds and nonlinear parameters. Test data are used to substantiate theoretical results where applicable.

## PUBLICATION REVIEW

This report has been reviewed and is approved.

FOR THE COMMANDER

  
HOWARD A. MAGRATH  
Technical Director  
Flight Dynamics Laboratory

ASD TR 61-177

## TABLE OF CONTENTS

<u>SECTION</u>		<u>PAGE</u>
I	INTRODUCTION . . . . .	1
II	THEORETICAL DISCUSSION . . . . .	9
	1. Equations Of Motion For Taxiing . . . . .	9
	2. Nonlinear Theory . . . . .	14
	3. Linearized Differential Equations . . . . .	16
	4. Affine Transformation Of The Equations . . . . .	17
III	TRANSFER FUNCTION DEVELOPMENT . . . . .	25
	1. Nonlinear System Power Spectral Analysis . . . . .	25
	2. Nonlinear System Cross Spectral Analysis . . . . .	25
	3. Nonlinear System Harmonic Analysis . . . . .	26
	4. Linearized System Analysis . . . . .	30
IV	RESULTS AND DISCUSSION . . . . .	39
	1. Direct Power Spectral Analysis Of The Nonlinear System. . . . .	40
	2. Cross-Spectral Analysis Results . . . . .	42
	3. Linearized System Results . . . . .	43
	4. Parametric Variations . . . . .	44
	5. Statistical Comparisons . . . . .	46
V	CONCLUSIONS . . . . .	49
VI	RECOMMENDATIONS . . . . .	51
	REFERENCED REPORTS . . . . .	157
 <u>APPENDIX</u>		
A	SUPPLEMENTARY EQUATIONS . . . . .	161
B	AIRPLANE CONFIGURATION DATA . . . . .	169
C	EQUIVALENT LINEAR SYSTEM SOLUTION . . . . .	177
D	COMPUTER APPLICATIONS IN DYNAMICS AND STATISTICS. . . . .	187
	1. Introduction . . . . .	187
	2. Generation of the Runway Profile for the Analog . . . . .	188
	3. Analog Simulation of Vehicle Response . . . . .	194

APPENDIX

PAGE

4.	Analog Methods of Power Spectral Analysis . . . . .	198
5.	Special Problems in Statistical Analysis on Analog Computers . . . . .	204
6.	Cross Spectrum Computation. . . . .	206
7.	Simulation of Continuously Variable Airplane Speed . . . . .	206
8.	Simulation of Gear Spacing with Electronic Time-Delay Networks . . . . .	208
9.	The Analog Computation Equipment . . . . .	208
10.	The Magnetic Tape System . . . . .	210
11.	Analog Filter Compensation for Amplitudes . . . . .	211
12.	Digital Approach to Power Spectral Analysis . . . . .	214
E.	NONLINEAR RESPONSE BY PERTURBATION METHODS . . . . .	217
F.	LINEARIZED TRANSFER FUNCTIONS FOR VARIATIONS IN STRUT DAMPING . . . . .	223
G.	FIRST APPROXIMATION TO THE LINEARIZED STRUT DAMPER. . . . .	233
H.	ANALYSIS OF THE SIMPLIFIED TWO DEGREES OF FREEDOM SYSTEM . . . . .	239
I.	COMPARISONS WITH ALTERNATIVE METHODS OF ANALYSIS . . . . .	247
	1. Nonlinear Harmonic Analysis . . . . .	249
	2. Cross Spectral Analysis of the Nonlinear System . . . . .	249
J.	ELLIPTIC FUNCTION SOLUTIONS FOR THE NONLINEAR SYSTEM . . . . .	263
	1. Summary of Applications to the Research Problem . . . . .	265
	2. Nomenclature . . . . .	271
	3. Introductory Discussion . . . . .	275
	4. Physical Characteristics of the System. . . . .	276
	5. Equations of Motion . . . . .	281
	a. Derivation of the Equations of Motion . . . . .	281
	b. Introduction of Dimensionless Variables. . . . .	283
	c. Transformation of the Equations . . . . .	285
	6. Solution of the Transformed Equation . . . . .	287
	a. Considerations Necessary to Obtain a Solution . . . . .	287
	b. Derivation of the Solution . . . . .	288
	c. Qualifications of the Solution . . . . .	293

APPENDIX

PAGE

7.	Evaluation of the Analytical Solution . . . . .	300
a.	Comparison with Solutions by the Runge-Kutto Method . . . . .	300
b.	Comparison with Experimental Dato. . . . .	303
K	COMPARISON OF ANALOG, DIGITAL, AND FLIGHT TEST RESULTS . . . . .	307
1.	Comparison of Analog Theory ond Flight Test Dato . . . . .	309
2.	Comparison of Analog and Digital Power Spectral Analysis . . . . .	314

## LIST OF SYMBOLS

- $A(\omega)$  - Amplitude of the frequency component,  $\omega$ , of  $y(t)$ , in.
- $A_{hi}$  - Hydraulic area of  $i^{\text{th}}$  strut, in.<sup>2</sup>
- $A_i$  - Arbitrary constant in oleo air spring term, empirically derived from drop test data. (Units depend upon the polytropic exponent.)
- $A$  - Wing area, in.<sup>2</sup>
- $A_{kn}$  - Effective modal area for cross coupling damping terms,  $k^{\text{th}}$  mode to  $n^{\text{th}}$  mode, in.<sup>2</sup>
- $A_L$  - (Appendix E only) magnitude of the linear contribution to the differential equation solution, in.
- $A_{NL}$  - (Appendix E only) magnitude of the nonlinear contribution to the differential equation solution, in.
- $A_{oi}$  - Area of opening in orifice plate of  $i^{\text{th}}$  strut, in.<sup>2</sup>
- $a_r$  - Cycles off resonance of filter edge (half-power point), 1/sec
- $A(\omega)$  - Amplitude of the frequency component,  $\omega$ , of a random function,  $y(t)$
- $a_{1i}$  - Coefficient of tire spring term. (Units depend upon  $a_{2i}$ .)
- $a_{2i}$  - Exponent of tire spring term
- $a_n(t)$  - Generalized LaGrangian coordinate displacement in the  $n^{\text{th}}$  mode, in.,  $n = 0, 1, 2, \dots, m$ .
- $B$  - Affine transformation constant, (nondimensional).
- $B_{cnq}$  - Modal unit bending moment coefficient,  $n^{\text{th}}$  mode, for  $q^{\text{th}}$  wing panel, lb-in.
- $B_{c\theta q}$  - Modal unit bending moment coefficient, pitch mode, for  $q^{\text{th}}$  wing panel, lb-in.<sup>2</sup>
- $b$  - Exponential coefficient in Wagner indicial delay function
- $b_i$  - Arbitrary constant in oleo air spring term (empirically derived from drop test data), in.
- $c_c$  - Critical damping constant, lb-sec/in.

- $c_d$  - Orifice coefficient
- $C_{fg}$  - Aerodynamic damper on  $M_f$  of equivalent system (linear), lb-sec/in.
- $C_{sg}$  - Aerodynamic damper on  $M_s$  of equivalent system (linear), lb-sec/in.
- $C_q$  - Wing chord length of outboard edge of  $q^{\text{th}}$  wing panel
- $C_L$  - Lift curve slope for the wing, per radian
- $c_n$  - Damping coefficient,  $n^{\text{th}}$  mode,  $\Upsilon c_c$ , lb-sec/in.
- $C_s$  - Damping coefficient between  $M_s$  and  $M_f$  for equivalent three mass linear system, lb-sec/in.
- $c_o$  -  $1/2 C_{L\alpha} \rho A \cdot V_H$ , lb-sec/rad-in.
- $C_{Di}$  - Coefficient of quadratic damping term, lb-sec<sup>2</sup>/in.<sup>2</sup>,  $\frac{\rho h^3 A_{hi}}{2(c_d A_{oi})^2}$
- $d$  - Differential operator,  $\frac{d}{dt}$
- $D_i$  - Coefficient of linearized damping term, lb-sec/in.
- $d_i$  - Orifice diameter,  $i^{\text{th}}$  gear, in.
- $d_1$  - Coefficient in Wagner indicial delay function
- $E$  - Energy change of system (with  $\Delta$  prefix), lb-in.
- $E_L$  - Energy dissipation of the linear system damper, lb-in.
- $E_{NL}$  - Energy dissipation of the nonlinear system damper, lb-in.
- $F_{ai}$  - Air compression force in strut,  $i^{\text{th}}$  gear, lb
- $F_{fi}$  - Axial friction force in strut,  $i^{\text{th}}$  gear, lb
- $F_d$  - Ground drag load, lb
- $F_o$  - Driving force magnitude divided by the nonlinear spring coefficient. (Units depend upon  $K_{NL}$ .)
- $F_K$  - Spring force, lb
- $F_{si}$  - Vertical strut force,  $i^{\text{th}}$  gear ( $F_s$ ), lb

$F_{ti}$	- Vertical tire force, $i^{\text{th}}$ gear ( $F_t$ ), lb
$G_r$	- Amplitude of $r^{\text{th}}$ cycle of oscillation of a quantity
$G_{rp}$	- Coefficients in the transfer function for the linear system, lb/in.
$G_0$	- Amplitude of $0^{\text{th}}$ cycle of oscillation of a quantity
$g$	- Gravitational constant, in/sec <sup>2</sup>
$h$	- Coefficient in Wagner indicial delay function
$H_k$	- Coefficient of the $k^{\text{th}}$ order harmonic in the nonlinear solution
$I_q$	- Moment of inertia about center of gravity of $q^{\text{th}}$ wing panel, lb-sec <sup>2</sup> -in.
$I_{\alpha q}$	- Moment of inertia of the $q^{\text{th}}$ wing panel about the elastic axis, lb-sec <sup>2</sup> -in.
$I_y$	- Total moment of inertia of the airplane in pitch about the center of gravity, lb-sec <sup>2</sup> -in.
$i$	- Complex number, $\sqrt{-1}$
$k_o$	- Statistical number of degrees of freedom
$K_{ai}$	- Linearized strut air spring constant, $i^{\text{th}}$ gear, lb/in.
$K_{bi}$	- Linearized strut air spring intercept, (at $s_i = 0$ ), lb
$K_f$	- Tire-plus-strut spring constant (function of $Z$ generally), lb/in.
$K_i$	- Constant derived from drop test data to match results, lb
$K_L$	- Lift ratio of airplane, $\frac{L}{W_o}$
$K_{NL}$	- Coefficient of the nonlinear term for strut stiffness, lb/(in.) <sup>n</sup>
$K_p$	- The positive number of standard deviations from the mean
$K_s$	- Spring constant for the elastically connected mass $M_s$ , lb/in.
$K_t$	- Linear tire spring constant, lb/in.
$L_{xi}$	- Distance along fuselage reference line from center of gravity to landing gear attachment point, (+ forward), in.
$L$	- Wing-lift force, positive up, for semi-span, lb

- $l(t)$  - Linear part of time-wise solution, in.
- $l_{xi}$  - Distance along fuselage reference line from elastic axis to landing gear attachment point,  $i$ , in.
- $M_f$  - Main mass of the simplified nonlinear system; or for the transformed three mass system, lb-sec<sup>2</sup>/in.
- $M_n$  - Generalized mass of  $n^{\text{th}}$  mode, (half airplane), lb-sec<sup>2</sup>/in.;  
 $n = 1, 2, \dots, m$
- $M_o$  - Mass of rigid body (half airplane), lb-sec<sup>2</sup>/in.
- $m$  - Exponential coefficient in Wagner indicial delay function.
- $m_o$  - Number of uniformly spaced points over the frequency range at which power estimates are desired.
- $m_q$  - Mass of the  $q^{\text{th}}$  wing panel, lb-sec<sup>2</sup>/in.
- $M_{ui}$  - Unsprung mass of  $i^{\text{th}}$  landing gear, lb-sec<sup>2</sup>/in.
- $M_s$  - Elastically connected mass for the transformed three mass system, lb-sec<sup>2</sup>/in.
- $M_{xq}$  - Wing bending moment,  $q^{\text{th}}$  panel, positive for up bending, lb-in.
- $M_{yq}$  - Wing torsion moment,  $q^{\text{th}}$  panel, positive nose down on left wing, lb-in.
- $n(t)$  - Nonlinear part of timewise solution, in.
- $N_o$  - Number of equally spaced readings in  $\Theta_T$
- $N_p$  - Occurrences; the number of times per unit time that the function,  $y$ , will exceed a magnitude of  $y_p = K_p \sigma$ , 1/sec
- $q_o$  - Maximum amplitude of harmonically oscillating ground profile, in.
- $q_i(t)$  - Runway vertical amplitude,  $i^{\text{th}}$  gear, in.
- $R_r$  - Ratio of nonlinear to linear solution magnitudes
- $R$  - Magnitude, =  $|T|$
- $S_{cnq}$  - Modal unit shear constants,  $n^{\text{th}}$  mode, for the  $q^{\text{th}}$  wing panel, lb
- $S_{c\theta q}$  - Modal unit shear constant, pitch mode, for the  $q^{\text{th}}$  wing panel, lb-in.

- $s_i(t)$  - Strut deflection for  $i^{\text{th}}$  strut, in.  
 $s$  - Laplacian operator (Appendix D only)  
 $S_{zq}$  - Wing shear at station  $q$ , positive up, lb  
 $S_{\alpha q}$  - Static mass unbalance of  $q^{\text{th}}$  wing panel, lb-sec<sup>2</sup>  
 $T_{cnq}$  - Modal unit torsion moment coefficient,  $n^{\text{th}}$  mode, for  $q^{\text{th}}$  wing panel, lb-in.  
 $T_{c\theta q}$  - Modal unit torsion moment coefficient, pitch mode, for  $q^{\text{th}}$  wing panel, lb-in.<sup>2</sup>  
 $T_O(\omega)$  - Transfer function for output response from power spectra  
 $T$  - Transfer function (subscript indicates the quantity)  
 $t$  - Time, sec  
 $t_{\text{preload}}$  - Time of preload, sec  
 $T_{O|}(i\omega)$  - Transfer function for output response from cross-spectral density  
 $V_H$  - Horizontal velocity, fps  
 $W_{nf}$  - Normalized bending deflection in the  $n^{\text{th}}$  mode at the nominal airplane center of gravity.  
 $W_{ni}$  - Normalized bending deflection in the  $n^{\text{th}}$  mode at the  $i^{\text{th}}$  landing gear location.  
 $W_{nq}$  - Normalized bending deflection in the  $n^{\text{th}}$  mode at the  $q^{\text{th}}$  wing panel or station.  
 $W_{ui}$  - Weight of the unsprung mass of gear  $i$ , lb  
 $W$  - Total weight of half the airplane, lb  
 $W_o$  - Airplane gross weight less the weight of the struts (per half airplane), lb  
 $X$  - Normalized amplitude of Universal Resonance Curves (Appendix D only)  
 $x$  - Independent variable of transformed nonlinear system in Appendix J.  
 $y_q$  - Wing coordinate for the  $q^{\text{th}}$  station, positive outward on left wing, in.

- $y(t)$  - A random function of time
- $y_p$  - The  $p^{\text{th}}$  level of  $y(t)$
- $\bar{y}$  - Arithmetic mean of  $y(t)$
- $Z_o$  - Wing lift less static weight,  $(K_L - 1)W_o$ , lb
- $Z$  -  $(s + Z_u) - Z_{\text{static}} =$  (Incremental strut-plus-tire deflection), in.
- $Z_{\text{static}}$  -  $(s + Z_u)_{\text{static}}$ , in.
- $Z_s$  - Equivalent system mass,  $M_s$ , displacement, in.
- $Z_f(t)$  - Airplane nominal center of gravity vertical displacement (also, Equivalent system main mass displacement), in.
- $Z_{ui}$  - Vertical displacement at the  $i^{\text{th}}$  landing gear axle, in.
- $Z_i$  - Vertical displacement of the  $i^{\text{th}}$  landing gear attachment point, in.
- $Z_T$  - Wing tip vertical displacement, in.
- $\Delta F_{si}$  - Incremental strut vertical force,  $i^{\text{th}}$  gear, lb
- $\Delta F_{ti}$  - Incremental tire vertical force,  $i^{\text{th}}$  gear, lb
- $\Delta M_{xq}$  - Incremental wing bending moments at station  $q$  (positive up bending), lb-in.;  
 $q = 1$  (nominal wing root station)  
 $q = 6$  (inboard of outboard nacelle)
- $\Delta M_{yq}$  - Incremental wing torsion moments at station  $q$  (positive nose down), lb-in.
- $\Delta S_{zq}$  - Incremental wing shears at station  $q$  (positive up), lb
- $\Delta t$  - Sampling interval, sec

GREEK SYMBOLS:

- $\alpha$  - Square of natural circular frequency ( $= \omega_0^2$ ), 1/sec<sup>2</sup>
- $\alpha_0$  - The average angle of attack of airplane wing, radians
- $\alpha_3$  - Skewness factor for frequency density distributions
- $\beta$  -  $K_{NL}/M_0$  (units depend upon the nonlinearity.)
- $\sigma$  - Root - mean - square (subscript indicates the quantity)
- $\sigma_{rw}$  - Root - mean - square level for runway amplitudes, ft or in.
- $\Phi(t)$  - Wagner function, indicial delay in lift build-up on air foil
- $\Phi_{nf}$  - Torsional deflection at the center of gravity in the n<sup>th</sup> mode, rad/in.
- $\Phi_{ni}$  - Torsional deflection at the i<sup>th</sup> landing gear location in the n<sup>th</sup> mode, rad/in.
- $\Phi_{nq}$  - Torsional deflection at q<sup>th</sup> wing station in the n<sup>th</sup> mode, rad/in.
- $\Phi(\omega)$  - Power spectral density (subscript indicates the quantity)
- $\Phi_I(\omega)$  - Power spectral input
- $\Phi_O(\omega)$  - Power spectral output
- $\Phi_{O_I}(i\omega)$  - Cross - spectral density
- $\psi$  - Angular variable, see Equation 60J
- $\Omega$  - Spatial frequency, rad/ft
- $\omega$  - Forcing frequency, rad/sec
- $\omega_0$  - Resonance frequency, undamped (In Appendix H, forcing frequency), rad/sec
- $\omega_r$  - Resonance frequency, damped, rad/sec
- $\omega_f$  - Resonance frequency, of  $M_f$  for equivalent system, rad/sec
- $\omega_s$  - Resonance frequency of  $M_s$  for equivalent system, rad/sec
- $\epsilon_i$  - Distance from airplane elastic axis to i<sup>th</sup> landing gear attachment point, positive forward, in.

- $\epsilon_{cp}$  - Distance from airplane center of gravity to airplane lift center of pressure ( + forward) , in.
- $\epsilon_{qo}$  - Longitudinal distance from the airplane center of gravity to the  $q^{\text{th}}$  mass center, positive forward, in.
- $\epsilon_x$  - Distance from airplane center of gravity to elastic axis, along X-axis, positive forward of elastic axis, in.
- $\epsilon_{cq}$  - Distance from airplane elastic axis to  $q^{\text{th}}$  wing panel center of pressure ( + forward), in.
- $\epsilon_q$  - Distance from elastic axis to center of gravity of  $q^{\text{th}}$  wing panel, in.
- $\delta_{i(t)}$  - Tire deflection for  $i^{\text{th}}$  landing gear, in.
- $\Theta$  - Angular displacement in pitch about the airplane center of gravity, positive nose up from the horizontal, radians
- $\theta_t$  - Nondimensional time (Appendix J only)
- $\theta_T$  - The stationary random time duration of a sample, sec
- $\xi_{nf}$  - Normalized modal deflection at the nominal airplane center of gravity in the  $n^{\text{th}}$  mode
- $\xi_{nq}$  - Normalized modal deflection at the  $q^{\text{th}}$  wing station in the  $n^{\text{th}}$  mode
- $\rho$  - Air density, lb-sec<sup>2</sup>/in.<sup>4</sup>
- $\rho_h$  - Density of hydraulic fluid, lb-sec<sup>2</sup>/in.<sup>4</sup>
- $\Psi$  - Phase angle of transfer function, degrees
- $\omega_n$  - Modal frequency of the  $n^{\text{th}}$  flexible mode, rad/sec
- $\lambda$  - Distance along runway; stations, ft
- $\Delta$  - Prefix, indicates incremental load or motion
- $\gamma$  - Ratio of damping to critical damping
- $\tau$  - Dummy variable for  $t$ ; ar, delay time in Appendix D, sec

## EXPONENTS:

- n - Exponent of nonlinear spring term.
- $\gamma_i$  - Polytropic air compression exponent

## SUBSCRIPTS AND INDICES:

- cp - Denotes center of pressure.
- f - Denotes nominal airplane center of gravity; or nominal fuselage station of airplane.
- h - Denotes hydraulic area of piston in strut.
- i - Denotes a landing gear number,  $i = 1, 2, 3$ . (1) refers to the nose (2) to the front main, and (3) to the rear main landing gear.
- k -  $k^{ih}$  coefficient of the  $k^{th}$  harmonic term in nonlinear solution.
- L - Lift; or linear.
- m - Is the total number of flexible modes in coupled vertical bending and torsion.
- n - Is a running index representing mode number.
- p - Columns in the transfer function matrix; or the  $p^{th}$  level of occurrence.
- q - Is a running index representing wing panel or stations.  $q = 1, 2, \dots, u$ .
- r - Rows in the transfer function matrix.
- s - Refers to the strut; or to the spring connected mass of transformed system.
- u - Is the total number of wing stations per half airplane.
- v - Total number of landing gears on the vehicle.

ABBREVIATIONS:

B.W.	Band width (of filter)
C.G.	Center of gravity
N.L.	Nonlinear
p.l.	Preload on a strut
rw	Runway
T.P.	Tire pressure, psi

Also:

.	Denotes differentiation with respect to time.
'	Denotes differentiation with respect to a space coordinate.
	Indicates the absolute value
PSD	Power spectral density
$\propto$	Indicates proportional to

## LIST OF ILLUSTRATIONS

<u>FIGURE</u>	<u>TITLE</u>	<u>PAGE</u>
1.	View of Example Airplane Showing the Landing Gear Arrangement Studied	4
2.	Sketch of Landing Gear Arrangement Studied	5
3.	Wing Chord and Modal Coordinate Sign Convention	6
4.	Three Degrees of Freedom System Considered in the Equivalent Linear Analysis	7
5.	Typical Nonlinear Frequency Response Variation for Single Degree of Freedom Analysis	52
6.	Simplified Nonlinear System, Spring Force Deflection Curve	53
7.	Transient and Steady State Response of Nonlinear System to Harmonic Excitation at $f = .50$ cps	54
8.	Transient and Steady State Response of Nonlinear System to Harmonic Excitation at $f = 1.0$ cps	55
9.	Transient and Steady State Response of Nonlinear System to Harmonic Excitation at $f = 1.25$ cps	56
10.	Transient and Steady State Response of Nonlinear System to Harmonic Excitation at $f = 1.7$ cps	57
11.	Transient and Steady State Response of Nonlinear System to Harmonic Excitation at $f = 3.3$ cps	58
12.	Steady State Response Time History for the Nonlinear System Tire Force, Driving Frequency: .5 cps	59
13.	Steady State Response Time History for the Nonlinear System Tire Force, Driving Frequency: 1.0 cps	59
14.	Steady State Response Time History for the Nonlinear System Tire Force, Driving Frequency: 1.25 cps	60
15.	Steady State Response Time History for the Nonlinear System Tire Force, Driving Frequency: 1.5 cps	60
16.	Steady State Response Time History for the Nonlinear System Tire Force, Driving Frequency: 1.70 cps	60

<u>FIGURE</u>	<u>TITLE</u>	<u>PAGE</u>
17.	Steady State Response Time History for the Nonlinear System Tire Force, Driving Frequency: 2.0 cps	61
18.	Steady State Response Time History for the Nonlinear System Tire Force, Driving Frequency: 3.3 cps	62
19.	Steady State Response Time History for the Nonlinear System Tire Force, Driving Frequency: 5.0 cps	62
20.	Steady State Response Time History for the Nonlinear System Wing Root Bending Moment, Driving Frequency: .5 cps	63
21.	Steady State Response Time History for the Nonlinear System Wing Root Bending Moment, Driving Frequency: 1.0 cps	63
22.	Steady State Response Time History for the Nonlinear System Wing Root Bending Moment, Driving Frequency: 1.25 cps	64
23.	Steady State Response Time History for the Nonlinear System Wing Root Bending Moment, Driving Frequency: 1.5 cps	64
24.	Steady State Response Time History for the Nonlinear System Wing Root Bending Moment, Driving Frequency: 1.7 cps	65
25.	Steady State Response Time History for the Nonlinear System Wing Root Bending Moment, Driving Frequency: 2.0 cps	65
26.	Steady State Response Time History for the Nonlinear System Wing Root Bending Moment, Driving Frequency: 3.3 cps	66
27.	Steady State Response Time History for the Nonlinear System Wing Root Bending Moment, Driving Frequency: 5.0 cps	66
28.	Steady State Response Time History for the Nonlinear System Wing Torsion Moment at Outboard Nacelle, Driving Frequency: .5 cps	67
29.	Steady State Response Time History for the Nonlinear System Wing Torsion Moment at Outboard Nacelle, Driving Frequency: 1.0 cps	67
30.	Steady State Response Time History for the Nonlinear System Wing Torsion Moment at Outboard Nacelle, Driving Frequency: 1.25 cps	68
31.	Steady State Response Time History for the Nonlinear System Wing Torsion Moment at Outboard Nacelle, Driving Frequency: 1.5 cps	68

<u>FIGURE</u>	<u>TITLE</u>	<u>PAGE</u>
32.	Steady State Response Time History for the Nonlinear System Wing Torsion Moment at Outboard Nacelle, Driving Frequency: 1.70 cps	69
33.	Steady State Response Time History for the Nonlinear System Wing Torsion Moment at Outboard Nacelle, Driving Frequency: 2.0 cps	69
34.	Steady State Response Time History for the Nonlinear System Wing Torsion Moment at Outboard Nacelle, Driving Frequency: 3.3 cps	70
35.	Steady State Response Time History for the Nonlinear System Wing Torsion Moment at Outboard Nacelle, Driving Frequency: 5.0 cps	70
36.	Time History of a Periodic Segment of the Nonlinear System Tire Force Response to Harmonic Excitation	71
37.	Study of Energy Change in Nonlinear System due to Harmonic Excitation, $f = 1.7$ Cycles Per Second	72
38.	Phase Plane Study of Strut Force Versus Strut Stroke	73
39.	Phase-Plane Study of Energy Absorption in the Strut, Nominal $f = .9$ cps	74
40.	Phase-Plane Study of Energy Absorption in the Strut, Nominal $f = 1.67$ cps	75
41.	Phase-Plane Study of Energy Absorption in the Strut, Nominal $f = 1.75$ cps	76
42.	Phase-Plane Study of Energy Absorption in the Strut, Nominal $f = 2.25$ cps	77
43.	Phase-Plane Study of Energy Absorption in the Strut, Nominal $f = 3.5$ cps	78
44.	Main Gear Force Versus Strut Stroke	79
45.	Main Gear Tire Deflection Versus Tire Force, Tire Pressure = 60 psi	80
46.	Main Gear Tire Deflection Versus Tire Force, Tire Pressure = 90 psi	81
47.	Main Gear Tire Deflection Versus Tire Force, Tire Pressure = 120 psi	82
48.	Strut Air Compression Force Versus Stroke, Nose Gear	83

<u>FIGURE</u>	<u>TITLE</u>	<u>PAGE</u>
49.	Nose Gear Tire Deflection Versus Tire Force, Tire Pressure = 60 psi	84
50.	Correction Factors for Finite Bandwidth Filters Operating on a Lightly - Damped Function Near a Peak Frequency	85
51.	Variation of System Damping, $c/c_c$ with Linearized Strut Damping Coefficient, D; Single Gear, 90 $c_{ps}$	86
52.	Variation of Damping Ratio with Speed for Any Tire Pressure at $f = .95$ cps Nominal Peak Frequency and for Strut Damper, $D = 185$	87
53.	Variation of Damping Ratio with Speed for Several Tire Pressures at an Average Peak Frequency of $f = 1.65$ cps and for a Strut Damper = 185	87
54.	Variation in Peak Amplitude of Tire Force with Linear Strut Damping Constant D	88
55.	Nyquist Diagram for Tire Force (Uncorrected for Filter Bandwidth)	89
56.	Time Histories of Loads and Motions for Single Gear Taxiing Standard Configuration, Taxi Speed = 88 fps	90
57.	Time Histories of Loads and Motions for Single Gear Taxiing Standard Configuration, Taxi Speed = 88 fps	91
58.	Time Histories of Loads and Motions for Multiple Gear Taxiing Standard Configuration, Taxi Speed = 88 fps	92
59.	Time Histories of Loads and Motions for Multiple Gear Taxiing Standard Configuration, Taxi Speed = 88 fps	93
60.	Power Spectrum of Vertical Tire Force for the Normal Configuration, Single Gear, Taxi Speeds 22 Ft/Sec and 44 Ft/Sec	94
61.	Power Spectrum of Vertical Tire Force for the Normal Configuration, Single Gear, Taxi Speeds 66 Ft/Sec and 88 Ft/Sec	95
62.	Power Spectrum of Strut Vertical Force for the Normal Configuration, Single Gear, Taxi Speed = 66 Ft/Sec	96
63.	Occurrences for $\Delta F_{t2}$ , Incremental Tire Vertical Force, Front Main Gear	97

<u>FIGURE</u>	<u>TITLE</u>	<u>PAGE</u>
64.	Cumulative Probability of the Nonlinear System for Vertical Force on Rear Main Gear	98
65.	Occurrences for $\Delta F_{t3}$ , Incremental Tire Vertical Force Rear Main Gear	99
66.	Cumulative Probability of the Nonlinear System for Vertical Force on Rear Main Gear	100
67.	Occurrences for $\Delta Z_f$ , Airplane Center of Gravity Vertical Acceleration	101
68.	Cumulative Probability of the Nonlinear System for Vertical Acceleration at the Center of Gravity	102
69.	Occurrences for $\Delta M_{x1}$ , Incremental Wing Bending Moments at Nominal Wing Root Station	103
70.	Cumulative Probability for the Nonlinear System for Wing Bending Moment at Nominal Wing Root Station	104
71.	Occurrences for $\Delta M_{y6}$ , Incremental Wing Torsion Moments Inboard of Outboard Nacelle (+ Nose Down)	105
72.	Cumulative Probability of the Nonlinear System for Wing Torsion Moments of Outboard Nacelle (+ Nose Down)	106
73.	Occurrences for $\Delta F_1$ , Incremental Tire Vertical Force (Single Gear)	107
74.	Comparison of Transfer Functions by Linear Harmonic and Power Spectral Density Methods for Landing Gear Tire Force, Single Gear Analysis for Normal Configuration	108
75.	Comparison of Transfer Functions by Linear Harmonic and Power Spectral Density Methods for Vertical Acceleration of Airplane Center of Gravity, Single Gear Analysis for Normal Configuration	109
76.	Comparison of Transfer Functions by Linear Harmonic and Power Spectral Density Methods for Wing Root Bending Moment, Single Gear Analysis for Normal Configuration	110
77.	Comparison of Transfer Functions by the Linear Harmonic and Power Spectral Density Methods for Wing Torsion Moment Inboard of Outboard Nacelle, Single Gear Analysis for Normal Configuration	111

<u>FIGURE</u>	<u>TITLE</u>	<u>PAGE</u>
78.	Comparison of Transfer Functions by Linear Harmonic and Power Spectral Density Methods for Landing Gear Tire Force, Single Gear Analysis for Normal Configuration	112
79.	Comparison of Output Power Spectra from Linear Harmonic and Power Spectral Density Methods for Landing Gear Tire Force, Single Gear Analysis	113
80.	Comparison of Output Power Spectra from Linear Harmonic and Power Spectra Density Methods for Wing Root Bending Moment, Single Gear Analysis	114
81.	Comparison of Transfer Functions for the Linear Harmonic System with Nose Gear In and Out of Phase with Main Gear for Wing Torsion Moment Inboard of Outboard Nacelle, Multi-Gear Analysis	115
82.	Comparison of Transfer Functions for the Linear Harmonic System with Nose Gear In and Out of Phase with Main Gear for Rear Main Gear Tire Force, Multi-Gear Analysis	116
83.	Comparison of Transfer Functions for the Linear Harmonic System with Nose Gear In and Out of Phase with Main Gear for Wing Torsion Moment Inboard of Outboard Nacelle, Multi-Gear Analysis	117
84.	Comparison of Transfer Functions by Linear Harmonic and Power Spectral Density Methods for Rear Main Landing Gear Tire Forces, Multi-Gear Analysis	118
85.	Comparison of Transfer Functions by Linear Harmonic and Power Spectral Density Methods for Vertical Acceleration at the Airplane Center of Gravity, Multi-Gear Analysis	119
86.	Comparison of Transfer Functions by Linear Harmonic and Power Spectral Density Methods for Wing Root Bending Moment, Multi-Gear Analysis	120
87.	Comparison of Transfer Functions by Linear Harmonic and Power Spectral Density Methods for Wing Torsion Moment Inboard of Outboard Nacelle, Multi-Gear Analysis	121
88.	Comparison of Nonlinear and Linearized Transfer Function Peaks for Main Gear Tire Force, Multi-Gear Analysis	122
89.	Comparison of Nonlinear and Linearized Transfer Function Peaks for Vertical Acceleration of the Center of Gravity	123

<u>FIGURE</u>	<u>TITLE</u>	<u>PAGE</u>
90.	Comparison of Nonlinear and Linearized Transfer Function Peaks for Wing Torsion Moments Inboard of Outboard Nacelle	124
91.	Variation of Linearized Spring Constant Versus Tire Pressure	125
92.	Ratio of Transfer Function Peak for Tire Force Over Linearized Spring Constant Versus Tire Pressure Variations	125
93.	Comparison of Nonlinear and Linearized Tire Force Transfer Functions for Variations with Velocity, Single Gear Analysis for Peaks at $f = 0.95$ cps and $f = 1.65$ cps	126
94.	Comparison of Nonlinear and Linearized Wing Root Bending Moment Transfer Functions for Variations with Velocity, Single Gear Analysis for Peaks at $f = 0.95$ cps	126
95.	Comparison of Nonlinear and Linearized Center of Gravity Vertical Acceleration Transfer Functions for Variations with Velocity, Single Gear Analysis for Peaks at $f = 0.95$ cps and $f = 1.65$ cps	127
96.	Comparison of Nonlinear and Linearized Wing Torsion Moment Transfer Functions Near Outboard Nacelle for Variations with Velocity, Single Gear Analysis for Peaks at $f = 0.95$ cps, $f = 1.65$ cps and $f = 3.4$ cps	128
97.	Variation of Transfer Function Peak with Damping of the Linear and Nonlinear Systems for Rear Main Landing Gear Tire Force, $F_{t3}$ , $f = 0.93$ cps	129
98.	Variation of Transfer Function Peak with Damping of the Linear and Nonlinear Systems for Rear Main Landing Gear Tire Force, $F_{t3}$ , $f = 1.65$ cps	130
99.	Variation of Transfer Function Peak with Damping of the Linear and Nonlinear Systems for Rear Main Landing Gear Tire Force, $F_{t3}$ , $f = 3.5$ cps	131
100.	Variation of Transfer Function Peak with Damping of the Linear and Nonlinear Systems for Center of Gravity Acceleration, $\ddot{Z}_f$ , $f = 0.95$ cps	132
101.	Variation of Transfer Function Peak with Damping of the Linear and Nonlinear Systems for Center of Gravity Acceleration, $\ddot{Z}_f$ , $f = 1.65$ cps	133

<u>FIGURE</u>	<u>TITLE</u>	<u>PAGE</u>
102.	Variation of Transfer Function Peak with Damping of the Linear and Nonlinear Systems for Center of Gravity Acceleration, $\ddot{z}_f$ , $f = 3.5$ cps	134
103.	Variation of Transfer Function Peak with Damping of the Linear and Nonlinear Systems for Wing Root Bending Moment, $M_{x1}$ , $f = 0.93$ cps	135
104.	Variation of Transfer Function Peak with Damping of the Linear and Nonlinear Systems for Wing Root Bending Moment, $M_{x1}$ , $f = 3.5$ cps	136
105.	Variations of Transfer Function Peak with Damping of the Linear and Nonlinear Systems for Wing Torsion Moment Inboard of Outboard Nacelle, $M_{y6}$ , $f = 0.95$ cps	137
106.	Variation of Transfer Function Peak with Damping of the Linear and Nonlinear Systems for Wing Torsion Moment Inboard of Outboard Nacelle, $M_{y6}$ , $f = 3.5$ cps	138
107.	Comparison Between Transfer Functions for Single and Multi-Gear Analyses of the Nonlinear System Tire Force	139
108.	Comparison of Output Power Spectra from Linear Harmonic and Power Spectral Density Methods for the Rear Main Gear Tire Force, Multi-Gear Analysis	140
109.	Comparison of Output Power Spectra from Linear Harmonic and Power Spectral Density for Vertical Acceleration of the Airplane Center of Gravity, Multi-Gear Analysis	141
110.	Comparison of Output Power Spectra from Linear Harmonic and Power Spectral Density Methods for Wing Root Bending Moment, Multi-Gear Analysis	142
111.	Comparison of Output Power Spectra from Linear Harmonic and Power Spectral Density Methods for Wing Torsion Moment Inboard of Outboard Nacelle, Multi-Gear Analysis	143
112.	Comparison of Load Occurrences for the Nonlinear and Linearized Systems for Incremental Tire Vertical Force Rear Main Gear, $\Delta F_{t3}$ , Multi-Gear Analysis, Tire Pressure = 60 psi	144
113.	Comparison of Load Occurrences for the Nonlinear and Linearized Systems for Incremental Tire Vertical Force Rear Main Gear, $\Delta F_{t3}$ , Multi-Gear Analysis, Tire Pressure = 90 psi	145

<u>FIGURE</u>	<u>TITLE</u>	<u>PAGE</u>
114.	Comparison of Load Occurrences for the Nonlinear and Linearized Systems for Incremental Tire Vertical Force Rear Main Gear, $\Delta F_{13}$ , Multi-Gear Analysis, Tire Pressure = 120 psi	146
115.	Comparison of Load Occurrences for the Nonlinear and Linearized Systems for Center of Gravity Acceleration, $\ddot{Z}_f$ , Multi-Gear Analysis, Tire Pressure = 60 psi	147
116.	Comparison of Load Occurrences for the Nonlinear and Linearized Systems for Center of Gravity Acceleration, $\ddot{Z}_f$ , Multi-Gear Analysis, Tire Pressure = 90 psi	148
117.	Comparison of Load Occurrences for the Nonlinear and Linearized Systems for Center of Gravity Acceleration, $\ddot{Z}_f$ , Multi-Gear Analysis, Tire Pressure = 120 psi	149
118.	Comparison of Load Occurrences for the Nonlinear and Linearized Systems for Incremental Wing Root Bending Moment, $\Delta M_{x1}$ , Multi-Gear Analysis, Tire Pressure = 60 psi	150
119.	Comparison of Load Occurrences for the Nonlinear and Linearized Systems for $M_{x1}$ , Wing Root Bending Moment, Multi-Gear Analysis, Tire Pressure = 90 psi	151
120.	Comparison of Load Occurrences for the Nonlinear and Linearized Systems for $M_{x1}$ , Wing Root Bending Moment, Multi-Gear Analysis, Tire Pressure = 120 psi	152
121.	Comparison of Load Occurrences for the Nonlinear and Linearized Systems for $M_{y6}$ , Wing Torsion Inboard of Outboard Nacelle, Multi-Gear Analysis, Tire Pressure = 60 psi	153
122.	Comparison of Load Occurrences for the Nonlinear and Linearized Systems for $M_{y6}$ , Wing Torsion Inboard of Outboard Nacelle, Multi-Gear Analysis, Tire Pressure = 90 psi	154
123.	Comparison of Load Occurrences for the Nonlinear and Linearized Systems for $M_{y6}$ , Wing Torsion Inboard of Outboard Nacelle, Multi-Gear Analysis, Tire Pressure = 120 psi	155
124.	Comparison of the Equivalent Linear and Nonlinear Damping Force Curves for the Standard Configuration	156
125.	Assumed Lift Variation for One-Half Airplane	170

<u>FIGURE</u>	<u>TITLE</u>	<u>PAGE</u>
126.	Average Main Gear Static Load Versus Taxi Speed, $V_H$	171
127.	Equivalent Three Mass System with Modal Damping	178
128.	Dynamic Response Analysis Flow Chart	186
129.	Analog Computer Diagram of Airplane Simulator	189
130.	Analog Computer Diagram for Seven Fourth-Order Pade' Circuits	191
131.	Computer Diagram for Regeneration of the Runway Slope Profile	193
132.	Runway Amplitude and Slope Profiles from 2870 to 3150 Ft	195
133.	Runway Derivative - Low Frequency Content Obtained from Follower and Filter Combination	196
134.	Integral of the Runway Derivative Obtained through the Complementary Filter Network	197
135.	Analog Flow Diagrams for Power Spectral Density Computations	201
136.	Frequency Response of the Five Pole Maximally Flat Filter	202
137.	Analog Computer Diagram for Each Power Spectral Density Point	203
138.	Analog Computer Diagram for Occurrence Counting and Probability Computations	205
139.	Block Diagram of Computer Circuit for Obtaining Cross Spectra	207
140.	Universal Resonance Curves	212
141.	Universal Phase Angle Curves	213
142.	Comparison Between Linear and Nonlinear Tire Force Transfer Functions with Increased Strut Damping	225
143.	Transfer Function for Vertical Acceleration of Airplane Center of Gravity, Single Gear Analysis	226
144.	Transfer Function for Wing Root Bending Moment, Single Gear Analysis	227
145.	Transfer Function for Wing Torsion Moment Inboard of Outboard Nacelle, Single Gear Analysis	228

<u>FIGURE</u>	<u>TITLE</u>	<u>PAGE</u>
146.	Transfer Function for Landing Gear Tire Force, Single Gear Analysis	229
147.	Transfer Function for Vertical Acceleration of Airplane Center of Gravity, Single Gear Analysis	230
148.	Transfer Function of Wing Root Bending Moment, Single Gear Analysis	231
149.	Transfer Function for Wing Torsion Moment Inboard of Outboard Nacelle, Single Gear Analysis	232
150.	Typical Two-Degree-Of-Freedom System Resonance Curves (Undamped)	243
151.	Main Mass Resonant Frequencies as a Function of Mass Ratio for $\omega_s \approx \omega_f$	245
152.	Comparison of Transfer Functions from the Nonlinear PSD and the Nonlinear Harmonic Methods for Main Gear Tire Force, Single Gear Analysis for Normal Configuration	253
153.	Comparison of Transfer Functions from the Nonlinear PSD and the Nonlinear Harmonic Methods for Wing Root Bending Moment, Single Gear Analysis for Normal Configuration	254
154.	Comparison of Transfer Functions from the Nonlinear PSD and the Nonlinear Harmonic Methods for Wing Torsion Moment Inboard of Outboard Nacelle, Single Gear Analysis for Normal Configuration	255
155.	Comparison of Transfer Functions by Cross-Spectral and Power Spectral Methods for Rear Main Tire Force, $F_{t3}$ , Multi-Gear Analysis for Normal Configuration, Taxi Speed = 44 fps	256
156.	Comparison of Transfer Functions by Cross-Spectral and Power Spectral Methods for Rear Main Tire Force, $F_{t3}$ , Multi-Gear Analysis for Normal Configuration, Taxi Speed = 88 fps	257
157.	Comparison of Transfer Function by Cross-Spectral and Power Spectral Methods for Acceleration of Center of Gravity, $\ddot{Z}_f$ , Multi-Gear Analysis for Normal Configuration, Taxi Speed = 44 fps	258
158.	Comparison of Transfer Function by Cross-Spectral and Power Spectral Methods for Acceleration of Center of Gravity, $\ddot{Z}_f$ , Multi-Gear Analysis for Normal Configuration, Taxi Speed = 88 fps	259
159.	Comparison of Transfer Function by Cross-Spectral and Power Spectral Methods for Wing Root Bending, $M_{x1}$ , Multi-Gear Analysis for Normal Configuration, Taxi Speed = 22 fps	260

<u>FIGURE</u>	<u>TITLE</u>	<u>PAGE</u>
160.	Sample Cross-Spectral Density (Correlated with Ground Profile Derivative) for Rear Main Gear Tire Force, Multi-Gear Analysis for the Normal Configuration	261
161.	Comparison of the True Force - Deflection Curve of the Tire and a Linear Approximation to the Tire Spring	279
162.	Plot of the Integration of the Incomplete Elliptic Integral of the Second Kind, $K(\nu)$ , with Respect to the Argument	294
163.	Comparison of the Actual Dimensionless Spring Force Curve and the Approximate Spring Force Curves for Various Initial Conditions	295
164.	Comparison of the True Maximum Dimensionless Lower Mass Displacement, $u_m$ , and the Approximation of $u_m$ for the Full Range of the Initial Velocity Parameter, $u_o'$	298
165.	Plot of the Ratio of Energy which the Linear Spring is Capable of Absorbing to the Total Energy which Both the Linear and Cubic Springs can Absorb, as a Function of the Initial Velocity Parameter, $u_o'$	299
166.	Comparison of Solutions for Lower - Mass Displacement and Upper - Mass Acceleration Obtained by the Runge-Kutta Procedure and from the Analytical Equation	301
167.	Comparison of Solutions for Upper - Mass Displacement Obtained by the Runge-Kutta Procedure and from the Analytical Equation	302
168.	Comparison Between Theoretical Results and Experimental Data on the Upper - Mass Acceleration for a Typical Impact	304
169.	Comparison Between Theoretical Results and Experimental Data on the Ground Vertical Force for a Typical Impact	305
170.	Comparison of Power Spectra from Flight Test Data with Results from Analog for Rear Main Gear Tire Force	310
171.	Comparison of Load Occurrences from Analytical and Flight Test Data for Incremental Tire Force, Rear Main Gear, $\Delta F_{13}$ ; Nominal Tire Pressure = 60 psi	311
172.	Taxi Loads per 1000 Flights	312
173.	Effect of Taxi Speed on Acceleration	313

<u>FIGURE</u>	<u>TITLE</u>	<u>PAGE</u>
174.	Comparison of Output Power Spectra from Analog and Digital Methods Applied to a Common Time History of Tire Force, Single Gear	315
175.	Comparison of Runway Power Spectra from Analog Computer with NASA Spectral Calculations for LaGuardia Runway	316
176.	Estimates of Reliability for Power Spectral Amplitudes	318

#### LIST OF TABLES

<u>TABLE</u>	<u>TITLE</u>	<u>PAGE</u>
1.	Airplane Mass and Inertia Data Versus Wing Stations at Maximum Take-Off Weight	172
2.	Free Free Mode Shapes	173
3.	Main and Nose Landing Gear Orifice Diameter Versus Orifice Coefficient	174
4.	Gear Force and Center of Gravity Deflection in Modes	175
5.	Amplitude and Phase Angle of Analytical Transfer Function for Tire Force	184
6.	Transfer Functions for Tire Force	250
7.	Transfer Functions for Wing Root Bending Moment	251
8.	Transfer Functions for Wing Torsion Moment at Outboard Nacelle	252
9.	Constants of the Physical System Used in Appendix J	300

## SECTION I

### INTRODUCTION

It is commonly recognized that structural design philosophy for aero-space vehicles should include considerations of fatigue life as well as concepts of critical or maximum loading. This is particularly true for taxiing, since present aircraft design criteria are usually somewhat arbitrary regarding taxi loads. The purpose of this research is to develop methods for repeated dynamic loads analysis so that improvements can be realized in ground operations of advanced flight vehicles.

The maximum loads resulting directly from the traverse of an airplane over a specific runway cannot in themselves be applied as design loads for all aircraft. Such an assumption would imply that both the runway and the airplane were "typical," which is highly unlikely. Specific aircraft response characteristics combined with a particular kind of forcing function can only be used, therefore, to establish trends with parametric variations for a given analysis technique.

Considering the variety of runways and the randomness of runway profile variations, a statistical evaluation of aircraft response parameters is assumed to offer the most useful approach. Therefore, a very extensive and detailed statistical study is performed on the loads and motions resulting from accurately simulated airplane response while taxiing over a runway having high density traffic and above average roughness. Power spectral densities, cross-spectra, and corresponding transfer functions are computed for several load points on an example vehicle. Although load occurrences can be calculated for normal distributions from the power spectral functions, the non-Gaussian nature of the data expected from a nonlinear system predicates the use of direct counting or integrating techniques for peak-count and probability studies. The tedious data processing that results is considered justified by the marked skewness of some of the data which are presented.

A detailed dynamic loads analysis is performed by either analog or digital computational schemes. In each case the computer simulates the transient response of the flexible airplane traversing the random runway profile at several speeds. Provision is made for many degrees of freedom in a generalized LaGrangian coordinate representation of the system. Various landing gear arrangements are considered. All possible parameters in the differential equations of motion are considered in the initial stages of the analysis, but where directly related effects are found to be negligible, further consideration is omitted. In the course of the investigation, at least three nonlinear properties of landing gears are found to be relevant to the dynamic analysis.

---

Manuscript released by the author 5 May 1961 for publication as an ASD Technical Report.

Both analog and digital computer solutions were obtained, but the analog techniques proved to be most successful for handling the non-linearities and the large amounts of random data required for power spectral analysis. A few comparisons have been made, however, indicating good agreement between analog and digital methods. The analog computer results are essentially complete, and these data are used in evaluating the analytical methods presented.

A closed-form elliptic function solution of the nonlinear system has been derived in an attempt to reduce or eliminate the need for machine computations. The mathematical forms are valid for boundary value problems only, however, and further research is recommended to determine more complete, forced solutions.

A prime objective of this program is to determine simplified approaches, where possible. Linearization of the nonlinear parameters of the system provides the most inclusive simplification that could be anticipated from an analytical point of view, but oleo-pneumatic shock struts are usually considered to be highly nonlinear devices not conducive to accurate linearization. This concept probably arises from numerous unsuccessful attempts in the past to achieve adequate results through linearization of landing gear systems for landing impacts. Landing loads design requirements include rather large initial conditions of velocity, which in turn generate rather high rates of strut closure. At these high telescoping velocities, the orifice resistance or damping force is highly nonlinear, and simplified analyses are inadequate.

There has been some evidence that the dynamic response of advanced flight vehicles during taxiing may be susceptible to linearization. Anticipated strut velocities are considerably lower for normal terrain operational conditions and shock struts are designed for maximum efficiency during landings, with the result that orifices are usually too large for effective damping during ground operations. This should be particularly true from a statistical, or fatigue loads viewpoint, according to known data on the random characteristics of runway roughness.

Under these assumptions, as part of this research program on ground handling loads, an investigation has been made to determine the optimum linearization procedures, and the adequacy of loads produced from such analyses. Standard techniques of nonlinear mechanics have been applied for this purpose where practical. However, generalization is often difficult because the mathematics of nonlinear systems is still in an immature state of development, except for a limited few classic cases. Therefore some unusual statistical and analytical techniques have occasionally been employed in developing simplified approaches.

An affine transformation of the linearized system is found to simplify the problem so that a closed form solution can be obtained. The linearized solutions are compared with the more exact nonlinear analog computer data, and good agreement is indicated in general.

Comparison of test and theoretical data is made where such data are available. Fully analyzed and substantiated taxi test data for the example vehicle, obtained from a dynamic response flight test program, are only meagerly available at this time. Profilometer data for one runway is available and a portion of the ground loads data from the corresponding tests has been included for comparison.

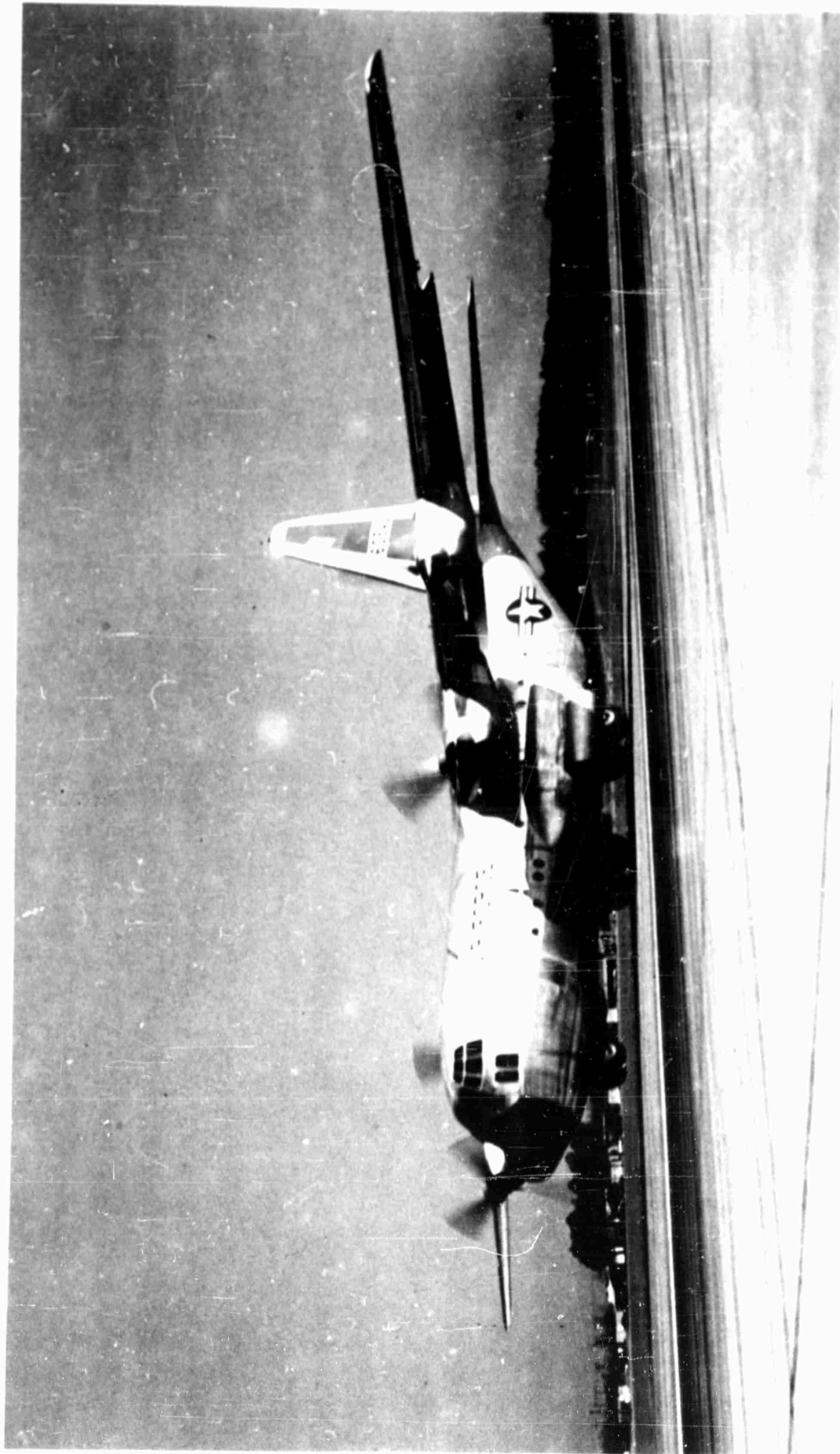


FIGURE 1: View of the Example Airplane Showing the Landing Gear Arrangement Studied

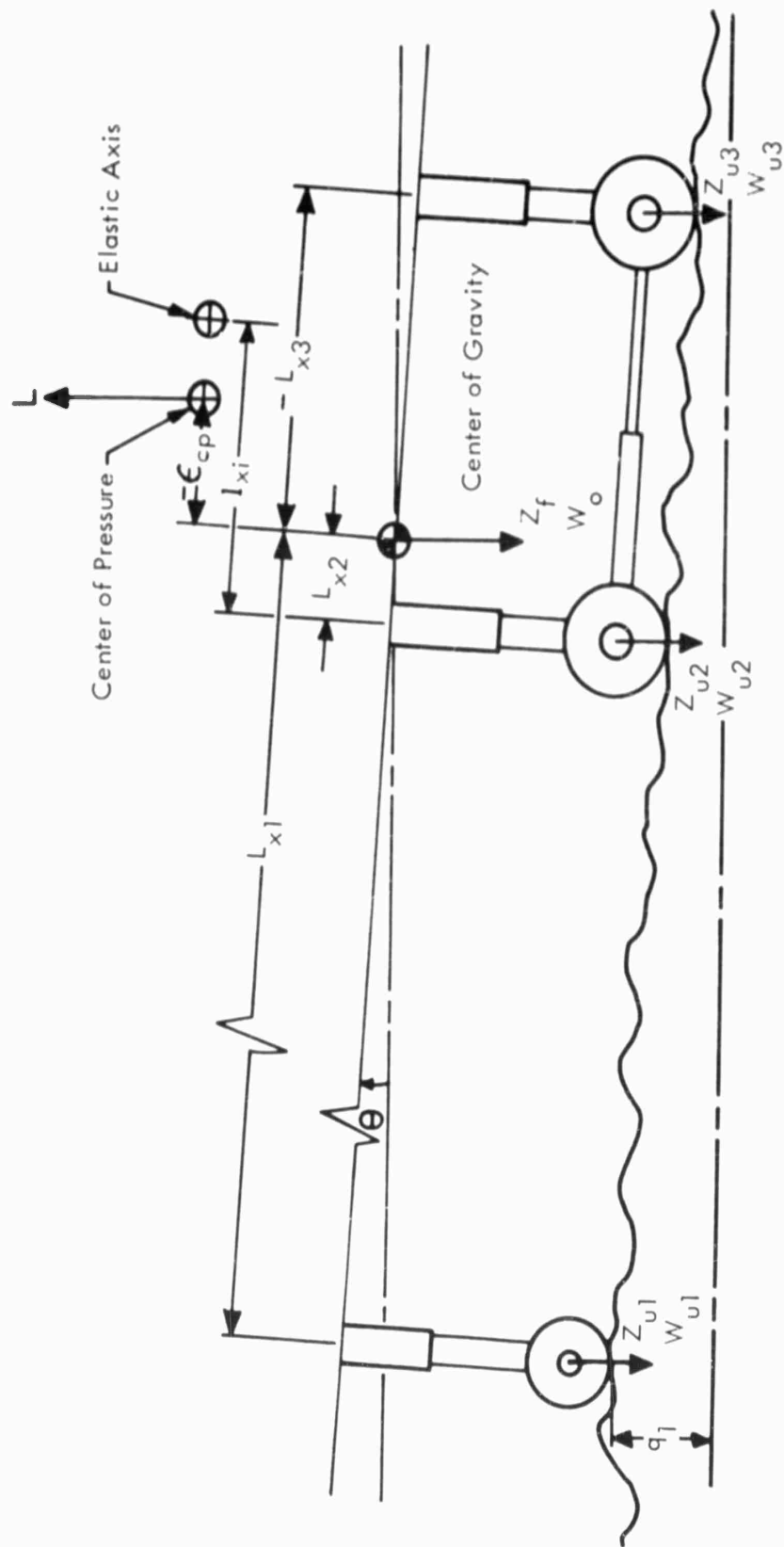


FIGURE 2 : Sketch Of Landing Gear Arrangement Studied

$q^{\text{th}}$  Panel

$$s_{nq} = W_{nq} - \epsilon_q \phi_{nq}$$

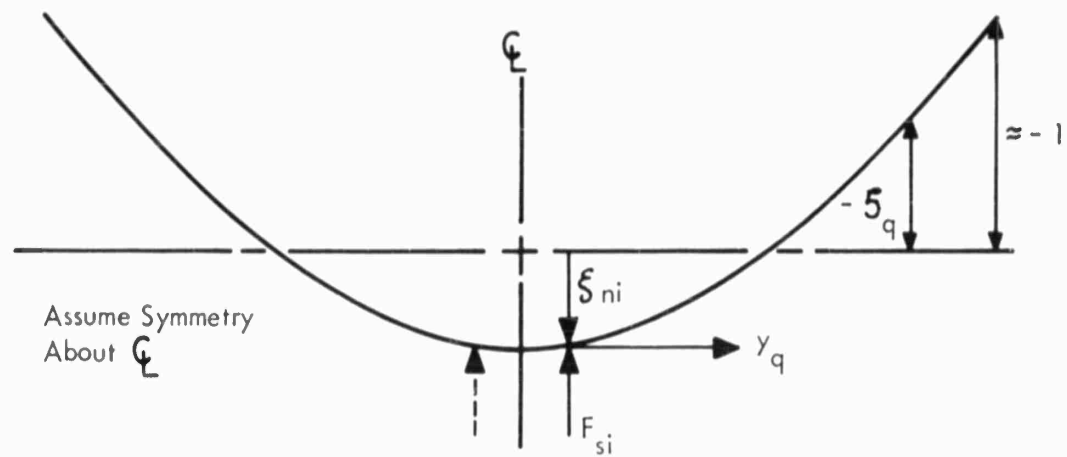
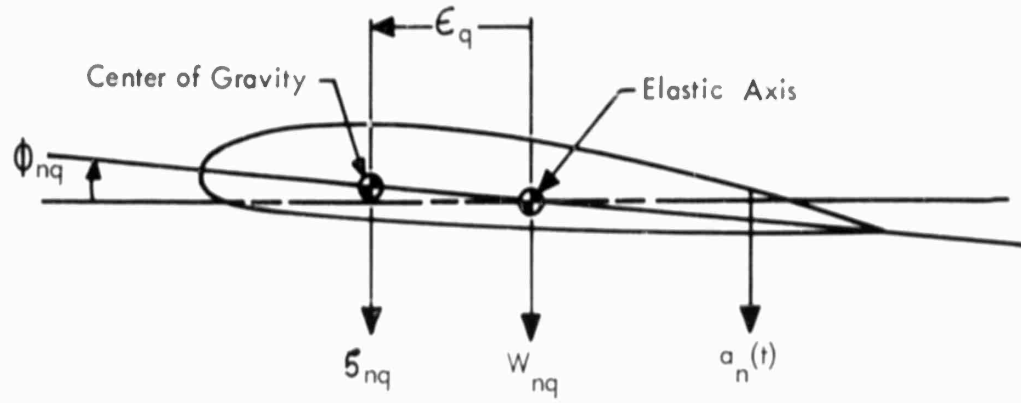


FIGURE 3 : Wing Chord and Modal Coordinate Sign Convention

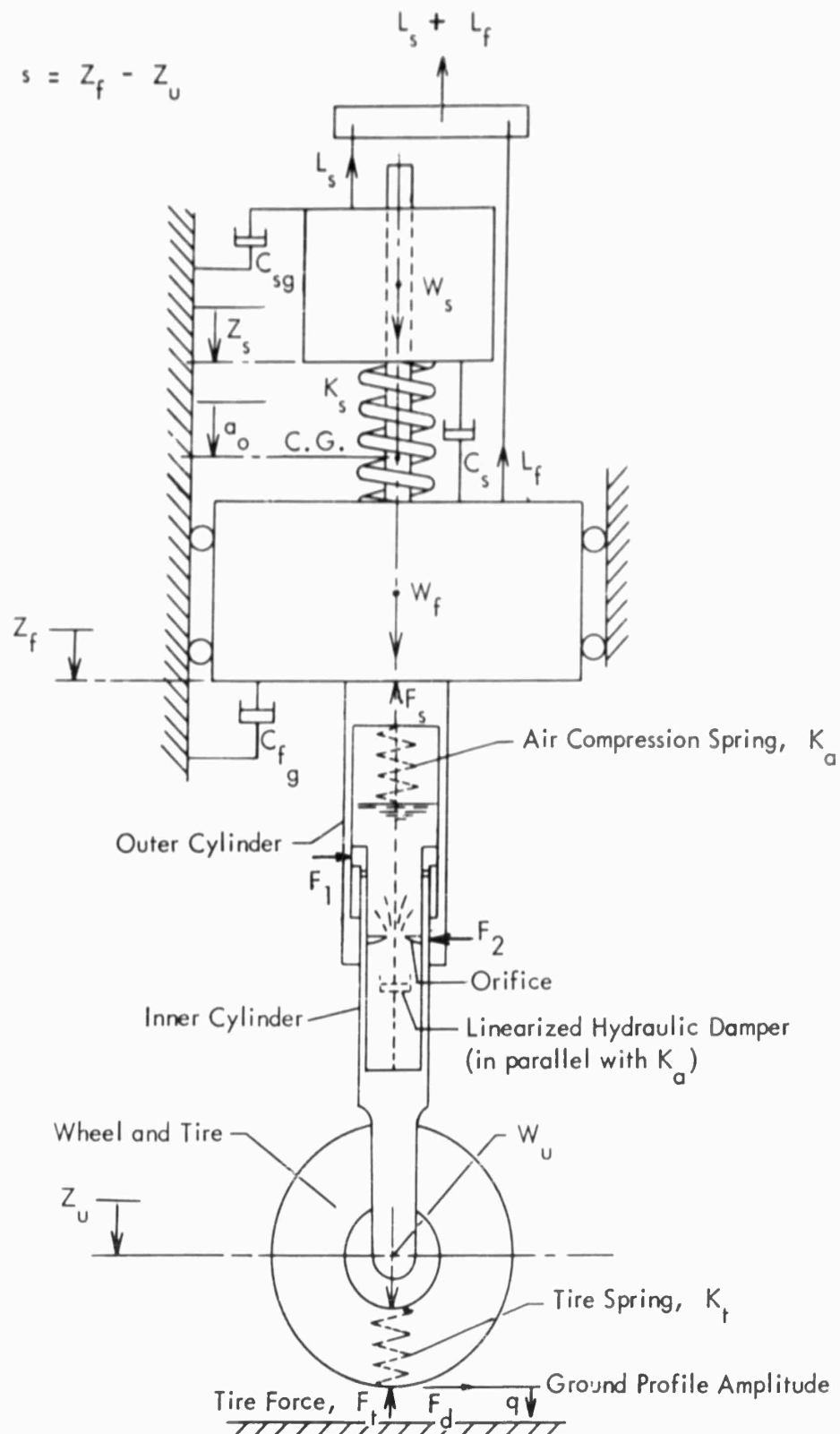


FIGURE 4 : Three Degrees of Freedom System Considered in the Equivalent Linear Analysis

## SECTION II

### THEORETICAL DISCUSSION

Solutions are obtained for the response of an aero-space vehicle while taxiing over a preselected random runway profile. The differential equations include the rigid body modes of pitch and translation, coupled with four flexible wing modes and up to five landing gears for ground loads application. Four nonlinear properties of the landing gear struts have been incorporated, and the effects of change in wing lift, non-steady aerodynamic damping and structural damping have been considered.

General information on modal terminology and the nature of the corresponding dynamic response may be found in Reference 17. Matrix iteration procedures are used in the determination of the natural modes of vibration of the vehicle as presented in Appendix B.

#### 1. Equations of Motion for Taxiing

The response of the airplane may be written in terms of the generalized LaGrangian coordinates for the normal modes of the system as follows:

(Refer to the List of Symbols and to Figures 2, 3, and 4 for quantities not defined here).

The translational response of the rigid body mode may be written in the form:

$$M_o \ddot{\alpha}_o = - \sum_{i=1}^v F_{si} + (1 - K_L) W_o - c_o \dot{\alpha}_o \quad i = (1, 2, \dots, 5) \quad (1)$$

where:  $c_o = 1/2 C_{L\alpha} A \rho V_H$

$A$  is the wing area

$C_{L\alpha}$  is the lift curve slope, per radian

$K_L = L/W_o$  and  $M_o = (W_o/g)$ , the rigid body mass

\* $L = 1/2 C_{L\alpha} \rho A V_H^2 \alpha_o$ , lbs.  $\alpha_o$  is the mean angle of attack, radians

\*Note: Down-wash effects and tail aerodynamics are neglected. Modal parameters such as  $M_n$  and  $\omega_n$  can be found in Appendices A and B. A more detailed derivation of the modal equations used here may be found in Reference 6.

The motion of the coupled-bending-and-torsion wing modes is defined by:

$$M_1 \ddot{a}_1 + M_1 \omega_1^2 a_1 = - \sum_{i=1}^v (F_{si} + W_{ui}) \xi_{1i} - \frac{C_{L\alpha} \rho V_H}{2} \int_0^t \sum_{k=0}^m \ddot{a}_k A_{k1} [1 - \Phi(t-\tau)] d\tau - c_1 \dot{a}_1 \quad (2)$$

$$M_n \ddot{a}_n + M_n \omega_n^2 a_n = - \sum_{i=1}^v (F_{si} + W_{ui}) \xi_{ni} - \frac{C_{L\alpha} \rho V_H}{2} \int_0^t \sum_{k=0}^m \ddot{a}_k A_{kn} [1 - \Phi(t-\tau)] d\tau - c_n \dot{a}_n \quad (3)$$

Where:  $n = (0, 1, 2, \dots, m)$  and  $m$  is the total number of flexible modes.

$A_{kn}$  is the effective modal wing area - (See Appendix A for the equation as simplified for the very low speed aerodynamics involved in taxiing).

$$c_n = \gamma c_c$$

$$c_c = 2M_n \omega_n$$

$\gamma$  = Percent critical damping

$a_n(t)$  = Generalized LaGrangian coordinate displacement in the  $n^{\text{th}}$  mode, ft,  $n = (0, 1, 2, \dots, m)$ .

$F_{si}$  = Strut Vertical Force,  $i^{\text{th}}$  gear, lbs.

$\xi_{ni}$  = Normalized  $n^{\text{th}}$  modal deflection at the point of the  $i^{\text{th}}$  gear force application

$M_n$  = Effective modal mass

$\omega_n$  = Modal frequency of the  $n^{\text{th}}$  flexible mode

$W_{ui}$  = Weight of unsprung mass of the  $i^{\text{th}}$  gear

$\Phi(t)$  = Wagner function, indicial delay in lift build-up on an airfoil

Pitch Equation:

$$I_y \ddot{\Theta} = \sum_{i=1}^v F_{si} L_{xi} + (K_L) W_o \epsilon_{cp} \quad (4)$$

where  $\Theta$  is the angular displacement in pitch about the airplane C.G., from the horizontal and  $\epsilon_{cp}$  is the longitudinal distance from the center of pressure to the C.G.

Strut Vertical Force:

For  $t \geq t_{p.l.}$  (preload)

$$F_{si} = F_{ai} + F_{si} + F_{fi} \frac{|\dot{s}_i|}{\dot{s}_i} \quad (5)$$

where:  $F_o$  is the strut polytropic air compression force

$F_s$  is the strut damping force

$F_f$  is the strut friction force magnitude

In more detail,

$$F_{si} = \frac{A_i}{(b_i - s_i)} v_i + K_i + C_{Di} \dot{s}_i |\dot{s}_i| + F_{fi} \frac{\dot{s}_i}{|\dot{s}_i|} \quad (6)$$

Note: The preload feature of struts is assumed to apply only with nose gear forces for taxiing. See Reference 6 and Appendix B for other details.

Vertical Tire Force:

$$F_{ti} = a_{1i} \delta_i^{c_{2i}} \quad (7)$$

$\delta_i > 0$  is the tire deflection

where:

$$\delta_i = Z_{ui} - q_i \quad (8)$$

and  $Z_{ui}$  = axle deflection

$q_i$  = the ground profile deflection

Definition of C.G. Acceleration:

$$\ddot{Z}_f = \sum_{n=0}^m \ddot{a}_n \xi_{nf} = \sum_{n=0}^m \ddot{a}_n (W_{nf} - \epsilon_x \Phi_{nf}) \quad (9)$$

Equation for Acceleration of  $i^{\text{th}}$  Landing Gear Attachment Point on the Airplane:

$$\ddot{Z}_i = -L_{xi} \ddot{\Theta} + \sum_{n=0}^m a_n \xi_{ni} \quad (10)$$

where  $L_{xi}$  is positive for  $i^{\text{th}}$  gear forward of the C.G.

Equation for Axle Vertical Acceleration:

After preload:  $t \geq t_{p.l.}$

$$M_{ui} \ddot{Z}_{ui} = F_{si} - F_{ti} + W_{ui} \quad (11)$$

Before preload:  $t \leq t_{p.l.}$

$$\ddot{Z}_{ui} \approx \ddot{Z}_i \quad (12)$$

The equation for the strut displacement of the  $i^{\text{th}}$  gear is as follows:

$$s_i = Z_i - Z_{ui} \quad (13)$$

A more detailed development of some specific terms in the equations may be found in Appendix A. Appendix B gives the magnitudes of most of the physical quantities used in the equations as they pertain to the example aircraft which is used for the investigation of strut characteristics.

In addition to the above terms, the digital program contains terms considering wing sweep angles, non-vertical struts, unsymmetry in roll, and asymmetric wing modes. The example airplane has very little wing sweep angle, and the struts are essentially vertical, so these terms are negligible. There is no statistically significant runway data indicating a marked degree of unsymmetry from the left to right sides, so terms resulting from unsymmetrical gear excitation are omitted.

The variation in wing lift ratio,  $K_L$ , is considered, since an increase in lift will tend to extend the struts, thus allowing the air compression "springs" to flex at a lower, less stiff portion of the nonlinear force-deflection curve. The nonsteady aerodynamic force term in Equation 3, involving the Wagner indicial delay in lift build-up, was studied early in the program. Removal of the indicial delay had no observed effect on the time history response at the relatively slow taxi speeds involved. It was also determined that the cross coupling damping terms were so out of phase that they had very little contribution. This conclusion is consistent with solutions made in Reference 18. Furthermore, the aerodynamic damping term is very small in magnitude for the taxi speeds considered in these analyses, and is about as effective as the structural damping term  $c_n \dot{a}_n$ .

Time histories of the wing response to pulse type loadings, as shown by gust analysis, indicate that approximately 15 percent of critical damping results from nonsteady aerodynamics at 560 fps. forward speed. Since the nonsteady term in Equation 3 is proportional to the velocity, average taxi speeds will result in less than 10 percent as much aerodynamic damping as that found in flight. Thus, approximately 1.5 percent of critical damping is to be expected on the average in this analysis. Furthermore, an accurate spanwise airload distribution cannot be determined because of dependence on flap setting, ground effects, power setting, trim and pitching angle, and cross-wind effects. Therefore, a reasonable degree of accuracy would appear to justify the combination of both the nonsteady aerodynamic and structural damping terms in the single damping term,  $c_n \dot{a}_n$ .

Structural hysteresis damping of about 3 percent has been measured on the example aircraft, and according to Reference 17, this indicates that 1.5 percent equivalent viscous damping is reasonable for the structure. Thus, the combined aerodynamic and structural effects are assumed to contribute about 3 percent of critical viscous damping to the solutions.

The strut friction force term in Equation 5 is omitted from this analysis, since drop test and taxi test results indicate that bearing friction forces are negligible for the example airplane for either landing or taxiing. Use of a strut tilted from the vertical, or the consideration of braking forces, would undoubtedly introduce strut binding loads as described in Reference 19. Reference 18 also neglected strut friction effects after indicating that this phenomenon would greatly complicate an analytical representation of the transfer function. The linearized transfer function to be derived in later sections of this report must consider discontinuous friction forces to be negligible.\* In any case, this assumption is valid for the example airplane, and future research on another airplane would be required for a detailed analysis of friction effects.

\*Note: However, a simplified friction force is derived, in Appendix J, so as to present essentially no further complication to the solution.

As described earlier, up to five landing gears with any possible mounting arrangement can be selected in the taxi analysis. However, an early analysis was made using a single landing gear mounted at the mid-point between the main landing gears of the example airplane. Several purposes are served by this approach:

1. A single-gear analysis can provide information on basic variations with taxiing speed as predicted in Reference 20, without unnecessary complications.
2. The most significant load stations can be selected for the more detailed multi-gear analysis.
3. The significance of minor parameters such as aerodynamic damping can be determined.
4. Certain phenomena which are expected to appear in all multi-gear analyses, but which are not dependent on nonlinearity, can be evaluated by comparison of single and multi-wheel transfer functions. Runway wavelengths in resonance with specific wheel spacings illustrate such a situation, as shown in Reference 20.

Finally, if symmetry about the airplane centerline is assumed, the tandem landing gear arrangement of the example airplane can be represented as shown in Figures 1 and 2 by three gears in sequence. The nose gear precedes the main gears by approximately 30 feet, and the main landing gears are independently suspended, with a spacing of approximately 5 feet between fore-and-aft struts.

## 2. Nonlinear Theory

The principal mathematical techniques employed in the study of a simplified nonlinear system will be summarized to aid in interpretation of the more detailed analysis. As stated earlier, the complete nonlinear system is generally solved by numerical or analog methods because of its complexity.

The nonlinear system under study indicates moderately low damping characteristics as exhibited by the rather sharp peaks in the transfer functions illustrated later in this report. For low system damping, the width of the resonance peaks at the half power amplitude is a direct measure of the percent of critical damping available. Since the strut damping force is one of the principal nonlinearities of the system, and otherwise is of small magnitude, it is apparent that small perturbation theory may be applicable in the study of the nonlinear solutions. This is particularly true if the nonlinear stiffnesses of the system, the tire and polytropic air compression forces in the strut, do not differ markedly from a linear spring force over the range of oscillations studied. The perturbations may be considered as small amplitude oscillations superposed on a solution of the system differential equations with only the linear terms appearing.

These quasi-periodic solutions may be derived for simple systems excited by a harmonically varying force of magnitude,  $K_f q_o$ , and frequency,  $\omega$ , by methods described in References 3 and 4. For example, assume a differential equation as follows:

$$\ddot{Z}_f + \lambda \dot{Z}_f |\dot{Z}_f| + \alpha Z_f + \beta Z_f^n = \beta F_o \cos \omega t \quad (1)$$

where:

$$\lambda = \frac{C_D}{M_f}$$

$$\alpha = \frac{K_f}{M_f}$$

$$\beta = \frac{K_{NL}}{M_f}$$

$F_o$  is the driving force magnitude divided by the nonlinear spring coefficient; the units for  $F_o$  depend upon the nonlinearity of the term involving  $K_{NL}$

$C_D$  is a nonlinear damping coefficient, lb-sec<sup>2</sup>/in.<sup>2</sup>

$M_f$  is the main mass of the simplified nonlinear system; or the equivalent transformed system. Refer to Figure 4 with  $M_s = 0$ .

$K_f$  is the linearized strut spring coefficient, lb/in.

$K_{NL}$  is the coefficient of the nonlinear component of strut stiffness.

$q_o$  is the amplitude of harmonically oscillating ground profile.

If the coefficients of the nonlinear terms and the forcing term are small, and of order  $\beta$ , then the solutions are approximately harmonic in nature. The nonlinearities of the solutions can be accounted for by ultra- or sub-harmonic oscillatory terms in the response. For purposes of determining the relative magnitude of the nonlinear terms, it is convenient to study simplified cases.

If  $\lambda$  is assumed to be zero and "hard" spring\* characteristics are used, with  $n = 3$ , a quasi-periodic solution can be determined to a second order approximation by methods of Reference 3 in the form,

\*Note: By definition, a "hard" spring possesses characteristics of increasing stiffness as deflection increases ( $\beta > 0$ ), as in Figure 6.

$$Z_f = H_0 \cos \omega t + H_1 \cos 3 \omega t \quad \dots, \quad (15)$$

neglecting the higher order, odd harmonic terms. The even harmonics are not present because they would disappear under the assumption of periodicity in higher order approximations.  $H_0$  is assumed to be the amplitude of the solution for the linearized differential equation, and  $H_1$  is the nonlinear term amplitude given by the expression

$$H_1 = \frac{\beta H_0^3}{32 \left[ \alpha + \frac{3\beta H_0^2}{4} - \frac{F_0 \beta}{H_0} \right]} \quad (16)$$

The ratio  $H_1/H_0$  is a measurement of the relative amplitude of nonlinear response in the system. Similarly, amplitude ratios can be derived for other integer exponents,  $n$ , and additional examples are evaluated in Appendix E. A typical frequency response curve for a hard spring system as derived is shown in Figure 5.

### 3. Linearized Differential Equations:

The linear differential equations will be identical to the nonlinear differential Equations 1 through 13, with the exception of portions of Equations 5, 6, and 7. Nonlinear terms have been replaced by equivalent linear terms as follows:

The strut polytropic air compression force,  $F_a$ , is approximated by

$$F_{ai} = \frac{A_i}{(b_i - s_i)^{n_i}} + K_i \approx K_{ai} s_i + K_{bi} \quad (17)$$

and the strut damping force,  $F_s$ , is given as

$$F_{si} = C_{Di} \dot{s}_i + D_i |\dot{s}_i| \approx D_i \dot{s}_i \quad (18)$$

where:

$K_{ai}$  and  $K_{bi}$  are the slope and intercept of the linearized spring force.

$D_i$  is the linearized damping coefficient for the  $i^{\text{th}}$  strut, lb-sec/ft.

$s_i$  is the strut deflection for the  $i^{\text{th}}$  gear, ft.

Therefore, Equation 6, as linearized, will now define the strut force,

$F_{si}$ , as

$$F_{si} = K_{ai}\dot{s}_i + K_{bi} + D_i\dot{s}_i \quad (19)$$

Similarly, the exponential tire force,  $F_{ti} = a_{1i}\delta_i^{a_{2i}}$ , may be replaced by the expression

$$F_{ti} = K_{ti}\delta_i \quad (20)$$

with  $\delta = (Z_u - q)$ ; where  $Z_u$  and  $q$  are defined in the list of Symbols,  $K_{ti}$  is the linearized tire spring constant, and  $\delta$  is the tire deflection.

The means for determining these coefficients for the linear terms will be discussed in the section on Transfer Function Development.

The Equations 1 through 13 as modified by the preceding paragraphs, were applied directly in the analog computer solutions for the linearized transfer functions. The analog circuitry, shown in Appendix D for nonlinear cases, is simplified accordingly, and a significant reduction in required computer components is achieved for the dynamic system.

#### 4. Affine Transformation of the Equations

Although the computer solutions for the linear system contained three coupled bending-and-torsion modes, the results indicate that a rather small percent of the total response is derived from the second and third modes. By inspection, the third coupled mode is predominantly a second pure-bending mode, and the second coupled mode is primarily a first pure-torsion mode. Experience indicates that, for landing gears mounted near the wing root, most of the gear response due to flexibility results from coupling with the first flexible mode. If the landing gears are mounted on the wing, criteria in the form of mass ratios, to be discussed later, can be developed to judge the relative importance of each mode to the landing gear forces, as shown in Reference 6.

Since the first coupled mode predominates for the example airplane, the transfer functions for strut force may be derived to a high degree of accuracy from consideration of the first flexible and rigid body modes only. If desired, the response of the higher modes may be derived using these previously computed strut force amplitudes as direct excitation, without coupling or feedback to the strut from the higher mode motions. Again, this will yield excellent approximations to the net dynamic motions, as would be expected from the principle of superposition.

The above conclusions suggest an alternative system representation which is useful for discussion purposes and for compactness of presentation. If the two lowest order modes only are considered, an affine (linear equivalent) transformation of the modal equations can be made, similar to that presented in Reference 6. The resultant equations are more tractable for analytical solution without the use of computers.

The equivalent system thus derived consists of three masses, one of which is the unsprung mass of the landing gear,  $M_U$ , as shown in Figure 4. The mass,  $M_f$ , corresponds to the landing gear attachment location on the airplane in the original equations, since  $Z_f \approx Z_f$  for main gears attached at the fuselage. Also,  $Z_f$  is often referred to as "nominal center-of-gravity acceleration" since corresponding flight test data is frequently obtained by mounting accelerometers in the fuselage. The true C.G. acceleration remains fixed relative to the mode nodal points or rigid body mode.

The elastically connected mass is referred to as  $M_s$ , with a spring constant  $K_s$ , and a damper  $C_s$  between  $M_s$  and  $M_f$ , as illustrated. The steady state lift force,  $L$ , of the modal system, as in Figure 2<sup>s</sup>, must be considered as applied to both the masses,  $M_f$  and  $M_s$ , by forces  $L_f$  and  $L_s$ .

The transformation leaves the landing gear weight and physical characteristics unchanged, so-landing gear forces will be identical in both systems.

Affine transformations will be assumed as follows:

$$Z_f(t) = a_o(t) + \xi_1 a_1(t) \quad (21)$$

$$Z_s(t) = a_o(t) + B a_1(t) \quad (22)$$

The selection of  $\xi_1$  as the normalized deflection of the landing gear station in the first mode insures that  $Z_f$  will represent the timewise variation of upper strut motion. The coefficient,  $B$ , must be determined by comparison of the coefficients in the differential equations for both systems to determine the physical constraints required for equivalence.

Assuming that the strut is deflected past preload conditions for taxiing, the equations of motion for the modal responses, Equations 1 and 2, are restated as follows:

$$M_1 \ddot{a}_1 + c_1 \dot{a}_1 + M_1 \omega_1^2 a_1 = - (F_t + M_U \ddot{Z}_U) \xi_1 = - (F_s + W_U) \xi_1 \quad (23)$$

$$M_o \ddot{a}_o + c_o \dot{a}_o = - (F_t + M_U \ddot{Z}_U - W_U) - Z_o = - (F_s + Z_o) \quad (24)$$

where:

$$Z_o = - (1 - K_L) W_o \quad (25)$$

$$Z_f = o_o + o_1 \xi_1 \quad (26)$$

and the other constants are defined in the List of Symbols. Note that only a single strut is considered for this simplified analysis. However, the multi-gear analysis, as will be shown, yields negligibly different results.

The equations of motion for the equivalent transformed system, Figure 4, of three masses may be written:

$$M_f \ddot{Z}_f - C_s (\dot{Z}_s - \dot{Z}_f) + C_{fg} \dot{Z}_f - K_s (Z_s - Z_f) + (L_f - W_f) = - F_s \quad (27)$$

$$M_f \ddot{Z}_f + M_s \ddot{Z}_s + C_{fg} \dot{Z}_f + C_{sg} \dot{Z}_s + (L_s + L_f) - (W_s + W_f) = - F_s \quad (28)$$

where  $C_{fg}$  and  $C_{sg}$  may be considered as aerodynamic damping terms for the new system.

Substitute  $Z_f$  and  $Z_s$ , with corresponding derivatives, from Equations 21 and 22 into Equations 27 and 28 and eliminate  $\ddot{a}_o$  and  $\dot{a}_o$  between these equations. It is necessary to assume that  $C_{sg}/C_{fg} = M_s/M_f$ , but this assumption will be verified later. The result is,

$$\begin{aligned} M_f (\xi_1 - B) \ddot{a}_1 + \left[ (-C_s B + C_s \xi_1 + C_{fg} \xi_1) \right. \\ \left. + \frac{M_f}{M_s} (-C_s B + C_s \xi_1 - C_{sg} B) \right] \dot{a}_1 + (K_s \xi_1 - K_s B) \left( 1 + \frac{M_f}{M_s} \right) a_1 \\ + (L_f - W_f) + \frac{M_f}{M_s} (W_s - L_s) = - F_s \end{aligned} \quad (30)$$

Using the same substitutions, Equation 27 may be subtracted from Equation 28 and like terms may be collected to obtain:

$$\begin{aligned} \ddot{a}_o + B \ddot{a}_1 + \frac{C_{sg}}{M_s} \dot{a}_o + \frac{1}{M_s} (C_{sg} B + C_s B - C_s \xi_1) \dot{a}_1 \\ \frac{K_s}{M_s} (B - \xi_1) a_1 + \frac{L_s}{M_s} - g = 0 \end{aligned} \quad (31)$$

Equation 23 may be rewritten as:

$$\frac{M_1}{\xi_1} \ddot{a}_1 + \frac{c_1}{\xi_1} \dot{a}_1 + \frac{M_1 \omega_1^2}{\xi_1} a_1 + W_u = -F_s \quad (32)$$

Equation 30 may be compared term by term with Equation 32. By subtracting Equation 23 from Equation 24 and normalizing to the coefficient of  $\ddot{a}_o$ , an equation may be obtained for comparison with Equation 31 as follows:

$$\ddot{a}_o - \frac{M_1}{M_o \xi_1} \ddot{a}_1 + \frac{c_o}{M_o} \dot{a}_o - \frac{c_1}{M_o \xi_1} \dot{a}_1 - \frac{M_1 \omega_1^2}{M_o \xi_1} a_1 + \frac{(Z_o - W_u)}{M_o} = 0 \quad (33)$$

Equating the coefficients of corresponding variables in Equations 30 and 32 and doing the same for Equations 31 and 33, the constants of the three-mass system may be determined as a function of known variables in the LaGrangian modal system. Solution of this set of nine simultaneous equations yields the following set of parametric constants for the transformed equations:

$$M_s + M_f = M_o \quad (34)$$

$$L_s + L_f = gM_o + Z_o \quad (35)$$

$$M_s = \frac{M_o^2 \xi_1^2}{M_1 + M_o \xi_1^2} \quad (36)$$

$$M_f = \frac{M_1 M_o}{M_1 + M_o \xi_1^2} \quad (37)$$

$$\frac{M_s}{M_f} = \frac{M_o \xi_1^2}{M_1} \quad (38)$$

$$K_s = M_1 \omega_1^2 \left[ \frac{M_o \xi_1}{M_1 + M_o \xi_1^2} \right]^2 \quad (39)$$

$$L_s = \frac{M_o \xi_1^2 (Z_o - W_u)}{M_1 + M_o \xi_1^2} + W_s \quad (40)$$

$$L_f = \frac{M_1 Z_o + M_o W_u \xi_1^2}{M_1 + M_o \xi_1^2} + W_f \quad (41)$$

$$C_s = (c_1 - c_o \frac{M_1}{M_o}) \left[ \frac{M_o \xi_1}{M_1 + M_o \xi_1^2} \right]^2 \quad (42)$$

$$C_{sg} = \frac{c_o M_o \xi_1^2}{M_1 + M_o \xi_1^2} \quad (43)$$

$$C_{fg} = \frac{c_o M_1}{M_1 + M_o \xi_1^2} \quad (44)$$

$$\frac{C_{sg}}{C_{fg}} = \frac{M_s}{M_f} = \frac{M_o \xi_1^2}{M_1} \quad (45)$$

where

$$B = - \frac{M_1}{M_o \xi_1} \quad (46)$$

and

$$Z_o = (K_L - 1)W_o \quad (47)$$

The linear transformation, Equation 22, may then be written:

$$Z_s(t) = a_o(t) - \frac{M_1}{M_o \xi_1} a_1(t) \quad (48)$$

The inverse transformations are also of interest:

$$\ddot{z}_o = \frac{M_f}{M_o} \ddot{z}_f + \frac{M_s}{M_o} \ddot{z}_s \quad (49)$$

and

$$\ddot{z}_1 = \frac{M_s}{\xi_1(M_s + M_f)} (\ddot{z}_f - \ddot{z}_s) \quad (50)$$

Substitution of the preceding relationships into Equations 27 and 28 will yield a pair of equations identically equivalent to Equations 23 and 24. Thus, the three-mass system, with physically constrained values of  $M_s$ ,  $M_f$ ,  $C_{sg}$ ,  $C_{fg}$ ,  $C_s$ ,  $K_s$ ,  $L_s$ , and  $L_f$ , will represent the airplane responding in its first two free-free modes while taxiing.

A useful conclusion from this analysis is that the structural characteristics of the vehicle are defined by five parameters: the total mass above the landing gear  $M_o$ , the mass ratio  $M_s/M_f$ , the natural frequency  $\omega_1$ , and the combined structural and aerodynamic damping constants  $c_o$  and  $c_1$  through the relationships for  $C$  as well as for the ratio  $C_{sg}/C_{fg}$ . This latter damping ratio, from Equation 45, verifies that the assumption of Equation 29 in the derivation is compatible with the transformation requirements, and is therefore justified.

Once the above flexibility characteristics are determined for a structural configuration, the landing gear parameters may be varied at will, without affecting those constants. The transformation is valid for either the nonlinear or the linear strut force as computed from Equations 17 through 20. However, inclusion of the nonlinearities requires that the solutions be obtained by numerical integration or analog computer methods which provide no major simplification over solutions obtained by the use of the modal equations as discussed earlier.

A nonlinear solution can be obtained in closed analytic form, as shown in Appendix J, using Equations 24, 26, and 51; provided  $a_1 = 0$ .

In the case of a linearized strut force,  $F_s$ , and tire force  $F_t$ , a major simplification does result in both the analysis and the physical interpretation of system response characteristics. The use of Equations 19, 20, 27 and 28 along with the relation

$$M_u \ddot{z}_u - W_u = F_s - F_t \quad (51)$$

enables the determination of an analytical solution in closed form for a specified ground profile variation,  $q$ , with time. A more detailed discussion of the solution, including a summary of constants pertinent to the standard aircraft configuration under study, is presented in Appendix C.

As mentioned previously, once the transfer function from strut force is determined, the response of the second and third coupled bending-and-torsion modes can be determined quite accurately as independent oscillators excited by a force applied at the strut mounting point. This neglect of coupling with the strut motions is of negligible importance to the higher modes, at least in this example, since the strut frequency response function is essentially flat beyond 2 cycles per second, where these modes tend to reach peaks.

Thus, multiplication of the complex transfer function  $T_{\ddot{a}_n}/F$ , from the strut force to the modal acceleration, times the transfer function  $T_{F_s}/q$ , for strut force due to ground profile undulations, will yield the net modal transfer function as follows:

$$T_{\ddot{a}_n}/q(i\omega) = T_{\ddot{a}_n}/F_s(i\omega) \cdot T_{F_s}/q(i\omega) \quad (52)$$

Summing these modal responses with those obtained from the transformed three-mass system, as shown in Appendix C, the complete response loads may be obtained with a negligible loss in accuracy compared with the more complete analog computer analysis.

Since the unsprung mass,  $M_u$ , is usually very small relative to  $M_f$  or  $M_s$ , some preliminary information on the coupled system resonant frequencies can be obtained by a simplified analysis of a two degree-of-freedom system obtained by setting  $M_u = 0$ , neglecting dampers, and assuming a single spring for the strut and tire spring in series.

Frequency response curves obtained therefrom are three-dimensional in character, as opposed to the two-dimensional curves usually presented in dynamics literature; so a model has been prepared as shown in Figure 150 of Appendix H to illustrate the nature of the response phenomena for a single mass ratio  $M_s/M_f = .10$ . Since the effects shown are observed frequently in vibration absorber studies for equipment mounting isolation, the more commonly known terminology of absorber mass and main mass have been applied to  $M_s$  and  $M_f$  respectively.

Two distinct resonant peaks (truncated for presentation purposes) can be observed in the figure as the forcing frequency,  $\omega_o$ , is varied while  $\omega_f$  and  $\omega_s$ , the system frequencies, are held constant. This is also typical of the transfer functions derived for  $\ddot{Z}_f$  in the nonlinear system, to be discussed later, and since

$$T_{\ddot{Z}_f}/q(\omega) = -\omega^2 T_{Z_f}(\omega) \quad (53)$$

the displacement function will have similar peaks.

The simplified study thus lends additional evidence that a linearized system may duplicate at least the peaking characteristics of the nonlinear system as observed from analog computer solutions.

## SECTION III

### TRANSFER FUNCTION DEVELOPMENT

In the derivation of linearized transfer functions for the more complete set of differential equations, as modified by Equations 17 to 20, the analog computer is employed to excite the nonlinear and the linearized systems with a harmonically varying ground profile. Time histories of response thus obtained yield additional information on the physical nature of both the transient and steady-state response of the nonlinear system; and the analog computer is more suited to the long running times required to attain a steady state for what appears to be a complex, low-damped system.

In addition, harmonic or sinusoidal excitation is an alternative but simpler method than the direct dynamic analysis, as described, which requires the tedious application of power spectral or cross spectral density analysis techniques in the generation of transfer functions. Mathematically, all three methods are dependent upon linear theory and may be inapplicable to any given nonlinear system.

The existence of the steady state solution for a set of nonlinear differential equations cannot be proven, in general, and its exact nature in time is usually dependent upon its initial or boundary conditions, whereas a damped linear system is not so dependent. Generalizations are therefore difficult to make, and one method of transfer function development may be superior to another in a given nonlinear example.

#### 1. Nonlinear System Power Spectral Analysis

The direct dynamic analysis yields recorded time histories of the stationary random responses of the aircraft to the runway profile input. The methods of generalized harmonic analysis may then be applied to both the input and the response to yield transfer functions for the structural loads of interest. The power spectral density (PSD) functions which result can be used to compute frequencies of load occurrences and probabilities. A primary purpose of this investigation is the development of methods applicable to the prediction of repeated loads resulting from ground operations of flight vehicles, and these generalized statistical procedures possess inherent advantages in such fatigue studies.

The mathematical procedures, as applied in both the digital and analog computer solutions for transfer functions, are presented in detail in Appendix D. Only the absolute magnitude of the transfer function can be obtained in a PSD analysis, but this is sufficient for most statistical purposes. Completed calculations for this study are presented in the Results and Discussion Section since it is considered to be the standard approach, and the power spectral results are used most extensively in evaluating alternative methods.

#### 2. Nonlinear System Cross Spectral Analysis

The random time histories from the direct analysis may also be applied to determine the cross spectral density, directly correlating the runway roughness with the output response. The technical approach is delineated in Appendix D, and some typical results of the cross spectral analysis are presented in Appendix K.

The cross-correlation technique calculates both the magnitude and argument of the transfer function. However, for a linear system, if no cross-correlation exists, the magnitudes of both the power spectral and cross spectral transfer functions should be identical.

### 3. Nonlinear System Harmonic Analysis

To check on alternative possibilities, for transfer function analysis, and to study steady-state energy absorption characteristics of the nonlinear system, it is useful to generate solutions of the nonlinear strut force resulting from sinusoidal excitation. For this purpose, the more complete set of flexible model equations is used except that only one strut is employed so as to minimize the number of parameters, other than nonlinearities, which could affect the solutions.

Time histories of the response generated while taxiing over a series of (1-cos) shaped ramps, as simulated on the analog computer, are shown in Figures 7 through 11. The taxi speed merely affects the aerodynamic damping present in the single gear case, so an average velocity was selected. The transient response is included to indicate the long time required for the nonlinear subharmonics and ultraharmonics of the system to damp out. The presence of these harmonics is anticipated for nonlinear systems; and they remain to some extent, subsequent to the establishment of a steady-state, as predicted by perturbation techniques in a previous section and in Appendix E.

The significant point is that a repeated, steady-state time history does result. The periodic segments are shown in more detail in Figures 12 through 35 for representative frequencies of excitation. The appearance of the segments is somewhat odd in that, for a linear system, the output loads must be a sine wave of the same frequency as the input ground profile; whereas these nonlinear results are, in general, not sinusoidal. Both the amplitude and the frequency vary throughout a periodic segment.

The simplest response cycle is typified by the vertical tire force time history as shown in Figure 36. The first half cycle of the response is for decreasing strut force and is characterized by a lower amplitude, longer wavelength curve compared with a sine wave of the average wavelength for the cycle. The second half cycle, for increasing strut force, is of shorter wavelength but higher amplitude than the basic sine wave which is referred to as the equivalent linear part. These observations on frequency could be surmised from the nonlinear landing gear spring force-deflection curve shown in Figure 6. System resonance frequencies,  $\omega_r = \omega_0 \sqrt{1-(c/c_c)^2}$ , are insensitive to the system damping for small critical damping ratios,  $c/c_c$ . Therefore, strut and tire springs may be assumed to be in series, and by using the formula,

$$K_f(Z) = \frac{K_t K_a}{K_t + K_a} \tag{54}$$

where:

$Z = (Z_u + s)$  is the tire-plus-strut deflection (for  $q = 0$ ).

$K_f$  is the instantaneous tire spring constant; or the slope of a tangent to the tire force-deflection curve at the stated value of  $Z_u$ .

$K_a$  is the instantaneous strut air spring constant; or the slope of a tangent to the strut force deflection curve at the stated value of  $s$ .

$K_f(Z)$  is the instantaneous series spring constant for the tire and strut combined

then the curve of Figure 6 may be derived.

Since  $\omega_o = K_f/M_o$ , and the slopes of tangents to the curve decrease for decreasing force, the lower frequency of the first half cycle of  $F_f$  is rationally expected. Similarly, the increase in frequency can be predicted for positively increasing force, in the second half-cycle of  $F_f$ .

Estimates of the magnitudes of these additional frequencies, not coinciding with the basic excitation frequency, is a more difficult matter. Some analyses of nonlinear systems, as represented by Equation 14, were described earlier. Using a quadratic or cubic polynomial fit to the curve as shown in Figure 6, ratios of the amplitude contribution from the nonlinear harmonics to the basic linear term amplitude are derived in Appendix F by the perturbation method. The quadratic spring term results in a dominant first harmonic with about 4 percent contribution to the system response, and the cubic spring approximation results in about 6 percent amplitude relative to the linear term. The summation of these two harmonics is less than the preliminary estimate of nonlinear harmonic amplitude which, as sketched in Figure 36 relative to the sinusoidal response, indicates less than a 20 percent contribution.

The resultant time history depends on the phasing between the harmonic terms, and the perturbation method does not yield accurate phase information. The method of "equivalent linearization" attributed to Kryloff and Bogoliuboff, Reference 5, may be more suited for this purpose since that approach yields slowly varying amplitude and phase relationships. However, for the small amplitudes involved, the additional detail does not appear to be warranted.

The magnitude of the nonlinear harmonics can best be determined by Fourier harmonic analysis of the periodic segments. The existence of nonlinear subharmonics (those of lower frequency than the driving frequency, or "basic") cannot generally be predicted because of limitations in Fourier analysis theory, but the ultra-harmonic can be predicted with fair assurance.

The corresponding amplitudes determined from such analyses are summarized for the dominant harmonics in Appendix I. Briefly, a moderately large first harmonic and a lesser second harmonic appeared in the results, as predicted in the simplified nonlinear analysis. The magnitudes are also similar, with the first harmonic reaching a maximum of about 17 percent of the fundamental at an applied frequency of about 1.7 cps for the tire force. An even larger first harmonic occurs at the same frequency for wing torsion

moment inboard of the outboard nacelle, but the fundamental amplitude is rather low at this frequency, so this is not significant. The time histories of Figure 24 and 32 also demonstrate this marked oscillation at about 3.4 cycles per second superposed on the driving frequency of 1.7 cycles per second. Since the wing modes constitute a linear set of differential equations, this cannot be a harmonic inherent within the wing structure. Rather, the predominant wing torsion mode is in resonance with the first nonlinear harmonic of gear excitation, and since wing torsion is usually less effectively damped, appreciable amplitude results. This observation does not indicate whether or not the harmonic term is in phase or out of phase with the maximum peak-to-peak amplitude of the fundamental. However, inspection of the data, and comparisons with the nonlinear power spectral density results to be shown later, indicate that these harmonics frequently are in phase with the steady state torsion moment over a broad range of the spectrum from one cycle per second to 3.4 cycles per second. This implies that the strut force must do some additional work, and there is an energy transfer which increases torsional response, at high frequency.

Similarly, inspection of the time histories for bending moment at frequencies of from 1.5 to 2 cycles per second, Figures 23, 24, and 25, indicates that appreciable subharmonic oscillation is present. The situation suggests the possibility that energy may be transferred to lower frequencies, particularly into the strut force, since the gear coupling is quite strong with wing bending modes. In fact, the effect does seem to be present in the strut force, as will be shown later. The explanation for subharmonic excitation can best be quoted directly from J. J. Stoker, Reference 3, as follows: "Any free oscillation of a nonlinear system contains the higher harmonics in profusion, and thence it is possible that an external force with a frequency the same as one of these might be able to sustain the harmonic of lowest frequency. Of course, that this actually should occur probably requires that the damping be not too great - - ." Such an explanation implies the transfer of energy from one frequency to another.

As discussed earlier, the transfer function may be obtained from the steady state oscillatory response of a linear system to a sinusoidal excitation. This suggests that a first approximation to the transfer function may be obtained by dividing the peak-to-peak amplitudes for response quantities from Figures 12 through 35, by the corresponding peak-to-peak input. A few representative values determined in this manner are plotted in figures in Appendix I, for qualitative comparison only, with the transfer functions obtained from the power spectral density analysis. In this simplified form, neglecting the amplitude and phase of the nonlinear harmonics, the magnitudes are not particularly accurate. However, it is significant that the predominant frequency response characteristics of the quantities, particularly tire force, are retained. The resonant frequencies are nearly the same, although the amplitudes are somewhat low, indicating that the harmonics are either out of phase near resonance or they shift energy to another part of the system.

The harmonically generated solutions shown in Appendix I figures are dependent upon the amplitude of the sinusoidal excitation. The greater the amplitude of oscillation, the more nonlinear harmonics are generated. This presents another problem since the transfer functions for linear systems are not dependent upon input amplitude.

Furthermore, the quadratic damping characteristics, as presented in Equation 18, tend to promote amplitude dependence. For values of strut velocity,  $\dot{s}$ , given approximately by,

$$\dot{s} < \frac{D}{C_D} \quad (55)$$

the quadratic damper will be less effective than the best average linear damper; and for

$$\dot{s} > \frac{D}{C_D} \quad (56)$$

the nonlinear damper will be more effective, thus attenuating the response more than proportional to the amplitude increase.

For a linear system, the damping force can only increase proportional to the amplitude of oscillation, as shown in Figure 124.

Thus, the selection of a driving amplitude is a problem. A reduction in drive on the nonlinear harmonic solutions can increase the transfer function peaks appreciably, since the resonances are sensitive to the lower resultant system damping. The drive amplitude was selected on the basis of the root mean square amplitude,  $\sigma_{rw} \approx .1$  ft., of the random runway data from LaGuardia International Airport, used in deriving the power spectral (PSD) transfer functions for the nonlinear system. A level of  $q = \pm .85$  inches corresponds to about  $\pm .72 \sigma_{rw}$ , which according to the normal frequency density distribution (Reference 10) should include approximately 50 percent of the runway amplitudes over all wavelengths. The driving amplitude used was slightly less for operational reasons; but the selection, though seemingly rational, was arbitrary to some extent. In Reference 23 it is indicated that  $\sigma$  is calculated from the equation (assuming a zero mean)

$$\sigma^2 = \int_0^{\infty} \Phi_q(\Omega) d(\Omega) \quad (57)$$

where,

$\Omega$  is the spatial frequency in radians per foot and  $\omega$  is the circular frequency with,

$$\omega = 2\pi f = V_H \Omega \quad (58)$$

At an average taxi speed,  $V_H = 55$  fps, it is known that most of the magnitude of  $\sigma_{rw}$  results from integration over the range from zero to 0.8 cycle per second of runway input, since the spectrum declines rapidly with frequency ( $\Phi^q(\Omega) \propto 1/\Omega^3$ , approximately). Since the system resonances occur at higher frequencies, a lower input  $q$  could rationally be selected. In fact, the input sinusoid amplitude,  $q_{max}$ , should possibly vary with frequency as follows:

$$q_{max}(f) = .72 \left[ \int_f^{\infty} \Phi(f) dt \right]^{1/2} \quad (59)$$

If this procedure were utilized, the peaks labeled as "nonlinear harmonic" in Appendix I figures would be brought in better agreement with the PSD method shown. Thus, the harmonic analysis method constitutes a valid approach in itself. Nevertheless, in view of the complexity of nonlinear representation, and the amplitude sensitivity, this approach is not warranted if useful results can be obtained by simpler methods.

#### 4. Linearized System Analysis

The principal conclusion to be derived from the preceding nonlinear analysis is that the magnitude of nonlinear effects is relatively small. Since a greater amplitude of strut oscillation would yield results more nonlinear in character, some doubt is engendered by the amplitude dependence of the strut response. However, the selection of the LaGuardia runway roughness data, as a basis for evaluation, limits the corresponding amplitude range to be applied in the development of linearization procedures. The use of a runway with above average roughness levels tends to be justified, since the adaptability of the methods studied to severe operational conditions should be an essential requirement.

The above conclusion suggests that linearization of the system nonlinearities may be feasible, provided that spring rates and energy absorption characteristics can be appropriately chosen by logical means. To test the feasibility, a more accurate method of linearization criteria is presented first, making use of the nonlinear harmonic analysis of the previous section. Later, alternative schemes with various degrees of simplification will be suggested, with the realization that a nonlinear system simulation on a computer will not always be available to the design engineer.

The foremost requirement for determining the equivalent linear damping characteristics of a nonlinear physical system is that the energy balance for the two systems be maintained on the average throughout a periodic segment of the steady state response. This implies that the instantaneous energy dissipation will usually be non-valid for the linearized system, but the principle of conservation of energy as applied to both systems will be periodically obeyed. Thus it is necessary for the equivalent linear strut damper to dissipate the same amount of energy for the same relative amplitude of strut motion.

The work done per cycle of gear motion by the damper is equal to the energy,  $E$ , dissipated by the damper per cycle, as follows:

$$E = \oint F_s \cdot ds \quad (60)$$

where the scalar product can be neglected, since force and displacement vectors are always parallel in a strut. For the nonlinear system under consideration,

$$F_s = C_D \dot{s} |\dot{s}| \quad (61)$$

where  $C_D$  is the nonlinear damping coefficient which is usually predetermined by requirements for design landing impact energy absorption. The value can be derived analytically, as indicated in Appendix J, or from drop test data on a specific shock strut. For metered orifices in the strut, the metering pins usually have a small taper ratio as positioned for the static level of strut deflection, so that  $C_D$  may be assumed essentially constant for moderate amplitudes of motion.

For the equivalent linear system, a viscous damper may be chosen as follows:

$$F_s = D\dot{s} \quad (62)$$

where  $D$  is a linear damping coefficient, to be determined by energy equivalence. With the damping forces thus defined, the equal energy requirements,  $E_{NL} = E_L$ , where NL and L refer to the nonlinear and linear system respectively, may now be stated as:

$$\oint D\dot{s}_L ds = \oint C_D \dot{s}_{NL} |\dot{s}_{NL}| ds \quad (63)$$

The nonlinear portion of Equation 63 may be evaluated directly in the computer as shown in Figures 37 and 38. The time history in Figure 37 defines the energy change,  $\Delta E$ , for the air spring and damper throughout several cycles of oscillation, and the net dissipation per cycle is given by the difference in ordinates from one peak to the next in the graph, since the spring replaces all the energy it absorbs over a cycle. Figure 38 is less useful since the small area in the elongated loop of strut force versus stroke cannot be accurately determined.

Alternatively, the energy may be obtained from phase-plane studies as shown in Figures 39 through 43. The phase relationship between damping force and strut displacement can be viewed directly in these figures. It is of interest to note that these energy loops, as they may be called, approach an ellipse in form. For a linear system they must be exact ellipses, as will be shown. The area enclosed by the quasi-elliptic curve represents the energy absorbed per cycle by the damper in the nonlinear system.

The solution for the equivalent linear coefficient,  $D$ , in Equation 63 can be obtained by making certain assumptions regarding the motion of the strut, as follows:

- (a) Assume sinusoidal motion for the linear system, so that  $\dot{s} = \omega s$   
(This is valid for steady state).
- (b) Assume that maximum strut displacement for the linearized strut is equal to that for the nonlinear strut.

From (a) above, and Equation 62, it follows that

$$F_s = D\dot{s} = D\omega s \quad (64)$$

and from (b),

$$s_{L_{\max}} \approx s_{NL_{\max}} \quad (65)$$

$s_{NL_{\max}}$  may be determined from the nonlinear phase-plane energy loops at the desired frequency. Integration of the left hand side of Equation 63 may be accomplished by noting that, for sinusoidal motion,

$$\begin{aligned} s &= s_{L_{\max}} \sin \omega t \\ D\dot{s} &= Ds_{L_{\max}} \omega \cos \omega t \end{aligned} \quad (66)$$

from which

$$\sin^2 \omega t + \cos^2 \omega t = \frac{s^2}{s_{L_{\max}}^2} + \frac{D\dot{s}^2}{(D\omega s_{L_{\max}})^2} = 1 \quad (67)$$

Hence, the integration is just the area of the ellipse defined above, or

$$E_L = \oint D\dot{s} ds = \pi D\omega s_{L_{\max}}^2 \quad (68)$$

Equating system energies, and using Equations 65 and 68, yields the relationship,

$$E_{NL} = D\omega s_{NL_{\max}}^2 \quad (69)$$

from which the equivalent linear damping coefficient can be solved as follows:

$$D = \frac{E_{NL}}{\pi \omega_s^2 N_{NL \max}} \quad (70)$$

Inspection of the several energy figures reveals that the energy per cycle and the strut amplitude vary from one steady-state frequency to another. Each set of values yields a different magnitude of  $D$  from Equation 70. However, the selection is simplified by considering the transfer function peaks and how they affect the repeated load occurrences which are of major importance in fatigue and maximum design loads prediction.

Tire force occurrences per second,  $N_p$ , may be defined according to References 2 and 12 as follows:

$$N_p = \frac{1}{2\pi} \left[ \frac{\int_0^\infty \omega^2 \Phi_{F_t}(\omega) d\omega}{\int_0^\infty \Phi_{F_t}(\omega) d\omega - \bar{F}_t^2} \right]^{1/2} \exp - \frac{(F_t - \bar{F}_t)^2}{2 \sigma_{F_t}^2} \quad (71)$$

where  $\bar{F}_t$  is the average level of tire force. Realizing that the output power spectrum,  $\Phi_{F_t}$ , is proportional to the square of the transfer function,  $T_{F_t/q}$ , since,

$$\Phi_{F_t} = \left| T_{F_t/q} \right|^2 \Phi_q \quad (72)$$

and noting that the transfer function peaks from the nonlinear solutions (which were derived prior to the linearized analysis) are nearly a decade higher than off-resonant points in the spectrum, then it can be concluded that the integral functions in Equation 71 will be most dependent upon the magnitude of the peaks in the response. Furthermore, only two principal peaks occur in the strut force which is the main source of

excitation for the remainder of the system. The high frequency peaks in the bending and torsion moment transfer functions are mostly uncoupled with gear force, apparently, and therefore will not affect strut damping estimates. Since the vehicles usually possess low damping, the resonances may be easily predicted to the desired degree of accuracy using linearized springs and the simplified approaches suggested in Appendix H.

With the above observations in mind, the energy calculations from Figures 39 and 40 will be of primary interest for the predetermined resonances of approximately 0.9 cps and 1.67 cps. Using Equation 70 with data from these figures results in two damping factors,  $D = 138$  lb-sec/in. and  $D = 231$  lb-sec/in. The most reasonable alternative at this point is to select the average value,  $D = 185$  lb-sec/in., as the equivalent viscous damping coefficient to study the feasibility of linearization.

To determine the sensitivity of this approach to the calculated resonance frequency, Figure 41 presents the phase-plane diagram at 1.75 cps, slightly off from the second resonance peak. A definite "beating" phenomena, characteristic of nonlinear systems, appears in the results. The large and small cycles of oscillation repeat indefinitely in the steady state. However, the average energy per cycle from both energy loops yields a value of  $D = 243$  lb-sec/in., or less than 5 percent deviation from the value at the 1.67 cps resonance.

Ultimately, the completely analytical method described in Appendix J is the ideal approach for deriving the nonlinear and linear damping relationships. Preliminary calculations indicate that the analytic solution for the nonlinear system predicts the correct average value,  $D = 185$  lb-sec/in., for appropriate boundary conditions. Further research is required to determine the validity of the method when applied to other aircraft and operational conditions.

If sufficient airplane data are not available to perform the more accurate preceding analyses, a very simple approximation to the linear damper may also be derived by the method shown in Appendix G. Such an analysis may be useful for preliminary design studies.

The polytropic air compression spring in the strut constitutes another nonlinear property of the system which must be linearized. The spring force-deflection curve shown in Figure 44 is exponential in character, since the slope increases markedly as the deflection increases.

For normally distributed data most of the load occurrences are grouped around the mean value, so it seems reasonable to select the linear slopes as tangents to the curve at the mean load level. The static load levels shown are approximately the mean values; and they vary with taxiing speed, since added wing lift will tend to relieve the "static" load on the main landing gears. This tangency yields a spring constant of  $K_a = 11,900$  lbs/in. at 88 fps and  $K_a = 16,910$  lbs/in. at 22 fps. The corresponding slopes are arbitrarily drawn in Figure 44 so as to intersect the curve at approximately  $\pm 2\sigma_F$  pounds

of load on either side of the mean at each speed. The normal curve, Reference 10, indicates that nearly 95 percent of the data should lie within this range of load, so that a study of the nonlinear slope variation in this broad band should give a very conservative estimate of possibilities. Using root-mean-square values from nonlinear data, brief inspection of the nonlinear curve indicates a fifty to four-hundred percent change in slope is possible depending on taxi speed. However, these are upper limits and will occur only rarely in practice.

A more reasonable selection can be made by selecting a narrower range of values such as  $\pm \sigma$  from the mean, which will still include 68 percent of the data, and then forcing the slope-intercept formula to give the same potential energy charge from maximum to minimum load for the linear and the nonlinear systems. This requires that the areas under the original curve and the linear approximation must be equal over the desired range of load. Thus a curve can be established by taking the median slope from the tangencies at 88 fps and 22 fps, and selecting a range from  $-\sigma_F$  (-5,500 lbs) below the high speed static level to  $+\sigma_F$  (-2,400 lbs) above the low speed static load level. The corresponding displacements may be labeled  $s_a$  and  $s_b$ , respectively, and an integration performed on Equation 17 for each strut as follows:

$$\int_{s_a}^{s_b} [K_a s + K_b] ds = \int_{s_a}^{s_b} \left[ \frac{A}{(b-s)} + K \right] ds \quad (73)$$

Since all other values are known, and  $K_a$  may be selected approximately as a median value of 14,075 lbs/in., the linear intercept,  $K_b$ , can then be solved as given in the figure.

The selection of load range is somewhat arbitrary, and root-mean-square levels may not always be known for the nonlinear system. However, aero-space craft load factors or center of gravity accelerations are frequently known for similar vehicles, as stated in Appendix G, so using Newton's law and steady-state assumptions an estimate of for strut force may be derived as,

$$\sigma_{F_s} \approx M_o \sigma_{Z_f} \quad (74)$$

At 88 fps the result is  $\sigma_{F_s} = 5260$  pounds which is a very good estimate compared with the true value of 5500 lbs for the nonlinear PSD data.

The tire force-deflection curves present much less of a problem from a nonlinear standpoint. Figures 45, 46, and 47 for three tire pressures indicate that these curves are nonlinear at low load levels, but near static load they tend to be quite linear. Most tires exhibit similar characteristics, as indicated in References 7 and 8, unless the tire is

bottomed on the wheel rim. Therefore a detailed linearization process is somewhat superfluous for the tire used in this analysis. In the event that a highly nonlinear tire appears in a specific case, an equivalent energy procedure similar to that described for the strut air spring can be applied; so the pertinent static and root-mean-square load levels are sketched in the figures as an illustration of the approach.

The nose landing gear strut and tire forces given in Figures 48 and 49 are linearized by the same procedures for use in the multi-gear analyses, where a tandem or tricycle-tandem gear arrangement is used on the vehicle.

The average (quasi-static) load on the nose gear depends on many unknown parameters such as wing lift, thrust, flap and elevator settings, center-of-gravity location, and pilot actions, so an arbitrary value of nearly 5,000 pounds per strut was selected. The nose gear of the aircraft used for analysis consists of two tires and a single strut; and since symmetry about the roll axis is assumed, the load parameters are divided up accordingly for use in the equations. The strut of the nose gear has an orifice nearly the same as that for the main landing gear, so the linear damping coefficient is assumed to be the same per strut for all gears.

The structural damping and the steady and nonsteady aerodynamics employed are essentially the same in both the linear and the nonlinear systems. Additional physical constants for the system may be found in Appendices B and C of this report as applied in the linear and nonlinear systems, respectively.

The analog simulation is conventional and involves equipment as described in Appendix D, with the exception that nonlinear function generators and FM tape recorders are not required. Frequency resolvers are employed to measure the phase angles for the complex transfer functions which result.

Initially some check runs were made to determine the magnitude of the transfer function for tire force  $T_{F_{t/q}}$  at the known resonances of the system, since these are the most important points. This could be accomplished by driving the system with a sinusoidally varying ground profile,  $q = q_0 \cos \omega t$ , until a steady state is observed on a recorder. The quantity of peak-to-peak response divided by input yields one point on the transfer function. Care must be exercised in varying the frequency input to be sure the true "peak" frequency is attained.

Before such results can be compared with transfer functions obtained by power spectral density (PSD) methods, the filter characteristics of the spectral analysis procedure must be considered. These characteristics and corresponding attenuation factors as shown in Figure 50, are described in detail in Appendix D. Thus, to determine the comparable load magnitudes, some knowledge of system damping characteristics near resonances must be calculated. This can be obtained by measuring the logarithmic decrement, or the rate of decay in the response, when a smooth harmonic excitation

of the system is suddenly removed. The formula for system critical damping,  $c/c_o$ , may be expressed decimally as:

$$c/c_c = \frac{1}{2 \pi r} \ln \frac{G_o}{G_r} \quad (75)$$

where  $G_r$  is the decayed amplitude  $r$  cycles beyond the initial amplitude  $G_o$ .

The variation of system damping with strut damping coefficient, or speed, at nominal peak frequencies of .95 and 1.65 cps, is presented for three tire pressures of interest in Figures 51, 52 and 53. By coincidence, it appears that both frequencies exhibit similar damping for the optimized linear strut damping,  $D = 185$ . An average taxi speed of 55 fps was selected for the first figure, since the variation with speed is presented for the .95 cps peaks in Figure 52 and for nominal 1.65 cps peaks in Figure 53, while holding strut damping constant. This latter figure indicates a slight variation of damping with tire pressure, whereas the .95 cps results show no similar dependence on tire pressure. The nonlinear transfer functions indicate similar trends, as will be shown in the Results and Discussion Section.

Some dependence on tire pressure may be expected, in general, since system critical damping may be defined approximately as

$$c_c \approx 2 \sqrt{K_f M_o} \quad (76)$$

which indicates a proportionality with the square root of tire and strut stiffness. The effect of tire pressure increase is to stiffen the tire, thus causing the strut to work harder and to absorb more energy from the system.

By using appropriate interpolations of the above figures, system damping may be estimated with negligible error for any combination of speed, strut damping and peak frequency. However, peaks in wing bending moments and torsion moments above 3 cycles per second are apparently insensitive to either speed or strut damping, and always indicate slightly over two percent of critical damping. These higher mode responses are nearly uncoupled with the remainder of the system as stated in earlier discussions.

The variation of transfer function peaks for tire force,  $F_{t/g}$ , versus strut damping  $D$ , is presented in Figure 54, after application of attenuation factors as described previously. The single landing gear program is applied initially to simplify results. These curves are useful for checking the accuracy obtained with the linearized damping coefficient,  $D = 185$  lb-sec/in., relative to peak magnitudes of the PSD transfer functions for tire force. At this average taxi speed, the maximums at both resonances agree quite well on the average, as will be shown in the Results and Discussion Section.

Subsequent to this preliminary analysis, the full frequency response curves are established by calculating the amplitude and phase from Nyquist diagrams. An example of this form of presentation is shown in Figure 55 as obtained directly from the computer on an X-Y plotter. The absolute magnitudes,  $R = |T(\omega)|$ , obtained therefrom are presented as a function of frequency in the Results and Discussion Section for the most significant load quantities.

## SECTION IV

### RESULTS AND DISCUSSION

The results obtained from the analyses are presented in time history, rate of occurrence, probability, power spectral, cross-spectral, and transfer function form. These quantities from the nonlinear system are used for the evaluation of the linearized transfer functions are developed in later phases of the research program.

The principal responses that are studied may be summarized as follows:

$\ddot{Z}_f$  Airplane center of gravity vertical acceleration.

$F_{ti}$  Vertical reaction force on the  $i^{\text{th}}$  landing gear (tire force).

$M_{x1}$  Wing root bending moment. (The nominal wing root station for testing and analysis is usually chosen as approximately 90 inches from the example airplane centerline, or wing station 90).

$M_{y6}$  Wing torsion moment inboard of the outboard nacelle. (This location corresponds approximately to wing station 350.)

In addition, the runway amplitudes,  $q$ , are analyzed as generated in the computer for excitation of the airplane. Several other load points on the airplane are selected, in addition to the primary quantities, to complete the load survey. It was difficult to select, at the initiation of the program, those stations which would be of greatest significance for transfer function development.

The sign conventions for displacements and loads may be found in Figure 2 or Figure 3, or as defined in the List of Symbols.

Results of the direct dynamic analysis are presented for 4 speeds while taxiing over the runway at LaGuardia International Airport which is designated in Reference 25 as runway 5L. A detailed tabulation of the amplitudes for this runway is given in Reference 27.

Parametric variations are made for two principal nonlinear components of the landing gear. In addition to the standard strut orifice diameters, larger and smaller orifices are examined for the main and nose landing gears. Also, the effects of higher and lower tire pressures are studied relative to the standard configuration for the example airplane. The particular values used are presented in detail in Appendix B, and also on the figures, where pertinent.

Unless specific statements are made in the key of each figure, it should be assumed that the configuration is standard for the example airplane.

Sample time histories as obtained from the analog computer are presented in Figures 56 - 59. The time scale can be derived by using the timing marks at the bottom of each page. The spaces between the marks represent exactly 11 feet of runway, so division by the taxi speed in feet per second will yield a time increment in seconds, as determined by the analog scaling.

In the multi-gear time history, Figure 58, the nose gear tire force,  $F_{t1}$ , contacts the beginning of the runway some time previous to the front main gear force,  $F_{t2}$ , because of the natural sequence of the struts in passing over the runway.

Most quantities are presented as increments from a static equilibrium or average value. Since wing lift is assumed to vary with speed, the equilibrium gear forces are plotted versus taxi speed in Appendix B for easy reference.

The synthesized power-spectral density of the LaGuardia runway amplitudes is presented in Appendix K in the space-plane. In the time-plane, the power density is expected to be a function of the velocity as follows:

$$\Phi(\omega) = \frac{1}{V_H} \Phi(\Omega) \quad (77)$$

where  $\Omega$  is the spatial frequency in radians per foot, and  $\omega$  is in radians per second. Also,  $\omega = V_H \Omega$ . (78)

The above relationships will not be satisfied by these results at every point in the spectrum, however, since time is scaled in the computer to simulate taxi speed. The scaling requires that a new set of active filters be "designed" or set-up for each speed; and, although great care is exercised to try to obtain the same filter characteristics at each frequency point, some small differences in components will distort the power density slightly.

### 1. Direct Power-Spectral Analysis of the Nonlinear System

Figures 60 - 62 present the power spectra of the main gear forces for the nonlinear, single gear analysis on the computer at four taxi speeds. As discussed earlier, the single gear analysis is useful for preliminary parametric studies. These results may be interpreted as representing a tricycle or tail wheel airplane taxiing with sufficient speed to lift all but the main gears off the ground.

A visual inspection of the data reveals that peaks on a given spectrum coincide in frequency with predominant harmonic content present in the corresponding time histories. It is apparent that forcing frequencies as well as natural frequencies could influence the peaks in output spectra; but the input spectrum is a smoothly declining function as shown in Appendix K, so the response is mostly determined by the transfer function as shown in Equation 6D in Appendix D. Each frequency point on a transfer

function is dependent on steady-state conditions where only the forcing frequency remains in the response. Since the transmittance of each transfer function is greatest at resonance, natural frequencies of the system are expected to appear predominantly in the response.

Both the tire force spectra, Figures 60 and 61, and the strut force spectra, Figure 62, are nearly identical in appearance. Therefore it can be assumed that the effects of the unsprung mass of the landing gears are not very significant in steady-state response at the most important frequencies. The two principal peaks occur at frequencies above and below the first wing bending frequency (about 1.27 cps), so the gear force coupling with the wing in steady state may at first appear to be small. However, the translational natural frequency of the rigid body mass of the vehicle on the main landing gears is approximately 1.25 cps, using linearized spring constants from Equation 54. In this instance, the wing and gear frequencies form a strongly coupled pair which at resonance split into two new system modes at higher and lower frequencies from those of the uncoupled system. Similar phenomena may be observed in vibration absorber theory as described in Appendix H. Also, the transformed linear system of Appendix C makes the analogy even more apparent, since the LaGrangian generalized coordinates are replaced by rectangular cartesian coordinates corresponding to those in Appendix H.

The broadest possible range of strut and tire parameters for this aircraft is selected for the parametric variations. The corresponding strut natural frequencies change noticeably, but this dual mode phenomena appears consistently in all results; so the phenomena is anticipated, in general, for any aircraft having flexible structural modes near the strut natural frequencies.

The response of the multi-gear, or normal tandem-gear configuration of the example airplane is also computed in power spectral form. Generally, the peaking characteristics of the curves are the same as those for the single gear analysis. The small differences that do appear will be discussed more fully in later comparisons with the linearized data.

Rate of load occurrence and probability data for the previously discussed loads are presented in Figures 63 through 73 for the multi-gear nonlinear analysis. All loads and accelerations are given as dynamic increments from a static equilibrium, or average value, corresponding to the zero on the load scale. The probability curves are normalized as the probability of equaling or exceeding a given load level. Direct data sampling techniques have been used, as described in Appendix D, rather than the assumed Gaussian distribution, Equation 5D in Appendix D. Therefore, the unsymmetry in the distribution of positive and negative increments is clearly observable in many cases. This is particularly true for the vertical tire force, as was expected from its nonlinear characteristics. However, since the strut is the predominant driving mechanism, the skewness of the load occurrences may appear in any output quantity.

For nearly all situations, the rate of load occurrences increases with increasing taxi speed, as may be intuitively expected.

The transfer functions as derived from Equation 6D in Appendix D for the above loads are presented in Figures 74 through 78 for comparison with the linearized results to be discussed later. The peak-frequency characteristics are very similar to those for the power spectrum, as is expected. The wing bending moment shows a relatively high peak at the second wing bending frequency, 4.9 cps; and torsion moment indicates a large response at 3.4 cps which is the predominant wing torsional frequency. Wing root bending moment shows very little response corresponding to the 1.65 cps. system mode. Further analysis indicates that at this frequency the first free-free wing mode and the strut are oscillating at large amplitude, but out of phase with each other. Thus, the rigid body translational mode tends to cancel the loads from the first uncoupled bending mode.

The nonlinear transfer functions are more useful than the power spectra in evaluating linearized transfer functions for later phases of the program. The more uniform distribution of peaks with frequency, for functions normalized to a smoothly varying input spectra, is more amenable to visual interpretation.

It is apparent that the primary usefulness of the occurrences and probability data is to indicate trends in the prediction of fatigue loads spectra for a given airplane or configuration. There is no doubt as to the validity of the direct sampling methods, whereas the Gaussian assumption may not be applicable to the response of a nonlinear system.

As discussed previously, the methods of generalized harmonic analysis are not applicable, strictly speaking, to nonlinear systems. However, these methods have been assumed valid in earlier studies (References 11, 18, 20, 21, and 28) and the results have appeared to be reasonably applicable. The research program discussed herein is somewhat more extensive than the previous studies, and a prime purpose is to check the validity, or possible omissions, of these theoretical techniques.

## 2. Cross-Spectral Analysis Results

An additional check can be made through a cross-spectral density analysis of the same data. It is recognized that consideration of phase relationships between the excitation and the response in the complex plane could possibly reveal additional information on nonlinear phenomena.

A sample cross-spectral density for rear main tire force,  $F_{t3}$ , cross correlated with the runway derivatives,  $\dot{q}_3$ , is presented in Appendix I for the standard multi-gear configuration of the example aircraft. Comparison of these data in the form of transfer functions from Equation 7D in Appendix D with corresponding PSD data, as shown in Appendix I, indicates that the peak frequencies and amplitudes are not appreciably different for tire force.

It seems apparent, then, that cross spectral analysis will not yield new information and that the power spectral transfer functions are valid, within the mathematical assumptions, as shown.

### 3. Linearized System Results

The linearized system has been analyzed by the procedures given in the Theoretical Discussion section of this report. The optimum linearized damping coefficient of  $D = 185$  lb-sec/in. is assumed to correspond to the normal gear configuration having a quadratic damping coefficient,  $C_D = 14.1$  lb-sec<sup>2</sup>/in<sup>2</sup>. The equivalent linear transfer functions shown are derived from the analog computer, but the analytical solutions in Appendix C yield essentially the same answers.

The linear results are compared with the nonlinear transfer functions for single gear analyses in Figures 74 to 77 for an average taxi-speed, and remarkably good agreement can be observed in general. Since the landing gear reaction forces constitute the principal nonlinearity of the system, results for tire force in Figure 74 are most significant in that the linearized dampers and springs do adequately duplicate the peaks. The absence of major resonances beyond 2 cycles per second indicates very little coupling between the higher modes and the strut.

The transfer functions for tire force are compared in Figure 78 at the highest taxi speed to see if the validity is impaired by any velocity dependence. Again the maxima are in agreement, but the linear system shows some minor attenuation off from resonances for both speeds. This may be expected, since the linear damper was selected to match the higher damping requirements of the nonlinear gear at the larger strut amplitudes near resonances. Therefore, slight overdamping occurs on sidebands in the spectrum.

The above result is not particularly disadvantageous, however, since for statistical purposes the load occurrences are dependent upon integral functions of the output power spectral densities computed from Equation 6D in Appendix D. Sample power spectra are shown in Figures 79 and 80, and low frequency peaks are greatly accentuated due to the nature of the input spectra,  $\Phi_g$ . Thus the integrals in Equation 5D in Appendix D are most sensitive to the accuracy at resonances rather than on sideband frequencies.

The next phenomenon investigated is possible aircraft pitching effects on a multi-gear arrangement. The main landing gears are mounted close together in tandem, with the nose gear over 30 feet forward, as described previously. It was surmised that a study of variable phasing between nose and main gear forcing functions would reveal any steady state pitch effects. The most noticeable effects should appear for comparisons between cases with these nose and main gears driven out of phase and in phase. Such results are shown in Figures 81, 82 and 83 for tire force and for wing torsion moment, respectively. No appreciable differences can be observed in these figures, except at a very low amplitude at 0.5 cps, or less, where computer solutions are impaired by low voltage "noise" levels. This frequency corresponds to the anticipated pitch resonance range in this case, and it is apparent that this frequency is sufficiently low that it has no noticeable coupling with the higher frequencies of the system. There is a

very slight tendency for torsion moment to be reduced on the resonance peak for the out-of-phase condition, so what little pitch is present tends to cancel some wing torsion. However, either result is within the accuracy of the nonlinear results used for comparison, so the difference is not significant. Similarly, the other sampled loads indicated no significant sensitivity to phasing or pitching effects.

To determine whether or not tire pressure variations, with corresponding strut frequency changes, could affect these results, in-phase and out-of-phase data were studied at different tire pressures for the principal loads and accelerations. Again, no phase sensitivities were observable during analysis, so only the in-phase results are given for comparison with nonlinear transfer functions obtained by PSD methods as shown in Figures 84 to 87. The agreement is very good over the frequency range, in general, as was true for the single gear examples.

#### 4. Parametric Variations

The maxima are of greatest interest, so they are presented as parametric variations with tire pressure, taxi speed and strut damping coefficient in the subsequent figures.

The peak variations with tire pressure are shown in Figures 88 through 90 for several load quantities, in comparison with corresponding nonlinear results. Only the nominal frequency of the transfer function peak is given, since the frequency varies with pressure. The agreement is relatively good in both magnitude and trend, except for the nominal 0.93 cps peak on torsion moment. This is probably explainable in terms of the shift of energy to other harmonics in the nonlinear system at this frequency, as was discussed in the section on nonlinear harmonic solutions. Other minor discrepancies also are probably attributable to this phenomena.

The tendency for tire force peaks to increase with increasing tire pressure is of interest, so these are studied additionally in Figures 91 and 92. The linearized tire spring constant,  $K_t$ , in Figure 91 increases nearly 30 percent in transition from 60 psi to 120 psi (maximum rated pressure) in the tire. However, the ratio of tire transfer function to tire spring constant only shows a minor decline with increasing tire pressure. Therefore the increase in the maximum tire force is nearly proportional to tire spring stiffness; but some attenuation from increased strut damping is observable, since a stiffer tire tends to work the strut more severely.

Since no additional effects due to phasing are observable in the preceding multi-gear parameter studies, the remainder of the data is determined principally for single gear analysis, although some additional multi-gear data are given for comparison.

Variations of peaks with taxi speed are presented in Figures 93 through 96 for comparison with nonlinear solutions. Logarithmic plots are more appropriate, since the analysis is primarily interested in response power, which is usually shown in this form for statistical purposes. Similarly, the variations with strut damping coefficient are given in Figures 97 through 106. Trends are nearly the same in most instances, and the magnitudes are in moderately good agreement.

At this point it seems apparent that the multi-gear PSD data on the tire force consistently falls below the single and multi-gear linear data, but by varying amounts. Yet the single gear nonlinear data, which are only available for the center condition on the cross-plots for tire pressure and damping, are higher and in relatively good agreement with the linear data.

A closer reanalysis of the nonlinear data given previously was made as shown in Figure 107 to examine this characteristic of the functions. Although the 0.95 cps peak for tire force shows fair agreement, both maxima are lower for the multi-gear analysis, especially at 1.65 cps. The situation is difficult to explain since the pitching differential equation, Equation 4, represents a predominantly linear response which should be no different in the linear and the nonlinear systems. No subharmonic response near the pitching frequency has been detected near these resonances in the transfer function. Therefore, the only conclusion possible is that some unknown increment of attenuation was present in either the direct dynamic analysis over the random runway profile, or in the PSD analysis of the multi-gear data.

The true source of discrepancy cannot be discovered without major reanalysis, but it is apparent that the single gear data are more consistent with the remainder of the linear data within rational arguments on pitching and gear force phasing effects.

As a result, the single gear nonlinear data are plotted, at the only available center point, in Figures 97 to 106. Parametric variations of the transfer function peaks with  $C_D$  are only available for the multi-gear nonlinear studies, so the variations of these data are extrapolated as shown on the figures by a dotted line through the known single-gear point. Viewed in this manner, which is believed to be more rationally correct, the data for the linear and nonlinear systems are in quite good agreement, except for torsion moment at low frequency, as explained before. Appendix F shows the complete transfer functions for the increased and decreased damping coefficients corresponding to the above parametric data.

The energy phase-plane diagrams discussed earlier are only available for the median (standard) damper of the nonlinear system. Therefore, within the simplified theory given in Appendix G, the linear dampers are just taken proportional to the nonlinear coefficients. The assumption is the best on the average; but, because the maximum strut amplitude varies nonlinearly with the damping in the true system, the linear damper should not be varied quite so much as indicated. This is most apparent in Figures 101 and 102 for C.G. acceleration.

Assuming the right hand side of Equation 63 can be approximated by an ellipse, and using Equation 64, the linear D may be solved as

$$D \approx \frac{\pi C_D \omega_s^2 NL^3}{\pi \omega_s^2 L} \quad (79)$$

Then, using Equation 65,

$$D \approx C_D \omega s_{NL} \quad (80)$$

Solving for  $s_{NL}$  from Equation 17, and ignoring  $\gamma_i$ ,  $K_i$ , and the subscripts:

$$s_{NL_{max}} \approx b - \frac{A}{F_{a_{max}}} \quad (81)$$

Substitute Equation 81 into Equation 80, then,

$$D \propto C_D \left( b - \frac{A}{F_{a_{max}}} \right) \quad (82)$$

where  $f_{a_{max}}$  can be obtained from a linear system curve as shown in Figure 54, with simple iteration on  $D$ , and using the approximation that  $F_i \approx F_a$ .

This proportionality can be used to estimate a more appropriate value for  $D$  than that used in the figures. The difference is small, but it would improve the agreement. Also, the theoretical methods of Appendix J can be extended to improve the damping estimates.

### 5. Statistical Comparisons

Since, for fatigue loads purposes, the statistics are of primary interest, the load rate of occurrence is calculated for 10 nominal levels from Equation 5D in Appendix D, which makes the assumption of a Gaussian - normal frequency density distribution. The input runway amplitudes are Gaussian distributed, so for the linear system, the output response must also be Gaussian in nature. The response power spectra for use in these calculations are presented in Figures 108 through 111 as obtained from the transfer functions applied in Equation 6D in Appendix D.

To obtain a common base of comparison, the nonlinear power spectra discussed previously are also integrated as shown in Equation 6D in Appendix D and presented on Figures 112 through 123 as nonlinear (Gaussian) results. The agreement with the linear (Gaussian) data is generally good, as would be expected from the agreement of the power spectra in Figures 108 through 111.

The curves in Figures 63 to 73 indicate that the nonlinear data is non-Gaussian distributed. Skewness factors,  $\alpha_3$ , as high as  $\pm 7$  or as low as  $\pm 0$  can be computed, depending on selected load level, where  $\pm 2$  is considered statistically significant in Reference 10. A sample load occurrences variation for tire force, obtained by direct sampling methods, is shown in Figure 113 for comparison. The data are somewhat

different in distribution curve shape, and about six times higher in average rate of occurrences. To eliminate the effects of local curvature, a Gaussian curve was fitted to the direct sampling curves in every case by the method of least squares. These resultant curves shown in Figures 112 to 123 are generally parallel to the linear occurrence variations, but they are consistently higher.

A qualitative explanation for this can easily be given. In the linear system, only one frequency of oscillation can result for one frequency input. Conversely, the nonlinear system is known to possess several harmonics of response over the fundamental, and possibly some subharmonics, as shown in Appendix I. For every cycle of input, therefore, many cycles of response can result at any load level, since these harmonics are distributed profusely throughout the spectrum. The average frequency over the resonances for tire force, preferably weighted according to spectral amplitudes from Figure 108 can be assumed at about 1.25 cps, which would be similar to the fundamental for the linear system. The corresponding first and second ultra-harmonics of the nonlinear response should average about 2.5 cps and 3.75 cps, respectively. The ratio of peaks present according to this simplified analysis would be about  $7.50/1.25$ , or about 6 more occurrences in the nonlinear system compared with the linear system. In practice, even higher ultra-harmonics could be present, although the data for Appendix I does not indicate this. Therefore, the generally higher level of load occurrences for the nonlinear data in the figures can be rationally explained.

The load occurrences for tire force in Figures 112, 113, and 114 indicate an interesting trend; increases in tire pressure increase the Gaussian peak load occurrences of the nonlinear system more than proportional to that for the linear system. At low incremental forces, the agreement between the two systems is good, within the Gaussian assumption. However, at very large load levels, a stiffened tire (higher pressure) will result in more strut telescoping action, thus increasing the magnitude of the damping forces for the nonlinear system more than proportional to those for the linear system. A study of Figure 124 for strut damping force versus strut velocity will reveal that the nonlinear system damping force is sensitive to load amplitude, whereas the linear damping force increases only proportional to amplitude.

A possible counteractive effect is the predicted appearance of more of the higher nonlinear harmonics for increased amplitudes of strut motion. This phenomena would tend to alter the load occurrences under the Gaussian assumption through the effects on the higher frequency power spectral amplitudes used in Equation 5D in Appendix D. The exact magnitude of this effect is difficult to predict analytically.

These results probably show an extreme effect, since the assumed tire pressures range from less than the minimum for the aircraft to the maximum rated pressure for the tire. At the average pressure, however, the linear system load occurrences on the tire are in excellent agreement with those for the nonlinear system, as shown in Figure 113 under the Gaussian label.

Even these minor deviations in the data could perhaps be removed by using a better system damping estimate. The closed form solution to the nonlinear system equations obtained in Appendix J, by the application of elliptic function analysis, offers the most promising means for improved system damping estimation. Only the feasibility of such a method is to be studied as part of this program, but the results for damping factors as shown in Appendix J are very encouraging. Further research is needed to determine the accuracy obtainable for other aircraft, and the possible simplifications that may be achieved.

Similarly, the effects of nonlinear ultrasonic subharmonics on repeated loads prediction should be the subject of future research. There is some question as to whether this larger number of cycles of load, at relatively low amplitude, can markedly reduce fatigue life of a vehicle. The various theories of fatigue life available, as indicated in Reference 16, do not always agree on the relative importance of cycles and stress levels. For example, resonance seems to be an essential factor in the fatigue failure of a panel subjected to jet noise or buffeting, which implies that, for root-mean-square stress levels low enough to result in long life, the damage is done by only a very few of the stress reversals, perhaps fewer than 2 percent; and these stresses are of high magnitude averaging over three times the root-mean-square level. On the other hand, the commonly accepted Miner's theory predicts that a large number of stress reversals at relatively low amplitude may be of most significance in many cases. Depending on which theory is applied, the nonlinear harmonics may or may not be important to the cumulative load occurrences.

The comparison with Flight Test data, shown in Appendix K, gives added encouragement that the methods of analysis developed in this investigation will yield valid predictions of aircraft loads.

## SECTION V

### CONCLUSIONS

Nonlinear and linearized alighting gear systems of advanced flight vehicles have been studied by mathematical and automatic computer techniques with the objective of determining methods of dynamic analysis. Repeated loads for ground operations of aerospace vehicles are of primary interest; and the development of simplified procedures, where accuracy permits, have been emphasized.

The principal conclusions of a general nature may be summarized as follows:

- (1) The direct dynamic analysis, using full nonlinear properties of shock struts, structural flexibility and a known runway profile, constitutes a useful and valid technique for the prediction of repeated loads during ground operations. Most organizations in the aero-space field possess analog equipment similar to that utilized herein, and application of the special circuits and techniques developed as a part of this research enables the determination of transfer functions for taxiing. The only remaining task is to select standardized runway spectra for application to design.
- (2) Repeated loads derived from the direct analysis are more accurate, in that the frequency density distributions are non-Gaussian in nature; and they apparently are an order of magnitude higher in rate of occurrences, due to nonlinear harmonic generation.
- (3) A detailed analysis of the nonlinear system, subjected to a cosinusoidally varying forcing function, indicates that the principal nonlinear characteristic of the solutions is the nonlinear ultra-harmonic content. However, these harmonics usually contribute less than about 20 percent of the principal amplitude of response, indicating that linearization can be expected to yield reasonable results.
- (4) Closed form analytical solutions obtained by perturbation methods applied to simplified nonlinear systems verify the order of magnitude of nonlinear effects as predicted by the more complete nonlinear harmonic analysis.
- (5) Equivalent energy requirements are established which enable equivalent linearization of the nonlinear system.
- (6) A closed form analytical solution of the linear system is derived, assuming a slight simplification, and the results agree very well with a more accurate representation on an analog computer.

- (7) The linearized results in the form of transfer functions, power spectral densities, and cumulative load occurrences are generally in good agreement with corresponding results from the nonlinear analysis, provided certain nonlinear system effects are considered. In particular, the ultra- and subharmonic frequencies which appear in the nonlinear solutions can be used to predict an amplification factor which should be applied to load occurrences obtained from a power spectrum through the Gaussian assumption.
- (8) Comparison of the analytical results with preliminary flight test data indicates relatively good agreement.

Some additional problems resulting from the nonlinear system harmonics are discussed, and additional research and development is recommended on the following page to clarify these details from related technical fields.

## SECTION VI

### RECOMMENDATIONS

In view of the results of this investigation, the following recommendations should be considered for future research.

- (1) A synthesis of the large amounts of terrain roughness data presently available through efforts of WADD, AGARD, and NASA should be attempted, so as to develop an optimum roughness spectra for design analysis. It should be remembered that a rough runway is not necessarily conservative, because of the nonlinearities present in the system. Subsequently, the possibility of generating this synthesized spectrum with a "shaped" white noise generator for use in a direct dynamic analysis should be investigated.
- (2) The possible existence of a closed-form analytical solution for the nonlinear system, including structural flexibility and a steady-state forcing function, should be investigated.
- (3) The general validity of statistical load occurrence formulae presently in common use throughout the industry should be examined, particularly as they are used for nonlinear systems. The techniques of engineering cybernetics as applied to closed loop servomechanisms, and control systems of aero-space craft, may be markedly effected by the results of such an investigation.
- (4) Further comparisons of analysis and flight test data should be made as more data become available.

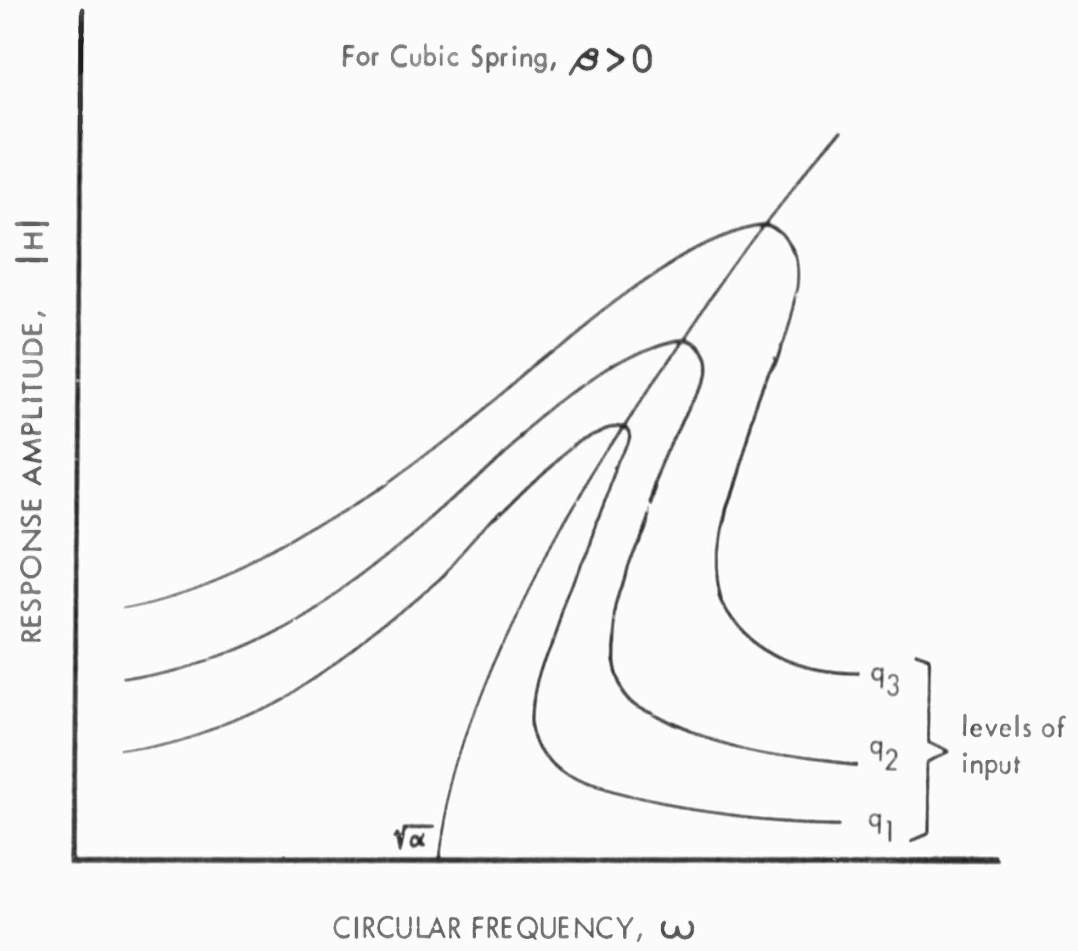


FIGURE 5 : Typical Nonlinear Frequency Response Variation For Single Degree of Freedom Analysis

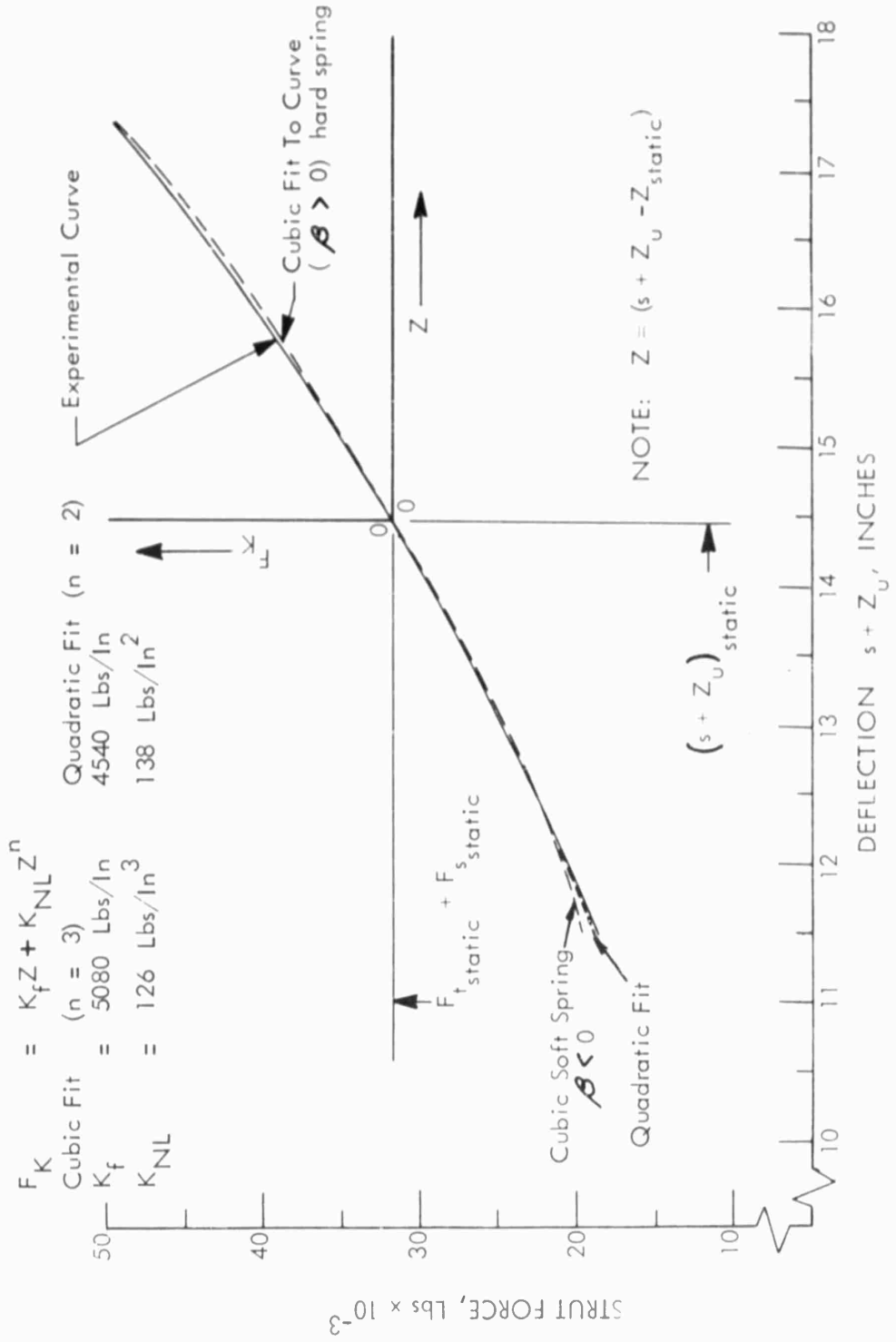


FIGURE 6 : Simplified Nonlinear System, Spring Force Deflection Curve

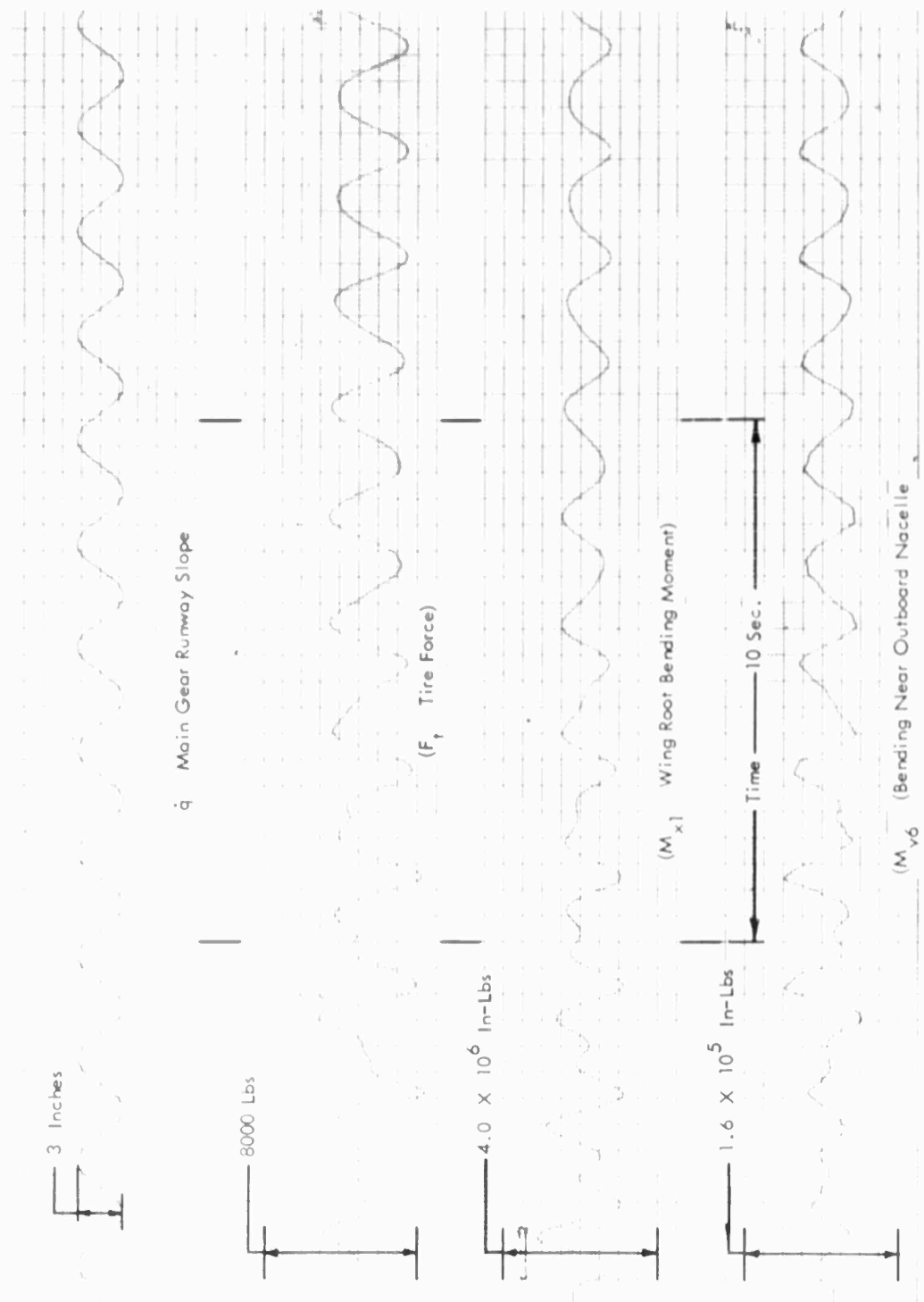


FIGURE 7 : Transient and Steady State Response of Nonlinear System to Harmonic Excitation at  $f = .50$  Cycles Per Second.

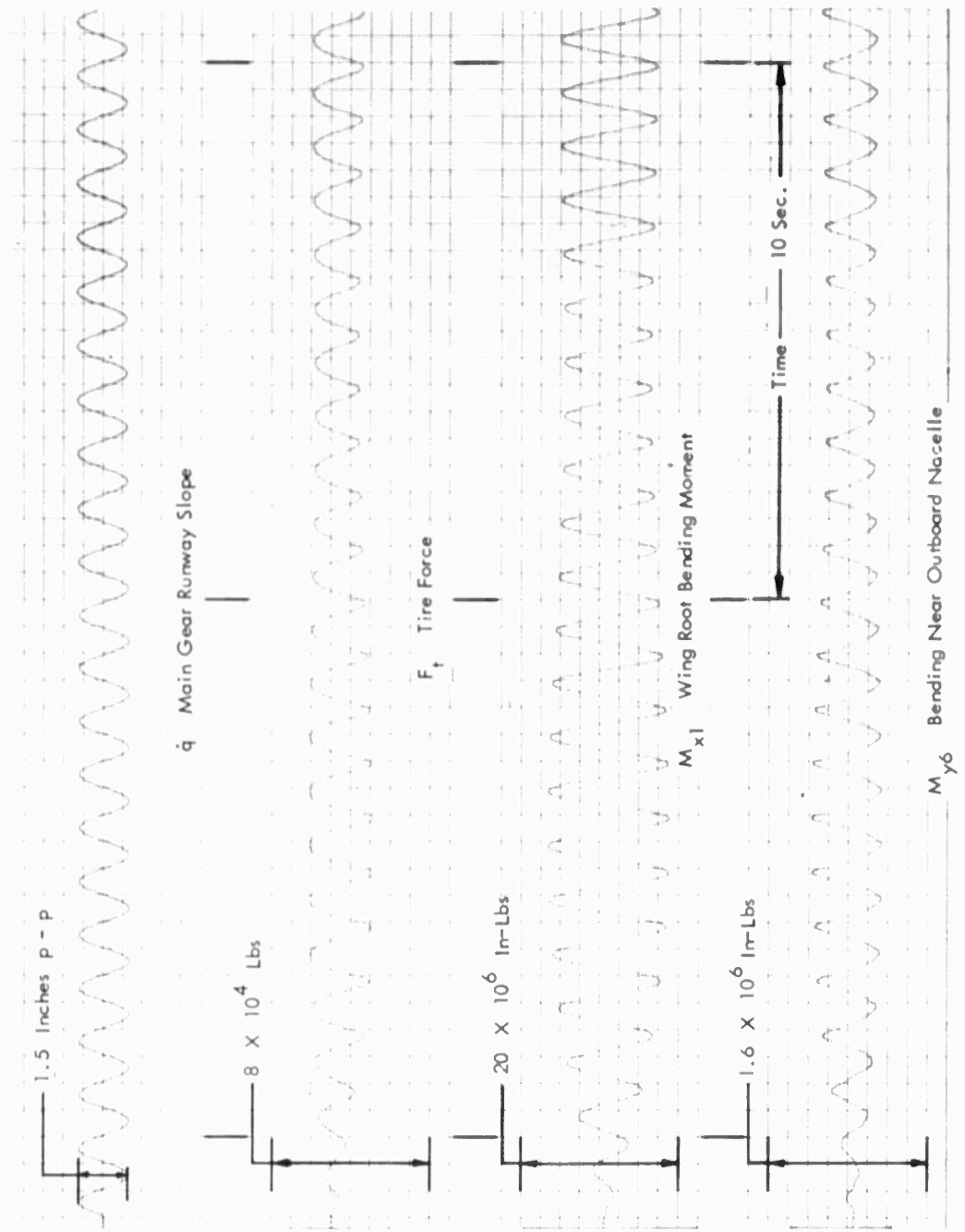


FIGURE 8 : Transient and Steady State Response Of Nonlinear System to Harmonic Excitation at  $f = 1.0$  Cycles Per Second.

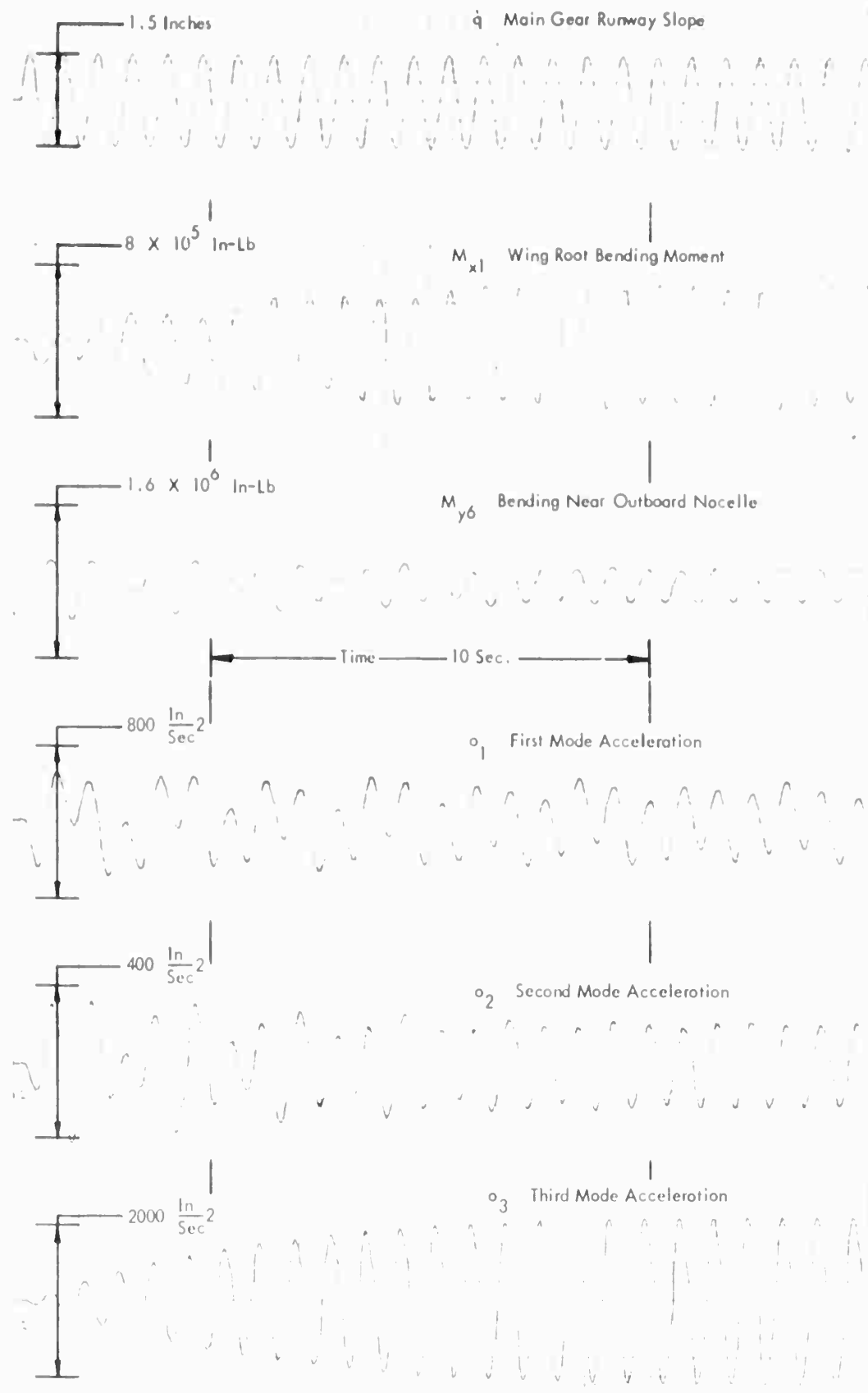


FIGURE 9 : Transient and Steady State Response of Nonlinear System to Harmonic Excitation of  $f = 1.25$  Cycles Per Second.

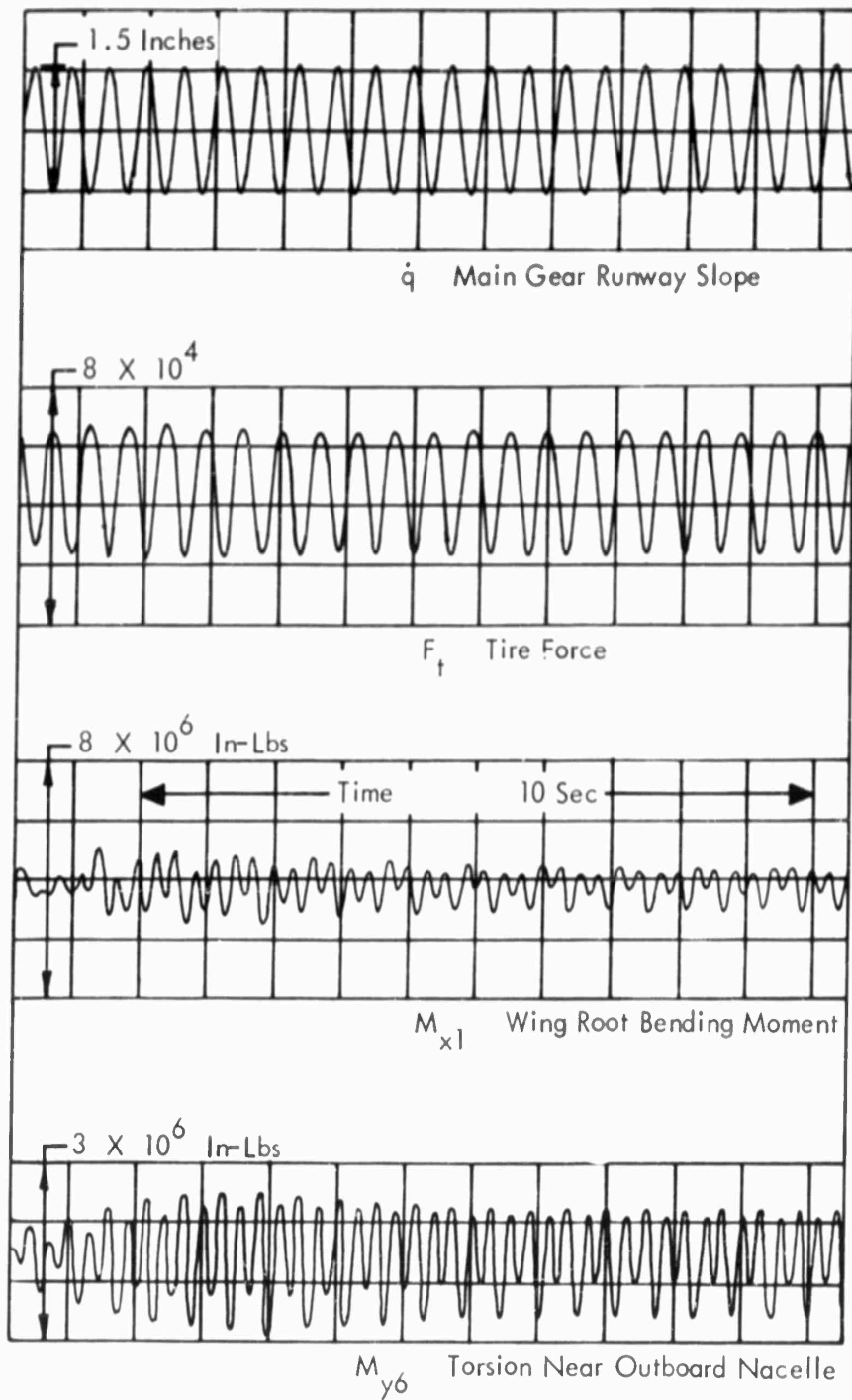


FIGURE 10 : Transient and Steady State Response of Nonlinear System to Harmonic Excitation at  $f = 1.7$  Cycles Per Second.

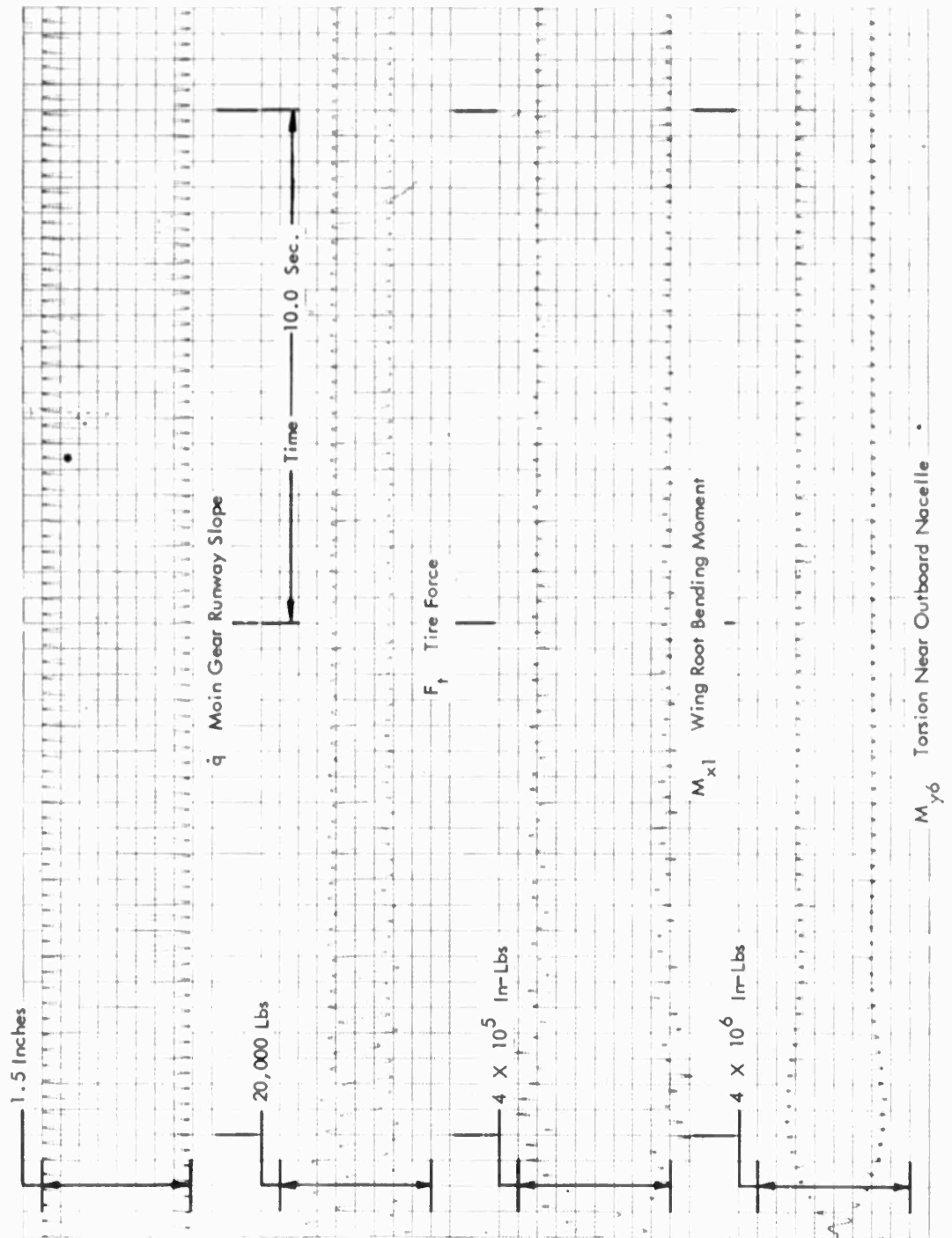


FIGURE 11 : Transient and Steady State Response of Nonlinear System to Harmonic Excitation at  $f = 3.3$  Cycles Per Second.

Time to Steady State: 22.5 Sec  
Input Amplitude: 3 inches peak to peak  
 $V_H = 55$  fps

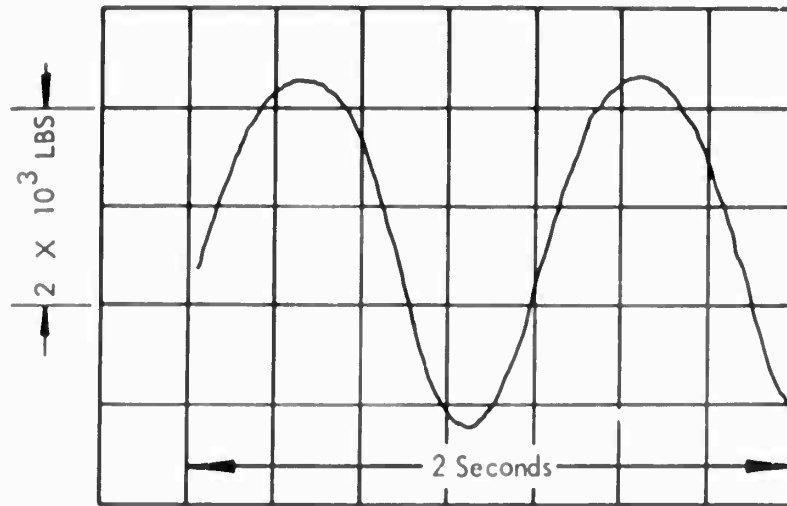


FIGURE 12 : Steady State Response Time History  
for the Nonlinear System Tire Force  
Driving Frequency: .5 cps

Time to Steady State: 22.75 Sec  
Input Amplitude: 1.5 inches peak to peak  
 $V_H = 55$  fps

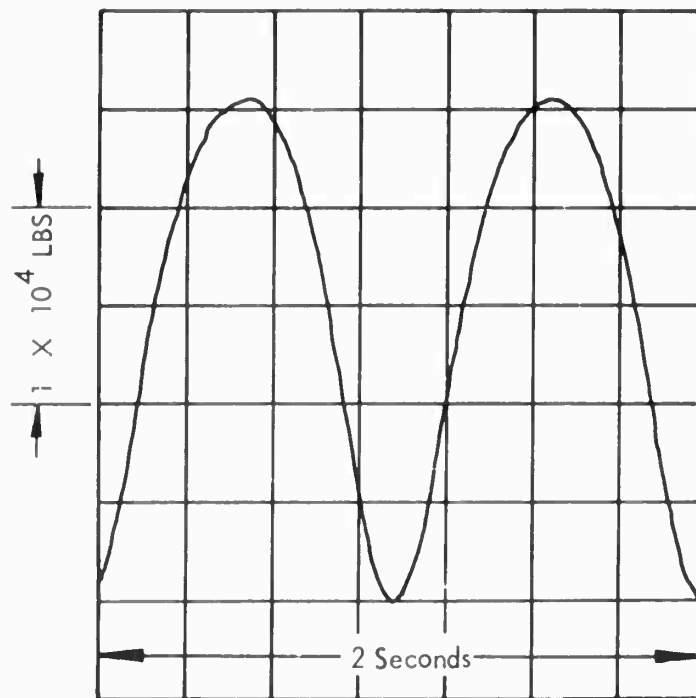


FIGURE 13 : Steady State Response Time History  
for the Nonlinear System Tire Force  
Driving Frequency: 1.0 cps

Time to Steady State: 17.5 Sec  
Input Amplitude: 1.5 inches peak to peak  
 $V_H = 55$  fps

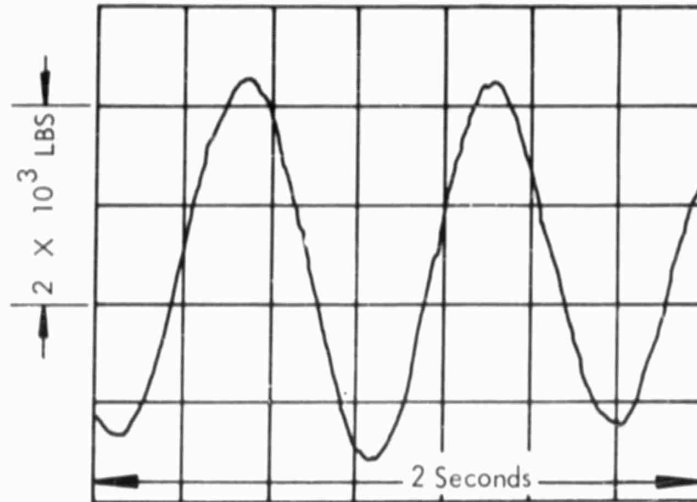


FIGURE 14 : Steady State Response Time History  
for the Nonlinear System Tire Force  
Driving Frequency: 1.25 cps

Time to Steady State: 13.0 Sec  
Input Amplitude: 1.5 inches peak to peak  
 $V_H = 55$  fps

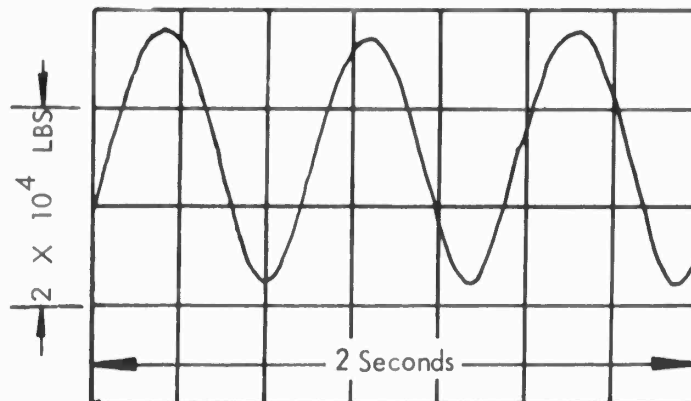


FIGURE 15 : Steady State Response Time History  
for the Nonlinear System Tire Force  
Driving Frequency: 1.5 cps

Time to Steady State: 8.75 Sec  
Input Amplitude: 1.5 inches peak to peak  
 $V_H = 55$  fps

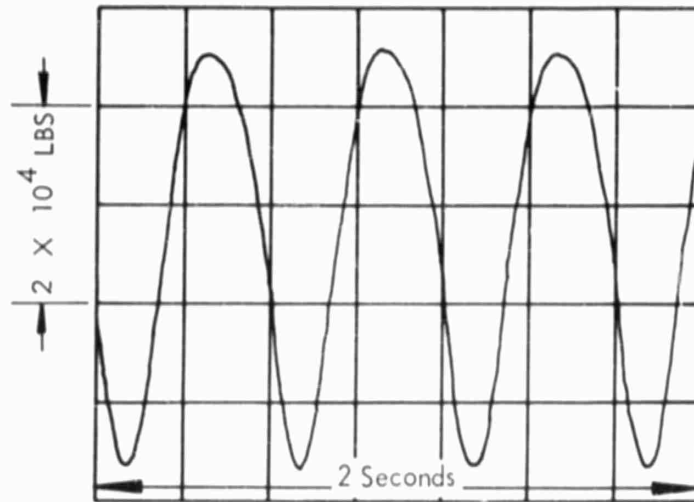


FIGURE 16 : Steady State Response Time History  
for the Nonlinear System Tire Force  
Driving Frequency: 1.70 cps

Time to Steady State: 21.6 Sec  
Input Amplitude: 1.5 inches peak to peak  
 $V_H = 55$  fps

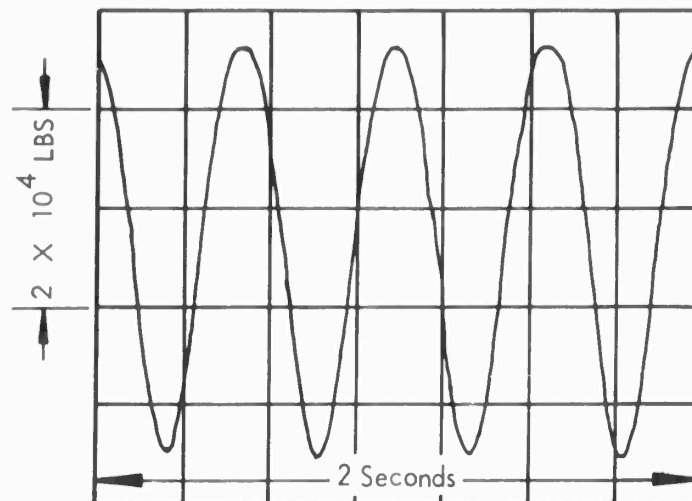


FIGURE 17 : Steady State Response Time History  
for the Nonlinear System Tire Force  
Driving Frequency: 2.0 cps

Time to Steady State: 22.0 Sec  
Input Amplitude: 1.5 inches peak to peak  
 $V_H = 55$  fps

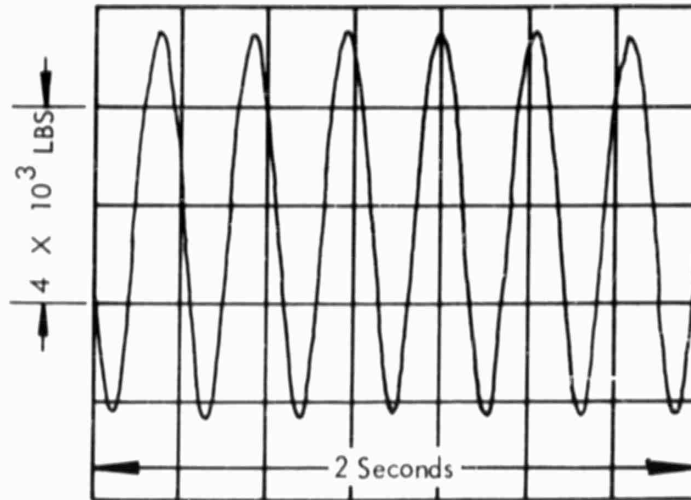


FIGURE 18 : Steady State Response Time History  
for the Nonlinear System Tire Force  
Driving Frequency: 3.3 cps

Time to Steady State: 11.5 Sec  
Input Amplitude: 1.5 inches peak to peak  
 $V_H = 55$  fps

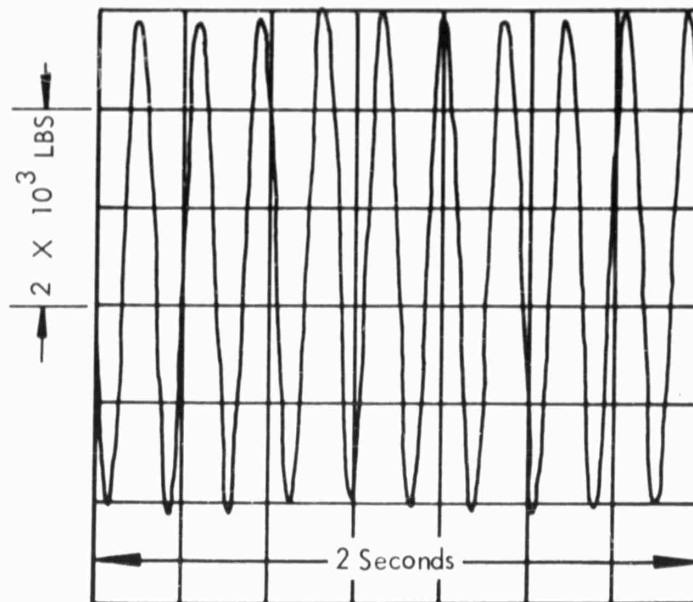


FIGURE 19 : Steady State Response Time History  
for the Nonlinear System Tire Force  
Driving Frequency: 5.0 cps

Time to Steady State: 22.5 Sec  
 Input Amplitude: 3 inches peak to peak  
 $V_H = 55$  fps

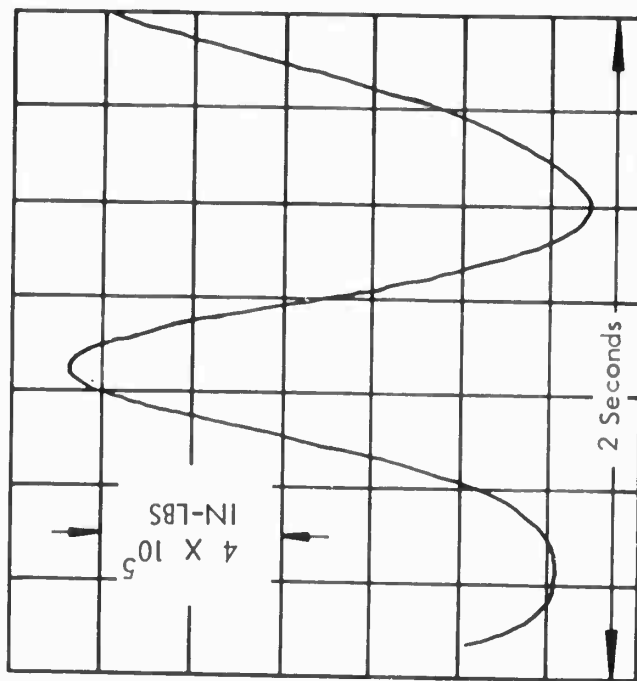


FIGURE 20 : Steady State Response Time History  
 for the Nonlinear System Wing  
 Root Bending Moment  
 Driving Frequency: .5 cps

Time to Steady State: 22.75 Sec  
 Input Amplitude: 1.5 inches peak to peak  
 $V_H = 55$  fps

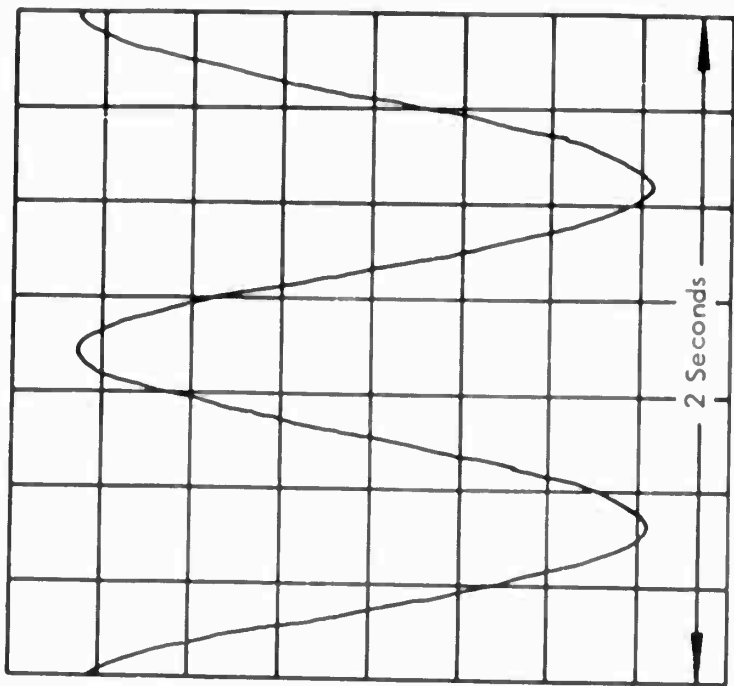


FIGURE 21 : Steady State Response Time History  
 for the Nonlinear System Wing  
 Root Bending Moment  
 Driving Frequency: 1.0 cps

Time to Steady State: 17.5 Sec  
Input Amplitude: 1.5 inches peak to peak  
 $V_H = 55$  fps

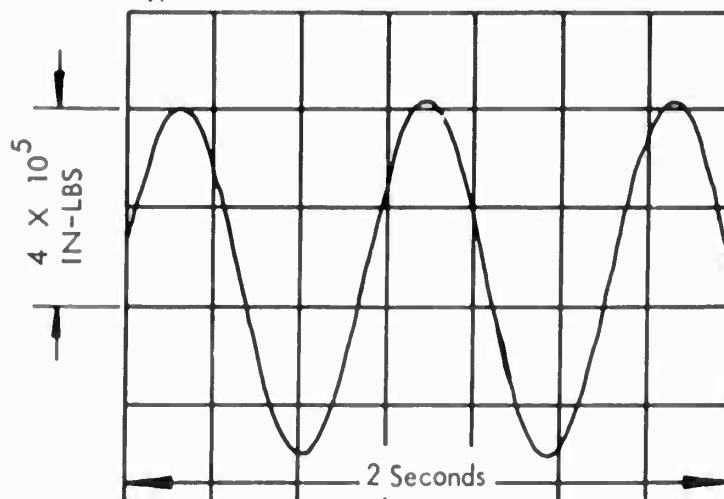


FIGURE 22 : Steady State Response Time History  
for the Nonlinear System Wing  
Root Bending Moment  
Driving Frequency: 1.25 cps

Time to Steady State: 13.0 Sec  
Input Amplitude: 1.5 inches peak to peak  
 $V_H = 55$  fps

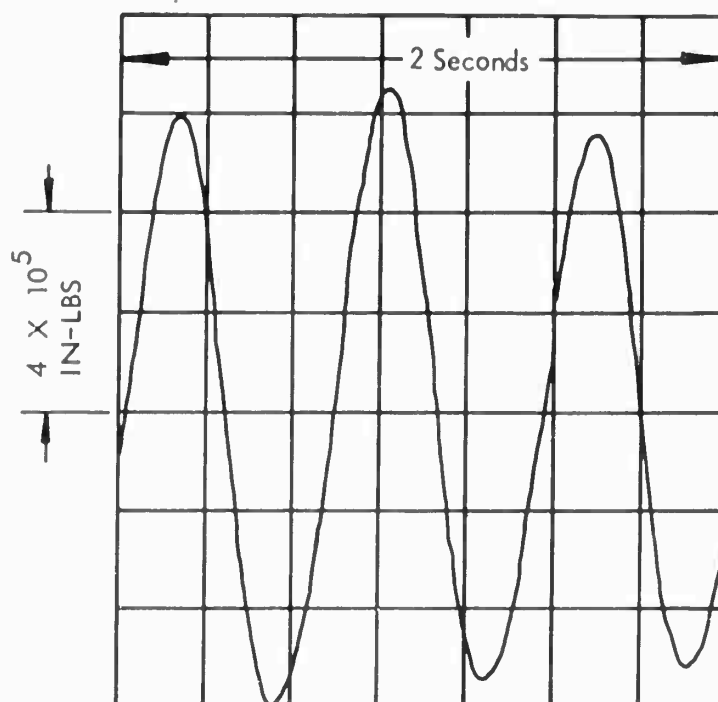


FIGURE 23 : Steady State Response Time History  
for the Nonlinear System Wing  
Root Bending Moment  
Driving Frequency: 1.5 cps

Time to Steady State: 8.75 Sec  
Input Amplitude: 1.5 inches peak to peak  
 $V_H = 55$  fps

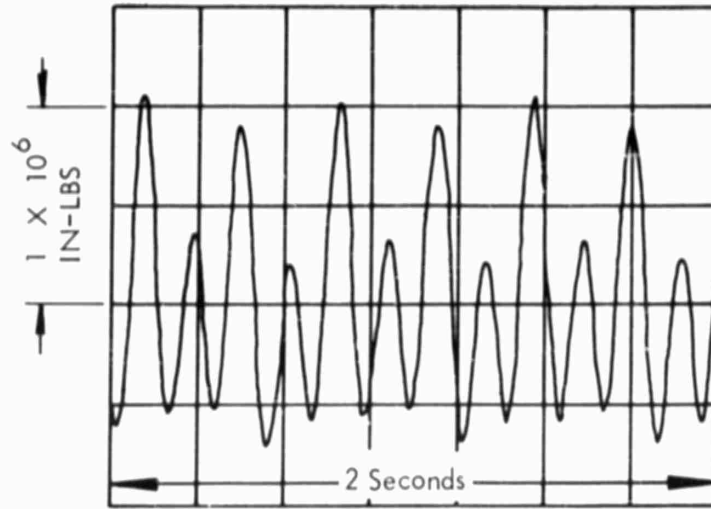


FIGURE 24 : Steady State Response Time History  
for the Nonlinear System Wing  
Root Bending Moment  
Driving Frequency: 1.70 cps

Time to Steady State: 21.6 Sec  
Input Amplitude: 1.5 inches peak to peak  
 $V_H = 55$  fps

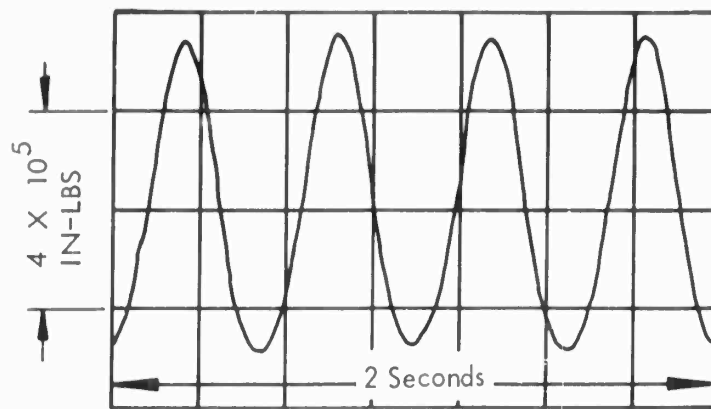


FIGURE 25 : Steady State Response Time History  
for the Nonlinear System Wing  
Root Bending Moment  
Driving Frequency: 2.0 cps

Time to Steady State: 22.0 Sec  
Input Amplitude: 1.5 inches peak to peak  
 $V_H = 55$  fps

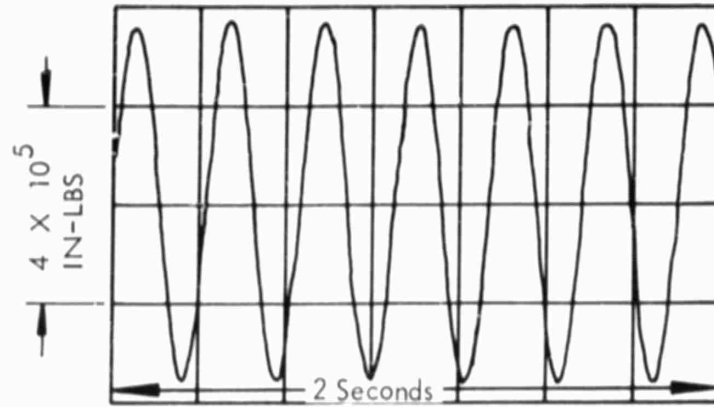


FIGURE 26 : Steady State Response Time History  
for the Nonlinear System Wing  
Root Bending Moment  
Driving Frequency: 3.3 cps

Time to Steady State: 11.5 Sec  
Input Amplitude: 1.5 inches peak to peak  
 $V_H = 55$  fps

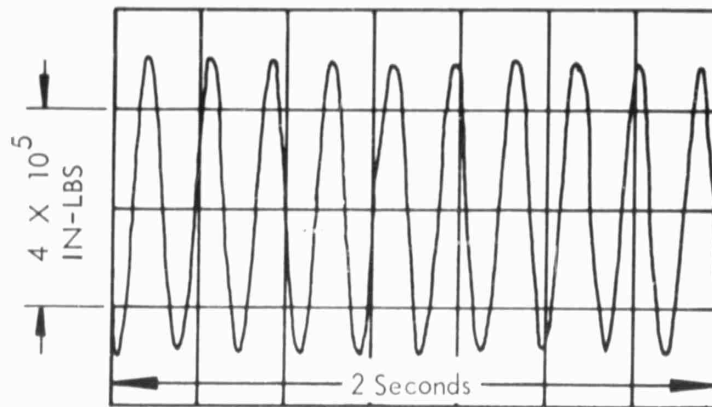


FIGURE 27 : Steady State Response Time History  
for the Nonlinear System Wing  
Root Bending Moment  
Driving Frequency: 5.0 cps

Time to Steady State: 22.5 Sec  
 Input Amplitude: 3 inches peak to peak  
 $V_H = 55 \text{ fps}$

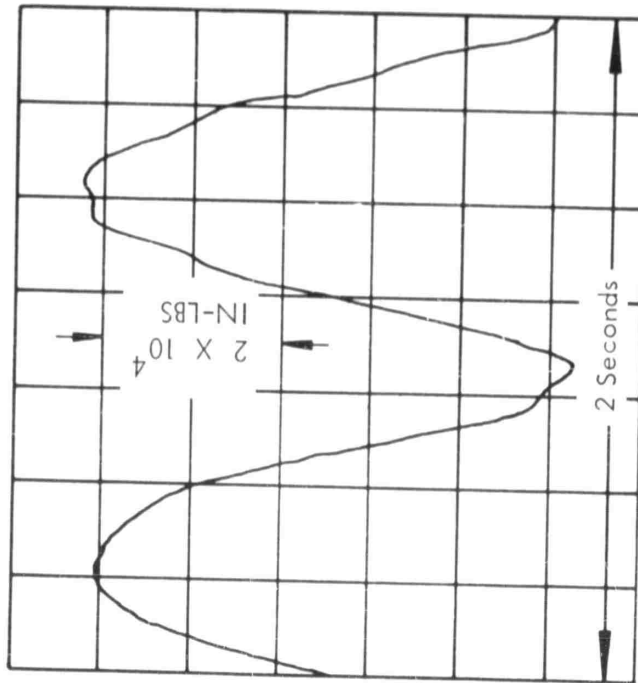


FIGURE 28 : Steady State Response Time History  
 for the Nonlinear System Wing  
 Torsion Moment at Outboard Nacelle  
 Driving Frequency: .5 cps

Time to Steady State: 22.75 Sec  
 Input Amplitude: 1.5 inches peak to peak  
 $V_H = 55 \text{ fps}$

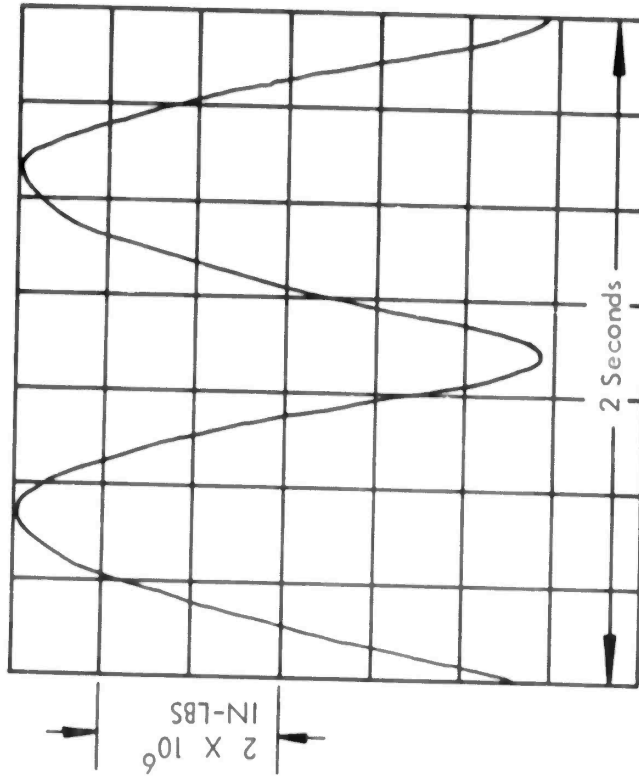


FIGURE 29 : Steady State Response Time History  
 for the Nonlinear System Wing  
 Torsion Moment at Outboard Nacelle  
 Driving Frequency: 1.0 cps

Time to Steady State: 1.75 Sec  
Input Amplitude: 1.5 inches peak to peak  
 $V_H = 55$  fps

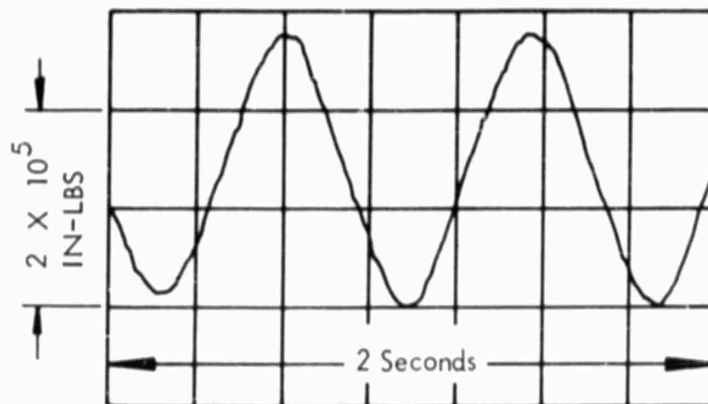


FIGURE 30 : Steady State Response Time History  
for the Nonlinear System Wing  
Torsion Moment at Outboard Nacelle  
Driving Frequency: 1.25 cps

Time to Steady State: 13.0 Sec  
Input Amplitude: 1.5 inches peak to peak  
 $V_H = 55$  fps

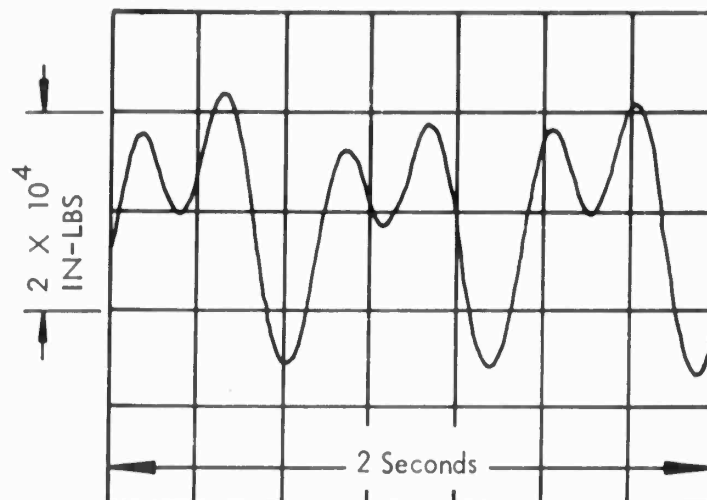


FIGURE 31 : Steady State Response Time History  
for the Nonlinear System Wing  
Torsion Moment at Outboard Nacelle  
Driving Frequency: 1.5 cps

Time to Steady State: 8.75 Sec  
Input Amplitude: 1.5 inches peak to peak  
 $V_H = 55$  fps

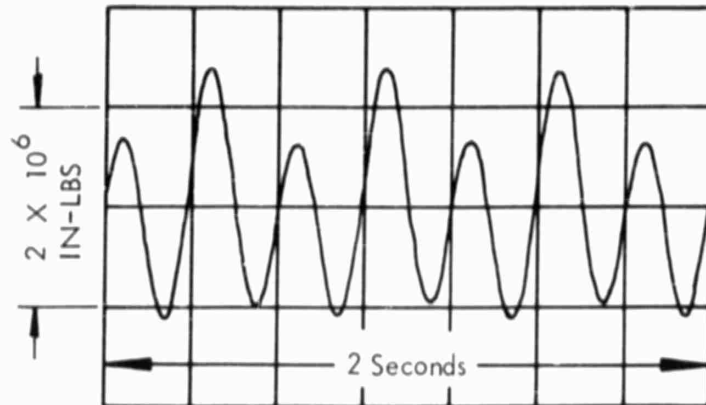


FIGURE 32 : Steady State Response Time History  
for the Nonlinear System Wing  
Torsion Moment at Outboard Nacelle  
Driving Frequency: 1.70 cps

Time to Steady State: 21.6 Sec  
Input Amplitude: 1.5 inches peak to peak  
 $V_H = 55$  fps

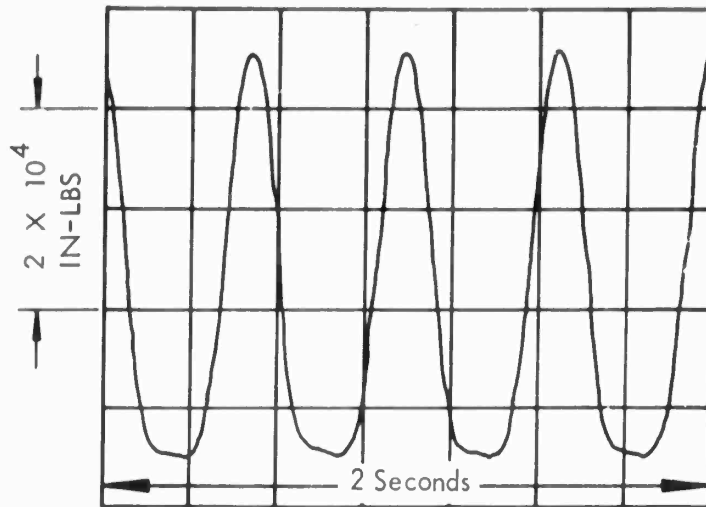


FIGURE 33 : Steady State Response Time History  
for the Nonlinear System Wing  
Torsion Moment at Outboard Nacelle  
Driving Frequency: 2.0 cps

Time to Steady State: 22.0 Sec  
Input Amplitude: 1.5 inches peak to peak  
 $V_H = 55$  fps

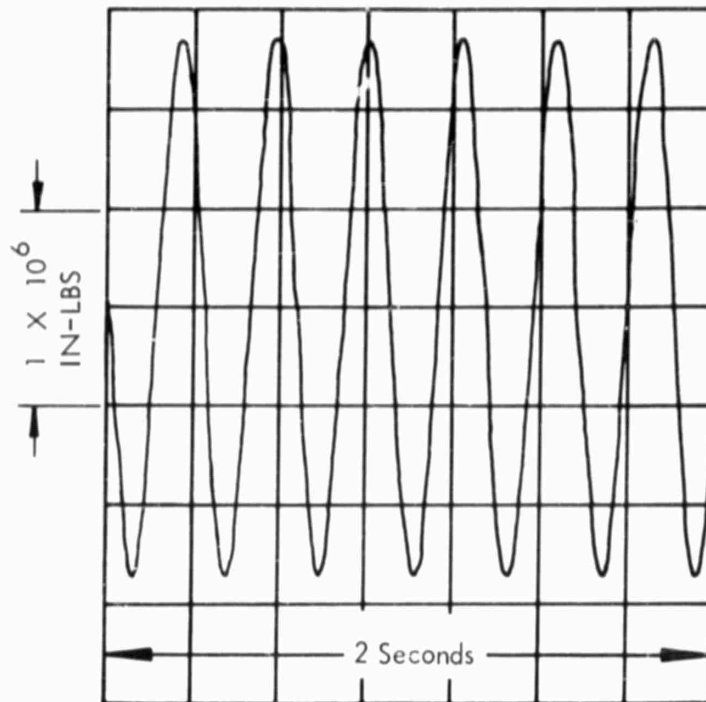


FIGURE 34 : Steady State Response Time History  
for the Nonlinear System Wing  
Torsion Moment at Outboard Nacelle  
Driving Frequency: 3.3 cps

Time to Steady State: 11.5 Sec  
Input Amplitude: 1.5 inches peak to peak  
 $V_H = 55$  fps

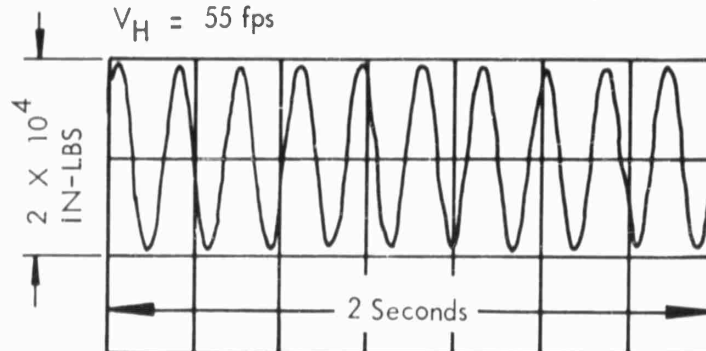


FIGURE 35 : Steady State Response Time History  
for the Nonlinear System Wing  
Torsion Moment at Outboard Nacelle  
Driving Frequency: 5.0 cps

Driving Frequency = 1.70 cps  
Driving Amplitude = 1.5" p - p  
 $V_H = 44$  ft/sec

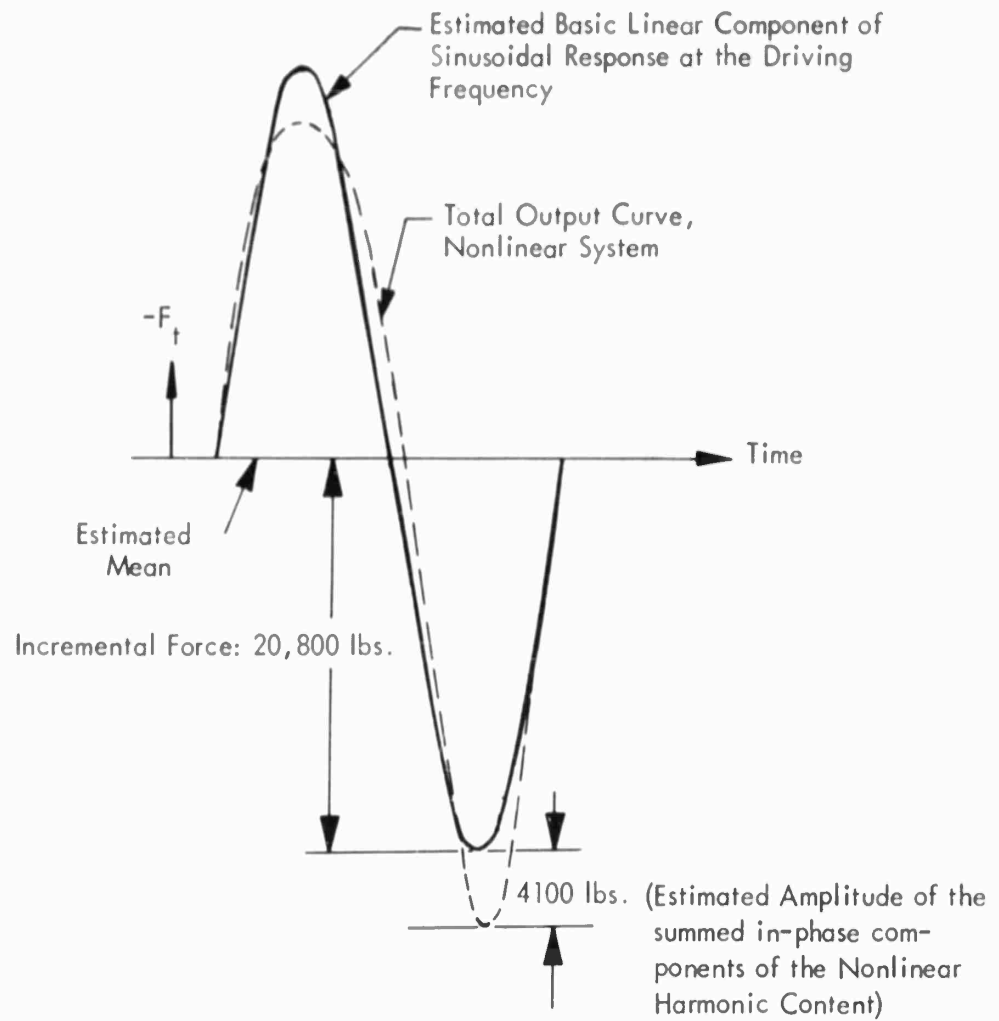


FIGURE 36 : Time History of a Periodic Segment of the Nonlinear System Tire Force Response to Harmonic Excitation

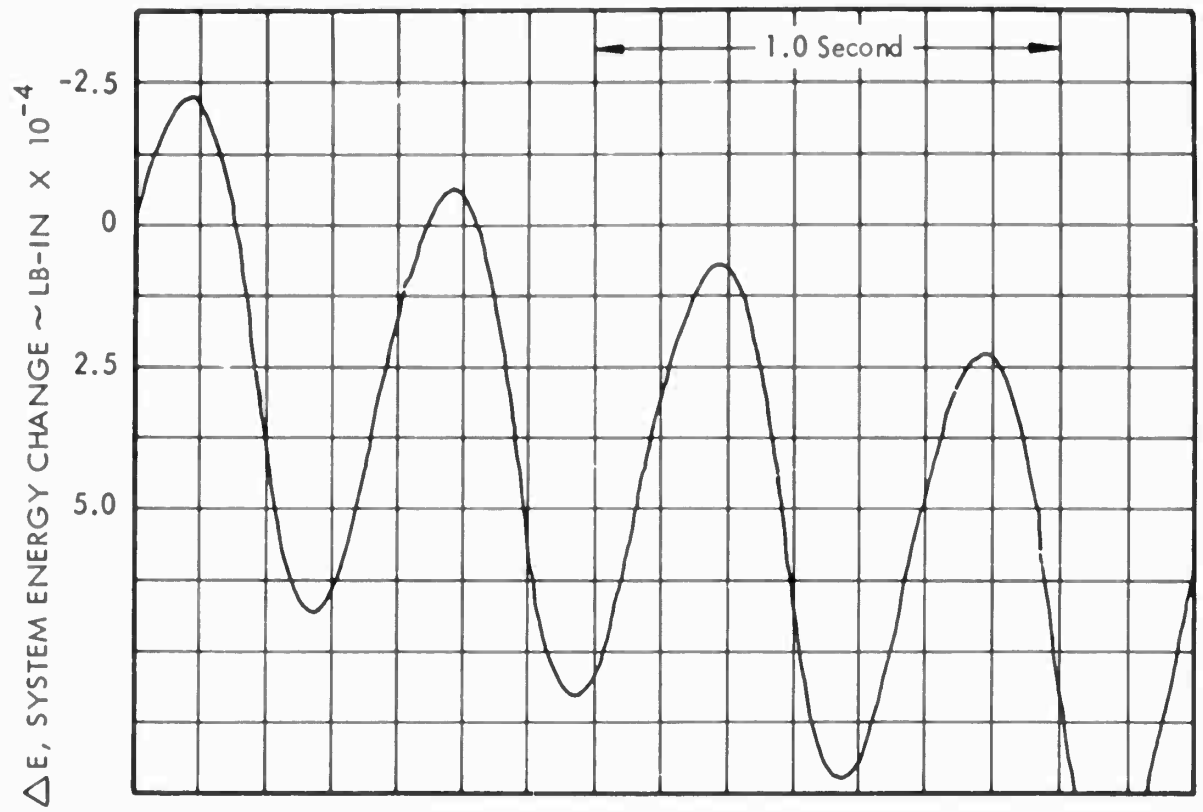


FIGURE 37: Study of Energy Change in Nonlinear System due to Harmonic Excitation,  $f = 1.7$  Cycles Per Second

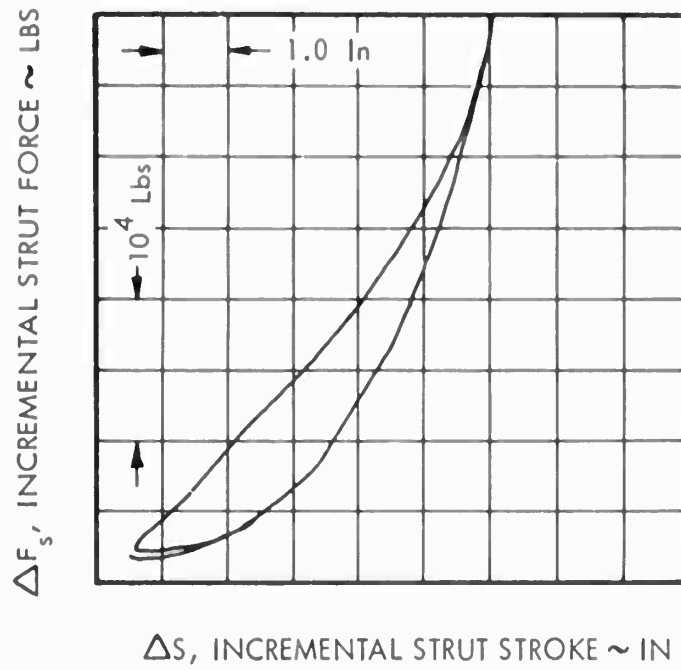


FIGURE 38: Phase Plane Study of Strut Force Versus Strut Stroke

$$C_D = 14.10 \text{ lb} \cdot \text{sec}^2/\text{in.}^2$$

$$V_H = 44 \text{ ft/sec}$$

$$\text{T.P.} = 90 \text{ p.s.i.}$$

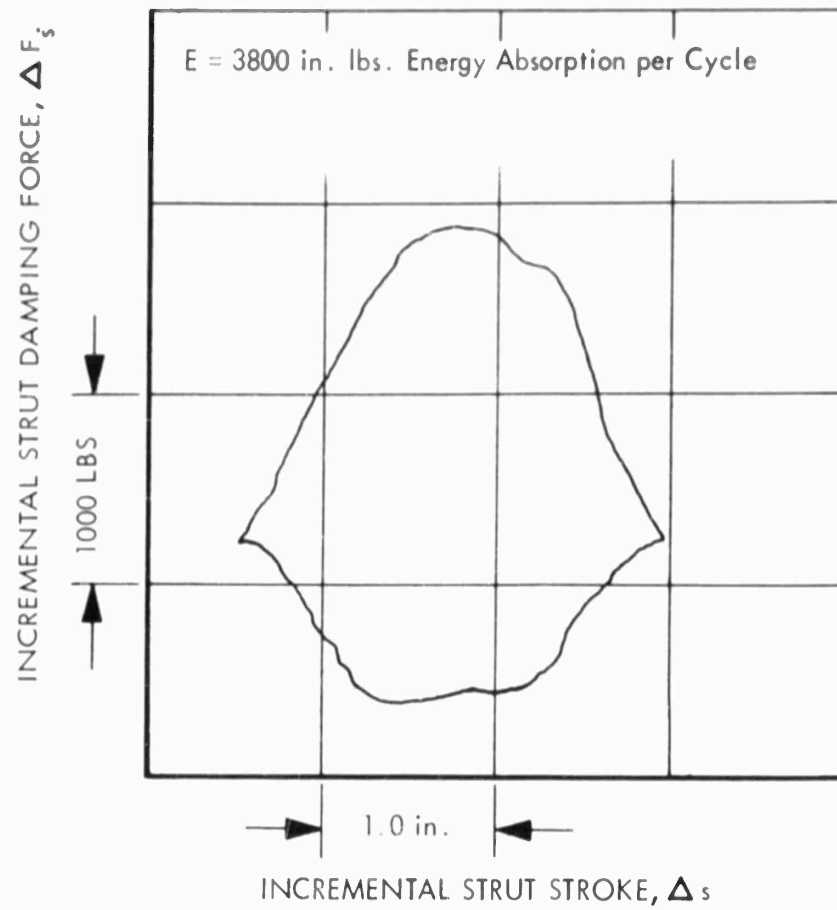


FIGURE 39 : Phase - Plane Study of Energy Absorption  
in the Strut  
Nominal  $f = .9 \text{ c.p.s.}$

$$C_D = 14.10 \text{ lb} \cdot \text{sec}^2 / \text{in.}^2$$

$$V_H = 44 \text{ ft/sec}$$

$$\text{T.P.} = 90 \text{ p.s.i.}$$

$$E = 17,040 \text{ in. lbs. Energy Absorption per Cycle}$$

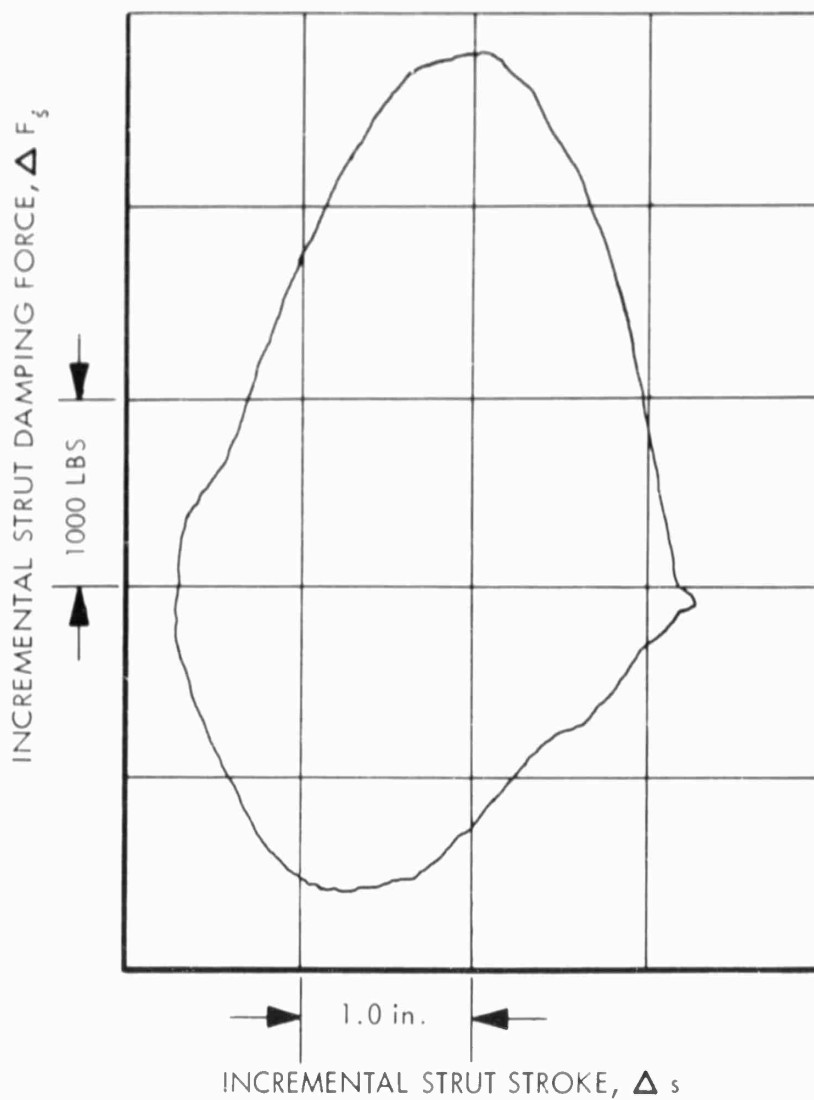


FIGURE 40 : Phase - Plane Study of Energy Absorption  
in the Strut

Nominal  $f = 1.67$  c.p.s.

$$C_D = 14.10 \text{ lb} \cdot \text{sec}^2 / \text{in.}^2$$

$$V_H = 44 \text{ ft/sec}$$

$$\text{T.P.} = 90 \text{ p.s.i.}$$

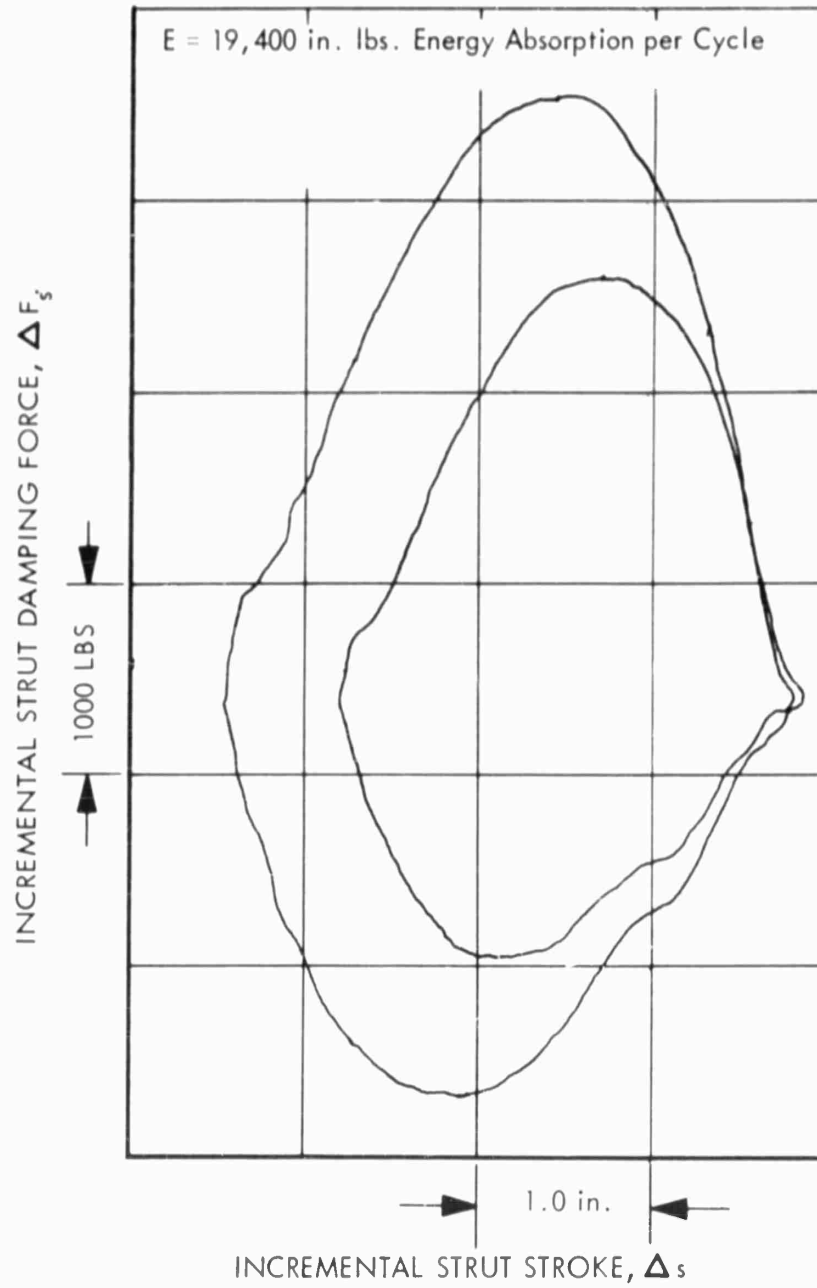


FIGURE 41 : Phase - Plane Study of Energy Absorption in the Strut

Nominal  $f = 1.75 \text{ c.p.s.}$

$$C_D = 14.10 \text{ lb} \cdot \text{sec}^2/\text{in.}^2$$

$$V_H = 44 \text{ ft/sec}$$

$$\text{T.P.} = 90 \text{ p.s.i.}$$

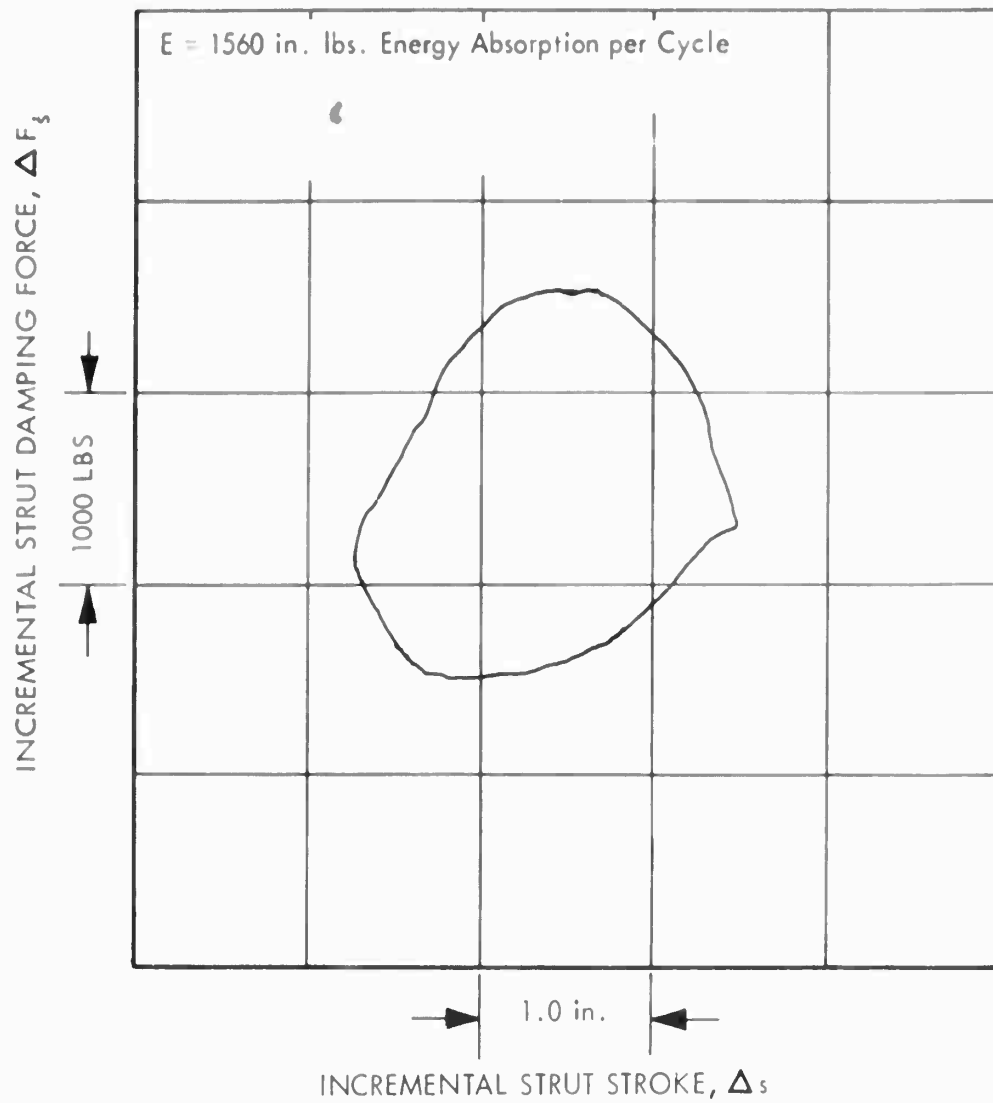


FIGURE 42 : Phase - Plane Study of Energy Absorption in the Strut  
Nominal  $f = 2.25 \text{ c.p.s.}$

$$C_D = 14.10 \text{ lb} \cdot \text{sec}^2 / \text{in.}^2$$

$$V_H = 44 \text{ ft/sec}$$

$$\text{T.P.} = 90 \text{ p.s.i.}$$

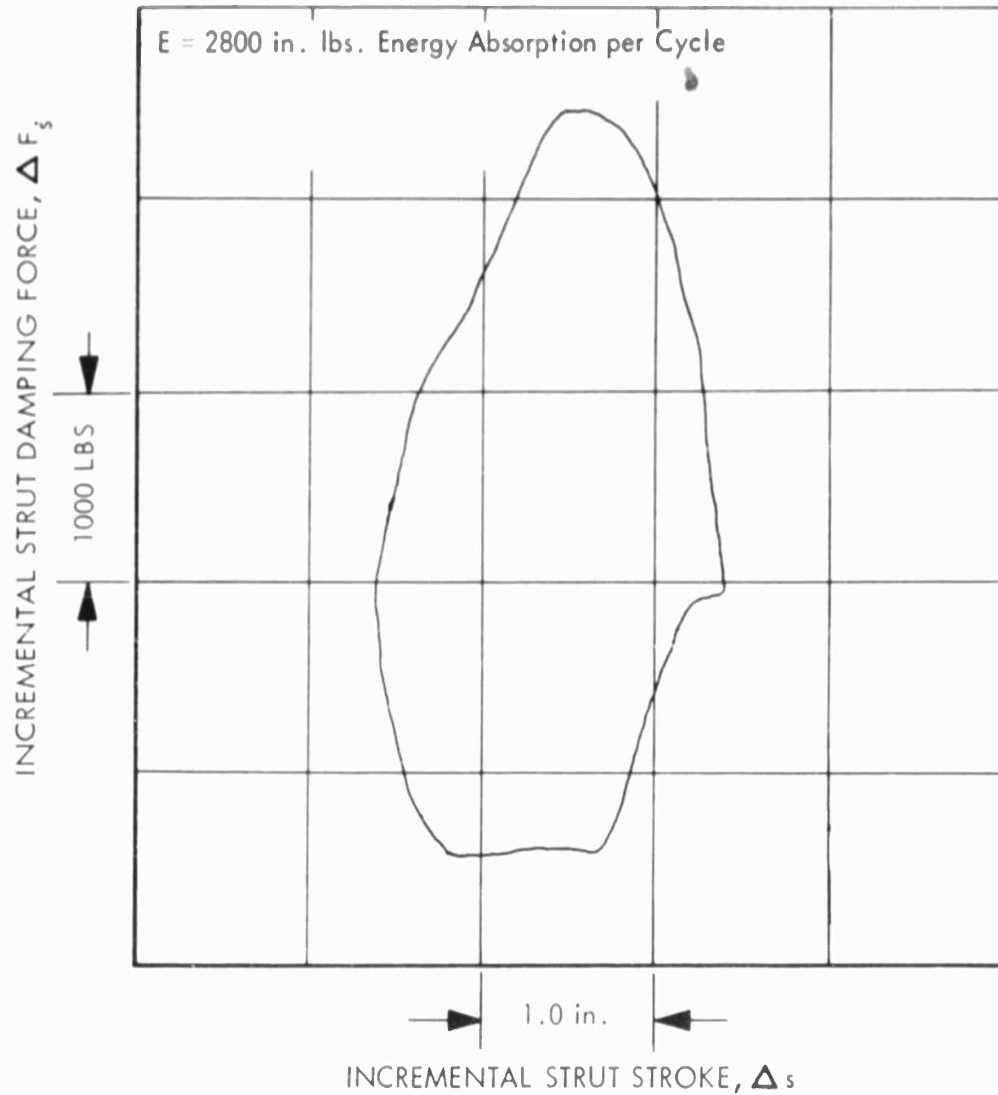


FIGURE 43 : Phase - Plane Study of Energy Absorption in the Strut  
Nominal  $f = 3.5 \text{ c.p.s.}$

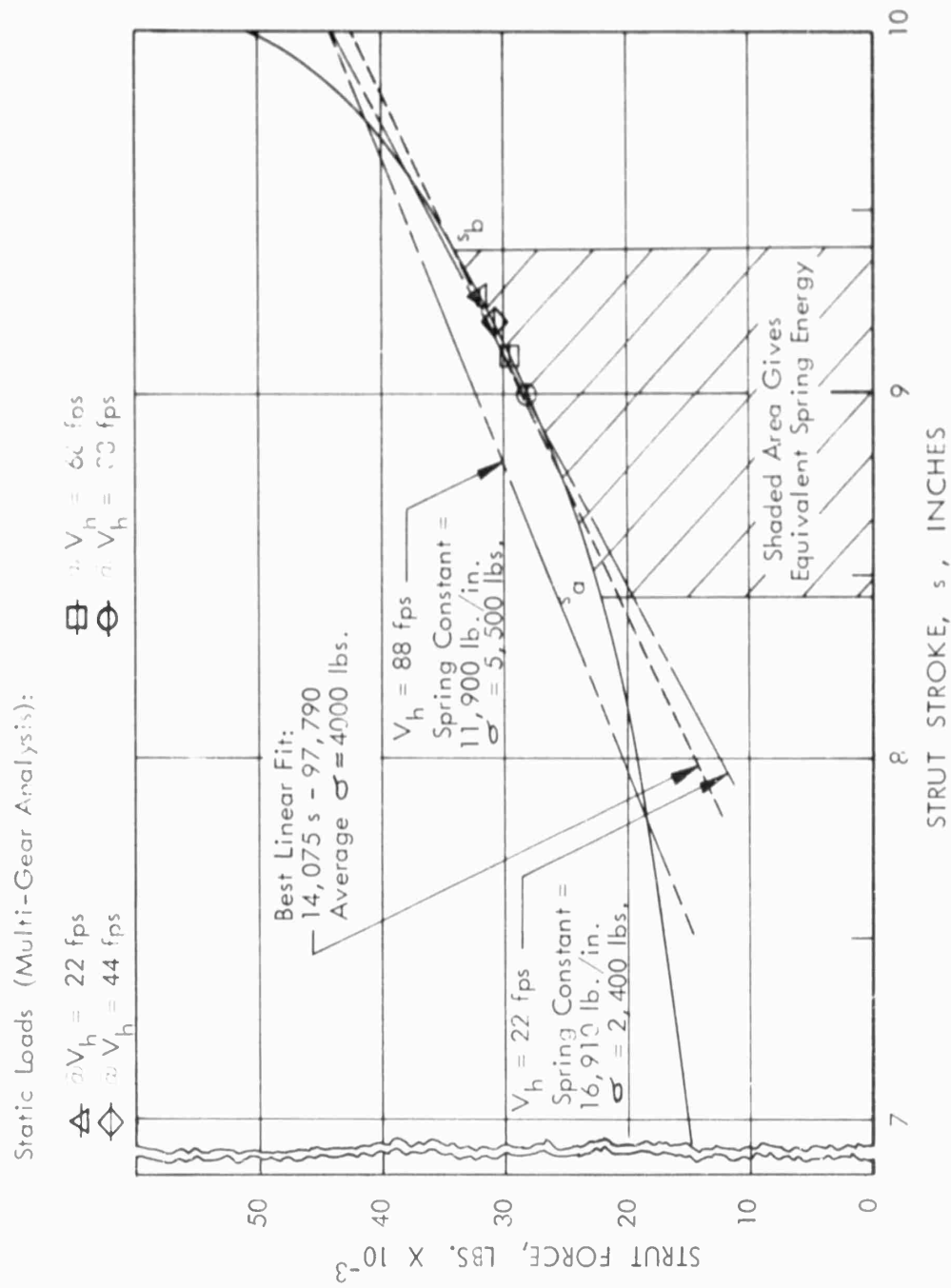


FIGURE 44 : Main Gear Strut Force Versus Strut Stroke

Tire Force, Static  
(Single Gear)

⊠ @  $V_H = 22$  fps

⊙ @  $V_H = 88$  fps

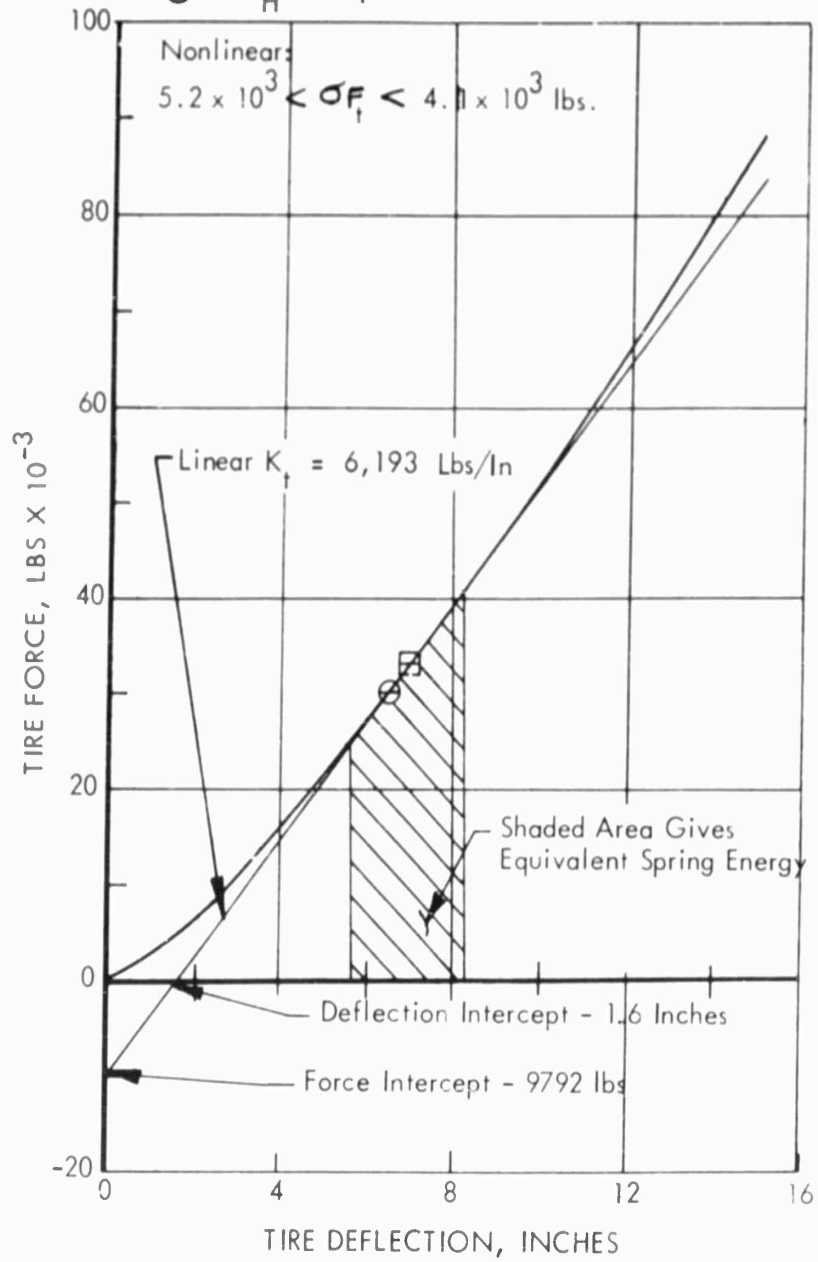


FIGURE 45: Main Gear Tire Deflection vs. Tire Force  
Tire Pressure = 60 p.s.i.

Tire Force, Static (Single Gear):

☐ @  $V_H = 22$  fps

⊖ @  $V_H = 88$  fps

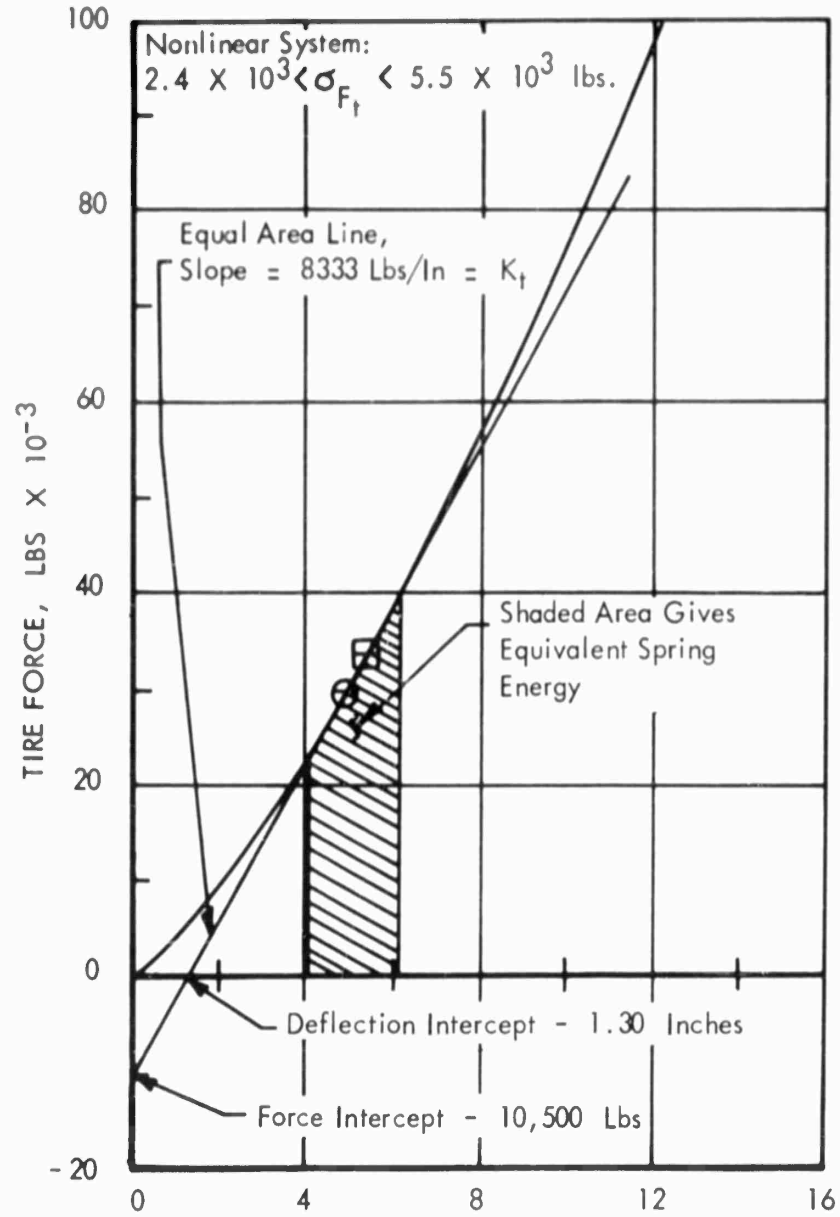


FIGURE 46 : Main Gear Tire Deflection versus Tire Force Tire Pressure = 90 PSI

Tire Force Static (Single Gear)

- ☐  $V_H = 22$  fps
- ⊖  $V_H = 88$  fps

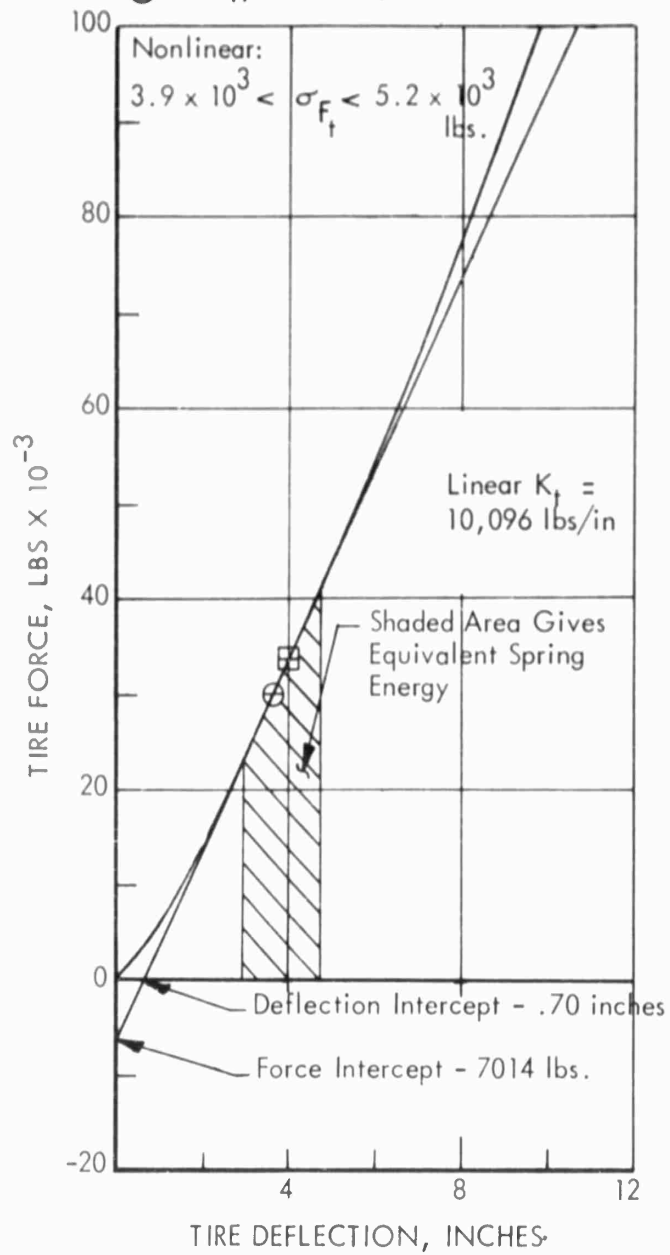


FIGURE 47 : Main Gear Tire Deflection vs. Tire Force

Tire Pressure = 120 p.s.i.

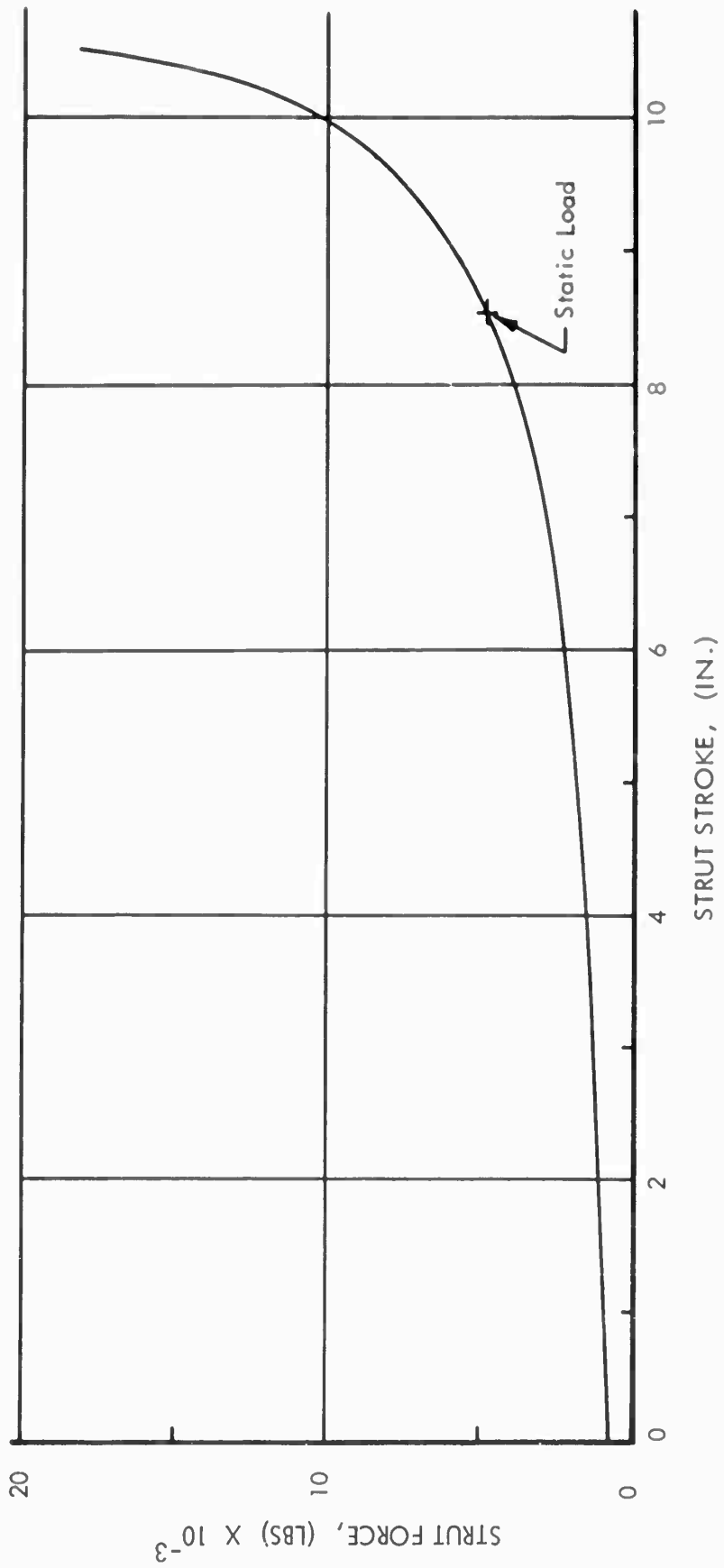


FIGURE 48 : Strut Air Compression Force versus Stroke, Nose Gear

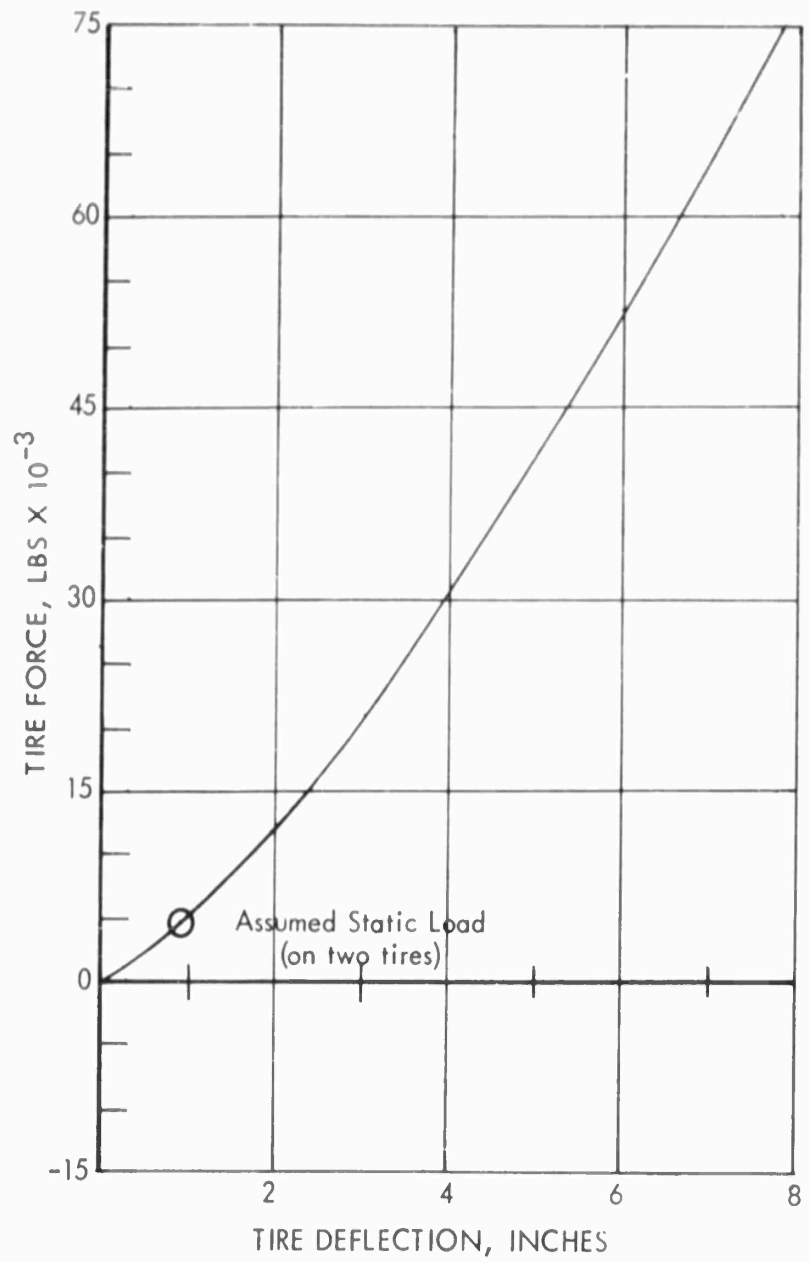


FIGURE 49 : Nose Gear Tire Deflection Versus Tire Force  
Tire Pressure 60 p.s.i.

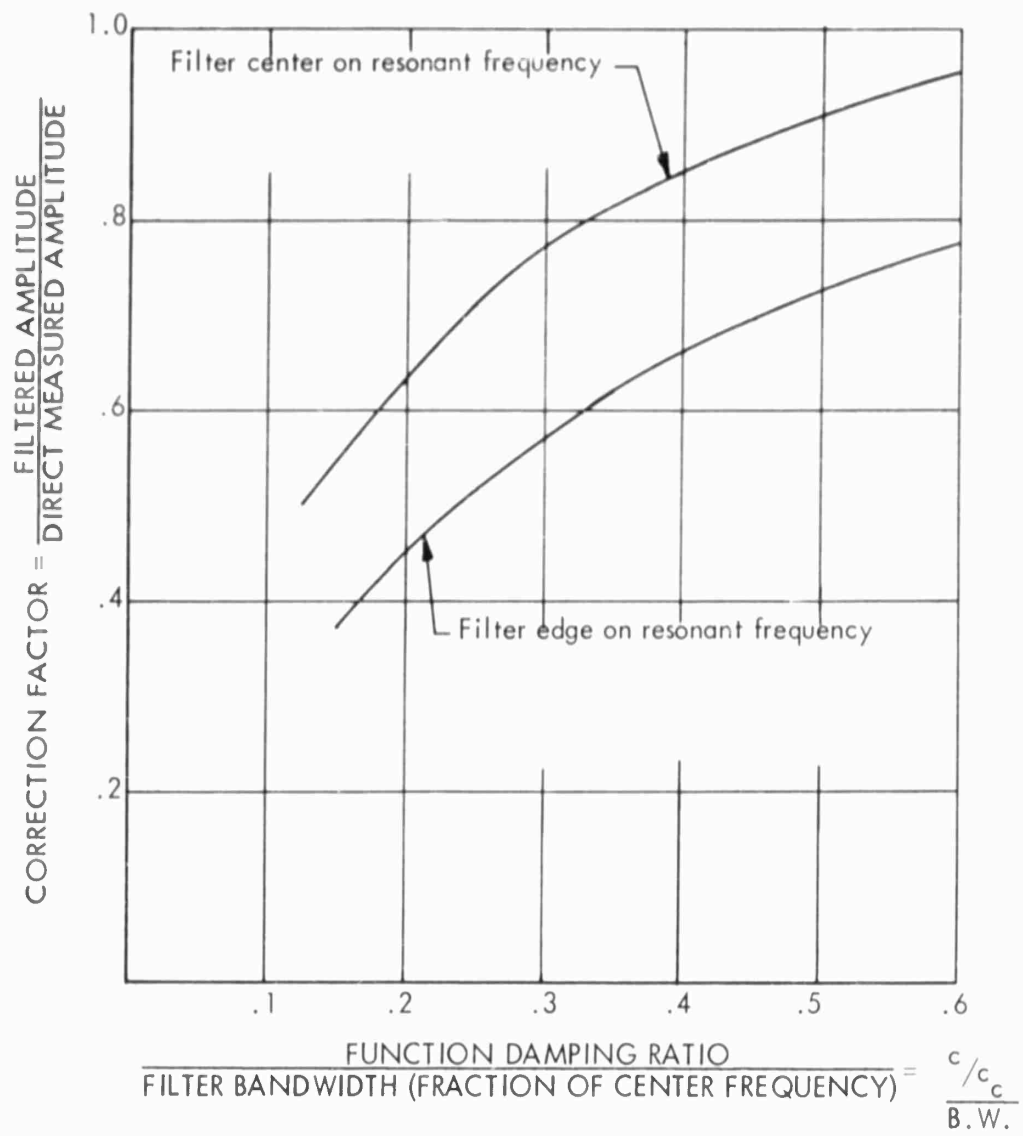


FIGURE 50 : Correction Factors For Finite Bandwidth Filters Operating on a Lightly-Damped Function Near a Peak Frequency

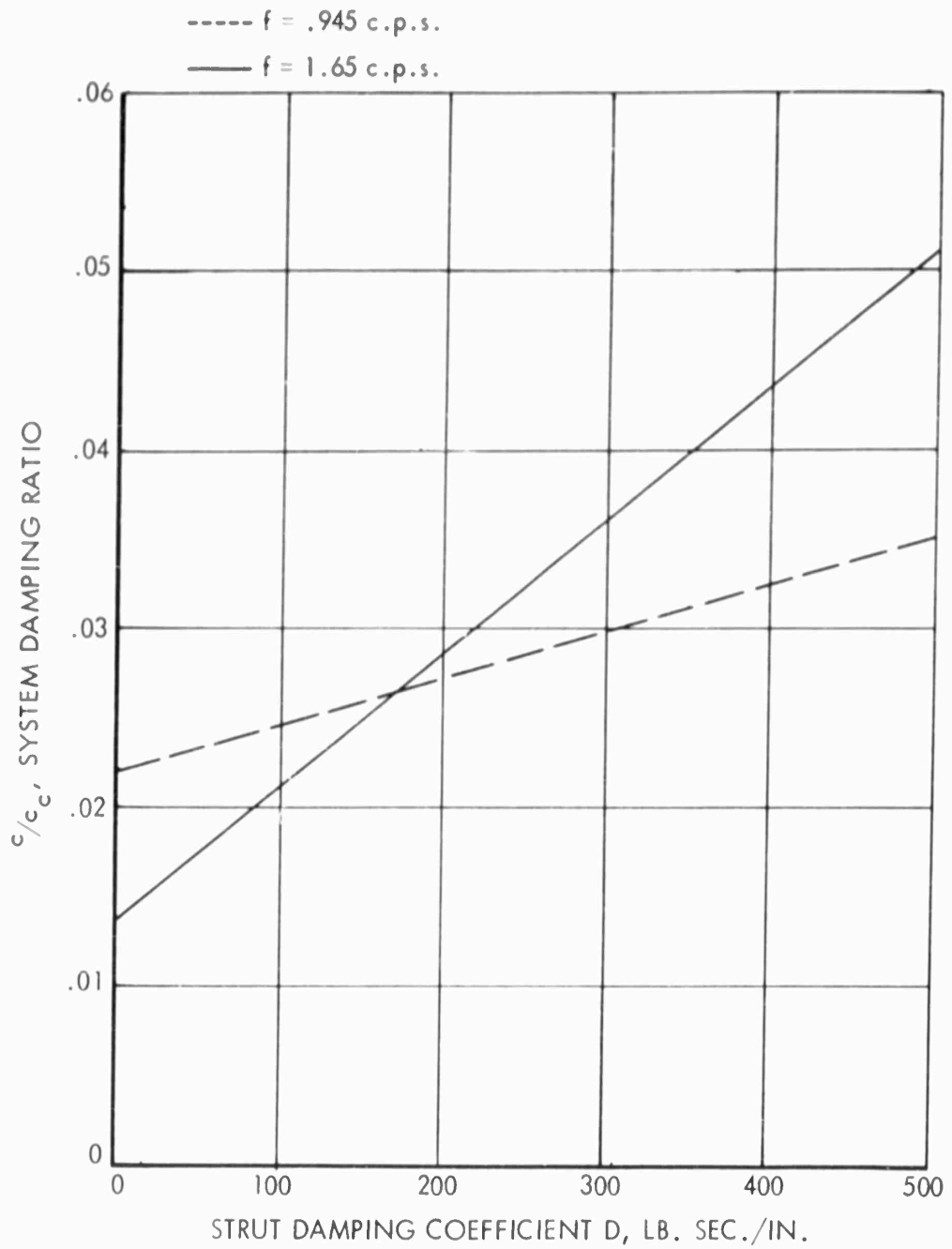


FIGURE 51 : Variation of System Damping,  $c/c_c$  With Linearized Strut Damping Coefficient D

Single Gear, 90 p.s.i.

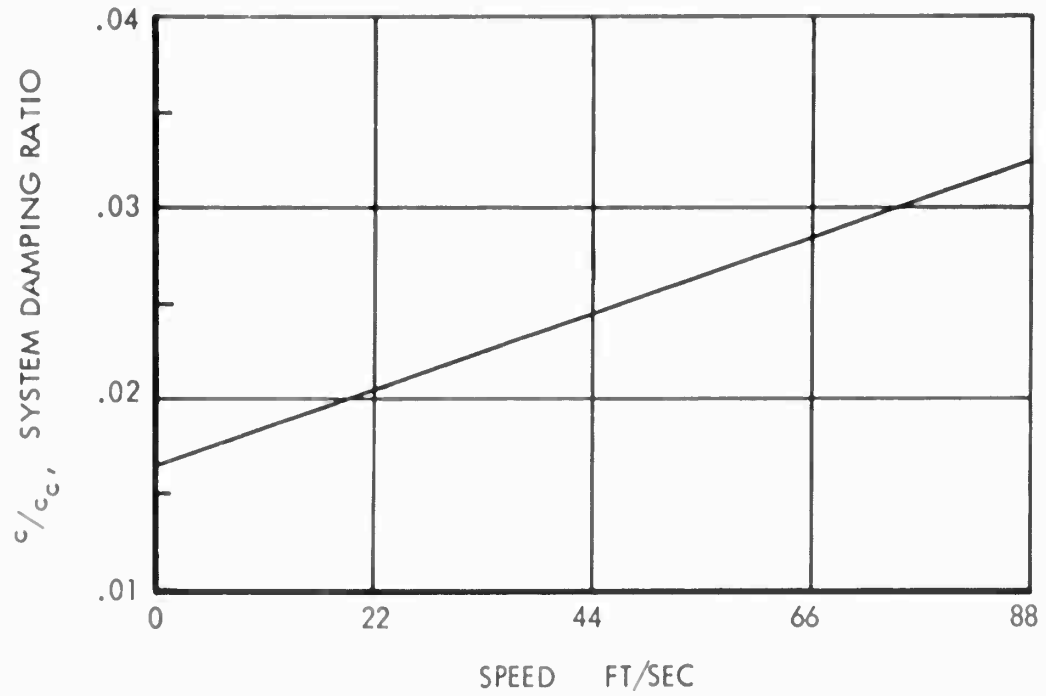


FIGURE 52 : Variation of Damping Ratio With Speed for Any Tire Pressure @  $f = .95$  cps Nominal Peak Frequency and for a Strut Damper of  $D = 185$  Lb-Sec/In.

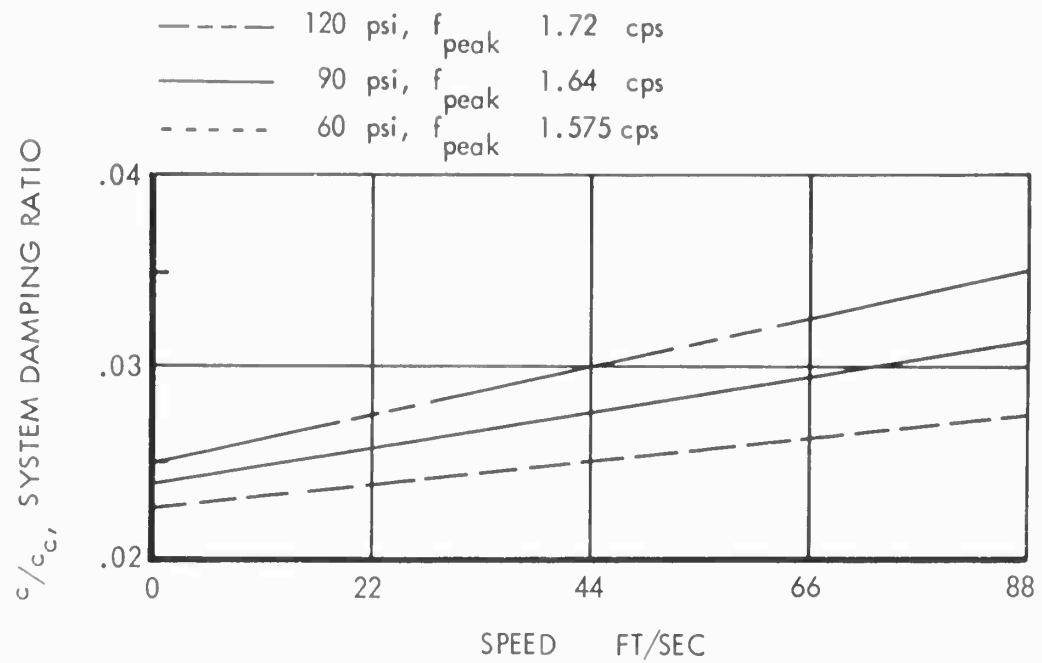


FIGURE 53 : Variation of Damping Ratio With Speed for Several Tire Pressures at an Average Peak Frequency of  $f = 1.65$  cps and for a Strut Damper of  $D = 185$  Lb-Sec/In.

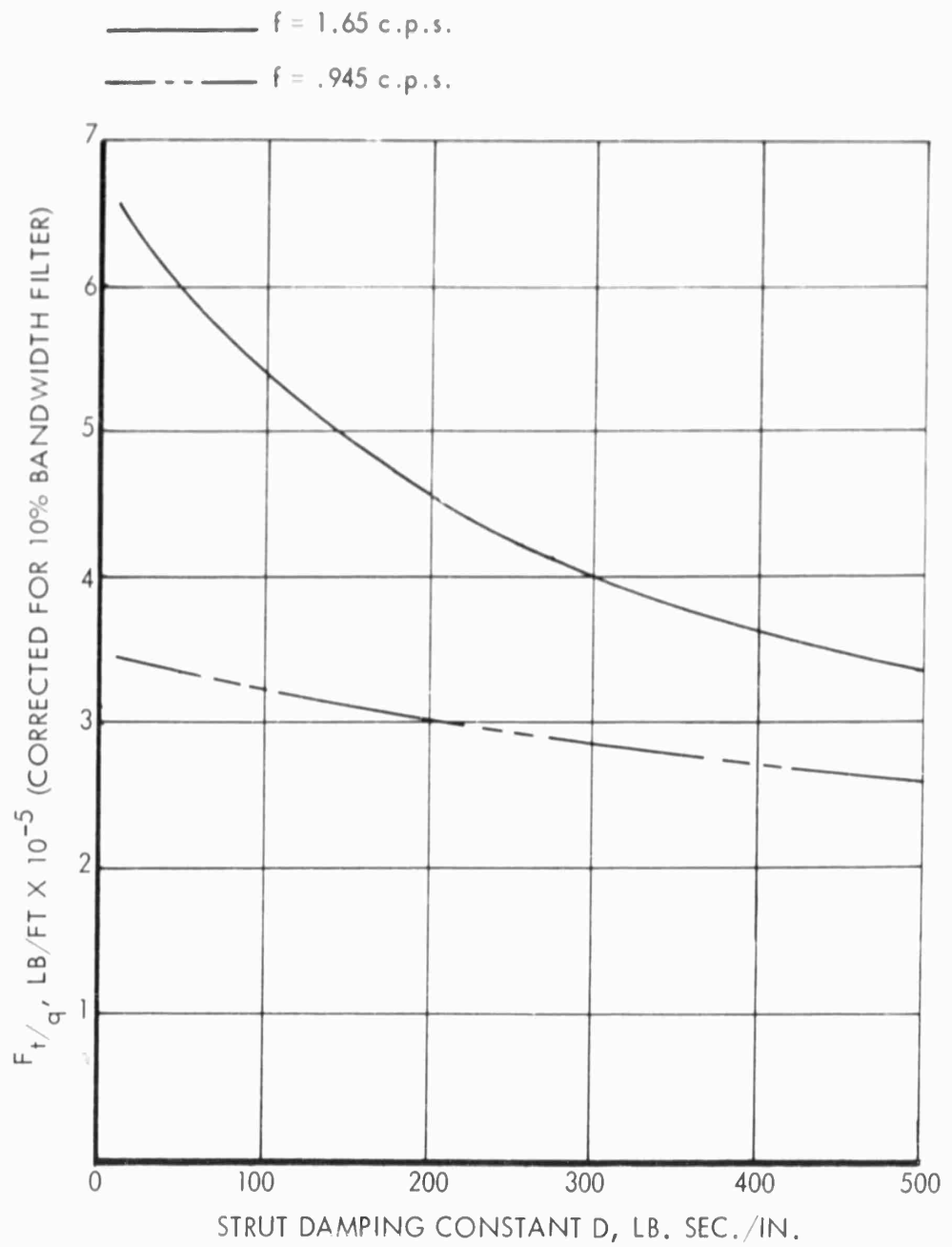


FIGURE 54: Variation in Peak Amplitude of Tire Force With Linear Strut Damping Constant D

Tire Pressure = 90 p.s.i.

Single Gear Analysis

$V_H = 55 \text{ fps}$

KEY:

R ~ Magnitude

$\Psi$  ~ Phase Angle (Relative To Drive), Radians

Drive At 2 Inches Peak-To-Peak, 10 Volts/In

T.P. = 90 psi

D = 1700 Lb-Sec/In

$K_a = 28,150$  Lb/In

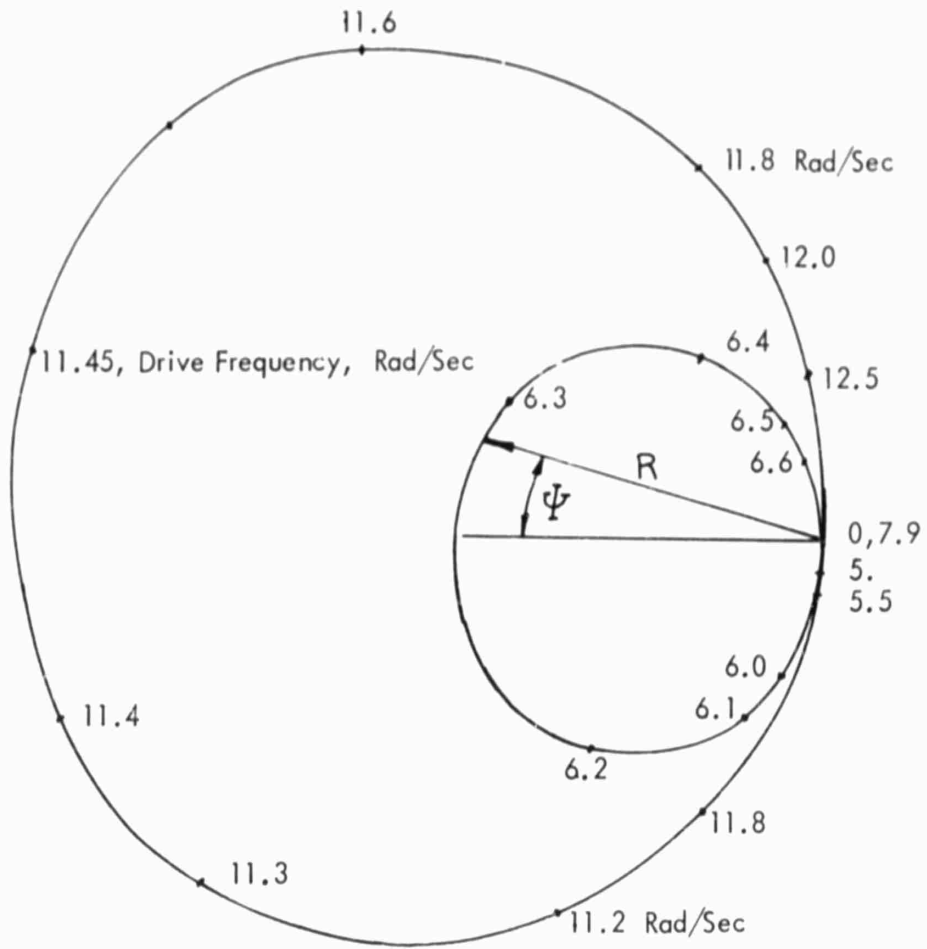


FIGURE 55 : Nyquist Diagram For Tire Force (Uncorrected For Filter Bandwidth)

$\Delta F_t$  - MAIN GEAR TIRE FORCE  
LBS X  $10^{-3}$

$Z_f$  - AIRPLANE CG ACCELERATION  
IN/SEC<sup>2</sup> X  $10^{-3}$

$\dot{Z}_f$  - AIRPLANE CG VELOCITY  
IN/SEC

$\Delta M_{x1}$  - WING ROOT BENDING MOMENT  
IN-LBS X  $10^{-6}$

$\Delta S_{z1}$  - WING ROOT SHEAR  
LBS X  $10^{-3}$

$\Delta M_{x6}$  - BENDING NEAR OUTBOARD NACELLE  
IN-LBS X  $10^{-6}$

$\dot{q}$  - MAIN GEAR RUNWAY DERIVATIVE  
IN/SEC

$\ddot{a}_0$  - RIGID BODY ACCELERATION  
IN/SEC<sup>2</sup> X  $10^{-3}$

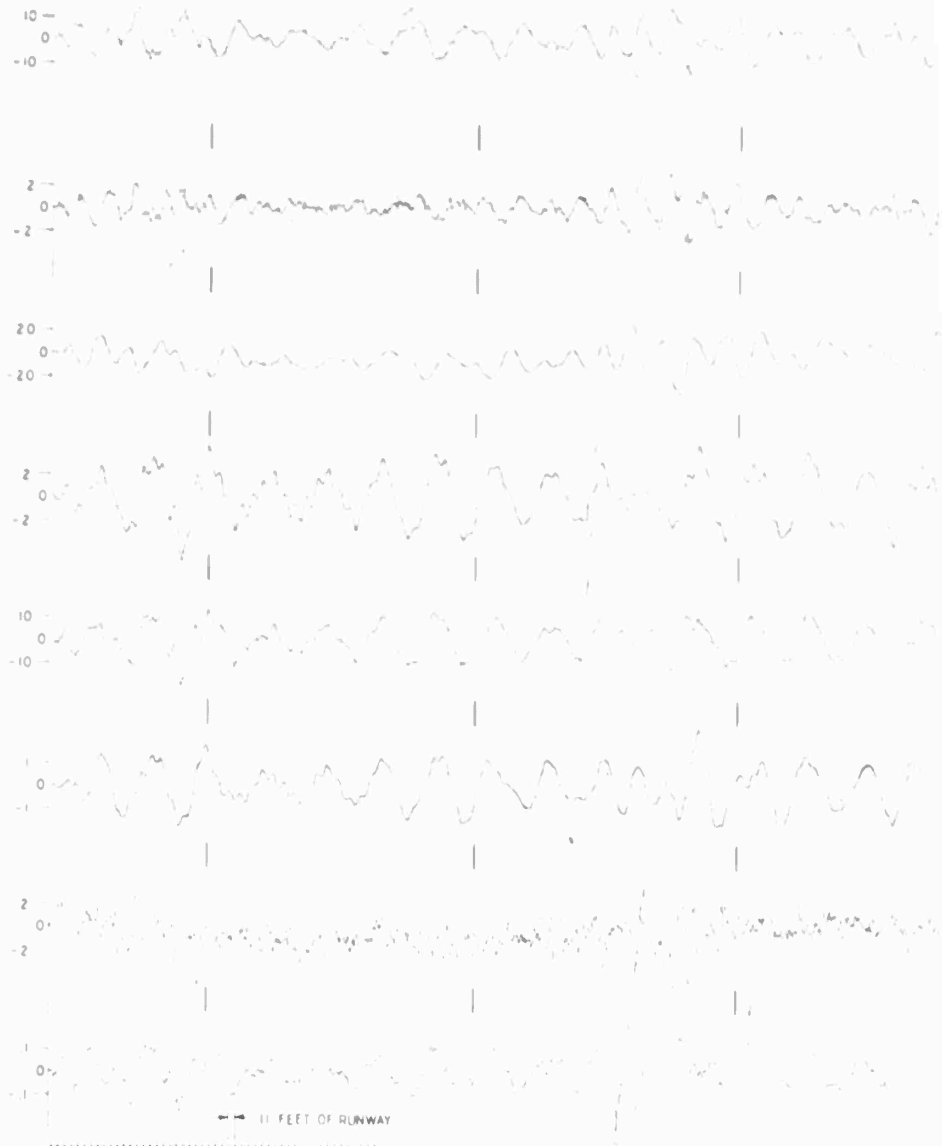
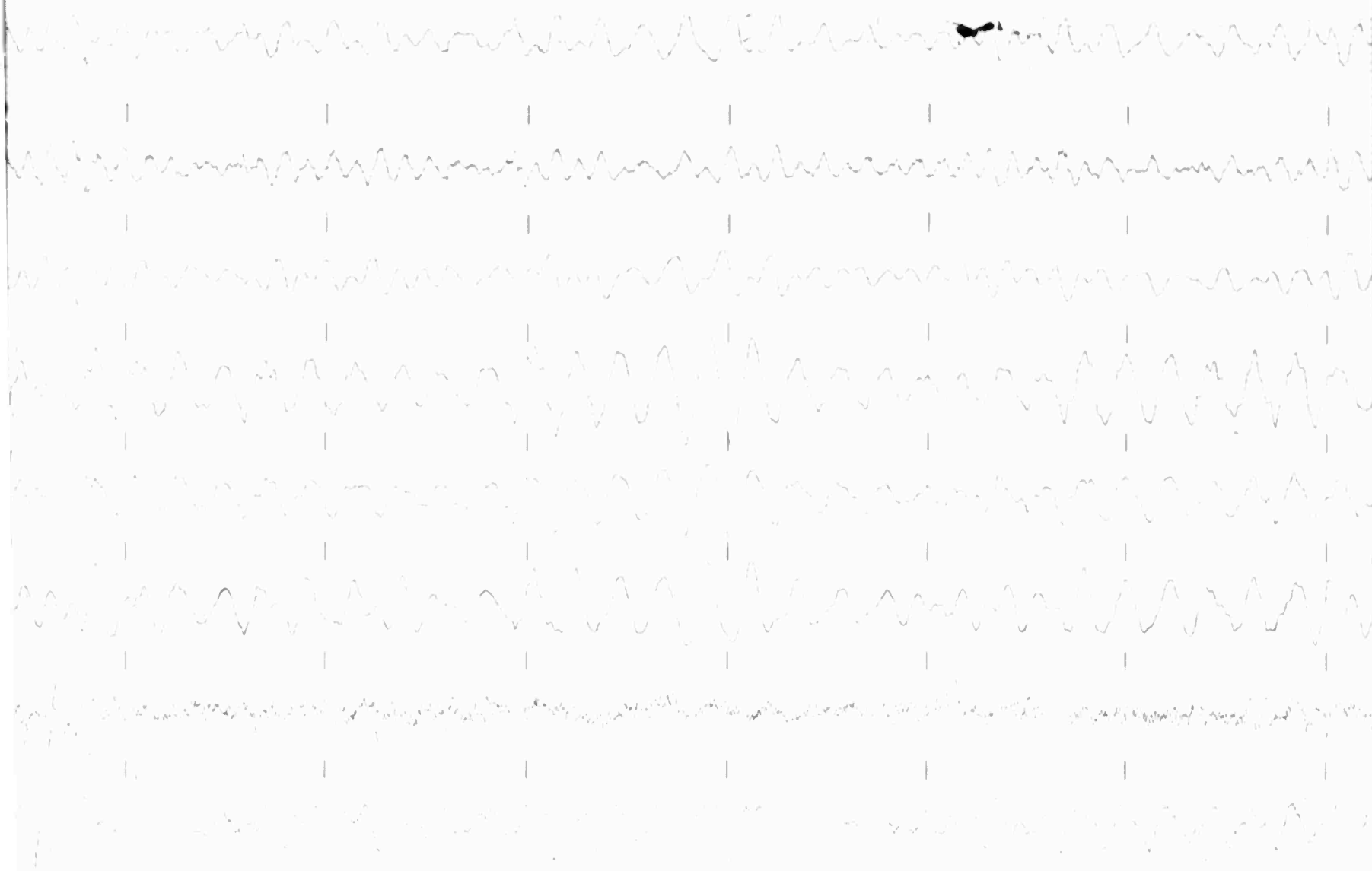


FIGURE 56:

TIME HIS

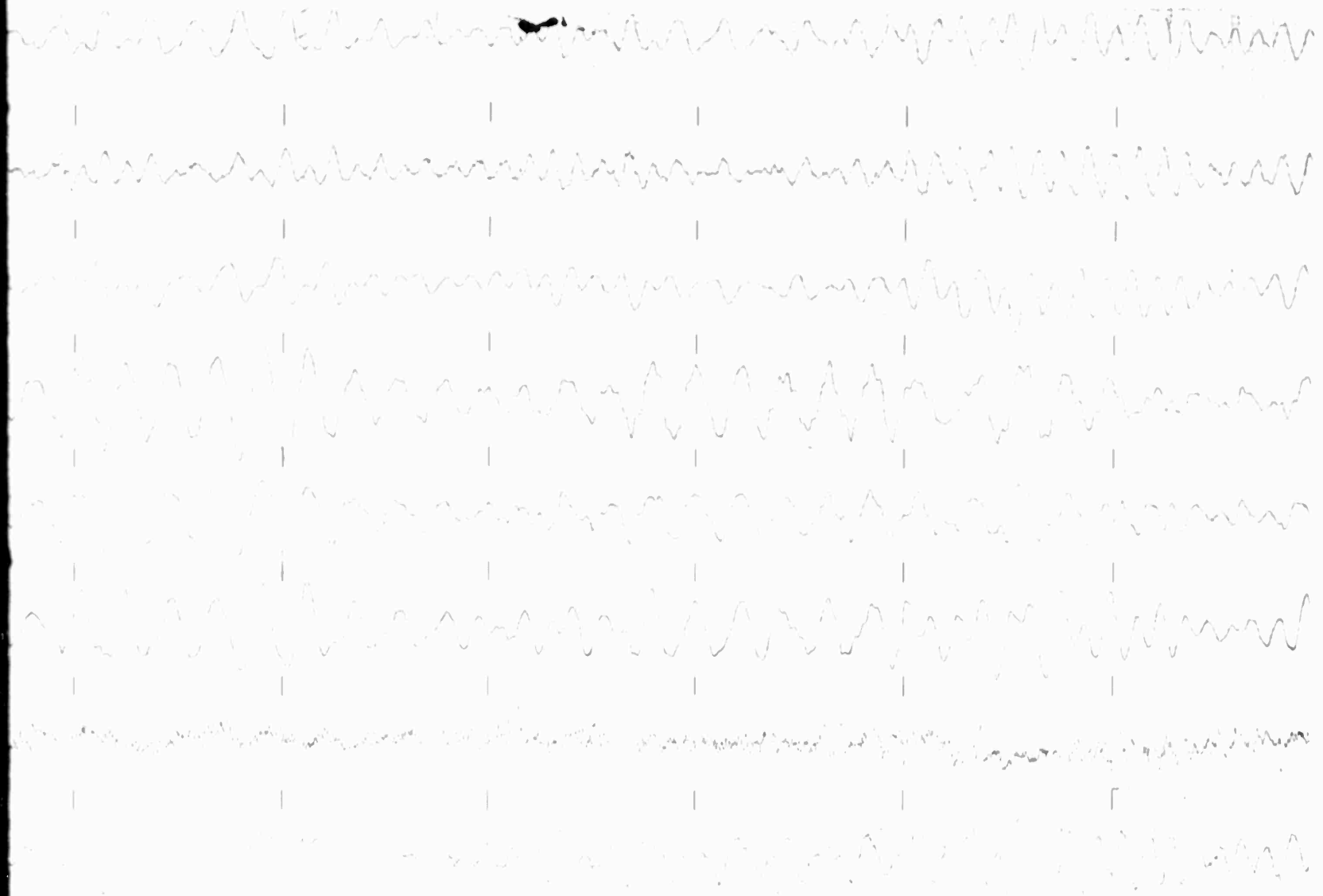




TIME HISTORY OF LOADS AND MOTIONS FOR  
SINGLE GEAR TAXIING

STANDARD CONFIGURATION  
TAXI SPEED -  $V_H$  = 88 FT/SEC





ND MOTIONS FOR  
AXIING  
RAT ION  
8 FT/SEC

3

$\Delta F_s$  - MAIN GEAR STRUT FORCE  
LBS X  $10^{-3}$

$Z_T$  - AIRPLANE CG ACCELERATION  
IN/SEC<sup>2</sup> X  $10^{-3}$

$\Delta M_{y_6}$  - TORSION NEAR OUTBOARD NACELLE  
IN-LBS X  $10^{-6}$

$\Delta M_{y_1}$  - WING ROOT TORSION MOMENT  
IN-LBS X  $10^{-6}$

$Z_T$  - WING TIP ACCELERATION  
IN/SEC<sup>2</sup> X  $10^{-3}$

$\Delta S_{z_6}$  - SHEAR NEAR OUTBOARD NACELLE  
LBS X  $10^{-3}$

$q$  - MAIN GEAR RUNWAY DERIVATIVE  
IN/SEC

$\delta_o$  - RIGID BODY ACCELERATION  
IN/SEC<sup>2</sup> X  $10^{-3}$



FIGURE 57:

TIME HI





TIME HISTORY OF LOADS AND MOTIONS FOR  
SINGLE GEAR TAXIING

STANDARD CONFIGURATION  
TAXI SPEED  $\sim V_H = 88$  FT/SEC





AND MOTIONS FOR  
AXIING  
URATION  
88 FT/SEC

3

$\Delta F_{t2}$  - FRONT MAIN TIRE FORCE  
LBS X  $10^{-3}$

$\Delta M_{x1}$  - WING ROOT BENDING MOMENT  
IN-LBS X  $10^{-6}$

$\Delta M_{y1}$  - WING ROOT TORSION MOMENT  
IN-LBS X  $10^{-6}$

$\Delta S_{z1}$  - WING ROOT SHEAR  
LBS X  $10^{-3}$

$Z_f$  - AIRPLANE CG ACCELERATION  
IN/SEC<sup>2</sup> X  $10^{-3}$

$q_1$  - NOSE GEAR RUNWAY DERIVATIVE  
IN/SEC

$\Delta F_{t1}$  - NOSE GEAR TIRE FORCE  
LBS X  $10^{-3}$

$\delta_0$  - RIGID BODY ACCELERATION  
IN/SEC<sup>2</sup> X  $10^{-3}$

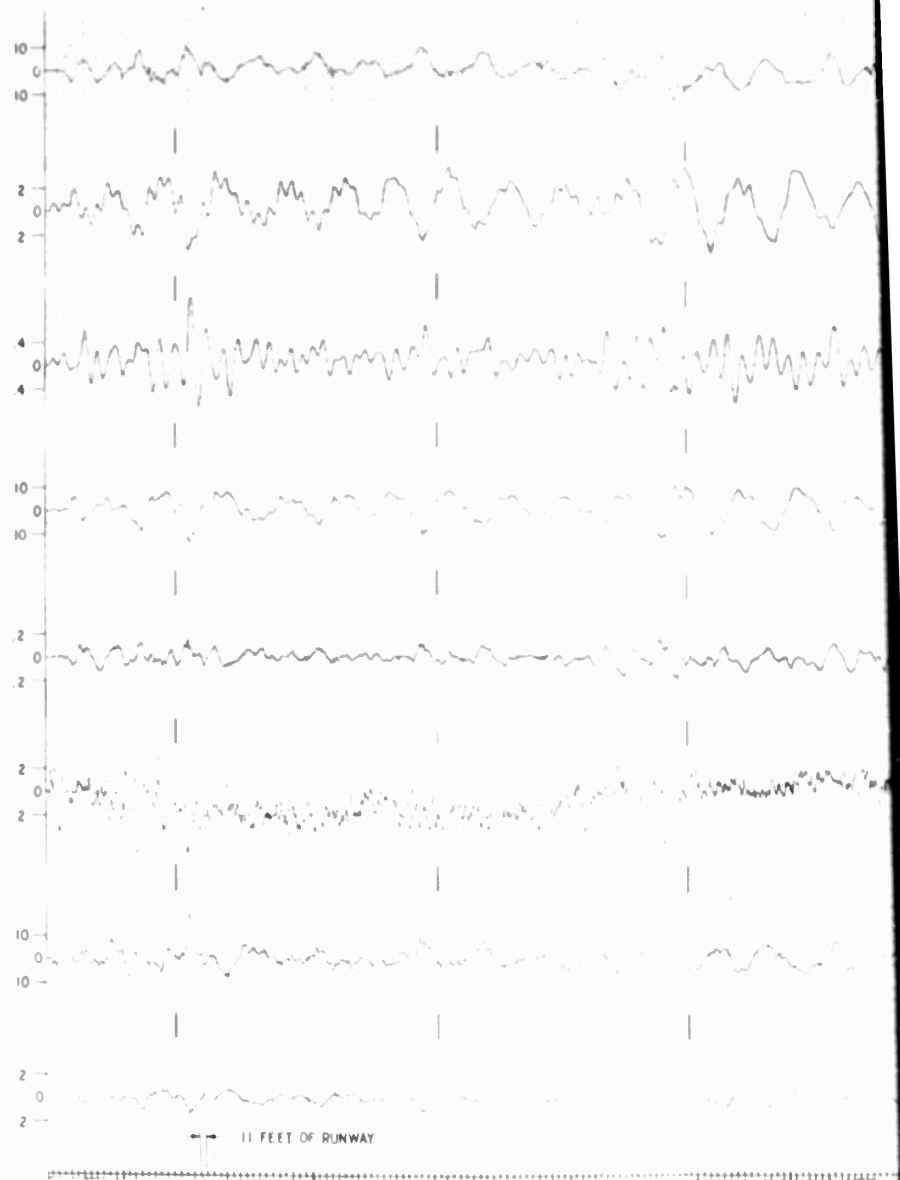
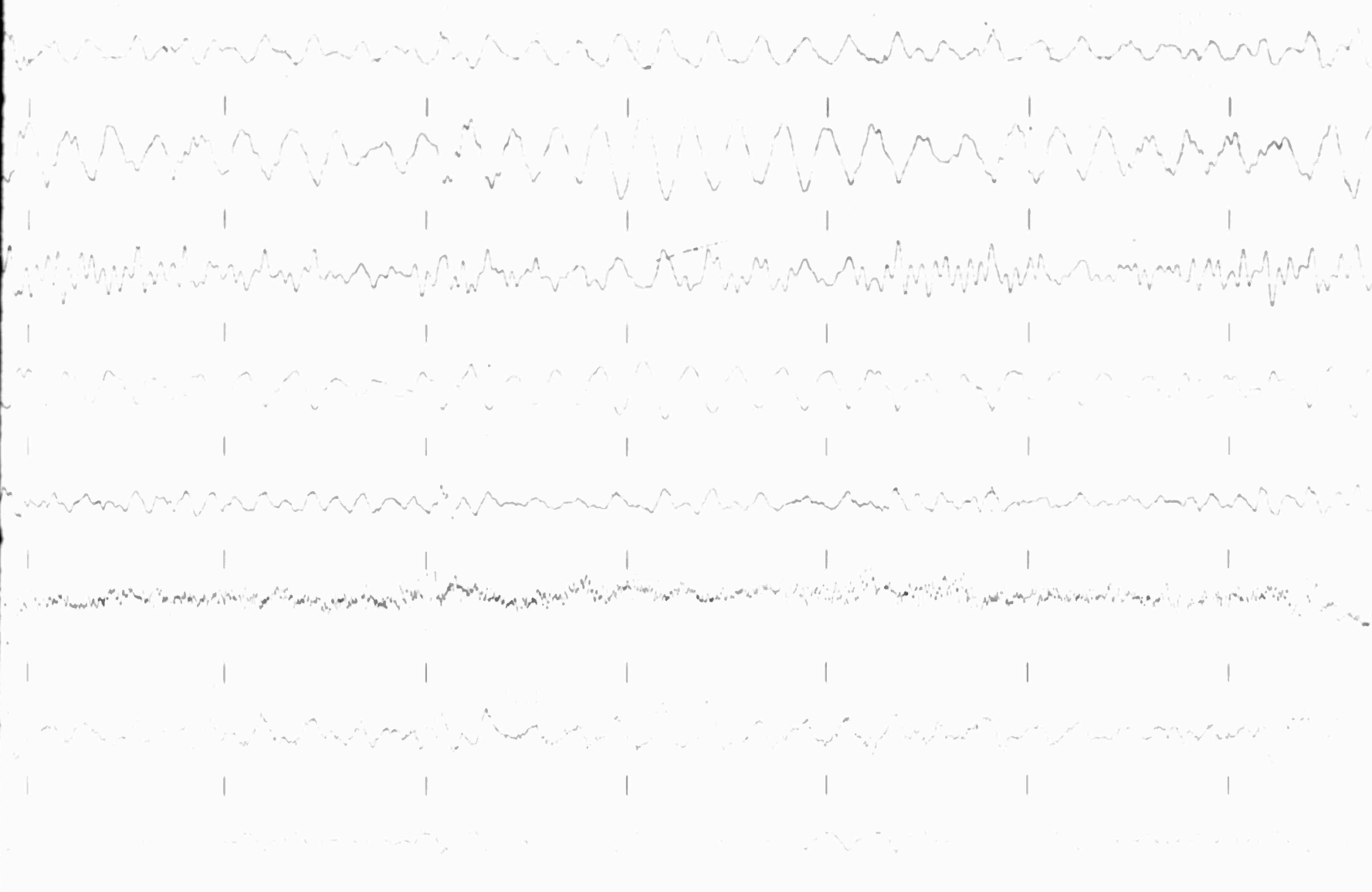


FIGURE 58:

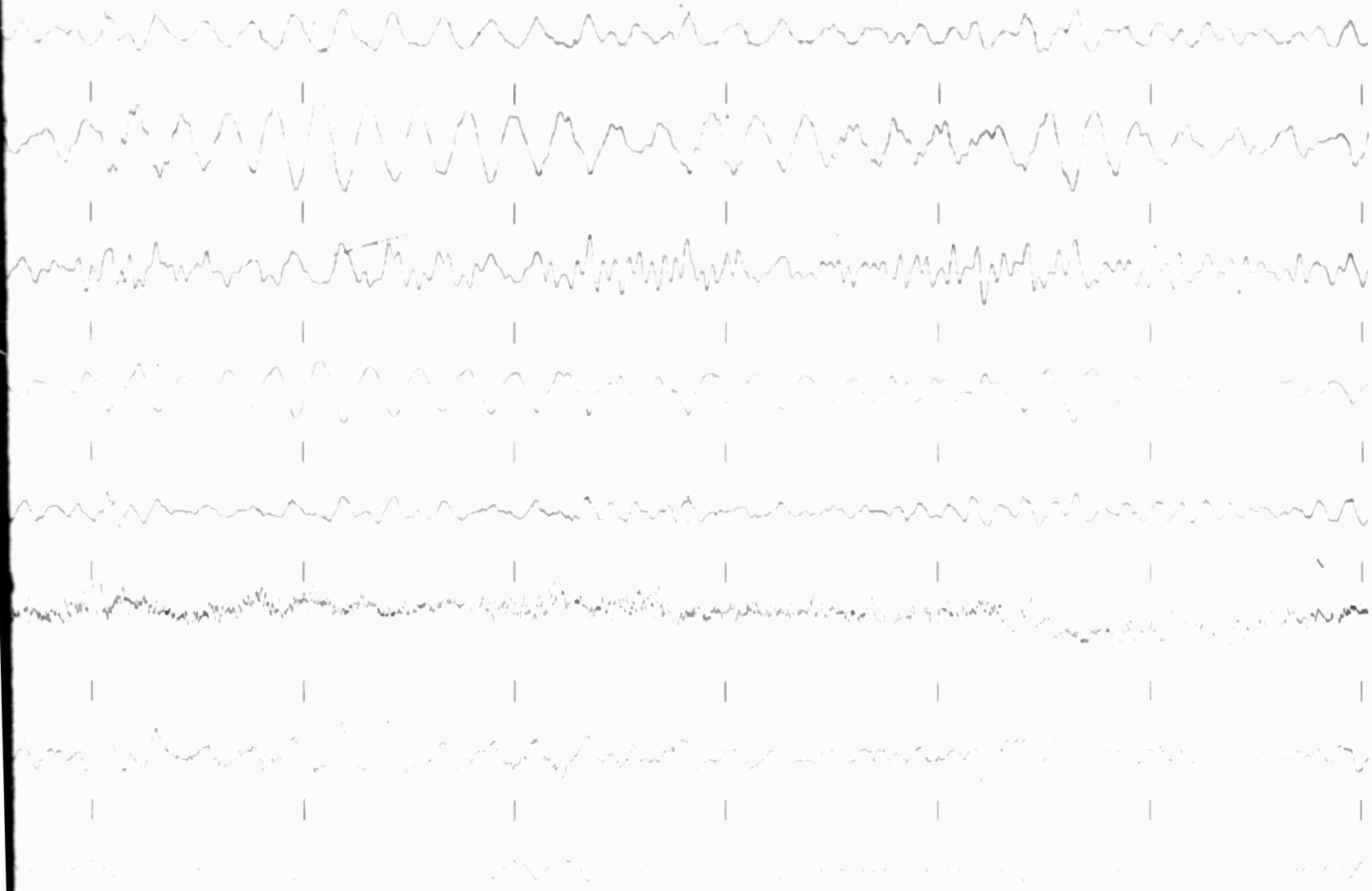
TIME





TIME HISTORY OF LOADS AND MOTIONS FOR  
MULTI-GEAR TAXIING  
STANDARD CONFIGURATION  
TAXI SPEED  $\sim V_H = 88 \text{ F/SEC}$





OS AND MOTIONS FOR  
R TAXIING

CONFIGURATION  
 $V_H = 88 \text{ F/SEC}$

3



FIGURE 59:

TIME HIST



TIME HISTORY OF LOADS AND MOTIONS FOR  
MULTI-GEAR TAXIING

STANDARD CONFIGURATION  
TAXI SPEED -  $V_H = 88$  FT/SEC





AND MOTIONS FOR  
TAXIING  
DURATION  
88 FT/SEC



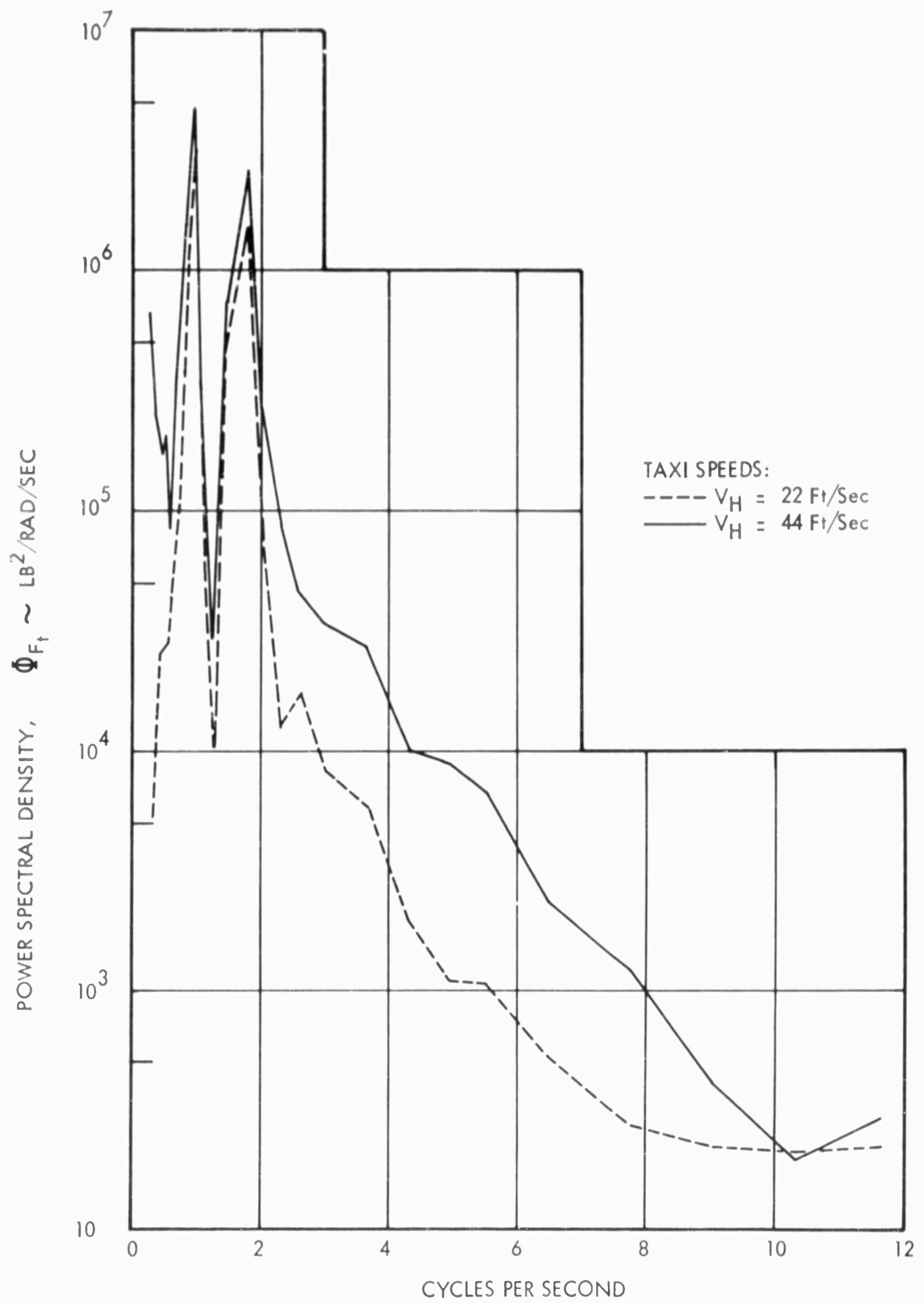


FIGURE 60 : Power Spectrum of Vertical Tire Force for the Normal Configuration (Single Gear)

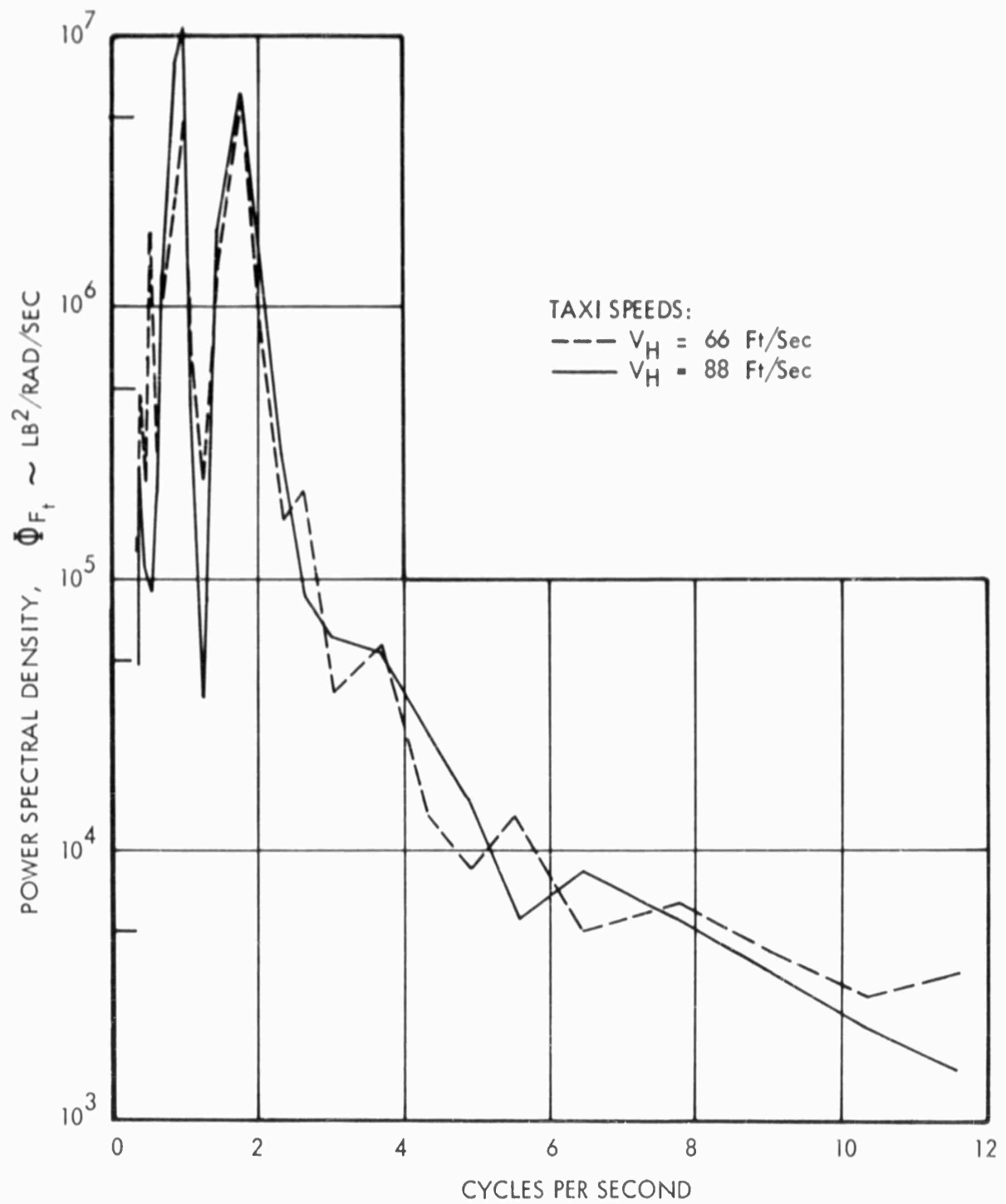


FIGURE 61 : Power Spectrum of Vertical Tire Force for the Normal Configuration (Single Gear)

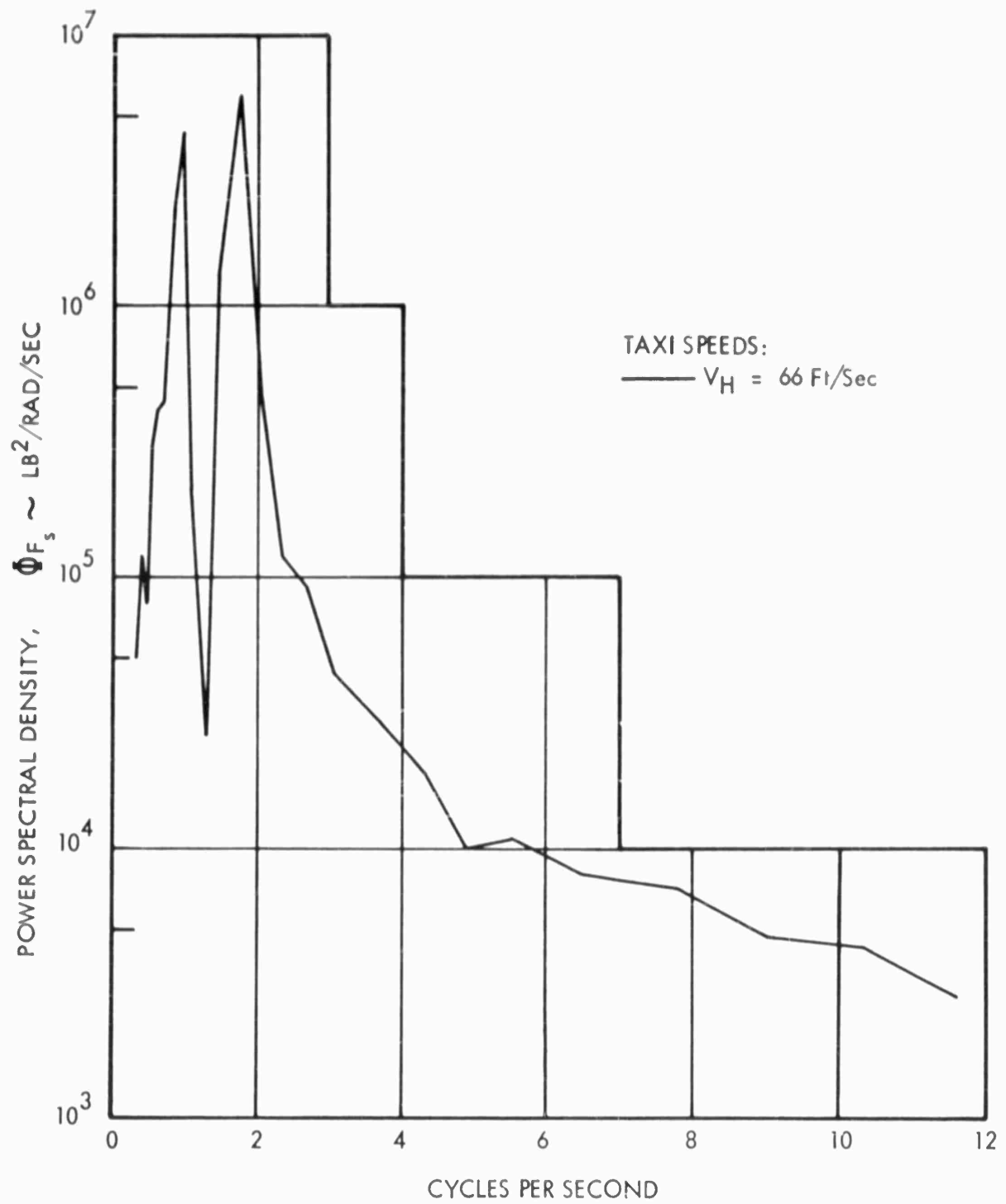


FIGURE 62 : Power Spectrum of Strut Vertical Force for the Normal Configuration  
 (Single Gear)

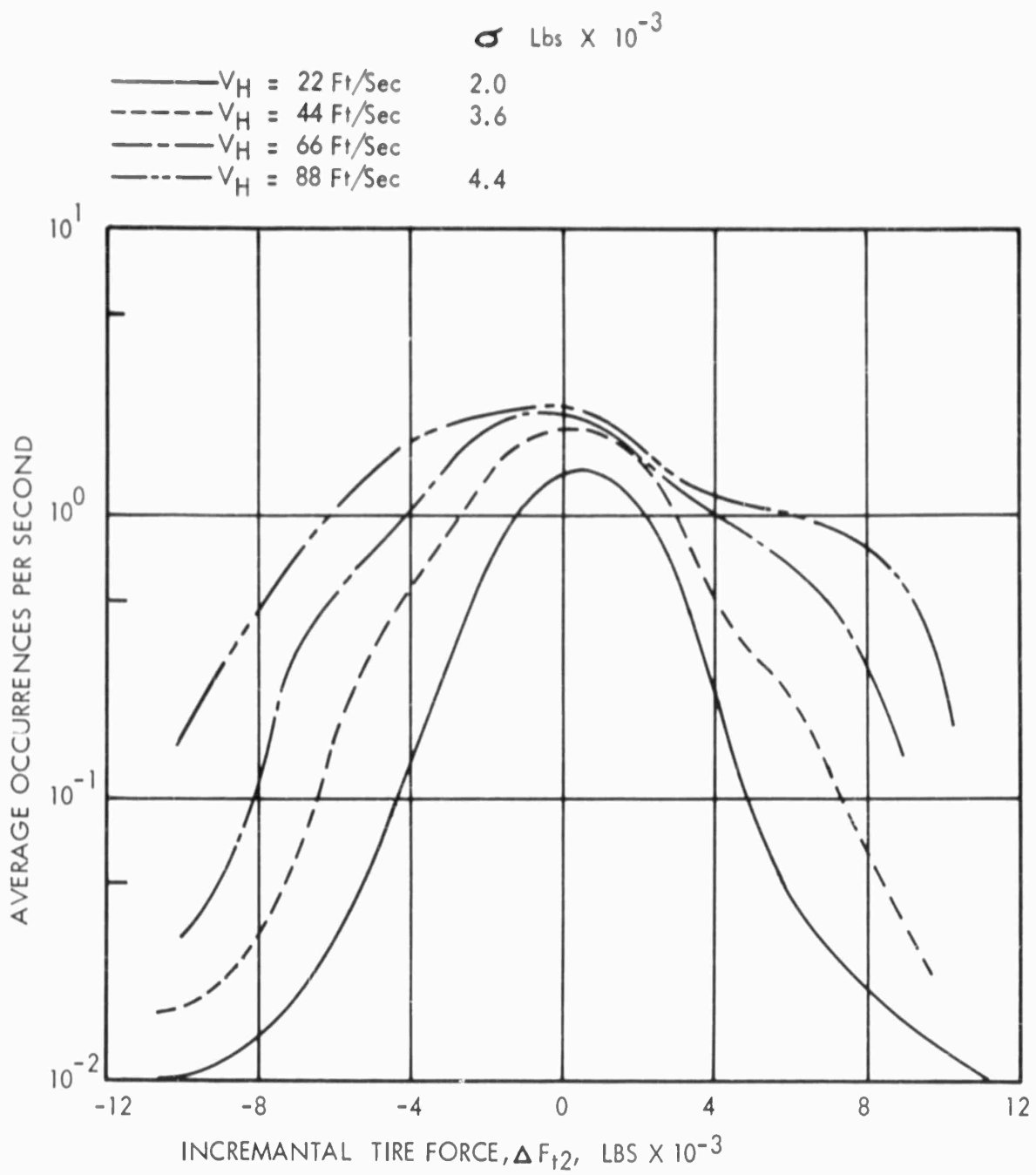


FIGURE 63 : Occurrences For,  $\Delta F_{t2}$ , Incremental Tire Vertical Force Front Main Gear

- - - - -  $V_H = 22$  Ft/Sec  
 - - - - -  $V_H = 44$  Ft/Sec  
 - - - - -  $V_H = 66$  Ft/Sec  
 - - - - -  $V_H = 88$  Ft/Sec

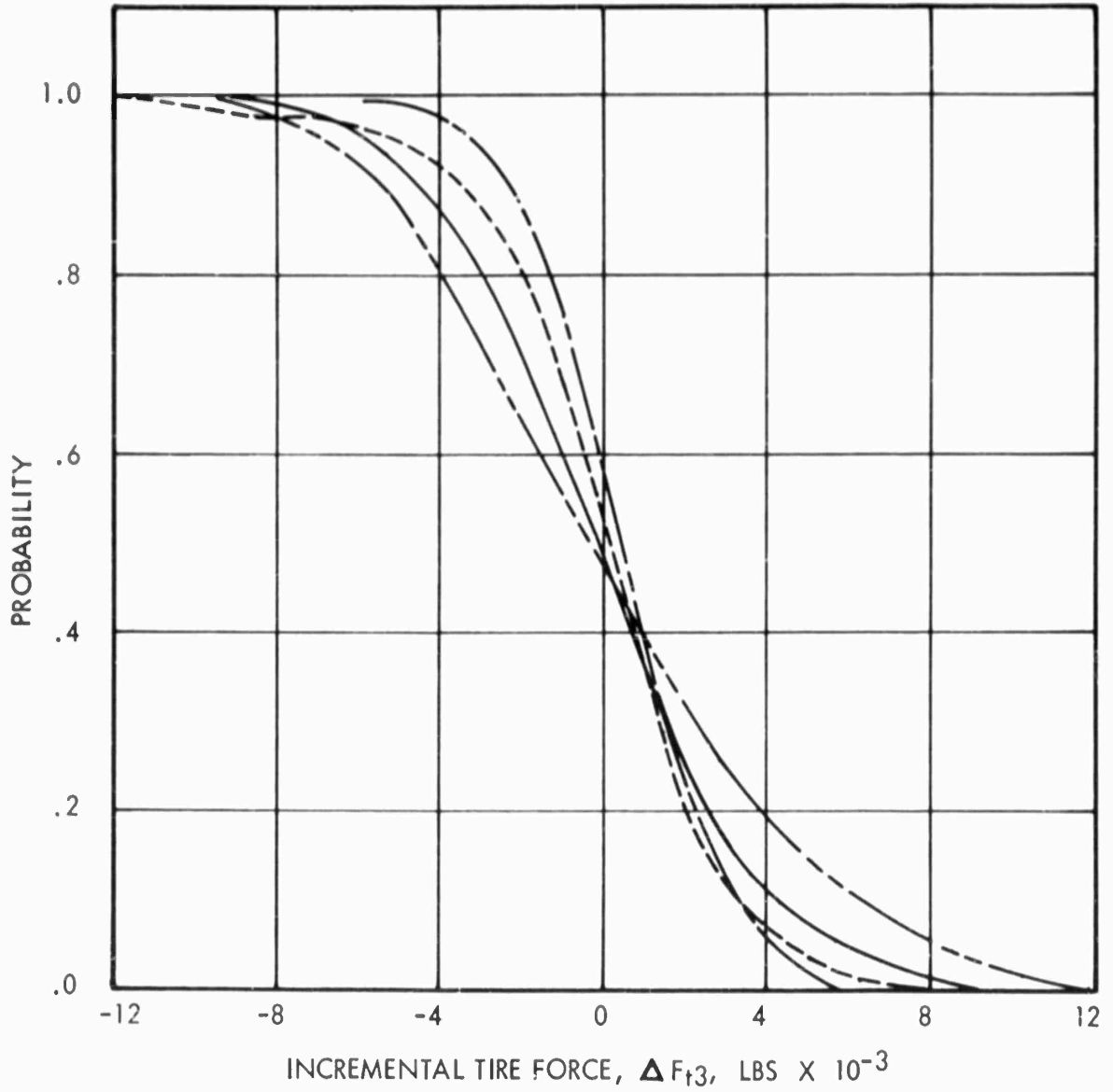


FIGURE 64 : Cumulative Probability of the Nonlinear System for Vertical Force on Rear Main Gear

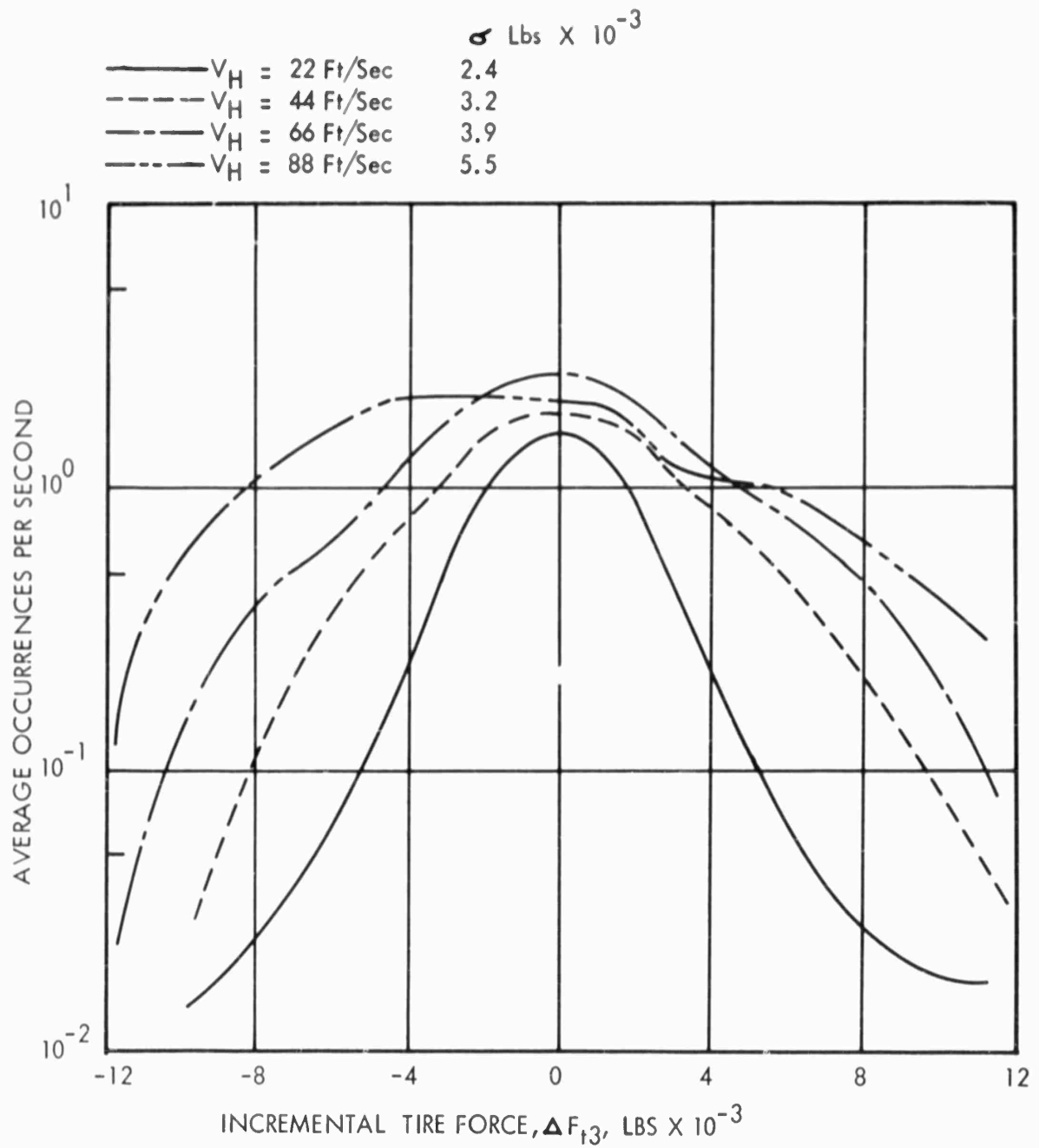


FIGURE 65 : Occurrences For,  $\Delta F_{t3}$ , Incremental Tire Vertical Force Rear Main Gear

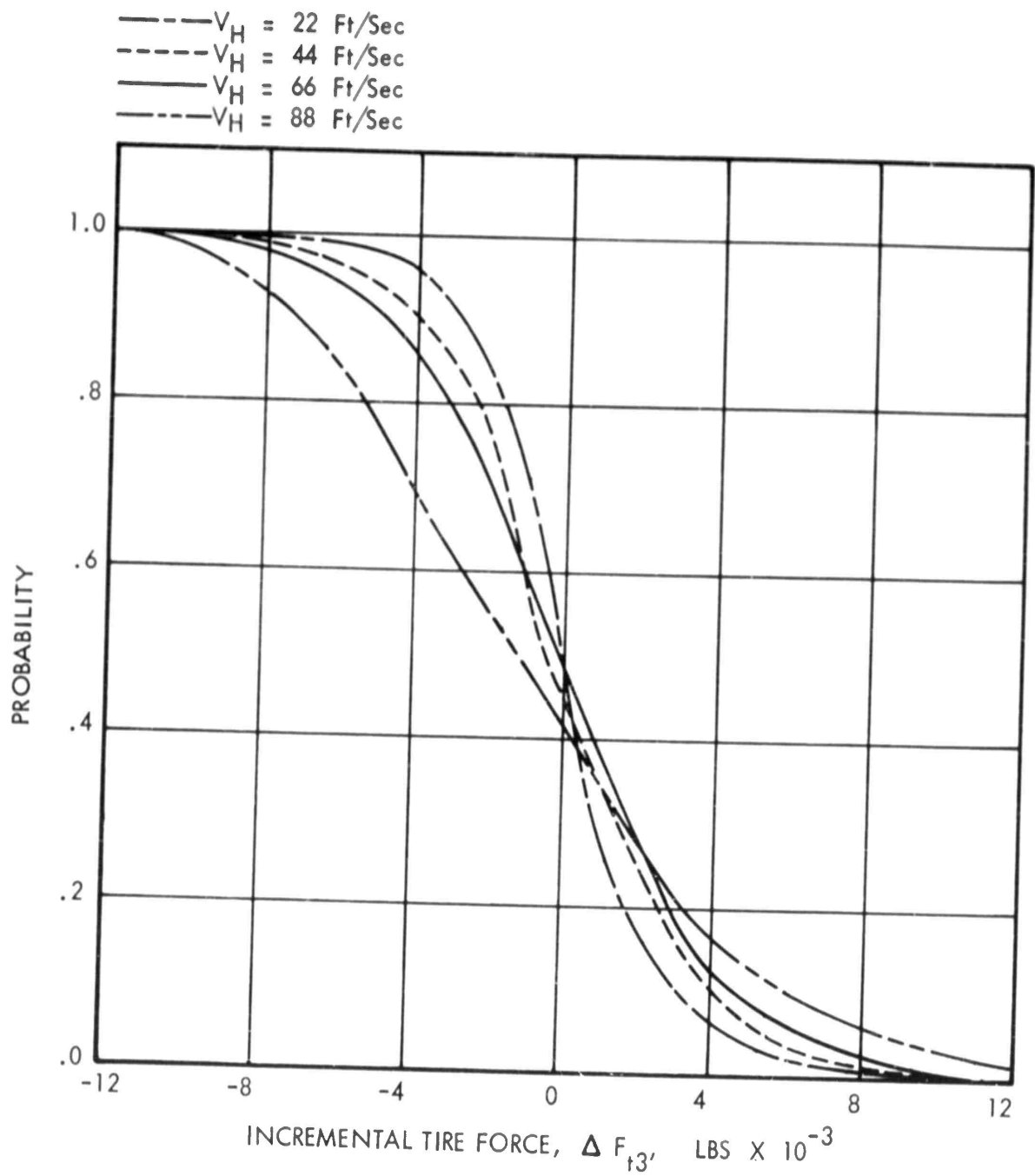


FIGURE 66: Cumulative Probability of the Nonlinear System for Vertical Force on Rear Main Gear

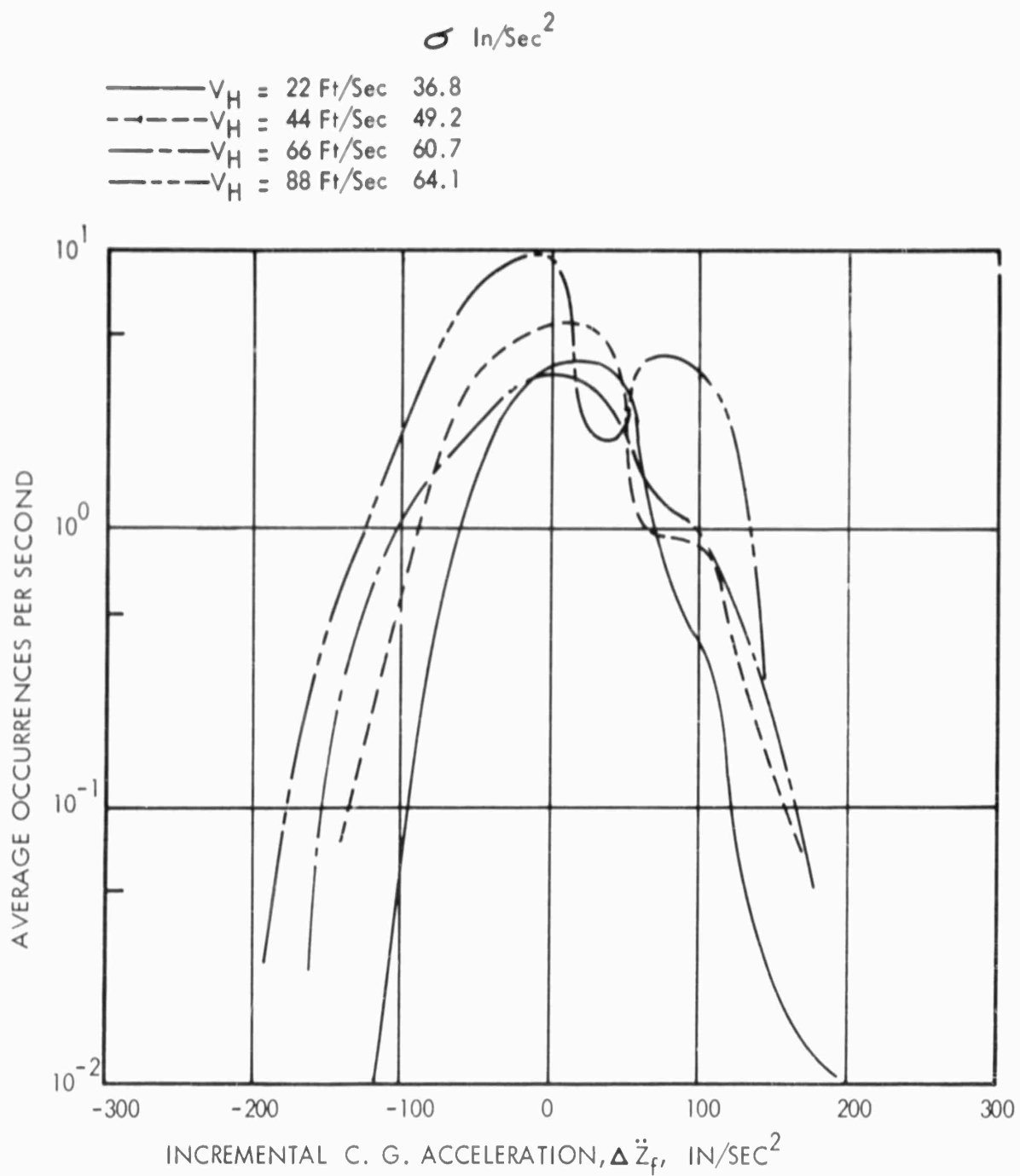


FIGURE 67 : Occurrences For,  $\Delta \ddot{z}_f$ , Airplane Center of Gravity Vertical Acceleration

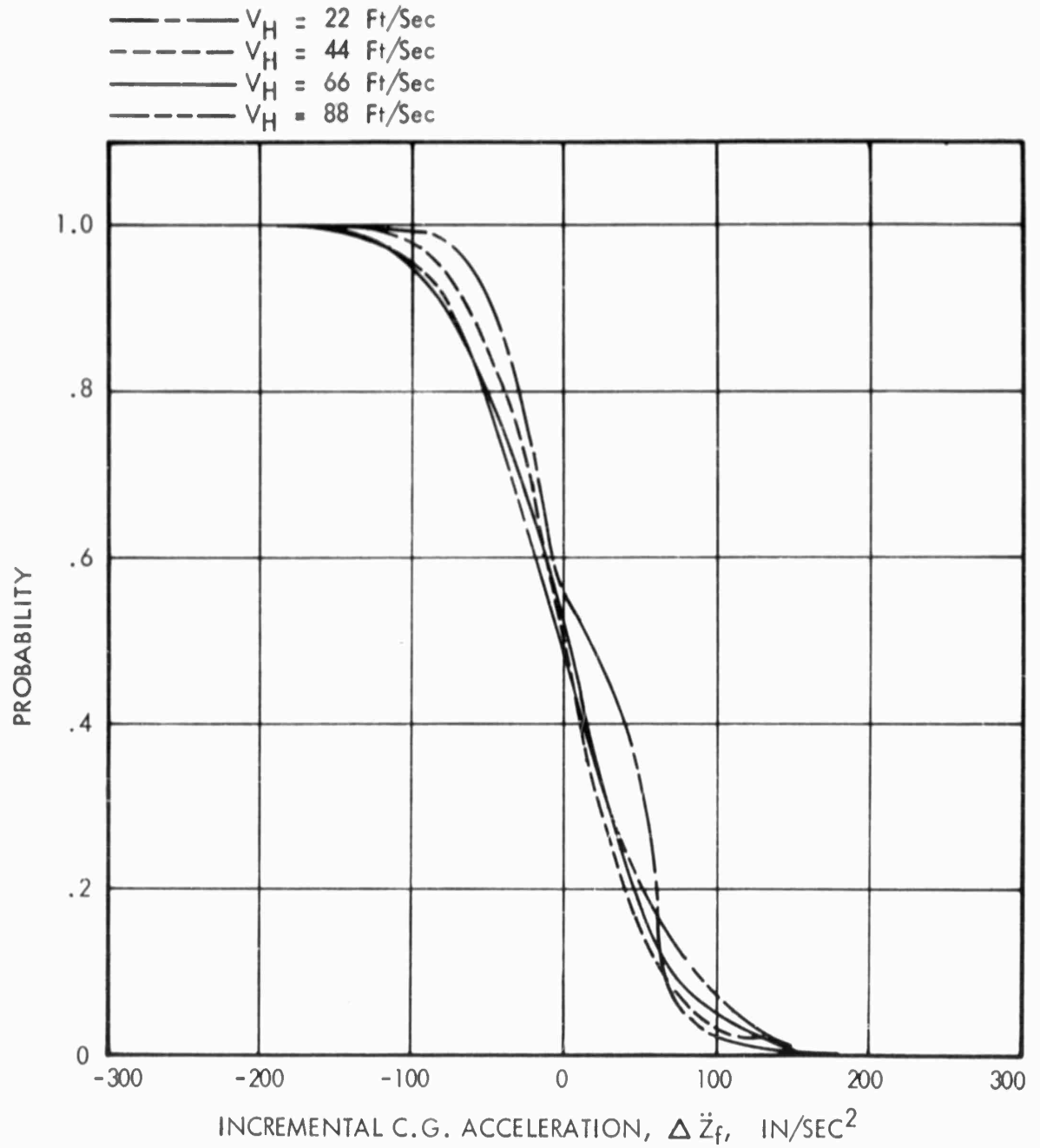


FIGURE 68 : Cumulative Probability of the Nonlinear System for Vertical Acceleration at the Center of Gravity

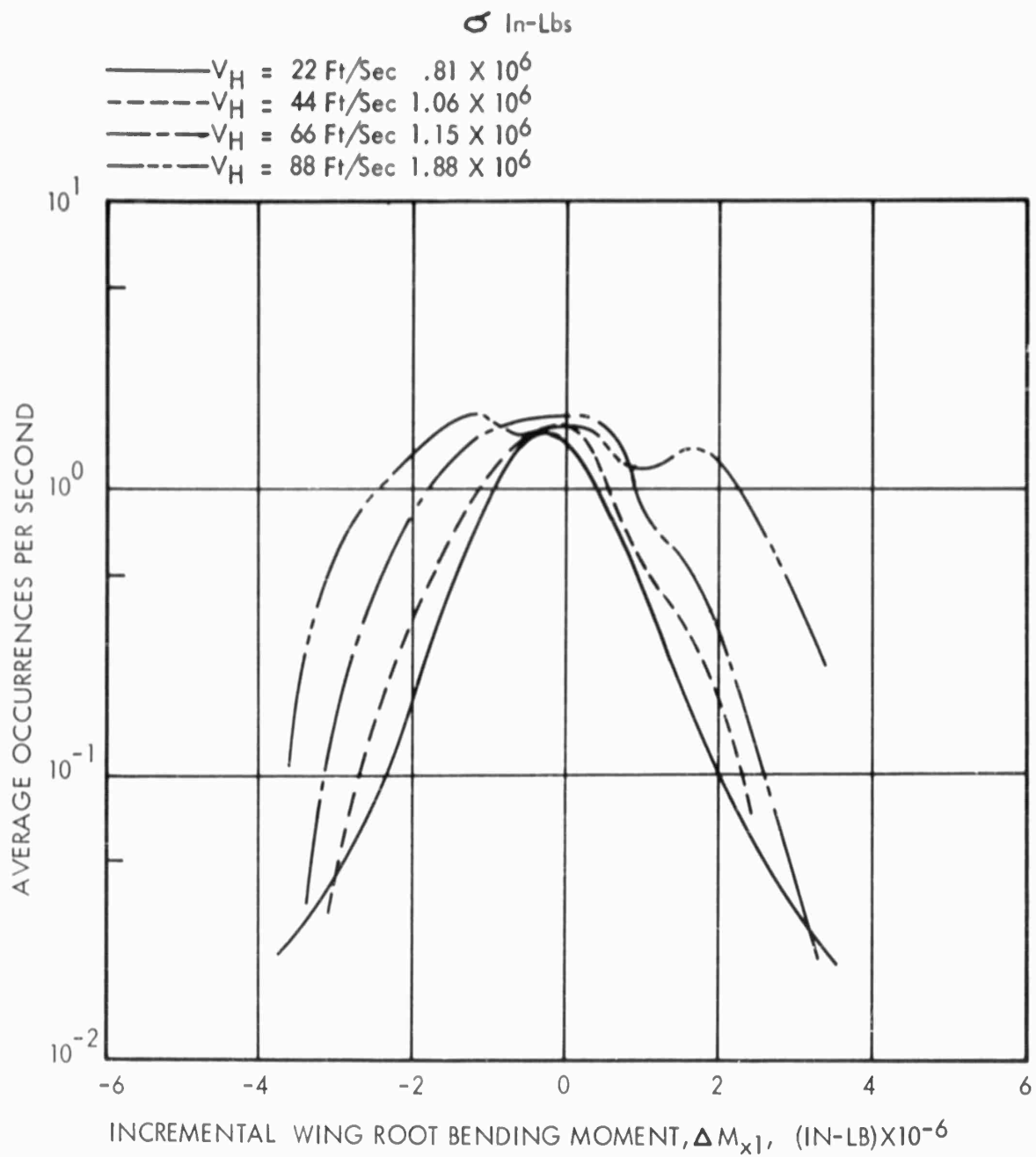
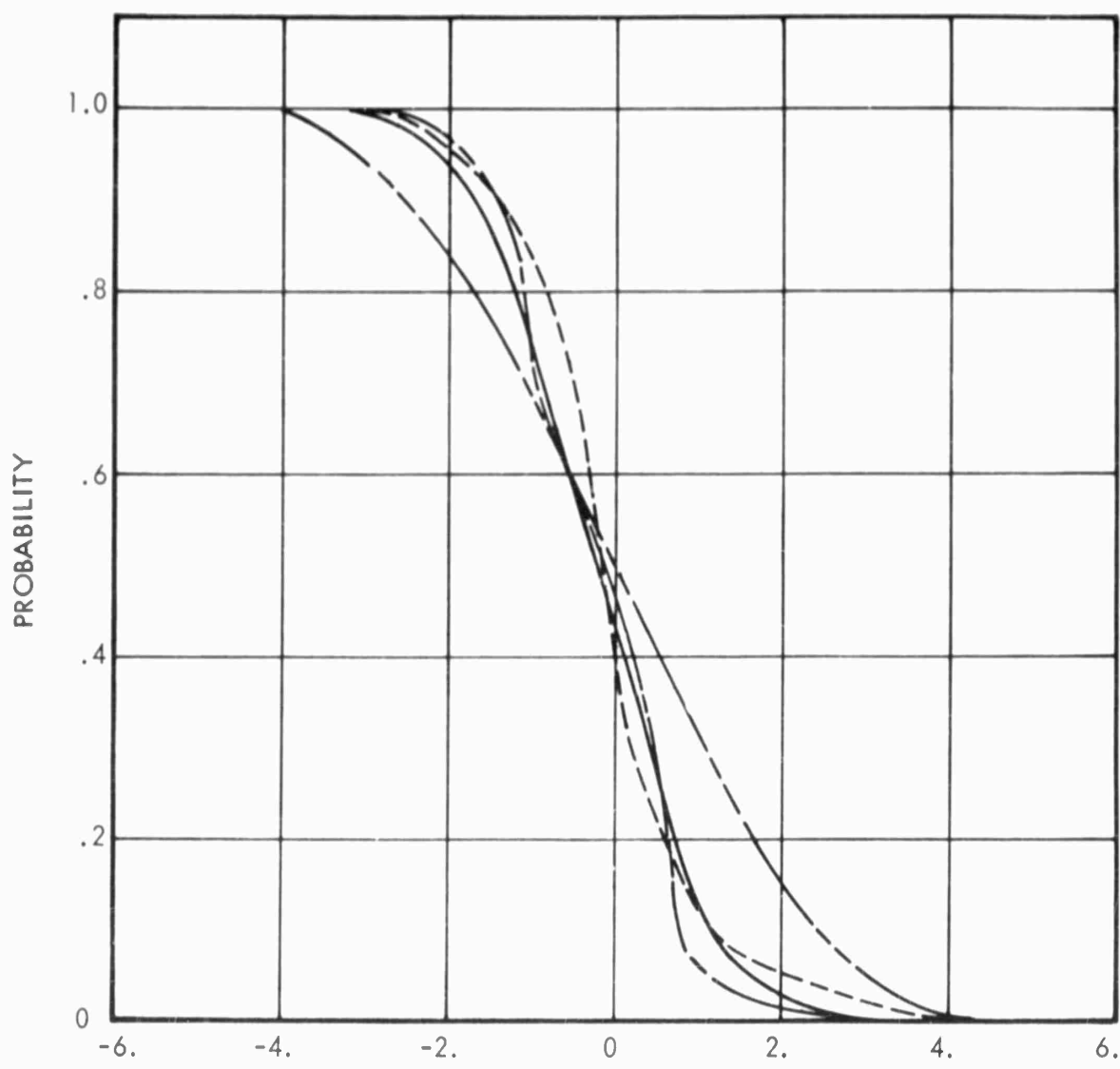


FIGURE 69 : Occurrences For,  $\Delta M_{x1}$ , Incremental Wing Bending Moments at Nominal Wing Root Station

- - - - -  $V_H = 22$  Ft/Sec  
 - - - - -  $V_H = 44$  Ft/Sec  
 - - - - -  $V_H = 66$  Ft/Sec  
 - - - - -  $V_H = 88$  Ft/Sec



INCREMENTAL WING ROOT BENDING MOMENT,  $\Delta M_{x1}$ , IN-LB  $\times 10^{-6}$

FIGURE 70 : Cumulative Probability of the Nonlinear System for Wing Bending Moment at Nominal Wing Root Station

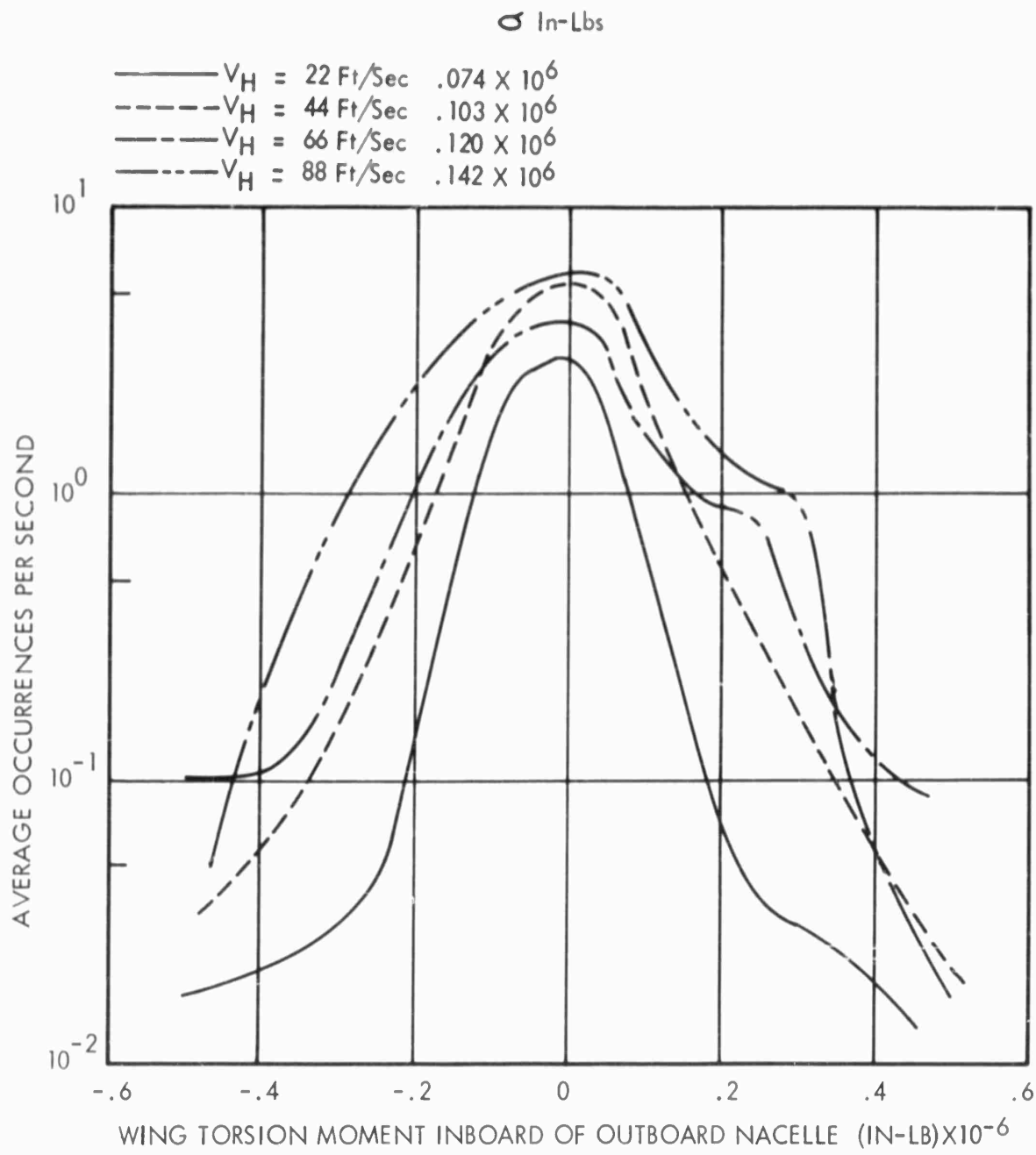


FIGURE 71 : Occurrences For,  $\Delta M_{y6}$ , Incremental Wing Torsion Moments Inboard of Outboard Nacelle (+Nose Down)

- - - -  $V_H = 22$  Ft/Sec  
 - - - -  $V_H = 44$  Ft/Sec  
 - - - -  $V_H = 66$  Ft/Sec  
 - - - -  $V_H = 88$  Ft/Sec

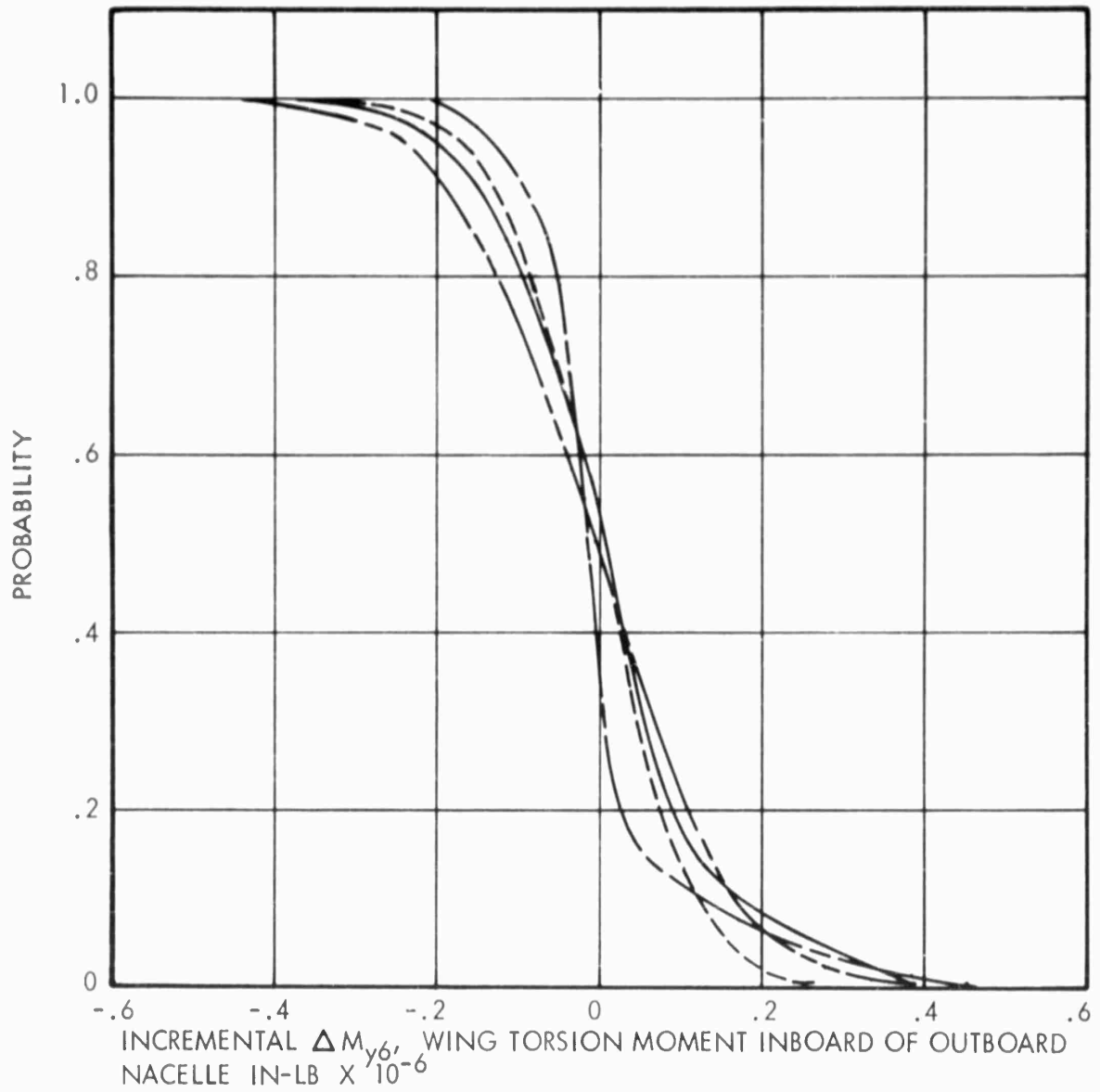


FIGURE 72 : Cumulative Probability of the Nonlinear System for Wing Torsion Moments Inboard of Outboard Nacelle (+Nose Down)

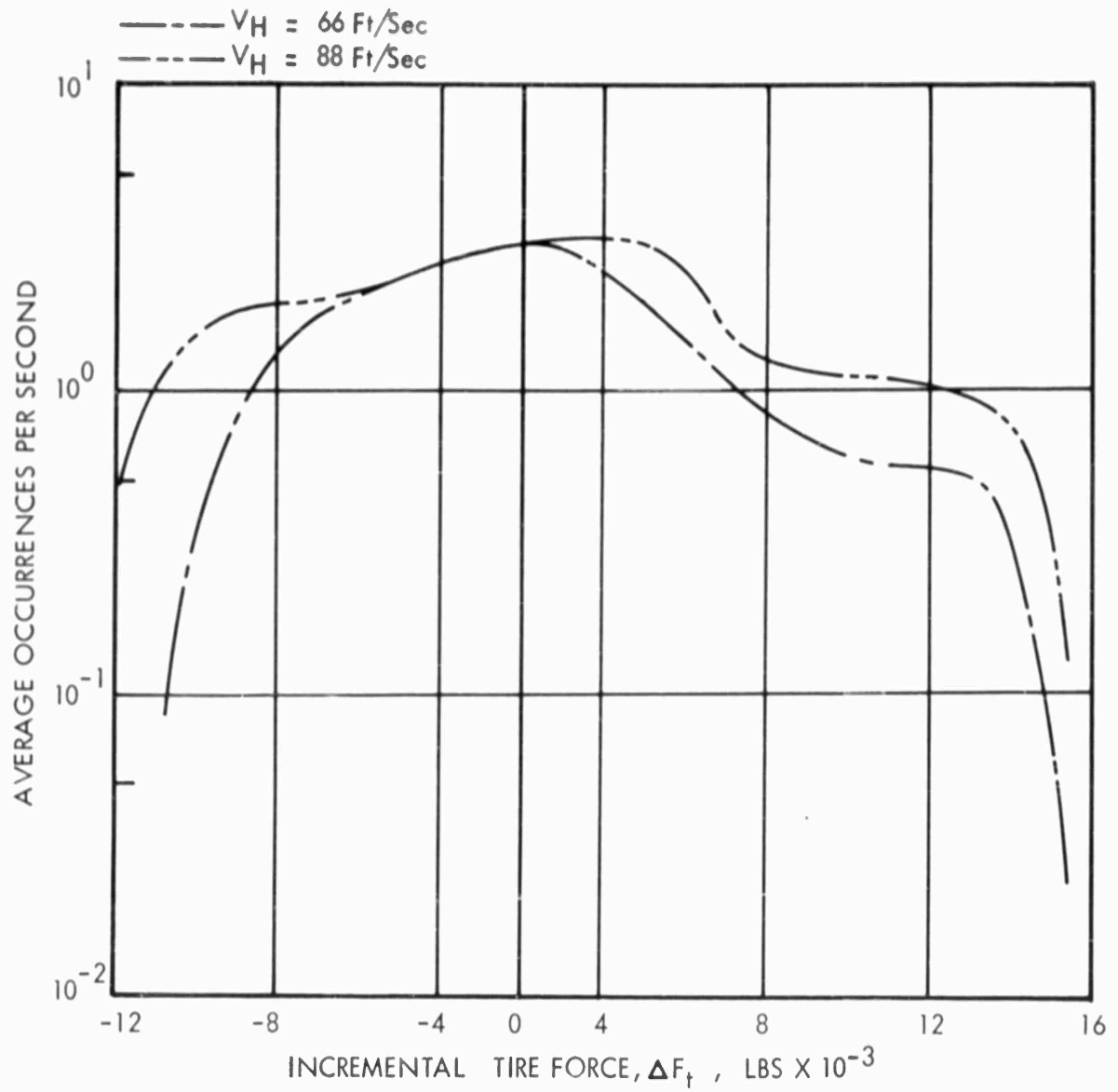


FIGURE 73 : Occurrences For,  $\Delta F_t$ , Incremental Tire Vertical Force (Single Gear)

Tire Pressure = 90 psi  
D = 185 Lb-Sec/In

ANALYSIS METHODS AND TAXI SPEEDS:

----- Linear Harmonic -  $V_H = 55$  Ft/Sec

———— Nonlinear PSD -  $V_H = 66$  Ft/Sec

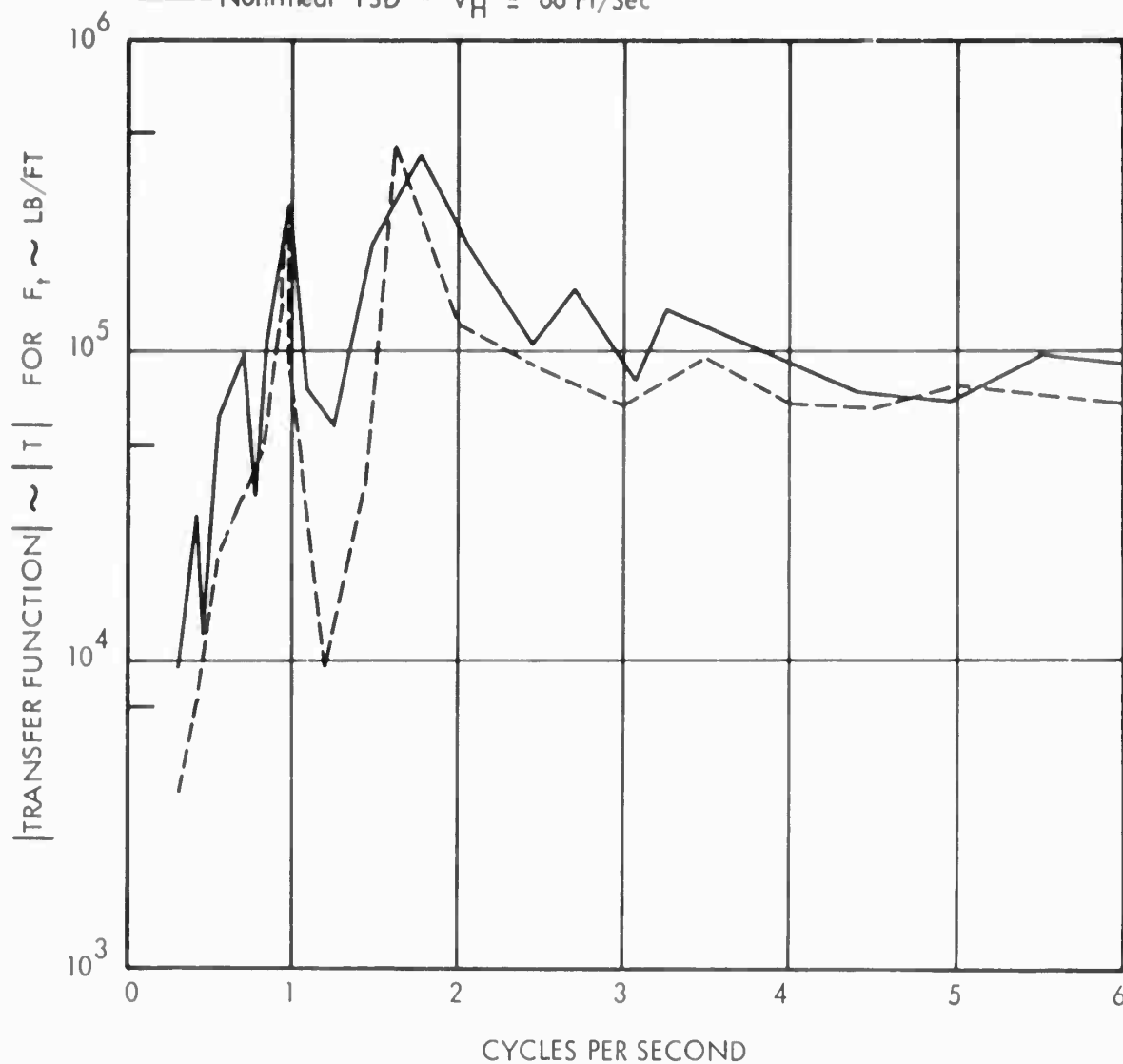


FIGURE 74 : Comparison of Transfer Functions by Linear Harmonic and Power Spectral Density Methods for Landing Gear Tire Force  
Single Gear Analysis for Normal Configuration

Tire Pressure = 90 psi  
D = 185 Lb-Sec/In

ANALYSIS METHODS AND TAXI SPEED:

-----Linear Harmonic -  $V_H = 55$  Ft/Sec

————Nonlinear PSD -  $V_H = 66$  Ft/Sec

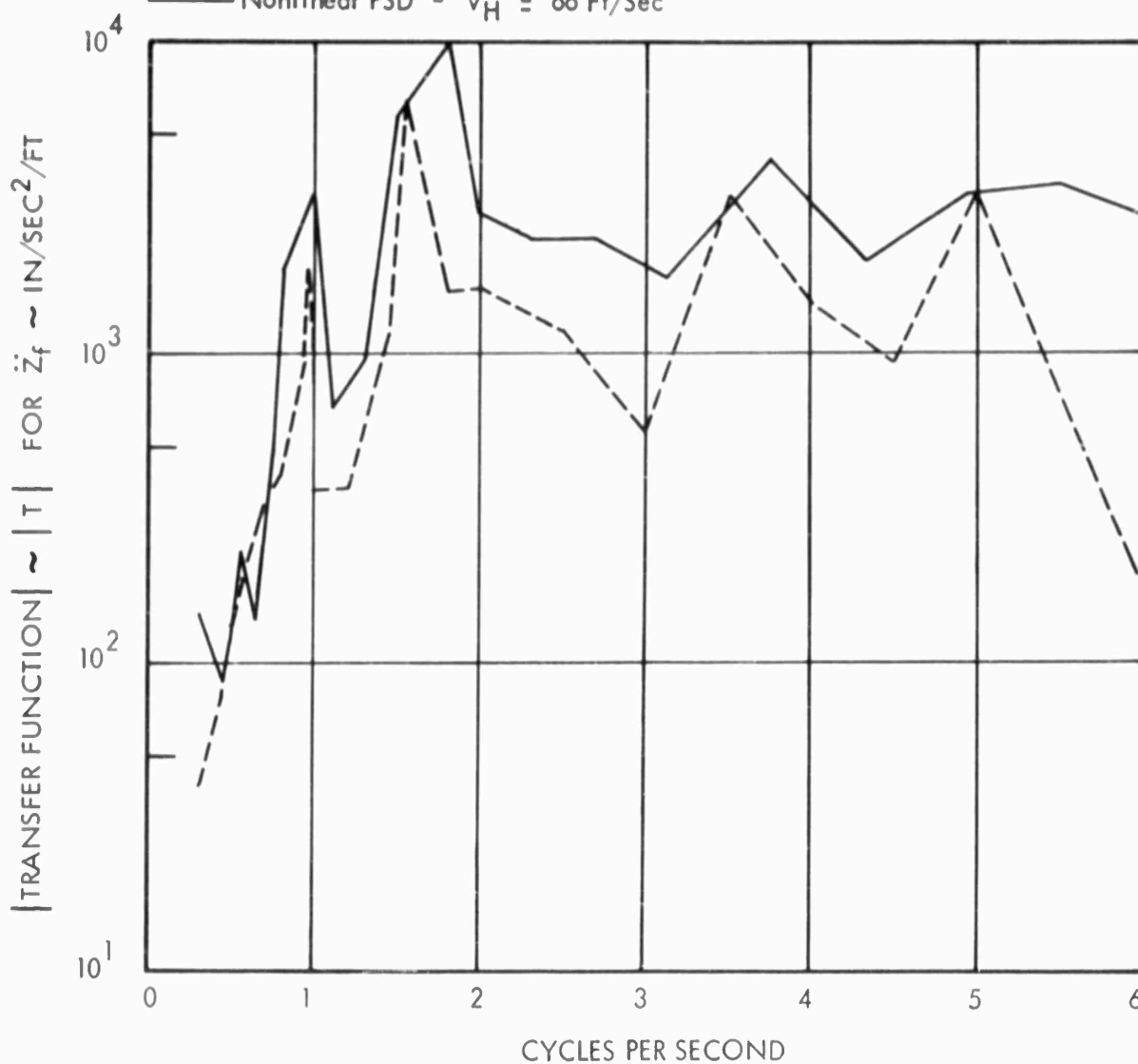


FIGURE 75 : Comparison of Transfer Functions by Linear Harmonic and Power Spectral Density Methods for Vertical Acceleration of Airplane Center of Gravity  
Single Gear Analysis for Normal Configuration

Tire Pressure = 90 psi  
D = 185 Lb-Sec/In

ANALYSIS METHODS AND TAXI SPEEDS:  
----- Linear Harmonic -  $V_H = 55$  Ft/Sec  
———— Nonlinear PSD -  $V_H = 66$  Ft/Sec

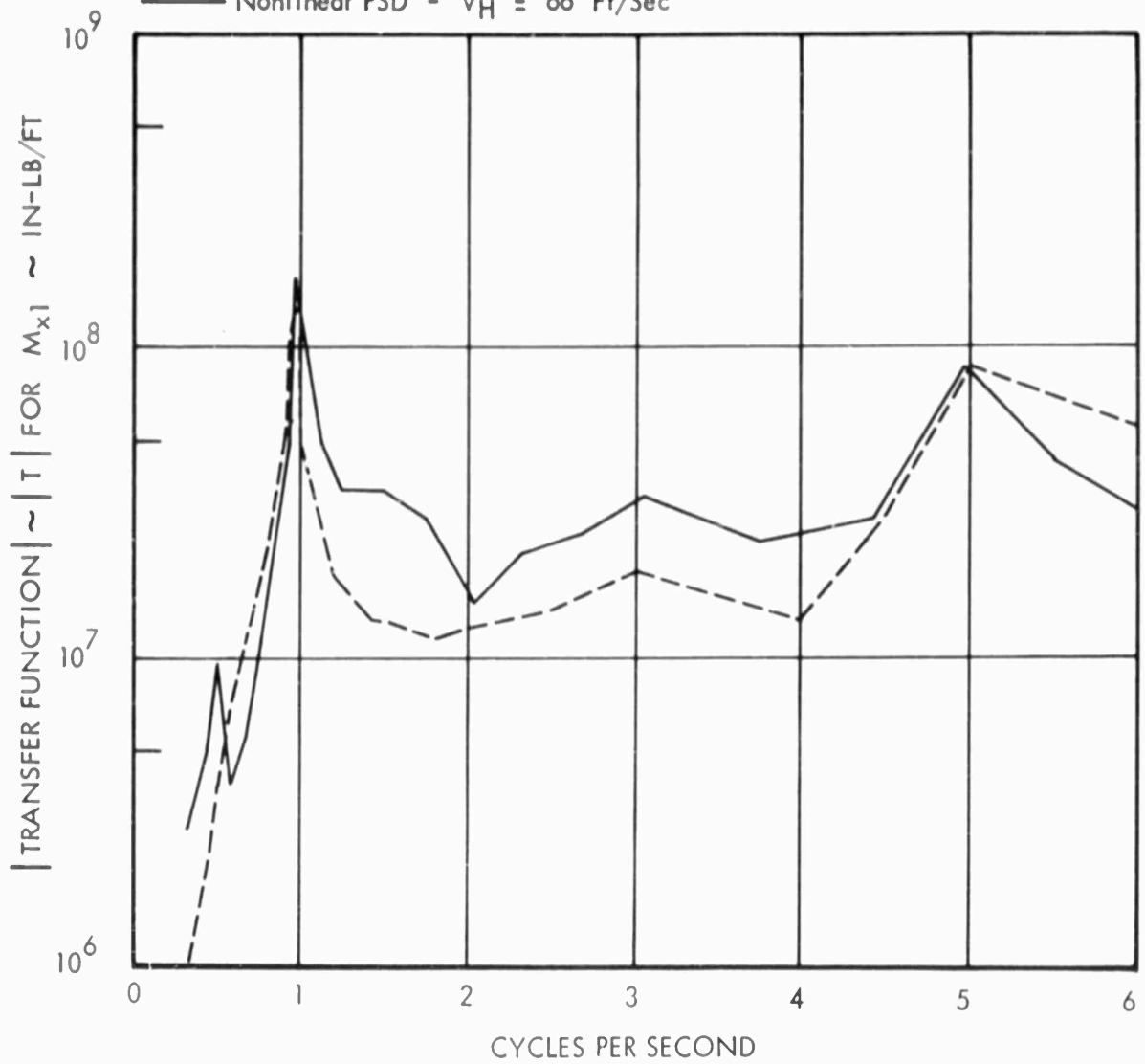


FIGURE 76 : Comparison of Transfer Functions by Linear Harmonic and Power Spectral Density Methods for Wing Root Bending Moment  
Single Gear Analysis for Normal Configuration

Tire Pressure = 90 psi  
D = 185 Lb-Sec/In

ANALYSIS METHODS AND TAXI SPEED:

----- Linear Harmonic -  $V_H = 55$  Ft/Sec  
———— Nonlinear PSD -  $V_H = 66$  Ft/Sec

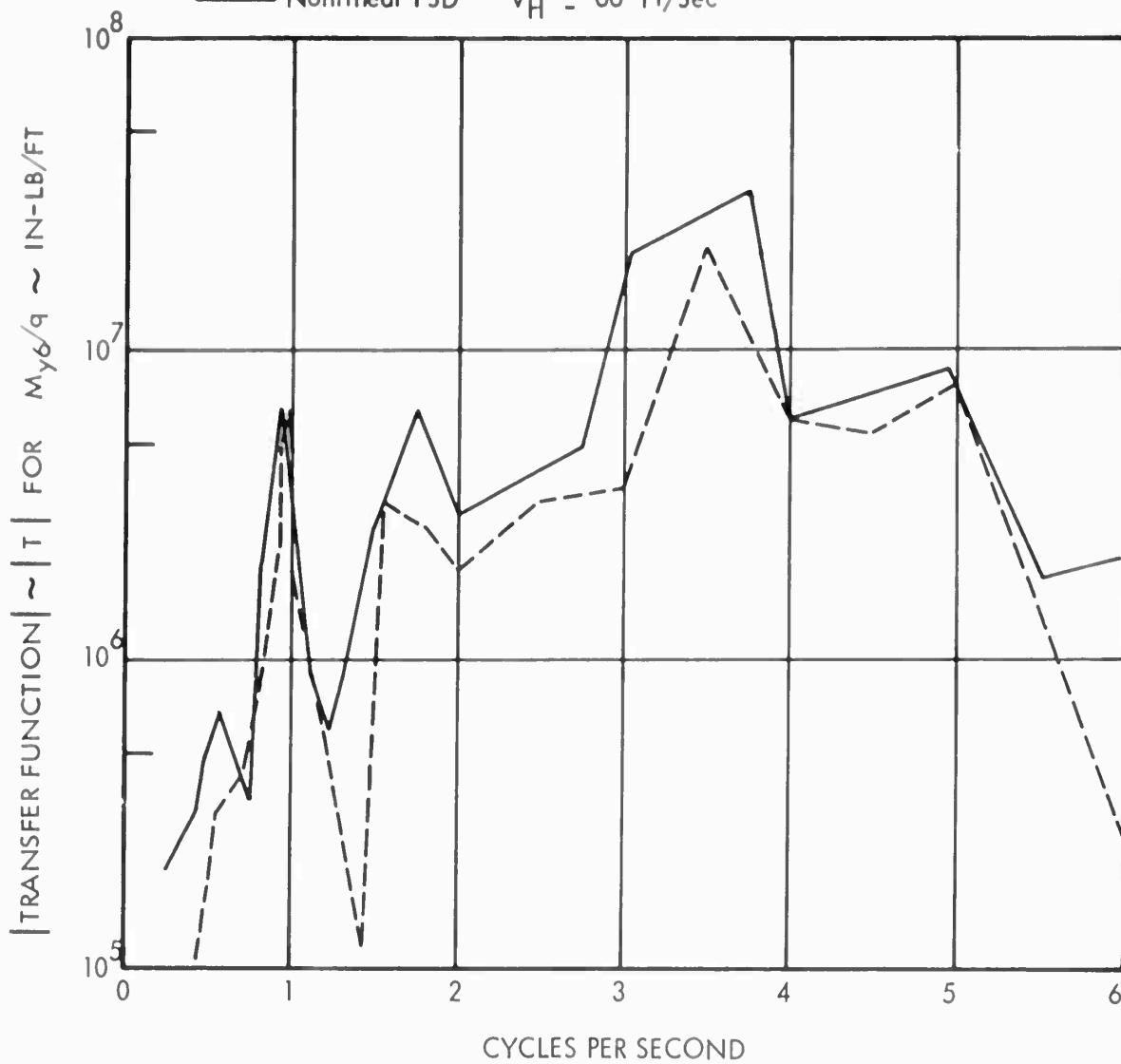


FIGURE 77 : Comparison of Transfer Functions by the Linear Harmonic and Power Spectral Density Methods for Wing Torsion Moment Inboard of Outboard Nacelle  
Single Gear Analysis for Normal Configuration

Tire Pressure = 90 psi

$V_H = 88$  fps

ANALYSIS METHODS:

-----Linear Harmonic -  $D = 185$  Lb-Sec/In

————Nonlinear PSD -  $C_D = 14.1$  Lb-Sec<sup>2</sup>/In<sup>2</sup>

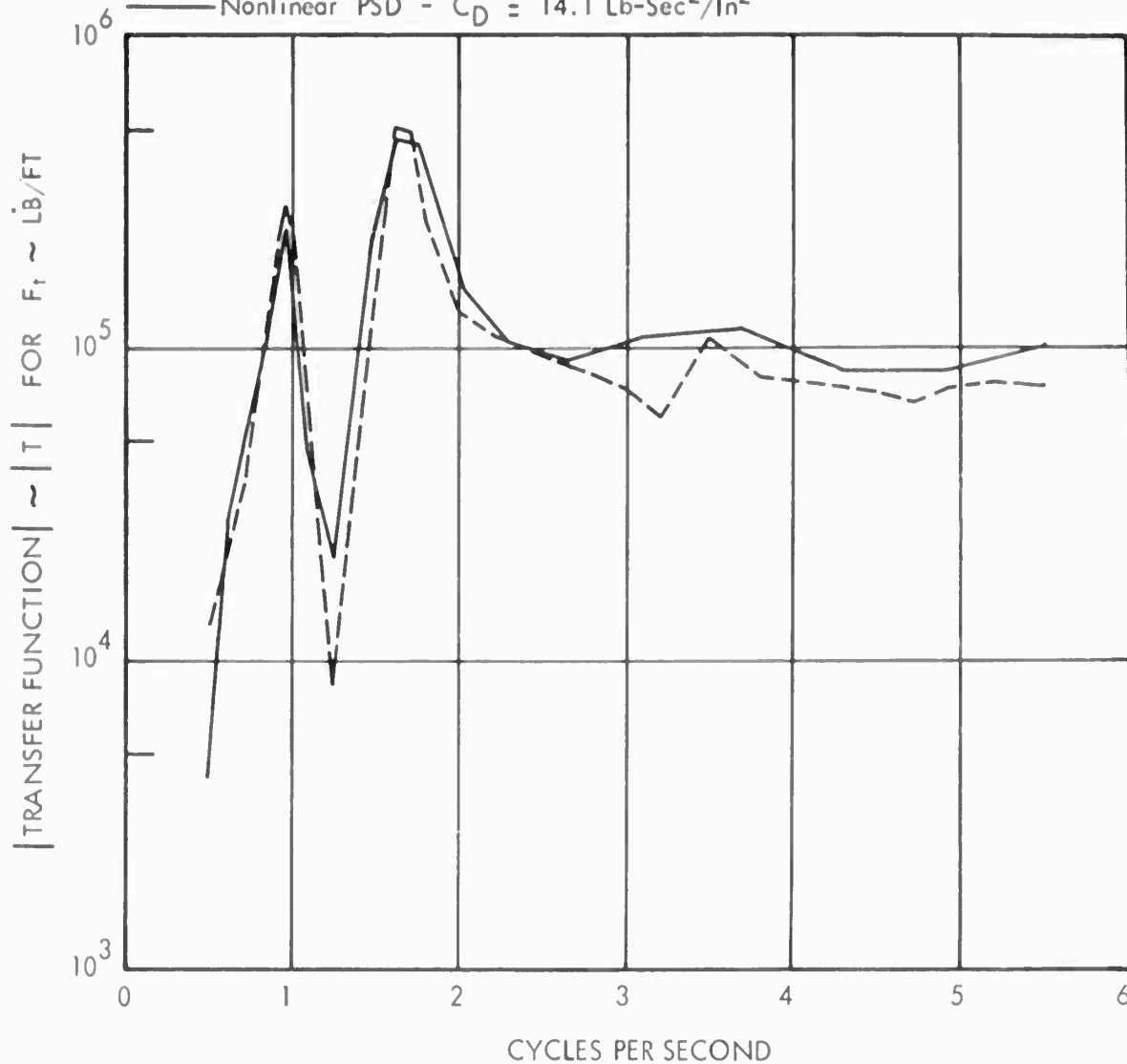


FIGURE 78 : Comparison of Transfer Functions by Linear Harmonic and Power Spectral Density Methods for Landing Gear Tire Force  
Single Gear Analysis for Normal Configuration

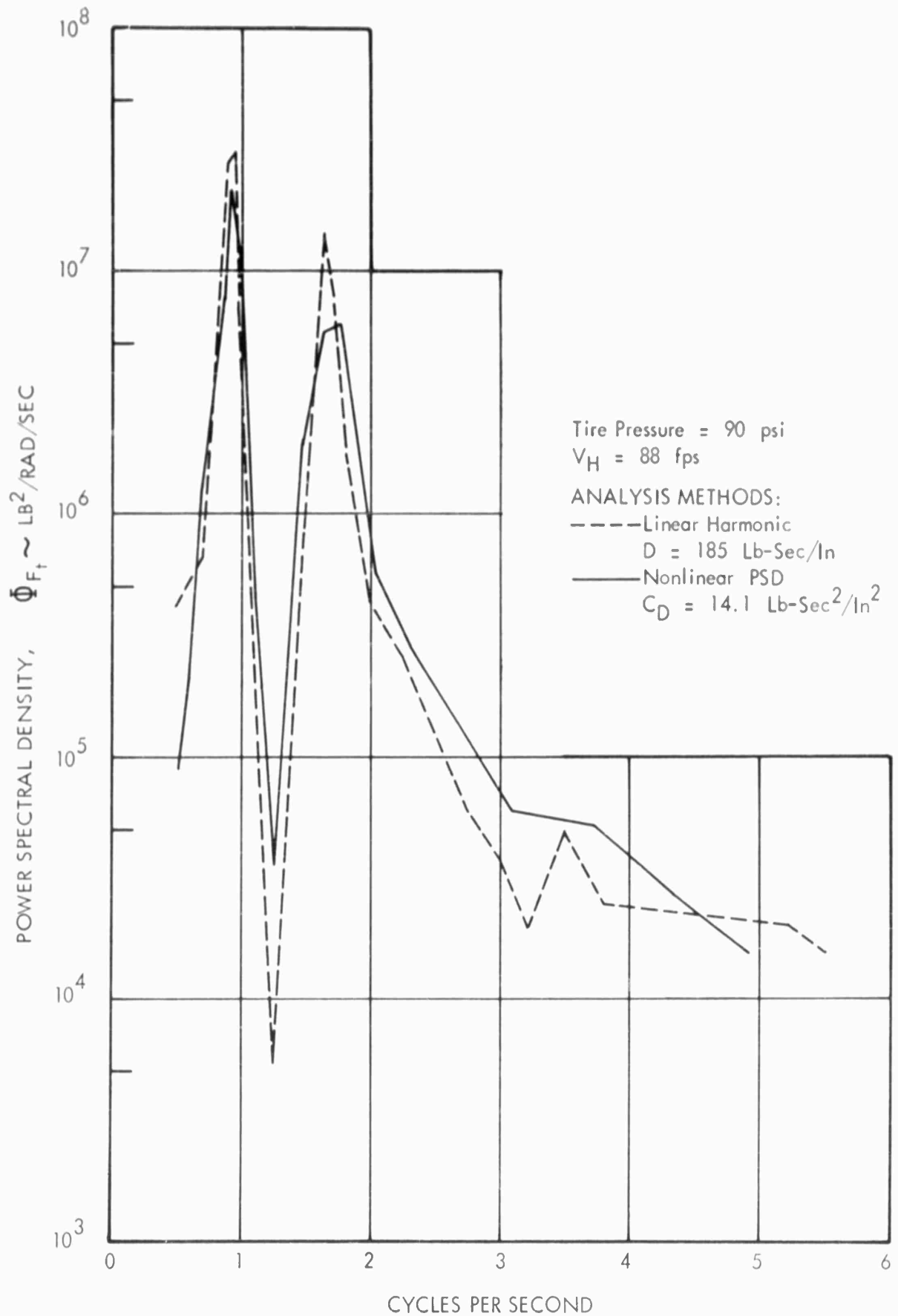


FIGURE 79 : Comparison of Output Power Spectra from Linear Harmonic and Power Spectral Density Methods for Landing Gear Tire Force Single Gear Analysis

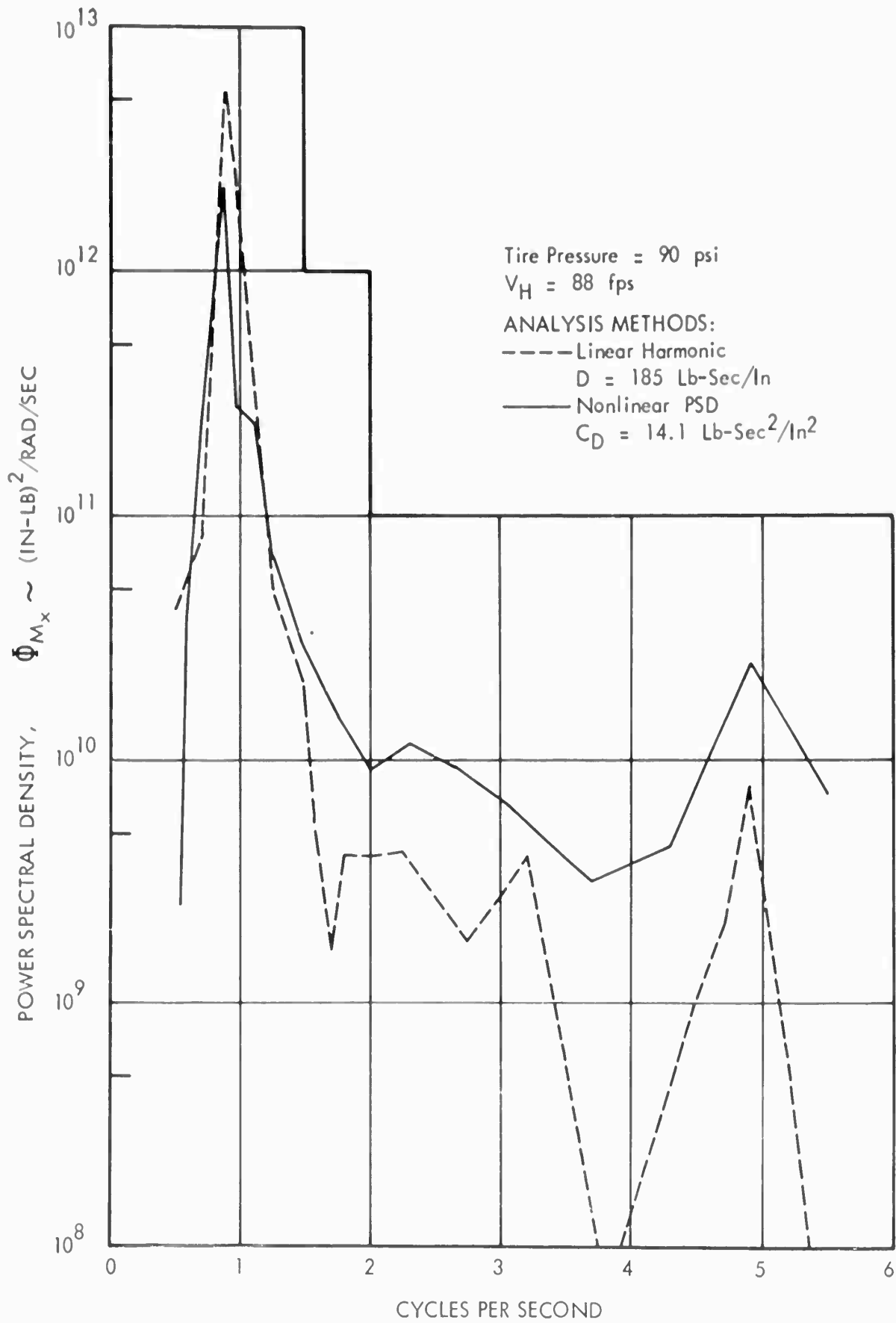


FIGURE 80 : Comparison of Output Power Spectra from Linear Harmonic and Power Spectral Density Methods for Wing Root Bending Moment Single Gear Analysis

Tire Pressure = 90 psi

$V_H = 55$  fps

$D^H = 185$  Lb-Sec/In

LINEAR HARMONIC METHOD:

— In Phase

- - - Out of Phase

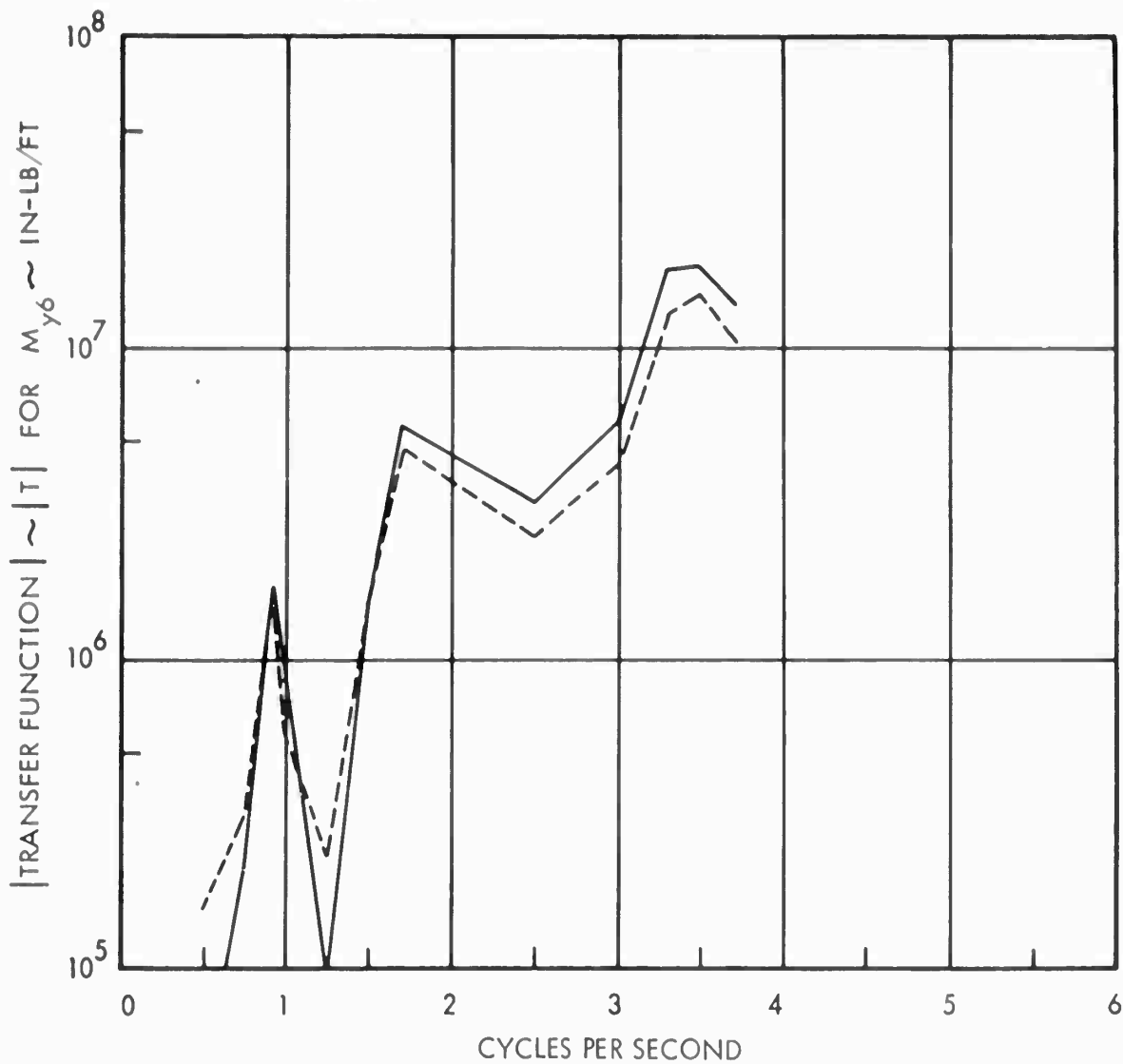


FIGURE 81 : Comparison of Transfer Functions for the Linear Harmonic System with Nose Gear In and Out of Phase with Main Gear for Wing Torsion Moment Inboard of Outboard Nacelle

Multi-Gear Analysis

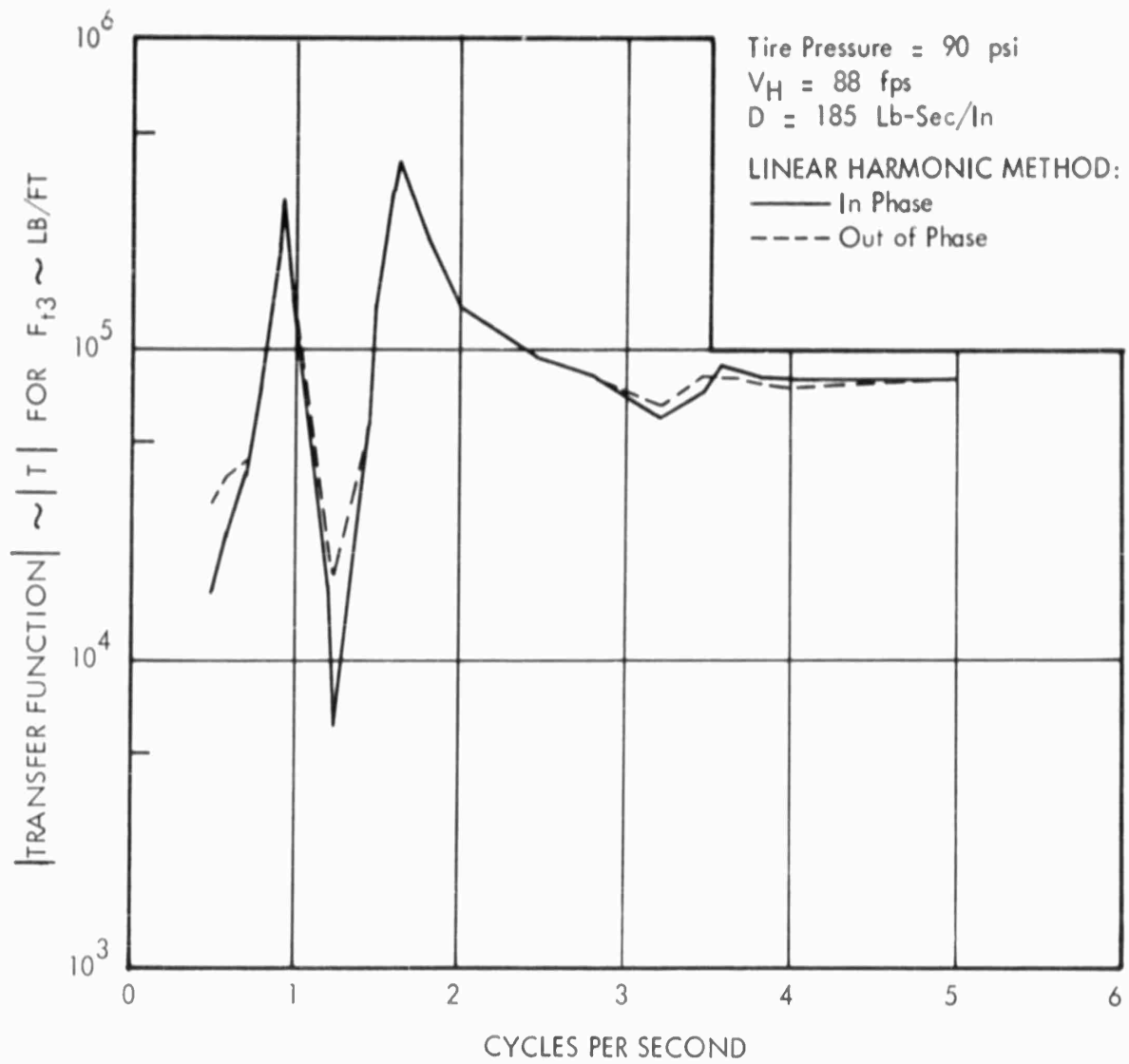


FIGURE 82 : Comparison of Transfer Functions for the Linear Harmonic System with Nose Gear In and Out of Phase with Main Gear for Rear Main Gear Tire Force

Multi-Gear Analysis

Tire Pressure = 90 psi

$V_H = 88$  fps

$D = 185$  Lb-Sec/In

LINEAR HARMONIC METHOD:

—— In Phase

----- Out of Phase

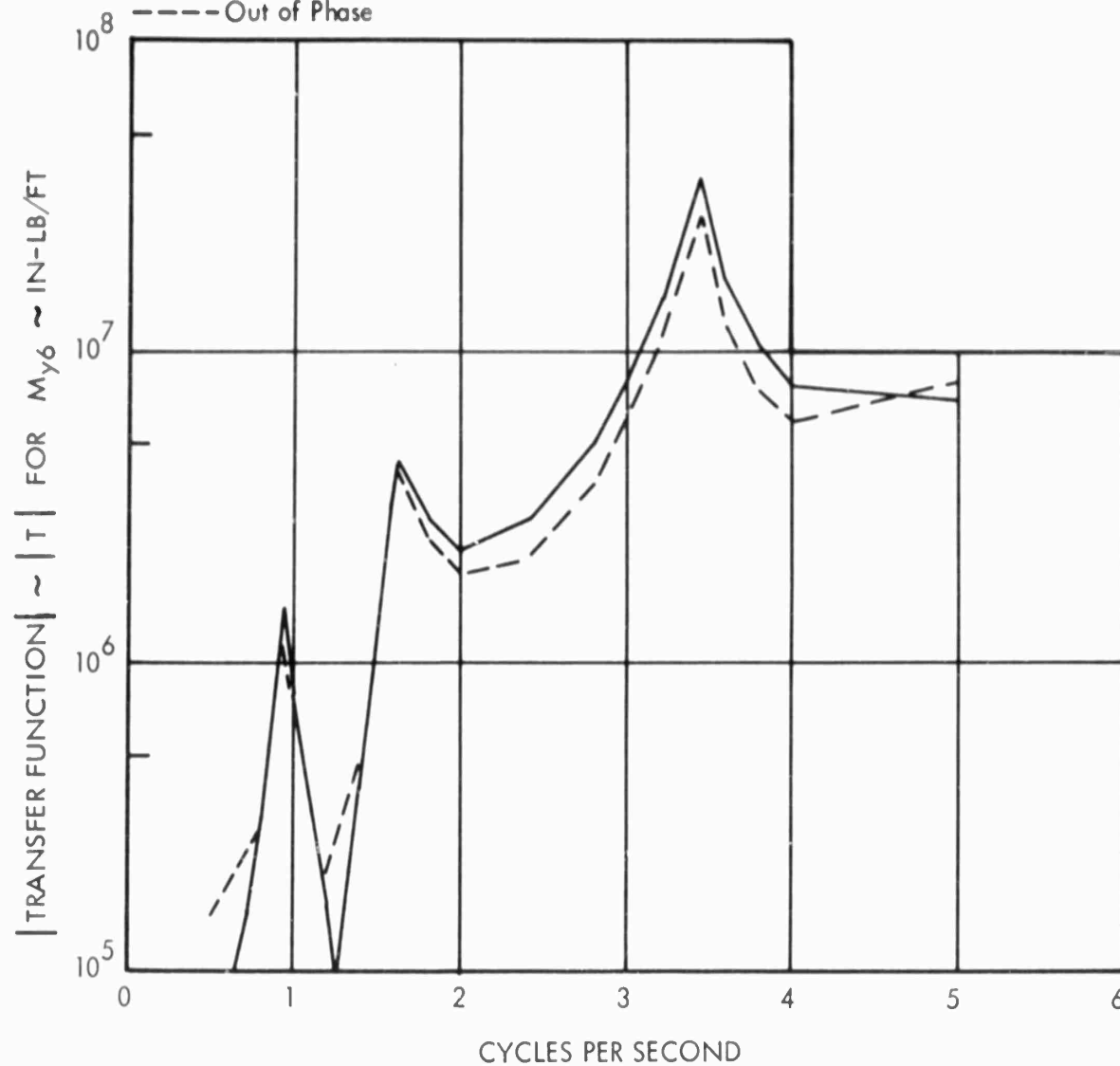


FIGURE 83 : Comparison of Transfer Functions for the Linear Harmonic System with Nose Gear In and Out of Phase with Main Gear for Wing Torsion Moment Inboard of Outboard Nacelle

Multi-Gear Analysis

Tire Pressure = 90 psi  
 $V_H = 88$  Ft/Sec  
 Nose Gear in Phase with Main Gear

ANALYSIS METHODS:

----- Linear Harmonic -  $D = 185$  Lb-Sec/In  
 ——— Nonlinear PSD -  $C_D = 14.1$  Lb-Sec<sup>2</sup>/In<sup>2</sup>

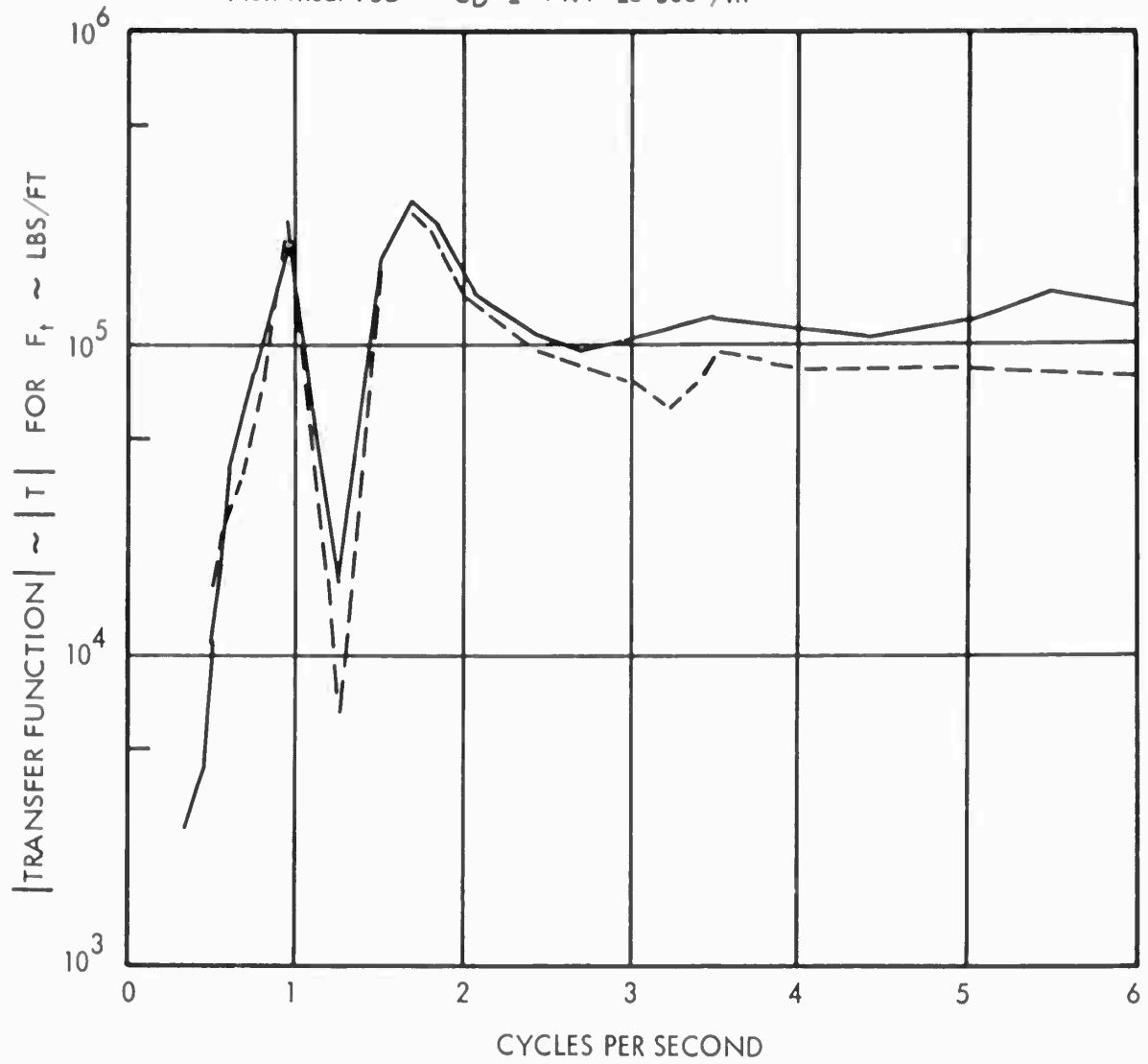


FIGURE 84 : Comparison of Transfer Functions by Linear Harmonic and Power Spectral Density Methods for Rear Main Landing Gear Tire Forces  
 Multi-Gear Analysis

Tire Pressure = 90 psi  
 $V_H = 88$  FPS  
 Nose Gear in Phase with Main Gear

ANALYSIS METHODS:

----- Linear Harmonic -  $D = 185$  Lb-Sec/In  
 ——— Nonlinear PSD -  $C_D = 14.1$  Lb-Sec<sup>2</sup>/In<sup>2</sup>

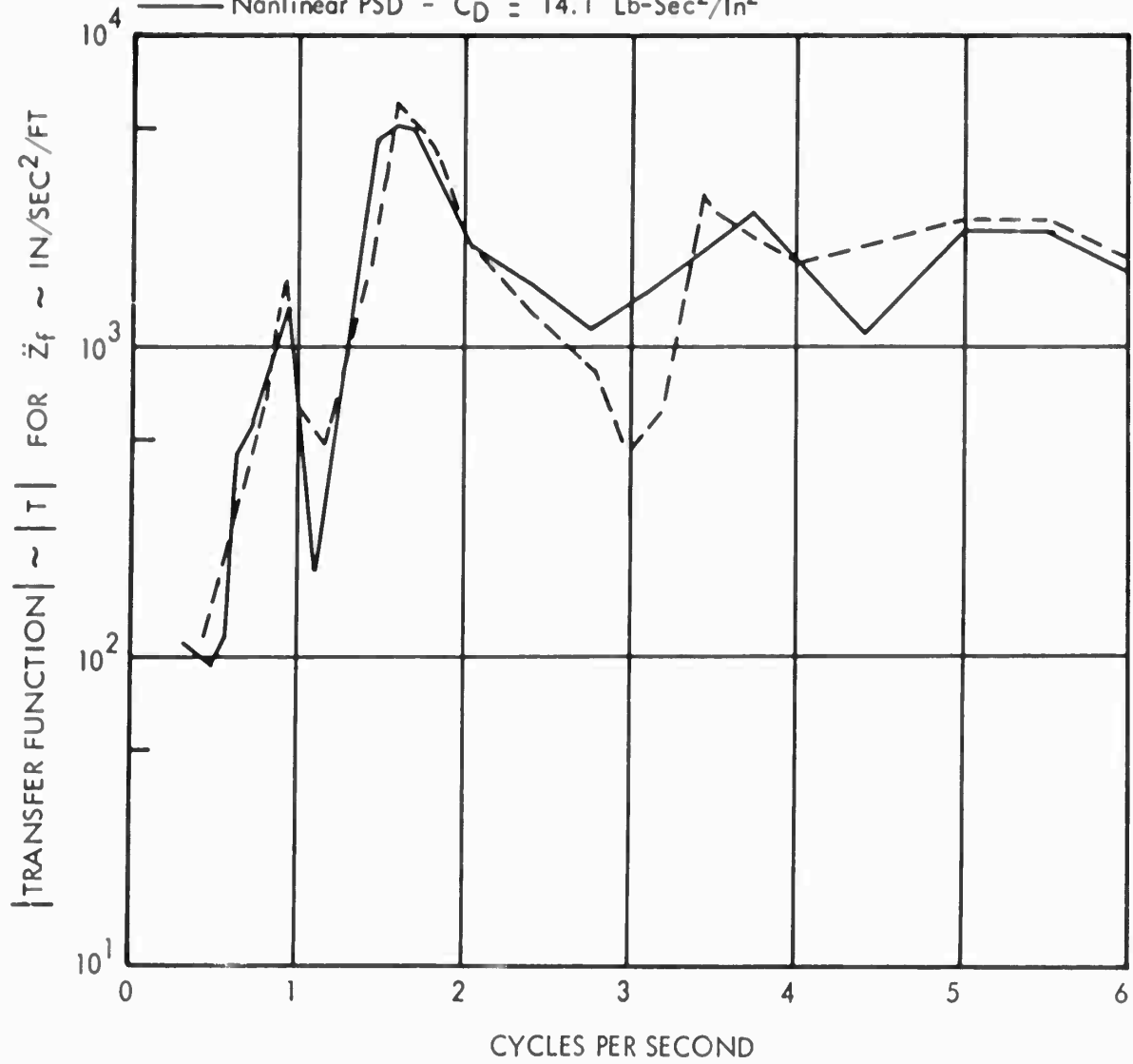


FIGURE 85 : Comparison of Transfer Functions by Linear Harmonic and Power Spectral Density Methods for Vertical Acceleration at the Airplane Center of Gravity

Multi-Gear Analysis

Tire Pressure = 90 psi  
 $V_H = 88$  FPS  
 Nose Gear in Phase with Main Gear

ANALYSIS METHODS:

----- Linear Harmonic -  $D = 185$  Lb-Sec/In  
 ——— Nonlinear PSD -  $C_D = 14.1$  Lb-Sec<sup>2</sup>/In<sup>2</sup>

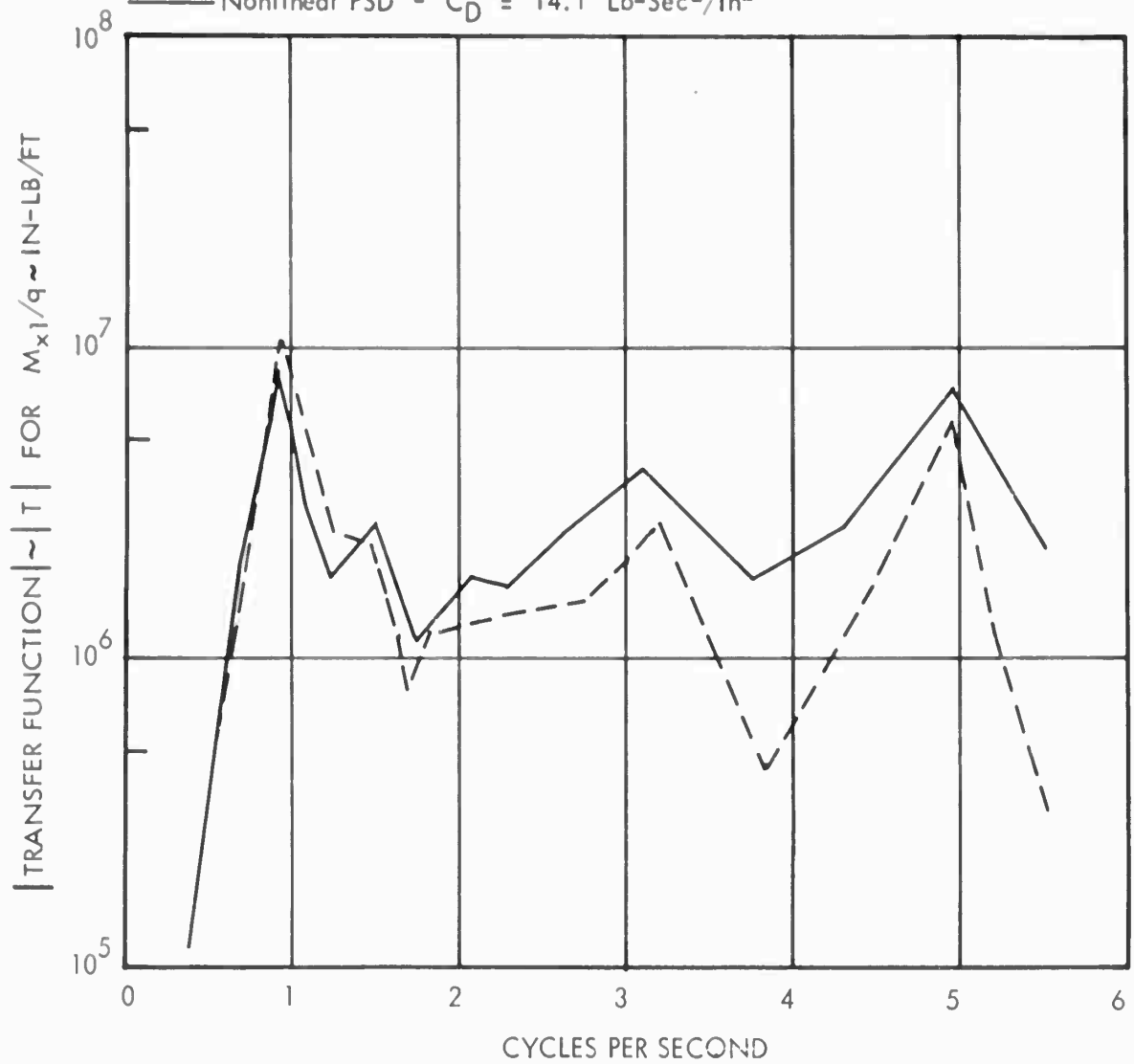


FIGURE 86 : Comparison of Transfer Function by Linear Harmonic and Power Spectral Density Methods for Wing Root Bending Moment  
 Multi-Gear Analysis

Tire Pressure = 90 psi  
 $V_H = 88$  fps  
 Nose Gear in Phase with Main Gear

ANALYSIS METHODS:  
 - - - Linear Harmonic -  $D = 185$  Lb-Sec/In  
 — Nonlinear PSD -  $C_D = 14.1$  Lb-Sec<sup>2</sup>/In<sup>2</sup>

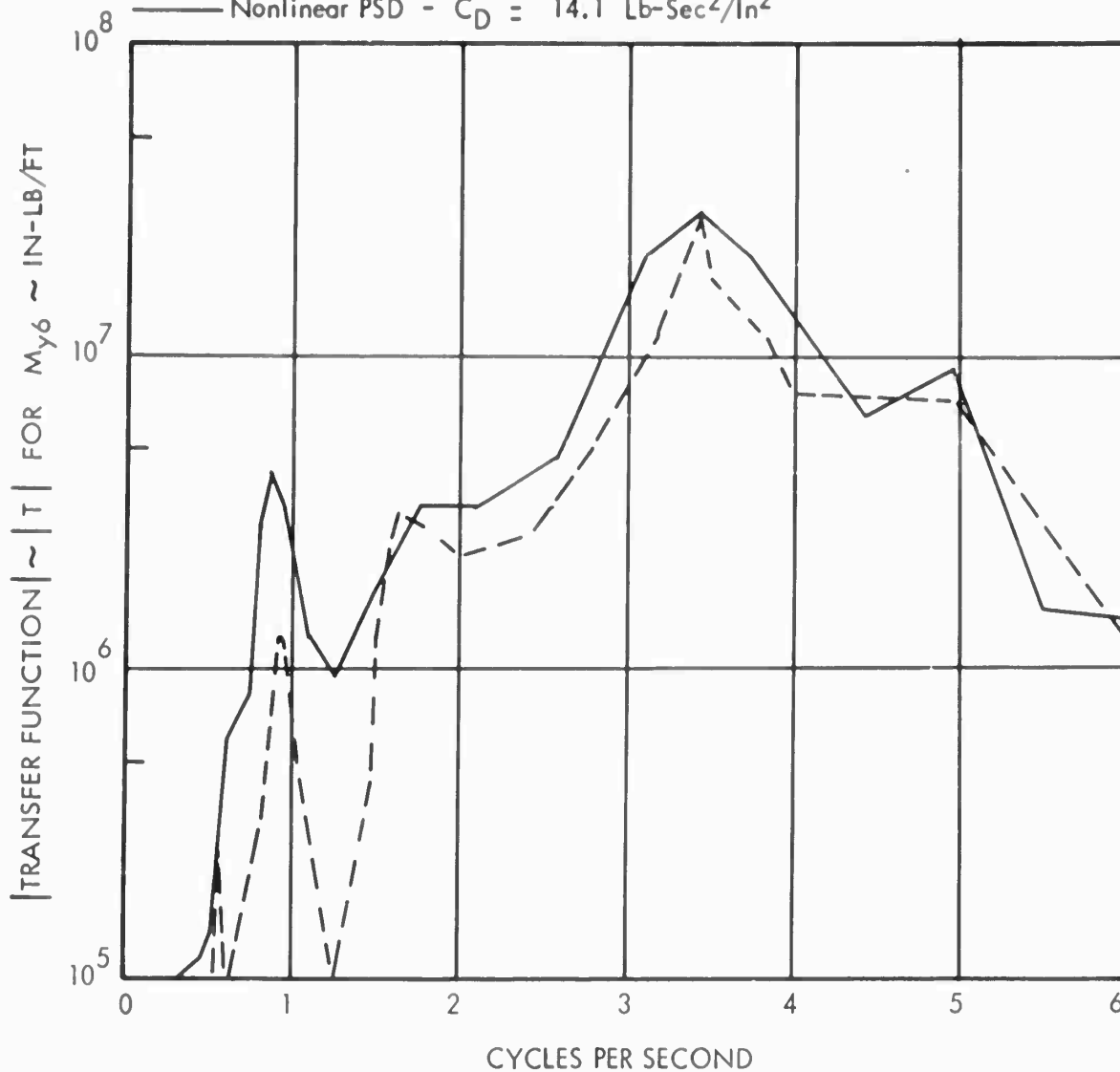


FIGURE 87 : Comparison of Transfer Functions by Linear Harmonic and Power Spectral Density Methods for Wing Torsion Moment Inboard of Outboard Nacelle

Multi-Gear Analysis

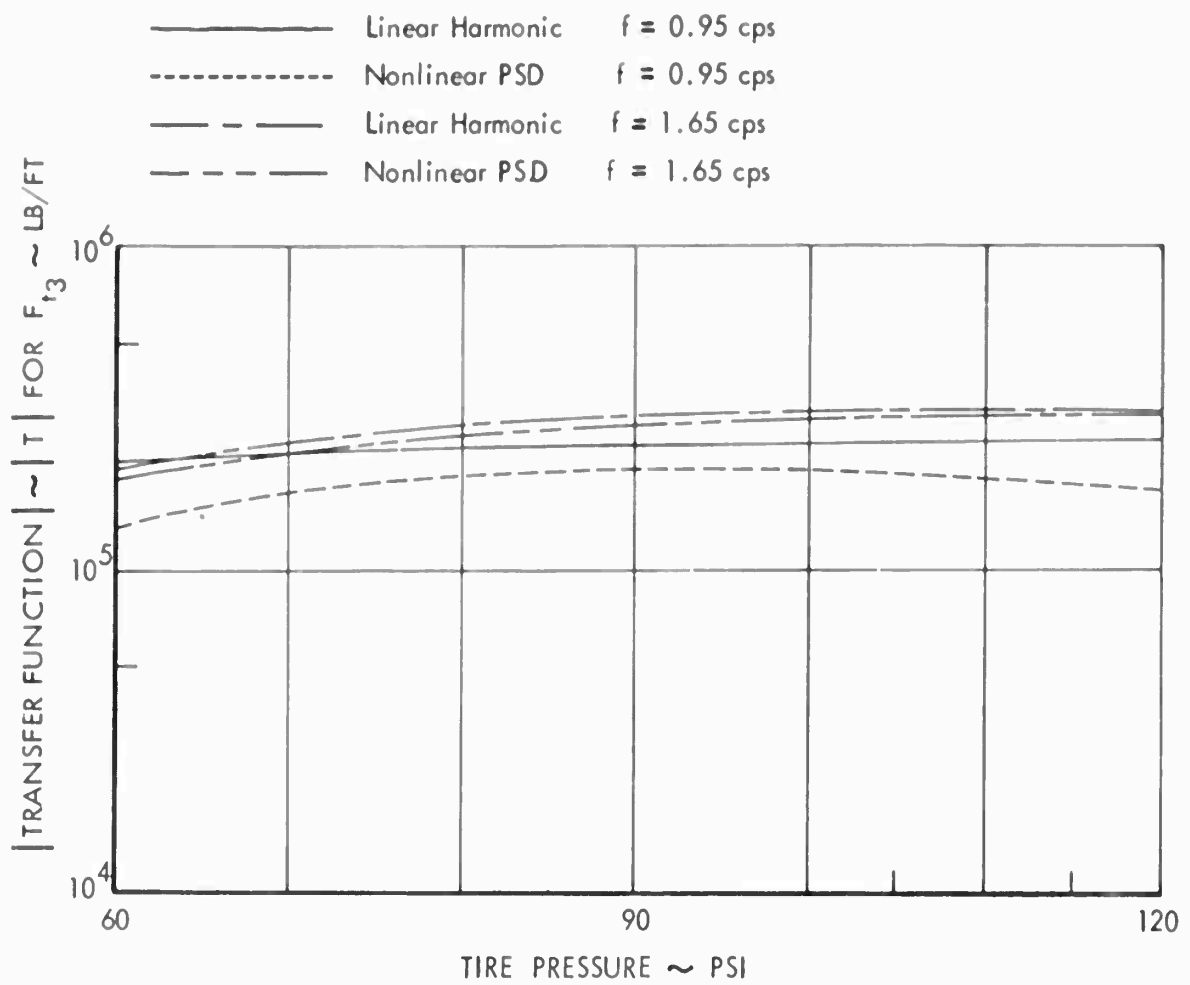


Figure 88: Comparison of Nonlinear and Linearized Transfer Function Peaks for Main Gear Tire Force

Multi-Gear Analysis  
 $V_H = 88$  fps

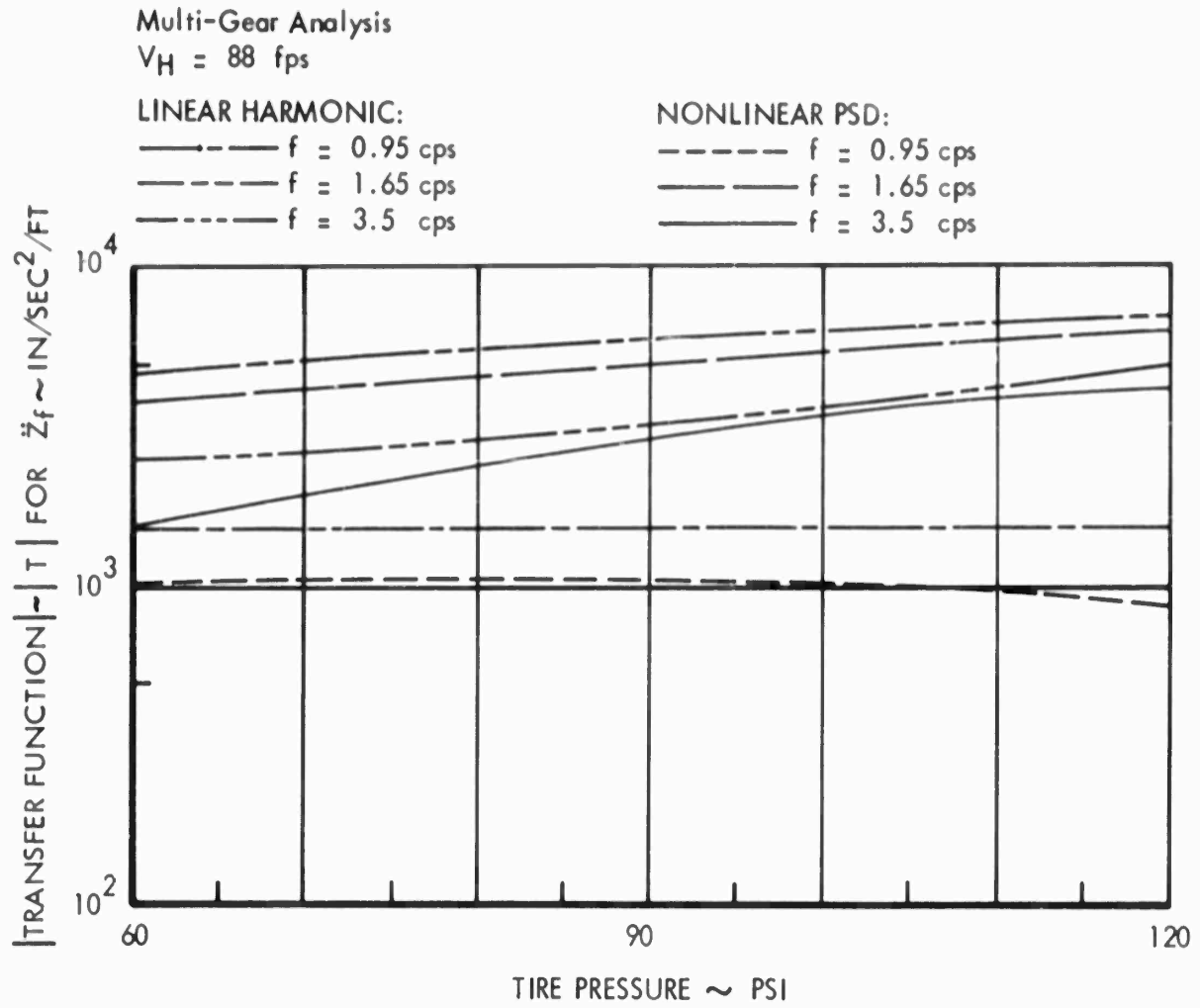


FIGURE 89 : Comparison of Nonlinear and Linearized Transfer Function Peaks for Vertical Acceleration of the Center of Gravity

Multi-Gear Analysis

$V_H = 88$  fps

LINEAR HARMONIC:

—  $f = 0.93$  cps

- - -  $f = 1.65$  cps

- · -  $f = 3.5$  cps

NONLINEAR PSD:

—  $f = 0.93$  cps

- - -  $f = 1.65$  cps

- · -  $f = 3.5$  cps

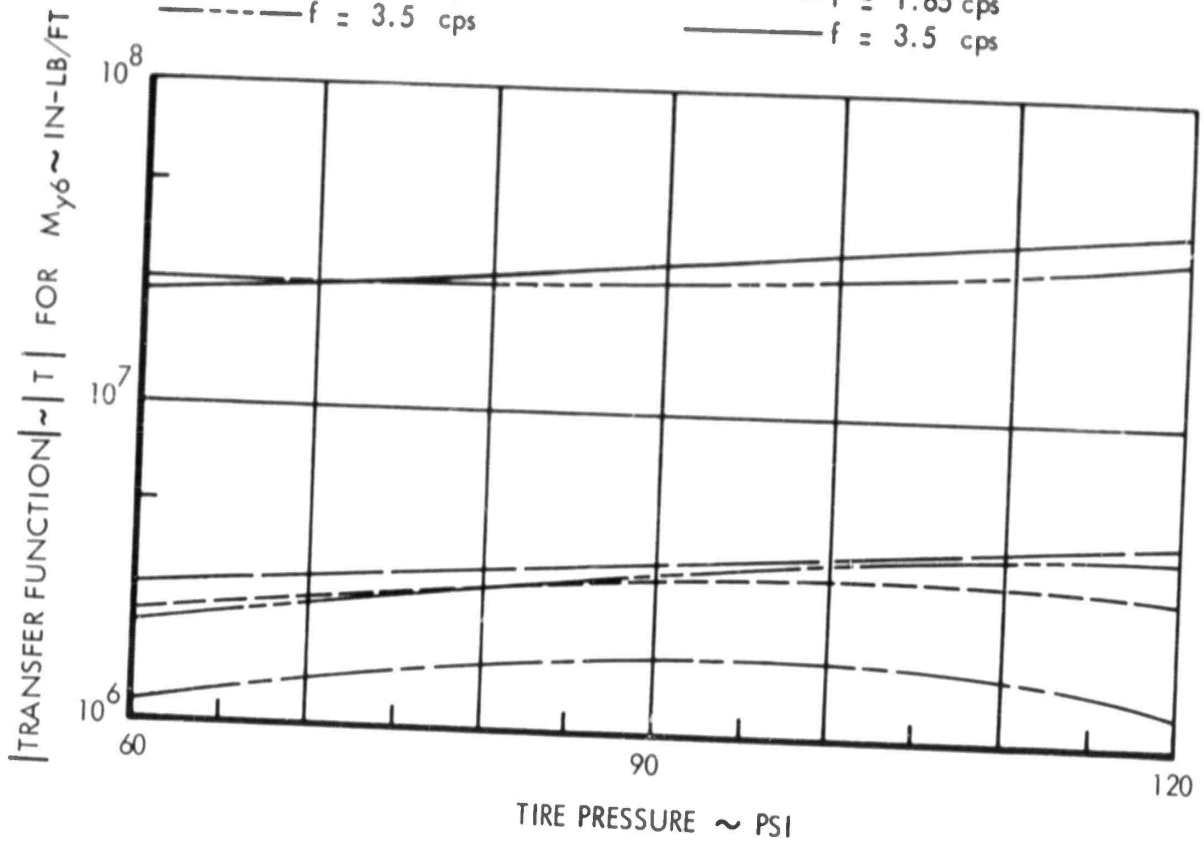


FIGURE 90 : Comparison of Nonlinear and Linearized Transfer Function Peaks for Wing Torsion Moment Inboard of Outboard Nacelle

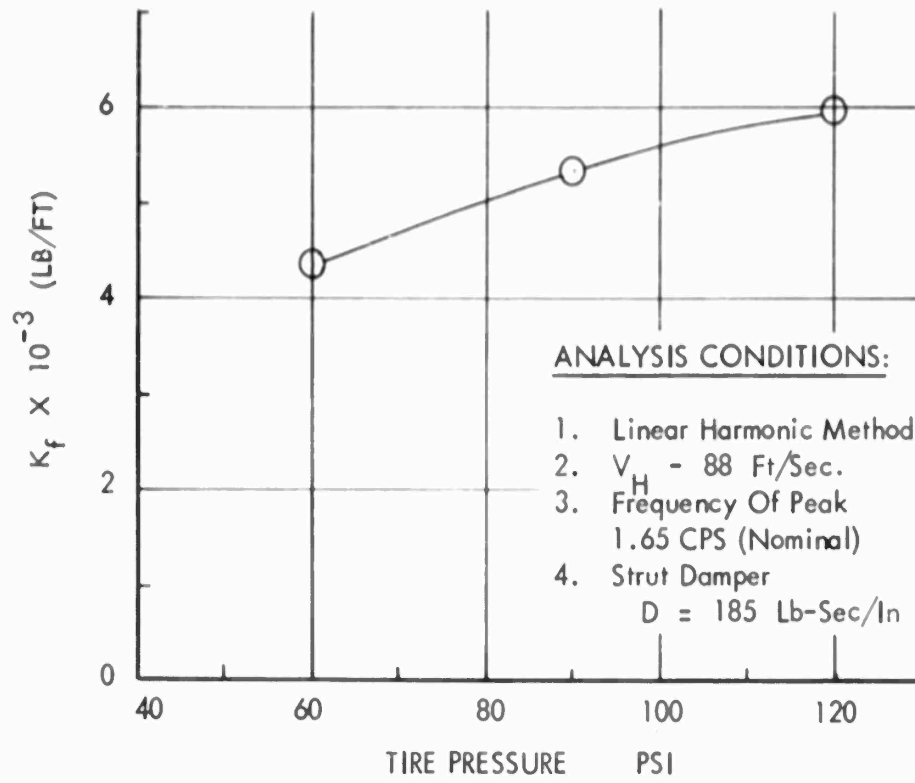


FIGURE 91 : Variation Of Linearized Spring Constant Versus Tire Pressure

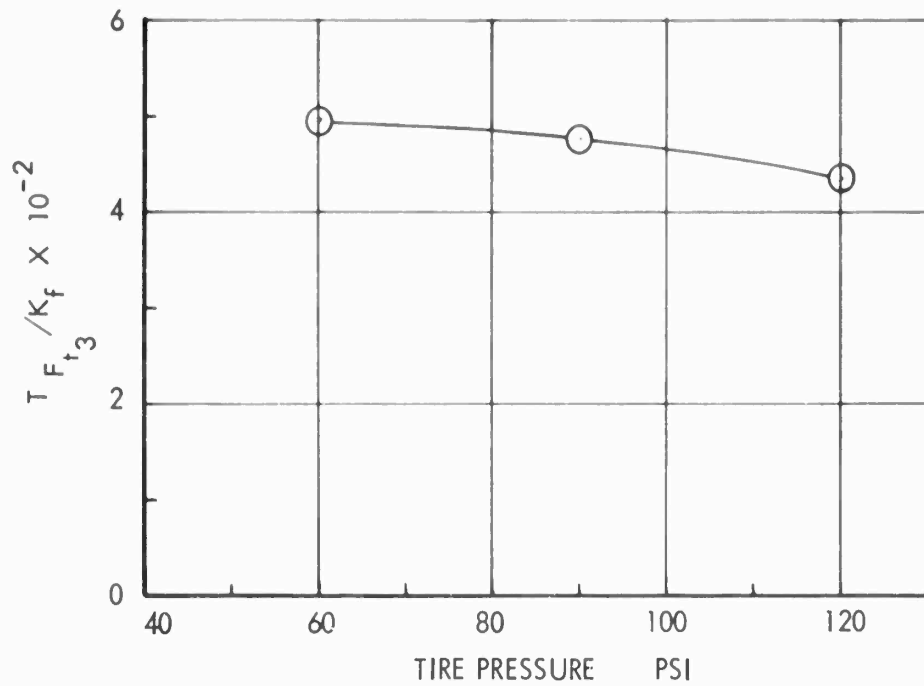


FIGURE 92 : Ratio Of Transfer Function Peak For Tire Force Over Linearized Spring Constant Versus Tire Pressure Variations

Tire Pressure = 90 psi

ANALYSIS METHODS:

Linear Harmonic -  $D = 185 \text{ Lb-Sec/In}$

-----  $f = 0.95 \text{ cps}$

—————  $f = 1.65 \text{ cps}$

Nonlinear PSD -  $C_D = 14.1 \text{ Lb-Sec}^2/\text{In}^2$

-----  $f = 0.95 \text{ cps}$

—————  $f = 1.65 \text{ cps}$

TRANSFER FUNCTION PEAKS

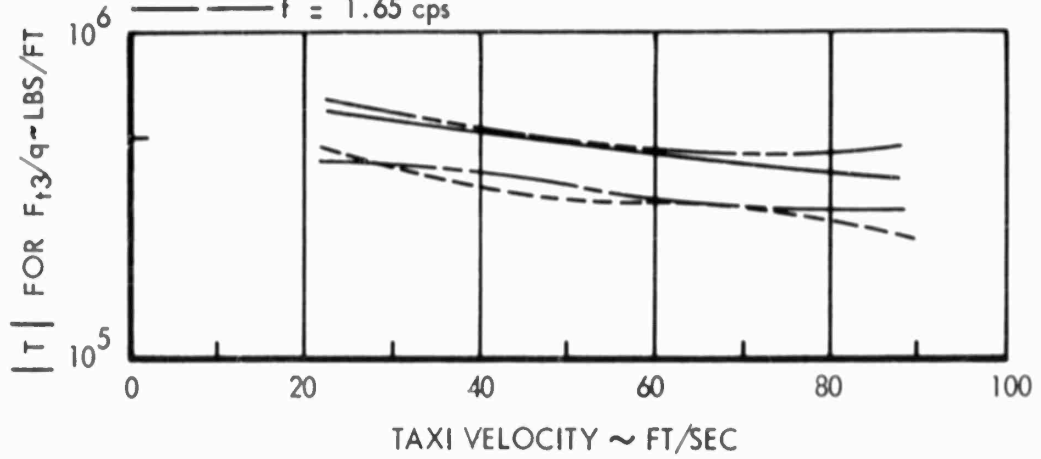


FIGURE 93 : Comparison of Nonlinear and Linearized Tire Force Transfer Functions for Variations with Velocity

Single Gear Analysis for Peaks at  $f = 0.95 \text{ cps}$  and  $f = 1.65 \text{ cps}$

Tire Pressure = 90 psi

ANALYSIS METHODS:

————— Linear Harmonic -  $D = 185 \text{ Lb-Sec/In}$

----- Nonlinear PSD -  $C_D = 14.1 \text{ Lb-Sec}^2/\text{In}^2$

TRANSFER FUNCTION PEAKS

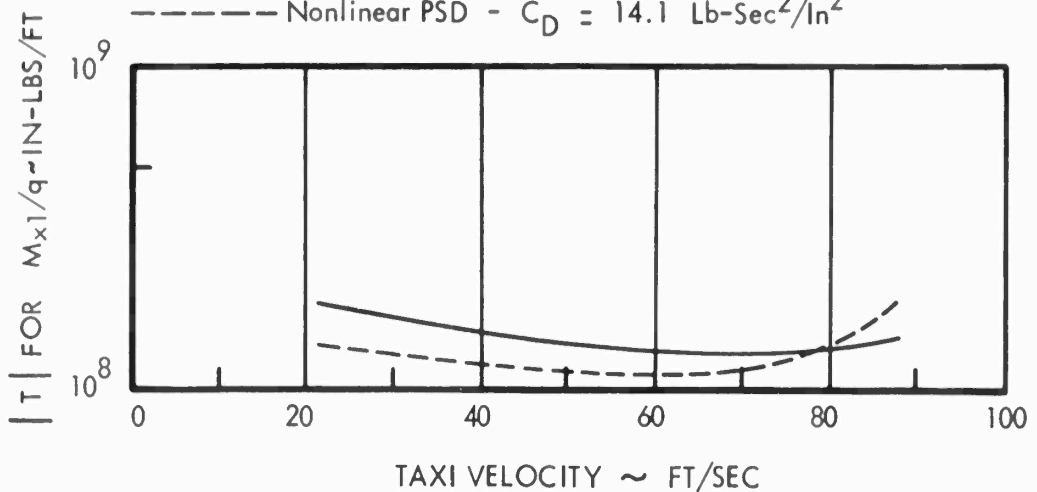


FIGURE 94 : Comparison of Nonlinear and Linearized Wing Root Bending Moment Transfer Functions for Variations with Velocity

Single Gear Analysis for Peaks at  $f = 0.95 \text{ cps}$

Tire Pressure = 90 psi

ANALYSIS METHODS:

Linear Harmonic -  $D = 185 \text{ Lb-Sec/In}$

-----  $f = 0.95 \text{ cps}$

-----  $f = 1.65 \text{ cps}$

Nonlinear PSD -  $C_D = 14.1 \text{ Lb-Sec}^2/\text{In}^2$

-----  $f = 0.95 \text{ cps}$

-----  $f = 1.65 \text{ cps}$

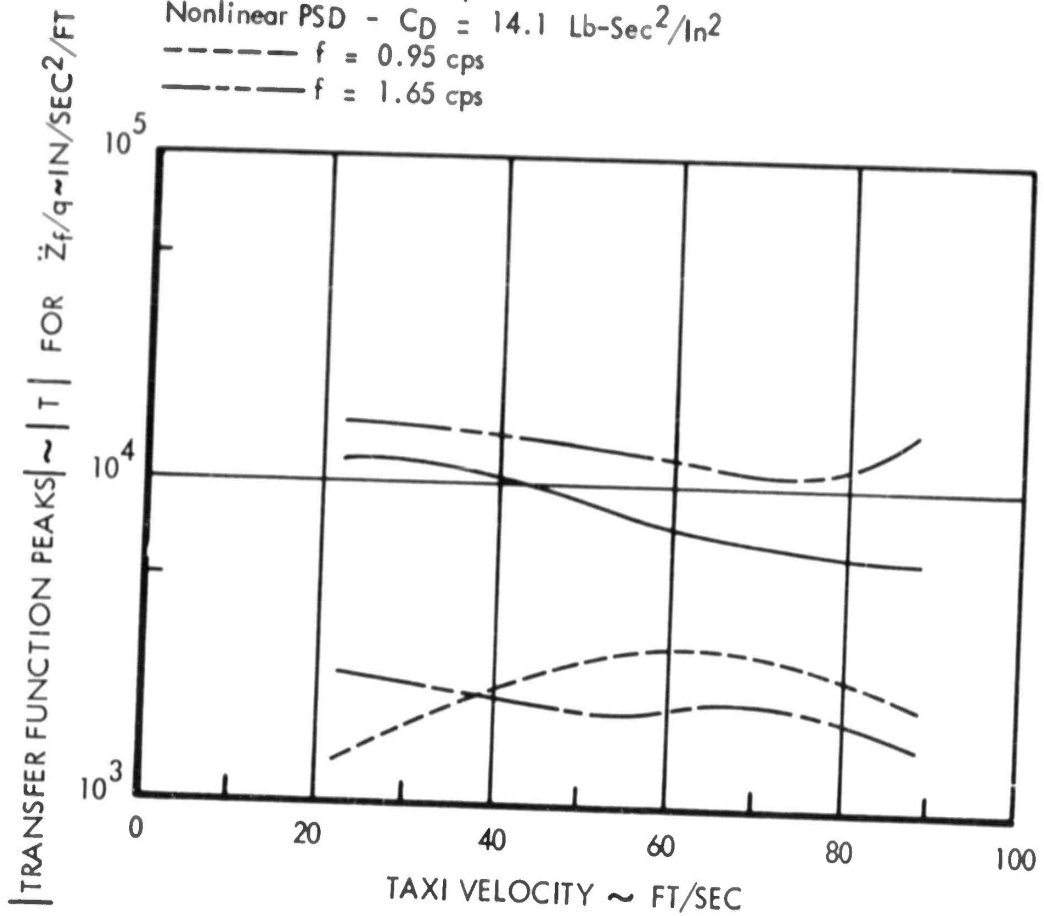


FIGURE 95 : Comparison of Nonlinear and Linearized Center-of-Gravity Vertical Acceleration Transfer Functions for Variations with Velocity

Single Gear Analysis for Peaks at  $f = 0.95 \text{ cps}$  and  $f = 1.65 \text{ cps}$

Tire Pressure = 90 psi

ANALYSIS METHODS:

Linear Harmonic -  $D = 185 \text{ Lb-Sec/In}$

-----  $f = 0.95 \text{ cps}$

-----  $f = 1.65 \text{ cps}$

-----  $f = 3.4 \text{ cps}$

Nonlinear PSD -  $C_D = 14.1 \text{ Lb-Sec}^2/\text{In}^2$

-----  $f = 0.95 \text{ cps}$

-----  $f = 1.65 \text{ cps}$

-----  $f = 3.4 \text{ cps}$

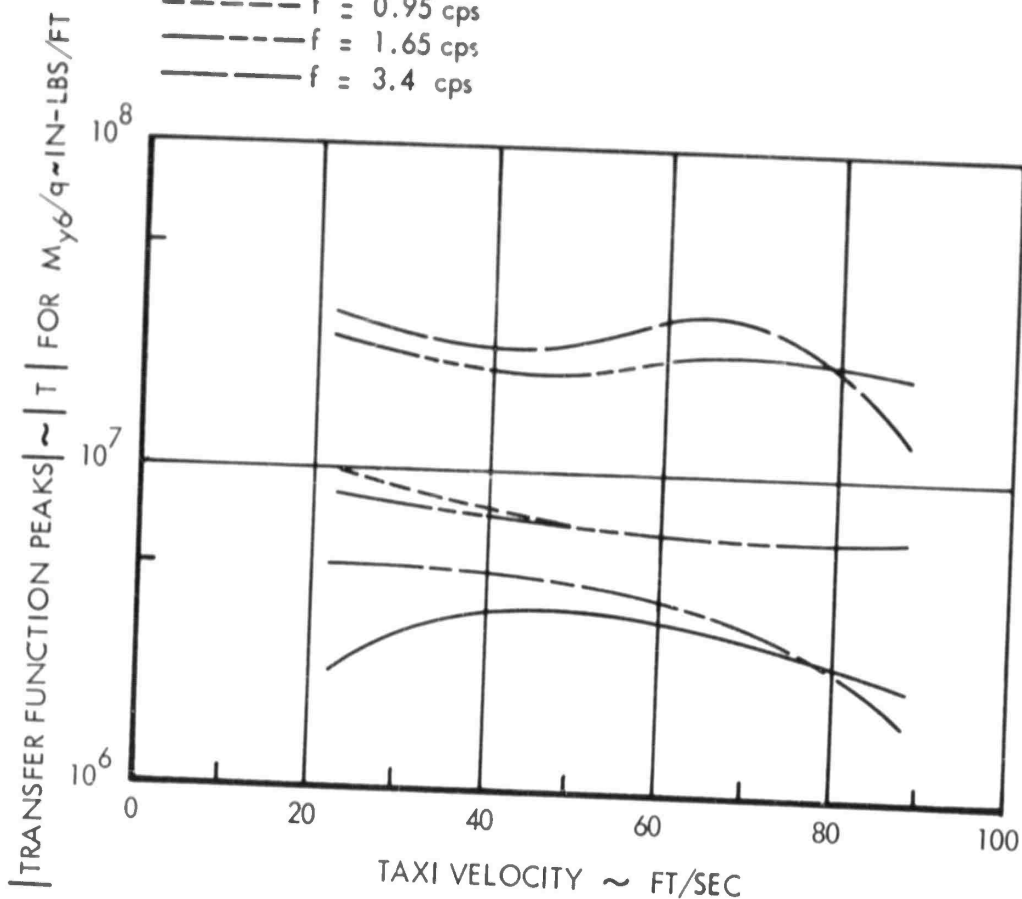


FIGURE 96 : Comparison of Nonlinear and Linearized Wing Torsion Moment Transfer Functions Near Outboard Nacelle for Variations with Velocity

Single Gear Analysis for Peaks at  $f = 0.95 \text{ cps}$ ,  
 $f = 1.65 \text{ cps}$  and  $f = 3.4 \text{ cps}$

Tire Pressure = 90 psi  
 $V_H = 88$  Ft/Sec

ANALYSIS METHODS:

Nonlinear PSD:

○ Multi-Gear

◇ Single Gear

---(Extrapolated)

Linear Harmonic:

□ Single Gear

▽ Multi-Gear

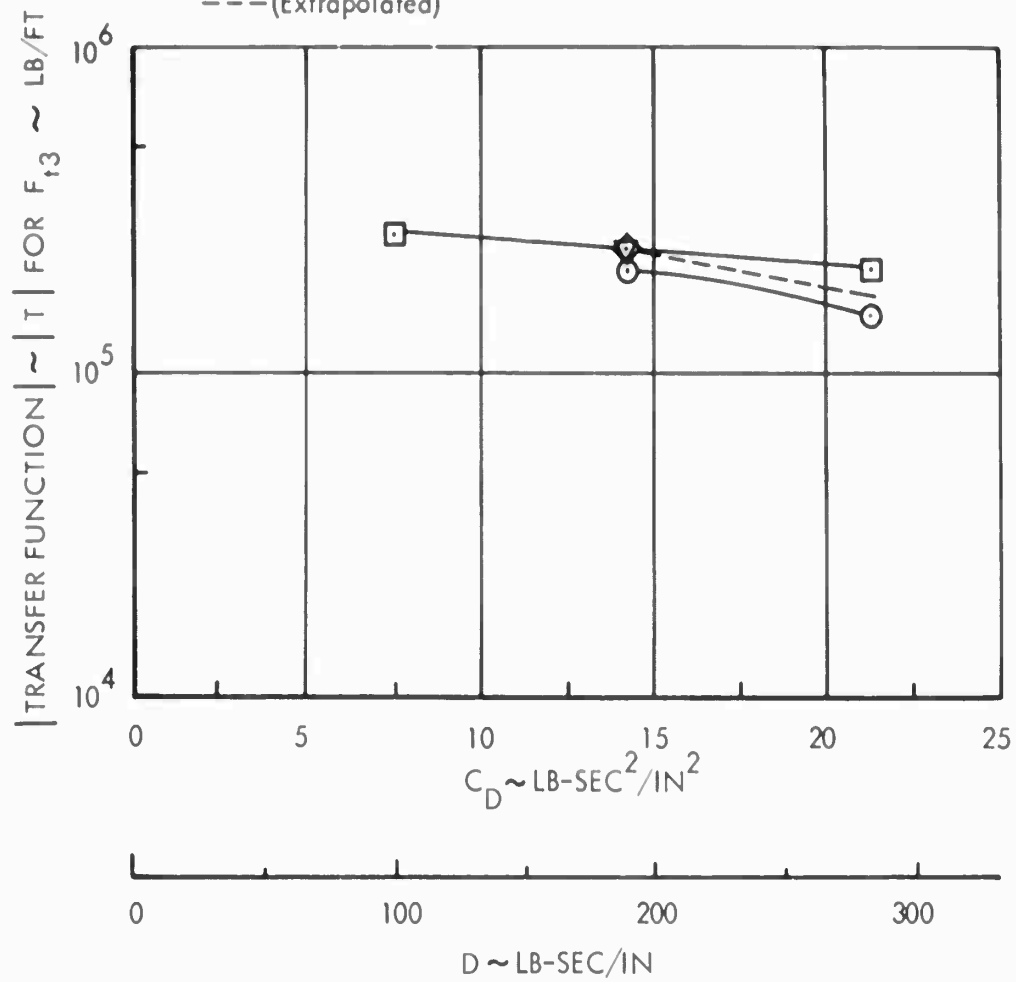


FIGURE 97: Variation of Transfer Function Peak with Damping of the Linear and Nonlinear Systems for Rear Main Landing Gear Tire Force,  $F_{t3}$

$$f = 0.93 \text{ cps}$$

Tire Pressure = 90 psi  
 $V_H = 88 \text{ Ft/Sec}$

ANALYSIS METHODS:

Nonlinear PSD:

○ Multi-Gear

◇ Single Gear

--- (Extrapolated)

Linear Harmonic:

□ Single Gear

▽ Multi-Gear

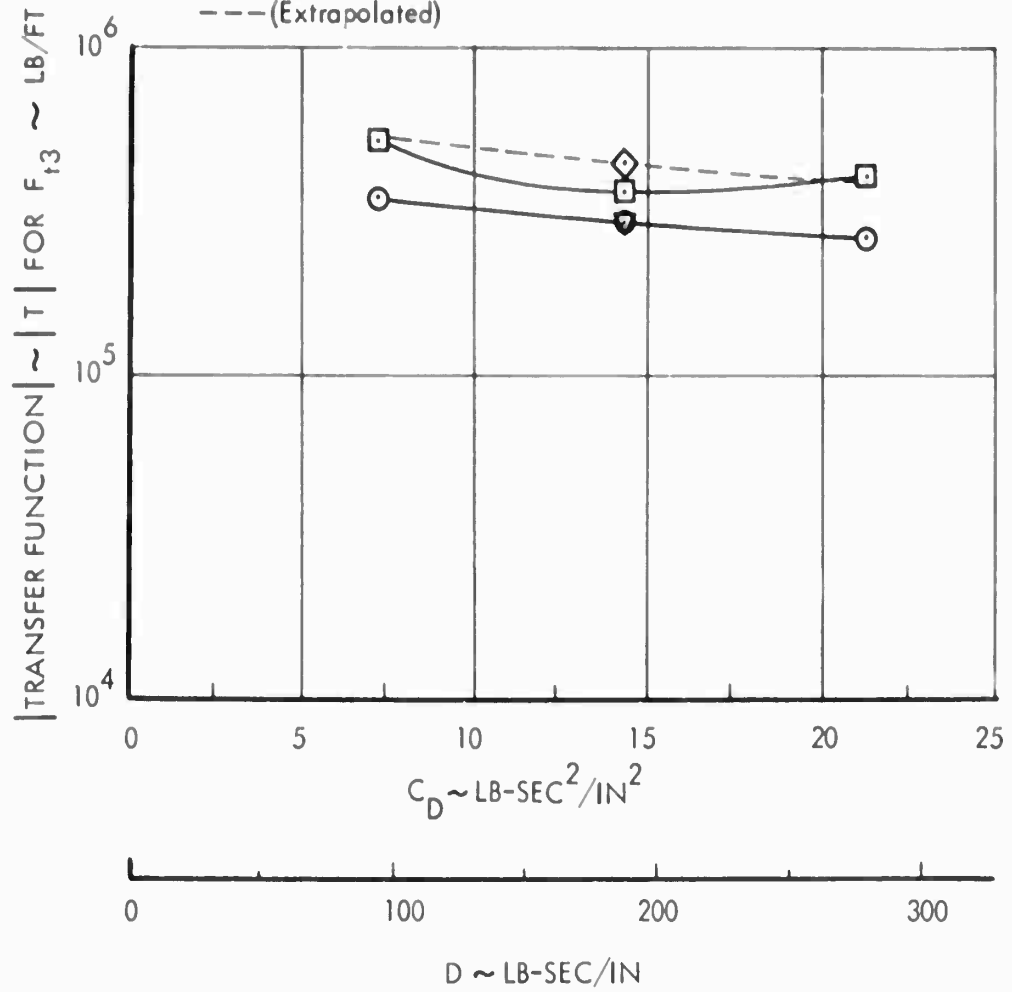


FIGURE 98: Variation of Transfer Function Peak with Damping of the Linear and Nonlinear Systems for Rear Main Landing Gear Tire Force,  $F_{t3}$

$f = 1.65 \text{ cps}$

Tire Pressure = 90 psi  
 $V_H = 88 \text{ Ft/Sec}$

ANALYSIS METHODS:

Nonlinear PSD:

○ Multi-Gear

◇ Single Gear

--- (Extrapolated)

Linear Harmonic:

□ Single Gear

▽ Multi-Gear

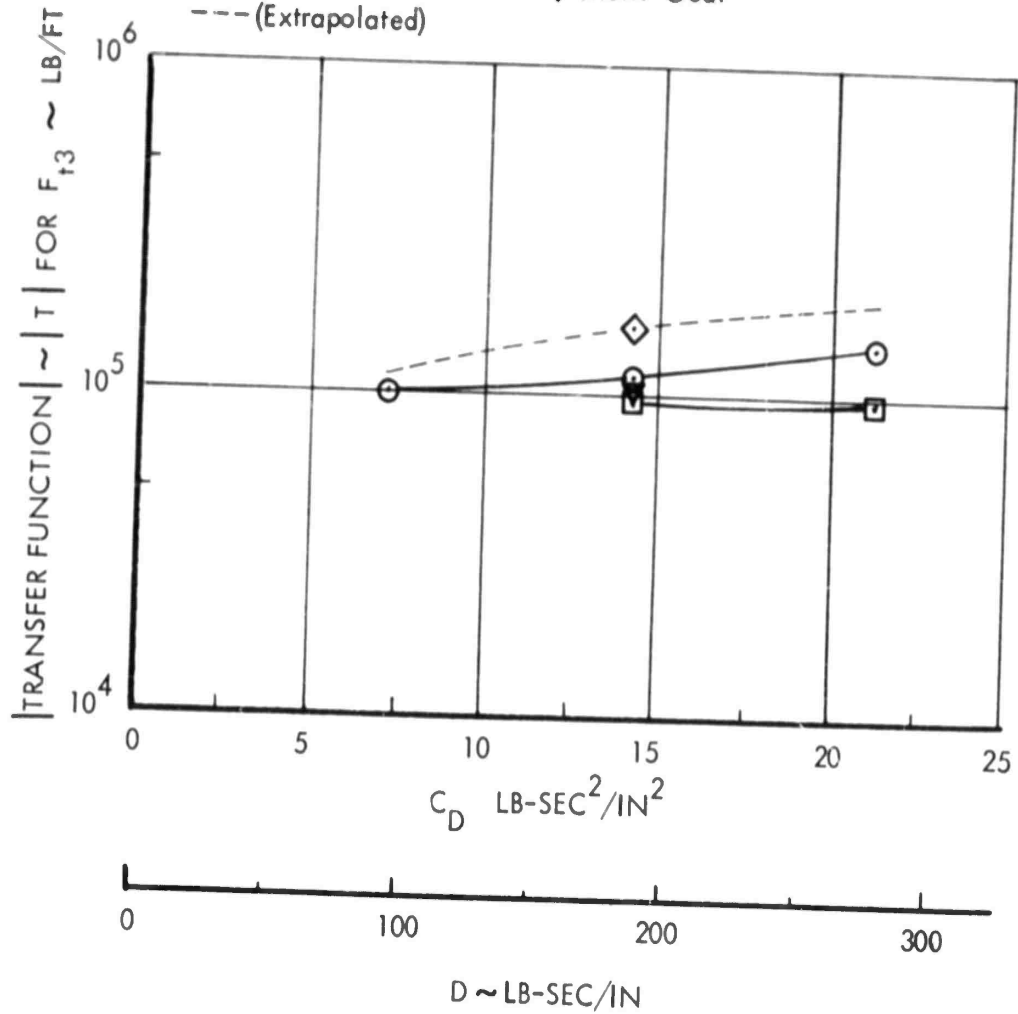


FIGURE 99: Variation of Transfer Function Peak with Damping of the Linear and Nonlinear Systems for Rear Main Landing Gear Tire Force,  $F_{t3}$

$f = 3.5 \text{ cps}$

Tire Pressure = 90 psi  
 $V_H = 88 \text{ Ft/Sec}$

ANALYSIS METHODS:

Nonlinear PSD:

○ Multi-Gear

◇ Single Gear

--- (Extrapolated)

Linear Harmonic:

□ Single Gear

▽ Multi-Gear

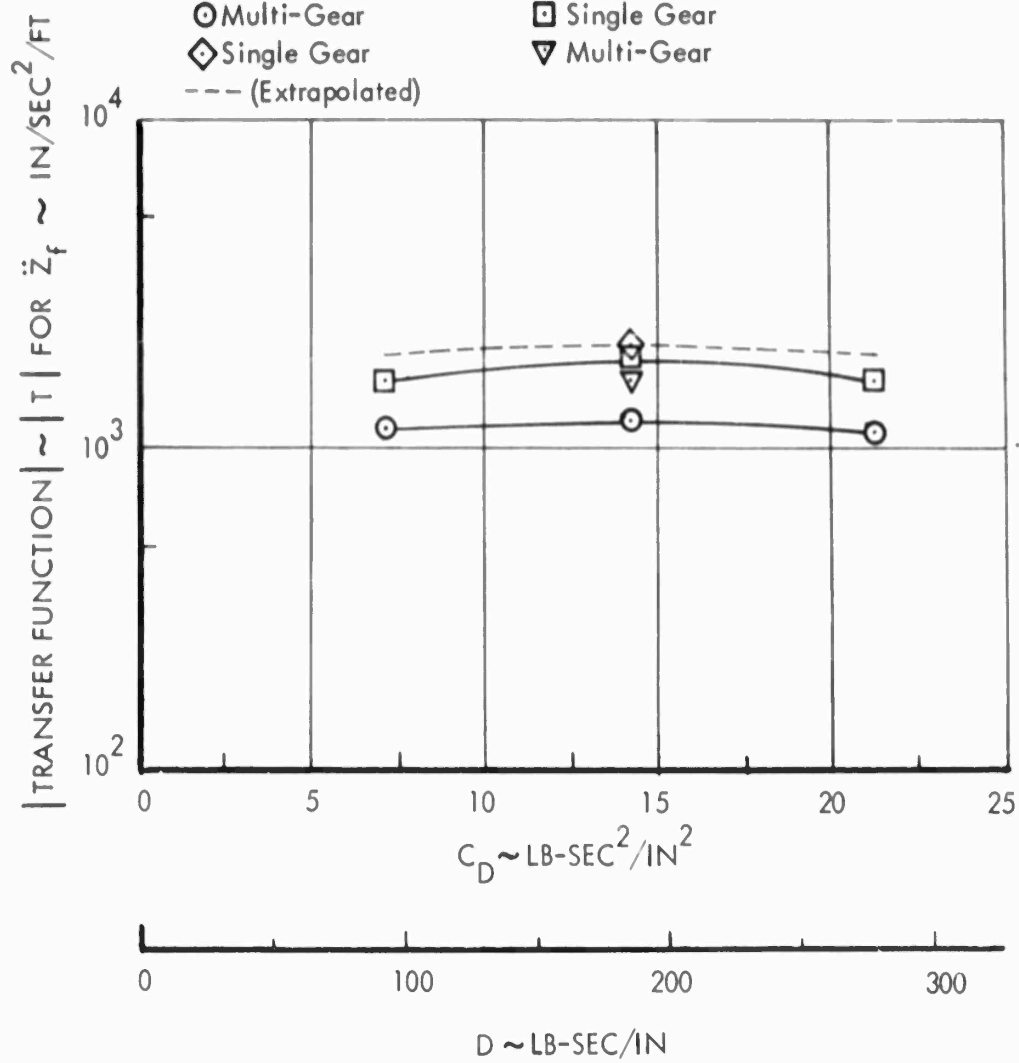


FIGURE 100: Variation of Transfer Function Peak with Damping of the Linear and Nonlinear Systems for Center of Gravity Acceleration,  $\ddot{z}_f$

$f = 0.95 \text{ cps}$

Tire Pressure = 90 psi  
 $V_H = 88 \text{ Ft/Sec}$

ANALYSIS METHODS:

Nonlinear PSD:

○ Multi-Gear

◇ Single Gear

---(Extrapolated)

Linear Harmonic:

□ Single Gear

▽ Multi-Gear

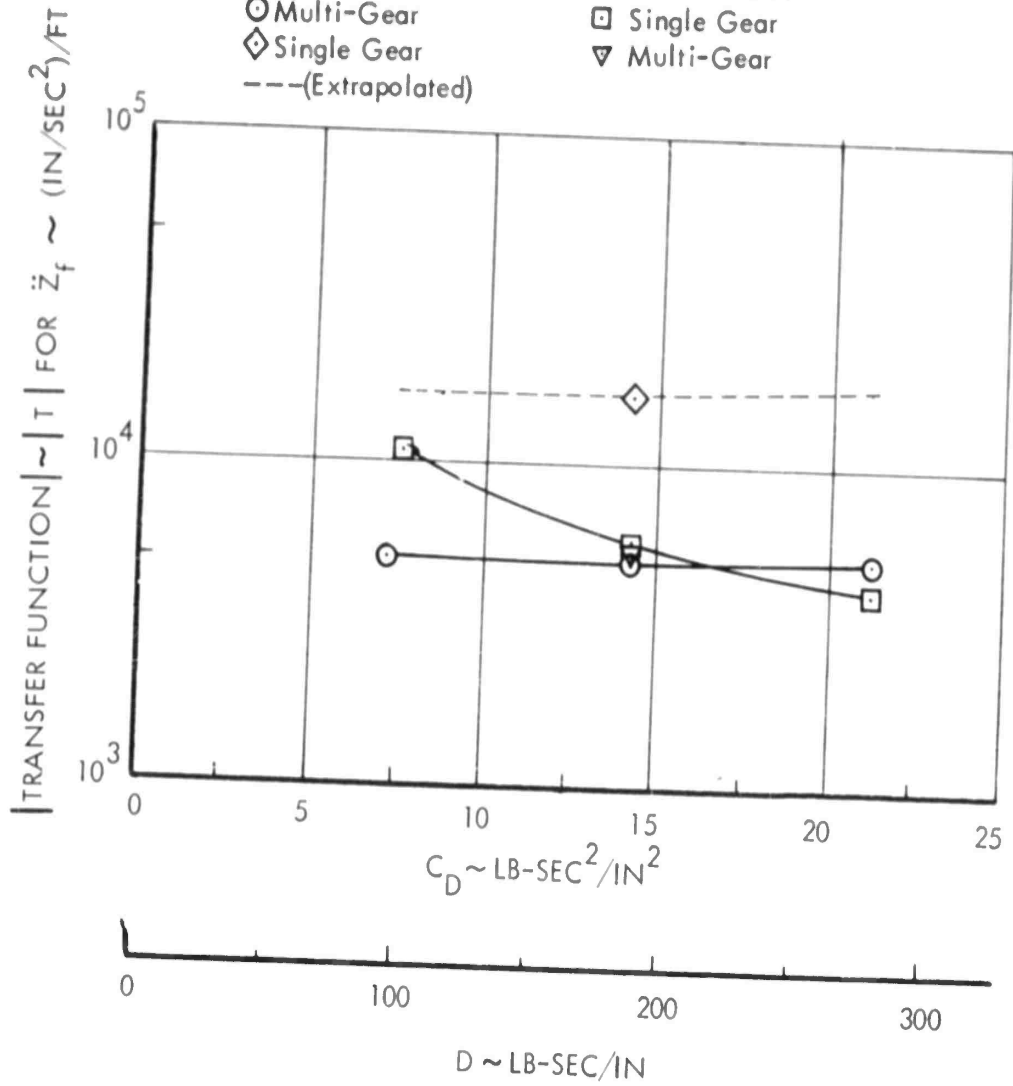


FIGURE 101: Variation of Transfer Function Peak with Damping of the Linear and Nonlinear Systems for Center of Gravity Acceleration,  $\ddot{z}_f$

$f = 1.65 \text{ cps}$

Tire Pressure = 90 psi  
 $V_H = 88 \text{ Ft/Sec}$

ANALYSIS METHODS:

Nonlinear PSD:

○ Multi-Gear

◇ Single Gear

--- (Extrapolated)

Linear Harmonic:

□ Single Gear

▽ Multi-Gear

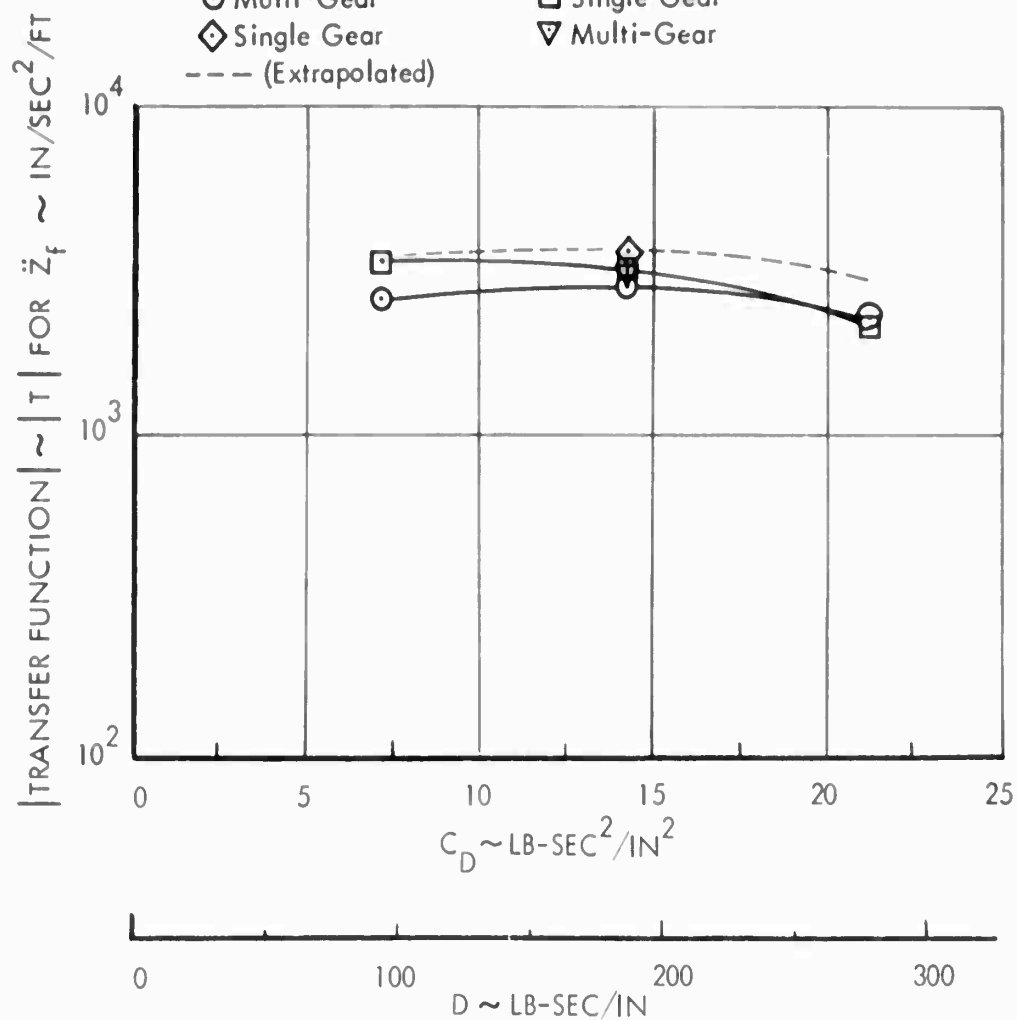


FIGURE 102: Variation of Transfer Function Peak with Damping of the Linear and Nonlinear Systems for Center of Gravity Acceleration,  $\ddot{z}_f$

$f = 3.5 \text{ cps}$

Tire Pressure = 90 psi  
 $V_H = 88$  Ft/Sec

ANALYSIS METHODS:

Nonlinear PSD:

○ Multi-Gear

◇ Single Gear

--- (Extrapolated)

Linear Harmonic:

□ Single Gear

▽ Multi-Gear

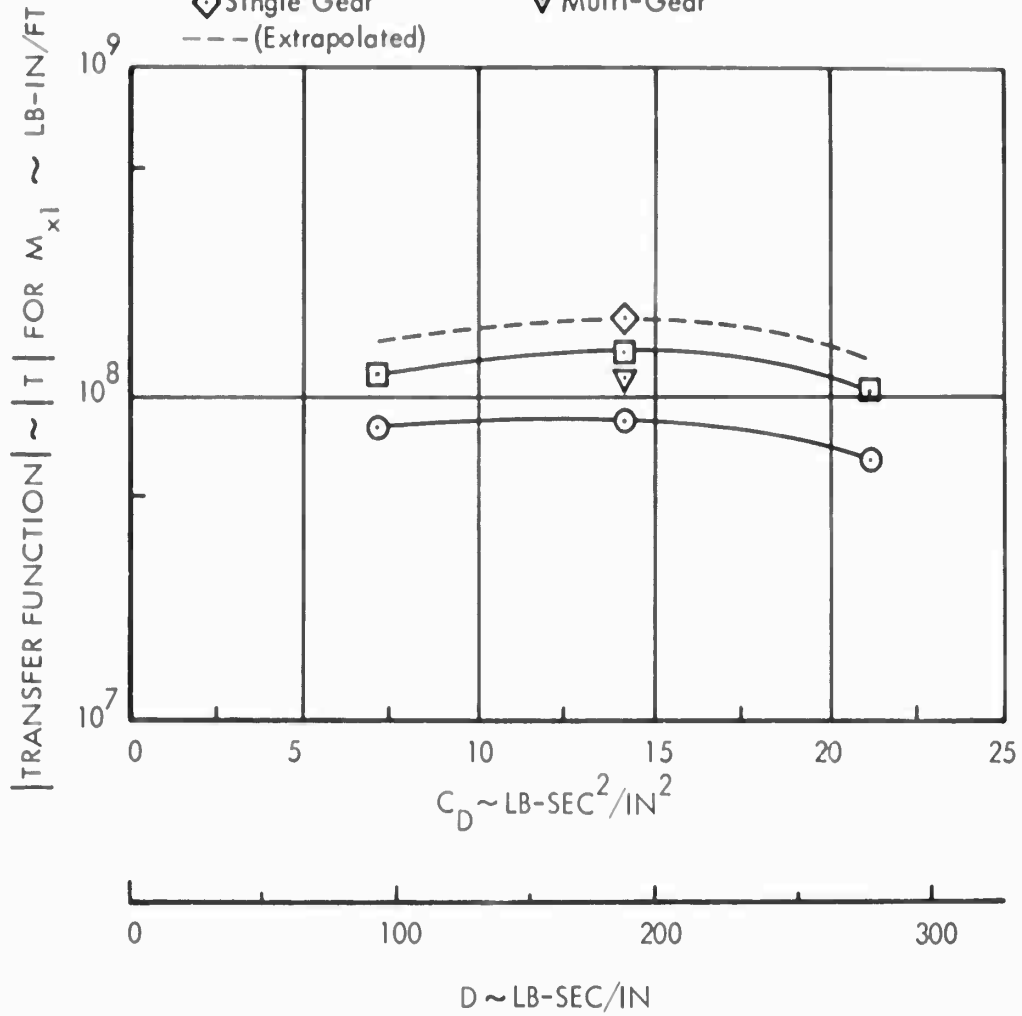


FIGURE 103: Variation of Transfer Function Peak with Damping of the Linear and Nonlinear Systems for Wing Root Bending Moment,  $M_{x1}$

$f = 0.93$  cps

Tire Pressure = 90 psi  
 $V_H = 88$  Ft/Sec

ANALYSIS METHODS:

Nonlinear PSD:

○ Multi-Gear

◇ Single Gear

---(Extrapolated)

Linear Harmonic:

□ Single Gear

▽ Multi-Gear

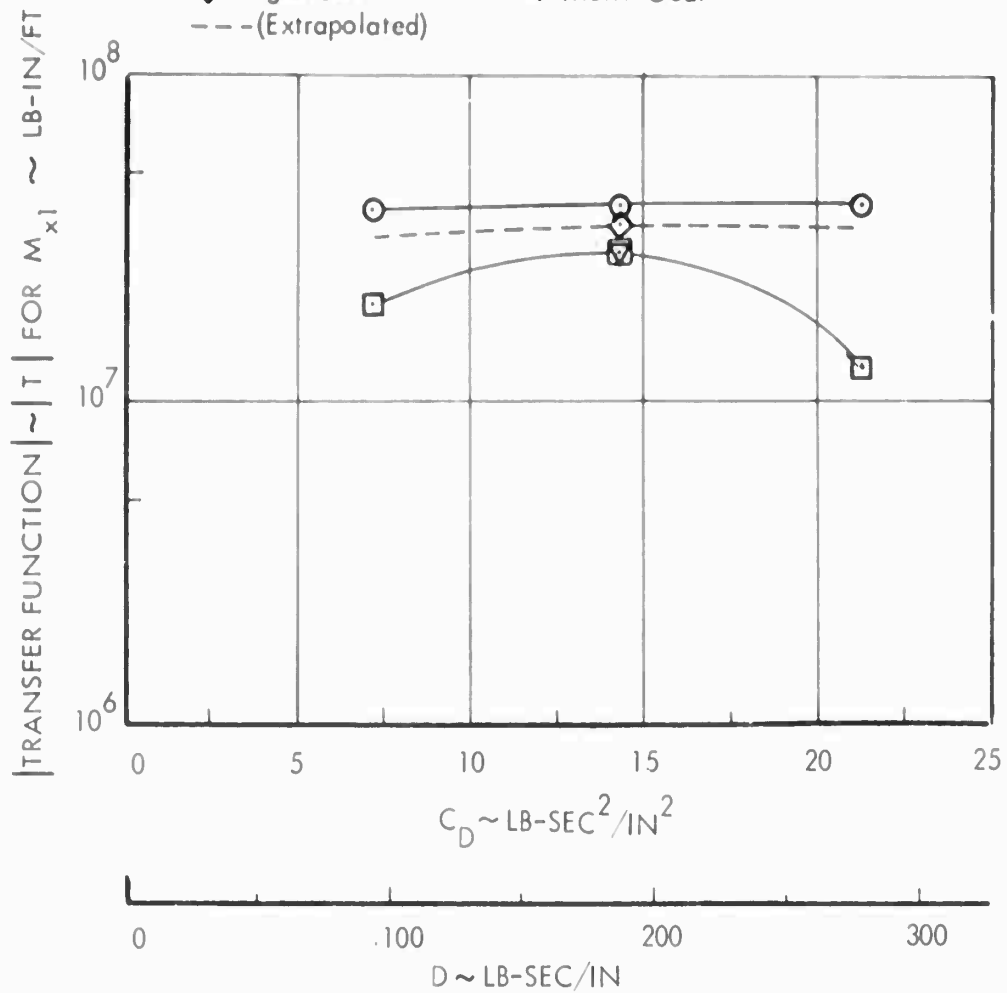


FIGURE 104: Variation of Transfer Function Peak with Damping of the Linear and Nonlinear Systems for Wing Root Bending Moment,  $M_{x1}$

$f = 3.5$  cps

Tire Pressure 90 psi  
 $V_H = 88$  Ft/Sec

ANALYSIS METHODS:

Nonlinear PSD:

○ Multi-Gear

◇ Single Gear

---(Extrapolated)

Linear Harmonic:

□ Single Gear

▽ Multi-Gear

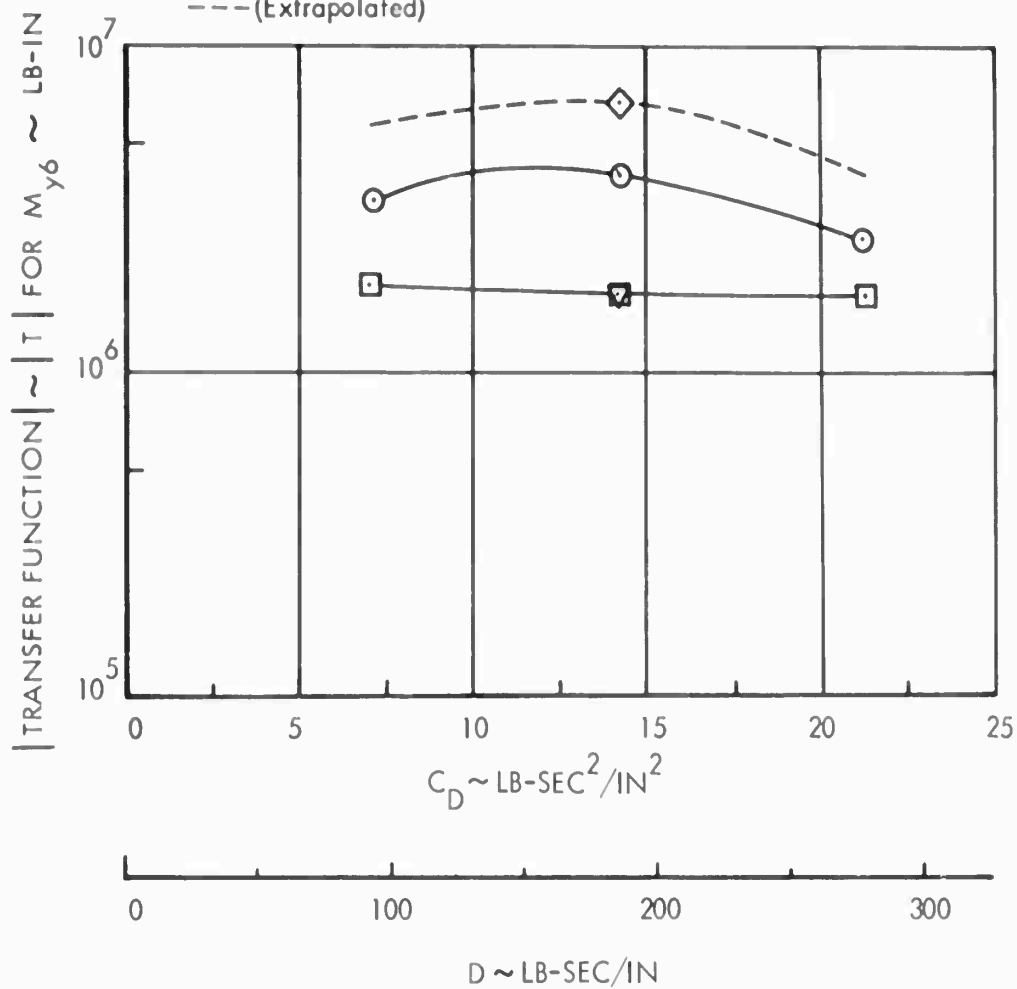


FIGURE 105: Variation of Transfer Function Peak with Damping of the Linear and Nonlinear Systems for Wing Torsion Moment Inboard of Outboard Nacelle,  $M_{y6}$

$f = 0.95$  cps

Tire Pressure 90 psi  
 $V_H = 88 \text{ Ft/Sec}$

ANALYSIS METHODS:

Nonlinear PSD:

○ Multi-Gear

◇ Single Gear

---(Extrapolated)

Linear Harmonic:

□ Single Gear

▽ Multi-Gear

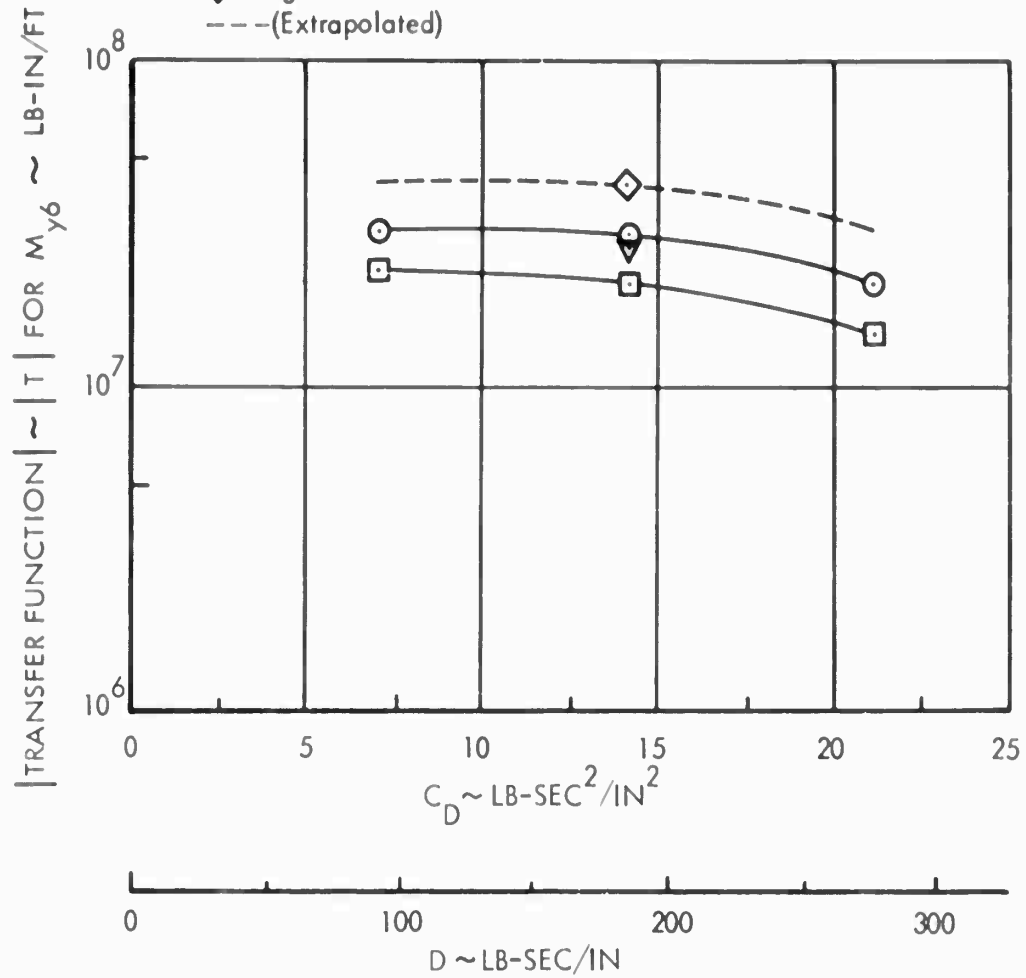


FIGURE 106: Variation of Transfer Function Peak with Damping of the Linear and Nonlinear Systems for Wing Torsion Moment Inboard of Outboard Nacelle,  $M_{y6}$

$f = 3.5 \text{ cps}$

Tire Pressure = 90 psi  
 $V_H = 88$  fps  
 Nonlinear PSD Methods  
 $C_D = 14.1$  lb-sec<sup>2</sup>/in<sup>2</sup>

ANALYSIS METHODS:

- Single Gear -  $F_{t1}$
- - - Multi-Gear -  $F_{t2}$
- · - Multi-Gear -  $F_{t3}$

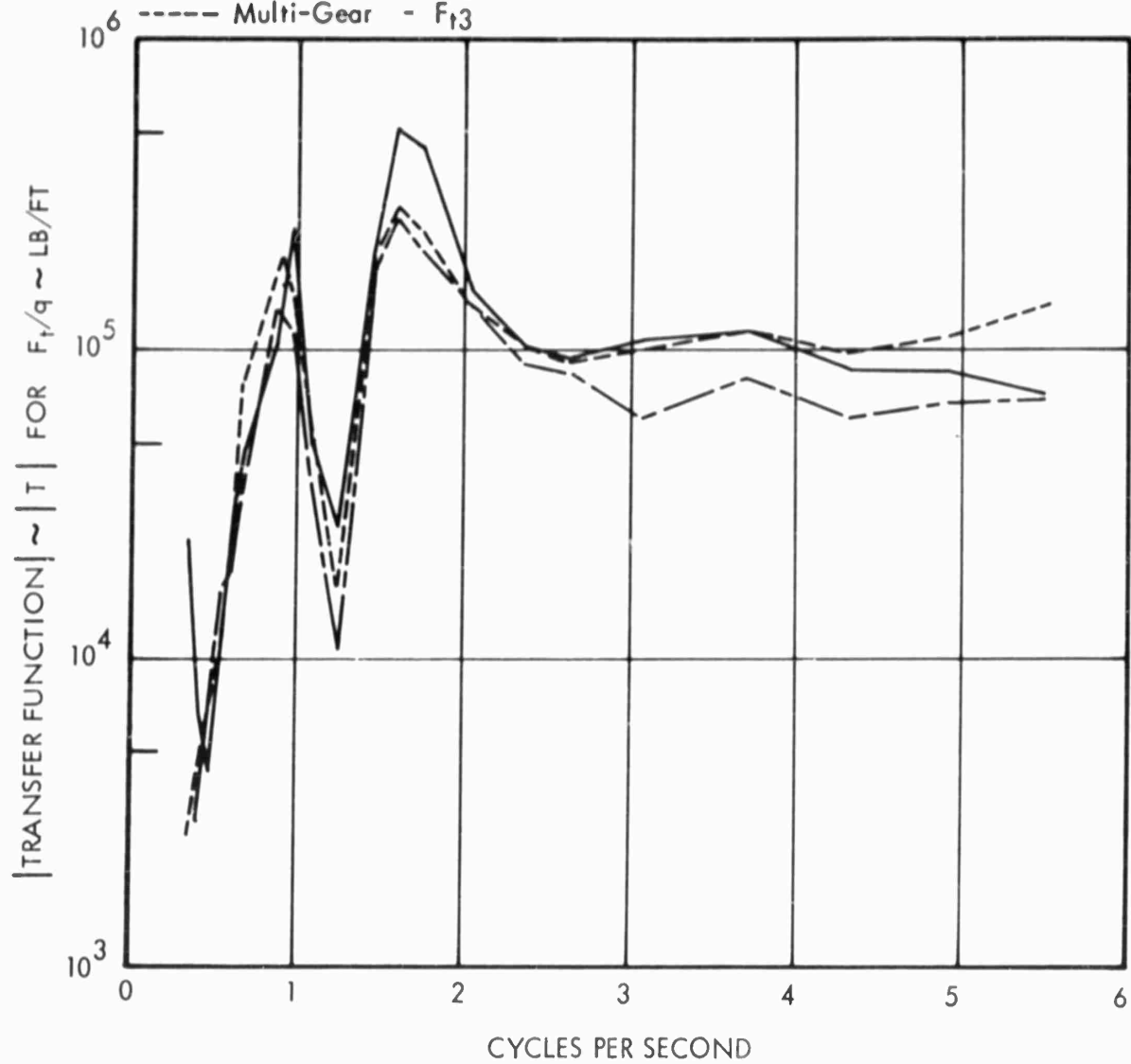


FIGURE 107 : Comparison Between Transfer Functions for Single and Multi-Gear Analyses of the Nonlinear System Tire Force

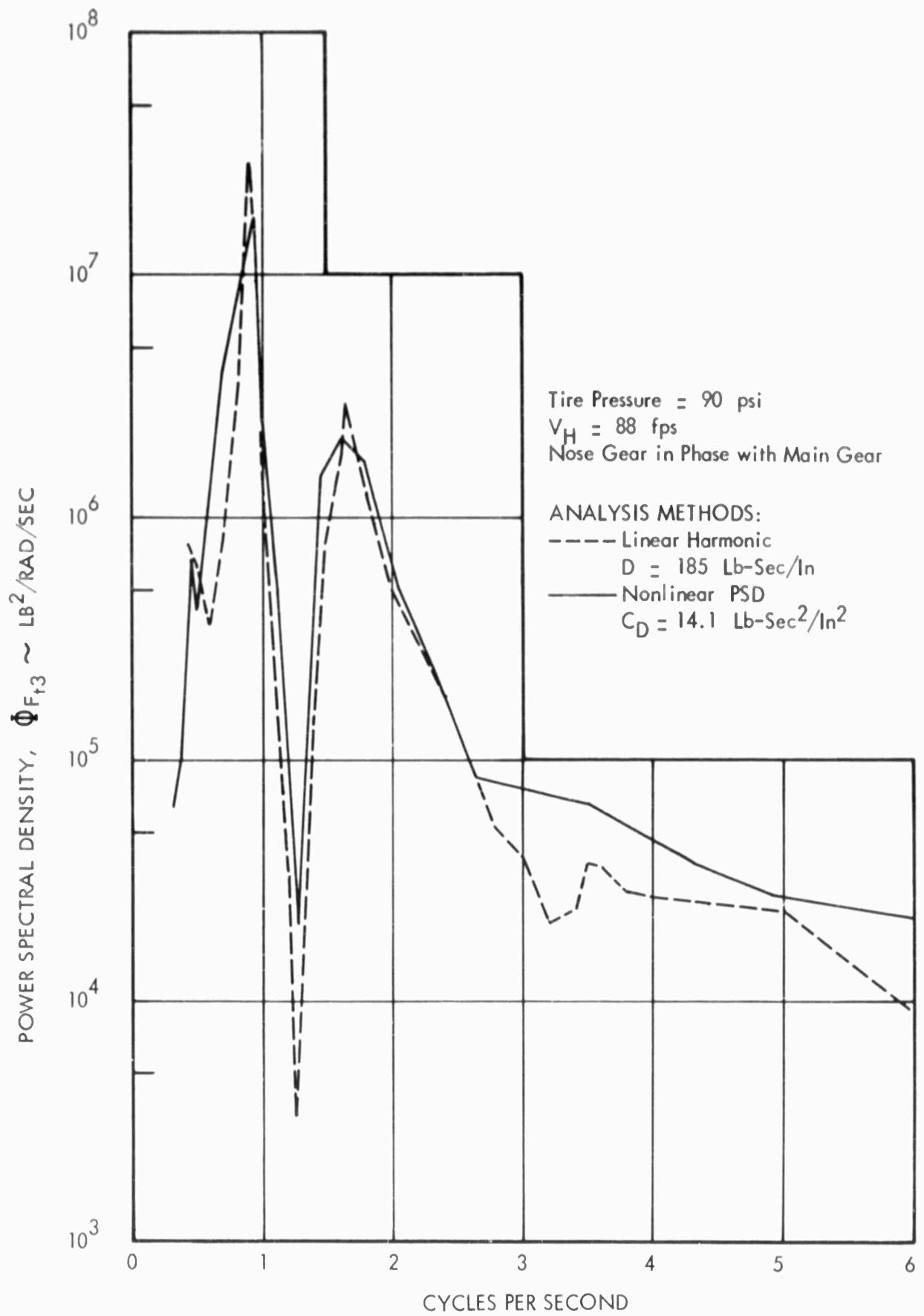


FIGURE 108 : Comparison of Output Power Spectra from Linear Harmonic and Power Spectral Density Methods for the Rear Main Gear Tire Force Multi-Gear Analysis

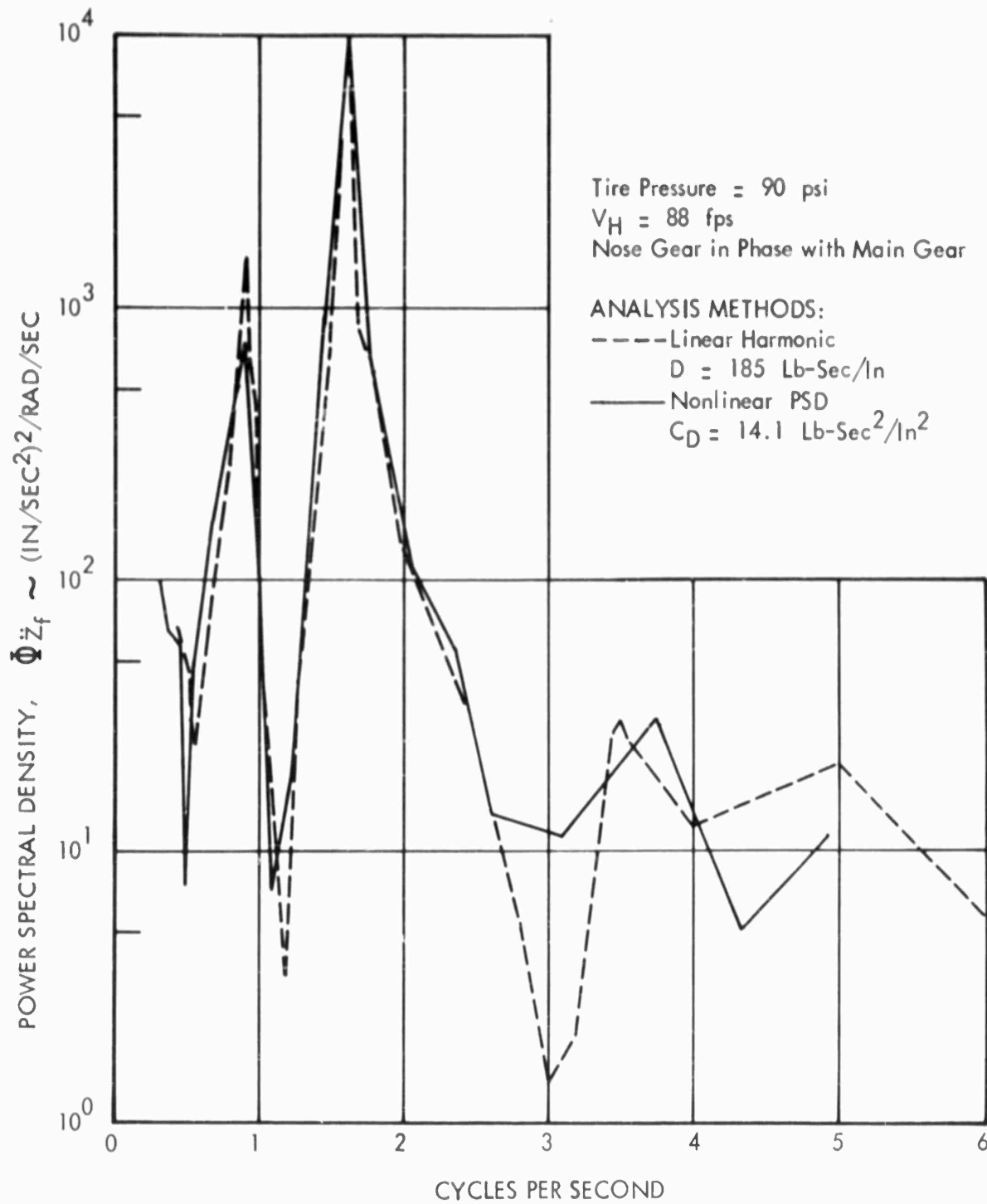


FIGURE 109 : Comparison of Output Power Spectra from Linear Harmonic and Power Spectral Density Methods for Vertical Acceleration of the Airplane Center of Gravity

Multi-Gear Analysis

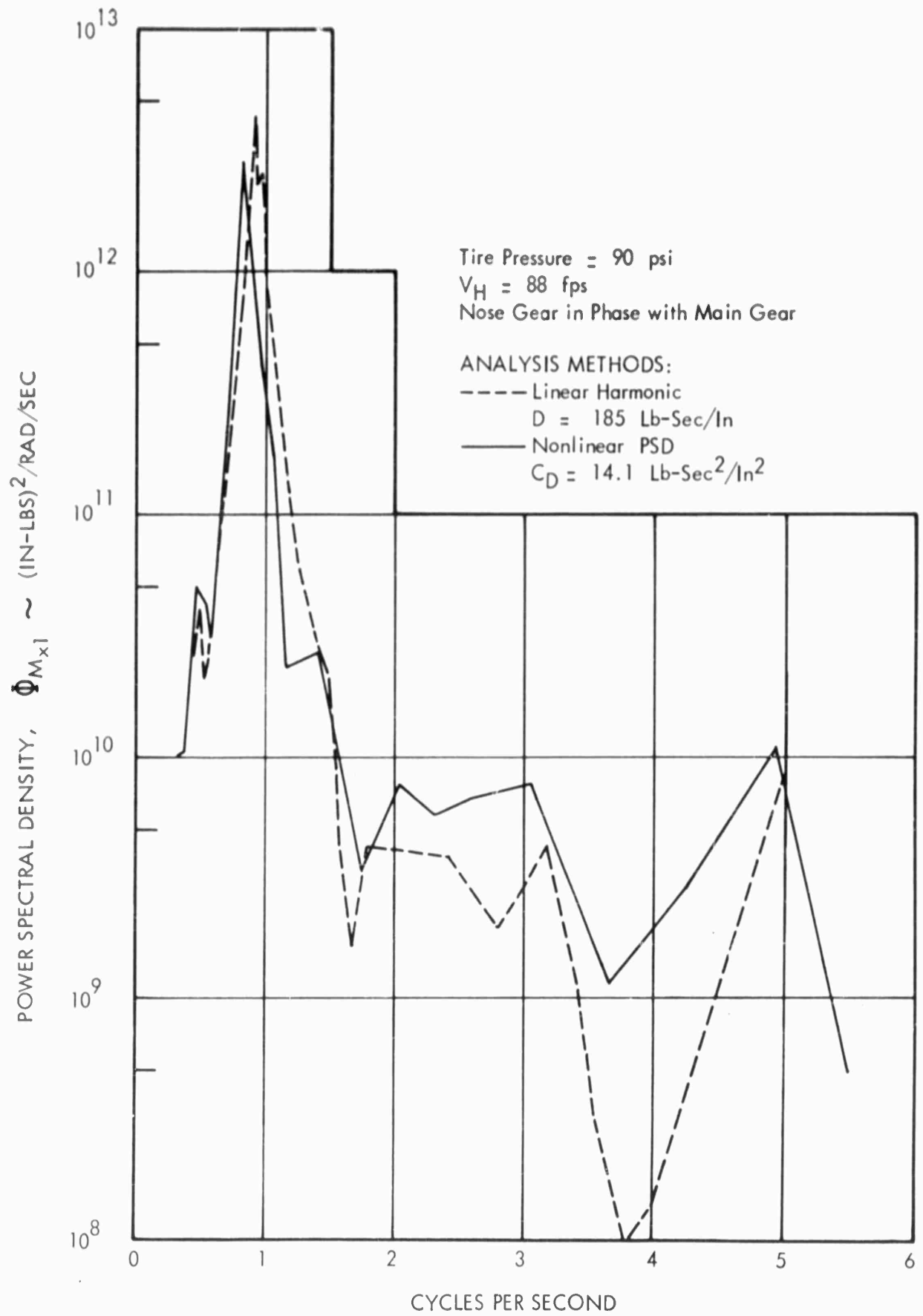


FIGURE 110 : Comparison of Output Power Spectra from Linear Harmonic and Power Spectral Density Methods for Wing Root Bending Moment  
Multi-Gear Analysis

Tire Pressure = 90 psi  
 $V_H = 88$  fps  
 Nose Gear in Phase with Main Gear

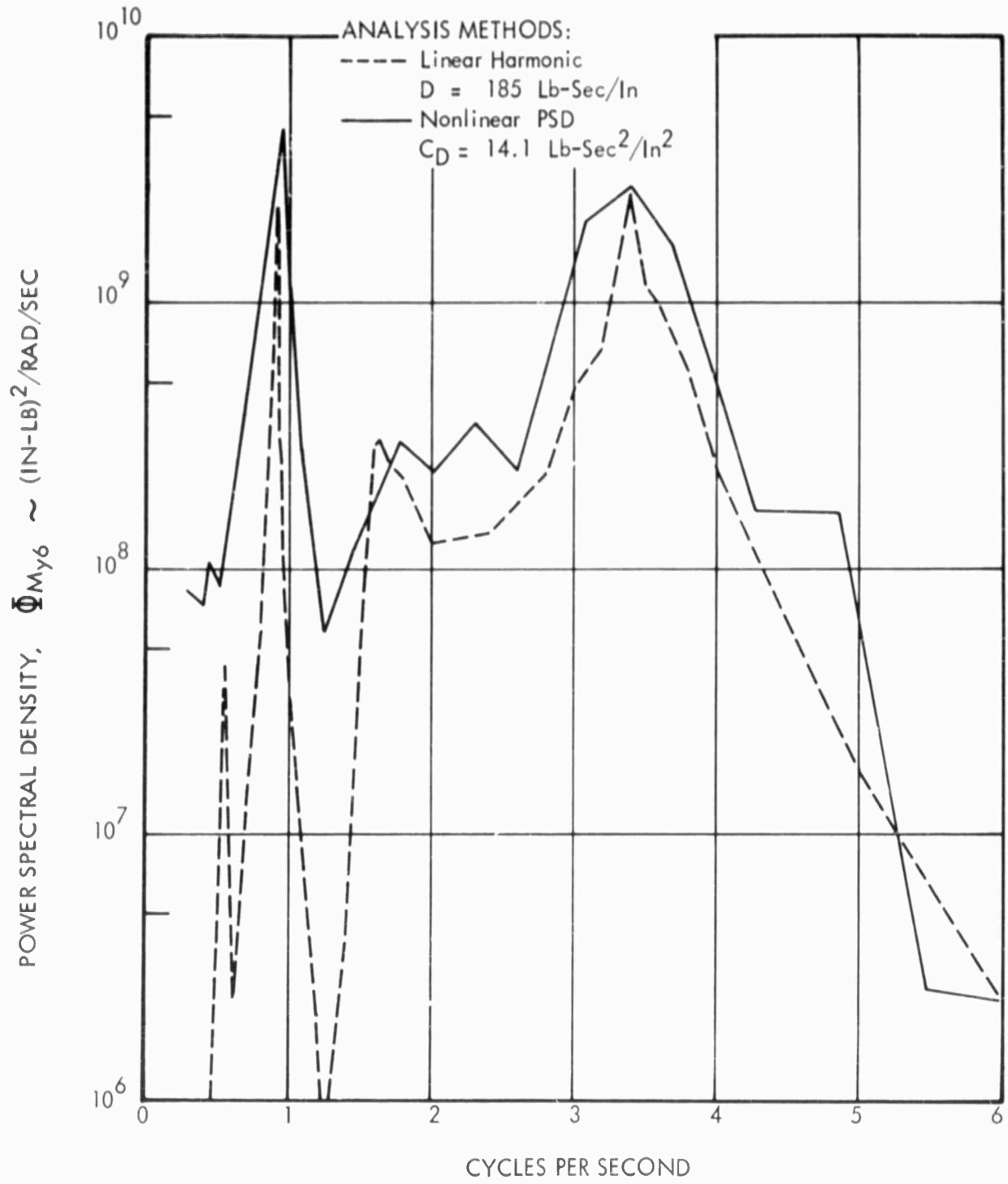


FIGURE 111 : Comparison of Output Power Spectra from Linear Harmonic and Power Spectral Density Methods for Wing Torsion Moment Inboard of Outboard Nacelle  
 Multi-Gear Analysis

$D = 185 \text{ Lb-Sec/In}$   
 $C_D = 14.1 \text{ Lb-Sec}^2/\text{In}^2$   
 $V_H = 88 \text{ fps}$

ANALYSIS METHODS:

- Nonlinear (Gaussian Fit to Direct Sampling)
- - - Linear (Gaussian)
- · - Nonlinear (Gaussian)

$\sigma \times 10^{-3} \text{ Lbs}$   
 4.06  
 4.44  
 3.58

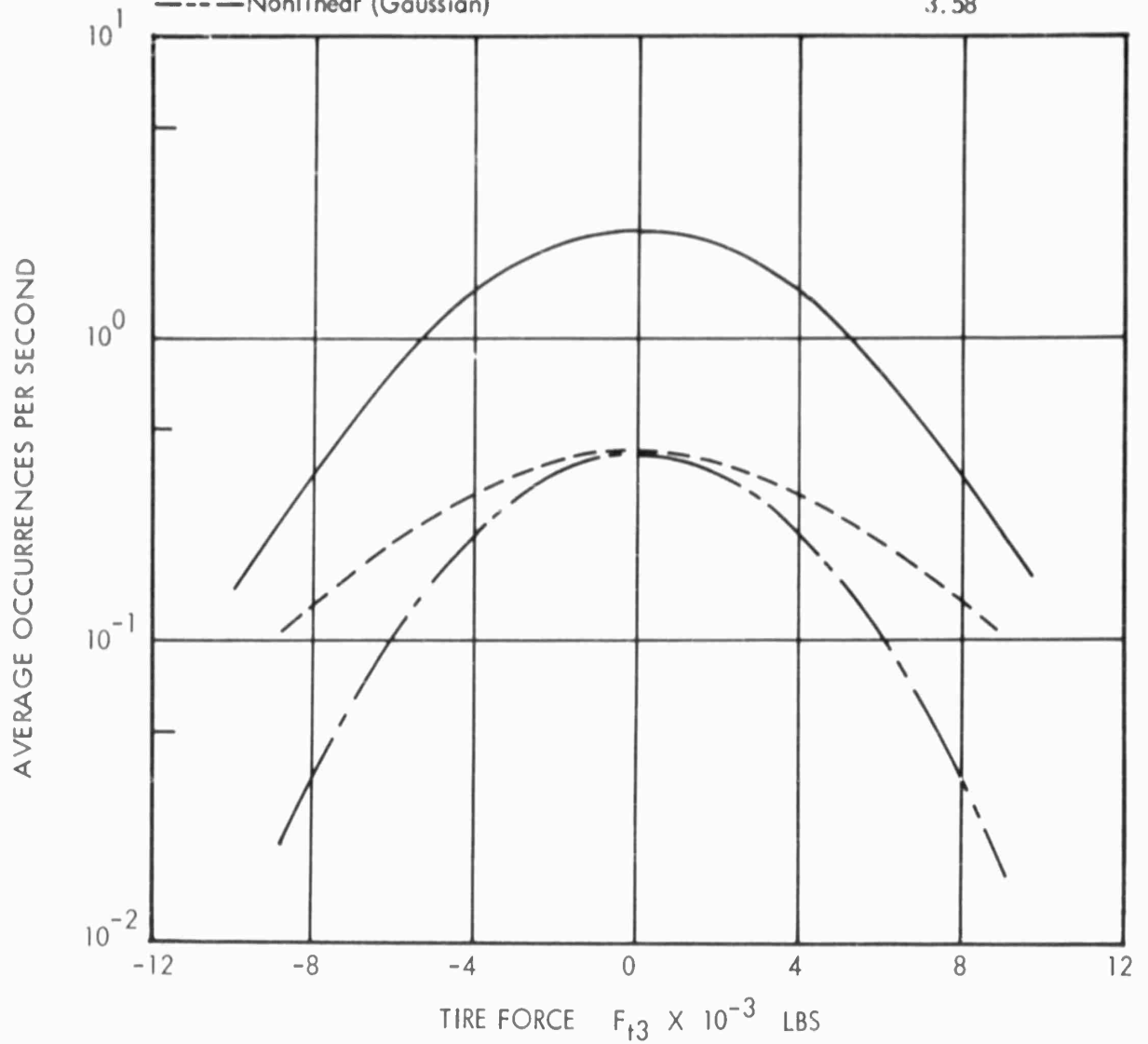


FIGURE 112 : Comparison of Load Occurrences for the Nonlinear and Linearized Systems for Incremental Tire Vertical Force Rear Main Gear,  $\Delta F_{t3}$

Multi Gear Analysis  
 Tire Pressure = 60 psi

$D = 185 \text{ Lb-Sec/In}$   
 $C_D = 14.1 \text{ Lb-Sec}^2/\text{In}^2$   
 $V_H = 88 \text{ fps}$

ANALYSIS METHODS:

- Nonlinear (Gaussian Fit to Direct Sampling)
- - - Linear (Gaussian)
- · - Nonlinear (Gaussian)
- - - Nonlinear (Direct Sampling)

$\sigma \times 10^{-3} \text{ Lbs}$   
 5.46  
 4.45  
 5.24  
 5.46

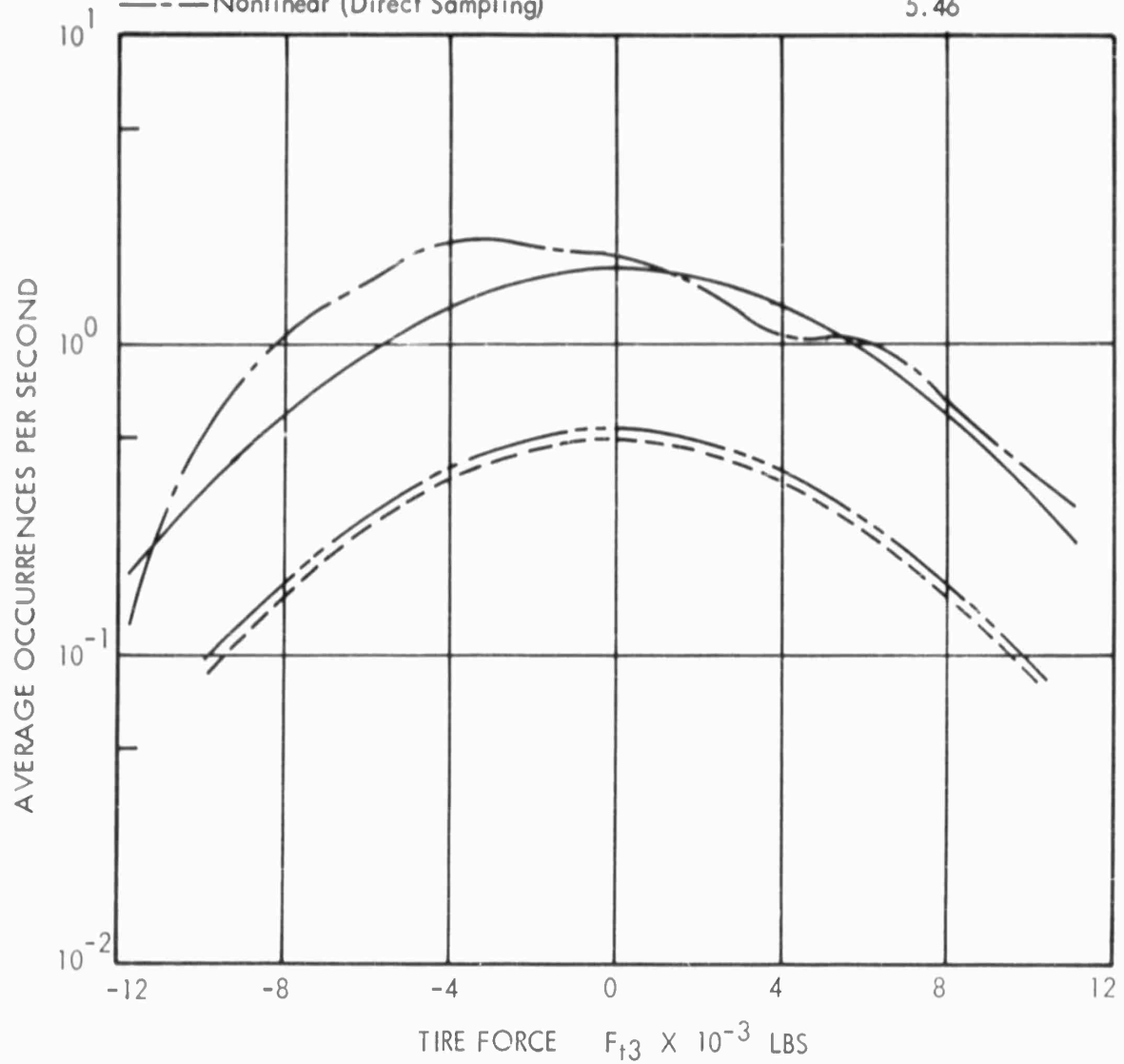


FIGURE 113 : Comparison of Load Occurrences for the Nonlinear and Linearized Systems for Incremental Tire Vertical Force Rear Main Gear,  $\Delta F_{t3}$

Multi Gear Analysis  
 Tire Pressure = 90 psi

$D = 185 \text{ Lb-Sec/In}$   
 $C_D = 14.1 \text{ Lb-Sec}^2/\text{In}^2$   
 $V_H = 88 \text{ fps}$

ANALYSIS METHODS:

— Nonlinear (Gaussian Fit to Direct Sampling)  
 - - - Linear (Gaussian)  
 - · - Nonlinear (Gaussian)

$\sigma \times 10^{-3} \text{ Lbs}$   
 5.22  
 4.32  
 5.07

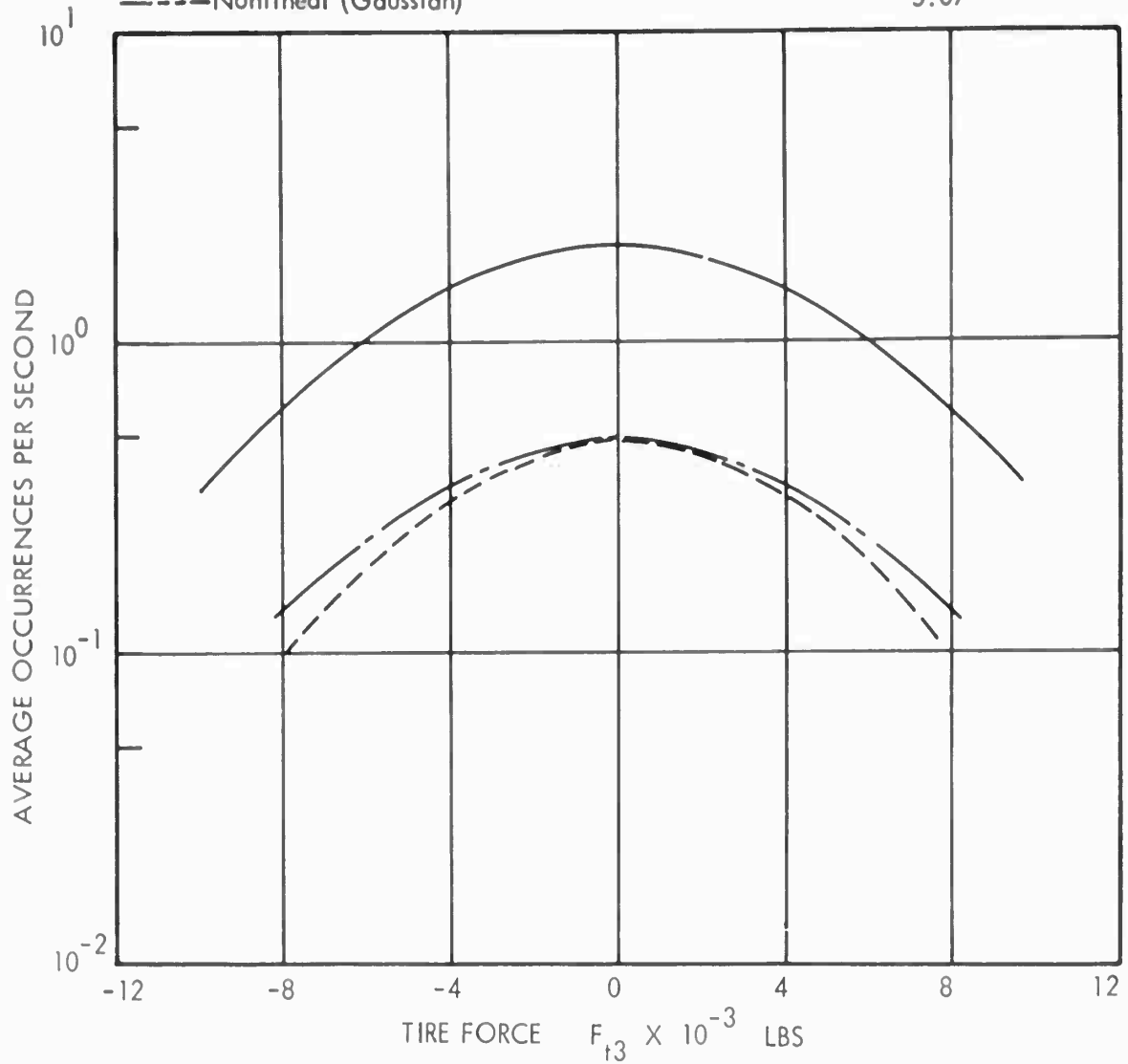


FIGURE 114 : Comparison of Load Occurrences for the Nonlinear and Linearized Systems for Incremental Tire Vertical Force Rear Main Gear,  $\Delta F_{t3}$

Multi Gear Analysis  
 Tire Pressure = 120 psi

$D = 185 \text{ Lb-Sec/In}$   
 $C_D = 14.1 \text{ Lb-Sec}^2/\text{In}^2$   
 $V_H = 88 \text{ fps}$

ANALYSIS METHODS:

- Nonlinear (Gaussian Fit to Direct Sampling)
- - - Linear (Gaussian)
- · - Nonlinear (Gaussian)

$\sigma \times 10^{-1} \text{ In/Sec}^2$   
 4.7  
 6.1  
 4.8

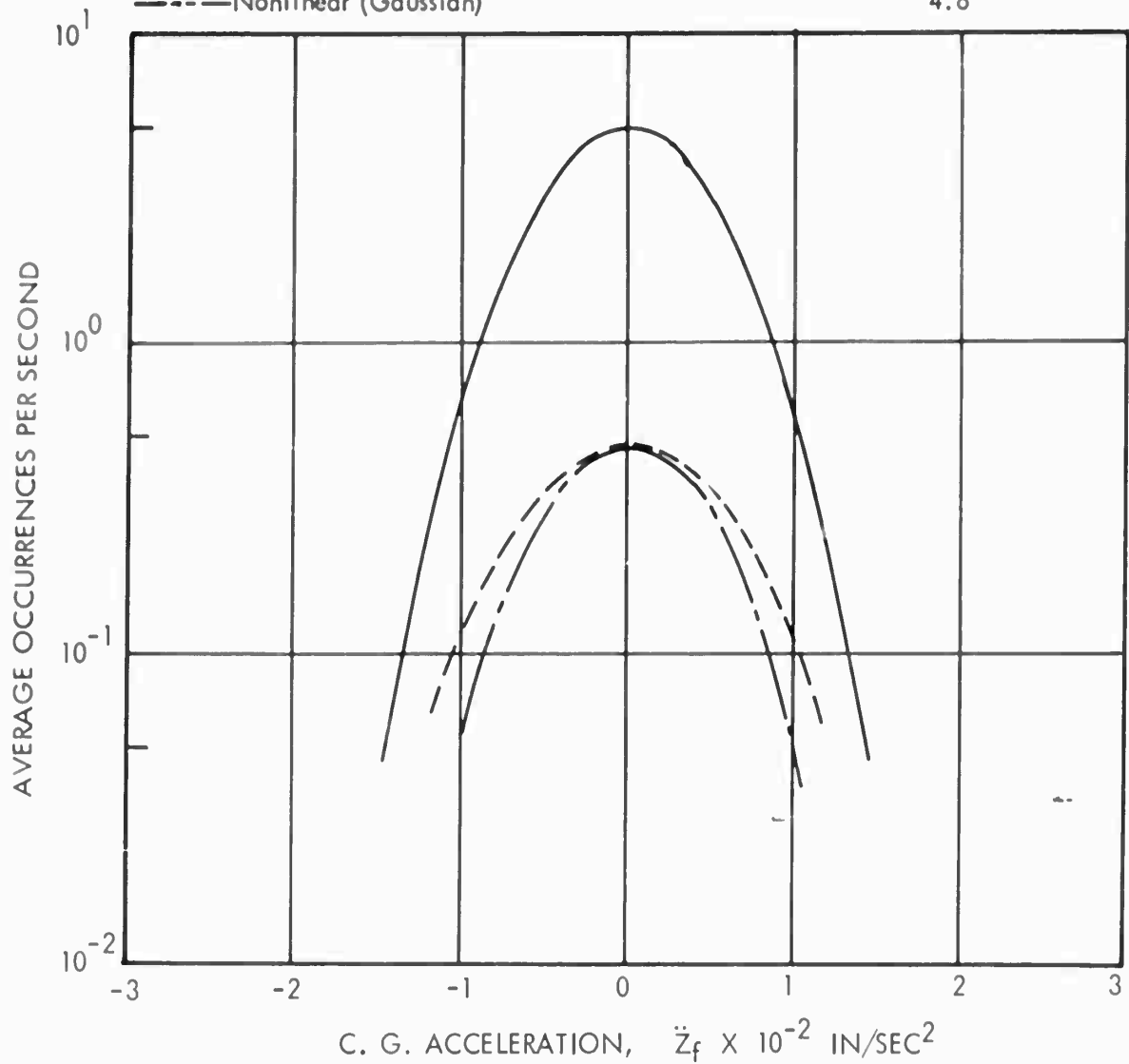


FIGURE 115 : Comparison of Load Occurrences for the Nonlinear and Linearized Systems for Center of Gravity Acceleration,  $\ddot{z}_f$

Multi Gear Analysis  
 Tire Pressure = 60 psi

$D = 185 \text{ Lb-Sec/In}$   
 $C_D = 14.1 \text{ Lb-Sec}^2/\text{In}^2$   
 $V_H = 88 \text{ fps}$

ANALYSIS METHODS:

— Nonlinear (Gaussian Fit to Direct Sampling)  
 - - - Linear (Gaussian)  
 - · - · Nonlinear (Gaussian)

$\sigma \times 10^{-1} \text{ IN/SEC}^2$   
 6.4  
 6.23  
 6.0

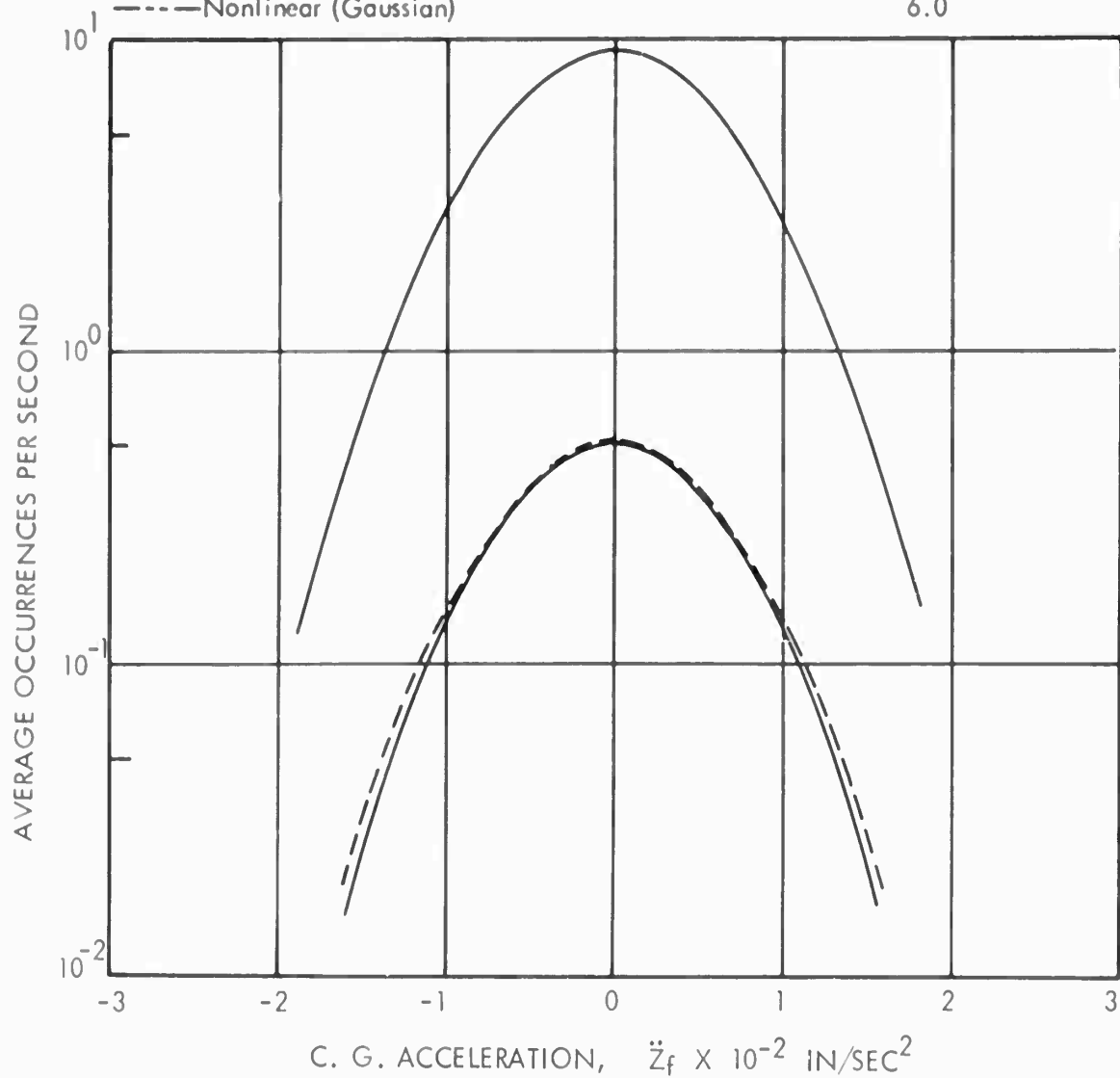


FIGURE 116 : Comparison of Load Occurrences for the Nonlinear and Linearized Systems for Center of Gravity Acceleration,  $\ddot{Z}_f$

Multi Gear Analysis  
 Tire Pressure = 90 psi

$D = 185 \text{ Lb-Sec/In}$   
 $C_D = 14.1 \text{ Lb-Sec}^2/\text{In}^2$   
 $V_H = 88 \text{ fps}$

ANALYSIS METHODS:

— Nonlinear (Gaussian Fit to Direct Sampling)  
 - - - Linear (Gaussian)  
 - · - Nonlinear (Gaussian)

$\sigma \times 10^{-1} \text{ In/Sec}^2$   
 6.7  
 5.9  
 6.0

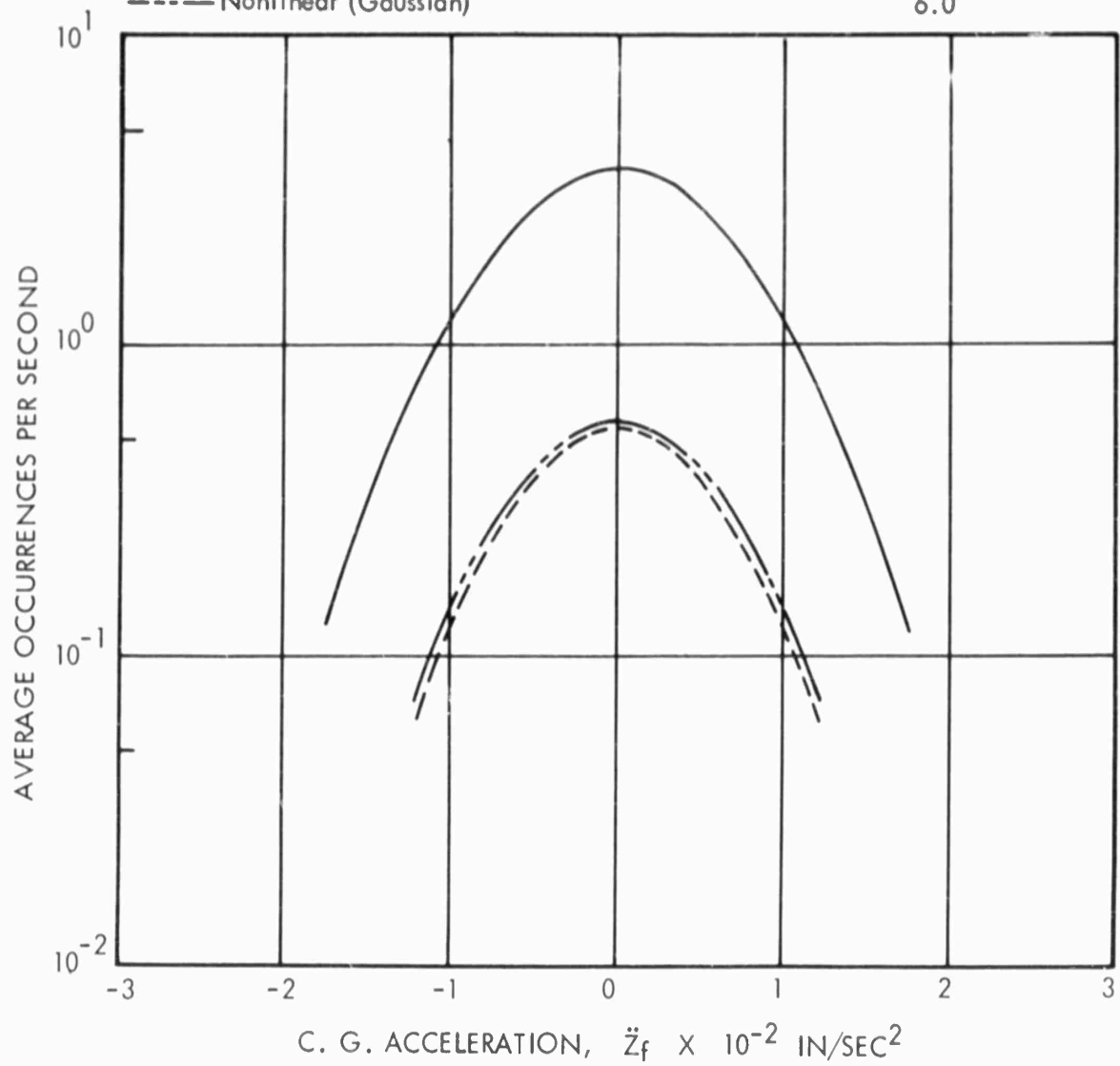


FIGURE 117 : Comparison of Load Occurrences for the Nonlinear and Linearized Systems for Center of Gravity Acceleration,  $\ddot{Z}_f$   
 Multi Gear Analysis  
 Tire Pressure = 120 psi

$D = 185 \text{ Lb-Sec/In}$   
 $C_D = 14.1 \text{ Lb-Sec}^2/\text{In}^2$   
 $V_H = 88 \text{ fps}$

ANALYSIS METHODS:  $\sigma \times 10^{-6} \text{ In-Lbs}$   
 ——— Nonlinear (Gaussian Fit to Direct Sampling) 1.49  
 - - - - Linear (Gaussian) 1.13  
 - · - · Nonlinear (Gaussian) 1.54

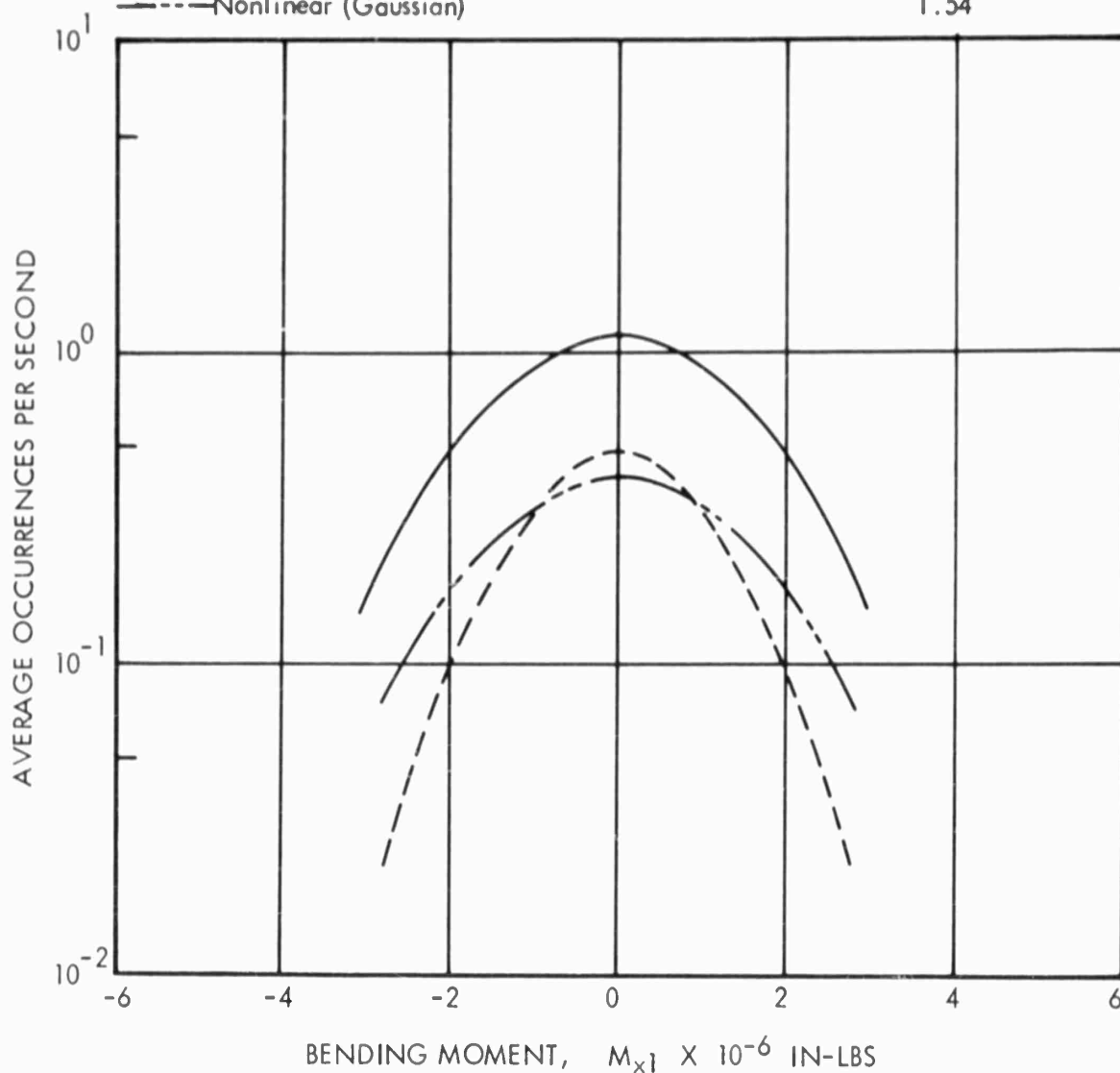


FIGURE 118 : Comparison of Load Occurrences for the Nonlinear and Linearized Systems for Incremental Wing Root Bending Moment,  $\Delta M_x |$

Multi Gear Analysis  
 Tire Pressure = 60 psi

$D = 185 \text{ Lb-Sec/In}$   
 $C_D = 14.1 \text{ Lb-Sec}^2/\text{In}^2$   
 $V_H = 88 \text{ fps}$

ANALYSIS METHODS:

- Nonlinear (Gaussian Fit to Direct Sampling)
- Linear (Gaussian)
- - - - Nonlinear (Gaussian)

$\sigma \times 10^{-6} \text{ In-Lbs}$   
 1.88  
 2.06  
 1.55

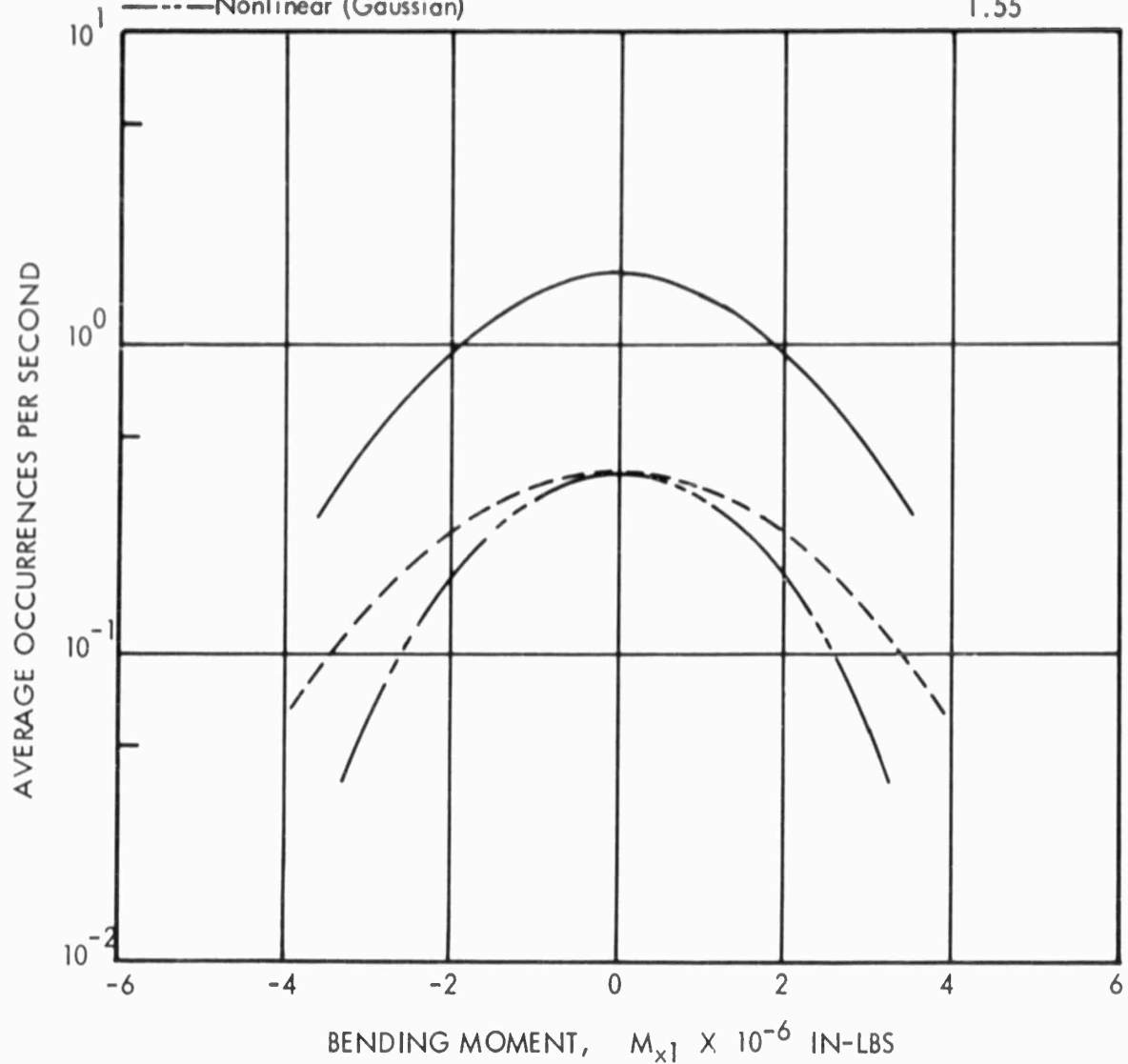


FIGURE 119 : Comparison of Load Occurrences for the Nonlinear and Linearized Systems for  $M_{x1}$ , Wing Root Bending Moment

Multi Gear Analysis  
 Tire Pressure = 90 psi

$D = 185 \text{ Lb-Sec/In}$   
 $C_D = 14.1 \text{ Lb-Sec}^2/\text{In}^2$   
 $V_H = 88 \text{ fps}$

ANALYSIS METHODS:

- Nonlinear (Gaussian Fit to Direct Sampling)
- Linear (Gaussian)
- Nonlinear (Gaussian)

$\sigma \times 10^{-6} \text{ In-Lbs}$   
 1.59  
 1.04  
 1.46

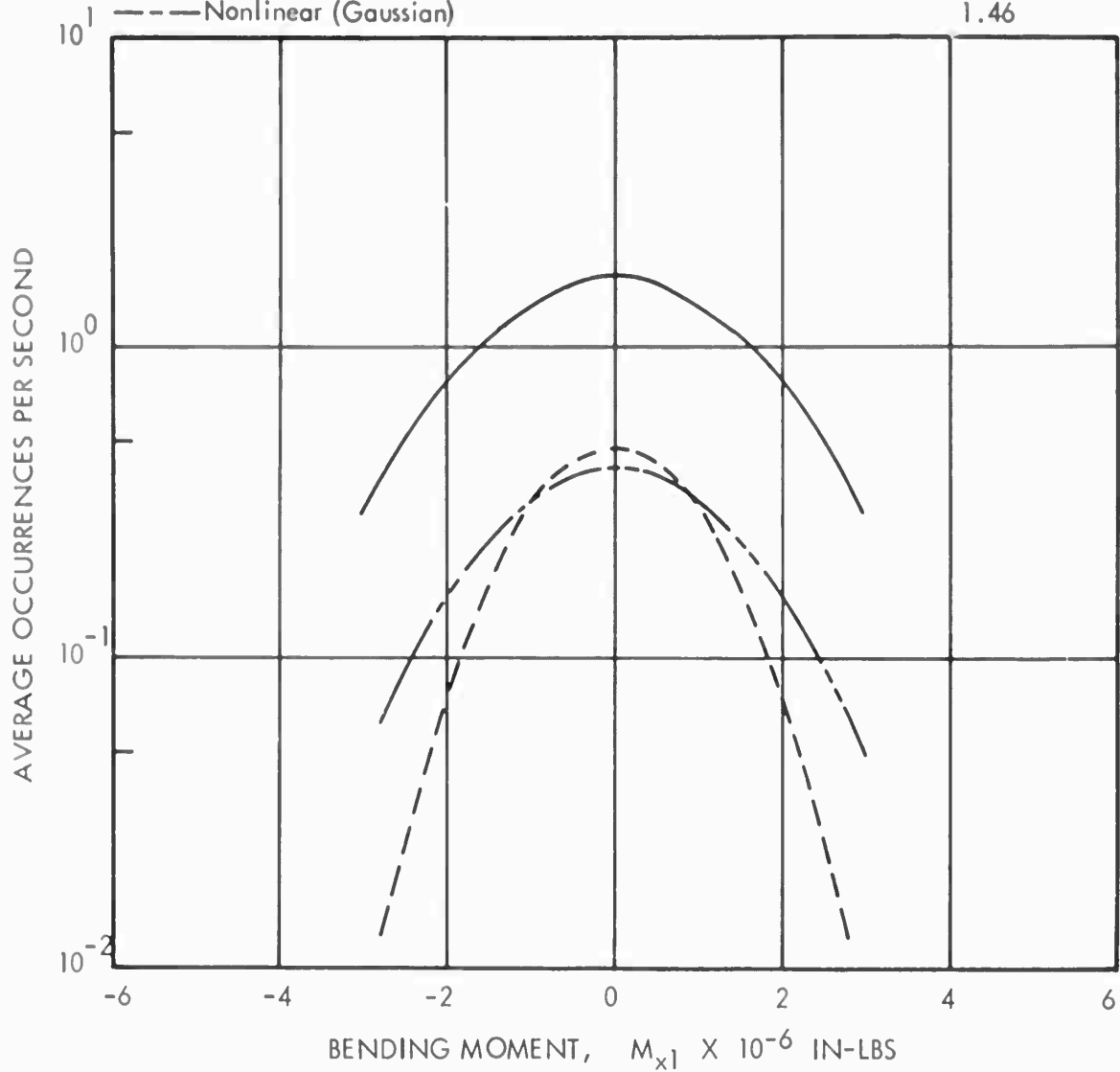


FIGURE 120 : Comparison of Load Occurrences for the Nonlinear and Linearized Systems for  $M_{x1}$ , Wing Root Bending Moment

Multi Gear Analysis  
 Tire Pressure = 120 psi

$D = 185 \text{ Lb-Sec/In}$   
 $C_D = 14.1 \text{ Lb-Sec}^2/\text{In}^2$   
 $V_H = 88 \text{ fps}$

ANALYSIS METHODS:

- Nonlinear (Gaussian Fit to Direct Sampling)
- - - Linear (Gaussian)
- · - Nonlinear (Gaussian)

$\sigma \times 10^{-5} \text{ In-Lbs}$   
 1.34  
 .964  
 1.13

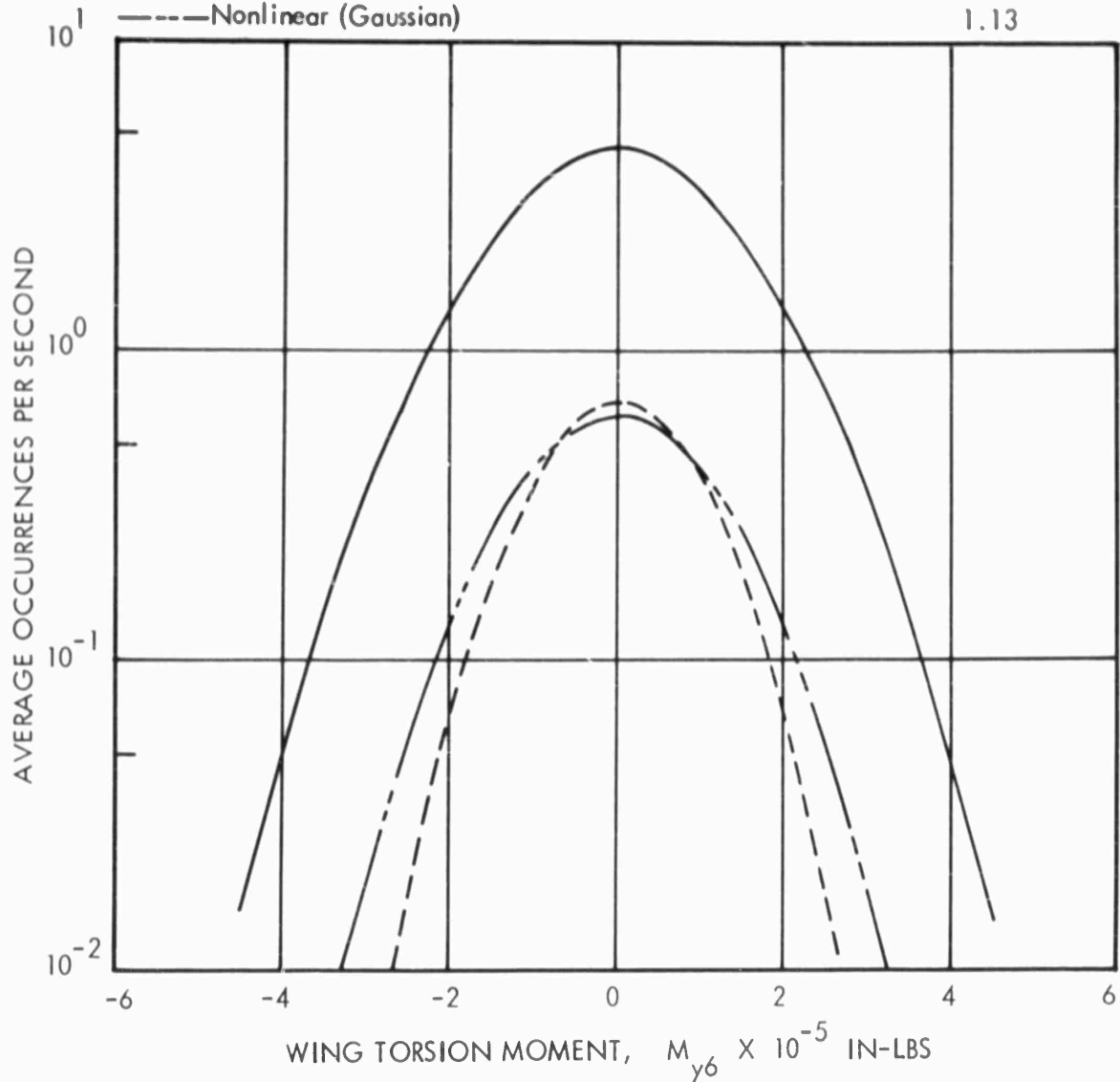


FIGURE 121 : Comparison of Load Occurrences for the Nonlinear and Linearized Systems for  $M_{y6}$ , Wing Torsion Inboard of Outboard Nacelle

Multi Gear Analysis  
 Tire Pressure = 60 psi

$D = 185 \text{ Lb-Sec/In}$   
 $C_D = 14.1 \text{ Lb-Sec}^2/\text{In}^2$   
 $V_H = 88 \text{ fps}$

ANALYSIS METHODS:

— Nonlinear (Gaussian Fit to Direct Sampling)  
 - - - Linear (Gaussian)  
 - · - · Nonlinear (Gaussian)

$\sigma \times 10^{-5} \text{ In-Lbs}$   
 1.42  
 .964  
 1.41

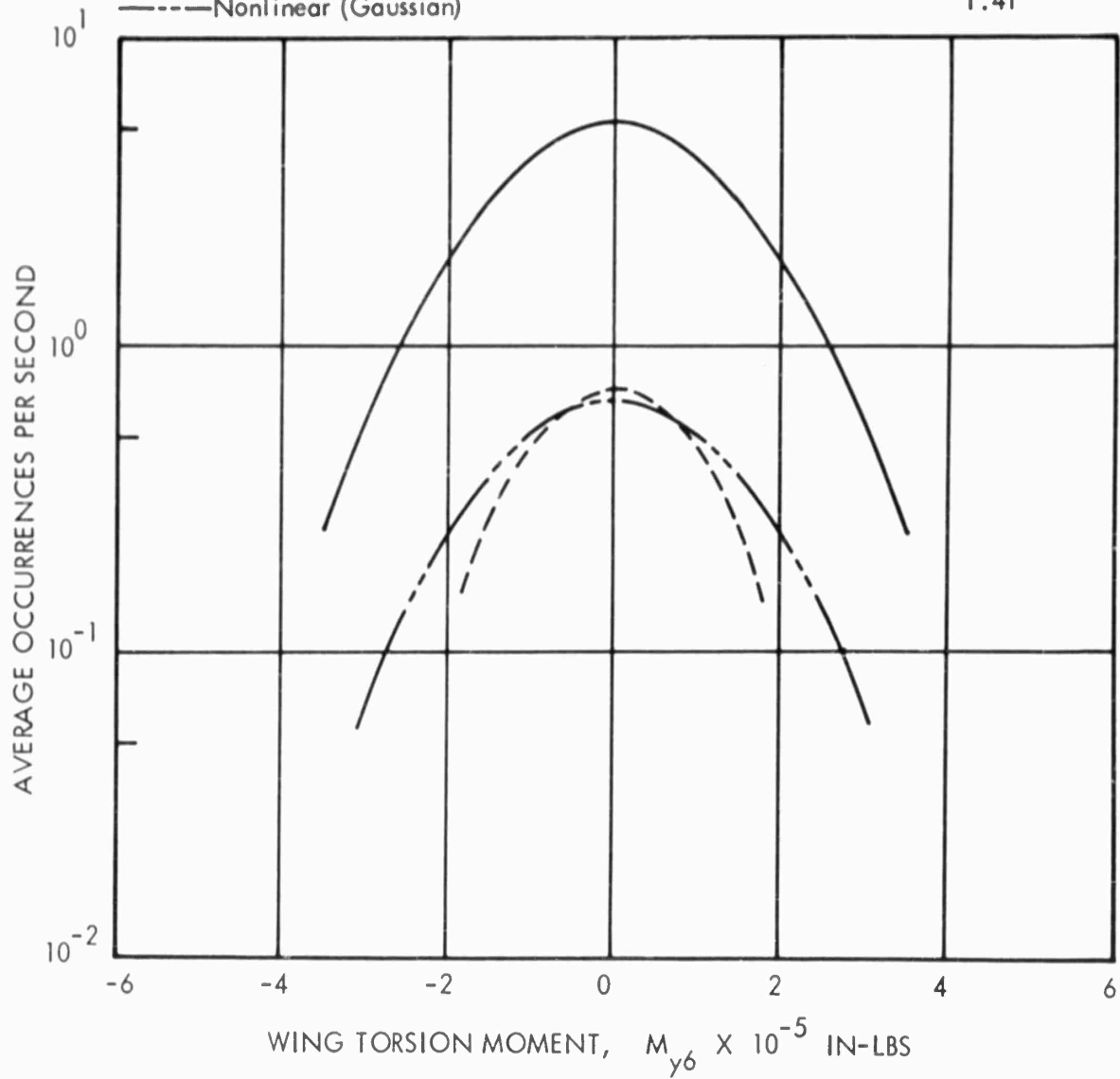


FIGURE 122 : Comparison of Load Occurrences for the Nonlinear and Linearized Systems for  $M_{y6}$ , Wing Torsion Inboard of Outboard Nacelle

Multi Gear Analysis  
 Tire Pressure = 90 psi

$D = 185 \text{ Lb-Sec/In}$   
 $C_D = 14.1 \text{ Lb-Sec}^2/\text{In}^2$   
 $V_H = 88 \text{ fps}$

ANALYSIS METHODS:

- Nonlinear (Gaussian Fit to Direct Sampling)
- - - - Linear (Gaussian)
- · - · Nonlinear (Gaussian)

$\sigma \times 10^{-5} \text{ In-Lbs}$   
 1.74  
 1.28  
 1.74

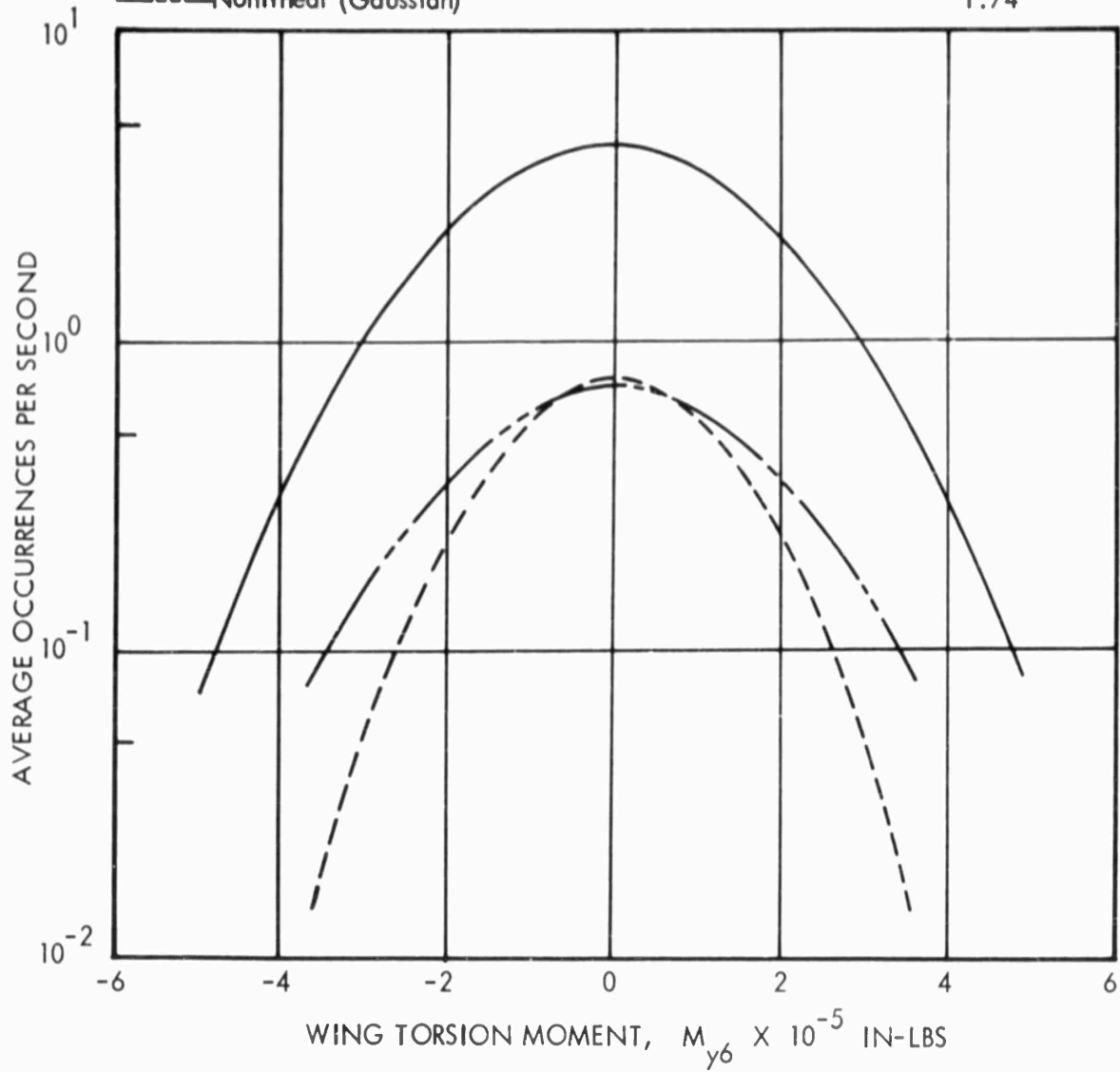


FIGURE 123 : Comparison of Load Occurrences for the Nonlinear and Linearized Systems for  $M_{y6}$ , Wing Torsion Inboard of Outboard Nacelle

Multi Gear Analysis  
 Tire Pressure = 120 psi

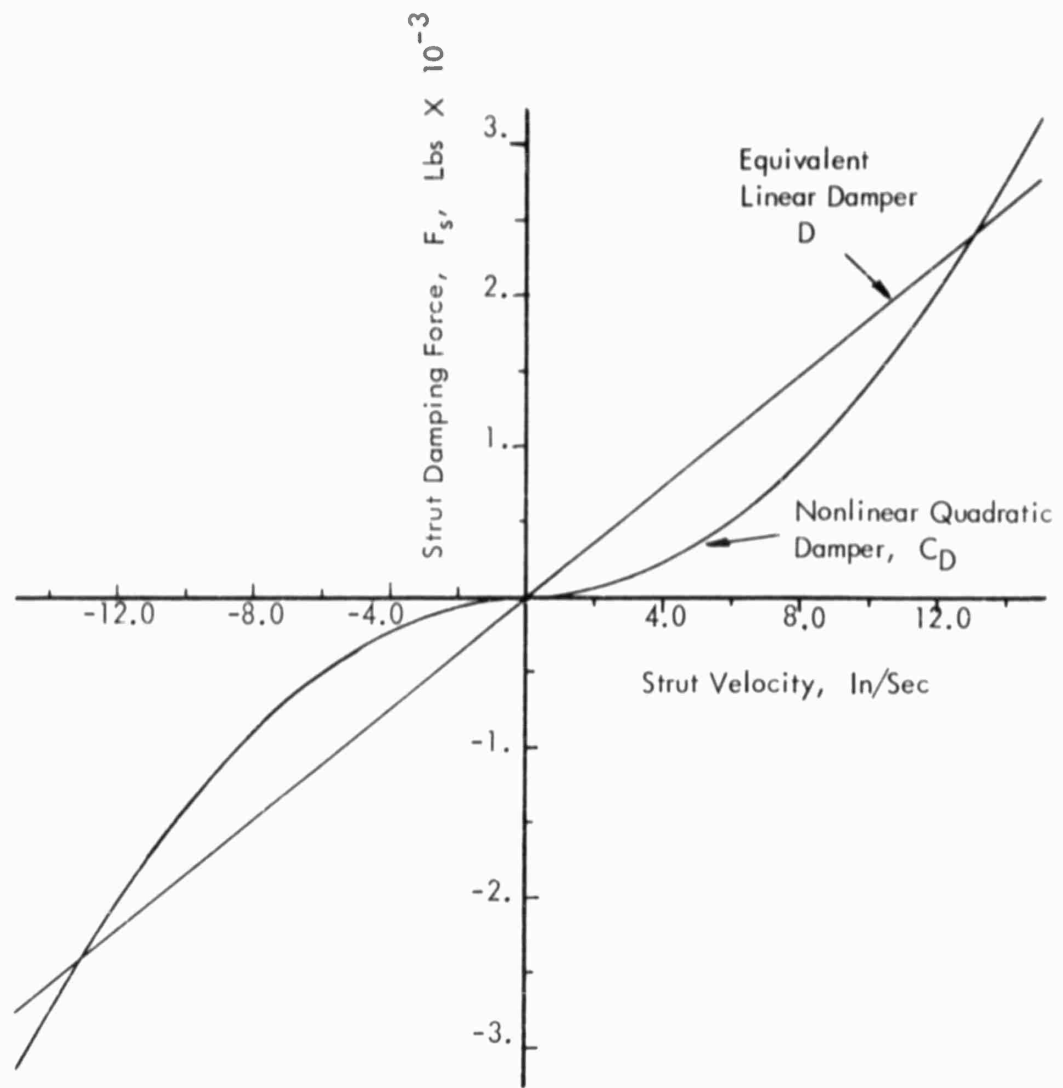


FIGURE 124 : Comparison of the Equivalent Linear and Nonlinear Damping Force Curves for the Standard Configuration

$$D = 185 \text{ Lb-Sec/In}$$

$$C_D = 14.1 \text{ Lb-Sec}^2/\text{In}^2$$

## REFERENCED REPORTS

1. Air Force Contract No. AF 33(616)-7546: Dynamic Loads Induced By Ground Operation of Aircraft, 14 July 1960.
2. Davenport, W. B., and Root, W. L.: An Introduction to the Theory of Random Signals and Noise, McGraw-Hill Book Company, Inc., New York, New York, 1958.
3. Stoker, J. J.: Nonlinear Vibrations, Interscience Publishers, New York, 1950.
4. McLachlan, N. W.: Ordinary Nonlinear Differential Equations, Oxford at the Clarendon Press, 1950.
5. Minorski, N.: Introduction to Nonlinear Mechanics, J. W. Edwards, Ann Arbor, 1947.
6. Milwitzky, B.; Cook, F. E.: Effects of Interaction on Landing Gear Behavior and Dynamic Loads in a Flexible Airplane Structure, NACA TN 3467, 1955.
7. Theisen, J. G.; Edge, Phillip M., Jr.: An Evaluation of an Accelerometer Method for Obtaining Landing-Gear Drag Loads, NACA TN 3247, Langley Aeronautical Laboratory, October, 1954.
8. Horne, W. B.: Static Force-Deflection Characteristics of Six Aircraft Tires Under Combined Loading, NACA TN 2926, May, 1953.
9. Timoshenko, S.: Vibration Problems in Engineering, 2nd Edition, D. Van Nostrand, Co., N. Y., 1937.
10. Cowden, F. E.; Croxton, D. J.: Applied General Statistics, Prentice-Hall, Inc., N. Y., 1946.
11. Milwitzky, B.: Study of Taxiing Problems Associated with Runway Roughness, NASA Memo 2-21-59L, March 1959.
12. Tsien, Hsue Shen: Engineering Cybernetics, McGraw Hill, New York, 1954.
13. Terman, Frederick E.: Radio Engineers' Handbook, McGraw Hill Co., 1943.
14. Korn & Korn: Electronic Analog Computers, 2nd Edition, McGraw Hill, 1956.
15. Milne Thomson, L. M.: Jacobian Elliptic Function Tables, Dover Publishing, 1950.
16. Anon, Proceedings, Fatigue of Aircraft Structures, WADC Symposium, WADC TR 59-507, August 11-13, 1959.

17. Scanlan, R. H.; Rosenbaum, R.: Introduction to the Study of Aircraft Vibration and Flutter, The Macmillan Company, 1951.
18. Grimes, C. K.: Development of a Method and Instrumentation for Evaluation of Runway Roughness Effects on Military Aircraft. AGARD Report 119, May 1957, North Atlantic Treaty Organization.
19. Milwitzky, B.; Cook, F. E.: Analysis of Landing Gear Behavior, NACA Rep. 1154, 1953 (Supersedes NACA TN 2755).
20. Houbolt, J. C.; Walls, J. H.; Smiley, R. F.: On Spectral Analysis of Runway Roughness and Loads Developed During Taxiing, NACA TN 3484, Washington, July 1955.
21. Walls, J. H.; Houbolt, J. C.; Press, H.: Some Measurements and Power Spectra of Runway Roughness, NACA TN 3305, Washington, November 1954.
22. Anonymous, Detail Requirements for Structural Fatigue Certification Programs, WADC TMWCLS-TM-58-4, 27 June 1958.
23. Press, H.; Tukey, J.: Power Spectral Methods of Analysis and Application in Airplane Dynamics, NATO AGARD Flight Test Manual, Vol. IV, Part IVC, June 1956.
24. Coleman, T. L.; Press, H.; Meadows, M. T.: An Evaluation of Effects of Flexibility on Wing Strains in Rough Air for a Large Swept Wing Airplane, NACA TN 4291, July 1958.
25. Thompson, W. E.: Measurements and Power Spectra of Runway Roughness at Airports in Countries of the North Atlantic Treaty Organization, NASA TN 4303, Washington, July 1958.
26. Rubin, M. R.; Smith, J. A.: Methods of Structural Dynamic Analysis with Applications to the B-36J and B-47E Aircraft; Part I - Determination of Wing Natural Modes, WADC TN 55-174, September 1955.
27. Potter, D. M.: Measurements of Runway Roughness of Four Commercial Airports, NACA RM L56126, Washington, 7 January 1957.
28. Morris, Garland, J.; Stickle, Joseph W.: Response of a Light Airplane to Roughness of Unpaved Runways, NASA TN D510, September 1960.
29. McPherson, Albert E.; Evens, J., Jr.; and Levy, Samuel: Influence of Wing Flexibility on Force-Time Relation in Shock Strut Following Vertical Landing Impact, NACA TN 1995, 1949.

30. Pian, T. H. H.; and Flomenhaft, H. I.: Analytical and Experimental Studies on Dynamic Loads in Airplane Structures During Landing, Journal of the Aeronautical Sciences, Volume 17, No. 12, December 1950, pp. 765-774, 786.
31. Stowel, Elbridge Z.; Houbolt, John C.; and Baidorf, S. B.: An Evaluation of Some Approximate Methods of Computing Landing Stresses in Aircraft, NACA TN 1584, 1948.
32. Walls, James H.: An Experimental Study of Orifice Coefficients, Internal Strut Pressures, and Loads on a Small Oleo-Pneumatic Shock Strut, NACA TN 3426, 1955.
33. Yorgiadas, Alexander J.: Graphical Analysis of Performance of Hydraulic Shock Absorbers in Aircraft Landing Gears, Journal of the Aeronautical Sciences, Volume 12, No. 4, October 1945, pp. 421-428.
34. Flugge, W.; and Coale, C. W.: The Influence of Wheel Spin-up on Landing Gear Impact, NACA TN 3217, Stanford University, 1954.
35. Flugge, W.: Landing Gear Impact, NACA TN 2743, Stanford University, 1952.
36. Lindquist, Dean C.: A Statistical Study of Wing Lift at Ground Contact for Four Transport Airplanes, NACA TN 3435, April 1955.
37. Painleve, P.: Acta Mathematica, Volume 25, No. 53, 1902, Original Not Seen, Secondary Source: Kamke, E.: Differentialgleichungen. Third Edition, Chelsea Publishing Company, New York, 1948, P. 548.

APPENDIX A  
SUPPLEMENTARY EQUATIONS

This appendix contains equations which will be helpful  
in interpreting the differential equations in the text.

The equations for the net modal deflection for coupled bending and torsion loads are as follows:

$$\xi_{ni} = W_{ni} - \epsilon_i \phi_{ni}$$

$$\xi_{nq} = W_{nq} - \epsilon_q \phi_{nq}$$

The generalized mass of the nth mode is written as:

$$M_n = \int_0^{b/2} m(y) \xi^2(y) dy$$

where:

$b/2$  is the semi-span of the wing and  $m(y)$  is the spanwise mass distribution.

The equation for the generalized modal area of the kth mode coupling with the nth mode for aerodynamic damping is given by:

$$A_{kn} = \frac{1}{2} \sum_{q=0}^u (C_{(q+1)} + C_q) \xi_{kq} \xi_{nq} (y_{(q+1)} - y_q)$$

where: (Neglect twist in  $\xi$  for  $A_{kn}$ )

$C_q$  is the chord-length at the qth wing panel.

$y_q$  is the wing station of the qth wing panel.

$u$  is the total number of wing panels used.

The Wagner idicial delay in lift build-up may be expressed as follows:

$$(1 - \Phi(t)) = 1 - d_1 e^{-bt} - h e^{-mt}$$

(Values used may be found in Reference 17)

The inertia wing loads at station q are computed as follows:  
(neglects steady and nonsteady aerodynamic loads).

Bending Moments:

$$M_{xq} = \left[ B_{c0q} \ddot{\Theta} + \sum_{n=0}^m B_{cnq} \ddot{\alpha}_n \right] \frac{l}{g}$$

Torsion Moments:

$$M_{yq} = \left[ T_{c0q} \ddot{\Theta} + \sum_{n=0}^m T_{cnq} \ddot{\alpha}_n \right] \frac{l}{g}$$

Shears:

$$S_{zq} = \left[ S_{c0q} \ddot{\Theta} + \sum_{n=0}^m S_{cnq} \ddot{\alpha}_n \right] \frac{l}{g}$$

The load coefficients are defined on the following pages.

## SHEAR COEFFICIENTS

For Pitch:

$$S_{c0q} = - \sum_{k=q}^u g m_k(y) \epsilon_{ko}(y)$$

For Each Mode:

$$S_{c0} = \sum_{k=q}^u g m_k \mathfrak{F}_{0k} \quad (\mathfrak{F}_0 = 1)$$

$$S_{c1} = \sum_{k=q}^u g m_k \mathfrak{F}_{1k}$$

$$S_{c2} = \sum_{k=q}^u g m_k \mathfrak{F}_{2k}$$

$$S_{c3} = \sum_{k=q}^u g m_k \mathfrak{F}_{3k}$$

General Form:  $S_{cnq} = \sum_{k=q}^u g m_k \mathfrak{F}_{nk} \quad n = 0, 1, 2, 3$

where  $\mathfrak{F}_{nq} = W_{nq} - \epsilon_q \phi_{nq}$

and  $m_q$  is the mass of the  $q^{\text{th}}$  panel

## BENDING MOMENT COEFFICIENTS

General Equation:

$$B_{cnq} = \sum_{k=q}^u gm_k (y_k - y_q) \mathfrak{F}_{nk} \quad n = 0, 1, 2, 3$$

Each Mode:

$$B_{coq} = \sum_{k=q}^u gm_k (y_k - y_q) \mathfrak{F}_{ok} \quad (\mathfrak{F}_o = 1)$$

$$B_{c1q} = \sum_{k=q}^u gm_k (y_k - y_q) \mathfrak{F}_{1k}$$

$$B_{c2q} = \sum_{k=q}^u gm_k (y_k - y_q) \mathfrak{F}_{2k}$$

$$B_{c3q} = \sum_{k=q}^u gm_k (y_k - y_q) \mathfrak{F}_{3k}$$

For Pitch:

$$B_{ceq} = - \sum_{k=q}^u gm_k \epsilon_{ko} (y_k - y_q)$$

## TORSION MOMENT CONTRIBUTED BY STATIC UNBALANCE

General Form:

$$T_{c \epsilon n q} = \sum_{k=q}^u g m_k \epsilon_k w_{n k} \quad n = 0, 1, 2, 3$$

Each Mode:

$$T_{c \epsilon 0 q} = \sum_{k=q}^u g m_k \epsilon_k w_{0 k} \quad (w_{0 k} \equiv 1)$$

$$T_{c \epsilon 1 q} = \sum_{k=q}^u g m_k \epsilon_k w_{1 k}$$

$$T_{c \epsilon 2 q} = \sum_{k=q}^u g m_k \epsilon_k w_{2 k}$$

$$T_{c \epsilon 3 q} = \sum_{k=q}^u g m_k \epsilon_k w_{3 k}$$

$$T_{c \epsilon 0 q} = - \sum_{k=q}^u g m_k \epsilon_x \epsilon_k$$

## TORSION MOMENT CONTRIBUTED BY INERTIA

General Form For Modes:

$$T_{cInq} = \sum_{k=q}^u gI_k \phi_{nk} \quad n = 1, 2, 3$$

Each Mode:

$$T_{cI0q} = 0 \quad \text{For } \ddot{a}_0$$

$$T_{cI1q} = \sum_{k=q}^u gI_k \phi_{1k}$$

$$T_{cI2q} = \sum_{k=q}^u gI_k \phi_{2k}$$

$$T_{cI3q} = \sum_{k=q}^u gI_k \phi_{3k}$$

Total torsion moment from unbalance and inertia:

$$T_{cnq} = -T_{cInq} + T_{ce nq}$$

Torsion moment coefficient for aircraft pitching inertia:

$$T_{ce q} = \sum_{k=q}^u gI_k$$

## APPENDIX B

### AIRPLANE CONFIGURATION DATA

This appendix contains configuration data for the airplane used as an example at maximum take-off gross weight. Spanwise mass and inertia data, free-free coupled bending and torsion mode shapes, landing gear deflections in the modes, and strut damping coefficients versus orifice diameters are presented.

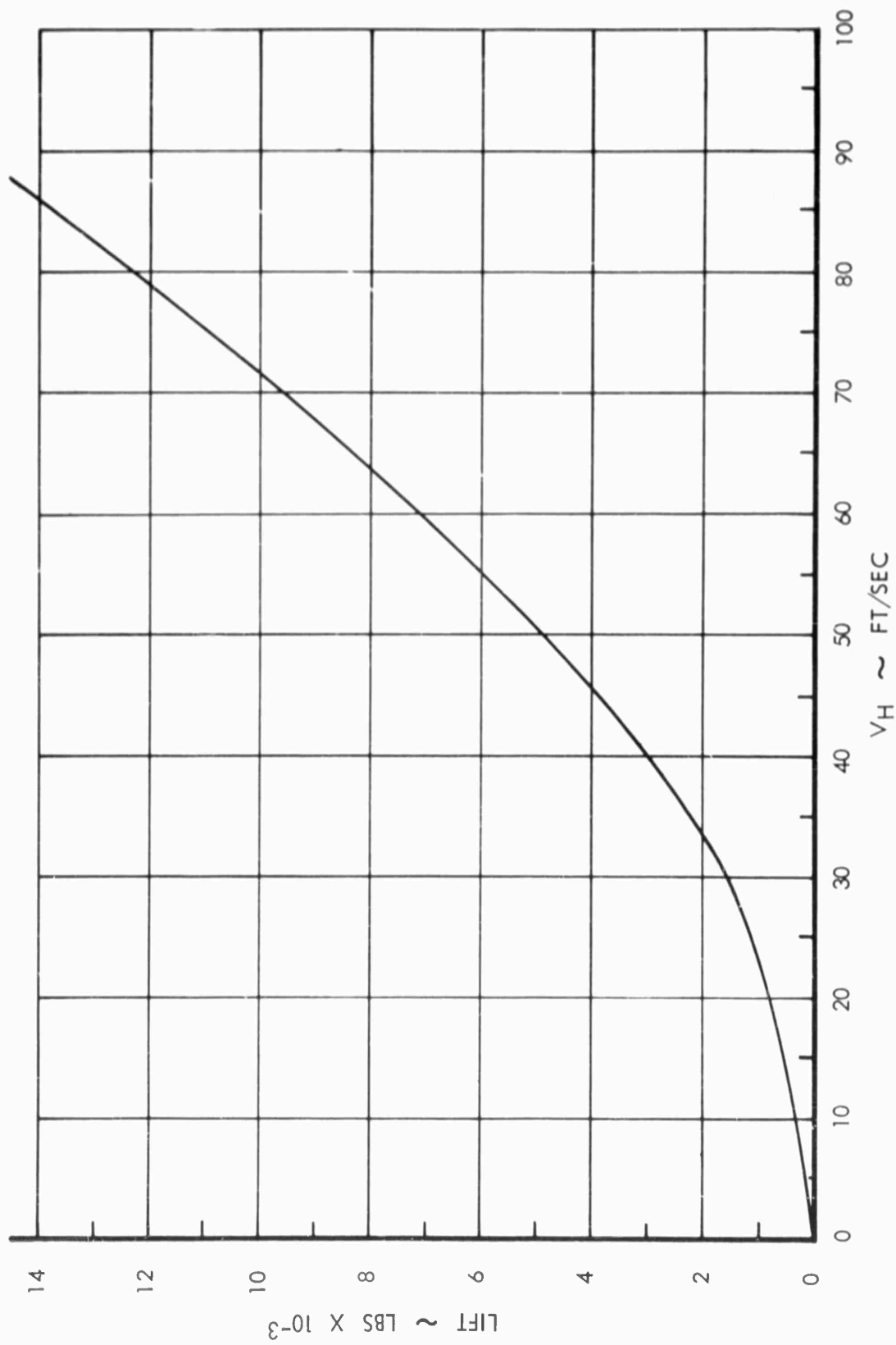


FIGURE 125 : Assumed Lift Variation for One-Half Airplane

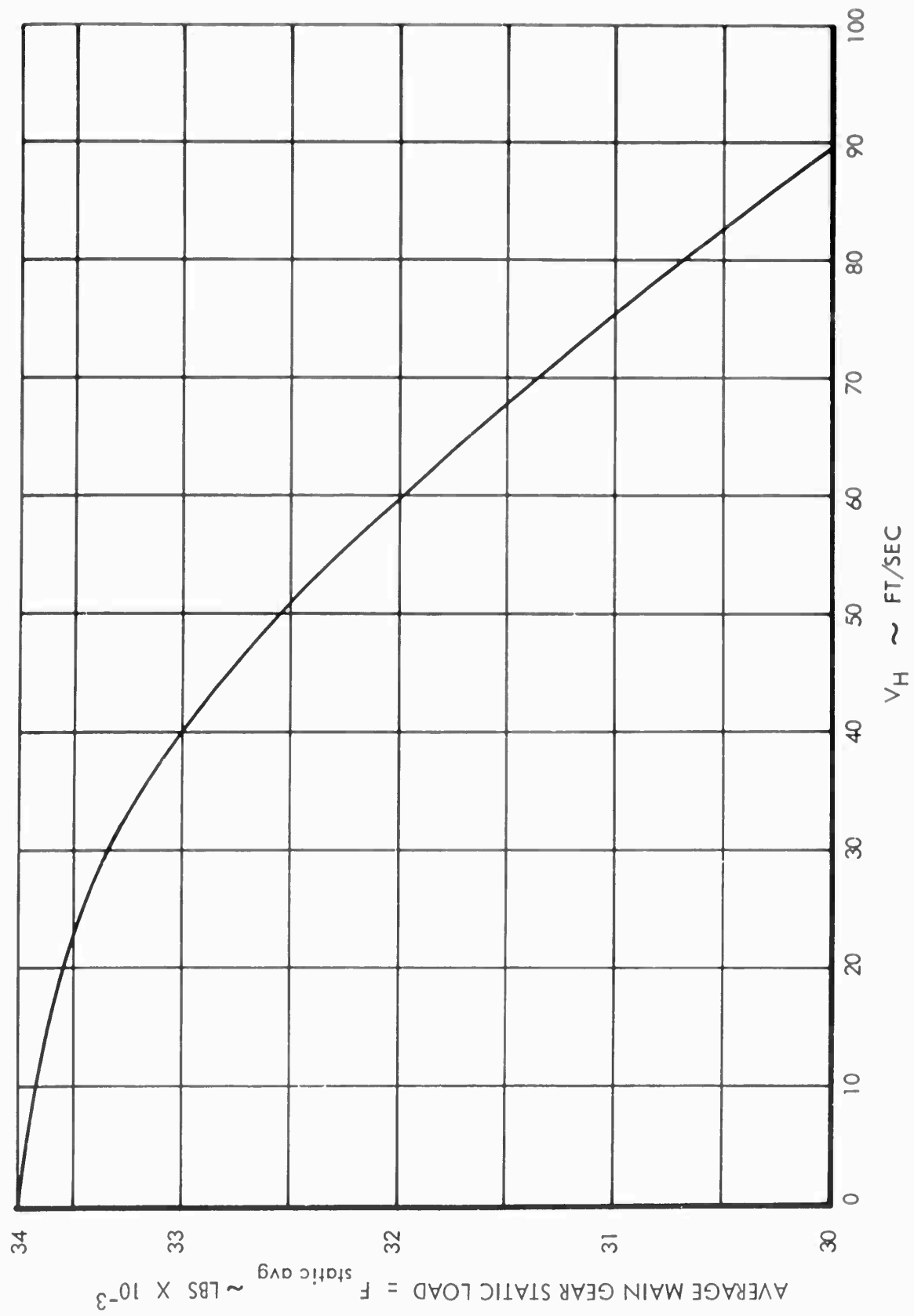


FIGURE 126 : Average Main Gear Static Load Versus Taxi Speed,  $V_H$

TABLE 1

(Airplane Mass and Inertia Data Versus Wing Stations at Maximum Take-Off Weight)

	(Wing Station) (inches)	(Empty Panel Weight) (lbs)	(Fuel Weight) (lbs)	(- $\epsilon_q$ ) (inches)	(Net Station Mass) (lb-sec <sup>2</sup> /in.)	(S $\alpha_q$ Net) (lb-sec <sup>2</sup> )	* (I $\alpha_q$ Net) (lb-sec <sup>2</sup> -in.)
0	60.00	24603.50	0.	-34.55663	63.73964	-2202.6269	4640804.250
1	87.50	937.50	2750.00	2.13220	9.55311	20.3691	8834.062
2	142.50	878.00	3514.00	2.13911	11.37824	24.3393	9057.344
3	196.00	1732.00	0.	-102.61406	13.26425	-1361.0984	183489.480
4	247.50	710.50	3575.00	1.89107	11.10233	20.9952	9207.568
5	298.00	600.50	2975.00	1.72833	9.26295	16.0094	7876.098
6	349.50	559.00	2055.00	1.33339	6.77202	9.0297	5576.382
7	400.00	1467.00	0.	-103.30952	12.26684	-1267.2813	165320.506
8	450.00	520.00	1645.00	1.23279	5.60881	6.9144	4354.577
9	500.00	390.50	1790.00	1.63090	5.64896	9.2129	3836.593
10	550.00	301.50	1540.00	0.98588	4.77073	4.7033	3096.879
11	600.00	278.00	1190.00	1.44986	3.80311	5.5139	2374.999
12	650.00	238.00	1140.00	0.80450	3.56995	2.8720	2031.498
13	700.00	202.00	890.00	1.58736	2.82902	4.4906	1659.075
14	750.00	173.00	686.00	1.16670	2.22539	2.5963	1248.707
15	785.50	43.00	0.	-0.50000	0.11140	-0.0556	49.769

\*  $I_q = I \alpha_q - m_q \epsilon_q^2$

TABLE 2

(Free Free Mode Shapes)

	$W_q$ Mode 1	$\Phi_q^*$ Mode 1	$W_q$ Mode 2	$\Phi_q^*$ Mode 2	$W_q$ Mode 3	$\Phi_q^*$ Mode 3
0	.1396	$.6639 \times 10^{-4}$	.1716	$-.4508 \times 10^{-3}$	.07055	$.1679 \times 10^{-3}$
1	.1383	.6640	.1676	$.1426 \times 10^{-3}$	.06680	-.1504
2	.1275	.6617	.1370	$.1389 \times 10^{-2}$	.03750	-.8208
3	.1061	.6565	.08248	.2701	-.01655	$-.1522 \times 10^{-2}$
4	.07495	.7570	.01353	.3859	-.08792	-.1952
5	.03264	.8724	-.06356	.5191	-.1703	-.2427
6	-.02244	$.1024 \times 10^{-3}$	-.1383	.6931	-.2543	-.3020
7	-.09022	.1223	-.1928	.9163	-.3273	-.3749
8	-.1706	.1191	-.2076	.9482	-.3754	-.4080
9	-.2646	.1149	-.1715	.9838	-.3779	-.4445
10	-.3722	.1102	-.07700	.01019	-.3108	-.4791
11	-.4921	.1047	.07706	.01055	-.1588	-.5117
12	-.6220	$.9844 \times 10^{-4}$	.2843	.01093	.07865	-.5443
13	-.7588	.9078	.5313	.01131	.3862	-.5730
14	-.8993	.8586	.8023	.01158	.7392	-.5927
15	-1.000	.8604	1.000	.01159	1.000	-.5943

$$f_1 = 1.2709 \text{ cps}$$

$$f_2 = 3.3641 \text{ cps}$$

$$f_3 = 4.9063 \text{ cps}$$

(Effective Modal Masses)

$$M_0 = 171.0 \text{ Lb-Sec}^2/\text{In} - \text{Exclusive of Landing Gear Weights}$$

$$M_1 = 8.9899 \text{ Lb-Sec}^2/\text{In}$$

$$M_2 = 29.2044 \text{ Lb-Sec}^2/\text{In}$$

$$M_3 = 6.7052 \text{ Lb-Sec}^2/\text{In}$$

\*Note:  $\Phi_q$  units are radians per unit tip deflection.

TABLE 3

(Main and Nose Landing Gear Orifice Diameter Versus Orifice Coefficient)

$$\text{Damping Coefficient} = C_D = \frac{\rho A_h^3}{2(C_d A_o)^2}$$

(Main Gear $C_D$ ) $\left(\frac{\text{Lb-Sec}^2}{\text{In}^2}\right)$	( Orifice Diameter ) (In)	(Nose Gear $C_D$ ) $\left(\frac{\text{Lb-Sec}^2}{\text{In}^2}\right)$	( Orifice Diameter ) (In)
14.1	.50	7.43	.159
7.05	.594	1.20	.25
21.15	.45	11.11	.143

(Standard Damping Coefficient: )

$$\text{Main Gear} = 14.1 \text{ Lb-Sec}^2/\text{In}^2$$

$$\text{Nose Gear} = 7.43 \text{ Lb-Sec}^2/\text{In}^2$$

TABLE 4

(Gear Force and Center of Gravity  
Deflection in Modes)

	Nose (i = 1)	Front Main (i = 2)	Rear Main (i = 3)
$\xi_{1i}$	0.1137	0.1375	0.1415
$\xi_{2i}$	0.3480	0.1868	0.1595
$\xi_{3i}$	0.0050	0.06495	0.0751

For Center of Gravity Translation:

$$\xi_{1c} = 0.1379$$

$$\xi_{2c} = 0.1908$$

$$\xi_{3c} = 0.06605$$

The strut air compression force,  $F_{ai}$ , versus stroke,  $s_i$ , variation is given by the following formula:

$$F_{ai} = \frac{A_i}{(b_i - s_i)^{\gamma_i}} + K_i$$

Where  $\gamma_i$  is the polytropic air compression exponent which is usually unity for the analysis.

Specific constants may be summarized as follows:

Nase Gear

$$\gamma_1 = 1$$

$$A = 14,150, (\text{lb-in.}, \text{ for } \gamma_1 = 1)$$

$$b_1 = 11.3, \text{ in.}$$

$$K_1 = - 333, \text{ lb}$$

Main Gear

$$\gamma_i = 1$$

$$A = 64,400, (\text{lb-in.}, \text{ for } \gamma_i = 1)$$

$$b_i = 11.3, \text{ in.}$$

$$K_i = - 333, \text{ lb}$$

APPENDIX C

EQUIVALENT LINEAR SYSTEM SOLUTION

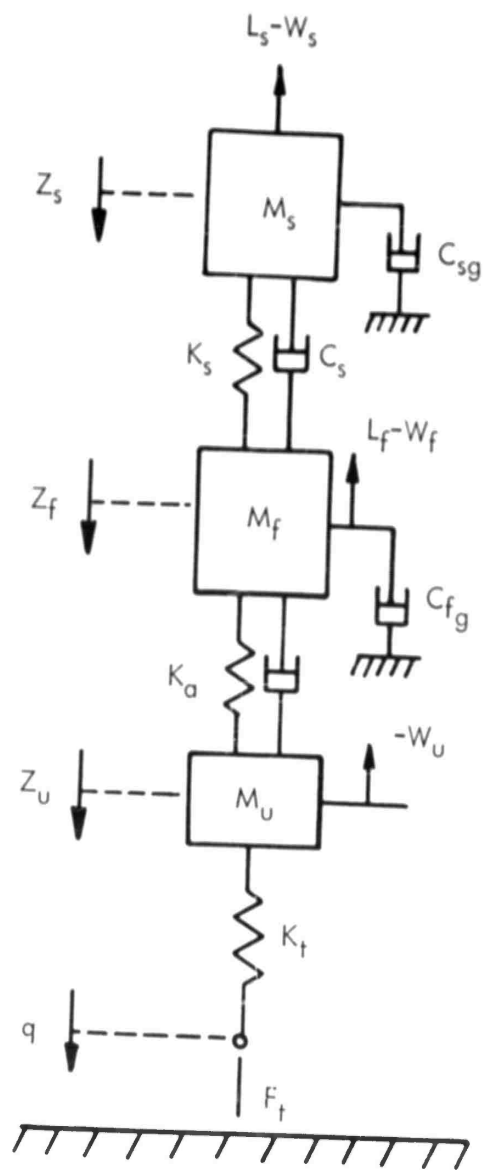


FIGURE 127 : Equivalent Three Mass System with Modal Damping

Summation of forces on each of the three masses separately, as shown in Figure 127, will result in the following equations of motion: (with  $d$  used as a differential operator)

$$\left[ M_s d^2 + (C_s + C_{sg})d + K_s \right] Z_s - (C_s d + K_s) Z_f = W_s - L_s \quad (1C)$$

$$-(C_s d + K_s) Z_s + \left[ M_f d^2 + (C_s + D + C_{fg})d + K_s + K_a \right] Z_f - (Dd + K_a) Z_u = W_f - L_f \quad (2C)$$

$$-(Dd + K_f) Z_f + \left[ M_u d^2 + Dd + K_a + K_t \right] Z_u - (K_t)q = W_u \quad (3C)$$

$$-(K_t) Z_u + (K_t)q = -F_t \quad (4C)$$

or, in matrix form:

$$\begin{bmatrix} M_s d^2 + (C_s + C_{sg}) + K_s & - (C_s d + K_s) & 0 & 0 \\ - (C_s d + K_s) & M_f d^2 + (C_s + D + C_{fg})d + K_s + K_a & - (Dd + K_a) & 0 \\ 0 & - (Dd + K_f) & M_u d^2 + Dd + K_a + K_t & - K_t \\ 0 & 0 & - K_t & K_t \end{bmatrix} \begin{bmatrix} Z_s \\ Z_f \\ Z_u \\ q \end{bmatrix} = \begin{bmatrix} W_s - L_s \\ W_f - L_f \\ W_u \\ -F_t \end{bmatrix} \quad (5C)$$

Assuming the following relationships:

$$G_{11} = M_s d^2 + (C_s + C_{sg})d + K_s \quad (6C)$$

$$G_{12} = - (C_s d + K_s) \quad (7C)$$

$$G_{22} = M_f d^2 + (C_s + D + C_{fg})d + K_s + K_a \quad (8C)$$

$$G_{23} = - (Dd + K_a) \quad (9C)$$

$$G_{33} = M_u d^2 + Dd + K_a + K_t \quad (10C)$$

$$G_{34} = - K_t \quad (11C)$$

$$G_{44} = K_t \quad (12C)$$

Omitting the constant forces  $L_s$ ,  $W_s$ ,  $L_f$ , and  $W_f$ , since this is a linear system, the matrix equations may be rewritten as follows: (The constant forces may be added in later by using the principle of superposition).

$$\begin{bmatrix} G_{11} & G_{12} & 0 & 0 \\ G_{12} & G_{22} & G_{23} & 0 \\ 0 & G_{23} & G_{33} & G_{34} \\ 0 & 0 & G_{34} & G_{44} \end{bmatrix} \begin{bmatrix} Z_s \\ Z_f \\ Z_u \\ q \end{bmatrix} = \begin{bmatrix} 0 \\ 0 \\ 0 \\ -F_t \end{bmatrix} \quad (13C)$$

Dividing all equations by  $q$  and solving for  $F_t/q$  yields:

$$\frac{F_t}{q} = - G_{44} + \frac{G_{34}^2 (G_{12}^2 - G_{11}G_{22})}{G_{33} (G_{12}^2 - G_{11}G_{22}) + G_{23}^2 G_{11}} \quad (14C)$$

Substituting  $j\omega$  for  $d$  in the transfer function gives the complex value of  $F_t/q$  for a constant input amplitude  $q$  at angular frequency  $\omega$ .

Numerical evaluation of the amplitude and phase angle of the transfer function involves the calculation of the coefficients  $G_{ip}$  for given constants of the physical system and substitution into equation 14C.

To compare the analytical results with results obtained from the analog computer runs, the amplitude of  $F_t/q$  must be modified to compensate for the finite filter bandwidth used on the computer. The method of determining the correction factor for  $F_t/q$

is derived by assuming the filters were ideal or "square" over the filter frequency range, and may be stated as follows:

$$\text{average } F_t/q = (F_t/q)_{\text{avg}} = \frac{1}{\omega_2 - \omega_1} \int_{\omega_1}^{\omega_2} \left| \frac{F_t}{q} \right| d\omega$$

where  $\omega_1$  and  $\omega_2$  correspond to filter edge points, centered on a peak of  $F_t$ .

To determine the compensated values of  $F_t/q$  about a frequency response peak, the following factor is applied:

$$\text{correction factor} = \left( \frac{F_t}{q} \right)_{\text{avg}} \cdot \frac{1}{(F_t/q)_{\text{peak}}}$$

Additional transfer functions are derived for the equivalent system and listed below. The evaluation of these are carried out in the same manner as  $F_t/q$ .

$$\frac{\xi}{q} = \frac{(F_t/q + G_{44}) (G_{33} + G_{23})}{-G_{34}} + G_{34} \quad (15C)$$

$$\frac{\ddot{Z}_u}{q} = -d^2 \left( \frac{F_t/q + G_{44}}{G_{34}} \right) \quad (16C)$$

$$\frac{\ddot{Z}_f}{q} = \frac{G_{33}d^2 (F_t/q + G_{44})}{G_{23}G_{34}} - \frac{d^2G_{34}}{G_{23}} \quad (17C)$$

$$\frac{\ddot{Z}_s}{q} = -d^2 \frac{G_{12}}{G_{11}} \left[ \frac{G_{33} (F_t/q + G_{44})}{G_{23}G_{34}} - \frac{G_{34}}{G_{23}} \right] \quad (18C)$$

$$\frac{\ddot{a}_o}{q} = \frac{B \frac{\ddot{Z}_f}{q} + \xi_1 \frac{\ddot{Z}_s}{q}}{B - \xi_1} \quad (19C)$$

$$\frac{\ddot{a}_1}{q} = \frac{\frac{\ddot{Z}_f}{q} - \frac{\ddot{Z}_s}{q}}{\xi - B} \quad (20C)$$

Thus, as shown in Appendix A, the wing loads can be determined from the following equations:

$$\frac{M_{xq}}{q} = B_{coq} \frac{\ddot{a}_o}{qg} + B_{clq} \frac{\ddot{a}_1}{qg} \quad (21C)$$

$$\frac{M_{yq}}{q} = T_{coq} \frac{\ddot{a}_o}{qg} + T_{clq} \frac{\ddot{a}_1}{qg} \quad (22C)$$

$$\frac{S_{zq}}{q} = S_{coq} \frac{\ddot{a}_o}{qg} + S_{clq} \frac{\ddot{a}_1}{qg} \quad (23C)$$

The contribution of the higher flexible modes to these loads can be determined as discussed relative to Equation 52 in the text.

A sample evaluation of the analytical solution, Equation 14C, is presented for comparison. The original physical values for the single gear linear system are: (these values are given per half airplane unless otherwise stated)

$$\begin{aligned} M_o &= 166 \quad \frac{\# \text{sec}^2}{\text{in}} \\ M_1 &= 8.99 \quad \frac{\# \text{sec}^2}{\text{in}} \\ M_u &= 1.68 \quad \frac{\# \text{sec}^2}{\text{in}} \quad (\text{per gear}) \\ D &= 185.0 \quad \frac{\# \text{sec}}{\text{in}} \quad (\text{per gear}) \\ c_o &= 40.9 \quad \frac{\# \text{sec}}{\text{in}}, \quad \text{at } V_H = 66 \text{ ft/sec} \\ c_1 &= 2.87 \quad \frac{\# \text{sec}}{\text{in}}; \quad \frac{c}{c_{cr}} = 2.5\% \text{ for 1st mode.} \\ \omega_1 &= 7.98 \quad \frac{\text{rad}}{\text{Sec}} \\ \xi_1 &= .1397 \end{aligned}$$

$$K_a = 14,170 \quad \text{lb/in. (per strut)}$$

$$K_t = 8,330 \quad \text{lb/in. (per tire at a pressure of 90 psi)}$$

The corresponding transformed linear system values (at  $V_H = 66$  ft/sec) are:

$$M_s = 43.97 \quad \text{lb-sec}^2/\text{in.}$$

$$M_f = 122.02 \quad \text{lb-sec}^2/\text{in.}$$

$$M_u = 1.68 \quad \text{lb-sec}^2/\text{in. (per gear)}$$

$$D = 185.0 \quad \text{lb-sec/in. (per gear)}$$

$$C_s = 2.27 \quad \text{lb-sec/in.}$$

$$C_{sg} = 10.87 \quad \text{lb-sec/in.}$$

$$C_{fg} = 30.2 \quad \text{lb-sec/in.}$$

$$K_s = 2055.0 \quad \text{lb/in.}$$

$$K_a = 14,170 \quad \text{lb/in. (per strut)}$$

$$K_t = 8330.0 \quad \text{lb/in. (per tire)}$$

$$\xi_1 = 0.1397$$

$$B = -.3877$$

$$\frac{M_s}{M_f} = 0.3604$$

The values of  $M_u$ ,  $D$ ,  $K_a$ , and  $K_t$  are doubled for the test case, since there are two gears driving one-half the airplane.

The results from a test case are presented in Table 5 as a single tire force frequency response function, and the values agree very favorably with results from the more detailed analog computer solutions shown in the text.

TABLE 5

(Amplitude and Phase Angle of Analytical Transfer Function for Tire Force)

(Frequency) cps	$\left( \frac{F_1}{q} \right)$ lb/ft	(Angle, Degrees)
0.5	1.292 X 10 <sup>4</sup>	354
0.6	2.151 X 10 <sup>4</sup>	354
0.7	3.653 X 10 <sup>4</sup>	352
0.8	6.986 X 10 <sup>4</sup>	349
0.86	1.097 X 10 <sup>5</sup>	344
0.90	2.160 X 10 <sup>5</sup>	329
0.94	*4.077 X 10 <sup>5</sup>	276
0.97	2.807 X 10 <sup>5</sup>	225
1.0	1.665 X 10 <sup>5</sup>	207
1.26	7.188 X 10 <sup>3</sup>	260
1.30	1.264 X 10 <sup>4</sup>	323
1.50	1.073 X 10 <sup>4</sup>	344
1.60	2.647 X 10 <sup>5</sup>	333
1.65	4.698 X 10 <sup>5</sup>	314
1.68	6.455 X 10 <sup>5</sup>	289
1.70	*7.033 X 10 <sup>5</sup>	267
1.73	6.175 X 10 <sup>5</sup>	238
1.75	5.249 X 10 <sup>5</sup>	225
1.80	3.617 X 10 <sup>5</sup>	208
1.90	2.277 X 10 <sup>5</sup>	196
2.25	1.233 X 10 <sup>5</sup>	188
3.0	8.641 X 10 <sup>4</sup>	187
4.0	7.517 X 10 <sup>4</sup>	188
5.0	7.139 X 10 <sup>4</sup>	190
6.0	6.994 X 10 <sup>4</sup>	192

\* Note: Peaks are uncompensated for filter effects.

APPENDIX D

COMPUTER APPLICATIONS IN DYNAMICS AND STATISTICS

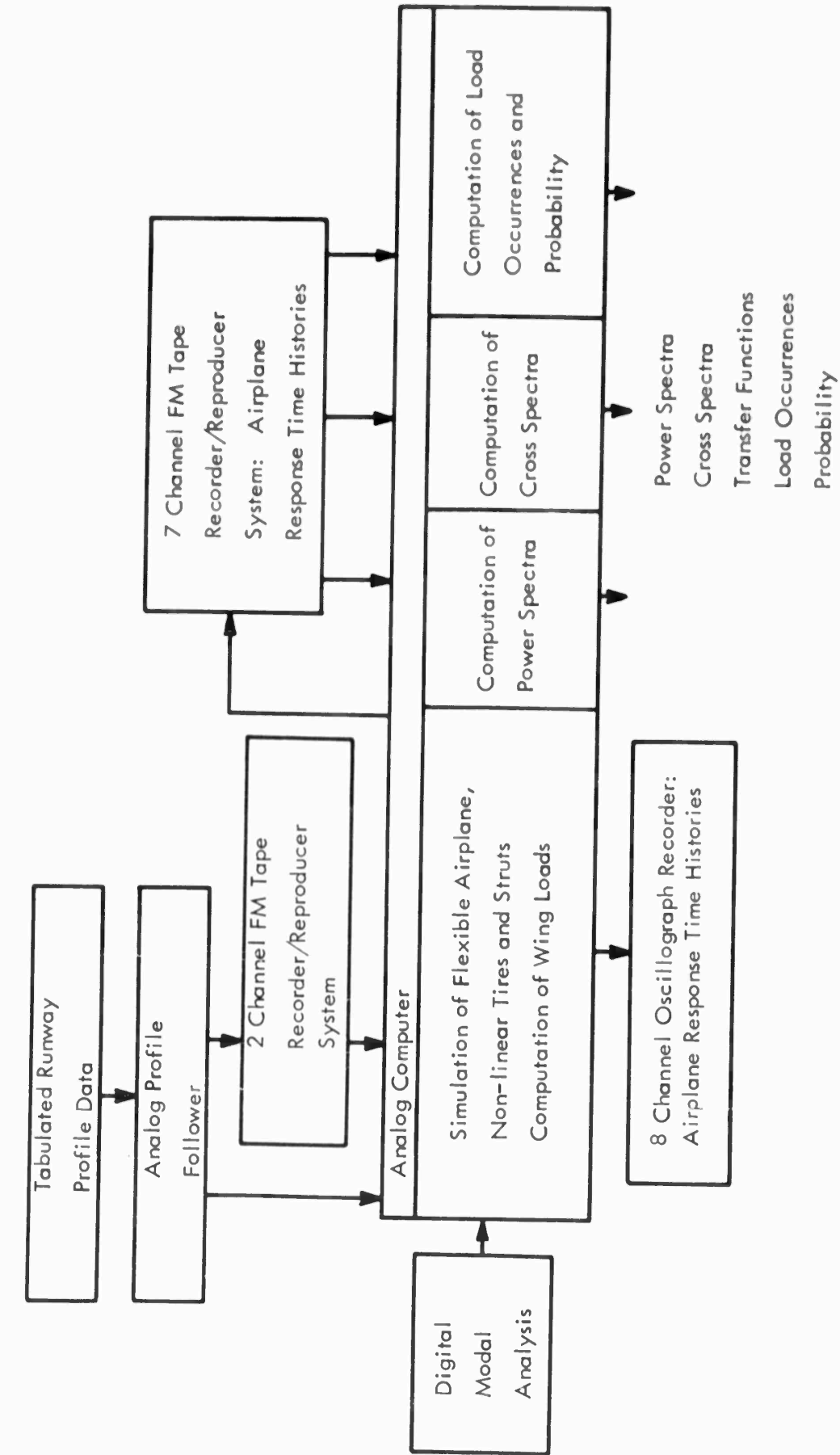


FIGURE 128 : Dynamic Response Analysis Flow Chart

## COMPUTER APPLICATIONS IN DYNAMICS AND STATISTICS

### 1. Introduction

Analog and digital computer techniques used for this investigation are presented in more detail in this appendix. A flow diagram showing the various applications of the analog and digital computers is shown in Figure 128.

Several computer solutions have been obtained for comparison of analog and digital results over sample runway segments. The digital program is inherently more accurate, and it is designed to include more details since it is used for more general problem solutions. The digital results include four flexible modes of vibration and present three components of loads at fifteen wing stations. However, the digital approach selected did not prove to be feasible since computational time became prohibitively expensive for the very long time-histories required for the direct dynamic analysis. Therefore, the analog computer was selected for the major task of aircraft simulation. The digital computer was used, however, in calculating the wing natural modes of vibration and for some PSD analysis.

The overall requirements of the problem from the view point of analog computation are as follows:

- a. To solve the equations which simulate a multi-gear, flexible aircraft performing taxi operations.
- b. To provide an input to this simulated aircraft which represents quite accurately the profile of a specified 5000-foot runway being traversed at several speeds.
- c. To preserve the spacing of the landing gears relative to the runway amplitude variations, and relative to each other.
- d. To record the time histories of specified airplane response functions.
- e. To measure the power spectra of these functions, as well as other statistical quantities.
- f. To obtain cross-spectra and transfer functions between specified pairs of the functions.

Following these operations, useful observations on parametric variations in the strut configuration are made; and subsequent to that, the equivalent linear system is developed to represent the nonlinear system, which constitutes the landing gear, and linearized solutions are obtained.

The simulation of the flexible vehicle on the computer is basically a standard procedure as applied in previous studies. However, the remaining items present problems in the reproduction, storage, and processing of much larger amounts of data than are

usually encountered in analog operations.

Figure 129 gives further details of the analog computer program network which simulates the example airplane, as discussed in the text. Figure 130 presents a typical time-delay network, of which seven were required as part of the runway input to the computer simulation, ensuring the proper sequencing of the landing gears as they pass over the runway.

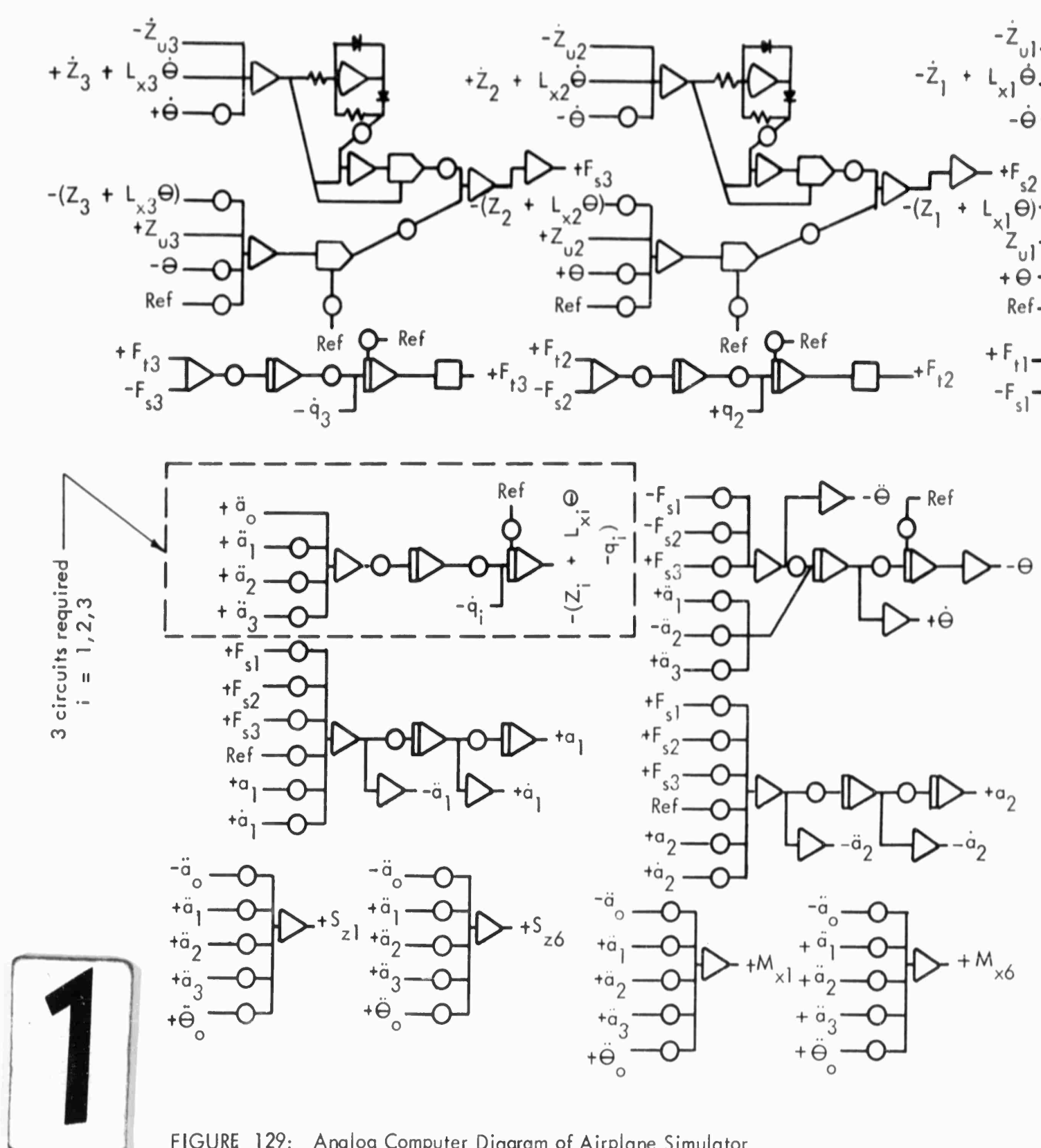
The intention of the flow diagrams and network figures is to provide a concept of the magnitude of the problem, the basic approaches, and the number and interrelation of components. Therefore, specific details are not necessarily intelligible from the figures. This appendix is intended to aid those technically versed in analog computation to comprehend the nature and scope of the problem set-up from a rather brief presentation.

The most significant of the analog computer problems are discussed in succeeding sections.

## 2. Generation of the Runway Profile for the Analog

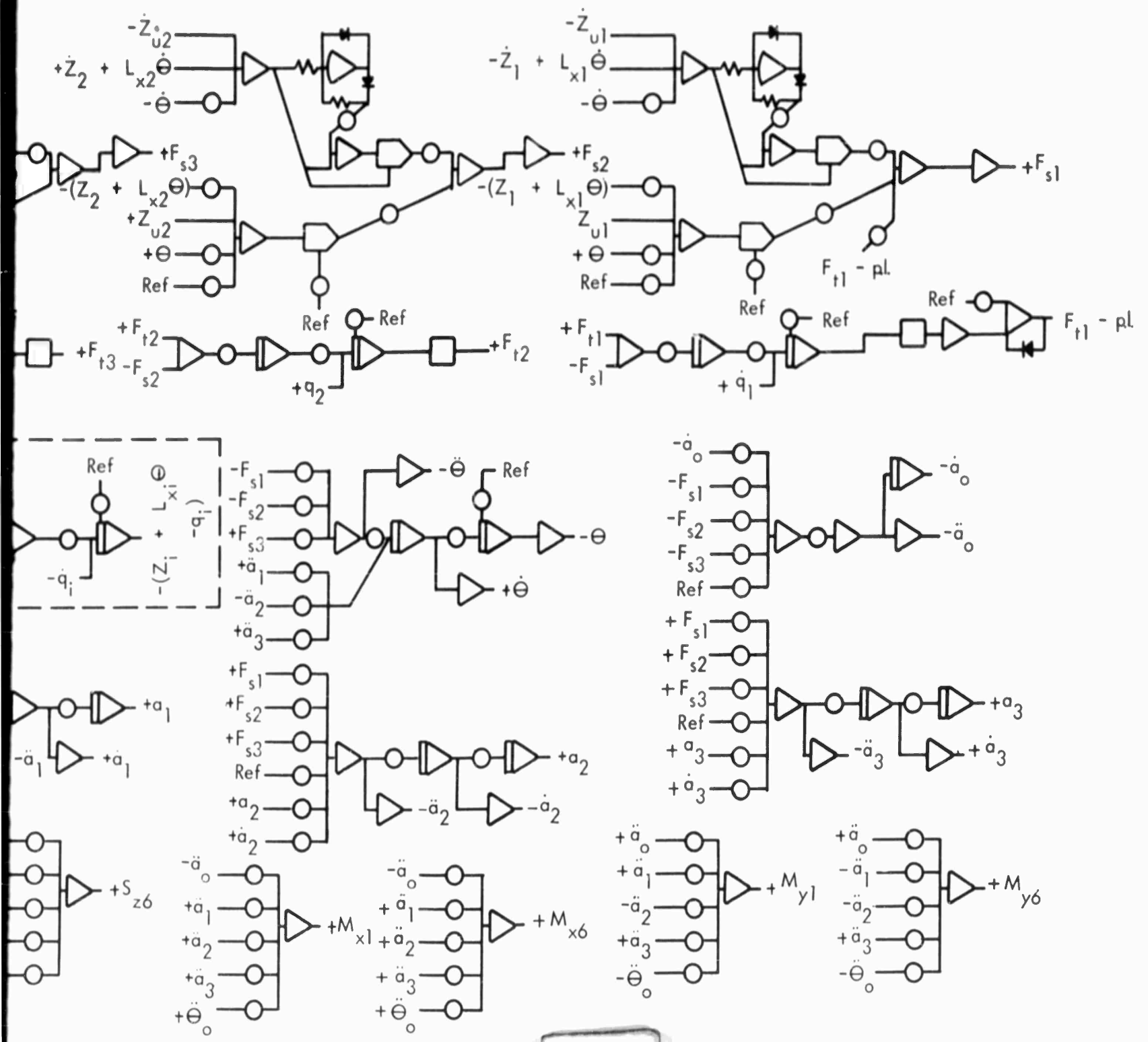
The principal problem concerning the generation of the runway amplitudes is the requirement for equal resolution of both the low amplitude, short wave length content of the runway as well as the large amplitude, long wave length content. Since the range of the amplitude of the variations in the runway is from the order of .001 ft. to 14 ft., (from short wavelength to long wavelength respectively) and a nominal precision of one percent is desired, the resolution of the short wavelength content must be to the order of .00001 ft.; this is 1/1,400,000 referred to the large amplitude variations. No ordinary analog equipment is available which is capable of such resolution; in fact, a graph of such a precision which could be followed by typical electromechanical following devices available today, accurate to  $\pm .05$  inches, would require a full scale travel of 280,000 inches. The length of the graph would be of a similar order. It is conceivable that an electromechanical follower could be passed over a curve of indefinite length, but the width or full scale required is a prohibitive value.

A diagram of the analog simulation of the taxiing aircraft makes it apparent that some advantages would result by using the slopes, or spatial derivatives, of the runway rather than the amplitudes for analog computational purposes. An inspection of the slopes of the runway (assumed to be the mean values between points on the elevation data obtained from direct measurement of the runway) reveals that the range of the slope function is only  $.075 \pm 0.05$  with a precision of  $\pm .00125$  or  $\pm 2.5$  percent of the full scale value. This is well within the accuracy of existing analog equipment - including magnetic tape record-reproduce systems.



**1**

FIGURE 129: Analog Computer Diagram of Airplane Simulator



Computer Diagram of Airplane Simulator



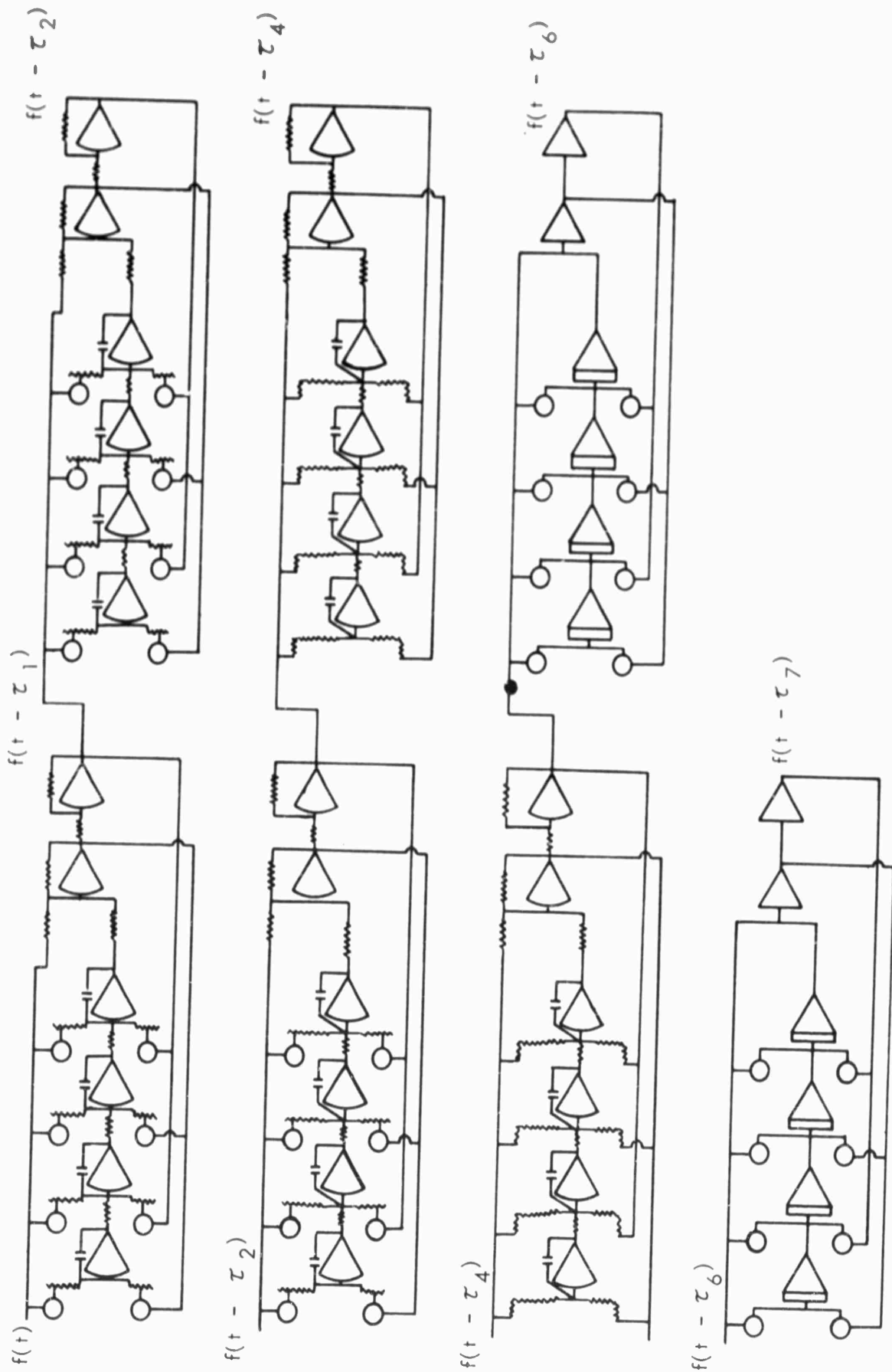


FIGURE 130: Analog Computer Diagram for Seven Fourth-Order Padé Circuits

The final procedure requires a recording of the slope function on frequency modulated magnetic tape. Playback of the tape yields a repeatable, accurate regeneration of the runway slope profile for reproduction as needed.

In more detail, the procedure is to plot the runway slope profile in one hundred 50-foot segments, each representing a full scale travel of an electromechanical plotter-follower. Each segment is recorded on magnetic tape from the follower, and subsequently the 100 segments of the tape are spliced together to form a single tape. Playback through the demodulators reproduces the runway slope profile with the same order of precision as the original measurements for the runway. One important exception is the long wavelength variations, which in this case are the same order of magnitude as the zero-drift in the tape record/reproduce system.

To obtain the same order of precision for both long and short wavelengths of the LaGuardia runway used in this study, a curve was set up for the follower which contained the general shape of the runway over the full 5000 feet, including principally the large amplitude-long wavelength variations. This curve was followed simultaneously with the magnetic tape playback, thus providing a source of good accuracy short wavelength and a separate source of equal accuracy long wavelength information. The accuracy of each of these channels deteriorated with wavelength as it approached the regime of the other. This was compensated for by utilizing a crossover network to combine these data as will be shown. Finally the runway profile amplitudes were reproduced by integrating the recorded slope functions as played back through the complementary filters and into the computer.

A block diagram of the system is shown in Figure 131. The output of the tape reproducer is the accurate, high frequency content of the runway slope plus low frequency error (drift). The output of the curve follower is the accurate low frequency content of the runway amplitude plus high frequency error (low level noise). Let these two outputs be defined as

$$sq(s) + E_L(s) = \text{output of tape}$$

$$q(s) + E_h(s) = \text{output of follower}$$

where  $q(s)$  is the true runway amplitude.

Now if filter  $F_1(s)$  has the operational characteristic

$$\frac{s}{s + \tau_1} \quad \text{operating on } (sq(s) + E_L)$$

and filter  $F_2$  has the characteristic  $\frac{s \tau_1}{s + \tau_1}$  operating on  $(q(s) + E_h)$ ,

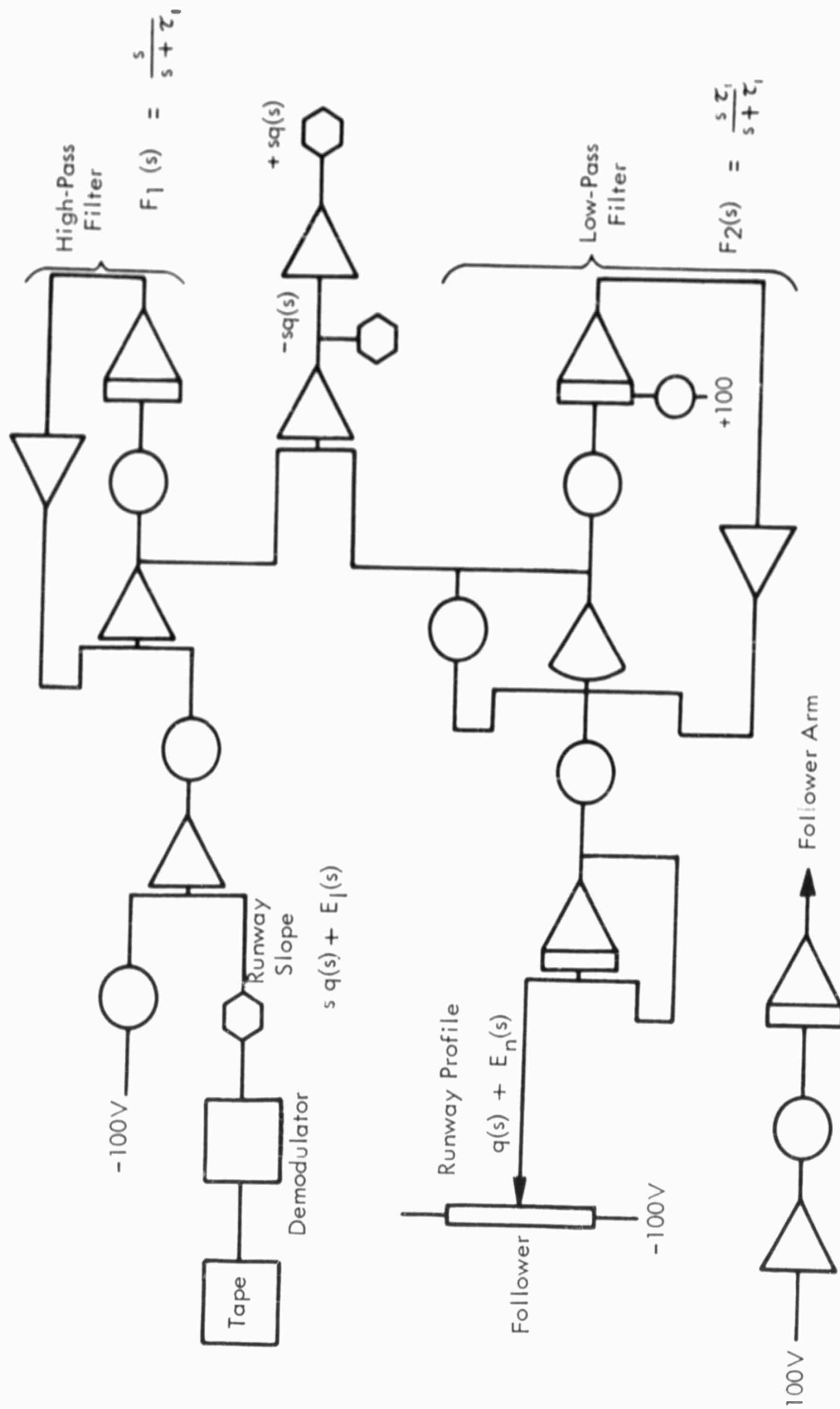


FIGURE 131 : Computer Diagram for Regeneration of the Runway Slope Profile

then the summed outputs of the two filters,  $e_o$  is

$$\begin{aligned}
 e_o &= \frac{s}{s + \tau_1} sq(s) + \frac{s}{s + \tau_1} E_L(s) + \frac{s\tau_1}{s + \tau_1} q(s) + \frac{s\tau_1}{s + \tau_1} E_h(s) \\
 &= \left( \frac{s}{s + \tau_1} + \frac{\tau_1}{s + \tau_1} \right) sq(s) + \frac{s}{s + \tau_1} E_L(s) + \frac{s\tau_1}{s + \tau_1} E_h(s) \\
 &= sq(s) + \frac{s}{s + \tau_1} E_L(s) + \frac{\tau_1}{s + \tau_1} sE_h(s)
 \end{aligned}$$

which is the desired runway slope profile  $sq(s)$  with the error terms attenuated. The low frequency error  $E_L(s)$  is attenuated to zero as  $s \rightarrow 0$  and the high frequency error in the slope profile  $sE_h(s)$  approaches zero as  $s \rightarrow \infty$ .

The choice of  $\tau_1$  was made by trial and error, integrating the regenerated slope function and observing the difference between it and the original runway amplitude both as to long period and short period errors. The value of  $\tau_1$  settled upon as giving the best overall fit corresponded to a wavelength of 66 ft. on the runway, with the speed of regeneration set at 11 ft/sec.

Figures 132, 133, and 134 show time histories of a typical segment of the regenerated runway slope and amplitude, the low-frequency derivative component obtained from the follower output, and a plot of the entire runway as obtained by integrating the output of the summation of the complementary filters.

The complex procedure described above resulted from the specified requirement that all the long wavelengths be considered; such technical complications involved a large amount of additional developmental work. The final results indicate that no significant response occurs below 0.8 cps in the vehicle, so these long wavelengths are not essential.

### 3. Analog Simulation of Vehicle Response

The simulation of the vehicle is performed by conventional analog procedures. The individual landing gear forces are introduced to the vehicle which is free to respond in rigid body translation and pitch and three flexible modes as described by Equations 1-13. The gear forces are derived from the motions of the aircraft over the runway profile.

The runway slope profile is introduced directly to the nose gear then passed through 7 fourth-order Pade' networks, each of which delays the profile signal by

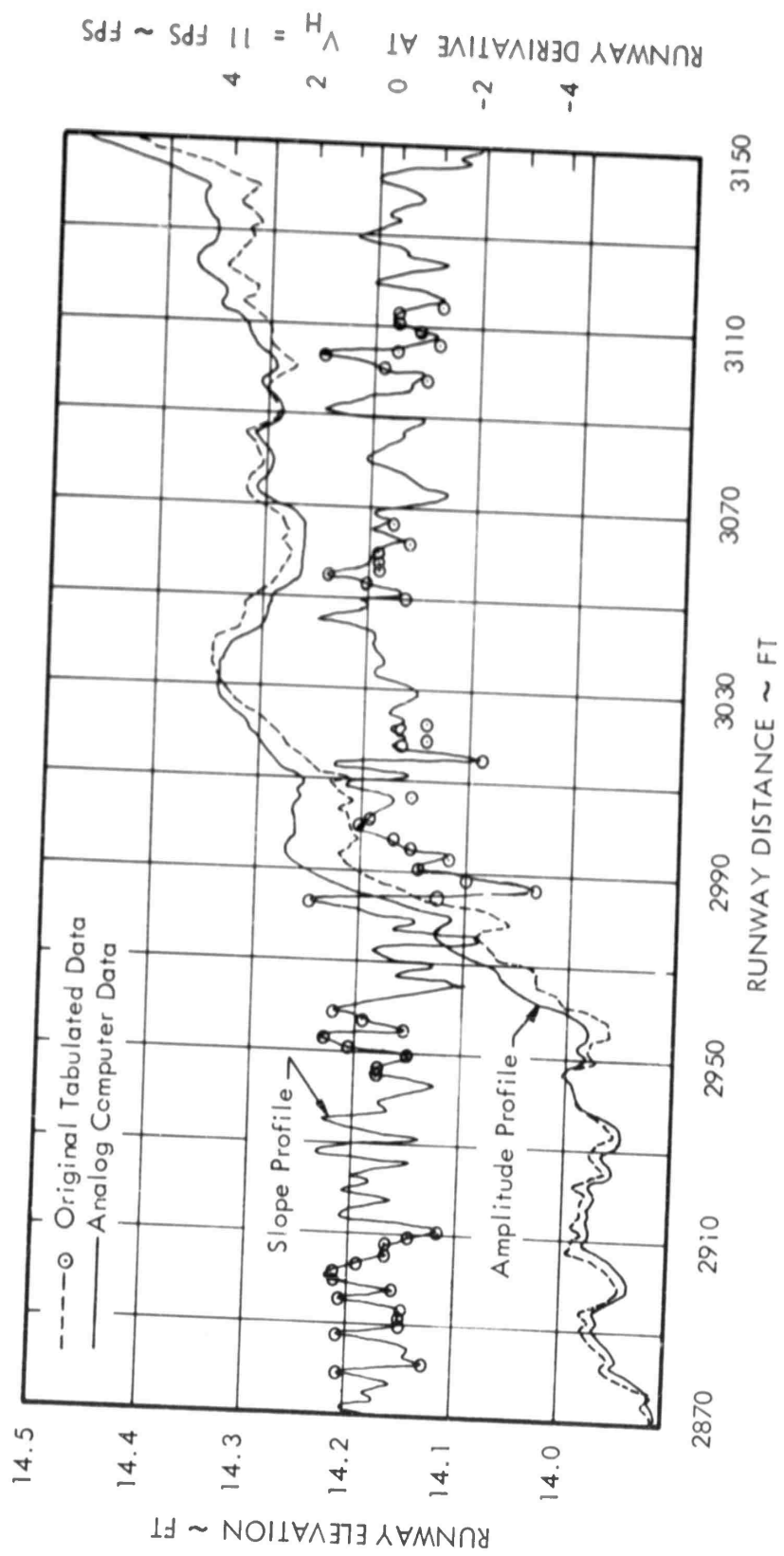


FIGURE 132: Runway Amplitude and Slope Profiles from 2870 to 3150 Ft

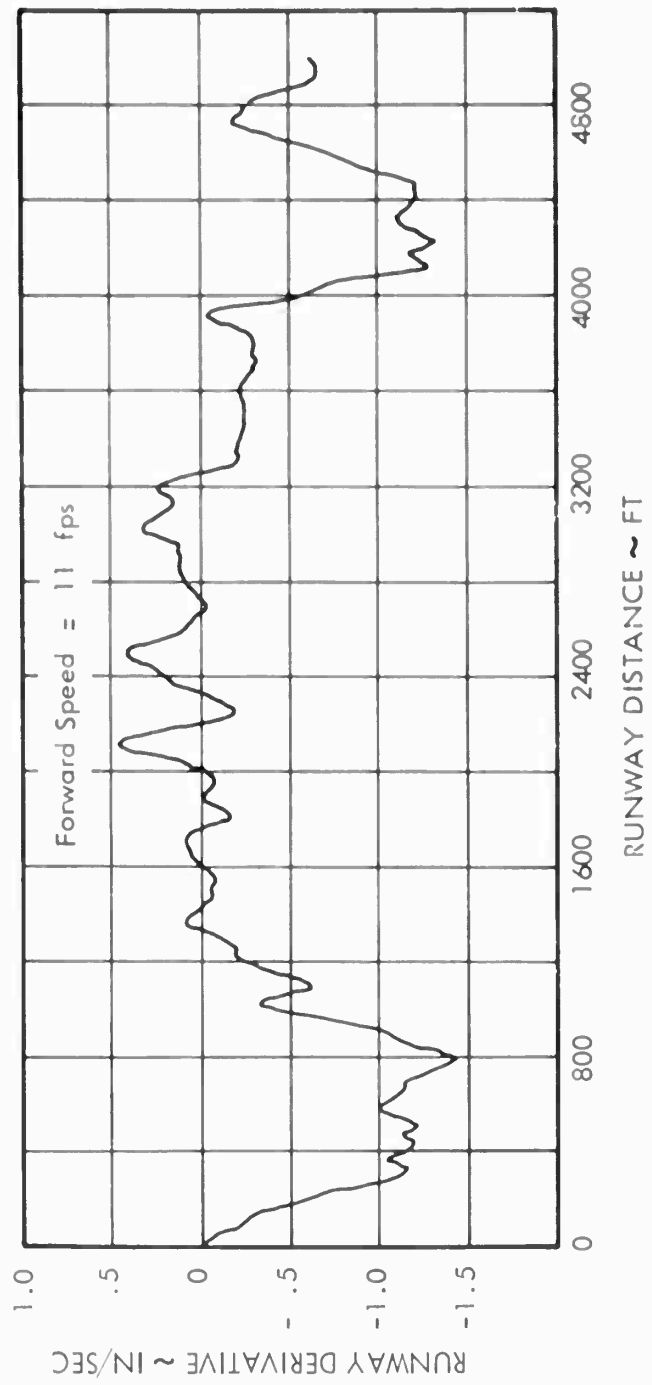


FIGURE 133: Runway Derivative - Low Frequency Content Obtained from Follower and Filter Combination

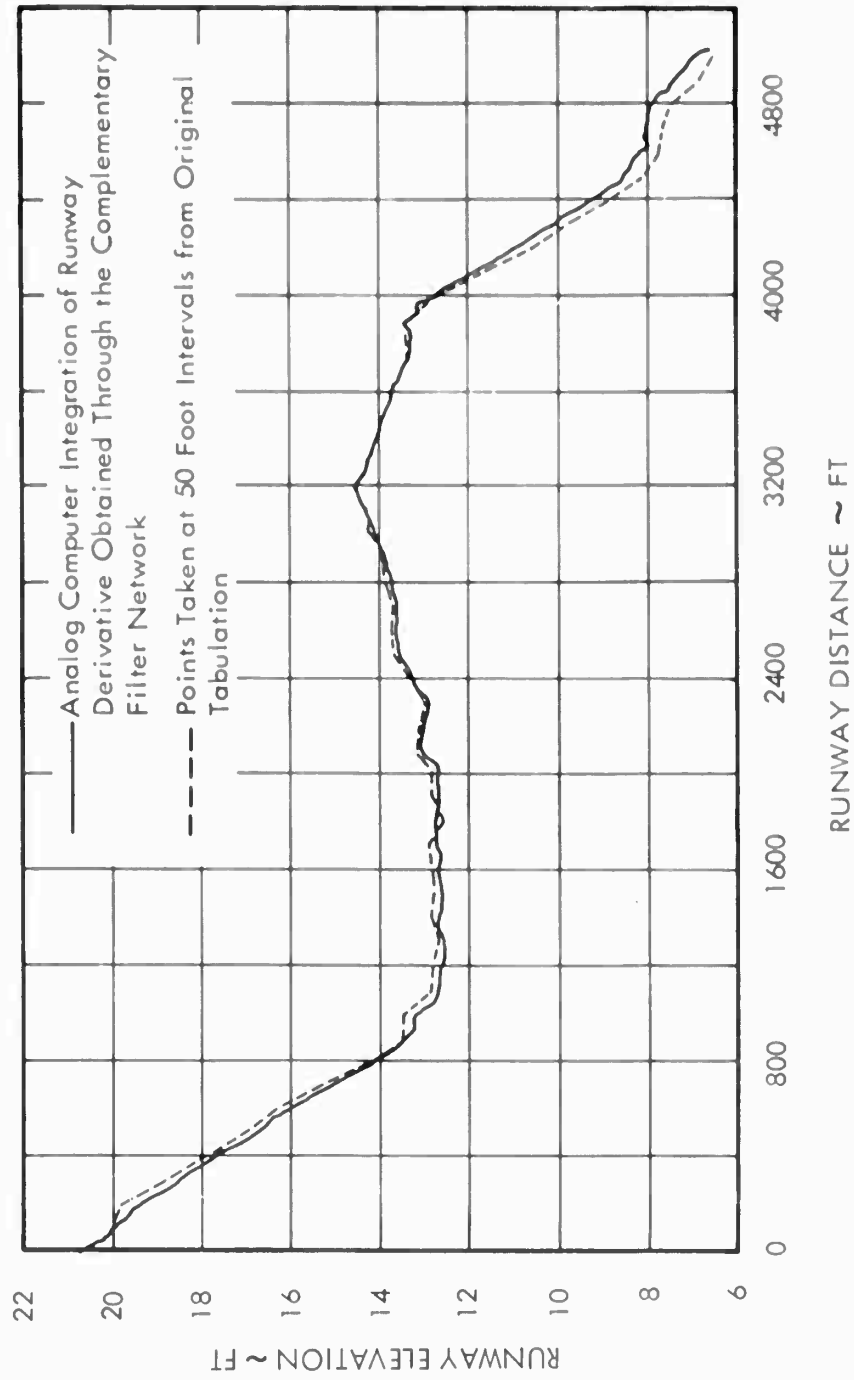


FIGURE 134: Integral of the Runway Derivative Obtained Through the Complementary Filter Network

time increments corresponding to 5 feet of runway travel, as discussed in Appendix D. The profile signal to the front main gear is taken from the 6th pad's circuit and the signal for the rear main from the 7th, to simulate the proper spacing of the nose and main gears of the example airplane, as shown in Figure 2 of the text.

Selected shears, bending, and torsion moments are computed as functions of the rigid and flexible modal response. Equations used to determine output loads at several stations are presented in Appendix A. The method of incorporating these in the dynamic computer simulation is presented in Figure 129.

Three nonlinear functions per gear are included: Strut orifice load as a function of strut velocity, strut air pressure as a function of a strut deflection or compression, and tire force as a function of tire deflection. These nonlinear functions, as used, have given excellent agreement between analysis and test data in prior analyses.

#### 4. Analog Methods Power Spectral Analysis

A brief description of the analog circuitry used for measuring power spectral density, load occurrences, and probability functions for the data obtained during the dynamic taxi analysis is given herein. In addition, the line of reasoning leading to the selection of specific techniques is presented in a chronological pattern.

The zero intermediate frequency (IF) low-pass filter technique is utilized to enable active elements to be used in the data reduction process and, thereby, to provide extremely "square" filters. Generally, the same circuits are used to perform both power spectral analyses and cross-spectral analyses, except for the parallel mode of operation of the circuits. Some of the considerations which led to the particular filter types and analysis techniques are:

a. The function follower, which was used to convert the plotted slope profile to a voltage which could be recorded on magnetic tape, was capable of following the desired amplitude variation accurately up to a frequency 3 cps. Above 3 cps, amplitudes were attenuated and considerable lag was experienced in the follower, which would lead to complete loss of data once the follower head lost the silver-ink line. On the other hand, a lower limit of 4 or 5 feet on the wavelength content of the runway data is desired. This sets an upper limit of 15 ft/sec on the rate at which the follower could actually traverse the runway data. Airplane speeds of 15, 30, 45, and 60 mph were of interest. Since each speed is an integral multiple of 11 ft/sec (22, 44, 66, and 88 ft/sec respectively) playback of the runway data at a rate of 11 ft/sec was fixed and then the computer simulation of the airplane was time-scaled by integral factors of 2, 4, 6, and 8. The time to carry out the simulated 5,000 ft. run is 454.5 sec for all airplane speeds.

b. Following the establishment of all time scaling, a conversion of the demodulators was accomplished so that the data recorded on the magnetic tape at 15 inches per second could be played back at 60 in/sec, thus speeding up the data reduction

process by a factor of four, and reducing the playback time to 113 seconds per pass. The read-out of end points, and rewind-reset time, remained the same.

The above considerations of follower-speed, computer time-scale for the problem, and playback speed, as well as the definition of certain frequencies in the power spectra of the airplane responses to the runway profile, led to the final selection of the number of points per PSD required, and the associated bandwidth of the filters used. The airplane frequencies of interest range from 0.3 to 12 cycles per second; and at the time-scales involved, this range corresponds to computer frequencies of from 0.0375 to 6 cycles per second. With the tape speed-up on playback, then, the filters are required to operate in the region from 0.15 to 24 cycles per second. Twenty-five points in the airplane spectrum were selected so as to define the desired frequencies.

The several methods of obtaining power spectral density measurements on analog equipment considered for this study were:

- a. Passive network filters
- b. Active network filters
- c. High intermediate frequency (IF), tuneable filters
- d. Zero frequency IF, fixed filters
- e. Tape-loop, repetitive data input
- f. Single-pass data input
- g. Sweep frequency analysis
- h. Parallel filter "comb" analysis

Additional considerations were: the time duration of the data, the frequency content, the precision required, the amount of equipment on hand or available, and the time required to perform the operations with suitable precision.

Since the data was obtained over a period of 454.5 seconds per run, the tape-loop method was impractical. Since the frequency range of interest was below 50 cps., passive element filters were ruled out in favor of the active filters composed of D.C. amplifiers, whose operation at or near zero cps. is accurate and reliable. The need for cross spectrum computation also led to the zero IF method which permits accurate phase detection.

The analysis of the requirements and capabilities led to the decision to use active network filters, zero frequency IF, multiple-filter, comb techniques.

The active network filters used were of the Butterworth or "maximally flat" design. Five poles were used, which produced a 30 db per octave roll-off beyond the cutoff frequency. The transfer function of the filter, a typical filter wiring diagram, and a complete block diagram for one PSD circuit are shown in Figure 135. The filter characteristic frequency is presented in Figure 136. Five filters were set up as shown in Figure 137 to obtain power spectral density points from the data. The spectrum of airplane frequencies of interest was divided into five regions: 0.30 - 0.63 cps, 0.63 - 1.30 cps, 1.30 - 2.80 cps, 2.80 - 5.80 cps, and 5.80 - 12 cps. Each of the filters was assigned a bandwidth equal to one-fifth of the width of one region. On the first playback of the function to be analyzed, one-fifth of each region was covered and the PSD at each point read. Next, the beat frequency oscillators were each advanced one filter-width, and a second pass made. This produced a second set of 5 PSD points, and so on through 5 passes, to completely cover the spectrum of interest.

In order to obtain readings for all levels of PSD for a given function, the gain frequently had to be adjusted before the squarer, or before the integrator, in order to prevent either the output of the squarer being entirely in the noise level, or the integrator operating beyond its linear limit. Experience with particular functions permitted better estimates of gains to be made, and the speeding up of the tape playback to 4 times the original recording rate (described later in this Appendix) decreased the lost time in re-running to obtain proper gain settings.

The equipment used in this program is among the best available in the industry, and repeated checks are made to eliminate the human factor. The frequency modulation equipment described above was modified from a 10 k.c. carrier to a 40 k.c. carrier, in order to speed up data reduction by tape speed change, sometime during the transition from single- to multi-gear power spectral analysis. Technically this should not affect results, but such operations at the upper limits of tape recorder and other equipment capabilities could generate subtle inaccuracies. Also, the Padé delay circuits used in the multi-gear analysis have some theoretical attenuation, as shown in Reference 14, but this should occur only at high frequencies, and the error relatively small.

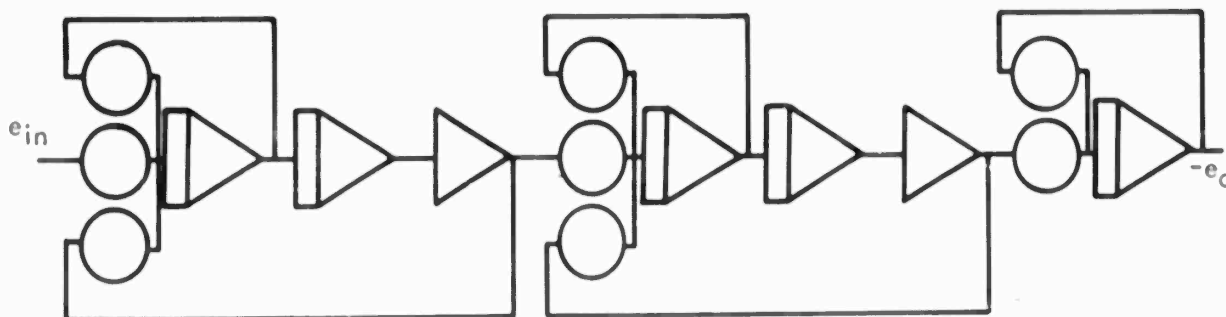
From the experience obtained, it is apparent that large electronic analog computation facilities (300 amplifiers or more) can be set up to process large amounts of data for obtaining rapid, accurate estimates of statistical quantities. Parallel circuits can be designed which will "comb" data rapidly, and with tape speed-up, exceed most normal accuracy requirements. Common practice can be made of recording at a low tape speed of 1 7/8 inches per second, and playing back at 60 inches per second, affording a net speed-up factor of 32. This capability is possible with complete record-reproduce systems commercially available.

Where a tape-loop machine is available, less analog computing equipment may be required since a single filter, sweep analysis is satisfactory. Sweep techniques permit continuous, smooth plots of power spectral density estimates to be made directly. A disadvantage of this technique is that it is difficult to eliminate the effects of the discontinuity encountered where the loop is joined; the subsequent impulse response of the filters will appear in the output.

Low-Pass Filter Transfer Function  
 (Where  $\omega_c$  is the Filter Cut Off Frequency)

$$\frac{e_o}{e_{in}} = \frac{1}{(s + \omega_c)(s^2 + 1.618 \omega_c s + \omega_c^2)(s^2 + .618 \omega_c s + \omega_c^2)}$$

Single Filter Circuit:



One Complete PSD Diagram:

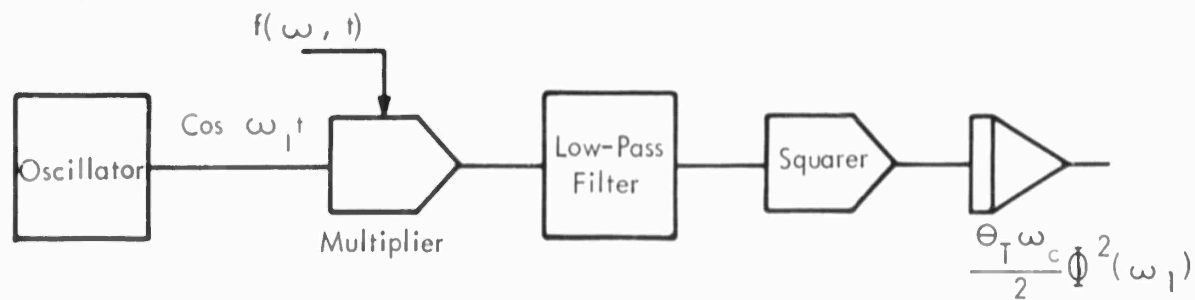


FIGURE 135: Analog Flow Diagrams for Power Spectral Density Calculations

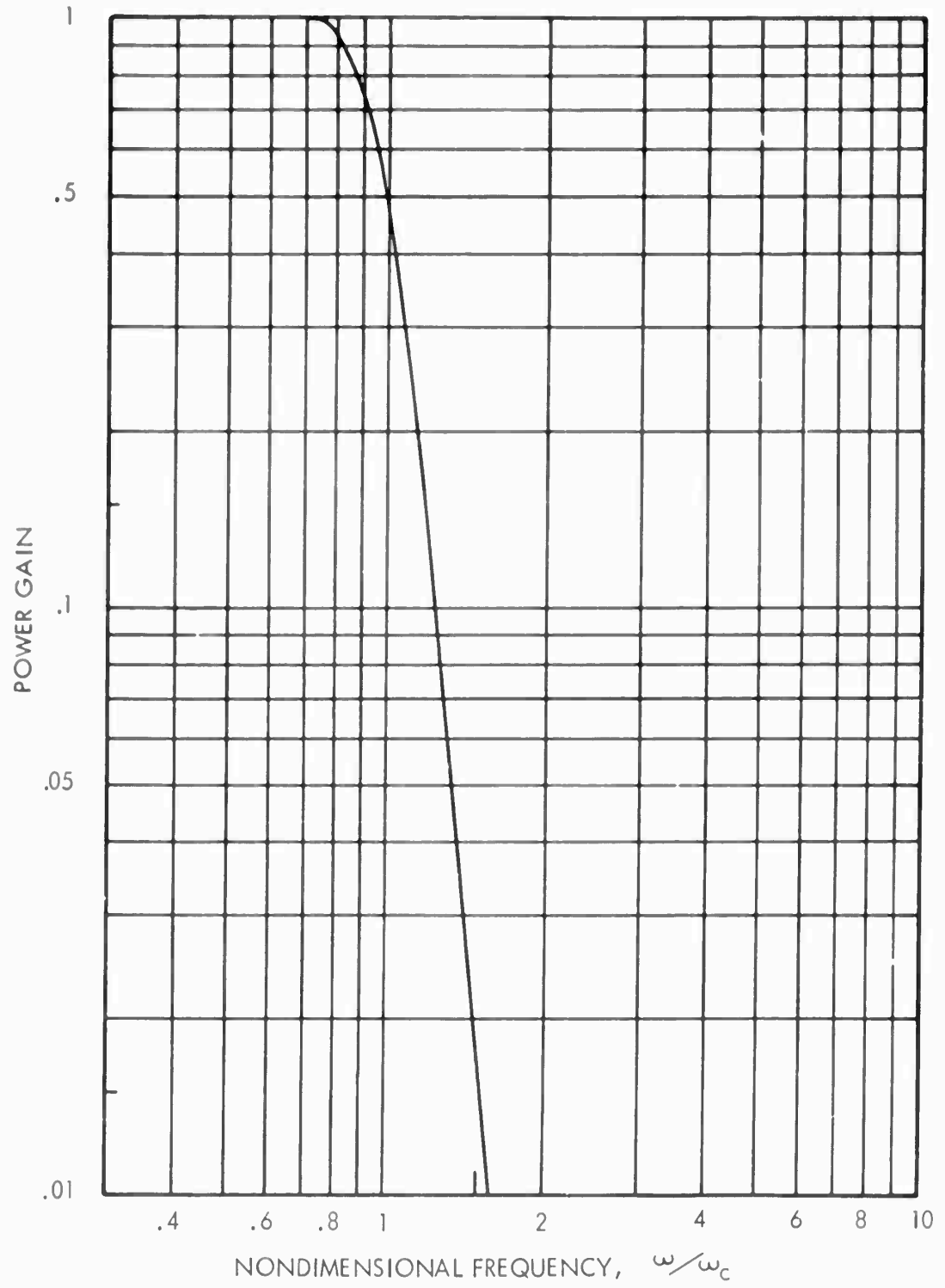


FIGURE 136 : Frequency Response of the Five-Pole Maximally Flat Filter

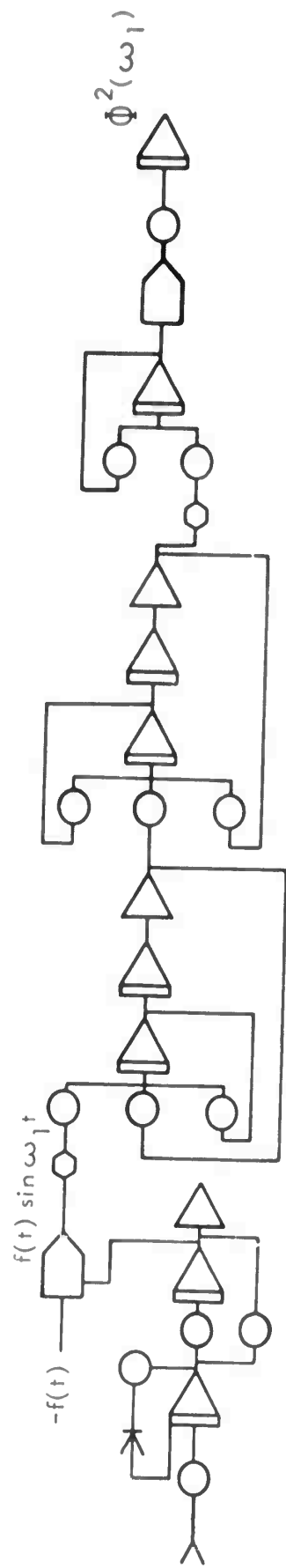


FIGURE 137: Analog Computer Diagram for Each Power Spectral Density Point

## 5. Special Problems in Statistical Analysis on Analog Computers

The special problems encountered in performing statistical computations on analog computers have been treated at length by many investigators. It was not the prime objective of this effort to obtain the most accurate or efficient technique, but rather to examine the feasibility of applying the analog computer to computations of a statistical nature.

The detection of coincidence (or occurrence) at a given amplitude, the counting of this event and subsequent ones, and the determination of the probability of this coincidence having been exceeded, is accomplished as shown in the computer diagram presented in Figure 138. The system operates as follows:

Amplifier  $A_1$  is held to zero output by a positive bias level,  $P_1$  and diode  $D_1$ . Capacitor  $C_1$  is discharged and amplifier  $A_3$  is inserted to ensure that  $e_1$  is zero and no voltage is present to drive integrator  $I_1$ . When  $f(t)$  falls more negative than  $P_1$ , the output of  $A_1$  switches to  $E_1$ .  $C_1$  must charge through  $D_2$ , and in doing so, must charge  $C_2$  on  $A_2$ . The voltage on  $A_2$  then changes by  $(C_1/C_2) E_1$ , constituting one count. Meanwhile,  $A_3$  and  $e_1$  go to  $-E_1$  and this is integrated by  $I_1$  until  $f(t)$  rises above the coincidence level again.

When  $f(t)$  does rise above the coincidence level,  $A_1$  returns to zero,  $C_1$  discharges through  $D_3$  and the count is held on  $A_2$ . After time  $t$ , the voltage  $e_2$  is proportional to the total time that  $f(t)$  has been below  $P$ . By choosing the opposite sign for the bias setting  $P$ , the system will work for positive occurrences. A set of five negatively biased and five positively biased circuits detects the number of occurrences at ten levels as well as the time in excess of each. The accuracy of the system was found to be within one or two of a known number of counts over 113 seconds, and the probability calculation was found to be as accurate as  $E_1$  could be set-about one percent of the nominal value. Further development of this circuit and technique should produce a highly accurate coincidence counting and probability computing system.

Since the runway was a single sample, used in its entirety, statistical reliability formulae are not particularly applicable to the estimates of power spectral density (PSD), cross spectra, transfer functions, load occurrence detection and counting, and probability functions obtained for the data on the analog computer. Multiplier offset and phase shift, integrator drift, potentiometer setting accuracy, and other analog computer error sources contribute to the overall accuracy of the measurements obtained. A further source of error is the magnetic tape system which will be described later in detail.

As mentioned briefly before, one of the problems encountered in doing statistical operations on active-network analog computers results from the necessity for a change in gains and scale factors to obtain consistently accurate results. This arises particularly in the field of power spectral analysis. Power spectra having a range in amplitude through several decades across the spectrum were desired, and if this range were

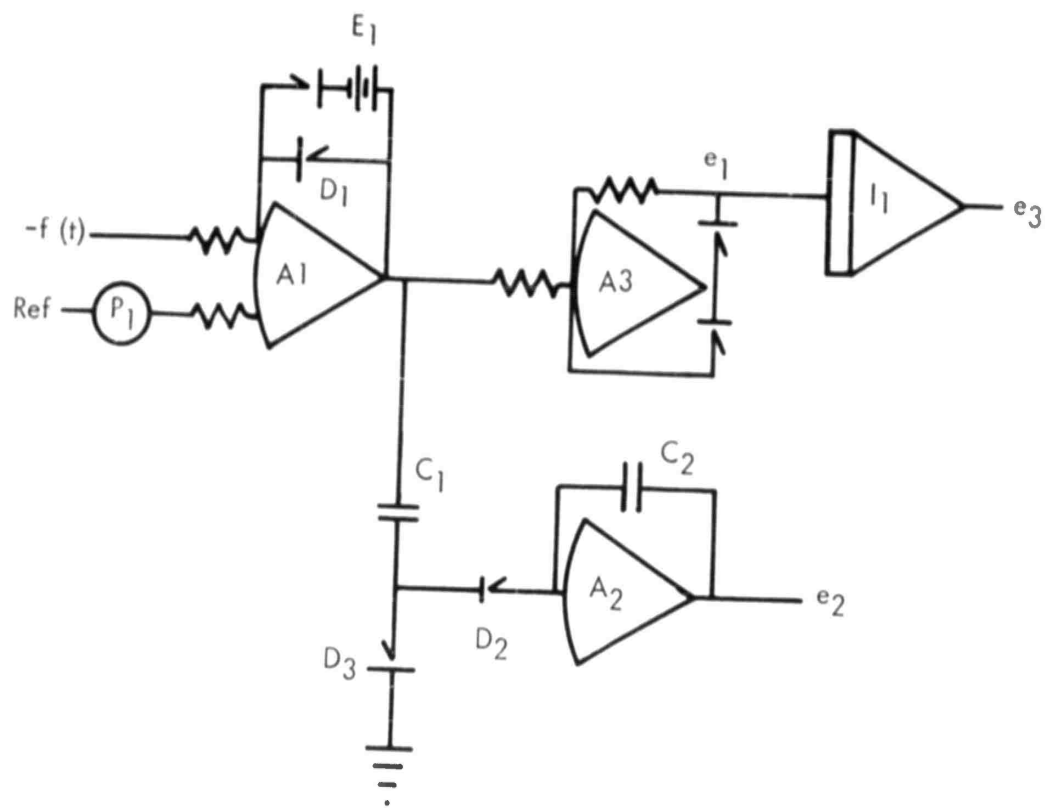


FIGURE 138 : Analog Computer Diagram for Occurrence Counting and Probability Computations

referenced to a constant-scaled analog system, it would represent output voltages from the order of 10-100 volts down to 10-100 millivolts.

In analog computation, a consistently high signal-to-noise ratio is necessary; and at the same time, the operational limits of the computer components must not be exceeded. In meeting these requirements, circuit gains and scale factors must be adjusted from one run to another to ensure reliability in the results. This operation greatly increases the time required to obtain results and to convert them to true magnitudes in tabular or graphical form. The technique can be somewhat improved when applied to a large mass of data; but at best, the results will be obtained in a form rather tedious for final data preparation.

The automation of these final data reduction steps may greatly speed up operations in the future.

#### 6. Cross Spectrum Computation

The cross spectrum computation was carried out as shown in Figure 139, in block diagram form. It is to be noted that three filters per point are needed, one to obtain the PSD of one function as reference amplitude, and one each to obtain the in-phase and out-of-phase components of the cross spectra. The cross spectra operation was further limited to two points per pass due to equipment limitations. Tentative conclusions are that the bandwidth of the filters for this type of computation must be fairly narrow relative to the frequency being studied to obtain useful phase information, while the values of the cross-spectra are of the same order of precision as the PSD in absolute magnitude.

#### 7. Simulation of Continuously Variable Airplane Speed

The problem of introducing variable taxi speed during a single pass over the prescribed runway has not been brought to a satisfactory conclusion, for the following reasons:

- a. The length of the runway requires an FM tape recording of the slope profile, which precludes a variation in speed of playback. (Tape speed variation only leads to a zero offset in the demodulated output signal).
- b. In order to accomplish the speed change, it is necessary to time-scale the airplane simulation in the computer. It is possible that all integrator gains could be simultaneously varied through servo- or electronic-multipliers at their inputs; however, the analysis of a record taken during such a procedure would be most tedious because the time scale would be changing from one point to the next throughout the run. This makes auto-correlation, cross-correlation, power spectral density or any other convolution-type analysis on the data, by presently indicated means, almost impossible.

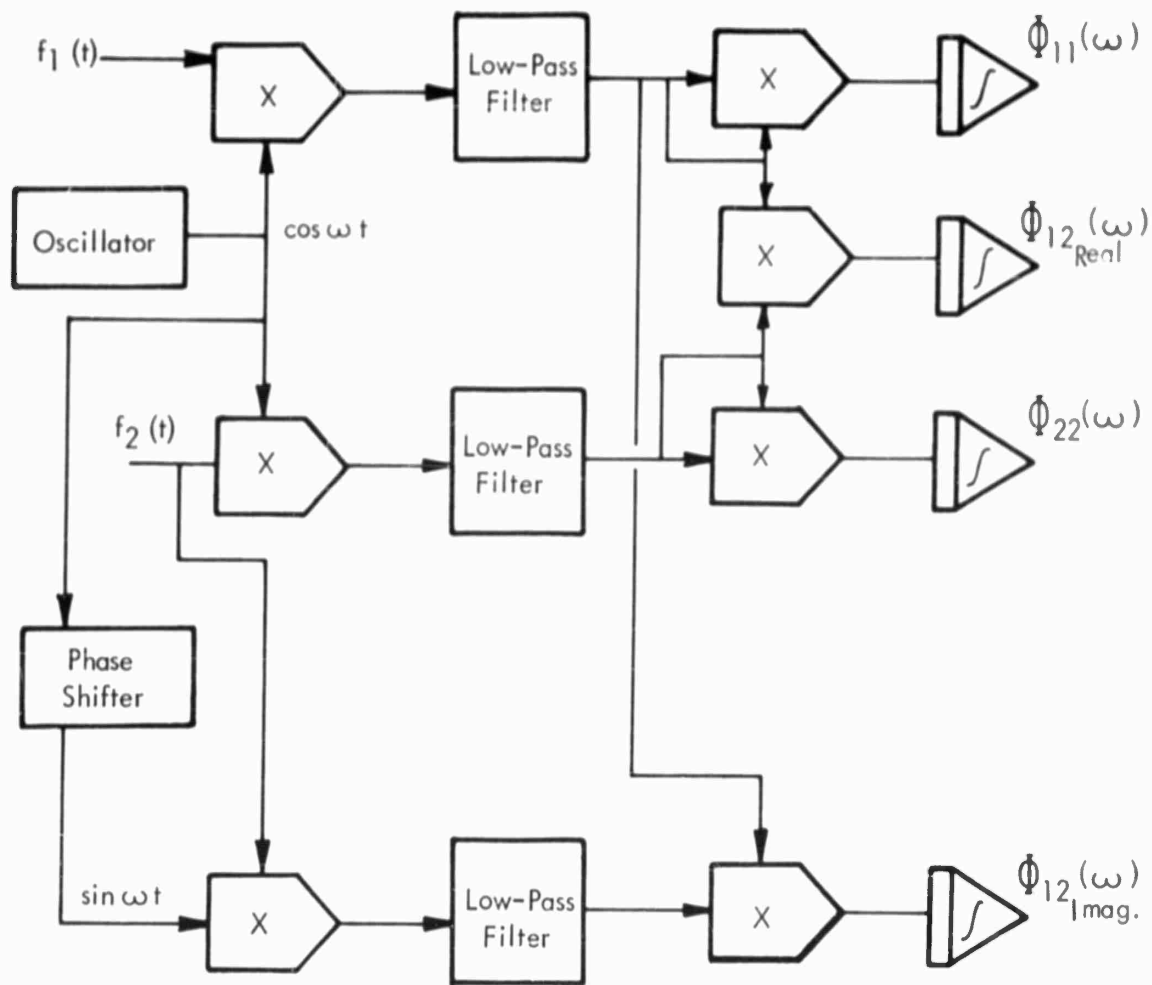


FIGURE 139 : Block Diagram of Computer Circuit for Obtaining Cross Spectra

It appears that variable speed may be accomplished by using another source of input, a noise generator with a shaping network, or filter, on the output which shapes the PSD of the noise so that it approaches the reference slope function of the runway. Speed variation can then be simulated on the input, leaving the computer time-scale of the airplane constant. Adjustment of the filter so that the PSD of the input will approach the PSD of the time derivative of the reference runway will produce the desired speed change.

The concept of replacing the specific runway slope with a "shaped" noise generator for making statistical studies of aircraft responses during taxi operation holds great promise, and deserves considerable attention in future studies. The disadvantage will be that instead of having an entire process, represented by a specific runway, only samples of the random function may be taken. This limits the results to the category of pure estimates with limits of confidence and reliability. However, with a high speed analog computer, a great many samples may be taken in an extremely short time and converted to statistical results with high levels of confidence and reliability.

#### 8. Simulating Gear-Spacing with Electronic Time-Delay Networks

The problem of including the spacing of the landing gear relative to the runway, and to each other, had to be solved on the analog computer by a time-delay network. The fourth order Pade' approximation was found to delay signals with adequate fidelity as long as the period of the signal is not less than the Pade' time-delay constant. A five foot wavelength of runway variation was determined as the minimum to be included in the analysis, since the original profile was read at intervals corresponding to only four foot wavelengths or longer. Also, this will still define the wavelength corresponding to main gear spacing, which is 5 feet. Since the runway regeneration on playback was fixed at 11 ft/sec, signals of a period of 5/11 sec and longer were to be utilized, introduced to the nose gear, then delayed and presented to the front main gear 30/11 sec later, and then 5/11 sec later, presented to the rear main gear.

Seven fourth-order Pade' circuits were programmed for the computer as shown in Figure 130, each of which has a 5/11 second delay time constant. The runway slope profile is introduced directly to the nose gear and to the Pade' circuits which are stacked end-to-end. Each circuit then delays the signal by the equivalent of 5 feet and the output of the sixth unit is 30 feet behind the nose gear, in proper sequence and phase for the front main gear. The seventh Pade' network provides runway profile information in proper sequence and phase for the rear main gear.

#### 9. The Analog Computation Equipment

The analog computation equipment utilized in this problem consists of three consoles having available a total of 130 operational amplifiers (not including those in the function generators, multipliers, etc.) for summing, integrating and high gain operations. The remaining equipment is presented in tabulated form below:

<u>Item</u>	<u>Quantity</u>
Servoset Coefficient Potentiometers	140
Manual Potentiometers	38
Decade Resistors	18
Electronic Multipliers	42
Servo Multipliers (high accuracy, 3 cup)	2
Diode Function Generators	14
Preset Clock, .01 sec to 99.99 sec	1
Variable D. C. Voltage Sources	30
Precision Voltage Dividers	2
Trunk Lines for Interconnection	60
Peripheral Equipment	
Oscillograph, 8 Channel	1
Oscillograph, 4 Channel	1
X-Y Plotter-Follower	2
Digital Voltmeter, 0.001-999.9 Volts	1
Oscilloscope, 0 - 5 Megacycles	1

The problems are divided into sections during programming which utilize the equipment's capability to the greatest advantage. For example: In the airplane - taxi simulation, the airplane and gear are programmed for the first computer, where rapid pot-set capability, as well as higher precision are available. The second computer and its manual pots are devoted to the Pade' circuits which do not change with taxi speed, and the third computer receives what fragments of the airplane are "left over," a few Pade' circuits, the runway regeneration, and the read outs for driving the FM modulators.

On playback of the data for power spectral density calculations, the filters are programmed on the third computer, and the input and output multipliers, the final integrators, and the beat-frequency oscillators are set up on the first computer.

### 10. The Magnetic Tape System

A magnetic tape record-reproduce system was developed when it became known that the reproduction of the entire 5000 feet of a runway would be required in the problem solution. Originally, the concept had been to record and reproduce the input and output data for the runway on the 11" X 17" X-Y plotter-followers, which had sufficed for previous limited studies.

The equipment immediately available was an airborne 14-channel system with frequency-modulation (FM) electronics and compound-modulation (CM) electronics available for all 14-channels of recording capacity. Several limitations were encountered in its use, so a seven-channel direct record-reproduce, multirange unit was obtained for use in this research program. The multirange feature of this equipment aided in the subsequent tape speed-up which was accomplished. Two additional 2-channel direct record-reproduce systems were utilized at various stages of the analysis.

The final technique employed was arrived at in the following manner:

The CM electronics (both the modulators and the demodulator) were found to operate only in the millivolt input-output region. Since the analog computer is scaled to operate in the region from -100 volts to +100 volts, there was trouble in getting the demodulated signal up to a level wherein the computer could accept it conveniently. (Tape speed-up with CM electronics would have been difficult, it later developed.)

The FM electronics employed a preamplifier to operate on low voltage inputs. It was determined that the multivibrators which generate the carrier are modulated by a +31 volt,  $\pm 10$  volt signal on the input grid, and it was possible to connect the computer amplifiers directly to these points. The demodulator consisted of a preamplifier which then differentiated, rectified, and clipped the playback signal, generating a pulse train of twice the instant frequency. This pulse train triggered a one-shot multivibrator which puts out a constant amplitude, constant time duration pulse at the double frequency of the input carrier. The output of the one-shot device was then filtered to reject the carrier, whereby the original signal was reproduced, although attenuated from  $\pm 10$  volts to  $\pm 0.60$  volts.

Later study revealed that this signal could be amplified by factors of 50 or 60, thus permitting its use in the analog computer. Also, if the tape was speeded up by a factor of 4, the 10KC carrier was converted to a 40KC carrier which the demodulator could not demodulate, the "on time" of the one-shot multivibrator being too long. However, the frequency-doubling in the pulse train was eliminated and a slightly shorter "on time" achieved, permitting the demodulation of a 40KC carrier.

Fortunately, the CM demodulator was found to contain the same FM section as the FM demodulator, so modifications developed for one unit applied to the other. (The AM portion of the CM demodulator was de-energized and by-passed). A filter for rejecting the carrier at the output of the CM unit was constructed of passive elements.

The direct record-reproduce units are used only to record the FM output from the modulators and to reproduce these signals for input to the demodulators. The measured linearity of the overall system is better than 5%, clouded a little by the D. C. drift of the output and the frequency drift of the modulators - none of these units being in temperature - controlled enclosures, nor supplied by particularly highly regulated D. C. power supplies.

### 11. Analog Filter Compensation for Amplitudes

The Figures 140 and 141 present the data for determining filter attenuation factors for essentially square filters. The term "quality factor,"  $Q$ , is often applied to system damping, since:

$$Q = \frac{1}{2c/c_c} \quad (1D)$$

For very low values of system damping, "universal" resonance curves can be prepared for single degree of freedom systems (see Appendix H) as shown in Figure 140. If the frequency above and below resonance which corresponds to filter half-power points is known as  $\omega_1$  and  $\omega_2$ , and the amplitude of Figure 140 is labeled  $X$ , then

$$\frac{-1}{(\omega_1 - \omega_2)} \int_{\omega_1}^{\omega_2} |X| d\omega = \text{the attenuation factor referred to in the text.} \quad (2D)$$

The application of this attenuation factor in the research program may be clarified as follows: If a nominally square filter is applied to a function which is flat or continually sloping in the frequency plane, the filter transmits the power at the center frequency very accurately. However, if the filter is centered over a very sharp peak, as is the case in a low damped system, it tends to read the peak as an average power spread over the bandwidth, and thereby attenuated. Similarly, two filters off center, but side-by-side so as to split the peak, will fail to read the true peak. To find the true peak reading, correction factors can be computed by applying the methods given in this appendix provided the system damping is known.

Since the PSD methods are used as a basis for validating the linearized analysis, the reverse procedure is used in this case; that is, the linear harmonic results are attenuated using correction factors on peaks only, to indicate values as seen by a

$$\frac{\text{Cycles off Resonance}}{\text{Resonant Frequency}} = \frac{a_r}{Q} = \text{Fractional Detuning}$$

$$a_r = Q \frac{\text{Cycles off Resonance}}{\text{Resonant Frequency}}$$

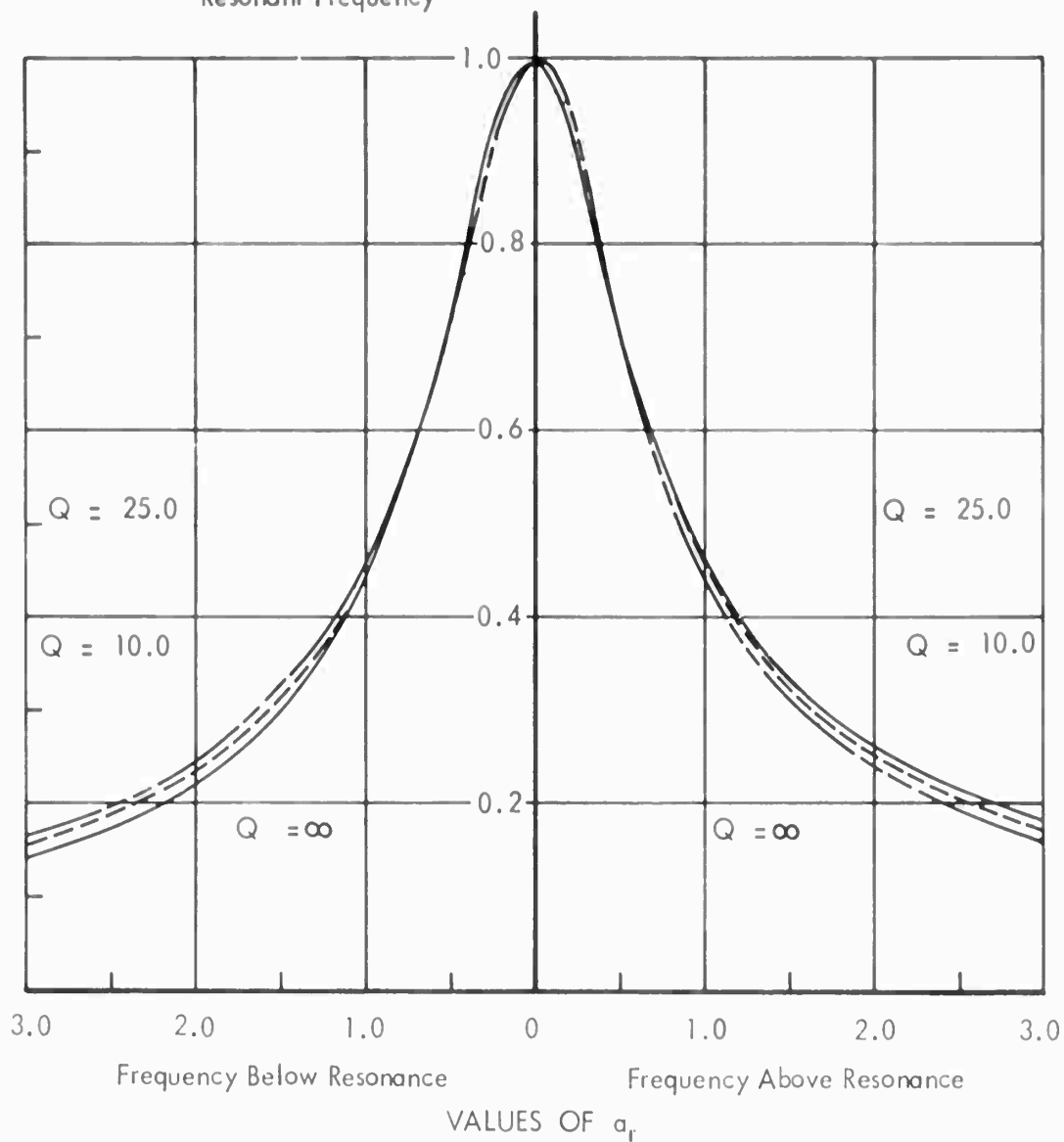


FIGURE 140 : Universal Resonance Curves (From Reference 13)

$$\frac{\text{Cycles off Resonance}}{\text{Resonant Frequency}} = \frac{a_r}{Q} = \text{Fractional Detuning}$$

$$a_r = Q \frac{\text{Cycles off Resonance}}{\text{Resonant Frequency}}$$

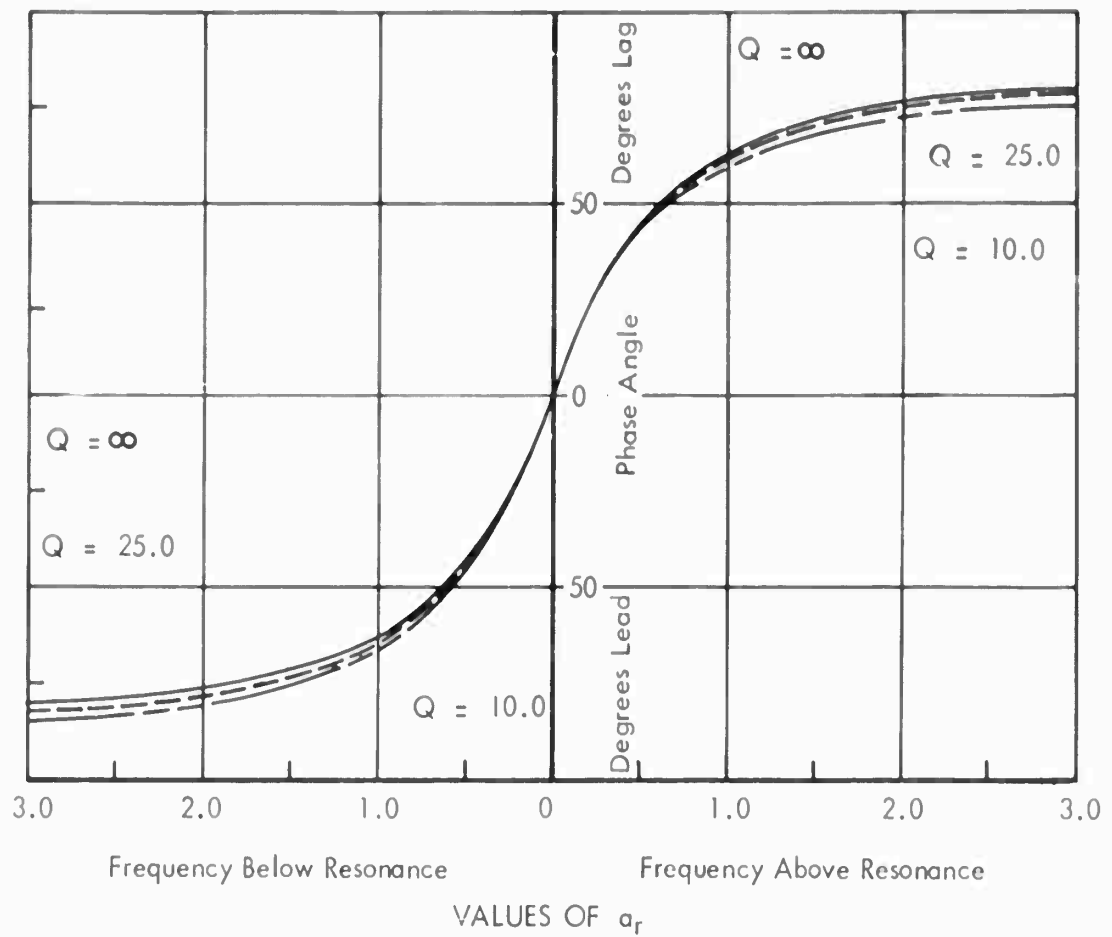


FIGURE 141 : Universal Phase Angle Curves (From Reference 13)

square filter. Such correction factors are shown in Figure 50 in the main text, as a function of percent of critical damping, for convenience in referencing. Note that a low damped system may show appreciable attenuation at peaks in response, as viewed through a 10 percent bandwidth filter.

## 12. Digital Approach to Power Spectral Analysis

The methods of generalized harmonic analysis are applied to determine the statistical properties of structural loads experienced on and within the airplane. From the power spectral density functions which result, frequencies of load occurrence and probabilities may be calculated.

If it is assumed that the load or disturbing phenomena is "stationary random," then its statistical properties will be invariant from one valid sample to another, taken at random from a given population. The variations cannot be described as a definite function of time, but the statistical properties can be determined from the power spectral density of the random function, as follows:

If  $A(\omega)$  is the amplitude of the frequency component  $\omega$  of the random function,  $y(t)$ , then an approximate interpretation of the power spectrum  $\Phi(\omega)$  may be expressed as in Reference 12:

$$\Phi(\omega) = \lim_{\Theta_T \rightarrow \infty} \frac{4\pi}{\Theta_T} |A(\omega)|^2 \quad (3D)$$

where  $\Theta_T$  is the stationary random time duration of the sample. However, for practical applications, a routine digital computation scheme has been developed for the evaluation of power spectra. A detailed description of the analysis procedure is given in References 12 and 23, but a few of the more important quantities will be summarized here:

The root mean square,  $\sigma$ , of the amplitude,  $y$ , is determined from

$$\sigma^2 = \left| \int_0^\infty \Phi(\omega) d\omega \right| - (\bar{y})^2 \quad (4D)$$

where  $\bar{y}$  is the arithmetic mean of  $y$ .

If  $k_p$  is the (positive) number of standard deviations from the mean, and the probability function is Gaussian distributed then the "peak-count",  $N_p$ , can be calculated as the probable number of times per unit time the function,  $y$ , will exceed a magnitude of  $y_p = k_p \sigma$ .

$$N_p(y_p) = \frac{1}{2\pi\sigma} e^{-\frac{(y_p - \bar{y})^2}{2\sigma^2}} \left[ \int_0^{\infty} \omega^2 \Phi(\omega) d\omega \right]^{1/2} \quad (5D)$$

The power spectral output,  $\Phi_O(\omega)$ , in terms of load (or stress) at a given location in an aircraft is related to an input spectrum  $\Phi_I(\omega)$  as follows:

$$\Phi_O(\omega) = |T_O(\omega)|^2 \Phi_I(\omega) \quad (6D)$$

The transfer function as obtained is the absolute magnitude of a frequency response function under steady state conditions, and it will not in general describe transient pulse loadings such as are encountered in landing and braking.

Similarly, a cross spectral density,  $\Phi_{OI}(j\omega)$ , directly correlating both input and output, may be evaluated as shown in Reference 23, and a transfer function calculated as follows:

$$T_{OI}(j\omega) = \frac{\Phi_{OI}(j\omega)}{\Phi_I(\omega)} \quad (7D)$$

Both the amplitude and phase of T is indicated in this case. However, for a linear system, if no cross-correlation exists, the magnitudes of both  $T_{OI}$  and  $T_O$  should be identical.

Statistical loads distributions for taxiing response can be determined from Equations 4D - 7D. However, it should be noted that where nonlinear phenomena are present, the methods of generalized harmonic analysis cannot be proven to be valid in general. Equation 5D, for example, assumes a normal Gaussian distribution of amplitudes in the data, and this implies a symmetry in positive and negative increments of loads. Non-linear phenomena, particularly landing gear forces, are typically known to be somewhat unsymmetrical in this respect.

APPENDIX E

NONLINEAR RESPONSE BY PERTURBATION METHODS

- (1) The perturbation method, References 3 and 5, may be applied to the differential equation,  $\ddot{Z} + \alpha Z + \beta Z^2 = \beta F_o \sin \omega t$ , to yield an approximate solution given by:

$$Z = H_o \sin \omega t - \left( \frac{\beta H_o^2}{2\alpha} \right) \left( 1 - \frac{4}{3} \cos \omega t + \frac{1}{3} \cos 2\omega t \right),$$

where

$$\alpha = \frac{K_f}{M_f}$$

$$\beta = \frac{K_{NL}}{M_f}$$

$K_f$  = coefficient of the linear part of  $F_K$

$K_{NL}$  = coefficient of the nonlinear part of  $F_K$

$M_o$  = rigid body mass

$$\beta F_o = \frac{\text{magnitude of driving force}}{M_f}$$

$F_K = K_f Z + K_{NL} Z^2$  = the spring force

$$H_o = \frac{\beta F_o}{2\sqrt{\alpha}(\sqrt{\alpha} - \omega)}$$

Let

$n$  = the nonlinear part of  $Z$ ,  $n = -\left( \frac{\beta H_o^2}{2\alpha} \right) \left( 1 - \frac{4}{3} \cos \omega t + \frac{1}{3} \cos 2\omega t \right)$

$l$  = the linear part of  $Z$ ,  $H_o \sin \omega t$

$A_{NL}$  = the minimax of  $n$  of greatest numerical value

$A_L$  = the minimax of  $l$  of greatest numerical value

$R_r = \frac{A_{NL}}{A_L}$  is the ratio of the nonlinear contribution of response to the linear response.

It can be shown that  $A_{NL} = \frac{-4H_o^2\beta}{3\alpha}$  and  $A_L = H_o$ , hence

$$R_r = \frac{4\beta H_o}{3\alpha}$$

Now, if

$$K_f = 4540 \text{ lbs/in}$$

$$K_{NL} = 138 \text{ lbs/in}^2$$

$$M_f = 82.9 \text{ lbs sec}^2/\text{in}$$

$$\beta F_o = 46 \text{ in/sec}^2$$

$$\omega = 10.36/\text{sec}$$

then

$$\alpha = 54.5/\text{sec}^2$$

$$\beta = 1.66/\text{in-sec}^2$$

and

$$R_r = 0.043$$

(2) When applied to

$$\ddot{Z} + \alpha Z + \beta Z^3 = \beta F_o \sin \omega t$$

the perturbation method yields an approximate solution given by:

$$Z = H_o \sin \omega t + \left( \frac{\beta H_o^3}{32\alpha} \right) (3\sin \omega t - \sin 3\omega t)$$

where  $\alpha$ ,  $\beta$ ,  $K_f$ ,  $K_{NL}$ ,  $M_f$ , and  $\beta F_o$  are defined as in (1); however

$$F_K = K_f Z + K_{NL} Z^3 = \text{the spring force.}$$

$H_0$  must satisfy the equation:

$$H_0^3 + \left( \frac{8\sqrt{\alpha}}{3\beta} \right) (\sqrt{\alpha} - \omega) H_0 - \frac{4F_0}{3} = 0$$

Although  $I$ ,  $A_{NL}$ ,  $A_L$ , and  $R_r$  are defined as in (1), one now has

$$n = \left( \frac{\beta H_0^3}{32\alpha} \right) (3\sin \omega t - \sin 3\omega t)$$

and it can be shown that

$$R_r = \frac{\beta H_0^2}{16\alpha}$$

where  $H_0$  is the numerically greatest real root of the above equation in  $H_0$ .

Now, if

$$K_f = 5080 \text{ lbs/in}$$

$$K_{NL} = 126 \text{ lbs/in}^3$$

$$M_f = 82.9 \text{ lbs-sec}^2/\text{in}$$

$$\beta F_0 = 46 \text{ in/sec}^2$$

$$\omega = 10.36/\text{sec}$$

then

$$\alpha = 61.3/\text{sec}^2$$

$$\beta = 1.52/\text{in}^2\text{-sec}^2$$

$$H_0 = -1.19 \text{ in}, -5.23 \text{ in}, 6.41 \text{ in}$$

$$R_r = 0.064$$

Note that the solution for the coefficient of the nonlinear harmonic term in (2) above differs slightly from that derived for the cubic spring case in the text. Equation 16 in the text was derived by Duffing's method, Reference 3, rather than the perturbation method, but the two answers agree within first order terms in  $\beta$ . Since  $\beta \ll \alpha$  in both approaches, the numerical results would be in good agreement.

APPENDIX F  
LINEARIZED TRANSFER FUNCTIONS FOR  
VARIATIONS IN STRUT DAMPING

The transfer functions presented herein are applied in the text as parametric variations for the peak values only. The complete frequency response functions are useful for observing shifts in resonant frequency, or other minor changes in form, so they are presented here for completeness.

Tire Pressure = 90 psi

$V_H = 88$  fps

ANALYSIS METHODS:

-----Single Gear

Linear Harmonic

$D = 277$  Lb-Sec/In

— Multi-Gear,  $F_{13}$

Nonlinear PSD

$C_D = 21.15$  Lb-Sec<sup>2</sup>/In<sup>2</sup>

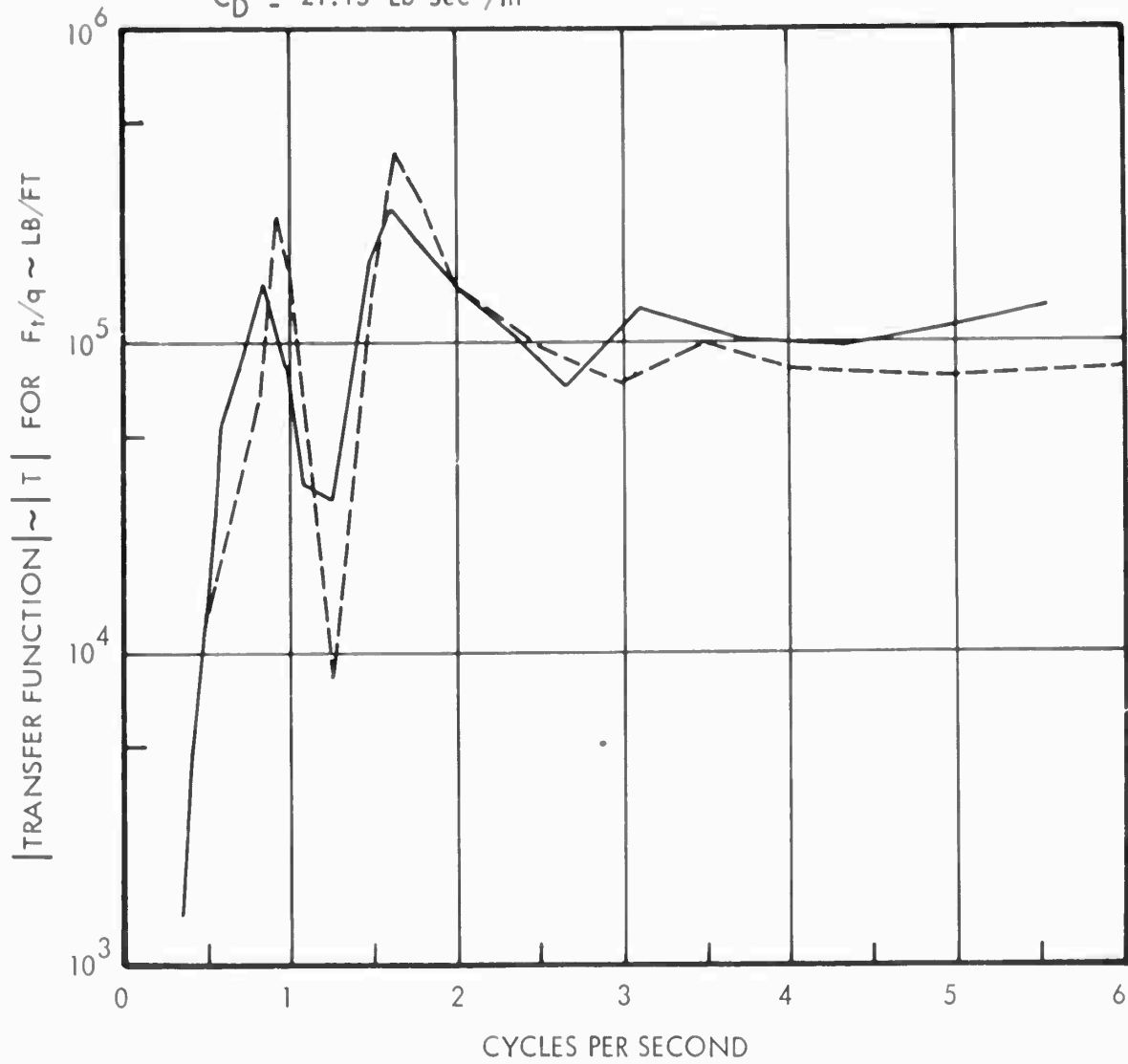


FIGURE 142 : Comparison Between Linear and Nonlinear Tire Force Transfer Functions with Increased Strut Damping

Tire Pressure = 90 psi  
 $V_H = 88$  fps

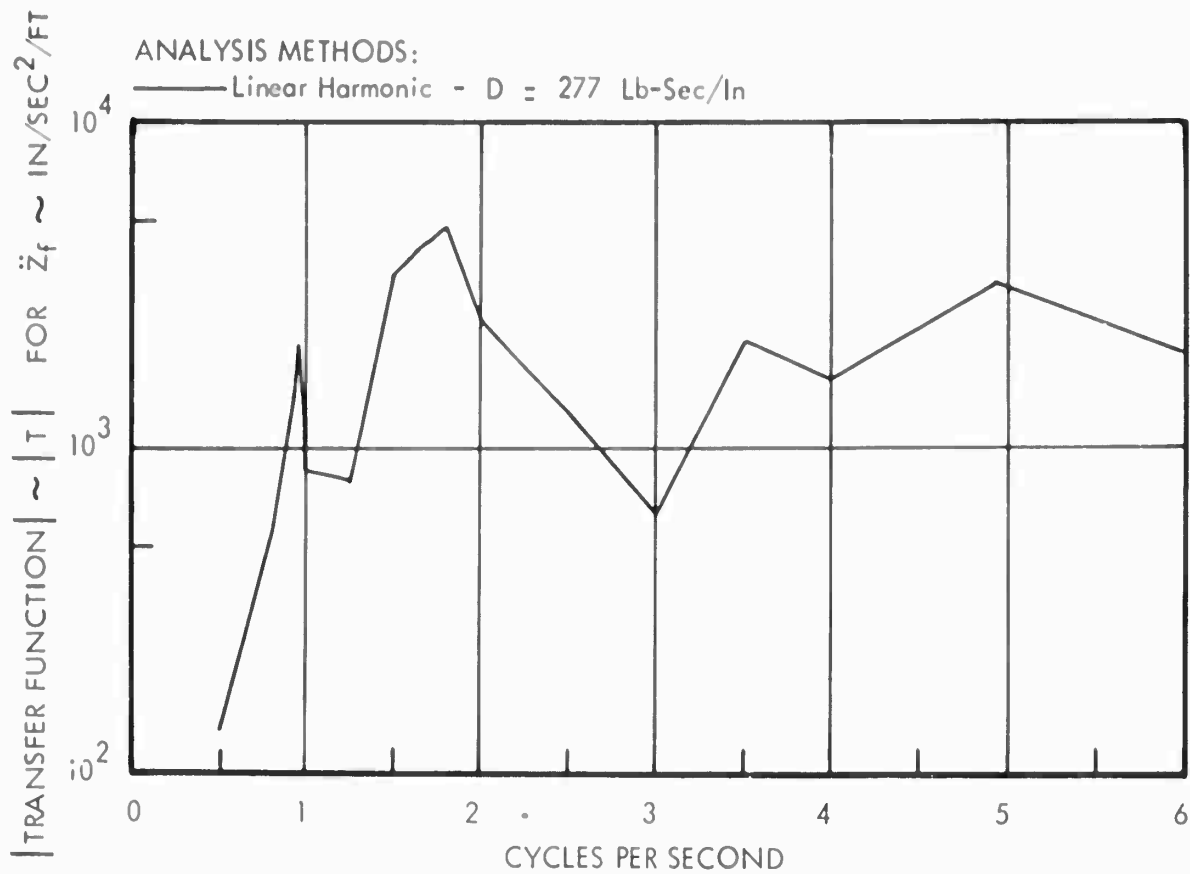


FIGURE 143 : Transfer Function for Vertical Acceleration of Airplane Center of Gravity

Single Gear Analysis

Tire Pressure = 90 psi  
 $V_H = 88$  fps

ANALYSIS METHODS:

— Linear Harmonic -  $D = 277$  LB-SEC/IN

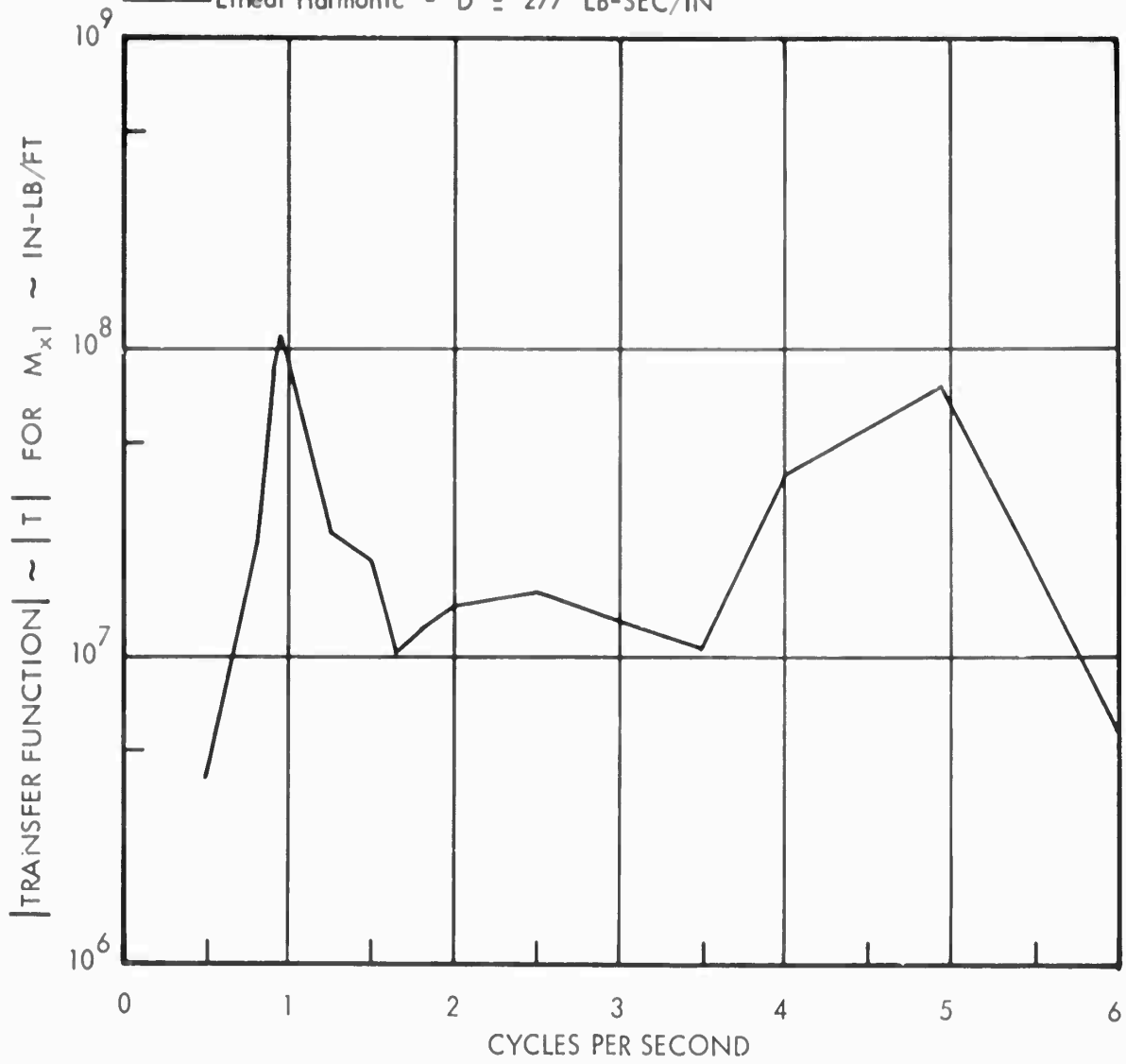


FIGURE 144 : Transfer Function for Wing Root Bending Moment  
Single Gear Analysis

Tire Pressure = 90 psi  
 $V_H = 88$  fps

ANALYSIS METHODS:

— Linear Harmonic -  $D = 277$  Lb-Sec/In

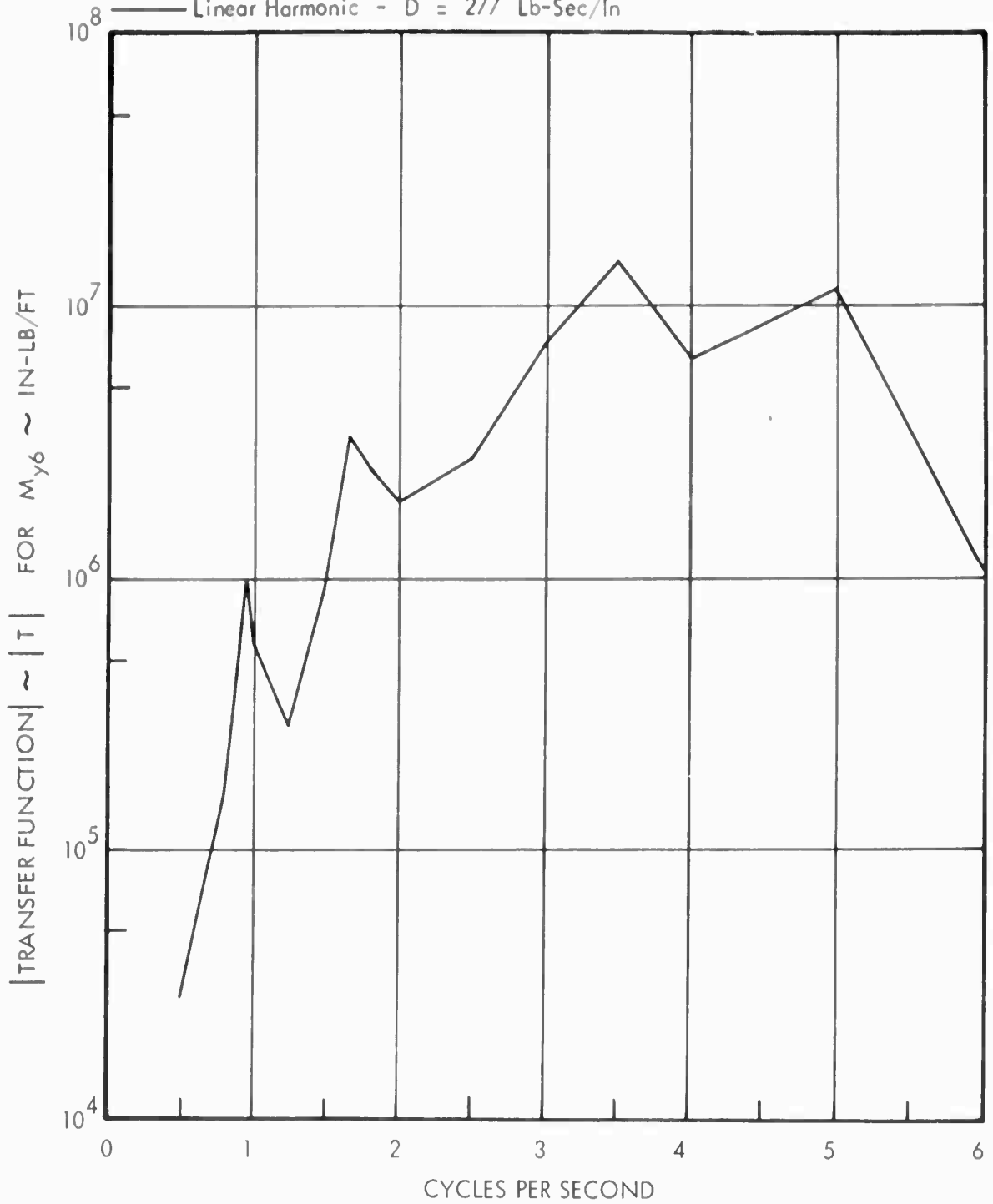


FIGURE 145 : Transfer Function for Wing Torsion Moment Inboard of Outboard Nacelle

Single Gear Analysis

Tire Pressure = 90 psi  
 $V_H = 88$  fps

ANALYSIS METHODS:

— Linear Harmonic -  $D = 93$  Lb-Sec/In

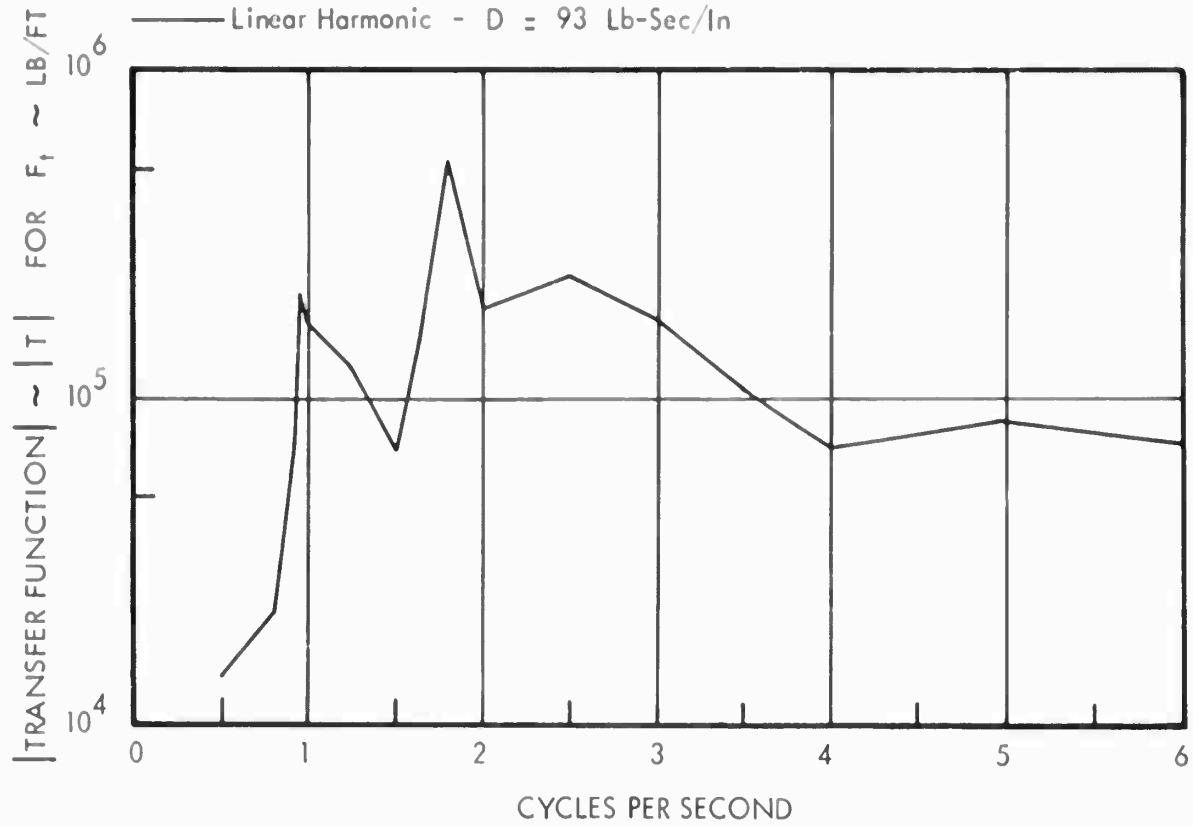


FIGURE 146 : Transfer Function for Landing Gear Tire Force  
Single Gear Analysis

Tire Pressure = 90 psi  
 $V_H = 88$  fps

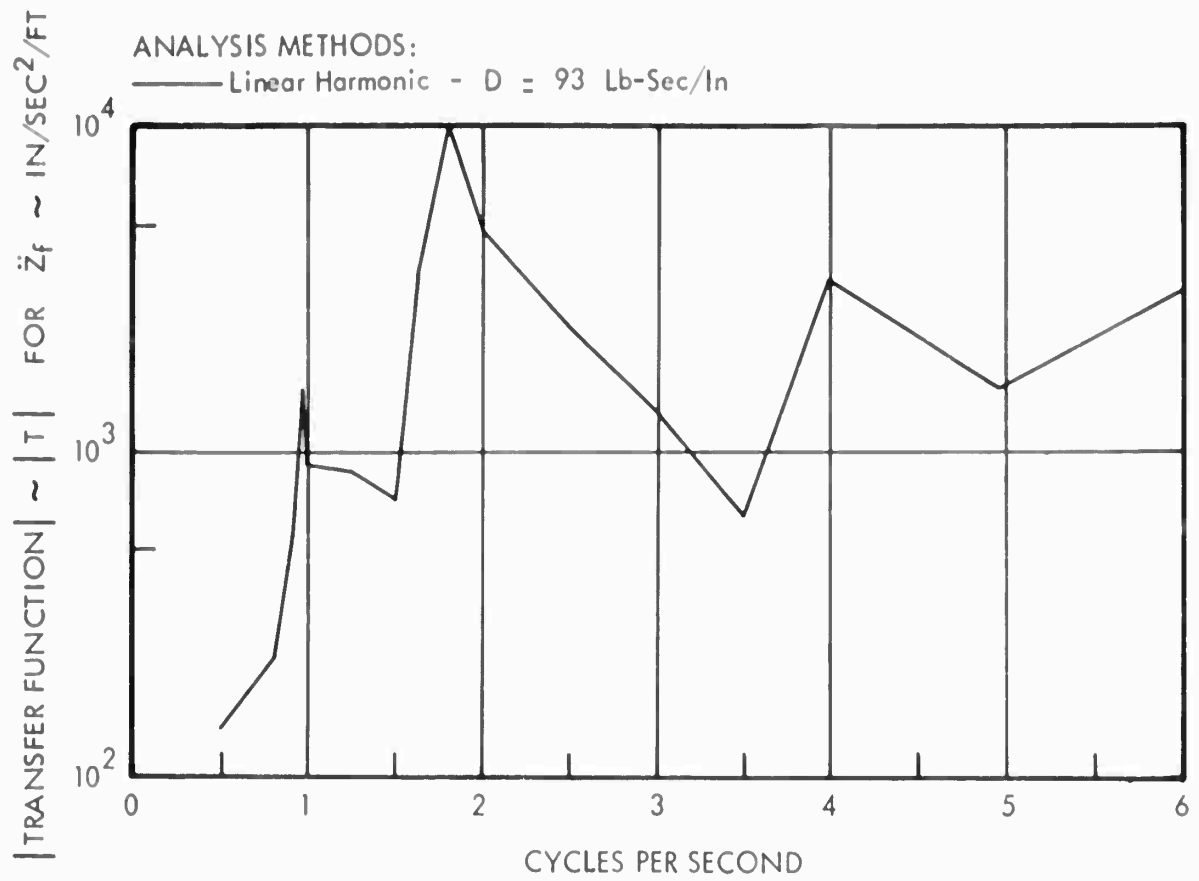


FIGURE 147 : Transfer Function for Vertical Acceleration of Airplane  
Center of Gravity  
Single Gear Analysis

Tire Pressure = 90 psi  
 $V_H = 88$  fps

ANALYSIS METHODS:

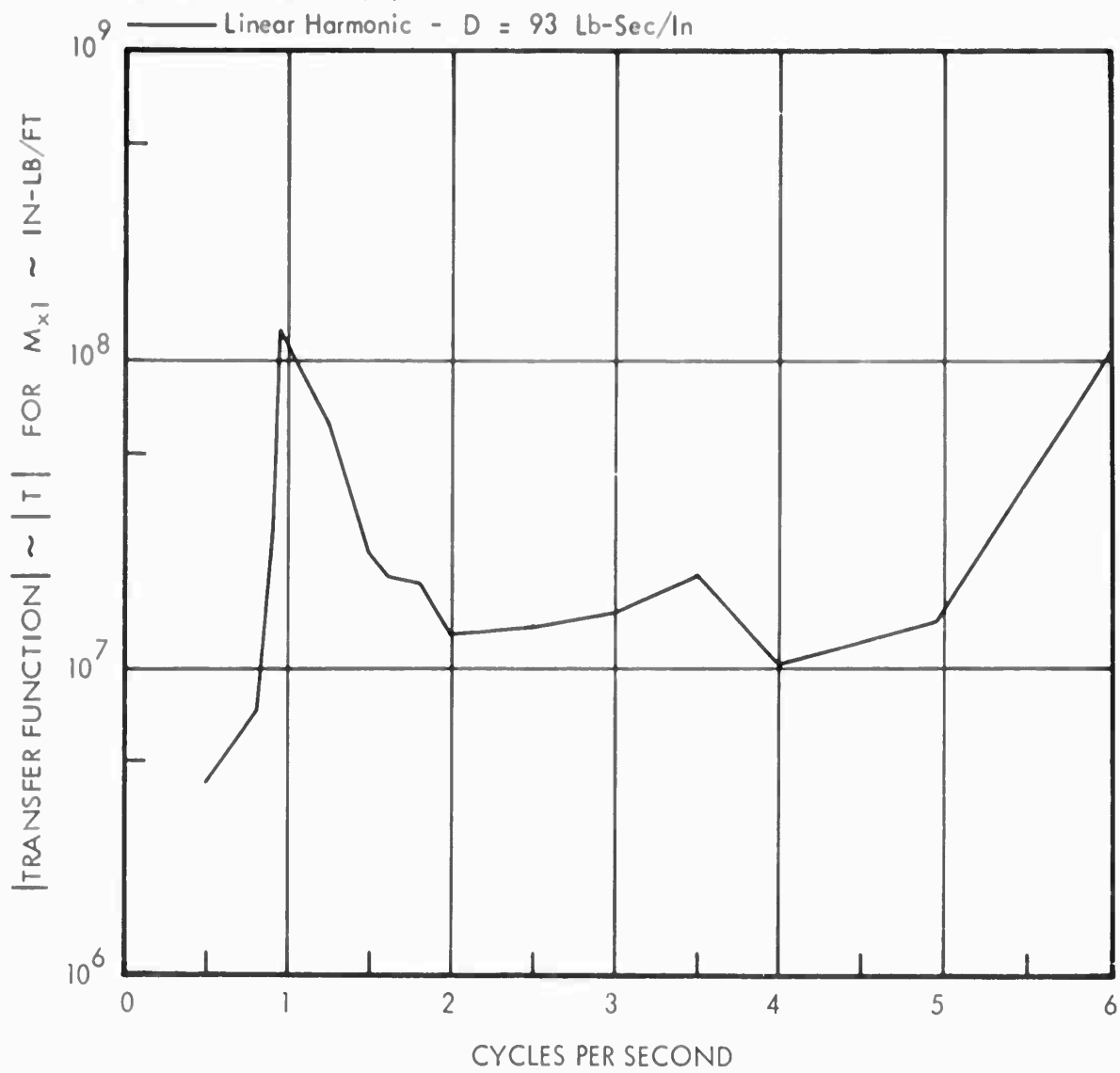


FIGURE 148 : Transfer Function for Wing Root Bending Moment  
Single Gear Analysis

Tire Pressure = 90 psi  
 $V_H = 88$  fps

ANALYSIS METHODS:

— Linear Harmonic -  $D = 93$  Lb-Sec/In

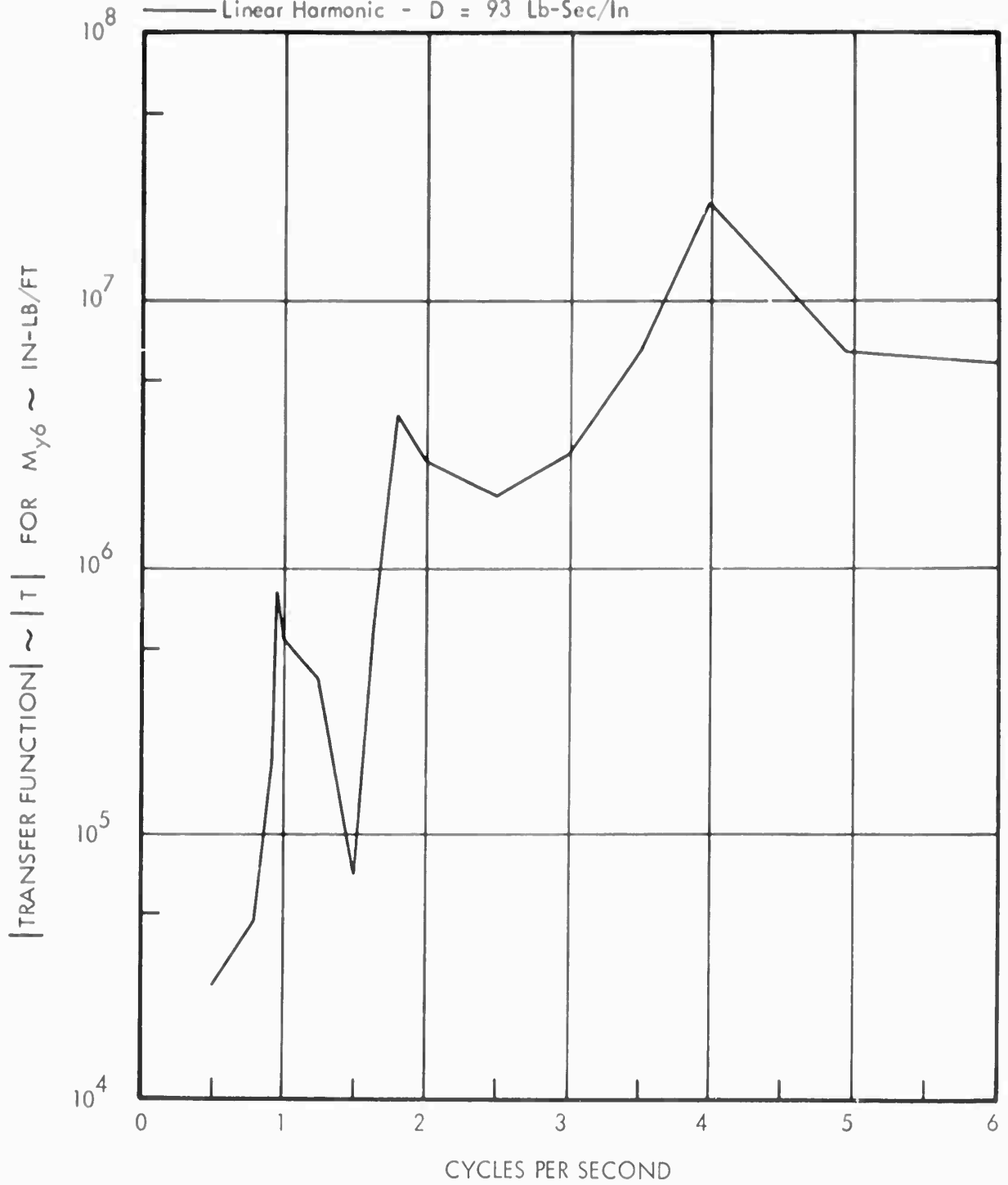


FIGURE 149 : Transfer Function for Wing Torsion Moment Inboard of Outboard Nacelle

Single Gear Analysis

APPENDIX G

FIRST APPROXIMATION TO THE LINEARIZED STRUT DAMPER

## FIRST APPROXIMATION TO THE LINEARIZED STRUT DAMPER

In the event that the nonlinear system solutions in the form of steady state time histories are not available, the following approximate method may be used to determine an equivalent  $D$  for a given  $C_D$ :

- (1) Assume that for stationary random response,  $\sigma_{\dot{z}} \approx \omega \sigma_z$ , where  $\sigma_z$  is the root-mean-square value of center of gravity acceleration. This relation is precisely true for pure harmonic functions; and it probably approaches validity for random functions with only one or two sharp resonant peaks in the neighborhood of the assumed value of  $\omega$ . Reference 12 derives a related function which implies that  $\dot{\Phi} = \omega^2 \Phi$  for stationary random data; and the application of this in Equation 57 of the text seems to indicate that the relationship in (1) is qualitatively plausible.
- (2) For frequencies of excitation away from resonances corresponding to the unsprung mass of the lower strut ( $f = 20$  cps), and the rigid body mode ( $f = 1.25$  cps) as sprung through the tires to the ground, an approximation to root-mean-square strut velocity,  $\sigma_{\dot{z}}$ , can be made by assuming  $\sigma_{\dot{z}} \approx \sigma_{\dot{s}}$ . (An analysis of elementary frequency response curves, such as in Reference 9, also suggest this, since  $\dot{s} = \dot{z}_f - \dot{z}_u$  and, at low frequencies,  $z_u$  will have very low amplitude response).

If the coupled resonant frequencies of the transformed three mass system, Appendix C, are chosen for analysis of damping in the strut, the above assumptions will be approximately valid, since these frequencies are about equidistant on either side of the low frequency, rigid-mode, single-degree-of-freedom resonance point. The relation in (1) may then be expressed as

$$\frac{\sigma_{\dot{z}}}{\omega} \approx \sigma_s \quad (G.1)$$

- (3) Assume the linear and nonlinear systems are to have the same maximum positive strut force and maximum velocity, i.e.

$$D \dot{s}_{L \max} = C_D \dot{s}_{NL \max}^2 \quad ; \quad \dot{s}_{L \max} = \dot{s}_{NL \max} \quad (G.2)$$

- (4) Use the relationship, from Reference 11, for the average peak values, such as:

$$\dot{z}_{\max \text{ avg}} = \sqrt{2} \sigma_{\dot{z}} \quad (G.3)$$

or,

$$\dot{s}_{\max_{\text{ovg}}} = \sqrt{2} \sigma_{\dot{s}} \quad (\text{G.4})$$

$$\begin{aligned} \text{then, } D &= C_D \dot{s}_{\text{NL}_{\max}} \\ &= \sqrt{2} C_D \frac{\sigma_{\dot{s}}}{\omega} \end{aligned} \quad (\text{G.5})$$

The right hand side of equation (G.5) will be completely known, thus allowing the calculation of an approximation to D.

The following is a calculation of D using the above outlined method for the subject nonlinear system: Assuming the standard configuration of a taxi speed,

$V_H = 88 \text{ ft/sec}$ , the following is known,

$$C_D = 14.1 \text{ lb-sec}^2/\text{in}^2$$

$$\sigma_{\dot{s}} = 64.0 \text{ in/sec}^2 \text{ (See Figure 116 in the text)}$$

Equation (G.5) may be evaluated at the significant resonant frequencies,  $f = .95$  and  $1.67 \text{ cps}$ .

Thus:

$$\text{@ } .95 \text{ cps } D = \frac{(1.41) (14.1) (64.0)}{(.95) (2)}$$

$$= 216 \text{ lb-sec/in}$$

$$\text{@ } 1.67 \text{ cps } D = \frac{(1.41) (14.1) (64.0)}{(1.67) (2)}$$

$$= 123 \text{ lb-sec/in}$$

the average of these values is then the desired value,

$$D = \frac{216 + 123}{2}$$

or

$$D = 170 \text{ lb-sec/in}$$

which compares favorably with the value of  $185 \text{ lb-sec/in}$  derived in the text.

It should be noted that test data on Air Force runway X, in Reference 11, would give a value of  $\sigma_z \approx 64$  in/sec<sup>2</sup> at an average taxi speed. Such values could be obtained from several sources for making estimates as demonstrated.

APPENDIX H

ANALYSIS OF THE SIMPLIFIED TWO DEGREES OF FREEDOM SYSTEM

The equivalent three mass system referred to in the text may be simplified to a two mass, undamped system for purposes of qualitative study involving system resonances. This simplification yields additional insight as to the basic dynamic phenomena involved in this problem.

Since the mass  $M_U$  is small, it may be neglected along with the relatively small system damping which cannot effect frequencies greatly. Therefore the springs  $K_a$  and  $K_t$  may be combined in series to give a single equivalent spring  $K_f$ , as follows:

$$K_f = \frac{K_a K_t}{K_a + K_t} \quad (H.1)$$

The equations of motion for the resulting system are then,

$$M_f \ddot{Z}_f + (K_f + K_s)Z_f - K_s Z_s = F_o \sin \omega t \quad (H.2)$$

$$M_s \ddot{Z}_s + K_s(Z_s - Z_f) = 0 \quad (H.3)$$

where  $F_o = K_f q_{\max}$ .

Equations (H.2) and (H.3) are discussed in detail in Reference 9, but the salient points will be summarized herein.

The solution of this system is given by

$$Z_f = Z_{fm} \sin \omega t \quad (H.4)$$

$$Z_s = Z_{sm} \sin \omega t$$

with  $Z_{fm}$  and  $Z_{sm}$  defined as the maximum magnitudes of  $Z_f$  and  $Z_s$  respectively and,

$$\frac{Z_{fm}}{Z_{static}} = \frac{1 - \frac{\omega^2}{\omega_s^2}}{\left(1 - \frac{\omega^2}{\omega_s^2}\right) \left(1 - \frac{K_s}{K_f} - \frac{\omega^2}{\omega_f^2}\right) - \frac{K_s}{K_f}} \quad (H.5)$$

where  $Z_{static} = F_o / K_f$

$$\frac{Z_{sm}}{Z_{static}} = \frac{1}{\left(1 - \frac{\omega^2}{\omega_s^2}\right) \left(1 + \frac{K_s}{K_f} - \frac{\omega^2}{\omega_f^2}\right) - \frac{K_s}{K_f}} \quad (H.6)$$

where

$$\omega_f = \sqrt{\frac{K_f}{M_f}} \quad , \quad \omega_s = \sqrt{\frac{K_s}{M_s}}$$

Figure 150 shows a three dimensional model representing the response,  $Z_f$ , of the mass,  $M_f$ , in a range of frequency near its resonant frequency. The mass ratio  $M_s/M_f$  is held constant at .10. The figure then shows that when the ratio of absorber frequency,  $\omega_s$ , to drive frequency,  $\omega_o$ , is made equal to 1.0, the response peak for  $M_f$ , the "main mass," is greatly attenuated. As  $\omega$  is varied, with  $\omega_f$  the same order of magnitude as  $\omega_s$ , it can be seen from the figure that  $Z_f$  passes through two resonant peaks on both sides of a null point. As observed in the text, this situation is indicative of the response of the center of gravity acceleration of the vehicle under study.

In the special situation where  $\omega_s = \omega_f$ , when  $\omega_o$  approaches  $\omega_s$ , the response of  $M_f$  as given by equation (H.5) and goes to zero, and the response of  $M_s$  as given by equation (H.6) goes to  $(-K_f/K_s)$ . Equations (H.5) and (H.6) for the case  $\omega_s = \omega_f$ , may be written as a function of drive frequency and mass ratio,  $\mu = M_s/M_f$  as follows:

$$\frac{Z_f}{Z_{static}} = \frac{\left(1 - \frac{\omega^2}{\omega_s^2}\right)}{\left(1 - \frac{\omega^2}{\omega_s^2}\right) \left(1 + \mu - \frac{\omega^2}{\omega_s^2}\right) - \mu} \quad (H.7)$$

$$\frac{Z_s}{Z_{static}} = \frac{1}{\left(1 - \frac{\omega^2}{\omega_s^2}\right) \left(1 + \mu - \frac{\omega^2}{\omega_s^2}\right) - \mu} \quad (H.8)$$

The denominators of (H.7) and (H.8) are identical, indicating that both  $M_s$  and  $M_f$  have the same resonant frequencies. These frequencies are determined by setting the denominator equal to zero and solving for the frequencies,

$$\left(1 - \frac{\omega^2}{\omega_s^2}\right) \left(1 + \mu - \frac{\omega^2}{\omega_s^2}\right) - \mu = 0 \quad (H.9)$$

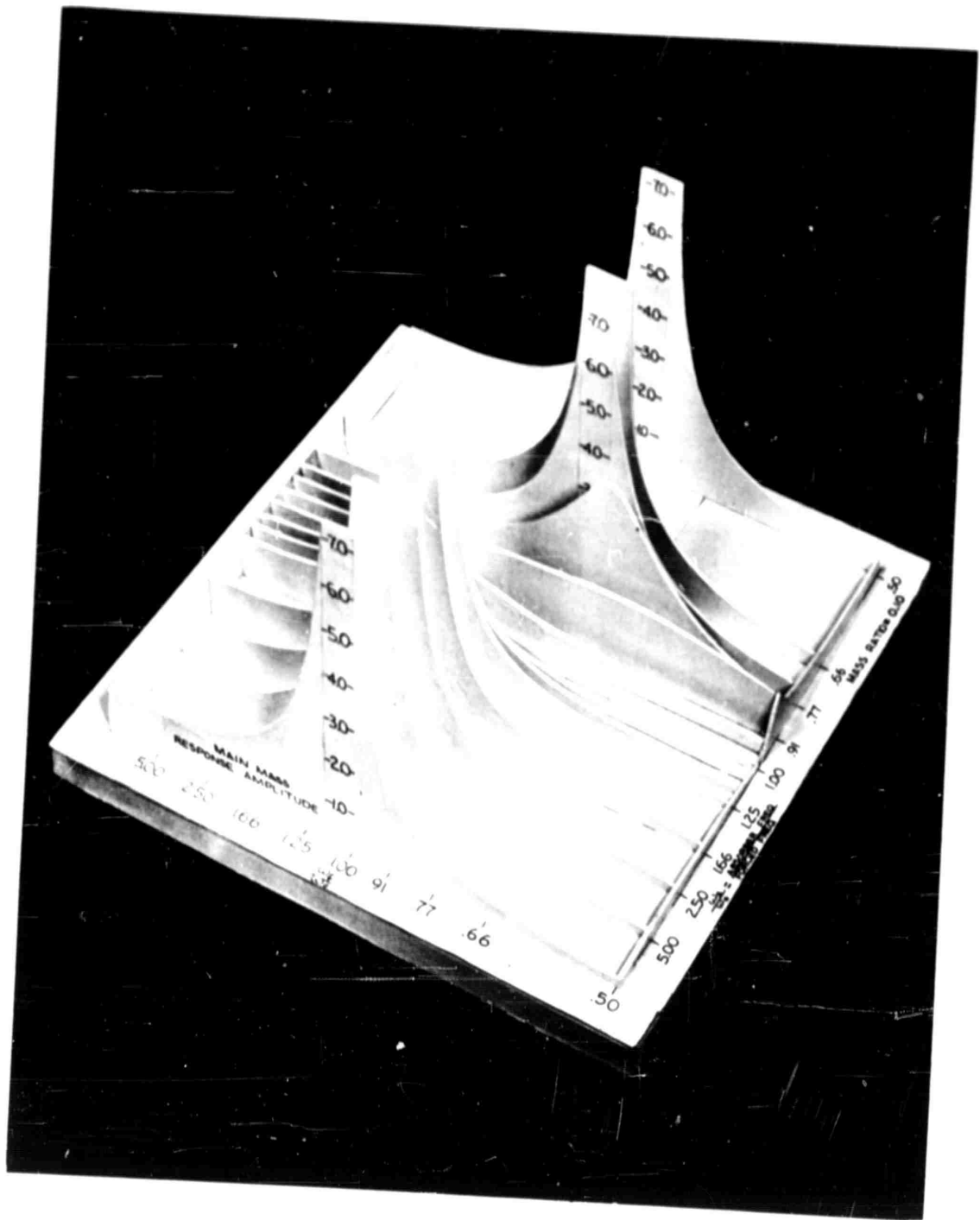


FIGURE 150: Typical Two-Degree-Of-Freedom System Resonance Curves (Undamped)

or,

$$\left(\frac{\omega}{\omega_s}\right)^4 - \left(\frac{\omega}{\omega_s}\right)^2 (2 + \mu) + 1 = 0 \quad (\text{H.10})$$

with the solutions

$$\left(\frac{\omega}{\omega_s}\right)^2 = \left(1 + \frac{\mu}{2}\right) \pm \left(\mu + \frac{\mu^2}{4}\right) \quad (\text{H.11})$$

These solutions are shown graphically in Figure 151. To relate this result to the response curves shown in Figure 150, take  $\mu = .10$ . From Figure 151 this gives resonant frequencies at 1.17 and .85 times the natural frequency. Since  $\omega = \omega_f$ , enter Figure (H.1) at 1/1.17 on both the  $\omega_f/\omega_0$  and  $\omega_s/\omega_0$  scales, this shows a resonant peak existing for these coordinates. Similarly a peak is found for .85.

For  $\omega \neq \omega_f$ , the resonant frequencies are determined by solving the response equations (H.5) and (H.6), so that each resonant frequency is a function of both  $\omega_s$  and  $\omega_f$  for a known mass ratio.

For the equivalent example airplane system, the frequencies are obtained as follows:

the equivalent main mass spring constant (for 1/2 airplane) is,

$$\begin{aligned} K_f &= \frac{K_a K_t}{K_a + K_t} = \frac{(2)(14,170)(8330)}{14,170 + 8330} \\ &= 10,480 \text{ Lb/In} \end{aligned}$$

and,

$$M_s = 44 \text{ Lb-Sec}^2/\text{In.}$$

$$M_f = 122 \text{ Lb-Sec}^2/\text{In.}$$

$$K_s = 2055 \text{ Lb/In.}$$

$$\omega_s = \sqrt{\frac{K_s}{M_s}} = 6.82 \text{ Rad/Sec,}$$

$$\omega_f = \sqrt{\frac{K_f}{M_f}} = 9.25 \text{ Rad/Sec}$$

Figure 151 may be used to an approximation if the above frequencies are averaged,

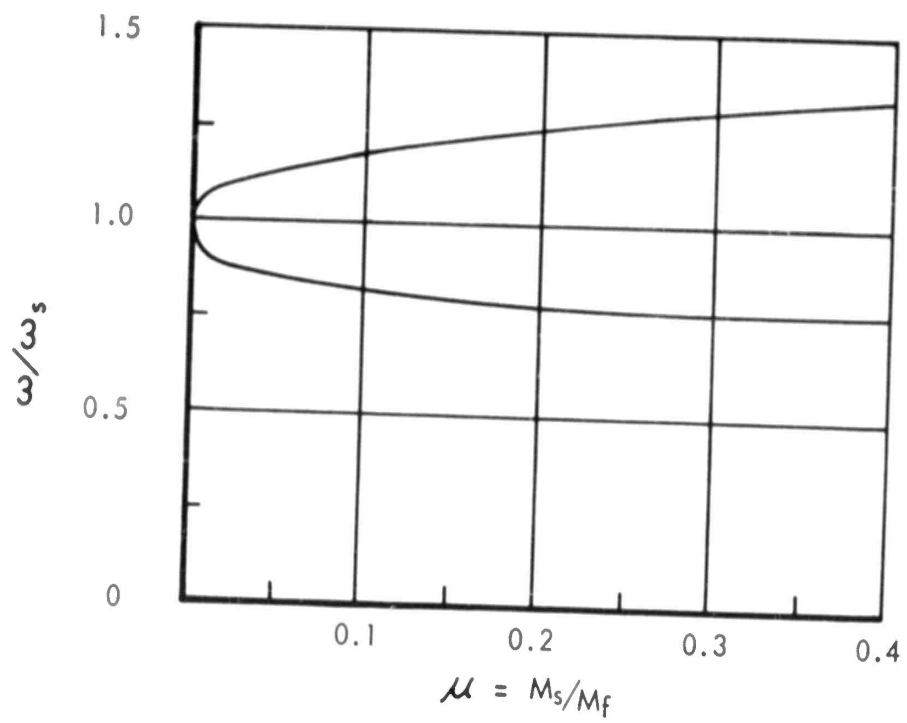


FIGURE 151 : Main Mass Resonant Frequencies as a Function of Mass Ratio for  $\omega_s \approx \omega_f$

$$\bar{\omega} = \frac{\omega_s + \omega_f}{2} = \frac{6.28 + 9.25}{2} = 8.04 \text{ Rad/Sec}$$

Also, the mass ratio is

$$\mu = \frac{M_s}{M_f} = .36$$

and from Figure 151 the resonance points may be obtained at .947 cps and 1.69 cps. Using equations (H.5) and (H.6) (i.e. the denominator) gives the solutions,

$$\omega^2 = \frac{\left[ \omega_f^2 + (1 + \mu) \omega_s^2 \right]}{2} \pm \left[ \frac{\left( \omega_f^2 + (1 + \mu) \omega_s^2 \right)^2}{4} - \omega_s^2 \omega_f^2 \right]^{1/2} \quad (\text{H.12})$$

yielding resonances at .941 cps and 1.69 cps; therefore, averaging the frequencies  $\omega_s$  and  $\omega_f$  and using Figure 151 to estimate resonances results in negligible error for a moderate range of values when  $\omega_s \neq \omega_f$ .

APPENDIX I  
COMPARISONS WITH  
ALTERNATIVE METHODS OF ANALYSIS

## COMPARISONS WITH ALTERNATIVE METHODS OF ANALYSIS

The feasibility and usefulness of two alternative methods for the determination of nonlinear system transfer functions have been examined as part of this program. Fourier series harmonic analysis and cross-spectral analysis may both be included in the broad category of generalized harmonic analyses along with power spectral techniques. Thus, results of these several methods will be compared briefly in this appendix.

### 1. Nonlinear Harmonic Analysis

This section presents the principal results of the Fourier harmonic analysis of the nonlinear system discussed in the text. Note that in Tables 6 through 8 the fundamental harmonic is always defined as being of the same frequency as the force exciting the system. Both the amplitudes and phase angles are tabulated for the harmonics which contribute most of the response.

Figures 152, 153 and 154 are shown for comparison of the amplitudes of the nonlinear transfer function obtained by PSD methods with the amplitudes of the same function calculated from peak-to-peak readings as discussed in the text.

Also shown on the figures is the amplitudes including the summation of all the harmonics from 1 to 10, regardless of phase angle, to see if any improvement can be obtained by this method. Since no improvement over the linearized results of the text can be observed, the method does not seem to be warranted.

### 2. Cross-Spectral Analysis of the Nonlinear System

Cross-spectral density analysis as defined in the text, could conceivably add new information through its cognizance of system phase relationships. However, comparisons with the PSD method in Figures 155 through 159 show no marked differences. Apparently the added complexity of cross-spectral analysis merely tends to add to random scatter in data reduction, and makes no significant contribution to nonlinear frequency response studies.

TABLE 6

(TRANSFER FUNCTIONS FOR TIRE FORCE, LB/FT)

Nonlinear Response Ultra-Harmonic Number		Applied Excitation Frequency, cps					
		$f_1 = 1.0$	$f_2 = 1.25$	$f_3 = 1.5$	$f_4 = 1.7$	$f_5 = 2.0$	$f_6 = 3.25$
Fundamental (0)	Amplitude	$1.96 \times 10^5$	$1.38 \times 10^4$	$1.02 \times 10^5$	$3.51 \times 10^5$	$1.75 \times 10^4$	$6.97 \times 10^4$
	Phase,deg.	207.0	260.0	344.0	255.0	196.0	187.0
(1)	Amplitude	$3.72 \times 10^4$	$0.76 \times 10^2$	$7.56 \times 10^3$	$5.86 \times 10^4$		
	Phase,deg.	212.0	6.0	304.0	307.0		
(2)	Amplitude	$5.12 \times 10^3$	$0.92 \times 10^2$				
	Phase,deg.	208.0	12.0				

TABLE 7

(TRANSFER FUNCTIONS FOR WING ROOT BENDING MOMENT, IN-LB/FT

Nonlinear Response Ultra-Harmonic Number		Applied Excitation Frequency, cps					
		$f_1 = 1.0$	$f_2 = 1.25$	$f_3 = 1.5$	$f_4 = 1.7$	$f_5 = 2.0$	$f_6 = 3.25$
Fundamental (0)	Amplitude	$1.00 \times 10^8$	$2.87 \times 10^7$	$2.33 \times 10^7$		$1.32 \times 10^7$	$3.22 \times 10^7$
	Phase,deg.	19.0	124.0	324.0		17.0	192.0
(1)	Amplitude	$3.86 \times 10^6$	$4.24 \times 10^5$	$7.99 \times 10^5$			
	Phase,deg.	30.0	143.0	145.0			
(2)	Amplitude	$1.31 \times 10^6$	$3.04 \times 10^5$				
	Phase,deg.	12.0	138.0				

TABLE 8

(TRANSFER FUNCTIONS FOR WING TORSION MOMENT AT OUTBOARD NACELLE, IN-LB/FT)

Nonlinear Response Ultra-Harmonic Number		Applied Excitation Frequency, cps					
		$f_1 = 1.0$	$f_2 = 1.25$	$f_3 = 1.5$	$f_4 = 1.7$	$f_5 = 2.0$	$f_6 = 3.25$
Fundamental (0)	Amplitude	$4.25 \times 10^6$	$8.43 \times 10^5$	$5.44 \times 10^5$	$4.75 \times 10^6$	$3.41 \times 10^6$	$1.89 \times 10^7$
	Phase,deg.	206.0	302.0	359.0	243.0	202.0	45.0
(1)	Amplitude	$6.86 \times 10^5$	$1.63 \times 10^4$	$5.24 \times 10^5$	$1.46 \times 10^7$		
	Phase,deg.	208.0	353.0	314.0	106.0		
(2)	Amplitude	$9.6 \times 10^4$	$1.89 \times 10^4$				
	Phase,deg.	217.0	181.0				

ANALYSIS METHODS:

Nonlinear PSD

○  $V_H = 66$  Ft/Sec

Nonlinear Harmonic

□  $V_H = 55$  Ft/Sec (Peak to Peak)

△  $V_H = 55$  Ft/Sec (Summed Harmonics)

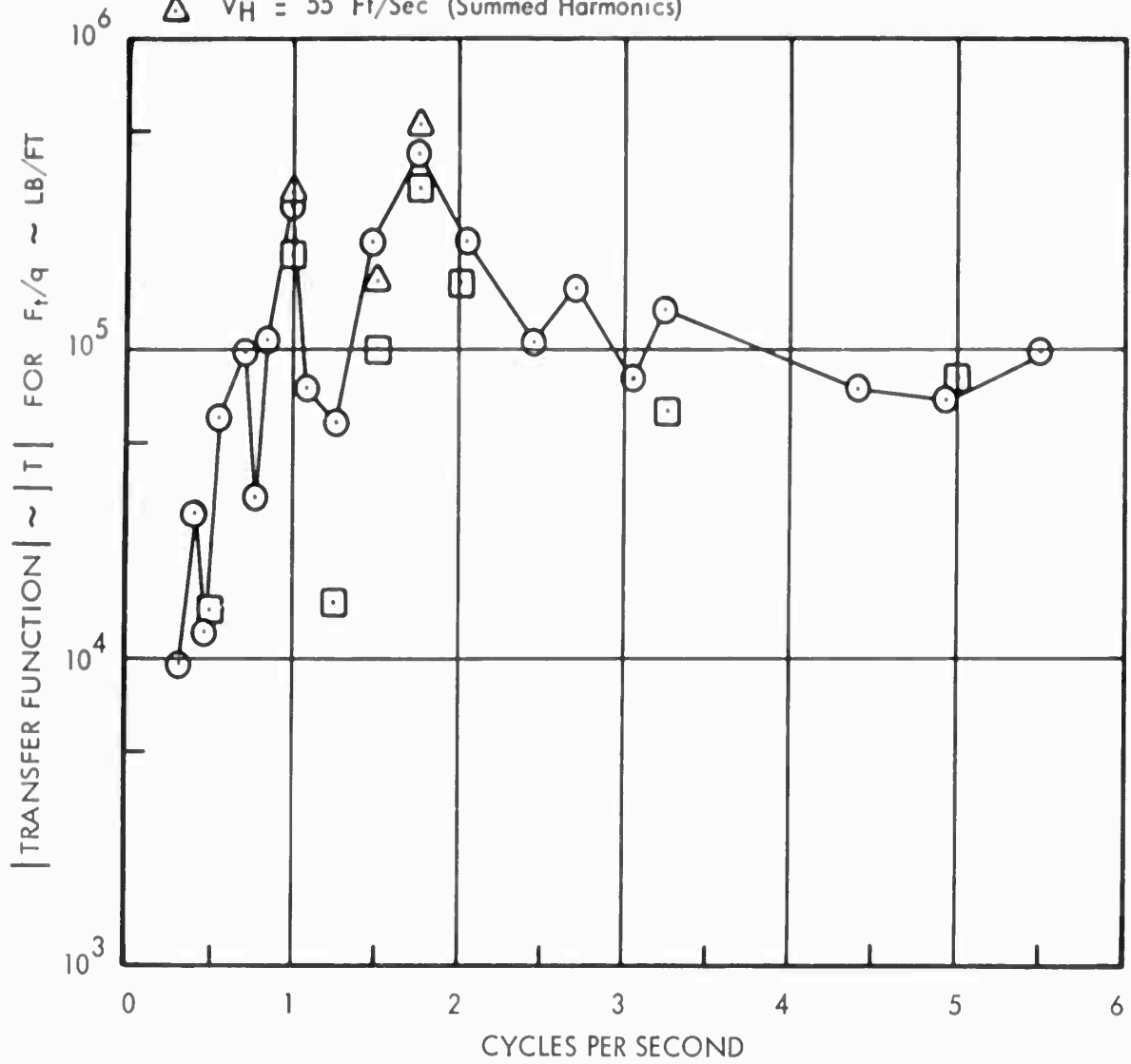


FIGURE 152 : Comparison of Transfer Functions from the Nonlinear PSD and the Nonlinear Harmonic Methods for Main Gear Tire Force  
Single Gear Analysis for Normal Configuration

ANALYSIS METHODS:

Nonlinear PSD

○  $V_H = 66$  Ft/Sec

Nonlinear Harmonics

□  $V_H = 55$  Ft/Sec (Peak to Peak)

△  $V_H = 55$  Ft/Sec (Summed Harmonics)

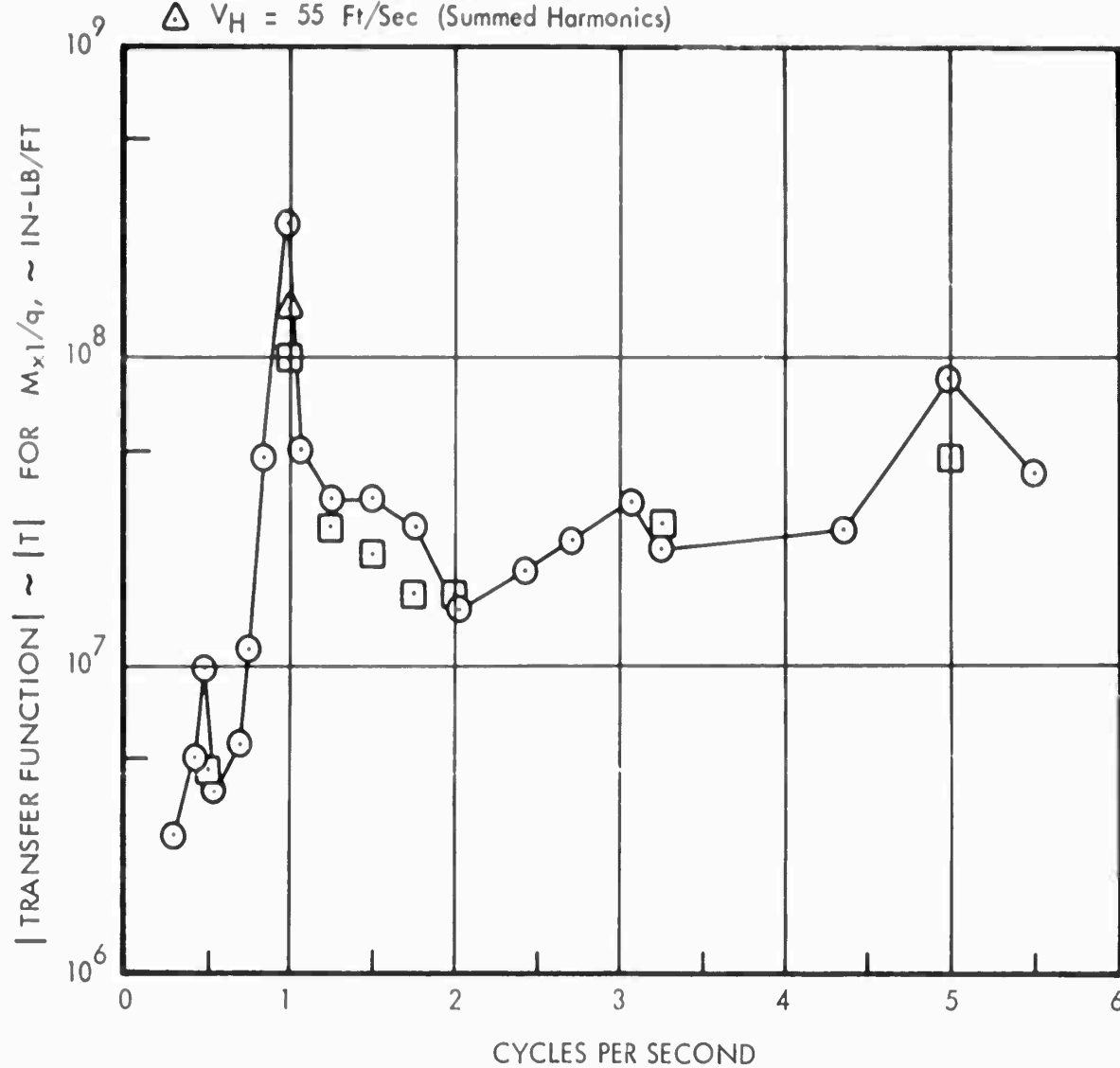


FIGURE 153 : Comparison of Transfer Functions from the Nonlinear PSD and the Nonlinear Harmonic Methods for Wing Root Bending Moment  
Single Gear Analysis for Normal Configuration

ANALYSIS METHODS:

Nonlinear PSD

○  $V_H = 66$  Ft/Sec

Nonlinear Harmonics

□  $V_H = 55$  Ft/Sec (Peak to Peak)

△  $V_H = 55$  Ft/Sec (Summed Harmonics)

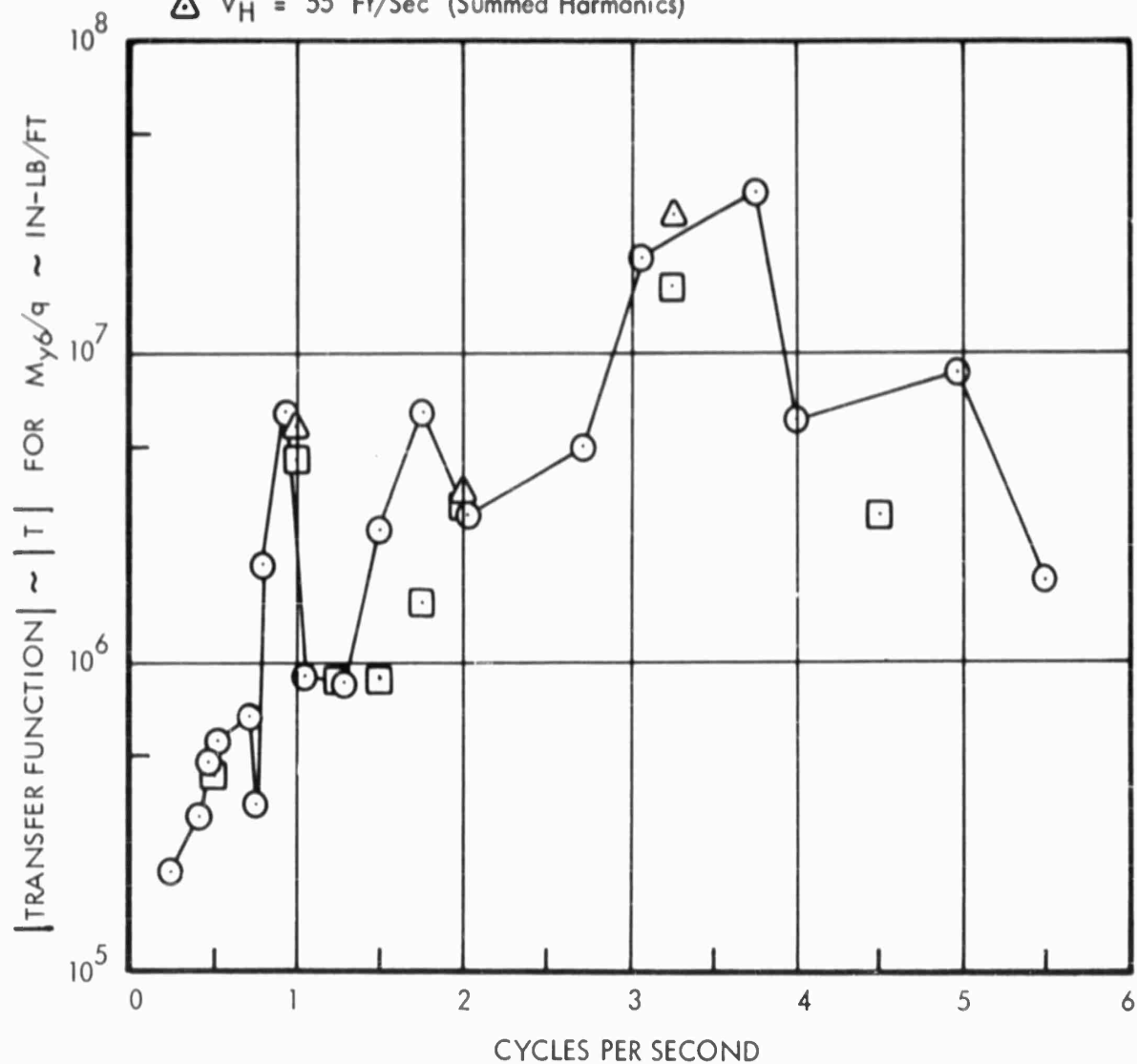


FIGURE 154 : Comparison of Transfer Functions from the Nonlinear PSD and the Nonlinear Harmonic Methods for Wing Torsion Moment Inboard of Outboard Nacelle

Single Gear Analysis for Normal Configuration

ANALYSIS METHODS:

----- Cross Spectral -  $V_H = 44 \text{ Ft/Sec}$   
 ——— Power Spectral -  $V_H = 44 \text{ Ft/Sec}$

Φ Input - q  
 Φ Output -  $F_{13}$

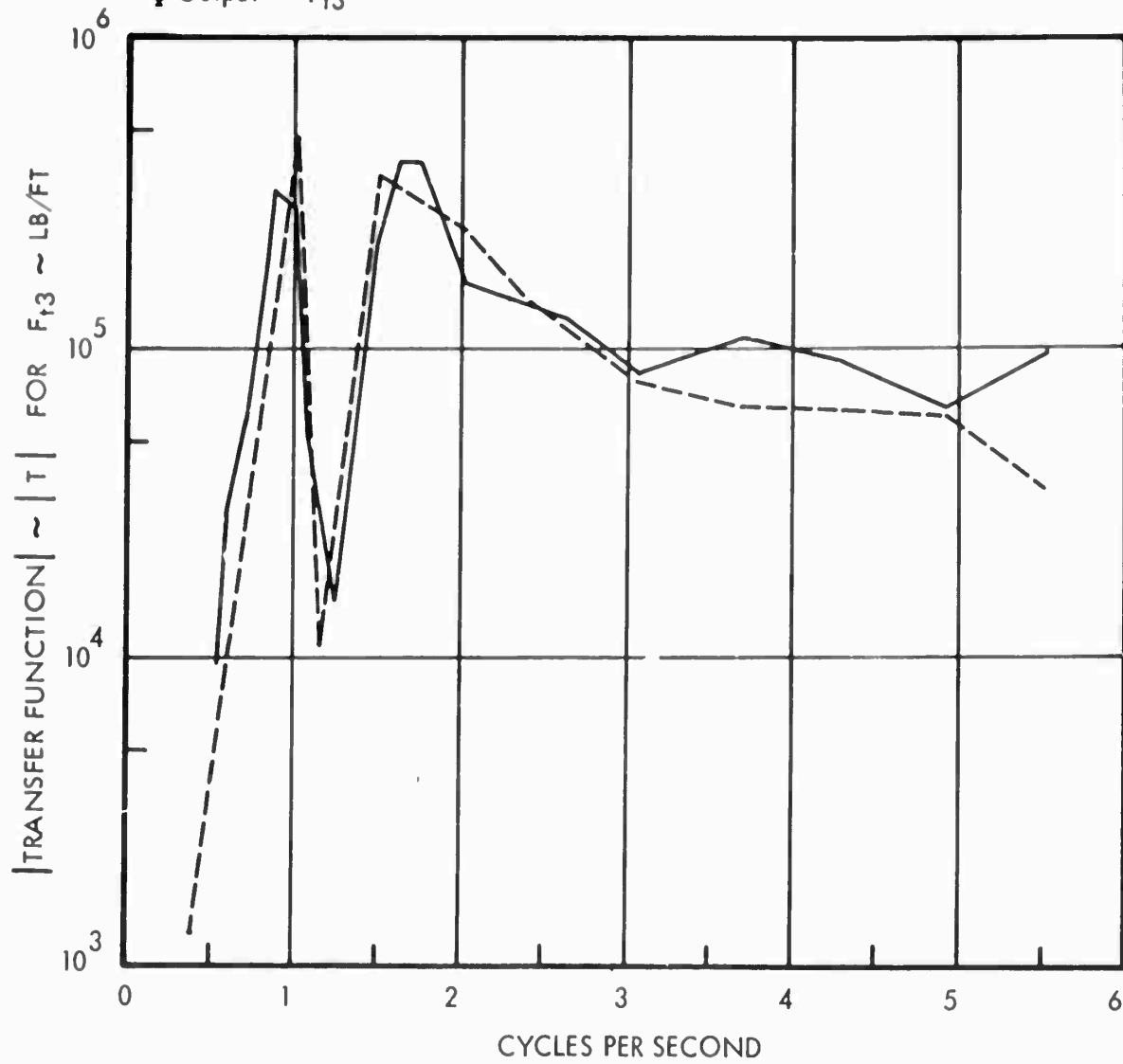


FIGURE 155 : Comparison of Transfer Function by Cross-Spectral and Power Spectral Methods for Rear Main Tire Force,  $F_{13}$   
 Multi-Gear Analysis for Normal Configuration

ANALYSIS METHODS:

----- Cross Spectral -  $V_H = 88 \text{ Ft/Sec}$

———— Power Spectral -  $V_H = 88 \text{ Ft/Sec}$

⊕ Input -  $q$

⊙ Output -  $F_{t3}$

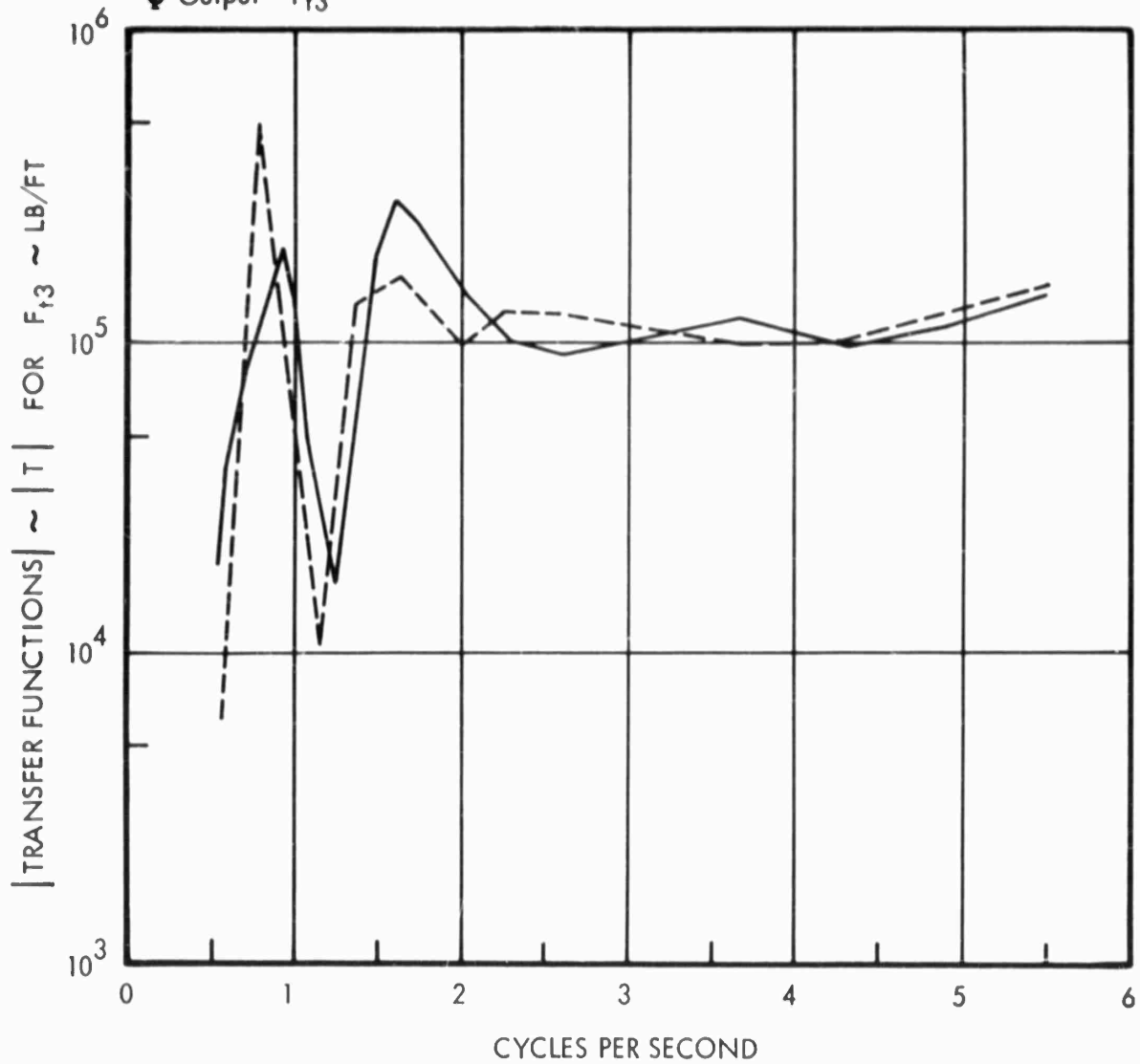


FIGURE 156 : Comparison of Transfer Functions by Cross-Spectral and Power Spectral Methods for Rear Main Tire Force,  $F_{t3}$   
Multi-Gear Analysis for Normal Configuration

ANALYSIS METHODS:

----- Cross Spectral -  $V_H = 44 \text{ Ft/Sec}$

———— Power Spectral -  $V_H = 44 \text{ Ft/Sec}$

⊙ Input -  $q$   
 ⊙ Output -  $\ddot{z}_f$

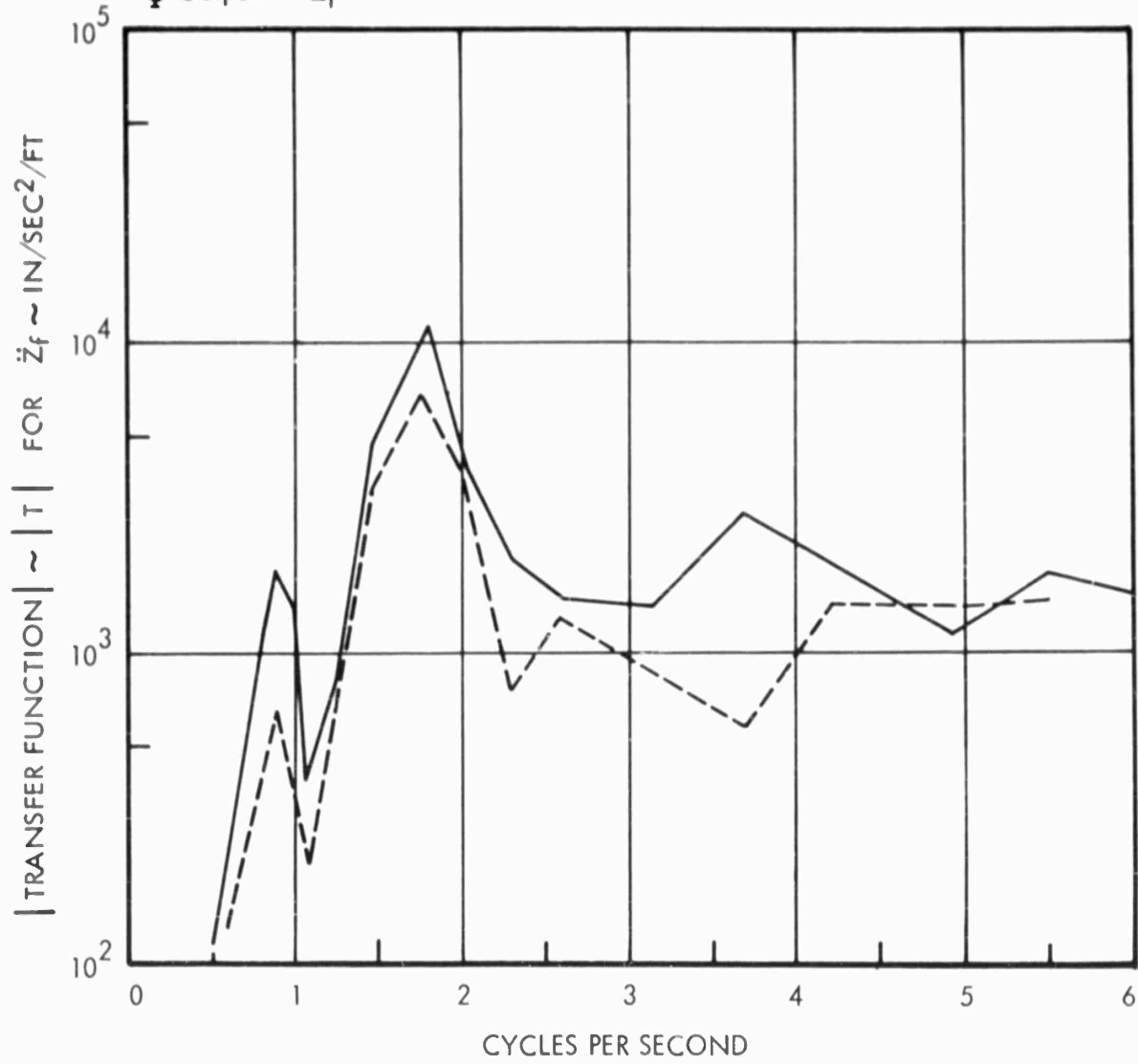


FIGURE 157 : Comparison of Transfer Function by Cross-Spectral and Power Spectral Methods for Acceleration of Center of Gravity,  $\ddot{z}_f$   
 Multi-Gear Analysis for Normal Configuration

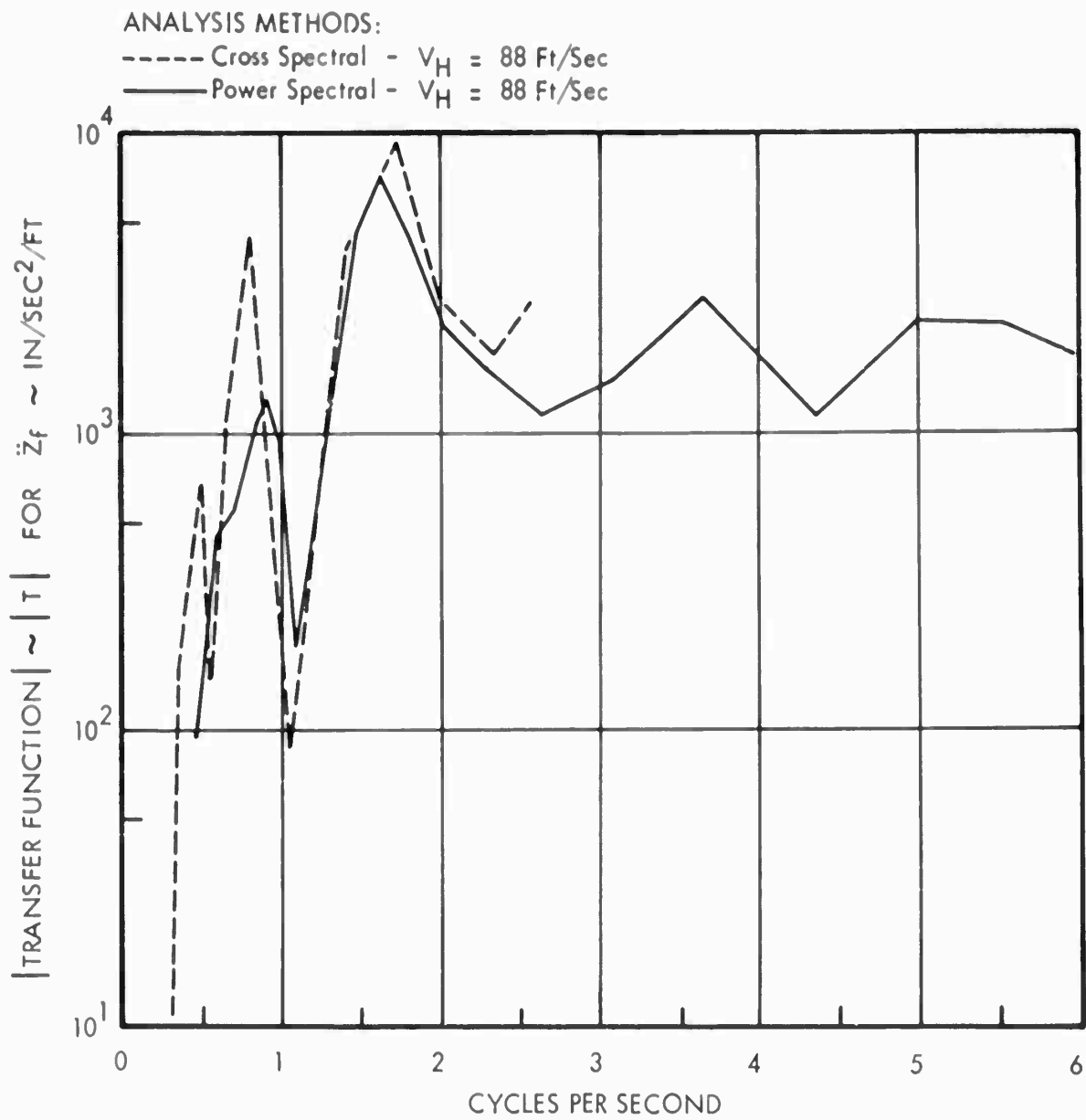


FIGURE 158 : Comparison of Transfer Functions by Cross-Spectral and Power Spectral Methods for Acceleration of Center of Gravity,  $\ddot{z}_f$   
 Multi-Gear Analysis for Normal Configuration

ANALYSIS METHODS:  
 ----- Cross Spectral -  $V_H = 22 \text{ Ft/Sec}$   
 \_\_\_\_\_ Power Spectral -  $V_H = 22 \text{ Ft/Sec}$

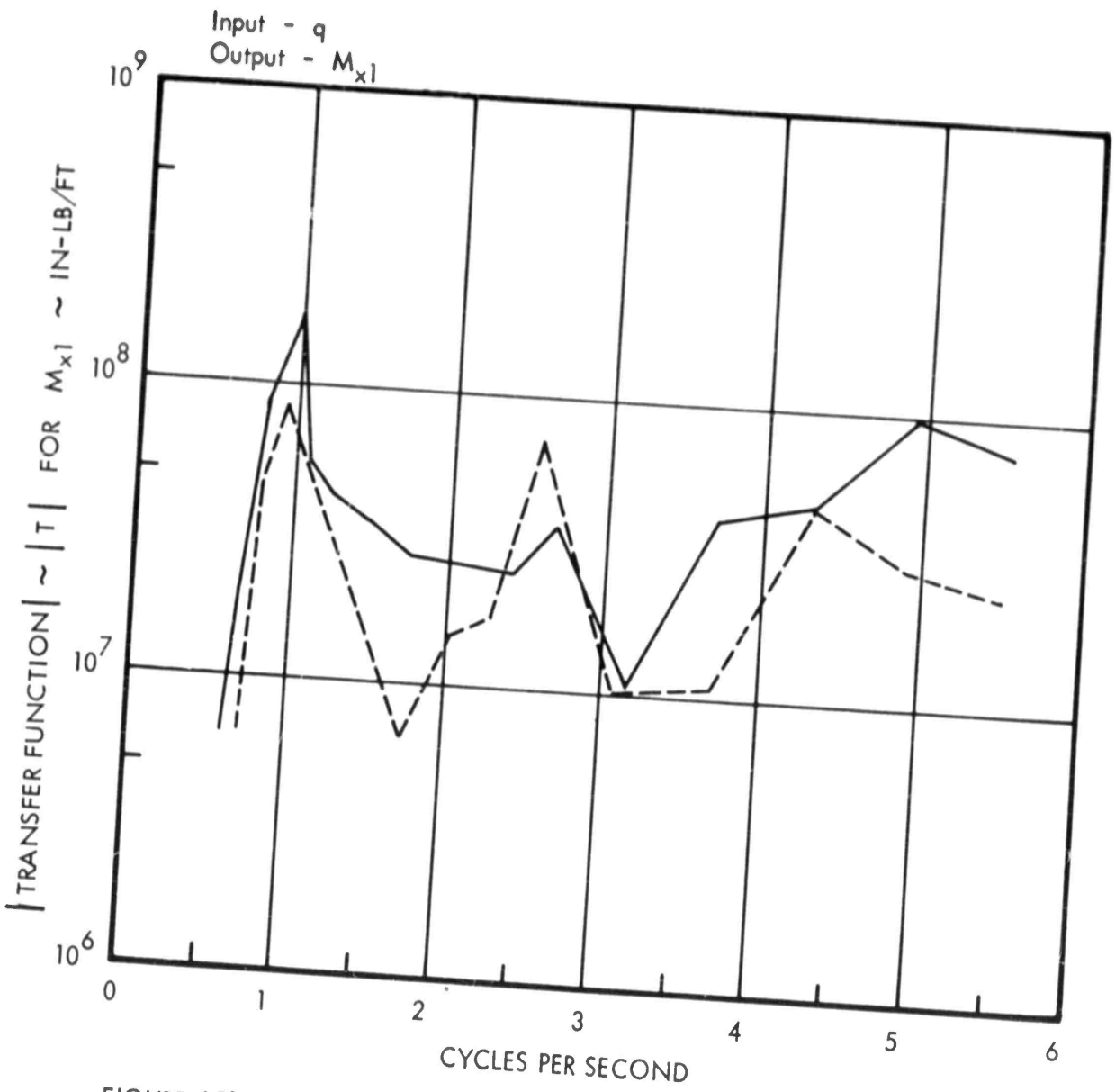


FIGURE 159 : Comparison of Transfer Function by Cross-Spectral and Power Spectral Methods for Wing Root Bending Moment,  $M_{x1}$   
 Multi-Gear Analysis for Normal Configuration

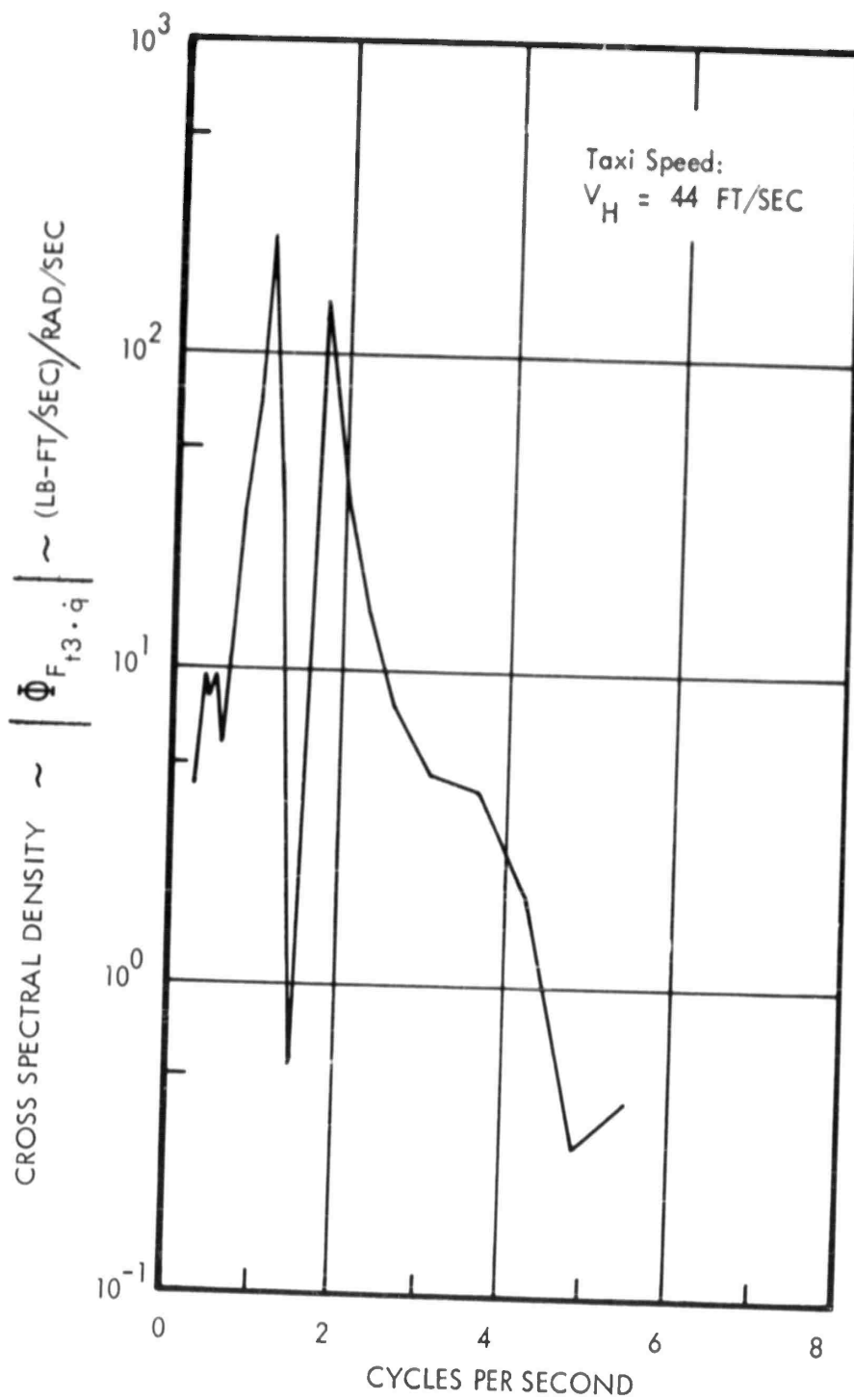


FIGURE 160: Sample Cross Spectral Density (Correlated with Ground Profile Derivative) for Rear Main Gear Tire Force

Multi-Gear Analysis for the Normal Configuration

APPENDIX J

ELLIPTIC FUNCTION SOLUTIONS FOR THE NONLINEAR SYSTEM

## ELLIPTIC FUNCTION SOLUTIONS FOR THE NONLINEAR SYSTEM

### 1. Summary of Applications to the Research Problem

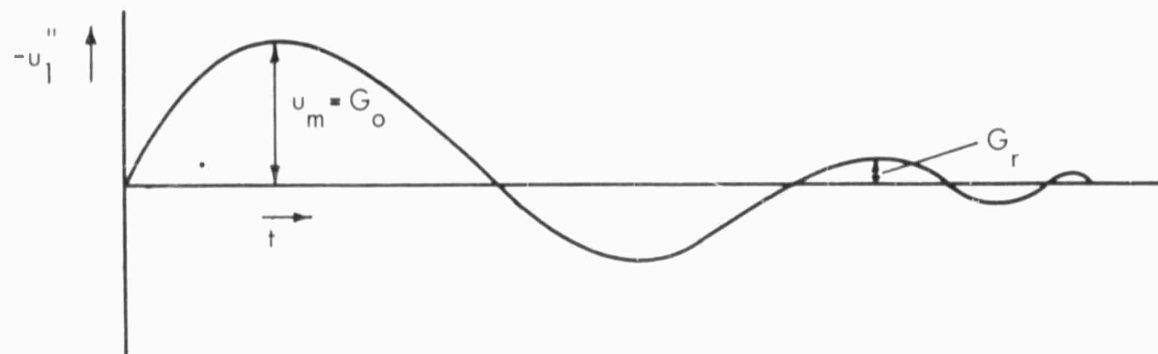
One of the desired references is not readily available to engineers in general, so a portion of it is reproduced in this appendix of the report.

A closed-form solution for the nonlinear differential equations was demonstrated in a thesis submitted to the Applied Mechanics Department at Virginia Polytechnic Institute.\* The method of solution is presented in a later section of this appendix. Since the nomenclature used in the method of solution differs somewhat from that used in the main body of this report, a separate list of terms and symbols appears in the next section of this appendix. In most cases the terminology is similar to that used in Reference 19, thus allowing the basic theory and detailed diagrams of that reference to be used as an aid in following the derivations in this appendix.

Since the analytic solutions are obtained only for landing conditions with an initial sinking velocity, the principal application to the taxiing problem arises through the prediction of the nonlinear strut damping energy absorption per cycle. This energy can then be used to predict the linear system damper required to produce equivalent performance.

The results are examined only briefly for validity of magnitudes, relative to strut damping prediction, since only the feasibility of solution by elliptic function analysis was to be studied as part of this methods research program.

In the most simple concept, if the system is given an initial velocity, the elliptic function solution amplitudes may be expected to decay as shown in the sketch that follows:



\* Thesis manuscript prepared by J. G. Theisen in August, 1956.

When this decaying function of upper mass acceleration,  $u_1''$ , is applied in Equation 62 in the text, a logarithmic decrement can be estimated, assuming a certain periodicity requirement for the equivalent linear system. Since the strut contributes all the damping in the closed form solution, the energy per cycle of strut oscillation can be computed for the nonlinear system by standard procedures. Finally, Equation 50 in the main report can be used to predict the equivalent linear damping coefficient.

Unfortunately, preliminary attempts to establish the damping in this manner resulted in physically untenable situations. The elliptic function solutions, at least for certain ranges of the airplane parameters, become discontinuous in time. This is probably due to the stipulation in the derivation that the differential equations as applied are only valid for strut closure, because of the quadratic damper. Further study is needed to test the feasibility of this method.

An alternative method was investigated briefly. The solution for  $u(\Theta)$  in the text of the thesis which is presented later in this appendix, is continuous in time for at least the first half period of motion during a landing impact. Although the "half period" of the nonlinear system is different from that of the linear system, knowledge of the energy dissipation of the nonlinear system over its first half period should yield sufficient information to predict the linear damper required to absorb the same amount of energy in the equivalent time period.

To check on feasibility of the method, the simplest mathematical conditions are selected within the limitations of a realizable physical system. In particular, it is assumed that there is no strut friction, so  $B_f = 0$ ; and that  $K_B = \frac{1}{9}$ , which results in  $H = 1$  for the thesis equations. Then if  $X(x)$  is defined as

$$X(x) = 3\sqrt{2u_0'} (1 - e^{-x/3}),$$

Equation 75J in the thesis text becomes

$$Y = \sqrt{u_0'/2} \left(1 - \frac{X}{3\sqrt{2u_0'}}\right) \text{sd} \left(X \middle| \frac{1}{2}\right) \quad (1J)$$

where the  $\text{sd}(X | 1/2)$  is an elliptic function, as defined in Reference 15, having the argument  $X$  and the parameter  $m = 1/2$ . The initial nondimensional sinking speed of the upper mass is  $u_0'$ .

Also, the appropriate combination of Equations 36J, 45J and 46J in the thesis yields the expression

$$dx = \sqrt{\frac{K_t q}{W_0}} \frac{dt}{2Y}$$

Since

$$dX = 2\sqrt{u_o'}/2 \left( \frac{X}{3\sqrt{2u_o'}} \right) dx = \frac{2Ydx}{sd \left( X \left| \frac{1}{2} \right. \right)}$$

then,

$$dt = \sqrt{\frac{W_o}{K_t g}} sd \left( X \left| \frac{1}{2} \right. \right) dX \quad (2J)$$

The strut telescoping velocity is defined as

$$\dot{s} = \dot{Z}_f - \dot{Z}_u$$

and, from Equations 35J and 40J in the thesis,

$$\dot{s} = (u_1' - u') \frac{1}{C_D} \sqrt{\frac{K_t W_o}{q}} = \left[ \frac{1}{C_D} \sqrt{\frac{K_t W_o}{q}} \right] \sqrt{u} \quad (3J)$$

Then, since  $Y = \sqrt{u}$ , the substitution of Equation 1J into 3J results in

$$\dot{s} = \frac{1}{C_D} \sqrt{\frac{K_t W_o u_o'}{2g}} \left( 1 - \frac{X}{3\sqrt{2u_o'}} \right) sd \left( X \left| \frac{1}{2} \right. \right) \quad (4J)$$

With  $H = 1$ , Equation 73J in the thesis may be written as

$$\Theta_r = 2\sin^{-1} \left[ -\frac{cd \left( X \left| \frac{1}{2} \right. \right)}{\sqrt{2}} \right] - \frac{7\pi}{2}$$

The total energy absorbed during the first half period of strut motion is given for the nonlinear system by

$$E_{NL} = \int_0^{s_{\max}} C_D \dot{s}^2 ds = \int_0^T C_D \dot{s}^3 dt \quad (5J)$$

where  $T$  is defined using Equation 36J of the thesis, with  $\Theta_r$ , the nondimensional time corresponding to the half period argument of the elliptic function solution, given by

$$(X = 2K) = \pi$$

Thus,

$$T = \pi \sqrt{\frac{W_o}{K_t g}} \quad (6J)$$

Substituting Equations 2J and 4J into Equation 5J, the nonlinear energy expression becomes

$$E_{NL} = \left[ \left( \frac{W_o \sqrt{K_t}}{g C_D} \right)^2 \sqrt{\left( \frac{u_o'}{2} \right)^3} \right] \int_0^{2K} \left( 1 - \frac{x}{3\sqrt{2}u_o'} \right)^3 \left( x \left| \frac{1}{2} \right. \right) dx \quad (7J)$$

The linear system corresponding to the previously solved nonlinear equations may be expressed as follows:

$$M_o \ddot{z}_f + D(\dot{z}_f - \dot{z}_u) + L - W_o = 0 \quad (8J)$$

$$D(\dot{z}_f - \dot{z}_u) - K_t z_u = 0 \quad (9J)$$

The same physical assumptions are made in the derivation of these equations as are made for the nonlinear system; i.e.,  $M_u = 0$ ,  $K_a = 0$ , and  $B_f = 0$ . However, for  $K_B = 1/9$  the wing lift,  $L$ , is approximately equal to the weight,  $W_o$ , within a few percent for the case selected; so the linear solution is simplified by the assumption that  $L = W_o$ . The error in strut energy dissipation resulting from this assumption is probably negligible.

The linear solution for strut stroke velocity may then be determined by standard procedures as

$$\dot{s} = \frac{p z_o}{J} \left[ - e^{-(p+J)t} + e^{-(p-J)t} \right] \quad (10J)$$

where

$$p = K_t / 2D$$

$$\omega_o^2 = K_t / M_o$$

and

$$J^2 = p^2 - \omega_o^2 \neq 0$$

The linear energy integral equivalent to Equation 5J may be written as

$$E_L = \int_0^T D \dot{s}^2 dt$$

Therefore, the linear system energy dissipated over the time corresponding to the first half-period of the nonlinear solution is

$$E_L = \frac{M_o \dot{z}_o^2}{2} \left[ 1 - \left( \frac{p-J}{2J^2} \right) p e^{-2(p+J)T} - \left( \frac{p+J}{2J^2} \right) p e^{-2(p-J)T} + \left( \frac{\omega_o^2}{J^2} \right) e^{-2pT} \right] \quad (11J)$$

The nature of the solution predicates a trial - and - error evaluation for the value of D which will satisfy the desired relation,

$$E_L = E_{NL} \quad (12J)$$

A set of parameters were selected to correspond approximately to the example airplane with 60 psi tires as used on the analog computer. The values are given per half airplane as follows:

$$C_D = 28.2 \text{ Lb-sec}^2/\text{In}^2 \quad (\text{two struts})$$

$$K_t = 10,466 \text{ Lb/In} \quad (\text{two struts})$$

$$W_o = 63,700 \text{ Lbs}$$

$$\dot{z}_o = 84 \text{ In/Sec}$$

For these conditions, the elliptic solution half period corresponds to a time, T, of approximately 0.39 seconds. In this time-period, Equation 5J yields

$$E_{NL} \approx 332,300 \text{ In-Lbs}$$

The required linear system energy, to satisfy Equation 12J, can be obtained with the value

$$D = 185 \text{ Lb-Sec/In.}$$

This result is in remarkably good agreement with the value of D predicted by the more complex analog solutions in the main text.

The most questionable value used in the above analysis is, possibly, the selection of  $\dot{z}_0 = 84 \text{ In/Sec}$ . This sinking speed was selected for the landing impact to insure operation at about the same position on the nonlinearity of the strut as that usually encountered in taxiing over the LaGuardia runway. The 84 In/Sec sinking speed yields a gear load factor of approximately  $(1 + \frac{2}{M_0} \sigma_F)$  for the example airplane. While taxiing, the gear load should correspond to less than this value about 84 percent of the time.

There is no contention that the form or magnitude of the linearized solution time history will conform with that of the nonlinear system. However, it does seem possible to establish an energy equivalence condition from these rather simple solutions.

The numerical evaluation of the elliptic function solution is only slightly more difficult than that of a simple trigonometric solution. The elliptic functions are tabulated in the most convenient form, however, in Reference 15. Most other tabulations are in an integral form not convenient in this problem.

The neglect of strut air compression force variation presents a problem requiring further investigation. Wing flexibility effects are only of secondary influence to strut damping force, so this neglect should not be important. However, some preliminary analysis indicates that further research could possibly develop methods for including these effects also.

The remainder of this appendix presents excerpts from the thesis which forms a basis for the previous derivations. Liberties have been taken to revise the text, at the discretion of the author, so as to reduce the length of presentation.

## 2. Nomenclature

$C_D$	coefficient of quadratic damping terms, $\frac{\rho A_h^3}{2(c_d A_o)^2}$ , Lb-Sec <sup>2</sup> /In <sup>2</sup>
$A_n$	pneumatic area, Ft <sup>2</sup>
$A_h$	hydraulic area, Ft <sup>2</sup>
$A_o$	area of opening in orifice plate, Ft <sup>2</sup>
$B_f$	coefficient of friction-force term, $\frac{2\mu d}{R_o}$
$c_d$	orifice discharge coefficient
$D$	linear viscous damping coefficient, Lb-Sec/Ft
$E(\Phi, k) \equiv E(\gamma)$	Legendre's incomplete elliptic integral of the second kind
$E_L$	energy dissipated by the linear system damper
$E_{NL}$	energy dissipated by the nonlinear system damper
$F(\Phi, k) \equiv \gamma$	incomplete elliptic integral of the first kind,
	$\gamma = 3\sqrt{2Hu_o'} (1 - e^{-x/3})$
$F_a$	air compression force in strut, Lb
$F_f$	axial friction force in strut, Lb
$F_h$	hydraulic resistance force in the strut, Lb
$F_s$	total axial shock-strut force, Lb
$F_t$	vertical force, applied at the ground, Lb
$F_1$	normal force on upper bearing (attached to inner cylinder), Lb

$F_2$	normal force on lower bearing (attached to outer cylinder), Lb
$H$	constant satisfying equal energy condition, $\sqrt{1 - \frac{2}{v_m} \left( \frac{1}{9} - K_B \right)}$
$K$	quarter period of elliptic function argument
$J$	$\sqrt{p^2 - \omega_o^2}$
$K_B$	nondimensional constant dependent on wing lift and strut friction $\frac{C_D (L - W_o)g}{K_t (1 - B_f)W_o}$
$K_t$	slope of the assumed tire deflection curve, Lb/Ft
$L$	wing-lift force, Lb
$M_o$	upper mass of airplane (above the strut), slugs
$R_o$	approximation to the average distance between bearing surfaces during the impact, $\left[ \left( R_1 + \frac{s_m}{2} \right) - \mu(b_1 - b_2) \right]$ , Ft
$R_1$	axial distance between upper and lower bearings, for fully extended shock strut, Ft
$W$	total weight of system, $W_o + W_u$ , Lb
$W_o$	weight of the upper mass above strut, Lb
$W_u$	weight of the lower mass below strut, Lb
$b_1$	outer radius of upper bearing, attached to inner cylinder, Ft
$b_2$	outer radius of lower bearing, attached to outer cylinder, Ft
$d$	horizontal distance from the axle to the strut centerline, Ft
$e$	base of natural logarithms ( $\approx 2.71828 \dots$ )

$g$	gravitational constant, Ft/Sec <sup>2</sup>
$k$	modulus of Jacobian elliptic functions and integrals
$\gamma$	polytropic exponent
$p$	$K_f/2D$
$P_a$	air pressure in upper strut, psi
$P_{a_0}$	initial air pressure in upper strut, psi
$P_h$	pressure in the lower chamber of the strut, psi
$s$	shock-strut stroke (displacement), $(Z_f - Z_u)$ , Ft
$s_m$	maximum possible stroke (fully closed strut), Ft
$t$	time after contact, Sec
$t_i$	time after contact before the equations of motion apply to the system, $\frac{0.0508}{\dot{z}_0}$ , Sec
$T$	time corresponding to the first half-period of nonlinear system, Sec
$u$	dimensionless lower-mass displacement from position at initial contact
$u_m$	maximum value of displacement during a given impact
$u_1$	dimensionless upper-mass displacement from position at initial contact
$u_0'$	dimensionless initial contact velocity
$v_0$	initial air volume within strut, Ft <sup>3</sup>
$X(x)$	elliptic function argument; function of $(x)$
$Z_f$	vertical displacement of the upper mass, Ft
$Z_u$	vertical displacement of the lower mass, Ft

$\dot{z}_0$	initial contact velocity, Ft/Sec
$Y(x)$	dimensionless displacement in the transformed equation of motion, $Y = u^{1/2}$
$Y_m$	maximum value of displacement during a given impact
$\theta_t$	dimensionless time from time of initial contact
$\mu$	coefficient of friction for the bearing surfaces
$\rho_h$	mass density of hydraulic fluid, slugs/Ft <sup>3</sup>
$\Phi$	am $\gamma$ = amplitude of $\gamma$
$\omega_0$	linear system natural frequency, $\sqrt{K_t/M_0}$ , 1/Sec

The use of dots over symbols indicates differentiation with respect to time,  $t$ .

Prime marks indicate differentiation with respect to dimensionless time,  $\theta_t$ , when the mark follows the symbol; and with respect to  $x$  when the mark is above the symbol.

### 3. Introductory Discussion

The solution of the equations of motion of an aircraft fuselage-landing gear configuration during landings is of interest to the designer who must predict the landing loads which an airplane encounters in service. In general such solutions are difficult because of the highly nonlinear characteristics of the oleo-pneumatic shock strut which couples the lower mass of the landing gear to the fuselage.

In the past, attempts to obtain solutions by linearization of these shock strut characteristics have resulted in unrealistic predictions of landing gear motions. Therefore, it has been necessary to carry out most of the theoretical analysis associated with landing gears by means of numerical integration procedures. These numerical methods are tedious, and as a result a large portion of design work has been carried out by means of trial and error drop testing of a system of masses representative of an airplane and landing gear. This in turn has proved to be time consuming and expensive.

This manuscript presents the closed-form analytical solution of the equations of motion for a basically nonlinear system which closely resembles an actual airplane and landing gear configuration. The nonlinear system considered has two degrees of freedom and is composed of a large mass representative of the fuselage-wing combination connected by an oleo-pneumatic shock strut to a wheel. The shock strut is assumed to have velocity-squared hydraulic damping and coulomb friction forces on the strut bearings. The nonlinear spring characteristic of the tire is represented by a sectionally linear spring.

In the first part of this paper the equations of motion for the nonlinear system are derived making use of a few simplifications which previous papers have shown to be justified. Also, the degree to which these assumptions limit the results is discussed. Next these equations of motion are solved in analytical form by a method which may be called "equivalent nonlinearization." It is shown that this solution is exact only for a specific combination of impact parameters, but that for a wide range of parameters the solution describes the motion of the system adequately for design purposes. Finally, a few analytical solutions are compared with solutions obtained by numerical integration methods; and the results are compared with experimental data for a typical landing impact.

#### 4. Physical Characteristics of the System

Other investigations have indicated that flexibility of the fuselage and wing structure of an airplane usually has only a small effect on landing gear shock strut performance (References 29, 30 and 31). For this reason, in the dynamical system to be investigated, the fuselage, wing, and empennage of the airplane may be represented by a single large mass,  $W_f$ , which is assumed to have freedom only in vertical translation designated by a coordinate  $Z_f$ . The lower mass,  $W_u$ , which is considerably smaller lies below the oleo strut and consists principally of the wheel, tire, axle, and strut inner cylinder assembly (as shown in Figure 4 of the main text). The strut is assumed to be infinitely rigid in bending. Horizontal forces at the axle, usually called drag or spring back loads, will not be considered in this investigation. Therefore, the lower mass has freedom only in vertical translation designated by the coordinate  $Z_u$ . Lift forces are externally applied to the system to represent aerodynamic lift, but nonsteady aerodynamic effects are neglected.

The shock strut axial force,  $F_s$ , has three principle components as follows:

$$F_s = F_h + F_a + F_f \quad (13J)$$

where

$F_h$  is the hydraulic resistance force resulting from the orifice within the strut (quadratic damping force).

$F_a$  is the polytropic air compression force within the strut.

$F_f$  is the strut axial friction force resulting from sliding friction of the bearing surfaces.

These quantities are derived and discussed in detail in Reference 19, so further elaboration will not be given here, except for a special form of  $F_f$ .

Friction forces within the strut result from the relative sliding of bearing surfaces on the inner and outer strut cylinders. Ground drag loads,  $F_d$ , produce forces  $F_1$  and  $F_2$  normal to the strut bearings (as shown in Figure 4 in the main text), but drag loads are neglected in this analysis. However, for some types of landing gears, vertical loads applied at the axle are eccentric to the strut center line and produce a bending moment which is resisted by forces,  $F_1$  and  $F_2$ , normal to the upper and lower bearing surfaces respectively. Conditions of relatively high normal pressures, slow sliding velocities of the bearing surfaces, and the poor lubricating properties of the hydraulic fluid lead to the conclusion that the internal friction forces may follow laws similar to those of dry (coulomb) friction; that is, the friction force is proportional to the normal force. Other landing gear studies have used this same relationship (References 19 and 34), although at present no conclusive experimental evidence in support of this assumption is available.

If it is assumed that the friction coefficient is the same on each sliding surface, then the strut axial friction force,  $F_f$ , may be determined from the equation

$$F_f = \frac{\dot{s}}{|\dot{s}|} \mu [ |F_1| + |F_2| ] \quad (14J)$$

or, since summation of horizontal forces indicates that  $F_1 = F_2$  for a strut with an excentric axle and no drag loads,

$$F_f = \frac{\dot{s}}{|\dot{s}|} 2\mu |F_1| \quad (15J)$$

where

$\mu$  coefficient of friction for bearing surfaces

$\frac{\dot{s}}{|\dot{s}|}$  factor to indicate sign of friction force

$F_1$  normal force on the upper bearing

$F_2$  normal force on the lower bearing

It is desirable to obtain  $F_1$  in terms of the resultant axial force within the strut expressed by  $F_s = F_f + F_a + F_1$ . If  $R_1$  is the distance between the upper and lower bearing surfaces for the fully extended strut, then this distance may be expressed as  $(R_1 + s)$  for any other strut position. Considering the forces applied to the lower strut piston as a free body, and taking moments about the intersection of the strut centerline and the line of action of  $F_2$  (refer to Figure 4 of the main text), the equation for  $F_1$  is

$$(R_1 + s)F_1 = \mu F_1(d + b_1) + \mu F_2(d - b_2) + d(F_s - \mu F_1 - \mu F_2) \quad (16J)$$

where  $b_1$  and  $b_2$  are the outer radii of the upper and lower bearings, respectively, and  $d$  is the distance from the axle to the strut center line. Since  $F_1 = F_2$ , the equation for  $F_1$  may be found as

$$F_1 = \frac{d}{[(R_1 + s) - \mu(b_1 - b_2)]} F_s \quad (17J)$$

In order to obtain a solution as presented in this paper, it is necessary to express the quantity  $[R_1 + s - \mu(b_1 - b_2)]$  as a constant. A similar assumption was made in Reference 34. If  $R_1$  is large with respect to the maximum value of  $s$  which is

possible,  $s_m$ , then a reasonable constant to use would be  $\left[ \left( R_1 + \frac{s_m}{2} \right) - \mu(b_1 - b_2) \right] = R_o$  where  $R_o$  is approximately an average distance between the bearing surfaces.  $s_m$  usually is quite well defined by the strut geometry, and the accuracy of this assumption for  $R_o$  depends on the particular strut being considered. The friction forces are often quite small for the simple vertical impact case; and the inclusion of friction, as will be shown, does not complicate the final solution obtained. Therefore it was felt that this term should be included for possible future studies on the qualitative effects of friction in the landing gear.

The normal bearing force from Equation 17J may now be expressed as

$$F_1 \approx \frac{d}{(R_o)} F_s \quad (18J)$$

and from Equation 15J

$$F_f = \frac{\dot{s}}{|\dot{s}|} \frac{2\mu d}{(R_o)} |F_s| \quad (19J)$$

$F_s$  is the total axial strut force, and as stated previously, it can be expressed as the summation of the strut internal forces:

$$F_s = F_h + F_a + F_f \quad (20J)$$

For this analysis the portions of mass comprising the inner and outer cylinder of the strut are considered to be weightless, and their weights are included with the major portion of the masses to which they are respectively attached. The assumption that the center of gravity of the lower mass lies at the axle center line also is a usual stipulation in such an analysis.

Recent data, References 19 and 35, indicates that the dynamic force deflection characteristics of the tire may be sharply nonlinear for small deflections, but can be represented by a linear approximation with only minor loss in accuracy for the major remaining portion of the curve. Thus a linear segment approximation to the true tire spring may be made as in Figure 161. For the 27-inch-diameter tire being considered in the appendix, this assumption gives no force for deflections less than  $Z_u = 0.0508$  foot, and a constant slope  $K_t$  thereafter. Such a representation seems to be entirely adequate for most practical purposes as shown in Reference 19.

If  $F_t$  is defined as the vertical force on the ground resulting from deflection of the spring  $K_t$ , then the force may be written

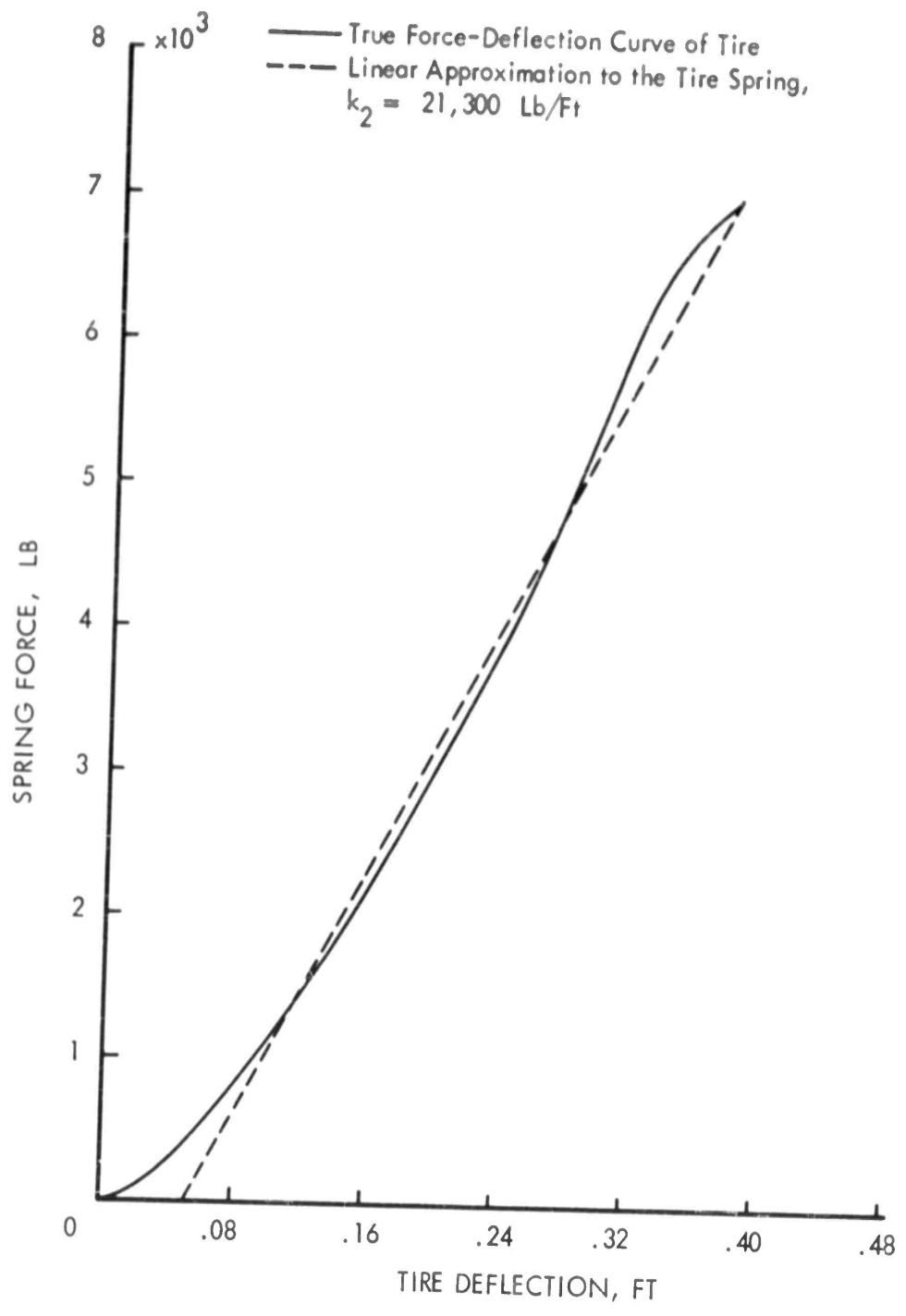


FIGURE 161 : Comparison of the True Force-Deflection Curve of the Tire and a Linear Approximation to the Tire Spring.

$$F_t = 0 \text{ for } 0 < Z_u < 0.0508 Ft \quad (21J)$$

$$F_t = K_t Z_u \text{ for } Z_u > 0.0508 Ft \quad (22J)$$

Finally, the wing lift from aerodynamic forces is represented by the force  $L$  acting through the center of gravity of the upper fuselage mass. Because of the very short time involved to complete the impact, the wing lift can reasonably be assumed to be a constant. Experimental data, Reference 36, indicates that for most landings the wing lift at ground contact is very nearly equal to the weight of the airplane. During the experimental drop tests used for comparisons with theory, in this appendix analysis, the wing lift force was simulated so that it was equal to the weight of the test model.

## 5. Equations of Motion

### a. Derivation of the Equations of Motion

With  $F_s$  and  $F_t$  defined as in the preceding section, the equations of motion may be written in single form. Considering the summation of vertical forces on the lower mass, Figure 4, the motion of the axle is given by the equation

$$F_s - F_t + W_u = \frac{W_u}{g} \ddot{z}_u \quad (23J)$$

Similarly, the vertical motion of the main mass,  $M_f = M_o$ , (assuming  $M_s = 0$ ) is determined by the equation

$$F_s + L - W_o = -\frac{W_o}{g} \ddot{z}_f \quad (24J)$$

Where  $L$  is the wing-lift force as defined earlier. If Equations 23J and 24J are combined, the overall balance of forces can be expressed by

$$F_t + L - W = -\frac{W_o}{g} \ddot{z}_f - \frac{W_u}{g} \ddot{z}_u \quad (25J)$$

where

$$W = W_o + W_u$$

Any two of these equations is sufficient to obtain a solution, since there are two degrees of freedom. In this derivation, Equations 23J and 25J will be used.

In order to obtain Equation 23J in a more desirable form we must express the strut axial force more explicitly. From Equation 20J

$$F_s = F_h + F_a + F_f$$

or, since the air pressure force is neglected for the reasons given in Reference 19,

$$F_s = \frac{\rho_h A_h^3}{2(c_d A_o)^2} \dot{s} |s| + \frac{\dot{s}}{|s|} \frac{2\mu d}{(R_o)} |F_s| \quad (26J)$$

Some simplifications become obvious at this point. Since the strut compression process only is of interest for landings, the strut velocity and strut axial force will always be positive. Therefore, the absolute value signs may be removed so that

$$F_s = C_D \dot{s}^2 + B_f F_s \quad (27J)$$

where

$$C_D = \frac{\rho_h A_h^3}{2(c_d A_o)^2}$$

$$B_f = \frac{2\mu d}{(R_o)}$$

Equation 27J can be solved for  $F_s$  giving

$$F_s = \frac{C_D}{(1 - B_f)} \dot{s}^2 \quad (28J)$$

Using the definition for  $\dot{s}$  substitute  $F_t$  and  $F_s$  from Equations 22J and 28J into Equations 23J and 25J with the result

$$\frac{W_u}{g} \ddot{z}_u - \frac{C_D}{(1 - B_f)} (\dot{z}_f - \dot{z}_u)^2 + K_t z_u - W_u = 0 \quad (29J)$$

$$\frac{W_o}{g} \ddot{z}_f + \frac{W_u}{g} \ddot{z}_u + K_t z_u + L - W = 0 \quad (30J)$$

Note that the net effect of including the friction force in the equations of motion is only to change the constant coefficient of the quadratic damping term. In References 19 and 38 it has been determined that since the lower mass is a relatively small fraction (less than 1/18) of the total mass, the system may be simplified even further. Calculations made in these references indicate that the lower mass may be assumed to be equal to zero without greatly modifying the results. Using this assumption, Equations 29J and 30J may be written as

$$(\dot{z}_f - \dot{z}_u)^2 - \left[ \frac{(1 - B_f)}{C_D} K_t \right] z_u = 0 \quad (31J)$$

$$\ddot{z}_f + \frac{gK_t}{W_o} z_u + (L - W_o) \frac{g}{W_o} = 0 \quad (32J)$$

These are the equations to be solved. The initial conditions for the vertical impact are given by

$$\begin{aligned} t &= 0 \\ Z_f &= Z_u = 0 \\ \dot{Z}_f &= \dot{Z}_u = \dot{z}_o \end{aligned} \tag{33J}$$

However, the assumption of Equation 21J implies that the system must move a distance equal to 0.0508 foot after initial contact before any finite ground reaction can develop. Since Equations 31J and 32J assume that the ground reaction increases linearly with deflection, these equations do not apply until some time  $t_i$  after contact. The initial velocity remains essentially constant over this very short interval of time, so  $t_i$  can be found from

$$t_i = \frac{0.0508}{\dot{z}_o} \tag{34J}$$

The initial conditions 33J still apply to the equations of motion in this case with the coordinate system transformed so that the tire force-deflection curve passes through zero. In plotting the solutions, all results must be displaced in time by  $t_i$  seconds, and the displacements will have 0.0508 foot added, to indicate the actual distance through which the model has moved.

b. Introduction of Dimensionless Variables

The solution of Equations 31J and 32J depends on six parameters, namely,  $C_D$ ,  $B_f$ ,  $\frac{W_o}{g}$ ,  $K_t$ ,  $L$ , and  $\dot{z}_o$ . It is desirable to reduce the number of parameters, and this can be done by introducing generalized variables  $u$  and  $u_1$  in the following transformations:

$$\begin{aligned} u &= \frac{C_D g}{W_o (1 - B_f)} Z_u \\ u_1 &= \frac{C_D g}{W_o (1 - B_f)} Z_f \end{aligned} \tag{35J}$$

and

$$\Theta_t = \sqrt{\frac{K_t g}{W_o}} t \tag{36J}$$

so that:

$$u' = \frac{du}{d\Theta_t} = \dot{z}_u \left[ \frac{C_D}{(1 - B_f)} \sqrt{\frac{g}{K_t W_o}} \right]$$

$$u_1' = \frac{du}{d\Theta_t} = \dot{z}_f \left[ \frac{C_D}{(1 - B_f)} \sqrt{\frac{g}{K_t W_o}} \right]$$

and

$$u_1'' = \frac{d^2 u_1}{d\Theta_t^2} = \ddot{z}_f \left[ \frac{C_D}{K_t (1 - B_f)} \right]$$

With those new variables, Equations 31J and 32J become

$$(u_1' - u')^2 - u = 0 \quad (37J)$$

$$u_1'' + u + K_B = 0 \quad (38J)$$

where

$$K_B = \frac{C_D (L - W_o) g}{K_t (1 - B_f) W_o}$$

Of special interest in this analysis is the case where the wing lift is equal to the weight of the system, as indicated earlier in this paper. When  $L = W_o$ , then  $K_B = 0$ ; and we see that Equation 31J and 32J will have single parameter only, the initial non-dimensional contact velocity, which is

$$u_o' = \dot{z}_o \left[ \frac{C_D}{(1 - B_f)} \sqrt{\frac{g}{K_t W_o}} \right] \quad (39J)$$

Equations 37J and 38J can be solved simultaneously to give a single equation in one variable. Rewrite Equation 37J as

$$u_1' - u' = u^{1/2} \quad (40J)$$

where the positive root must be used since the equations of motion are applicable only for positive strut-stroke velocity, and this implies that  $(u_1' - u')$  must be positive. Differentiate Equation 40J with respect to  $\Theta_t$ . Then

$$u_1'' - u'' = \frac{1}{2} u^{-1/2} u' \quad (41J)$$

Solve Equation 38J for  $u_1''$  and substitute in Equation 41J. This gives

$$u'' + u + \frac{1}{2} u^{-1/2} u' + K_B = 0 \quad (42J)$$

c. Transformation of the Equations

In order to obtain Equation 42J in a form more amenable to solution, use the following transformation:

$$u = Y^2 \quad (43J)$$

Then Equation 42J may be written

$$\frac{d}{d\theta_1} \left[ \frac{d(Y^2)}{d\theta_1} \right] + \frac{1}{2Y} \frac{d(Y^2)}{d\theta_1} + K_B + Y^2 = 0 \quad (44J)$$

Apply the transformation

$$x = \int_0^{\theta_1} \frac{d\alpha}{2 Y(\alpha)} \quad (45J)$$

or

$$dx = \frac{d\theta_1}{2Y(\theta_1)} \quad (46J)$$

The final equation obtained is

$$\frac{d^2 Y}{dx^2} + \frac{dY}{dx} + 2K_B Y + 2Y^3 = 0 \quad (47J)$$

To determine the initial conditions for this equation, rewrite Equation 46J as

$$d\theta_1 = \frac{d(Y^2)}{dY} dx$$

By substituting Equation 43J, it can be seen that

$$\frac{du}{d\theta_r} = \frac{dY}{dx} \quad (48J)$$

Therefore, the initial conditions are:

for  $x = 0$

$$Y = u_o^{1/2} = 0$$

$$\frac{dY}{dx} = u_o' \quad (49J)$$

## 6. Solution of the Transformed Equation

### a. Considerations Necessary to Obtain a Solution

An exact analytical solution for Equation 47J is obtainable only for a specific value of  $K_B$ . An equation similar in form to Equation 47J for which a solution is known, is

$$\frac{d^2Y}{dx^2} + \frac{dY}{dx} + \left(\frac{2}{9}\right)Y + 2H^2Y^3 = 0 \quad (50J)$$

where  $H$  is an arbitrary constant. This is a special case of an equation studied in Reference 37. It is apparent, then, that the solution of Equation 47J is identical to the solution of Equation 50J with the values  $K_B = 1/9$  and  $H = 1$ .

For any given landing gear configuration, this value of  $K_B$  implies that only one value of wing lift,  $L \neq W_0$ , will suffice. As was indicated earlier in this paper, for most landings  $L = W_0$ ; and in general the value of wing lift will not satisfy the condition that  $K_B = 1/9$ . However, it will be shown that with other values of  $K_B$ , Equation 50J has solutions reasonably representative of the solutions of Equation 47J for certain values of initial conditions and the parameter  $H$ .

A device sometimes used in nonlinear mechanics is to replace a nonlinear spring or damper system by an equivalent system which will have an equal absorption of energy within the range of the variable which is of interest as shown in References 4 and 5. Usually this method is used only when the nonlinear equation is a small perturbation from a corresponding linear differential equation, so that the nonlinear terms may be replaced by equivalent linear expressions which may then be handled analytically. In Equation 47J the nonlinearity is so large that equivalent linearization results in solutions for landing impacts that are greatly distorted. Since an analytical solution to Equation 50J is available, in this case the energy considerations may be equally useful in replacing the linear and cubic terms in Equation 50J by equivalent linear and cubic terms with coefficients adjusted to those in Equation 47J. Considering these expressions as spring forces, the energy stored within the springs is the integral of the force with respect to the displacement. For this study the primary interest is in the transient response during the first half cycle only; so if the maximum value of displacement in this interval is designated by  $Y_m$  the energy relationship between the actual and equivalent spring is

$$\int_0^{Y_m} \left[ \left(\frac{2}{9}\right)Y + 2H^2Y^3 \right] dY = \int_0^{Y_m} \left[ 2K_B Y - 2Y^3 \right] dY \quad (51J)$$

where

$$Y_m = u_m^{1/2}$$

The determination of the value of  $u_m$  is to be discussed later in the section entitled "Qualifications of the Solution." Since the other constants are fixed,  $H$  must be adjusted to satisfy the condition of equal energy. By performing the integration, the following expression is found

$$H = \sqrt{1 - \frac{2}{Y_m^2} \left( \frac{1}{9} - K_B \right)} \equiv \sqrt{1 - \frac{2}{u_m} \left( \frac{1}{9} - K_B \right)} \quad (52J)$$

For a value of  $H$  thus determined, Equations 50J and 47J may be considered as equivalent.

b. Derivation of the Solution

The solution to Equation 50J may be determined as follows: Let differentiation with respect to  $x$  be denoted by prime marks above symbols. Then Equation 50J becomes

$$Y'' + Y' + \frac{2}{9} Y + 2H^2 Y^3 = 0 \quad (53J)$$

Multiplying through by  $e^{2x/3}$  and rearranging terms, Equation 53J may be written as

$$\left( Y'' + \frac{1}{3} Y' \right) e^{2x/3} + \frac{2}{3} \left( Y' + \frac{1}{3} Y \right) e^{2x/3} = -2H^2 Y^3 e^{2x/3} \quad (54J)$$

This equation may be rewritten

$$\frac{d}{dx} \left[ e^{2x/3} \left( Y' + \frac{1}{3} Y \right) \right] = -2H^2 Y^3 e^{2x/3} \quad (55J)$$

Multiply through by  $\left[ e^{2x/3} \left( Y' + \frac{1}{3} Y \right) dx \right]$  to obtain

$$\left[ e^{2x/3} \left( Y' + \frac{1}{3} Y \right) \right] d \left[ e^{2x/3} \left( Y' + \frac{1}{3} Y \right) \right] = -2H^2 \left( Y e^{x/3} \right)^3 \left( Y' + \frac{1}{3} Y \right) e^{x/3} dx \quad (56J)$$

Equation 56J may be integrated, and the resulting expression is

$$e^{4x/3} \left( \dot{Y} + \frac{1}{3} Y \right)^2 = \left[ 1 - \left( \frac{3Ye^{x/3}}{c_1} \right)^4 \right] \left( \frac{c_1}{3} \right)^4 H^2 \quad (57J)$$

where  $c_1$  is the constant of integration. Take the square root of both sides and solve for  $Hc_1^2$

$$Hc_1^2 = \frac{e^{2x/3}}{\frac{1}{9} \sqrt{1 - \left( \frac{3Y}{c_1} e^{x/3} \right)^4}} \left( \dot{Y} + \frac{1}{3} Y \right) \quad (58J)$$

Multiply through Equation 58J by  $\left( \frac{1}{3c_1} e^{-x/3} dx \right)$  and rearrange factors to obtain

$$\frac{1}{3} Hc_1 e^{-x/3} dx = \frac{dx}{\sqrt{1 + \left( \frac{3Y}{c_1} e^{x/3} \right)^2}} \left[ \frac{\left( \dot{Y} + \frac{1}{3} Y \right) \frac{3}{c_1} e^{x/3}}{\sqrt{1 - \left( \frac{3Y}{c_1} e^{x/3} \right)^2}} \right] \quad (59J)$$

If a quantity  $\psi$  is defined as

$$\psi = \sin^{-1} \left( \frac{3Y}{c_1} e^{x/3} \right) \quad (60J)$$

so that

$$d\psi = \frac{dx}{\sqrt{1 - \left( \frac{3Y}{c_1} e^{x/3} \right)^2}} \left[ \left( \dot{Y} + \frac{1}{3} Y \right) \frac{3e^{x/3}}{c_1} \right] \quad (61J)$$

then substitution of Equations 60J and 61J into Equation 59J results in the expression

$$\frac{1}{3} H c_1 e^{-x/3} dx = \frac{d\psi}{\sqrt{1 + \sin^2 \psi}} \quad (62J)$$

This may be written in elliptic integral form as follows

$$\int \frac{1}{3} H c_1 e^{-x/3} dx = \int_0^{\Phi} \frac{d\psi}{\sqrt{1 - k^2 \sin^2 \psi}} \quad (63J)$$

where  $k^2 = -1$  is the modulus. The result of the integration may be written in standard notation as

$$-H c_1 e^{-x/3} + c_2 = F(\Phi, k) \equiv \Upsilon \quad (64J)$$

where  $c_2$  is a constant of integration and by definition

$$\operatorname{sn} \Upsilon = \sin \Phi \quad (65J)$$

Therefore, in terms of the Jacobian elliptic function, Equation 64J may be written as

$$\operatorname{sn}_{k=-1} \left( c_2 - H c_1 e^{-x/3} \right) = \frac{3\Upsilon}{c_1} e^{x/3} \quad (66J)$$

The solution is, then,

$$Y = \frac{1}{3} c_1 e^{-x/3} \operatorname{sn}_{k=-1} \left( c_2 - H c_1 e^{-x/3} \right) \quad (67J)$$

Using the initial conditions from Equation 49J, the constants of integration may be determined as

$$c_1 = 3 \sqrt{\frac{u_o'}{H}} \quad (68J)$$

$$c_2 = 3 \sqrt{H u_o'}$$

By substitution of these constants, Equation 67J becomes

$$Y = \sqrt{\frac{u_o'}{H}} e^{-x/3} \operatorname{sn}_{k=-1} \left[ \sqrt{H u_o'} \left( 1 - e^{-x/3} \right) \right] \quad (69J)$$

This is a valid solution, but the modulus usually is tabulated for positive, real values. By applying a transformation to the modulus, as shown in Reference 15, Equation 69J may be written

$$Y = \sqrt{\frac{u_o'}{2H}} e^{-x/3} \operatorname{sd}_{k^2=1/2} \left[ 3\sqrt{2Hu_o'} (1 - e^{-x/3}) \right] \quad (70J)$$

where, for convenience, the modulus  $k^2 = 1/2$  is understood to apply to all elliptic functions expressed herein unless otherwise stated. Since  $u = Y^2$ , it can be seen that

$$u = \frac{u_o'}{2H} e^{-2x/3} \operatorname{sd}^2 \left[ 3\sqrt{2Hu_o'} (1 - e^{-x/3}) \right] \quad (71J)$$

Keeping in mind that  $\theta_t$  is defined implicitly as a function  $x$  by Equation 45J, then Equation 45J may be rewritten as

$$\theta_t = \int_0^x 2Y(\xi) d\xi \quad (72J)$$

where the limits on  $x$  are chosen to satisfy the initial conditions for  $\theta_t$ .

Performing the indicated integration, it is seen that

$$\theta_t = \frac{2}{H} \sin^{-1} \left\{ -\frac{1}{\sqrt{2}} \operatorname{cd} \left[ 3\sqrt{2Hu_o'} (1 - e^{-x/3}) \right] \right\} - \frac{7\pi}{2H} \quad (73J)$$

Thus the solution for  $u(\theta_t)$  is in parametric form with Equations 71J and 73J. This form is convenient for obtaining the higher derivatives. The solution may be expressed in explicit form, however, as

$$u(\theta_t) = \frac{u_o'}{2H} \left( 1 - \frac{1}{3\sqrt{2Hu_o'}} \Theta \right)^2 \operatorname{sd}^2 \Theta \quad (74J)$$

where

$$\Theta = \operatorname{cd}^{-1} \left[ -\sqrt{2} \sin \left( \frac{H}{2} \theta_t + \frac{7\pi}{4} \right), k^2 = 1/2 \right] \quad (75J)$$

The nondimensional velocity of the lower mass can be obtained by use of Equation 48J as

$$u'(\theta_t) = u_o' \left( 1 - \frac{1}{3\sqrt{2Hu_o'}} \theta \right)^2 \frac{cd\theta}{dn\theta} - \left[ \frac{1}{3} \sqrt{\frac{u_o'}{2H}} \left( 1 - \frac{1}{3\sqrt{2Hu_o'}} \theta \right) sd\theta \right] \quad (76J)$$

For design purposes, the motion of the upper mass is also of interest. The non-dimensional acceleration can be obtained from Equation 38J.

$$u_1''(\theta_t) = -\frac{u_o'}{2H} \left( 1 - \frac{1}{3\sqrt{2Hu_o'}} \theta \right)^2 sd^2\theta - K_B \quad (77J)$$

The nondimensional velocity of the upper mass may be derived by use of Equation 37J.

$$u_1'(\theta_t) = u_o' \left( 1 - \frac{1}{3\sqrt{2Hu_o'}} \theta \right)^2 \frac{cd\theta}{dn\theta} + \left[ \frac{2}{3} \sqrt{\frac{u_o'}{2H}} \left( 1 - \frac{1}{3\sqrt{2Hu_o'}} \theta \right) sd\theta \right] \quad (78J)$$

The dimensionless displacement of the upper mass, may be obtained by graphical integration of Equation 78J, or more simply, perhaps, by substituting  $u_1(\theta_t)$  from Equation 40J in an integral relationship as follows:

$$u_1(\theta_t) = \int_0^{\theta_t} u_1'(r) dr = \int_0^{\theta_t} \left[ u^{1/2}(r) + u'(r) \right] dr = \int_0^{\theta_t} u^{1/2}(r) dr + u(\theta_t) \quad (79J)$$

Then, using the transformation Equations 43J and 45J, and selecting limits of integration which satisfy the initial conditions, it can be shown that

$$u_1(x) = 2 \int_0^x u(\xi) d\xi + u(x) \quad (80J)$$

Then  $u_1(\theta_1)$  is available in parametric form with Equation 73J. However, using Equations 80J and 71J the following expression may be derived:

$$u_1(x) = u(x) - \frac{2}{3H^2} \left\{ \left[ E(\gamma) - \frac{1}{2} \gamma - \frac{1}{2} \operatorname{sn} \gamma \operatorname{cd} \gamma \right] \left[ 3\sqrt{2Hu_0'} - \gamma \right] + \ln(\operatorname{dn} \gamma) - \frac{\gamma^2}{4} + \int_0^\gamma E(\gamma) d\gamma \right\} \quad (81J)$$

where

$$\gamma = 3\sqrt{2Hu_0'}(1 - e^{-x/3})$$

$\equiv F(\Phi, k)$  incomplete elliptic integral of the first kind

$\Phi = \operatorname{am} \gamma \equiv$  amplitude of  $\gamma$

$E(\gamma) \equiv E(\Phi, k)$  incomplete elliptic integral of the second kind

The integral term of Equation 81J may be evaluated graphically, and the result is presented for convenience in Figure 162.

#### c. Qualifications of the Solution

Since the solutions contain the parameter  $H$  which is a function of  $u_m$ , we must find a value for this maximum displacement before a calculation can be attempted. It may be indicated that the actual value of  $u_m$  which is used as the limit of integration in Equation 51J is not critical with respect to the final solution. This limit is the most logical and convenient, but any good approximate value for  $u_m$  will suffice, since the spring force-deflection curves will be negligibly different for small variations in the limit. This may be seen from Figure 163 where the effects on these curves are very small for large changes in  $u_m$ . A very good approximation for  $u_m$  as a function of  $u_0'$  may be derived using only Equations 52J and 71J as follows.

The solution for the actual maximum value of  $u$  would require the evaluation of Equation 76J for  $u' = 0$ . The corresponding value of  $\theta_1$  would be very difficult to obtain from this expression. For purposes of this paper any good approximate value of  $u_m$  is sufficient, and Equation 71J which is in the parametric form for  $u$  is much simpler to work with as follows:

$$u = \frac{u_0'}{2H} e^{-2x/3} s_{d^2}^2 \Big|_{k^2=1/2} \left[ 3\sqrt{2Hu_0'} (1 - e^{-x/3}) \right] \quad (82J)$$

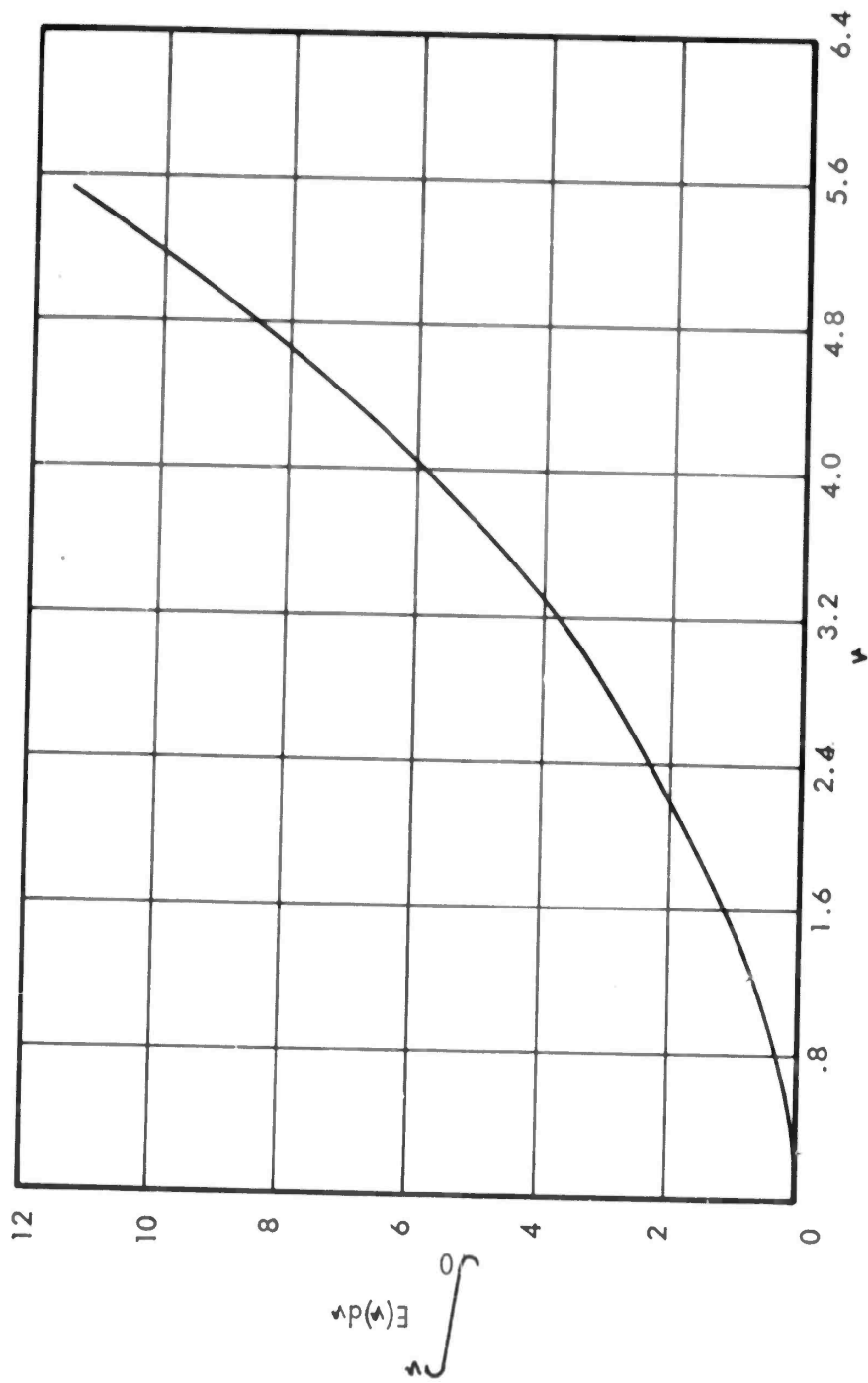


FIGURE 162 : Plot of the Integration of the Incomplete Elliptic Integral of the Second Kind,  $E(v)$ , with Respect to the Argument  $v$ .

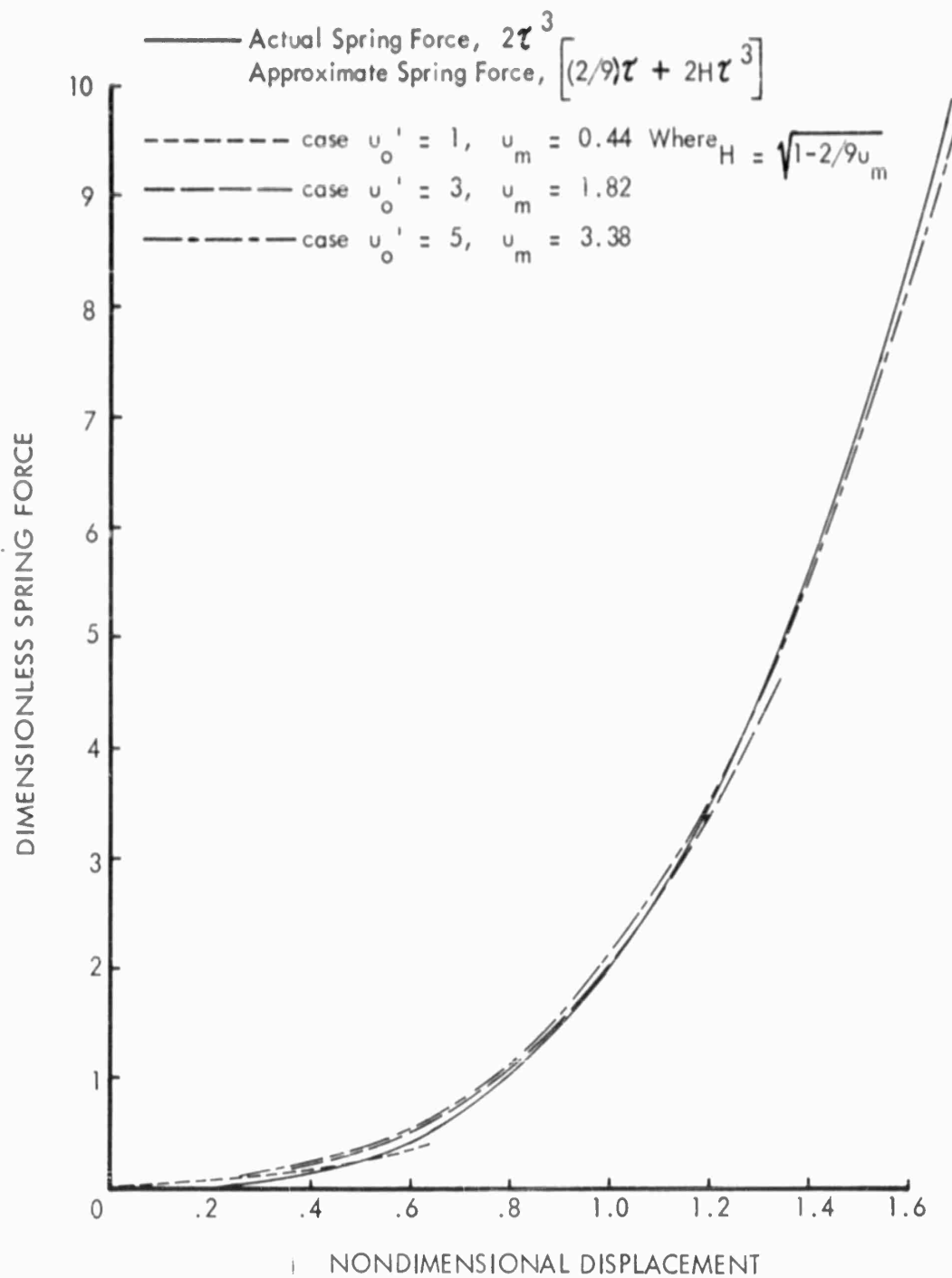


FIGURE 163 : Comparison of the Actual Dimensionless Spring-Force Curve and the Approximate Spring-Force Curves for Various Initial Conditions.

Under the assumption that the exponential term is relatively slowly varying, the value of the argument  $\gamma$  corresponding to  $u_m$  can be found by differentiating  $sd(\gamma, 1/2)$  with respect to  $\gamma$ , and equating<sup>m</sup> the result to zero as shown:

$$\frac{d}{d\gamma} sd(\gamma, 1/2) = \frac{cn}{dn} (\gamma, 1/2) = 0 \quad (83J)$$

or, since the  $dn(\gamma, 1/2)$  is always finite

$$\gamma = cn^{-1}(0, 1/2)$$

so that

$$\gamma = K \approx 1.85407. . . \quad (84J)$$

where  $k$  is the value of the argument at the quarter period. Substitution of this value in the argument of Equation 82J yields the result

$$\gamma = 3 \sqrt{2Hu_o'} (1 - e^{-x/3}) = K \quad (85J)$$

where the value of  $x$  now corresponds to the value of  $u = u_m$  in the first approximation. From Equation 85J it may be seen that

$$e^{-x/3} = 1 - \frac{K}{3 \sqrt{2Hu_o'}} \quad (86J)$$

Noting that

$$sd^2(K, 1/2) = 2 \quad (87J)$$

Expressions 86J and 87J may be substituted in Equation 82J to obtain

$$u_m = \frac{u_o'}{H} \left[ 1 - \frac{K}{3 \sqrt{2Hu_o'}} \right]^2 \quad (88J)$$

where, from Equation 52J

$$H = \sqrt{1 - \frac{2}{9u_m}} \quad (\text{for } K_B = 0) \quad (89J)$$

From Equations 88J and 89J the desired approximate solution for  $u_m$  may be obtained. However, by combining the two equations and solving for  $u_o'$  a more explicit expression may be obtained as follows:

$$u_o' = \frac{H}{9} \left[ 3\sqrt{u_m} + \frac{K}{H\sqrt{2}} \right]^2 \quad (90J)$$

This equation is easier to use for obtaining  $u_m$  as a function of  $u_o'$ . This function yields good agreement when compared with the true values for  $u_m$  as shown in Figure 164.

The degree to which the solution obtained by the method of "equivalent non-linearization" represents the solution of the original Equation 47J depends primarily on the proportion of energy stored by the linear and cubic spring terms. As indicated before, if  $K_B = 1/9$  then the original equation and the equivalent, Equation 50J, becomes less representative of the original equation.

It may be indicated, however, that this limitation is primarily concerned with the frequency characteristics and shape of the response curves. The energy considerations used in deriving the equivalent nonlinear spring imply that the maximum deflection of the approximate spring system will be close to that of the original system, since the work done in deflecting the springs to this maximum position is the same for either spring system.

The energy ratio spoken of indicates, then, to what extent the shape of the response curves may be in error. This ratio of energy,  $r$ , can be obtained from Equation 51J for the case of  $K_B = 0$ , as

$$r = \frac{\int_0^{Y_m} \frac{2}{9} Y dY}{\int_0^{Y_m} \left[ \frac{2}{9} Y + 2H^2 Y^3 \right] dY} = \frac{1}{1 + \frac{9}{2} H^2 Y_m^2}$$

or, by use of Equations 43J and 52J

$$r = \frac{2}{9u_m} \quad (91J)$$

Since  $u_m$  is known as a function of  $u_o'$ , Figure 164, this ratio of energy may also be presented as a function of  $u_o'$  as shown in Figure 165. Where the ratio of energy stored by the linear spring is a small fraction of the total energy stored in the springs, the solution would be expected to be very good. From Figure 165 it can be seen that for  $r > 1/5$  and for corresponding initial conditions  $u_o' \leq 2$ , a more quantitative analysis of the solution would be desirable.

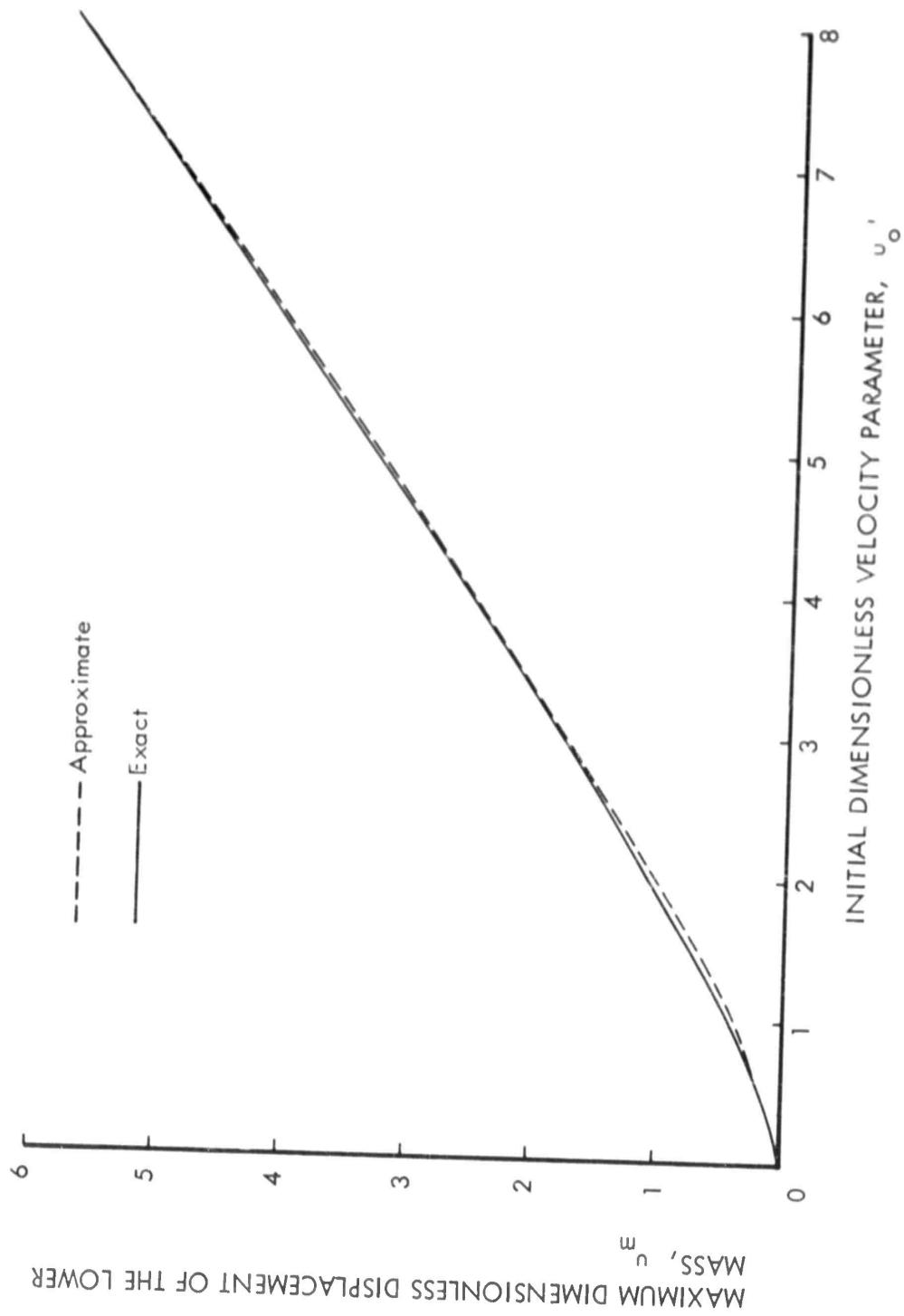


FIGURE 164 : Comparison of the True Maximum Dimensionless Lower Mass Displacement,  $u_m$ , and the Approximation of  $u_m$  for the Full Range of the Initial Velocity Parameter,  $u_o'$ .

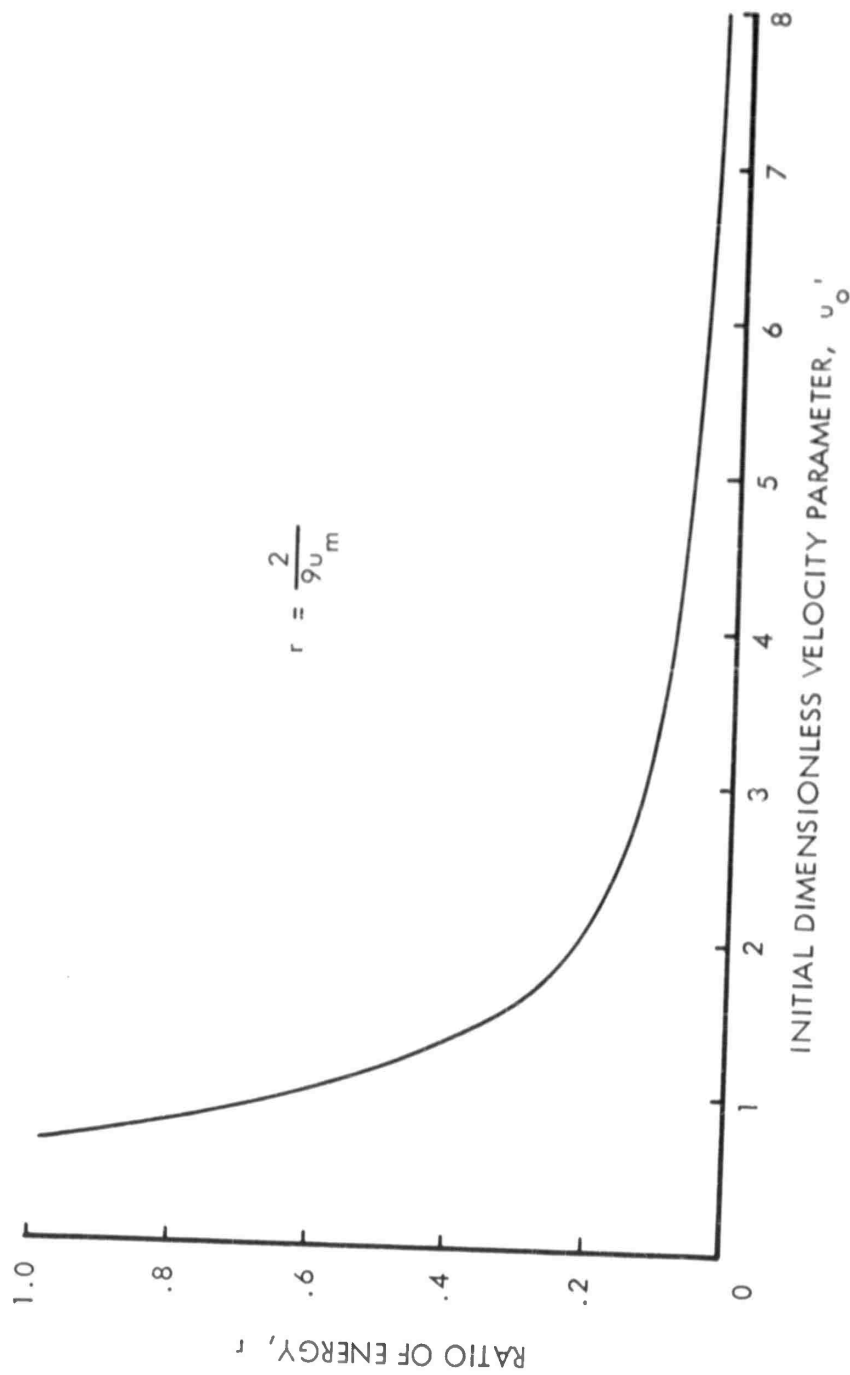


FIGURE 165 : Plot of the Ratio of Energy Which the Linear Spring is Capable of Absorbing to the Total Energy Which Both the Linear and Cubic Springs Can Absorb, as a Function of the Initial Velocity Parameter,  $u_0'$ .

## 7. Evaluation of the Analytical Solution

### a. Comparison with Solutions by the Runge-Kutta Method

Solutions for Equations 37J and 38J have been obtained by numerical integration methods in Reference 19. The two equations were solved simultaneously and the Runge-Kutta procedure applied as given in Reference 38. These results were thoroughly checked for a few specific values of the initial conditions and may be considered as nearly exact solutions for the motion of the system. Therefore, comparisons made between the results presented in Reference 19 and the solutions obtained in this paper should be a good indication of the accuracy of the analytical solutions.

The system analyzed in the reference did not have an eccentrically located axle, so that  $d = 0$  and no normal bearing forces were developed. Thus for these solutions there were no friction forces. Other constants for the physical system are presented in Table 9. Values for the Jacobian elliptic functions were obtained from Reference 15.

TABLE 9

(Constants of the Physical System Used in Appendix J)

$A_a$ , sq ft . . . . .	0.05761
$A_h$ , sq ft . . . . .	0.04708
$A_o$ , sq ft . . . . .	0.0005585
$v_o$ , cu ft . . . . .	0.03545
$P_{a_o}$ , lb/sq ft . . . . .	6,264
$R_1$ , ft . . . . .	0.5521
$W_o$ , lb . . . . .	2,411
$W_u$ , lb . . . . .	131

The dimensionless displacement and acceleration of the upper mass, and the dimensionless displacement of the lower mass are presented as functions of dimensionless time,  $\theta_1$ , in Figures 166 and 167. The solutions are discontinued when  $(u_1' - u') = u^{1/2} = 0$ , since this corresponds to the time after which  $\dot{s}$  becomes negative, and the equations of motion are no longer applicable. A wide range of  $u_o'$  necessary for design purposes is considered, and in most cases the agreement between the analytical solution and results obtained by means of the Runge-Kutta procedure is good. Note that the acceleration of the lower mass is not presented since this quantity is of little

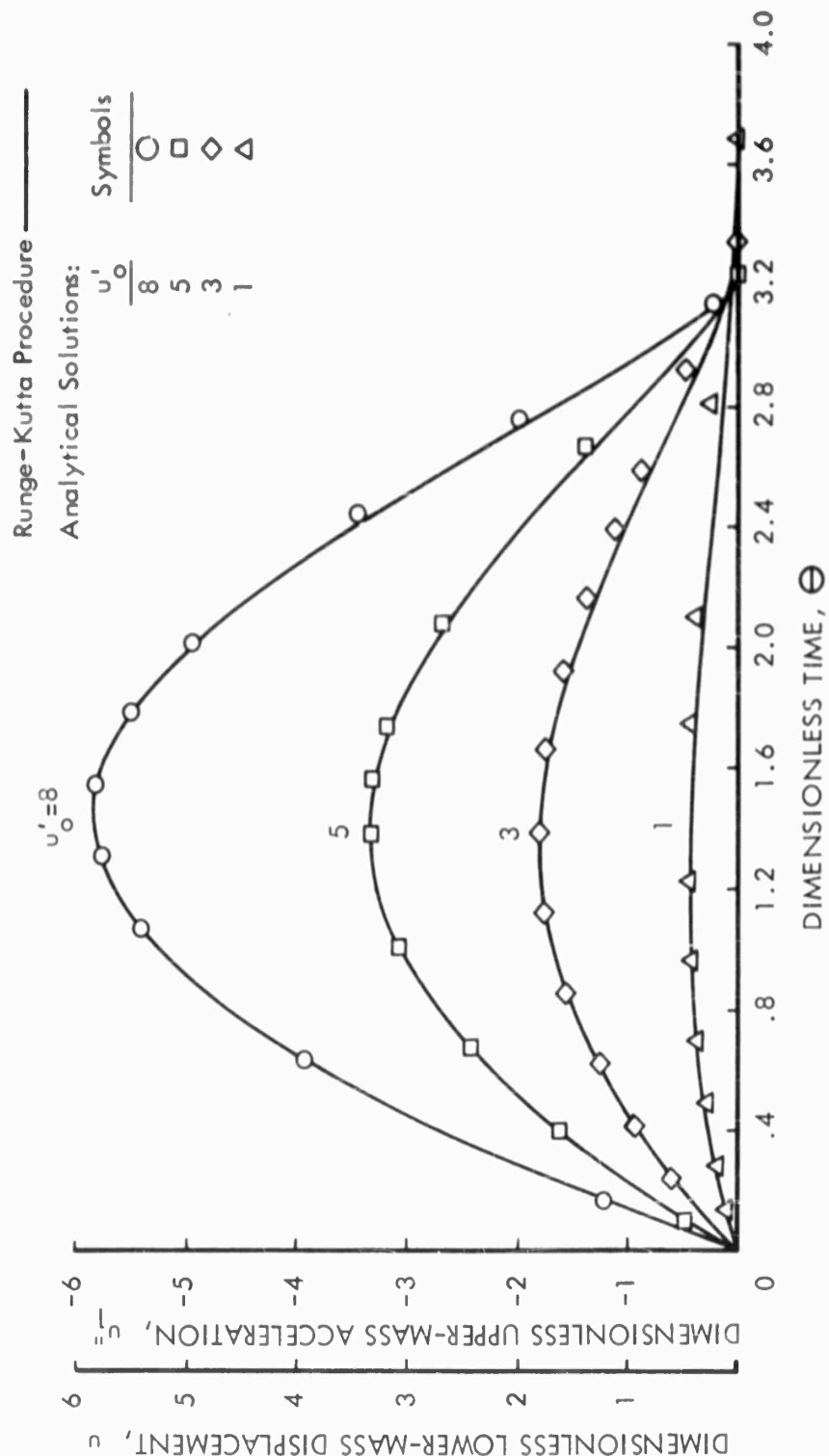


FIGURE 166 : Comparison of Solutions for Lower-Mass Displacement and Upper-Mass Acceleration Obtained by the Runge-Kutta Procedure and from the Analytical Equation.

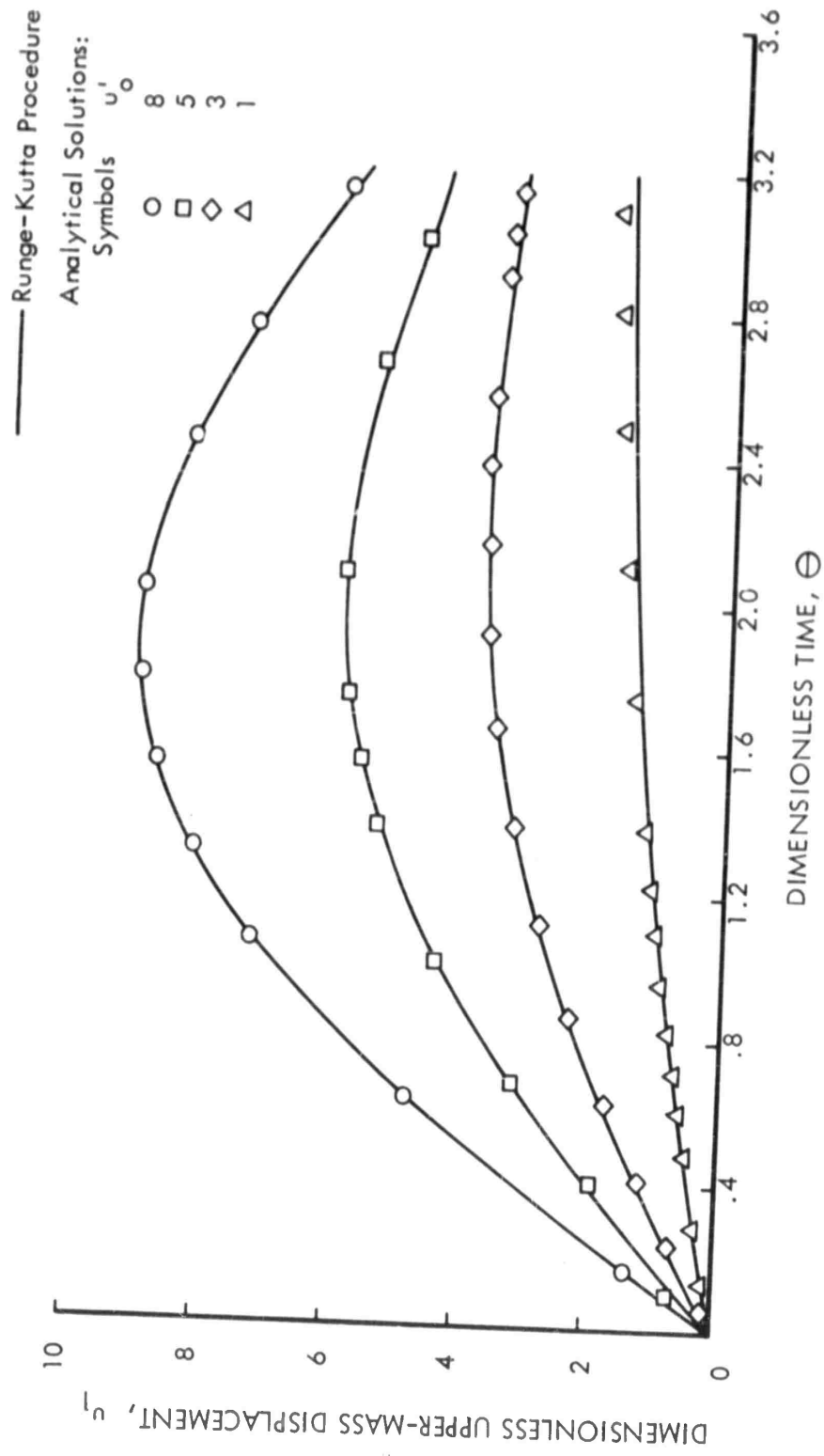


FIGURE 167 : Comparison of Solutions for Upper-Mass Displacement Obtained by the Runge-Kutta Procedure and from the Analytical Equation.

importance to the designer, and the corresponding inertia force was neglected in order to obtain Equations 37J and 38J.

Some differences are apparent at the very lowest initial conditions considered. As was indicated before, for  $u_0' = 1$  the ratio  $r$  (Figure 165) is rather large, indicating that the linear term in the equivalent spring force is accounting for the major portion of the work done by the springs. Therefore the method of equivalent nonlinearization applied to the transformed equations in this paper is approaching the case of equivalent linearization for the very lowest initial conditions. Linearization is expected to be impractical in the solution of the landing impact problem, so the results may be less good in this range. However, it is of interest that the original Equations 31J and 32J remain nonlinear through the transformations, even though Equation 53J becomes linear.

b. Comparison with Experimental Data

Reference 19 describes experimental drop tests conducted with a conventional oleopneumatic landing gear which closely represents the system in Figure 4 with  $M_2 = 0$ . Data obtained from these tests, in which a value of wing lift equal to the weight of the test model was simulated, are used for comparisons with the theoretical solutions presented in this paper.

Application of the transformation Equations 35J and 36J enables the calculation of the displacements, forces, and accelerations in dimensional terms. The acceleration of the upper mass is presented in Figure 168 along with the corresponding experimental data for the impact initial condition of  $\dot{z}_0 = 8.86$  feet per second. This value, according to data from Table 9, is equivalent to the dimensionless parameter  $u_0' = 2.39$ . The ground vertical reaction force  $F_1$  is presented in Figure 169 for comparison with the experimentally obtained forces. In general the results are in good agreement. The small differences that appear are attributable to the neglect of the air pressure force, the omission of the lower mass, to differences between the actual and the assumed tire characteristics, and to experimental errors.

In view of the observed good agreement between theory and experiment it seems that the solution presented will enable a designer to determine with reasonable accuracy the loads a landing gear may experience and thus aid him in preliminary design calculations.

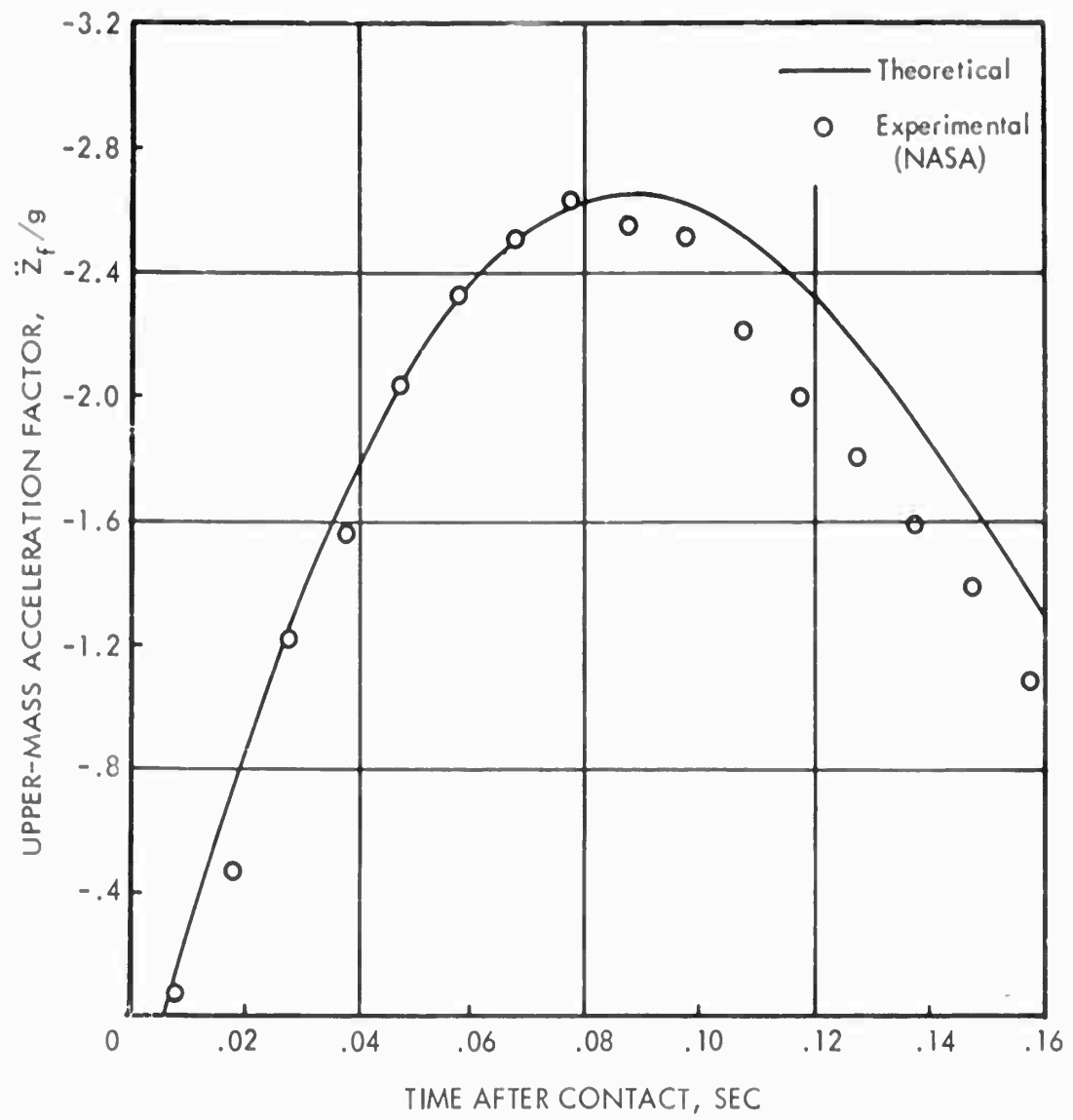


FIGURE 168: Comparison Between Theoretical Results and Experimental Data on the Upper-Mass Acceleration for a Typical Impact.

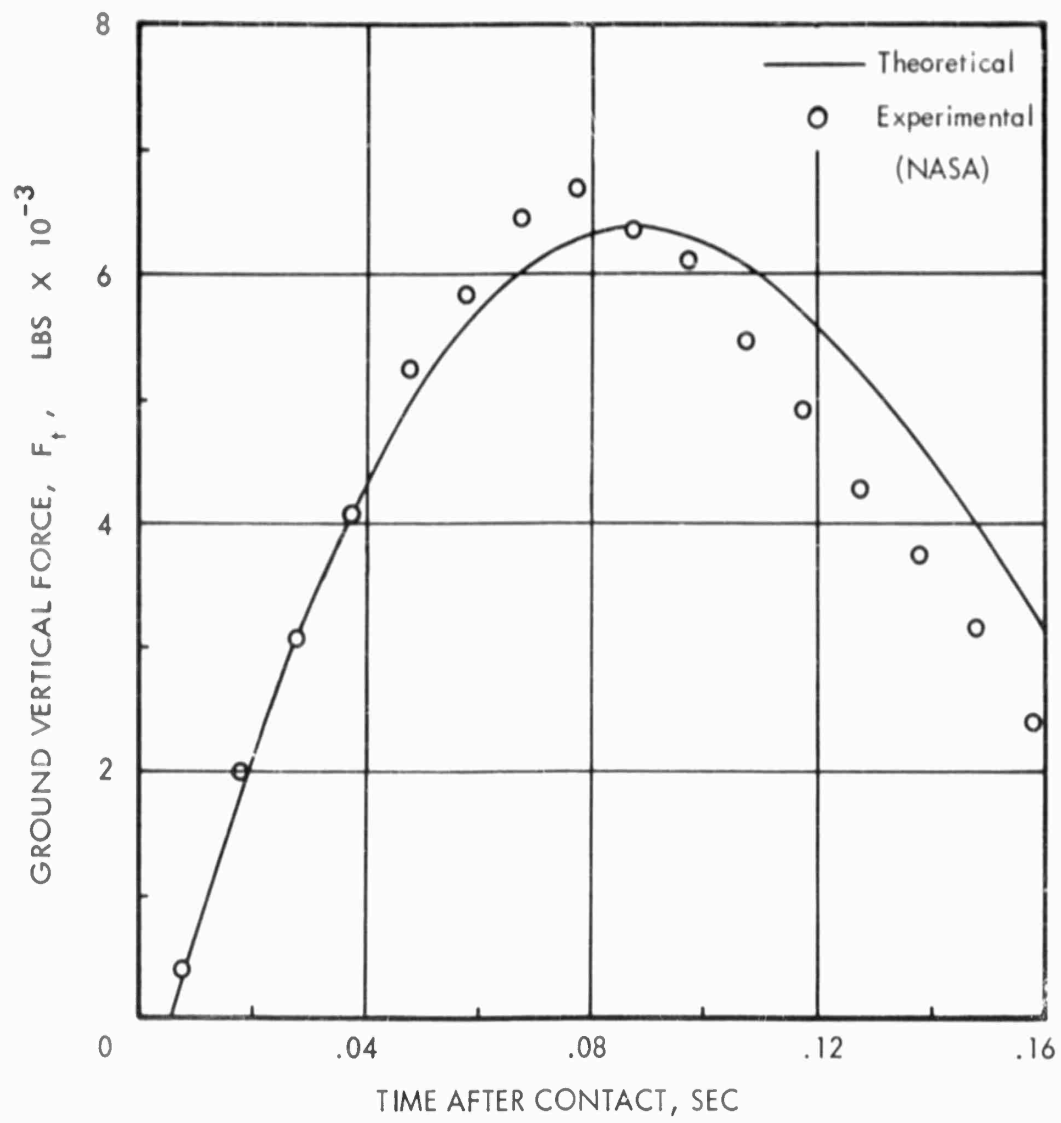


FIGURE 169: Comparison Between Theoretical Results and Experimental Data on the Ground Vertical Force for a Typical Impact.

## 8. Appendix Conclusions

An analytical solution has been presented for the equations of motion of a two-degree-of-freedom nonlinear system representing an airplane and landing gear configuration subjected to an impact load. The following conclusions can be made from the evaluation:

1. The friction forces developed on the strut bearing surfaces because of bending forces applied at the axle may be included in the equations of motion without adding to the complexity of the final differential equation. It is necessary to replace the variable distance between bearing surfaces by an approximate mean distance.

2. The equations of motion for the system may be transformed to an equation which closely resembles one having an exact elliptic solution. For a given airplane, a certain value of wing lift during landing will result in the two equations of motion being identical, and the exact solutions will describe the impact.

3. Since in general the wing lift force is approximately equal to the weight of the airplane, a method of "equivalent nonlinearization" must be employed to obtain the equation of motion in a form amenable to solution. The equivalent equation is derived on the basis of equal energy considerations and the major nonlinear character is retained, thereby presenting an improvement over the usual linearization methods which have been unsuccessful in this problem.

4. Comparison with more exact solutions obtained by numerical integration methods reveals that the analytical solutions obtained herein are very accurate within a wide range of initial conditions.

5. Comparison with experimental results indicates that notwithstanding the numerous simplifications made, the solutions obtained describe the motion of the system adequately for design purposes.

APPENDIX K  
COMPARISON OF ANALOG, DIGITAL  
FLIGHT TEST RESULTS

## 1. Comparison of Analog Theory and Flight Test Data

Taxi test data from a dynamic response test program for the example airplane as delineated in Reference 22, is still in preliminary stages of analysis. Runway roughness data for a Wright-Patterson AFB runway was measured by ASD for the test program. Comparisons of theory and preliminary test data from that runway are of interest to indicate whether the general levels of load are in agreement.

The analog analysis results and flight test data for strut force on the example airplane are compared in Figure 170, and relatively good agreement is indicated. From a fatigue loads point of view, the differences in local variations in the load spectra may be unimportant in general, as long as the average power at the low frequency end is the same. The next figure substantiates this point. Figure 171 compares the gear load occurrences from the previously discussed test data and the analog linear and nonlinear analyses. All three curves assume a symmetrical Gaussian distribution of amplitudes as derived from Equation 5D in Appendix D. The linear analysis agrees with the test data in shape of the distribution, but the nonlinear analysis agrees better in average occurrence level over a range of load that should include about 96 percent of the data. A more complete collection of the test data being processed is needed before any more definite statistical conclusions can be made.

Figures 172 and 173 are of general interest for comparison of center of gravity accelerations. The response of the test airplane over the LaGuardia runway, as determined from the analog, is compared with experimental data and other analog analysis data from Reference 11.

Average peak acceleration,  $\ddot{Z}$ , is defined as in Reference 11,

$$\ddot{Z} = \sqrt{2} \sigma_{\ddot{Z}}$$

where  $\sigma_{\ddot{Z}}$  is the c.g. acceleration r.m.s. level. The response over the LaGuardia runway, which doesn't have a particularly smooth profile, shows up about as would be expected in the figures.

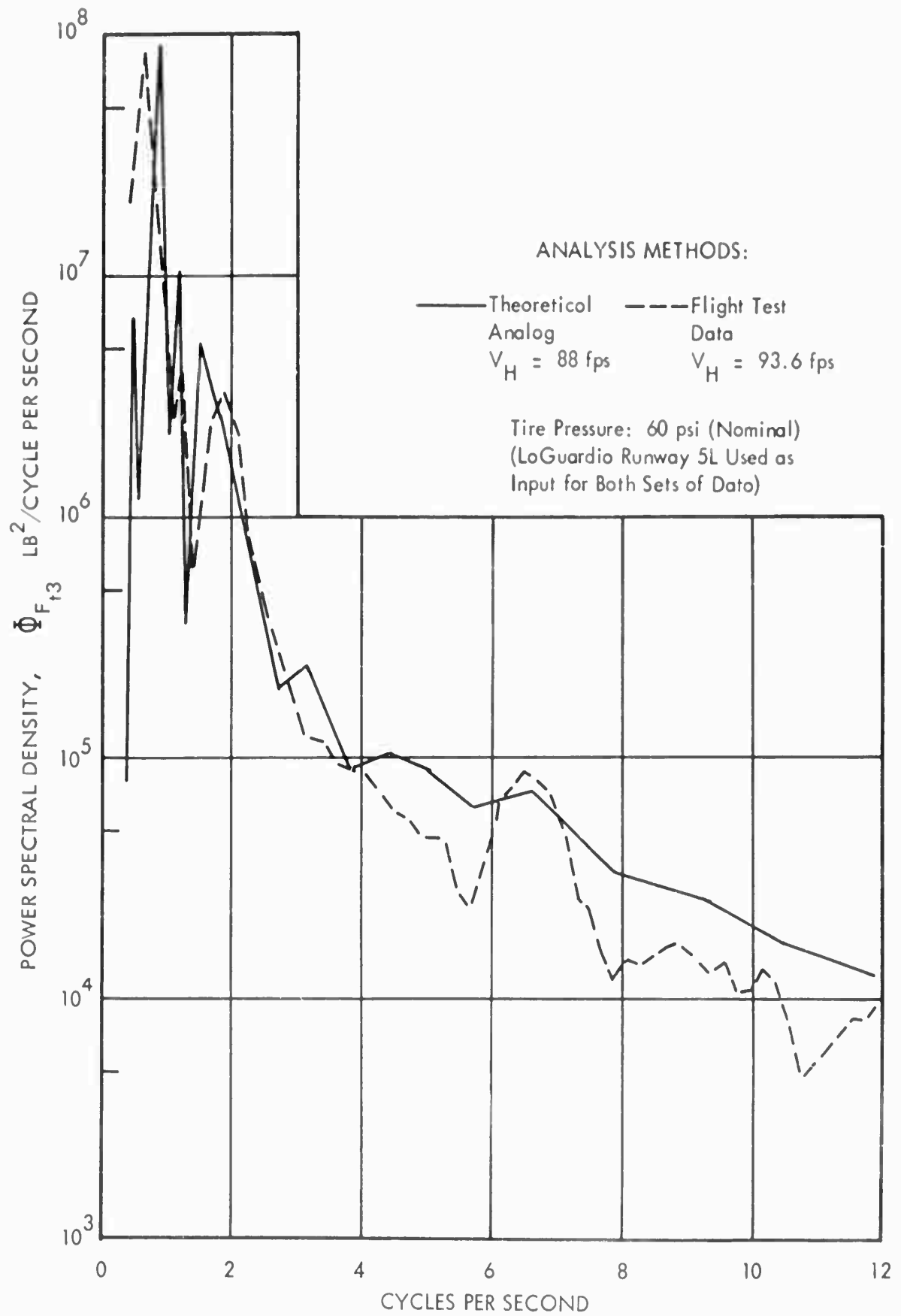


FIGURE 170 : Comparison of Power Spectra from Flight Test Data With Results from Analog for Rear Main Gear Tire Force

Source of Data: (LaGuardia Runway 5L Used As Common Input)

Flight Test Data ---  
 $C_D = 14.1 \text{ Lb-Sec}^2/\text{In}$   
 $V_H = 93.6 \text{ fps}$   
 $\sigma = 5250 \text{ Lb}$

Theoretical PSD ———  
 Nonlinear  
 $C_D = 14.1 \text{ Lb-Sec}^2/\text{In}^2$   
 $V_H = 88 \text{ fps}$   
 $\sigma = 3580 \text{ Lb}$

Theoretical ---  
 Linear Harmonic  
 $D = 185 \text{ Lb-Sec/In}$   
 $V_H = 88 \text{ fps}$   
 $\sigma = 4440 \text{ Lb}$

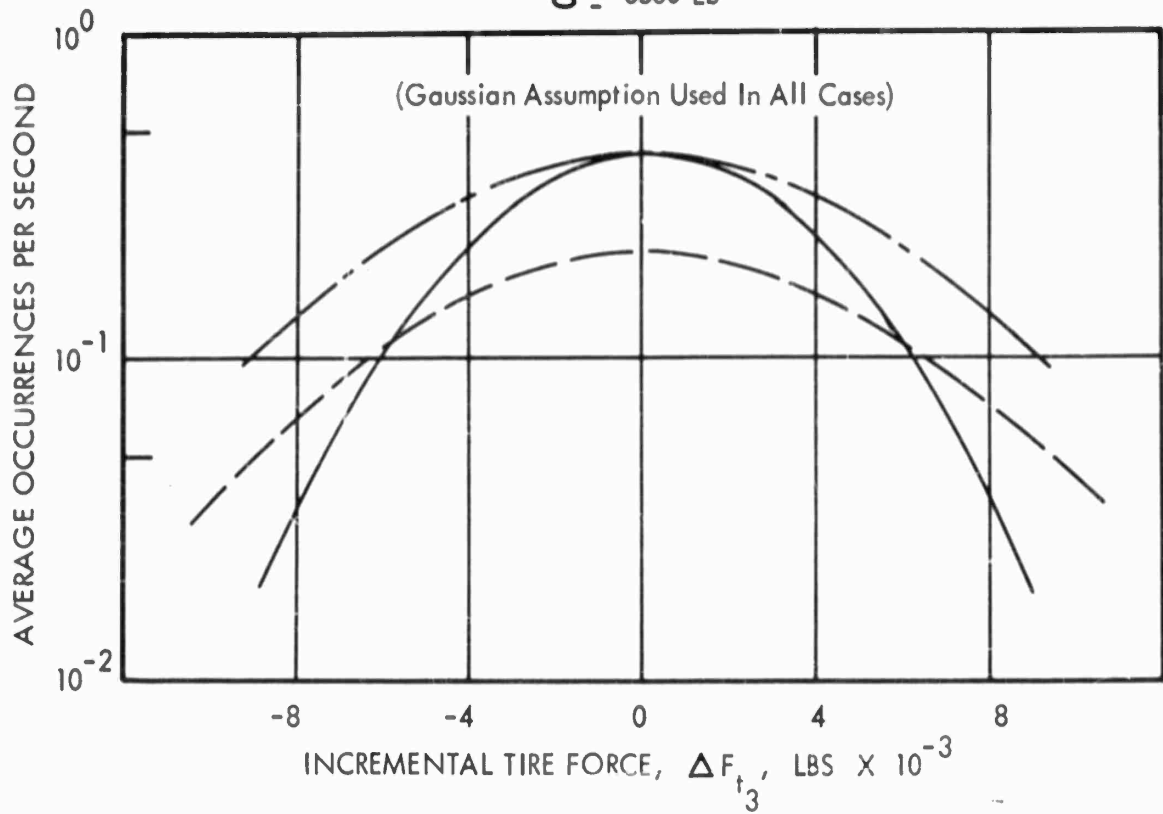


FIGURE 171 : Comparison of Load Occurrences from Analytical and Flight Test Data for Incremental Tire Force, Rear Main Gear,  $\Delta F_{t_3}$

(Nominal Tire Pressure: 60 psi)

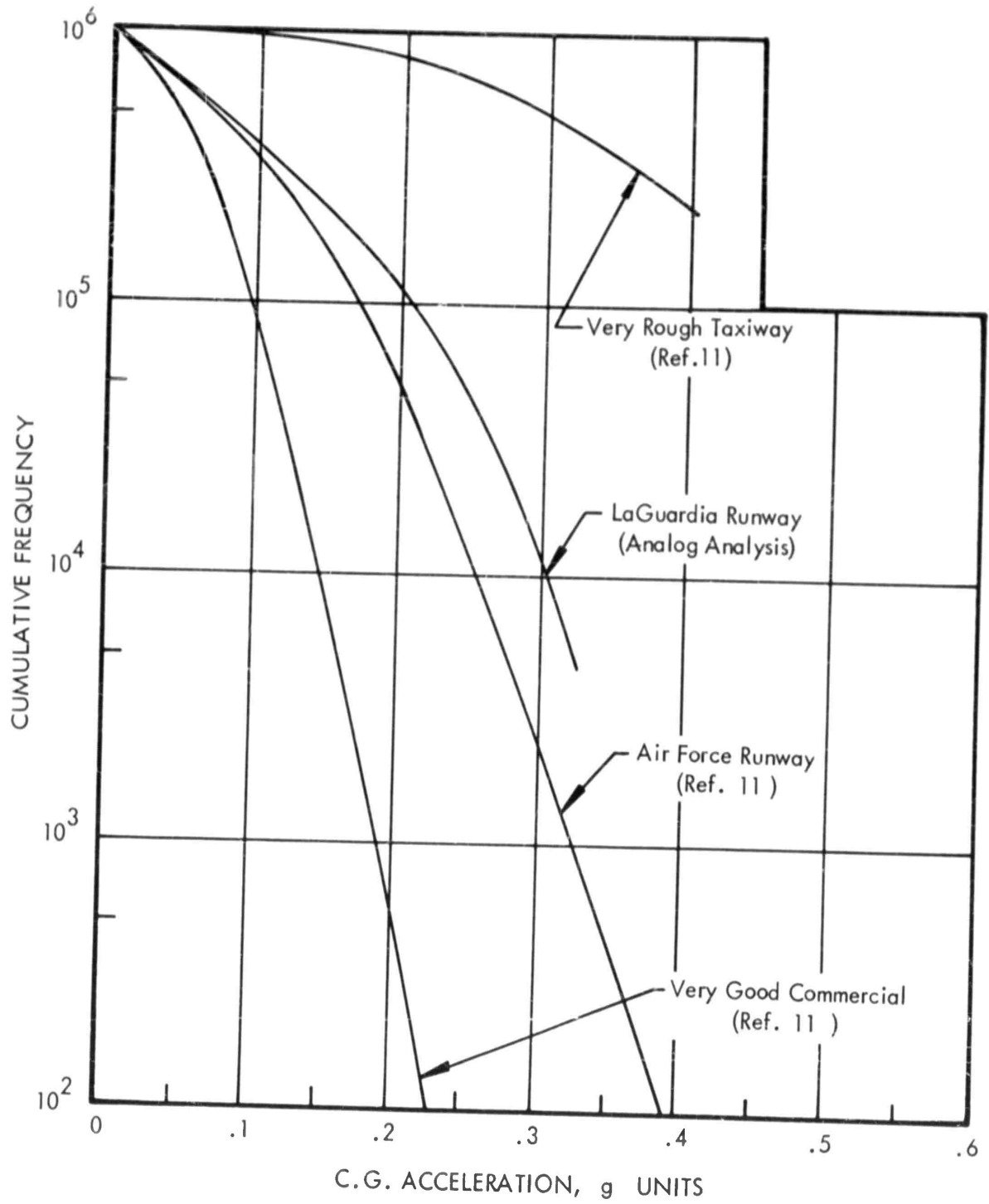


FIGURE 172 : Taxi Loads Per 1000 Flights

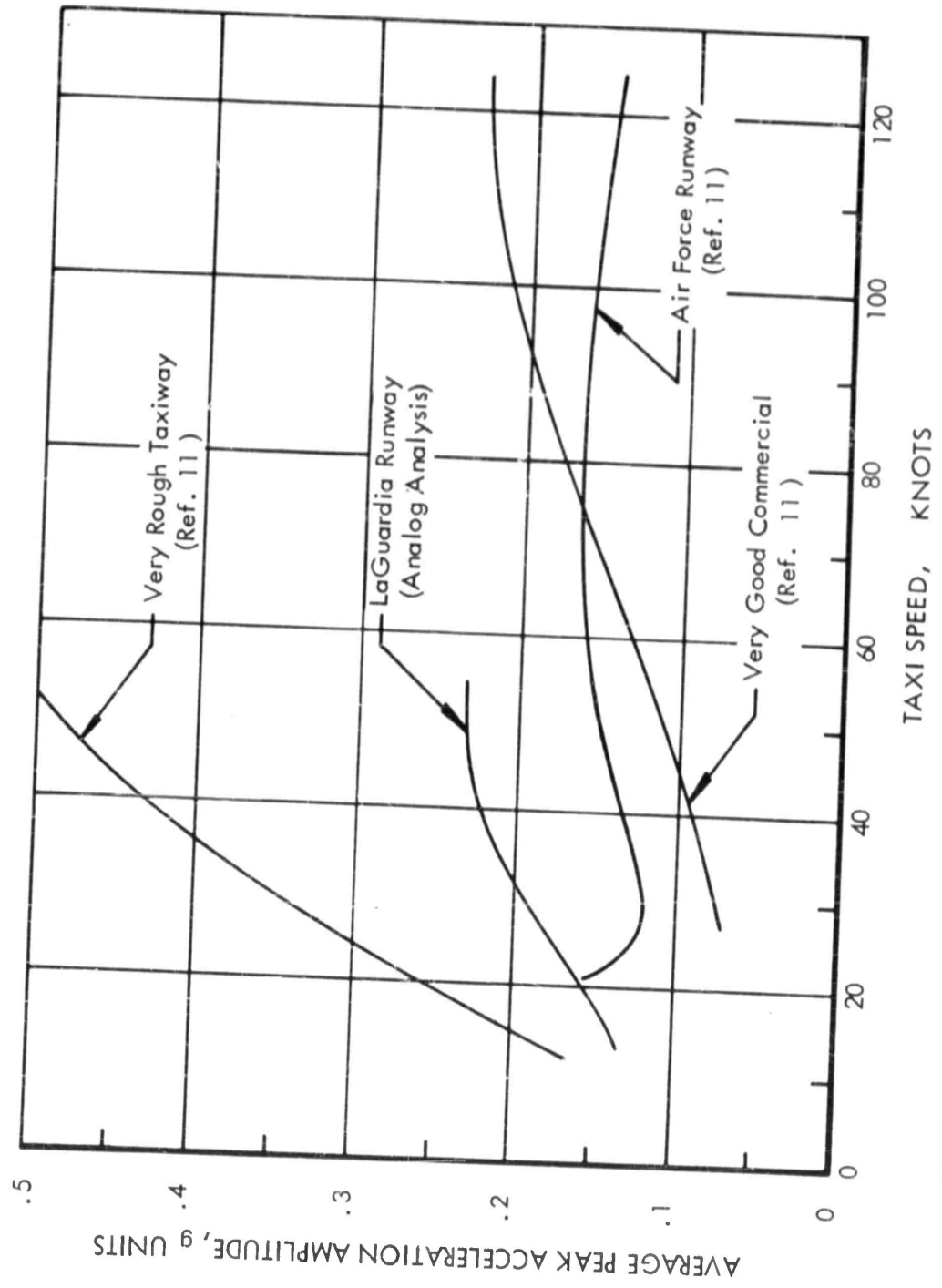


FIGURE 173 : Effect of Taxi Speed on Acceleration

## 2. Comparison of Analog and Digital Power Spectral Analysis

One of the analog time histories of strut force was tabulated and converted to digital form on tape for IBM 704 processing. The digital program is essentially composed of the equations for power spectral density analysis as given in Reference 23.

The comparison of analog and digital power spectra is shown for the strut force in Figure 174. Considering the differences in basic techniques involved, the results are in remarkably good agreement.

The power spectra of the runway amplitudes in the time-plane are a function of the taxi speed as shown by Equation 77 in the text. Therefore, the runway amplitude spectra can be converted to the space frequency-plane as shown in Figure 175. The results are synthesized by taking mean densities from 4 power spectra calculated at speeds of 22, 44, 66, and 88 fps.

A comparison is made with the spectrum for the LaGuardia runway number 5L as computed by digital methods in Reference 25. The agreement is very good at the low frequency end of the spectrum. Some attenuation is apparent at the high frequency end of the analog results. This may be attributed to the differences in spectral analysis, or to some loss in high frequency content of the runway as recorded on tape for the analog analysis. Some differences may occur as a result of the prewhitening procedures used by NASA in Reference 25, since the analog used electronic pre-filtering techniques. Also, the analog analysis is made on the runway derivatives,  $\dot{q}$ , rather than the amplitudes,  $q$ , using relationships similar to those applied in Reference 12. It is assumed that:

$$\Phi_{\dot{q}}(\omega) = (\omega^2) \Phi_q(\omega)$$

The mathematics of the problem should be examined more thoroughly for random functions.

Regardless of the above small differences, the root mean square,  $\sigma$ , of the runway amplitudes are negligibly different in either case as indicated on Figure 175. This results because the formula for  $\sigma$ , (Equation 4D in Appendix D), is predominantly dependent on the lowest frequency amplitudes where the two spectra agree in magnitude.

The statistical reliability of the power spectral density calculations is dependent upon the method of analysis and upon specific parameters involved in the calculation. A more detailed technical discussion of reliability estimates is given in Reference 23, but a few useful values will be summarized herein.

Given a stationary random data sample  $\theta_T$  seconds in duration, the total number of readings,  $n_o$ , can be calculated from

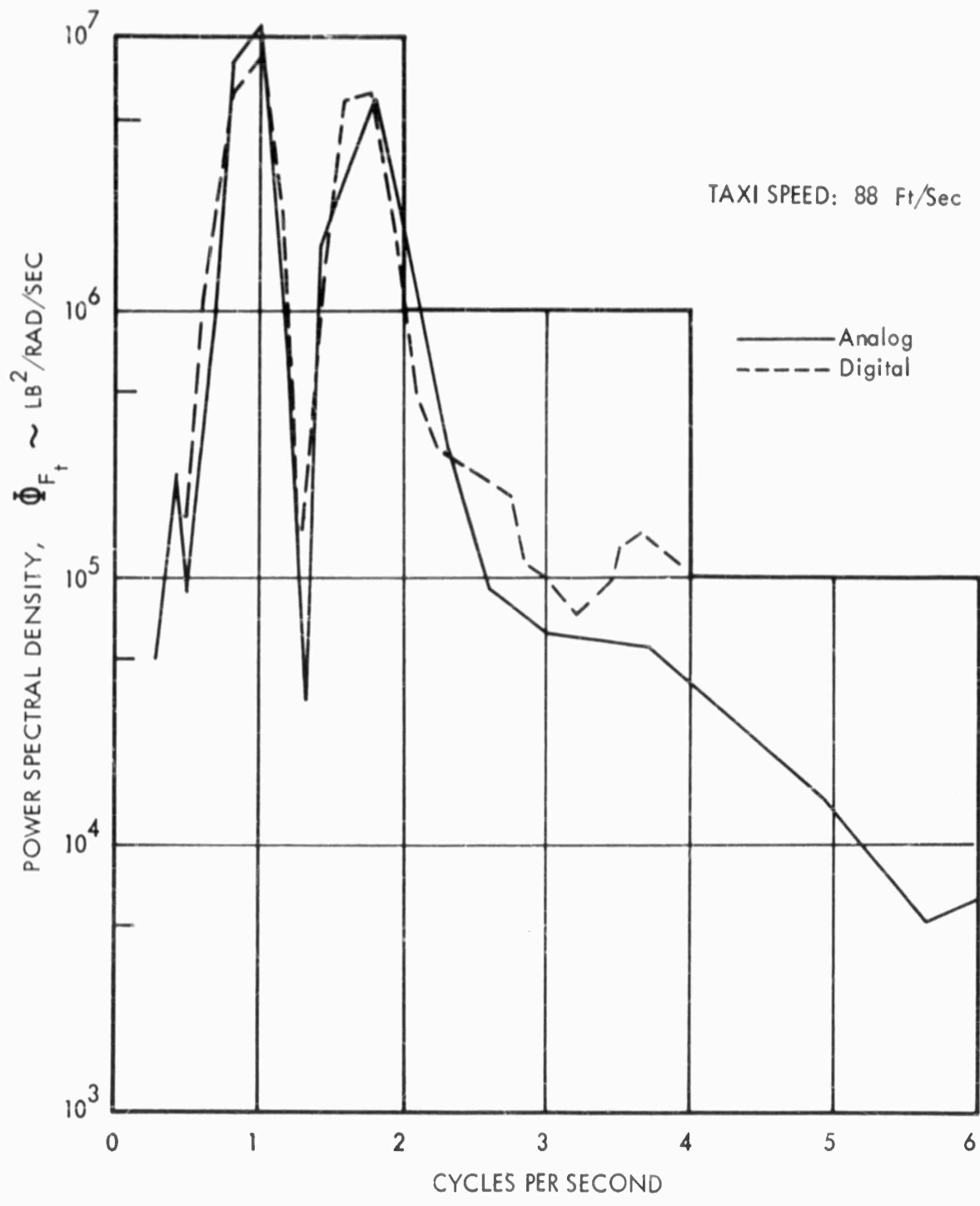


FIGURE 174 : Comparison of Output Power Spectra from Analog and Digital Methods Applied to a Common Time History of Tire Force (Single Gear)

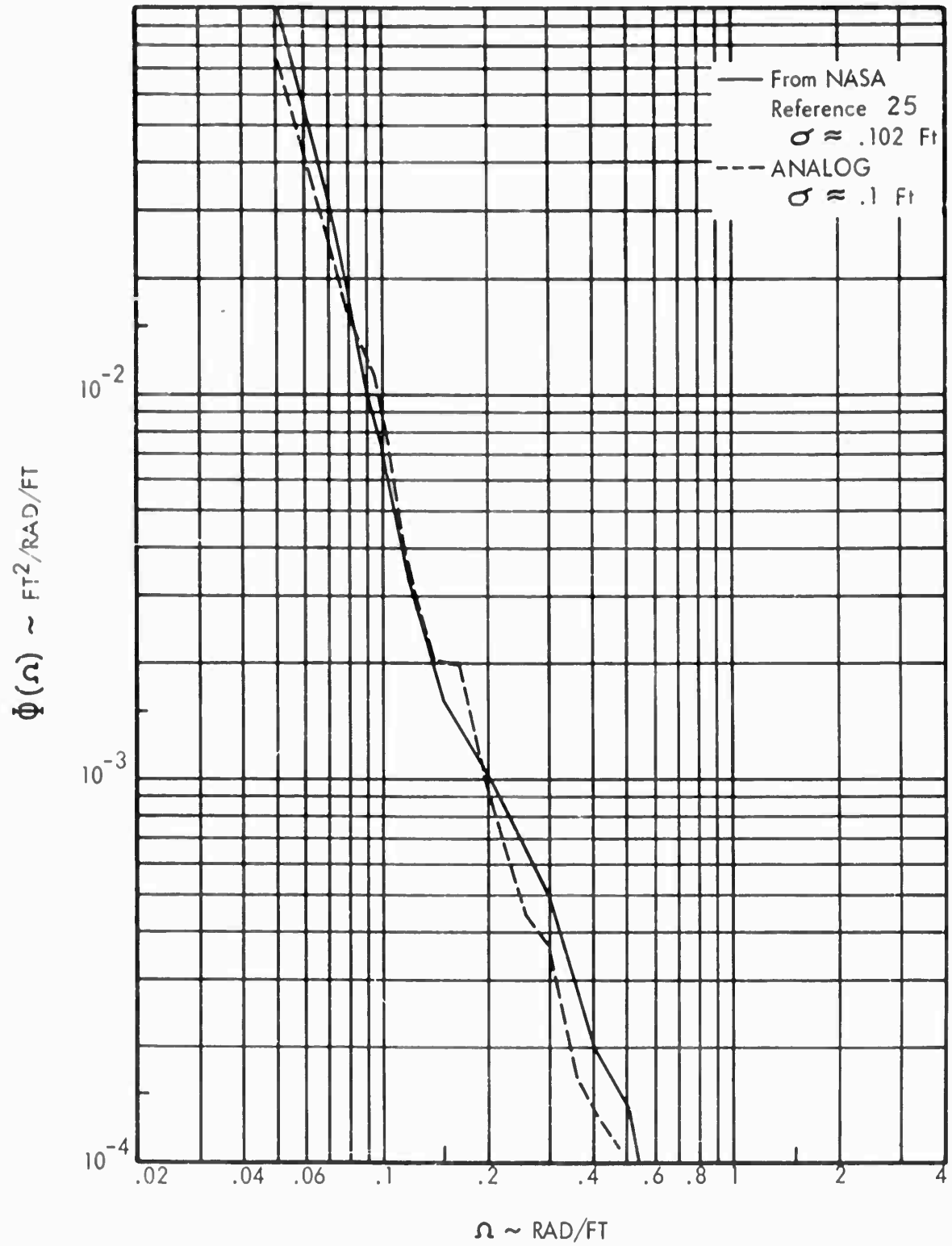


FIGURE 175 : Comparison of Runway Power Spectra from Analog Computer with NASA Spectral Calculations for Laguardia Runway

$$n_o = \theta_T / \Delta t$$

where  $\Delta t$  is the sampling interval in seconds. If  $m_o$  is defined as the number of uniformly spaced points over the frequency range at which the power estimates are desired, then the number of statistical degrees of freedom,  $k_o$ , may be computed as

$$k_o = \frac{n_o - m_o/5}{m_o/2}$$

The confidence limits corresponding to the power spectral amplitude of interest can then be determined by applying  $k_o$  in Figure 176. The envelope shown in the figure corresponds to the limits within which 90 percent of the power estimates will lie.

The probability density of values is chi-square distributed (as defined in Reference 10) around the mean power density for small values of  $k_o$ . However, as  $k_o$  increases, the estimates become symmetrical and approach a Gaussian distribution. Usual engineering practice is to maintain  $k_o$  on the order of 100 or greater if possible, although allowable sampling rates sometimes prevent this.

The digital computer examples shown herein may be summarized as follows:

Figure 174,

$$\Delta t = 1/8 \text{ sec}, \quad n_o \approx 500, \quad m_o = 25, \quad k_o \approx 40$$

Figure 170

$$\Delta t = 1/40 \text{ sec}, \quad n_o \approx 9600, \quad m_o = 99, \quad k_o \approx 97$$

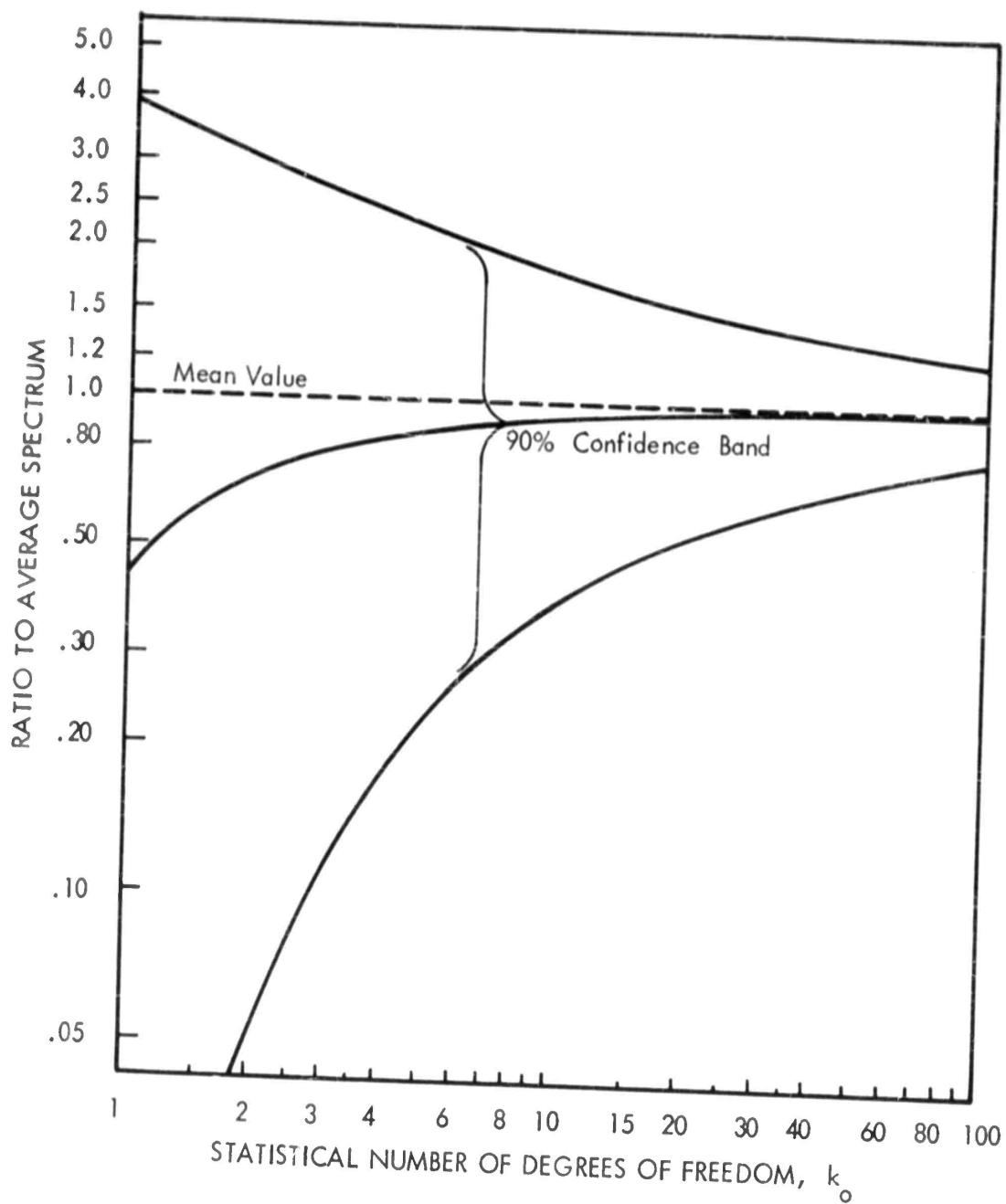


FIGURE 176 : Estimates of Reliability for Power Spectral Amplitudes

Aeronautical Systems Division, Wright-Patterson Air Force Base, Ohio.  
 Rep. No. ASD-IR-61-177. METHODS FOR ANALYZING FLIGHT VEHICLES DURING THE TAXI CONDITION. Final Report, January 1962, 334 p. incl illus., tables.  
 Unclassified Report.  
 Methods are developed for the prediction of ground taxing loads for advanced flight vehicles. The theory presented is generally applicable to determining the taxing response of vehicles operated on prepared or unprepared terrain with random distributed surface undulations. The vehicle, with many degrees of flexibility and nonlinearities of the shock strut, is represented in a generalized Lagrangian coordinate system. Nonlinear solutions are obtained in closed

( over )

analytical form, and on analog and digital computers, to various degrees of approximation for taxing over an existing runway profile. Equivalent linearized transfer functions are developed for comparison on the basis of power and cross spectral densities, load occurrences, and probabilities for a variety of speeds and nonlinear parameters. Test data are used to substantiate theoretical results where applicable.

UNCLASSIFIED  
 I. Project 1367, Task 13451, Contract AF 33(616) 7547  
 III. Lockheed-Georgia Company  
 IV. Theisen, J. G.  
 V. Secondary Report No. FR 517, AvalfrOTS  
 VII. In ASTIA collection

UNCLASSIFIED

UNCLASSIFIED

Aeronautical Systems Division, Wright-Patterson Air Force Base, Ohio.  
 Rep. No. ASD-IR-61-177. METHODS FOR ANALYZING FLIGHT VEHICLES DURING THE TAXI CONDITION. Final Report, January 1962, 334 p. incl illus., tables.  
 Unclassified Report.  
 Methods are developed for the prediction of ground taxing loads for advanced flight vehicles. The theory presented is generally applicable to determining the taxing response of vehicles operated on prepared or unprepared terrain with random distributed surface undulations. The vehicle, with many degrees of flexibility and nonlinearities of the shock strut, is represented in a generalized Lagrangian coordinate system. Nonlinear solutions are obtained in closed

( over )

analytical form, and on analog and digital computers, to various degrees of approximation for taxing over an existing runway profile. Equivalent linearized transfer functions are developed for comparison on the basis of power and cross spectral densities, load occurrences, and probabilities for a variety of speeds and nonlinear parameters. Test data are used to substantiate theoretical results where applicable.

UNCLASSIFIED  
 I. Project 1367, Task 13451, Contract AF 33(616) 7547  
 III. Lockheed-Georgia Company  
 IV. Theisen, J. G.  
 V. Secondary Report No. FR 517, AvalfrOTS  
 VII. In ASTIA collection

UNCLASSIFIED

UNCLASSIFIED

UNCLASSIFIED

<p>Aeronautical Systems Division, Wright-Patterson Air Force Base, Ohio.      Report No. ASD-IR-61-177, METHODS FOR ANALYZING LIGHT VEHICLES DURING THE TAXI CONDITION. Final Report, January 1962, 334 p. incl illus., tables.      Unclassified Report</p> <p>Methods are developed for the prediction of ground taxing loads for advanced flight vehicles. The theory presented is generally applicable to determining the taxing response of vehicles operated on prepared or unprepared terrain with randomly distributed surface undulations. The vehicle, with many degrees of flexibility and nonlinearities of the shock strut, is represented in a generalized Lagrangian coordinate system. Nonlinear solutions are obtained in closed</p> <p style="text-align: right;">( over )</p>	<p>UNCLASSIFIED</p> <p>I. Project 1307, Task 13451      II. Contract AF 33(616)-7546      III. Lockheed-Georgia Company      IV. Theisen, J. G.      V. Secondary Report No. FR 517,      VI. Avaltr OIS      VII. In AS 11A collection</p>
<p>Aeronautical Systems Division, Wright-Patterson Air Force Base, Ohio.      Report No. ASD-IR-61-177, METHODS FOR ANALYZING LIGHT VEHICLES DURING THE TAXI CONDITION. Final Report, January 1962, 334 p. incl illus., tables.      Unclassified Report</p> <p>Methods are developed for the prediction of ground taxing loads for advanced flight vehicles. The theory presented is generally applicable to determining the taxing response of vehicles operated on prepared or unprepared terrain with randomly distributed surface undulations. The vehicle, with many degrees of flexibility and nonlinearities of the shock strut, is represented in a generalized Lagrangian coordinate system. Nonlinear solutions are obtained in closed</p> <p style="text-align: right;">( over )</p>	<p>UNCLASSIFIED</p> <p>I. Project 1307, Task 13451      II. Contract AF 33(616)-7546      III. Lockheed-Georgia Company      IV. Theisen, J. G.      V. Secondary Report No. FR 517,      VI. Avaltr OIS      VII. In AS 11A collection</p>
<p>analytical form, and on analog and digital computers, to various degrees of approximation for taxing over an existing runway profile. Equivalent linearized transfer functions are developed for comparison on the basis of power and cross-spectral densities, load occurrences, and probabilities for a variety of speeds and nonlinear parameters. Test data are used to substantiate theoretical results where applicable.</p>	<p>UNCLASSIFIED</p> <p>I. Project 1307, Task 13451      II. Contract AF 33(616)-7546      III. Lockheed-Georgia Company      IV. Theisen, J. G.      V. Secondary Report No. FR 517,      VI. Avaltr OIS      VII. In AS 11A collection</p>

Aeronautical Systems Division, Wright-Patterson Air Force Base, Ohio.  
Rpt No. ASD-TR-61-177. METHODS FOR ANALYZING FLIGHT VEHICLES DURING THE TAXI CONDITION. Final Report, January 1962, 334 p. incl illus., tables.

Unclassified Report

Methods are developed for the prediction of ground taxing loads for advanced flight vehicles. The theory presented is generally applicable to determining the taxing response of vehicles operated on prepared or unprepared terrain with randomly distributed surface undulations. The vehicle, with many degrees of flexibility and nonlinearities of the shock strut, is represented in a generalized Lagrangian coordinate system. Nonlinear solutions are obtained in closed

( over )

analytical form, and on analog and digital computers, to various degrees of approximation for taxing over an existing runway profile. Equivalent linearized transfer functions are developed for comparison on the basis of power and cross spectral densities, load occurrences, and probabilities for a variety of speeds and nonlinear parameters. Test data are used to substantiate theoretical results where applicable.

8 JUL 67 1M

UNCLASSIFIED

- I. Project 1367, Task 13451
- II. Contract AF 33(616)-7546

III. Lockheed-Georgia Company

IV. Theisen, J. G.

V. Secondary Report

No. ER 517

VI. Avail for OTS

VII. In ASTIA collection

UNCLASSIFIED

Aeronautical Systems Division, Wright-Patterson Air Force Base, Ohio.  
Rpt No. ASD-TR-61-177. METHODS FOR ANALYZING FLIGHT VEHICLES DURING THE TAXI CONDITION. Final Report, January 1962, 334 p. incl illus., tables.

Unclassified Report

Methods are developed for the prediction of ground taxing loads for advanced flight vehicles. The theory presented is generally applicable to determining the taxing response of vehicles operated on prepared or unprepared terrain with randomly distributed surface undulations. The vehicle, with many degrees of flexibility and nonlinearities of the shock strut, is represented in a generalized Lagrangian coordinate system. Nonlinear solutions are obtained in closed

( over )

analytical form, and on analog and digital computers, to various degrees of approximation for taxing over an existing runway profile. Equivalent linearized transfer functions are developed for comparison on the basis of power and cross spectral densities, load occurrences, and probabilities for a variety of speeds and nonlinear parameters. Test data are used to substantiate theoretical results where applicable.

8 JUL 67 1M

UNCLASSIFIED

- I. Project 1367, Task 13451
- II. Contract AF 33(616)-7546

III. Lockheed-Georgia Company

IV. Theisen, J. G.

V. Secondary Report

No. ER 517

VI. Avail for OTS

VII. In ASTIA collection

UNCLASSIFIED

UNCLASSIFIED

UNCLASSIFIED

<p>Aeronautical Systems Division, Wright-Patterson Air Force Base, Ohio. Rpt No. ASD-TR-61-177. METHODS FOR ANALYZING FLIGHT VEHICLES DURING THE TAXI CONDITION. Final Report, January 1962, 334 p. incl illus., tables. Unclassified Report</p> <p>Methods are developed for the prediction of ground taxing loads for advanced flight vehicles. The theory presented is generally applicable to determining the taxing response of vehicles operated on prepared or unprepared terrain with randomly distributed surface undulations. The vehicle, with many degrees of flexibility and nonlinearities of the shock strut, is represented in a generalized Lagrangian coordinate system. Nonlinear solutions are obtained in closed</p> <p style="text-align: right;">( o o o )</p>	<p>UNCLASSIFIED</p> <p>Project 1367, Task 13451 Contract AF33(616)-7546</p> <p>Lockheed-Georgia Company Theisen, J. G. Secondary Report No. ER 5179 Aval tr OTS In ASTIA collection</p>	<p>Aeronautical Systems Division, Wright-Patterson Air Force Base, Ohio. Rpt No. ASD-TR-61-177. METHODS FOR ANALYZING FLIGHT VEHICLES DURING THE TAXI CONDITION. Final Report, January 1962, 334 p. incl illus., tables. Unclassified Report</p> <p>Methods are developed for the prediction of ground taxing loads for advanced flight vehicles. The theory presented is generally applicable to determining the taxing response of vehicles operated on prepared or unprepared terrain with randomly distributed surface undulations. The vehicle, with many degrees of flexibility and nonlinearities of the shock strut, is represented in a generalized Lagrangian coordinate system. Nonlinear solutions are obtained in closed</p> <p style="text-align: right;">( o o o )</p>	<p>UNCLASSIFIED</p> <p>Project 1367, Task 13451 Contract AF33(616)-7546</p> <p>Lockheed-Georgia Company Theisen, J. G. Secondary Report No. ER 5179 Aval tr OTS In ASTIA collection</p>
<p>analytical form, and on analog and digital computers, to various degrees of approximation for taxing over an existing runway profile. Equivalent linearized transfer functions are developed for comparison on the basis of power and cross spectral densities, load frequencies, and probabilities for a variety of speeds and nonlinear parameters. Test data are used to substantiate theoretical results where applicable.</p>	<p>UNCLASSIFIED</p> <p>Project 1367, Task 13451 Contract AF33(616)-7546</p> <p>Lockheed-Georgia Company Theisen, J. G. Secondary Report No. ER 5179 Aval tr OTS In ASTIA collection</p>	<p>analytical form, and on analog and digital computers, to various degrees of approximation for taxing over an existing runway profile. Equivalent linearized transfer functions are developed for comparison on the basis of power and cross spectral densities, load frequencies, and probabilities for a variety of speeds and nonlinear parameters. Test data are used to substantiate theoretical results where applicable.</p>	<p>UNCLASSIFIED</p> <p>Project 1367, Task 13451 Contract AF33(616)-7546</p> <p>Lockheed-Georgia Company Theisen, J. G. Secondary Report No. ER 5179 Aval tr OTS In ASTIA collection</p>

UNCLASSIFIED

UNCLASSIFIED

UNCLASSIFIED